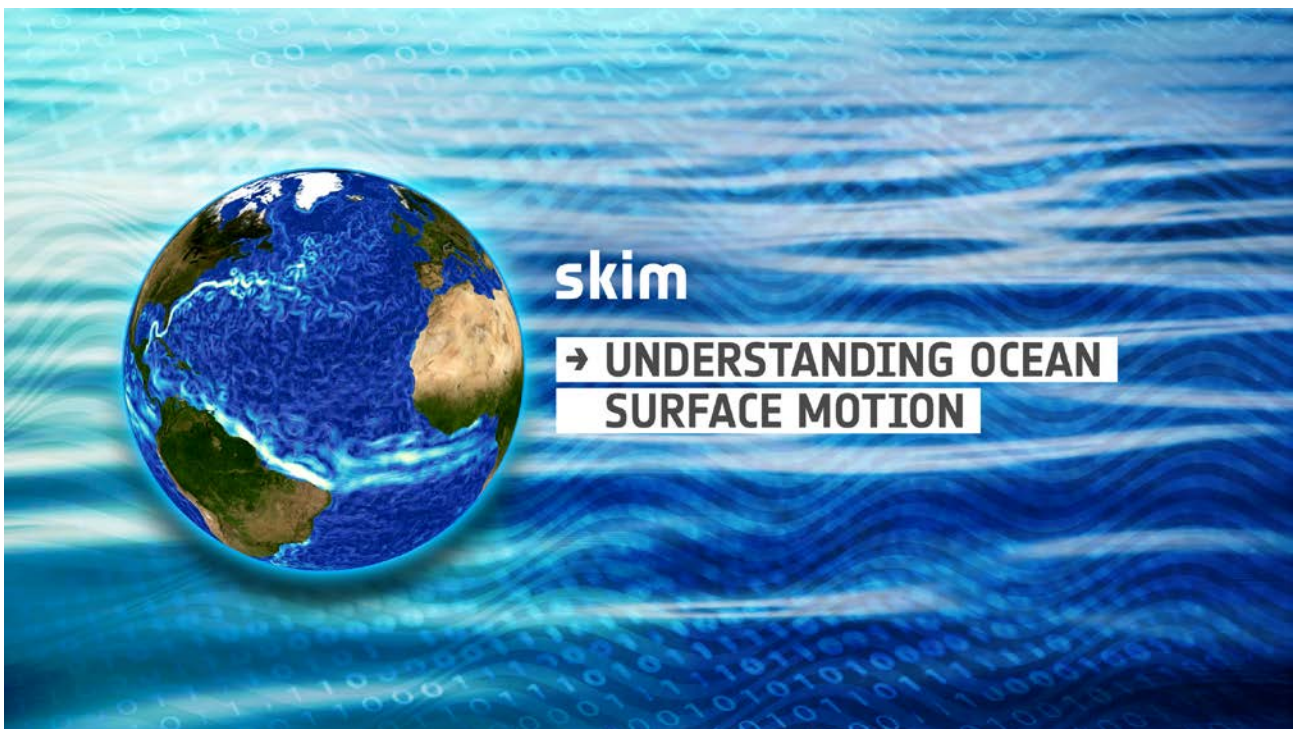


Earth Explorer 9 Candidate Mission SKIM – Report for Mission Selection



Reference
Issue/Revision
Date of Issue
Status

ESA-EOPSM-SKIM-RP-3550
1.0
21/06/2019
Issued



ACKNOWLEDGEMENTS

This report is based on contributions from the SKIM Mission Advisory Group (MAG):

Fabrice Ardhuin (LOPS Laboratory of Ocean Physics and remote Sensing, FR)
Alessandro Battaglia (University of Leicester, UK)
Peter Brandt (Geomar, DE)
Fabrice Collard (OceanDataLab, FR)
Geir Engen (NORCE Norwegian Research Center AS, NO)
Paco Lopez-Dekker (Delft University of Technology, NL)
Adrien Martin (National Oceanography Center, UK)
Jamie Shutler (University of Exeter, UK)
Detlef Stammer (University of Hamburg, DE)
Michel Tsamados (University College London, UK)
Erik van Sebille (Utrecht University, NL)
Ernesto Rodriguez (Observer, NASA JPL, USA)

The scientific content of the report was compiled by Craig Donlon (Scientific Coordinator) based on inputs derived from the MAG, supporting scientific studies and campaign activities, with contribution from Björn Rommen, Tania Casal and Gerhard Ressler. Additional contributions were made by Gérald Dibarboure, François Boy, Pierre Dubois, François Soulat, Clement Ubelmann, Bertrand Chapron, Lucile Gaultier, Frederic Nougier, Jean-Marc Delouis, Goulven Monnier, Stéphane Méric, Charles Peureux, Mickael Accensi, and Tom Holden via supporting science studies and campaign work.

The technical content of the report was compiled by Erik De Witte (Technical Coordinator) with contributions from Ana Piris Niño, Andrea Tromba, Björn Frommknecht, Björn Rommen, Elena Daganzo-Eusebio, Maarten van den Oever, Martin Suess (Payload Technical Coordinator) and Paolo Bensi, based on inputs derived from the industrial Phase A system and technical activities under the responsibility of the Future Missions and Instruments Division. Special thanks go to the industrial teams who have supported ESA to bring this report together in a very short time after the Preliminary Requirements Review.

Recommended citation:

ESA(2019). *Report for Mission Selection: SKIM*, European Space Agency, Noordwijk, The Netherlands, ESA-EOPSM-SKIM-RP-3550, 264pp.

Cover image design: Earth Observation Graphics Bureau (EOGB)
Copyright: © 2019 European Space Agency



TABLE OF CONTENTS:

ACKNOWLEDGEMENTS.....2

TABLE OF CONTENTS:3

EXECUTIVE SUMMARY 8

1 INTRODUCTION..... 12

2 BACKGROUND AND SCIENTIFIC JUSTIFICATION 15

2.1 The Importance of Ocean Currents: Scientific and Societal Issues of Concern..... 20

2.2 Relevance to the ESA Research Objectives for Earth Observation 24

2.3 User Needs for Ocean Surface Current Measurements.....25

2.3.1 User Needs for TSCV..... 26

2.3.2 User Needs for Ocean Waves27

2.3.3 User Needs for Nadir Altimetry 28

2.4 Why SKIM?..... 29

2.5 Unique Characteristics of TSCV..... 31

2.5.1 Stokes Drift and Waves33

2.6 Measuring TSCV Globally: Estimating Currents from Satellite Observations of Sea Level35

2.6.1 Effective Resolution of Sea-level Measurement35

2.6.2 Challenges when Estimating Ocean Currents from Sea Level Measurements 36

2.6.3 Quantifying the Observation Gap 36

2.7 Innovation and Advancement of European Earth Observation Capability: Inventing Doppler Oceanography from Space37

2.8 TSCV and Numerical Modelling 39

2.8.1 The Scientific Delta of SKIM..... 41

2.8.2 Complementarity 42

2.9 Timeliness..... 42

2.10 Summary of SKIM User Needs 43

3 RESEARCH OBJECTIVES 46

3.1 Aim and Objective 46

3.1.1 The Ocean–Atmosphere Interface in the Earth System..... 46

3.1.2 Transport of Material at the Ocean Surface Including Marine Plastic Debris. 49

3.2 Potential Additional Research Contributions of SKIM 50

3.3 SKIM Mission Objectives 51



3.3.1 Summary	51
4 OBSERVATIONAL REQUIREMENTS	52
4.1 Observational Approach.....	52
4.1.1 From Doppler Velocity to TSCV: the SKIM Measurement Principle.....	53
4.2 Level-2 Product Requirements to Address Mission Objectives	56
4.3 Level-1b Observation Requirements.....	58
4.3.1 Beam Pointing Requirements.....	58
4.3.2 Doppler Performance.....	61
4.3.3 Loose Formation Flight with MetOp-SG(1B)	61
4.3.4 Mission Phasing	63
4.3.5 Swath Width.....	64
4.3.6 Coverage and Revisit.....	64
4.3.7 Number of Beams and Beam Characteristics	65
4.3.8 Radar Performance	65
4.3.9 Precise Orbit Determination.....	70
4.3.10 Geolocation Requirements	71
4.3.11 Product Delivery Latency.....	71
4.3.12 Mission Lifetime	71
4.3.13 Scientific Diagnostics and Algorithm Evolution	72
4.4 Level-1 SKIM Products.....	72
5 MISSION ELEMENTS	73
5.1 Mission Architecture Overview.....	73
5.2 Mission Analysis and Orbit Selection	74
5.2.1 Flight Configuration with MetOp-SG(1B)	74
5.2.2 Mission Profile	79
5.3 Space Segment.....	80
5.3.1 Overview.....	80
5.3.2 Satellite Configuration	81
5.3.3 Payload	83
5.3.4 Platform.....	116
5.3.5 System budgets	129
5.4 Launcher.....	131
5.5 Ground Segment and Data Processing	133



5.5.1	Overview of Ground Segment	133
5.5.2	Flight Operation Segment.....	134
5.5.3	Payload Data Ground Segment.....	136
5.5.4	Level-1 Data Processing	138
5.6	Operations, Utilisation and Disposal.....	140
5.6.1	Overview.....	140
5.6.2	Launch and Early Operations Phase (LEOP) and Commissioning.....	140
5.6.3	Nominal Operations.....	141
5.6.4	International Telecommunications Union (ITU) Constraints.....	141
5.6.5	Contingency Operations.....	142
5.6.6	Disposal.....	143
6	SCIENTIFIC DATA PROCESSING AND VALIDATION CONCEPT	144
6.1	SKIM Geophysical Retrieval Framework.....	144
6.2	The SKIM Retrieval Algorithm	148
6.2.1	Retrieving the Geophysical Doppler U_{GD} (Level-2a L2A_UGD Product).....	149
6.2.2	Retrieving NRCS and Doppler Modulation Spectra (Level-2a L2A_WR product) .	153
6.2.3	Retrieval of 1D Wave Spectra (Level-2b L2B_WDS Product)	156
6.2.4	Retrieval of the Radial Surface velocity (Level-2b L2B_U Product)	156
6.2.5	Retrieval of TSCV: Level-2b L2B_U to Level-2c Processing.....	160
6.2.6	Multitemporal Processing to Level-2d	162
6.2.7	SKIM Nadir Beam Processing: Conventional Altimetry	163
6.3	Algorithm Development and Evolution after Launch	163
6.4	Validation Concept.....	164
6.4.1	Validation Using In Situ Measurements.....	165
6.4.2	Validation Using Coastal HF-Radar	166
6.4.3	Validation Using Dedicated Campaigns	167
6.4.4	Validation Using Other Satellite Data in Synergy	167
6.4.5	Use of Numerical Models.....	167
7	PERFORMANCE ESTIMATION	168
7.1	Performance Assessment Approach	168
7.1.1	Assessment Strategy.....	170
7.2	End-to-End Mission Performance Tools	171
7.2.1	SKIM End to End Performance Simulator (SEEPS)	173



7.2.2	Level-2 Global Coverage Parametric SKIM Simulator.....	175
7.2.3	Simulator Test Scenario Descriptions	178
7.3	Level-1b Performance.....	180
7.3.1	Nadir Altimetry Performance	180
7.3.2	Pulse-Pair Phase Performance.....	181
7.3.3	Level-1b Pointing Performance.....	187
7.3.4	Radiometric Performance.....	193
7.3.5	Geo-location Performance	194
7.3.6	Summary of Level-1b Requirements and Performance of the SKIM Mission.....	194
7.4	Level-2 Retrieval Performance	196
7.4.1	Fine Pointing Algorithm Performance	196
7.4.2	Nadir Altimetry Performance	201
7.4.3	Performance of Level-2 Wave Products	203
7.4.4	Performance of Level-2b U _{CD}	206
7.4.5	Performance of Level-2c U _{CD}	209
7.5	Level-2 Performance Assessment Based on Experimental Data	214
7.5.1	Campaign Implementation.....	214
7.5.2	Results.....	216
8	MISSION CONTEXT.....	220
8.1	Science and societal benefit	220
8.1.1	Contribution to International Programmes	220
8.1.2	Global Climate: Atmosphere-Ocean Fluxes and Transport of Heat and Carbon ...	221
8.1.3	Marine life: Drifting Ecosystems and Debris	223
8.2	Readiness of the Multiple User Communities	224
8.3	Applications.....	225
8.3.1	Marine Energy, from Oil and Gas to Renewables	225
8.3.2	Global Circulation for Disaster Management (e.g. Oil or Chemical Spill, Downed aircraft, Safety of Life at Sea).....	226
8.3.3	Marine Meteorology and Ship Routing.....	226
8.4	European Earth Observation innovation and Advancement	227
8.5	Conclusion.....	228
9	PROGRAMMATICS.....	229
9.1	Scientific Maturity, Critical Areas and Risks	229



9.1.1 Scientific Maturity: Key Questions for SRL..... 230

9.1.2 Critical Scientific Areas and Risks 232

9.1.3 Scientific Roadmap237

9.2 Technical Maturity, Critical Areas and Risks 238

9.2.1 Summary 238

9.2.2 Satellite and Platform 239

9.2.3 SKaR 240

9.3 Development Approach and Schedule..... 243

9.3.1 Overall Development Approach and Model Philosophy 243

9.3.2 Schedule 244

9.4 Conclusion245

REFERENCES246

ACRONYMS AND ABBREVIATIONS 260



EXECUTIVE SUMMARY

This report forms the basis for the selection of the ninth Earth Explorer mission within ESA's Earth Observation Programme. Two competing 'Fast Track' mission candidates, the Far-infrared Outgoing Radiation Understanding and Monitoring (FORUM) mission and the Sea surface Kinematics Multiscale monitoring (SKIM) mission, have undergone a rapid and compressed Phase A feasibility study. This report covers the SKIM mission.

The aim of SKIM is to measure directly and simultaneously the ocean Total Surface Current Velocity (TSCV - an Essential Climate Variable) and its component Stokes drift with the directional wave spectrum. SKIM will also provide a conventional nadir altimeter capability, enabling a unique and detailed exploration of the TSCV and Stokes drift relative to geostrophic currents – therefore going beyond geostrophy.

SKIM will be used to quantify the role of joint TSCV, Stokes drift and directional waves on fundamental coupling ocean–atmosphere processes within the Earth system and their societal impact at the global and regional scale. The SKIM mission will provide scientists with an unprecedented measurement data set to study in great detail the exchange of heat, gas, mass and momentum between the atmosphere and the ocean, filling knowledge gaps in upper-ocean biogeochemical processes, kinetic energy fluxes and vertical motion in the upper ocean. It will also improve mapping of marine pollutant drift (marine plastic debris, oil), and monitoring ocean wave regimes, extremes and shifts. SKIM, through data assimilation, will improve modelling capabilities to quantify the dynamics and spatial distribution of lateral eddy fluxes and vertical exchanges in the upper ocean that are fundamental to a better understanding of trans-oceanic species dispersal and marine biogeography evolution. SKIM benefits will be essential in the poorly measured equatorial and polar areas. This will lead to a major increase in our understanding of the complex equatorial dynamics and of the role of ocean surface currents and waves in the rapidly changing Arctic and Antarctic regions.

Remarkably, in most parts of the world ocean, very few, if any, *in situ* measurements of the TSCV or Stokes drift are made on a regular basis – yet on a regional scale, new ocean surface currents are still being discovered today when data are available. These currents will certainly have to be re-mapped as they shift as the climate crisis deepens. Despite their importance for science and society, direct measurements of the ocean TSCV and Stokes drift, acquired from space with regular coverage and dense sampling, have so far eluded the Earth observation community. As a consequence, the level of scientific scrutiny required to fully address the ESA Living Planet ocean challenges (ESA 2015a) and United Nations Sustainable Development Goals (SDGs, United Nations 2015) is not yet available.

SKIM will be the first satellite mission providing Doppler measurements to directly retrieve the TSCV and its components every few days. SKIM is a multi-scale mission, resolving, for the first time, the wave-induced Stokes drift that is required to estimate surface transport that is essential for ocean-atmosphere exchange, to manage oil and chemical spills, and to monitor the trajectory and fate of floating marine plastic debris. The unique combination of SKIM and MetOp-SG(1B) flying in loose formation will enable wind–wave–TSCV synergy to be fully developed for scientific and societal benefits. Improvements in scatterometer wind estimates are anticipated based on the application of SKIM data that, for the first time, will systematically account for the impact of wave–TSCV interaction on the retrievals. SKIM will



also be used to study the altimeter sea state bias correction which is one of the largest sources of uncertainty in the satellite sea level record, with direct application to Copernicus Sentinel-6 and Sentinel-3.

Shore-based High Frequency (HF) radars are used to measure the ocean-surface currents in coastal seas and are unique in their capability of measuring the TSCV, including the Stokes drift, and its time and space variability. At the very heart of the SKIM Doppler mission is the simple idea that a technique analogous to the highly successful coastal HF-radar can be used in low Earth orbit to measure directly ocean TSCV and Stokes drift. This will provide a quasi-synoptic, regular and dense sampling over the global ocean. SKIM will extend coastal HF-radar network to the global ocean to address the Living Planet ocean challenges. SKIM is our *HF-radar in space*.

The space segment will be implemented as a single spacecraft carrying a Ka-band radar called the SKIM Ka-band radar (SKaR). The satellite will fly in a near-polar, Sun-synchronous quasi-circular frozen orbit at an average altitude of 832 km. The orbit is designed to maximise collocated and simultaneous observations with MetOp-SG(1B)'s scatterometer (SCA) and Microwave Imaging radiometer (MWI) instruments. Vega-C is the baseline launcher in a dual-launch configuration.

The SKaR includes a multi-beam conically scanning antenna that samples the ocean surface over a wide swath of approximately 315 km. As the satellite flies, a spiral-like beam ground track pattern emerges as each beam sweeps across the instrument swath. A rapid succession of radar pulses is transmitted and echoes from the surface are processed onboard to reduce noise. Subsequent pulses are correlated to compute the Doppler shift, which combines the satellite motion and the motion of the ocean surface. Subtracting the satellite motion with sufficient accuracy is one of the technical challenges of the mission. To this end, data-driven calibration approaches have been developed and tested.

Four types of fundamental measurements are provided by SKaR:

- **Line of Sight (LoS) velocity measurements:** the high Pulse Repetition Frequency (PRF) of 32 kHz ensures the coherence of consecutive radar pulses. By correlating pairs of consecutive pulses and by coherent averaging, pulse-pair echoes are obtained so as to provide directly the LoS Doppler velocities from the phase signal of the pulse-pair echoes.
- **Wave scatterometry:** using off-nadir beams, the azimuth diversity of backscatter modulation spectrum is obtained through incoherent processing of the Real Aperture Radar (RAR) waveforms. This is used to compute Stokes drift and directional wave spectrum.
- **High-precision nadir altimetry:** this is implemented for the nadir beam using non-ambiguous unfocussed SAR processing. The unique combination of simultaneous surface wave and current information will, for the first time, help to better understand and reduce altimeter sea-state bias uncertainties.
- **Delta-k LoS velocity measurements:** this experimental product involves a particular use of chirp signals to capture a beat pulse between slightly different carrier frequencies. A resonant spike appears, which corresponds to the propagation velocity of gravity waves with wavelength satisfying the dispersion relation of ocean waves and its anomalies (current). The intent is to measure vertical shear in the surface ocean.



Onboard processing is implemented using technologies that allow in-orbit reconfiguration of the processing routines. SKaR has a very-high range resolution to help estimate the phase of the range-resolved pulse-pair echoes, and a corresponding Doppler spectrum to be used in the higher-level processing. Together with the backscatter modulation, the component of the measured LoS velocity due to the circular orbital motion of the waves, containing the signal of underlying currents, can be calculated.

The operations scenario foresees a continuous observation over all large water and sea ice surfaces between the latitudes of 82° North and South. The SKaR data will be downlinked to the ground station with a radio link in the X-band. The generic Earth Explorer ground segment infrastructure will be used for the SKIM mission.

The space segment is designed for a nominal lifetime of five years with enough propellant to last seven years. The SKIM satellite is largely based on a recurrent three-axis stabilized Earth-pointing platform, with specific mission adaptations, which ensure a streamlined satellite development approach to meet the stringent programmatic boundary conditions while minimising the development risks.

SKIM is considered a technically feasible mission. Critical technologies have been identified and dedicated pre-development activities have been initiated during Phase A. Based on the results of pre-developments achieved so far, and assuming successful completion of the pre-developments planned to be initiated in phase B1, it is expected to reach at least a Technology Readiness Level of 5 or 6 by the end of Phase B1. The main critical technologies and pre-developments initiated during the Phase A are:

- Embedded software for onboard processing
- Grid modulator in the high-power amplifier power supply
- RF rotary joint in the antenna

Scientific maturity was assessed at the start and at the end of the Phase A by conducting, within the community assessments based on the definitions of the Scientific Readiness Levels (SRLs). The mission and research objectives have remained stable with respect to the original proposal. However, changes with respect to the initial concept have been made during the Phase A in order to enhance the scientific return, in particular by moving from an orbit coordinated with Copernicus Sentinel-1 to one flying in a loose formation with MetOp-SG(1B). SKIM and MetOp-SG(1B) form an innovative wind–wave–current measurement combination. In addition, MetOp-SG(1B) provides an elegant solution for obtaining auxiliary information important for SKIM, including precipitation, water vapour, sea-ice and surface wind vector information. End-to-end system performance simulations demonstrate that the mission objectives are met for single-swath TSCV at $\leq 0.15 \text{ m s}^{-1}$ or 15%, whichever is smaller. This can be reduced to $\leq 0.1 \text{ m s}^{-1}$ (the mission goal) by improving the wave Doppler algorithm, for which a development plan is in place or by temporally averaging products over 10 days to approach the Global Climate Observing System target of 0.05 m s^{-1} . Stokes drift and directional wave spectrum retrieval simulations demonstrate that SKIM meets all requirements. Using airborne and ground campaign data, the TSCV retrieval approach has been consolidated and the target requirements for accuracy and spatial resolution have been fulfilled by comparing to different drifting buoy measurements and



coastal HF-radar measurements. Based on simulations and dedicated campaign activities, SKIM was demonstrated to be compliant with its scientific mission requirements.

The SKIM scientific community has been nurtured with dedicated user workshops held during the Phase A and access to open source simulation tools and output data sets. These enable scientists and applications specialists to explore SKIM data sets and prepare their applications and services. Over twenty scientific publications have been generated during the Phase A demonstrating how SKIM data can be used in applications. There is a significant community interest in the SKIM mission.

The critical scientific areas of maturity and risk have been assessed and there are no major issues of concern regarding the scientific development of SKIM. The mission and research objectives have remained stable with respect to the original proposal. Evidence of SRL evolution has been collected based on two Scientific Readiness Assessments that demonstrate SRL evolution from SRL=4 to SRL=5. On the basis of the above, it is considered that SKIM has reached the required Scientific Readiness Level of 5 at the end of Phase A. A roadmap of science activities to further develop the SKIM mission has been established to address future scientific development.

Assuming the expected successful outcome of on-going and planned technology pre-developments, the maturity of critical technologies will reach the required level prior to the start of the implementation phase. The development schedule is driven by the instrument development, characterization and test phases. The Design Development and Validation Plan and the associated schedule are not yet fully consolidated. Further improvements would be necessary to recover - with margins - the launch date by the end of 2025.

SKIM will be the first satellite mission to provide wide-swath Doppler measurements that can directly retrieve the global ocean surface current at space scales of about 30 km every few days. SKIM will directly address one of the most challenging and fundamental questions in modern oceanography and marine meteorology: *How do the kinematics and dynamics of the ocean TSCV influence the integrated Earth system at the ocean atmosphere interface?*

The SKIM mission concept has reached the expected scientific and technical readiness levels at the end of Phase A, and is sufficiently mature for implementation as Earth Explorer 9. The development schedule is compatible with a launch in the 2026 timeframe.



1 INTRODUCTION

The Earth Observation Envelope Programme is a rolling programme designed to underpin European efforts in Earth Observation from space. The Earth Explorer element of the programme consists of a series of space missions addressing critical Earth science issues.

To date ESA has developed and launched five such Earth Explorer research missions:

- GOCE - Gravity field and steady-state Ocean Circulation Explorer
- SMOS - Soil Moisture and Ocean Salinity
- CryoSat - Polar Ice Monitoring
- Swarm - Earth's Magnetic Field and Environment Explorer
- Aeolus - Doppler Wind Lidar

and is currently implementing a further three:

- EarthCARE - Clouds, Aerosols and Radiation Explorer
- Biomass - to take global measurements of forest biomass
- FLEX – Fluorescence Explorer

The Agency aims to achieve a clear appreciation of the science community's views on what mission concepts will give the highest scientific return and best response and solution to scientific challenges and issues society is facing (Earth Observation Science Strategy for ESA: A New Era for Scientific Advances and Societal Benefits, ESA SP-1329/1 and ESA's Living Planet Programme: Scientific Achievements and Future Challenges – Scientific Context of the Earth Observation Science Strategy for ESA, ESA SP-1329/2, European Space Agency, Noordwijk, the Netherlands, 2015).

This series of pioneering Earth Explorer satellite missions represents the epitome of Europe's technical endeavour in conceiving and realising new Earth-observing capabilities. Each of these research missions offers new innovative measurement techniques to explore and understand different aspects of the Earth system. Meanwhile, the guiding principle remains to define, develop and operate these Earth Explorer missions in close cooperation with the scientific community to address the most critical Earth-science questions in as comprehensive and effective a manner as possible.

In 2016, ESA initiated a call to invite proposals for mission concepts that exhibit a certain degree of maturity, or “readiness”, and that demonstrate the potential of new innovative Earth Observation techniques of relevance to both the scientific and the applications communities. Mission Proposers were encouraged to make use of recurrent hardware and software, of formation and constellations (possibly via national and/or international partnerships), and launch opportunities. Specific to this Call, the scope of the EE-9 mission was to address science questions that have a direct bearing on societal issues such as:

- Food security
- Availability of fresh water
- Management of the Earth's resources and energy
- Health of the planet and humankind
- Disaster risk reduction and improvement of disaster resilience
- Climate change



Not only the feasibility of the concept in terms of realising its scientific objectives and meeting its technical challenges has to be demonstrated, but also the capacity of the mission to address scientific questions in the context of above major societal issues.

In 2017, two Earth Explorer 9 candidates were selected for feasibility study (Phase A): FORUM and SKIM.

FORUM aims to measure the Earth's top-of-atmosphere emission spectrum in the 100 to 1600 cm^{-1} (6.25 μm to 100 μm) spectral region covering the observational gap of the far-infrared 100-667 cm^{-1} (15 μm to 100 μm), which has never been observed from space, spectrally resolved, and in its entirety. This measurement will provide an improved understanding of the climate system by supplying, for the first time, most of the spectral features of the far-infrared contribution to the Earth radiation budget, particularly focusing on the water vapour contribution related to the continuum absorption in the rotational band, cirrus cloud and ice/snow surface emissivity.

The Sea surface Kinematics Multiscale monitoring (SKIM) mission aims to measure directly and simultaneously, the ocean Total Surface Current Velocity (TSCV, an Essential Climate Variable), and its component Stokes drift with the directional wave spectrum, to quantify their role in ocean–atmosphere processes and the societal impact at the global and regional scale. At the very heart of it is the simple idea that a Doppler technique analogous to coastal HF-radar can be used in low Earth orbit to measure directly ocean TSCV. This will extend the highly successful coastal HF-radar network to the global ocean in order to address the Living Planet ocean challenges and important Societal Development Goals set by the United Nations. SKIM will be the first satellite mission to provide Doppler measurements that can directly retrieve the TSCV and its components every few days. SKIM is a multi-scale mission, resolving, for the first time from space, the wave-induced Stokes drift that is required to estimate surface transport that is essential for ocean-atmosphere exchange, to manage oil and chemical spills, and monitor the trajectory and fate of floating marine plastic debris.

Owing to the fact that concepts were invited where scientific as well as technological investigation/validation have progressed, the Agency has implemented a streamlined schedule as compared to previous Earth Explorer Missions.

The Reports for Mission Selection capture the status of the respective mission Concept at the end of Phase A activities. The two volumes will be provided to the Earth-observation community as a basis for the User Consultation Meeting held in July 2019, and for the subsequent recommendation for selection of a single Earth Explorer 9 mission by the Advisory Committee for Earth Observation.

Each Report for Mission Selection follows a common format and logic. Each identifies the scientific questions and related key societal issues motivating the mission and its research objectives. After establishing the scientific basis and rationale, the specific mission objectives are outlined and traced to a set of requirements used for system concept definition. Consolidated descriptions of two competing technical concepts are provided for each candidate mission, the designs of which are optimised to respond to the mission requirements. Based on each design concept, the end-to-end performance is simulated and the maturity of the geophysical data processing is outlined. The results are used to establish



the feasibility and maturity of the concept as well as to evaluate the capability to fulfil the mission requirements and scientific objectives.

Each report comprises this introductory first chapter and eight subsequent chapters as follows:

Chapter 2 identifies the background and scientific issues to be addressed by the mission. It provides justification for the mission and includes a review of the current scientific understanding of the issue in question while identifying the potential advances in knowledge that the mission could provide.

Chapter 3 draws on arguments presented in Chapter 2, and summarizes specific research objectives and related mission objectives.

Chapter 4 outlines the mission requirements, including required Level-2 geophysical data products and observational parameters, the need for these observations to be made from space, and aspects of timeliness and timing of the mission.

Chapter 5 provides an overview of the system elements, including the space and ground segments, operations, calibration and the data processing up to Level-1b.

Chapter 6 details the scientific data processing and validation concept, including processing and calibration/validation as well as the data processing techniques that need to be implemented to meet the data product requirements.

Chapter 7 makes a comparison of the expected versus the required performance and ability to fulfil the research/observational objectives based on the documented system concept.

Chapter 8 documents the readiness of the scientific user community in respect to planned use of the unique scientific products, the global context in terms of complementary missions as well as the operational or applications potential of the data products. This chapter also outlines the societal benefit of the mission.

Chapter 9 outlines a programme of implementation. It also addresses the technical maturity, the development status of key technologies, and schedules.

2 BACKGROUND AND SCIENTIFIC JUSTIFICATION

Measurements of the powerful, complex and highly variable ocean surface currents and surface waves are fundamental to our understanding of ocean circulation and air–sea interaction. This is because they influence the Earth system at time scales from wind waves, weather through to climate (GCOS, 2015). The motivation for better knowledge and understanding of ocean surface currents has its foundation in traditional maritime activities serving society at all levels including: shipping, maritime safety, marine operations, increasing maritime activities with sea-ice, fisheries, renewable energy, pollution events, environmental management, resource exploitation, ports and harbour operations, recreation, numerical weather prediction, ocean forecasting, and climate monitoring, amongst others. Mariners initially relied on their own observations to map the mean ocean surface current, collating ships records into the first mariners’ charts with great dedication and care. They wanted to understand why some ships travelling westward from England to North America made the crossing more quickly than others. In 1786, Poupard and Franklin (1786) discovered the Gulf Stream western boundary current.

Ocean Surface Currents

Ocean-surface currents are usually described as a combination of basin-scale circulations driven by the tides, wind, and differences in water density. The mean surface-circulation is organised into gyres that are almost closed circulation loops covering the longitudinal extent of an ocean basin, with an intensified current on the western boundary such as the Gulf Stream, with powerful equatorial currents. Divergence and convergence of ocean-surface current determines the vertical exchange between water at the ocean surface and the interior ocean beneath. At the largest scales, ocean water-masses are formed at the surface that replace or ventilate older water in deeper layers with surface water.

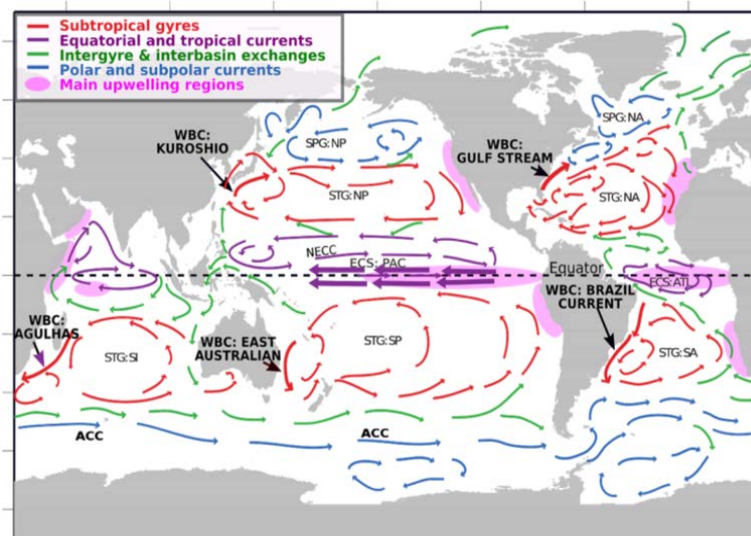


Figure 2.1. Left: the general ocean-surface circulation decomposed into gyres and large current systems with coastal and equatorial upwelling systems marked as purple areas. (Adapted from Vallis, 2017, with permission)

Textbook images of ocean currents and their surface expression (Fig. 2.1) portray a simplified view of the average surface ocean flow obtained from the compilation of drifting buoy measurements, complemented by satellite altimetry, over at least four decades (e.g.



Kennedy et al., 2011). This simple schematic of ocean circulation ignores to the complexity of the different processes and their interactions that define the Total Surface Current Velocity (TSCV).

Where the surface flow diverges, subsurface water brings nutrients close to the surface that feed the whole ecosystem with the most important fisheries located in these upwelling regions. Where the surface water converges, in the middle of the subtropical gyres, they gather floating material, including the infamous marine plastic ‘garbage patches’ (van Sebille et al., 2015). But such a simple view of surface-ocean circulation does not do justice to the complexity of the upper oceanic surface velocity field that is strongly influenced by the forcing acting through ocean–atmosphere interactions. This is because surface water movement involves a continuum of variability across all space and time scales subject to small- and large-scale random perturbations and nonlinear interactions.

The ocean-surface layer is the interface between the ocean and the overlying atmosphere: divergence and convergence of the ocean-surface current determines the vertical exchanges between the ocean surface and the interior ocean beneath. Stokes drift, for which no measurement is currently available from space, is extremely important to explain the transport of all material at the surface of the ocean (Fraser et al., 2018). In these ways, the TSCV and the component Stokes drift play a fundamental role in surface ocean transport of energy, heat, gases important for life and climate (e.g. oxygen, carbon dioxide), momentum, biology, along with many other globally and biogeochemically important trace gases (e.g. dimethyl sulphide, methane, nitrogen dioxide, methyl bromide, and many volatile pollutants) throughout the ocean, atmosphere and, between different Earth system components; notably within hydrological and biogeochemical cycles. In fact, the TSCV and Stokes drift *impact everything* that is in the upper ocean, natural or anthropogenic including ships, sea-ice, marine life, carbon dioxide, oil and other pollutants. These are the key variables required to manage the contemporary challenge of floating marine plastic debris transport and knowledge of its fate. This includes long-range transport and dispersion by convergent and divergent flow regimes that are not well known. Most importantly, within the interconnected Earth system, ocean–atmosphere interaction across the perpetually moving ocean surface is fundamental to regulating our climate (IPCC, 2014).

Ocean Total Surface Current Velocity

The perpetual motion of the ocean surface in contact with the atmosphere is the result of a superposition of different forces acting on the same ocean surface and those connected to the deeper ocean layers (Chapron et al., 2017). At the local scale, wind stress acting on the surface drives surface currents, induces shear and vertical turbulent exchange, and generates waves that themselves, drive important Stokes drift flows that have a profound effect on all floating material (Fraser et al., 2018). Thus, the concept of wind-wave-current interaction is central to understanding the kinematics and dynamics of the ocean surface current (e.g. Villas Bôas et al. 2019, Cronin et al., 2019).

The actual velocity of a water parcel in contact with the atmosphere at any given location and time (i.e. the surface ocean current) is called the Total Surface Current Velocity (TSCV). The TSCV can be formally defined as the Lagrangian mean velocity at the sea surface (Andrews and McIntyre, 1978): *the TSCV is the actual velocity of water parcels that are right at the ocean surface in contact with the atmosphere*. The depth of the surface layer representative of the TSCV in the upper ocean depends on its vertical stratification. It includes a multiscale

continuum of variability across all space and time scales governed by quasi-random forcing perturbations and nonlinear interactions at a given time and location. Motion at the ocean surface is the result of a superposition of different forces acting on the same ocean surface and those connected to the deeper ocean layers (Fig. 2.2). These include amongst others (Chapron et al., 2017):

- Frictional stress of the wind acting on the sea surface (water or sea ice)
- Ocean surface wave-induced inertia and pressure gradient, leading to Stokes drift (e.g. Ardhuin et al., 2009)
- Coriolis force related to Earth’s rotation, Ω (the magnitude of rotation vector)
- Large scale (>10 km) pressure gradients due to variations in surface elevation (gravitation, including tides, atmospheric pressure, local topography) and to variation in density, including effects of stratification.

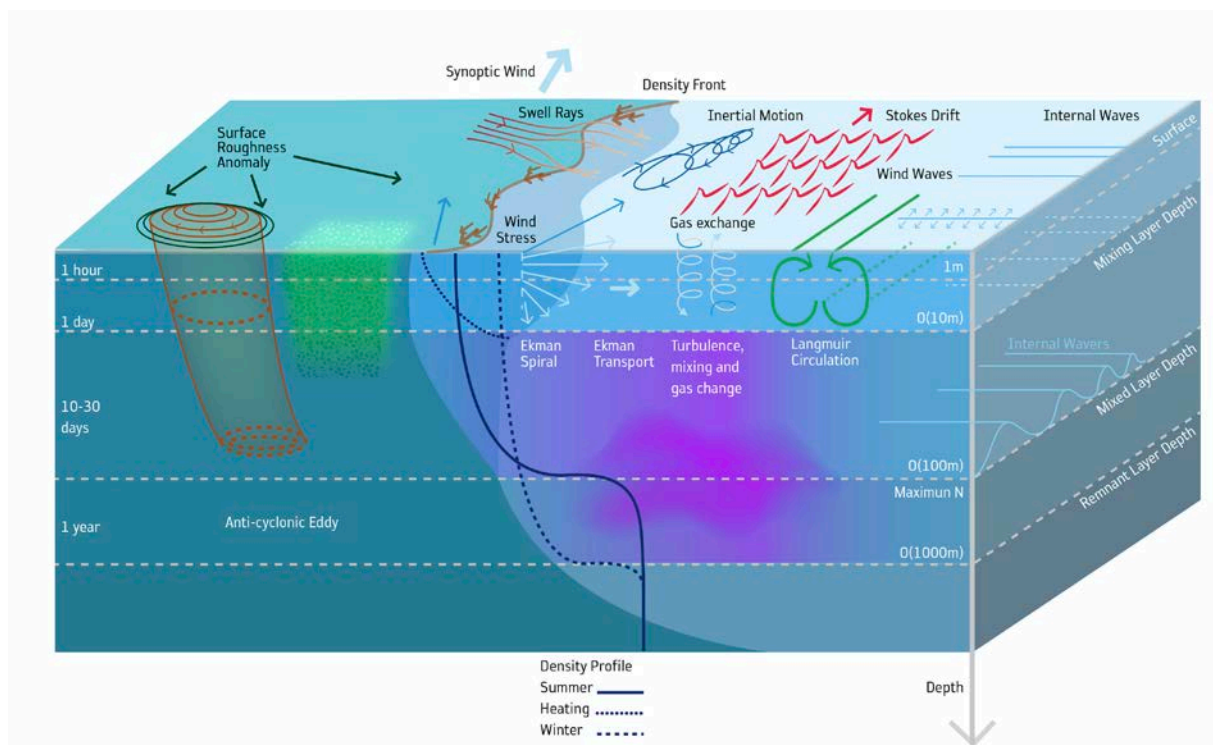


Figure 2.2. Motions of the oceans and their many complexities. The image shows processes that influence the TSCV, including density fronts, wind-generated waves, Langmuir turbulence. (Credit: ESA)

Only in recent years have numerical ocean models started to include the necessary large range of space and time scales to represent these and the reader is referred to <https://bit.ly/2XsokAe> for one example realisation (D. Menemenlis personal communication, see Torres et al., 2018 for analyses). Thus, the processes resolved today in state-of-the-art models are only part of the full range of motions that contribute to the upper-ocean velocity field as illustrated by Fig. 2.2 (e.g. Fox-Kemper et al., 2019).

Where are the TSCV observations?

Remarkably, in most parts of the world ocean, very few, if any, *in situ* measurements of the TSCV have been made – yet new ocean surface currents are still being discovered today, such as those recently found close to Madagascar (Ramanantsoa et al., 2018) and close to Iceland

(Harden and Pickard, 2018). These will certainly have to be remapped tomorrow as they shift with climate change – although this will be extremely challenging using today’s observing systems.

The primary constraint on our knowledge of TSCV is a lack of measurements having regular, quasi-synoptic, global repeat coverage. Ironically, we still face the same challenge as Poupard and Franklin in 1786: in the words of Walter Munk, “*If I were to choose a single phrase to characterize the first century of modern oceanography, it would be a century of under-sampling*” (2002).

The truth is that today, we are practically blind to the TSCV over most of the ocean.

Despite their importance for science and society, regular, repeat coverage and densely sampled and direct measurement of the ocean TSCV from space have, so far, eluded the Earth observation community. As a consequence, the level of scientific scrutiny required to fully address the ESA Living Planet ocean challenges (ESA 2015a) and United Nations Sustainable Development Goals (SDGs, United Nations 2015) is not available.

We are unable to properly answer the question: Where are all the surface ocean currents going?

The way forward: Doppler oceanography from space

One notable exception is the undisputed success of High Frequency (HF) radars, that are used to measure the ocean-surface currents in coastal seas (Gurgel et al., 1999). These measurement systems are unique in their capability of measuring the TSCV (including the Stokes drift), and both the time and space variability of the TSCV. Figure 2.3 shows the analysis of data from the Oregon coast that is dominated by Near-Inertial Oscillations (NIOs). Kim and Kosro (2013) have shown that these oscillations are, on average, coherent over time scales up to six days and spatial scales larger than 100 km. Such properties are completely unknown for the open ocean where no such data exists.

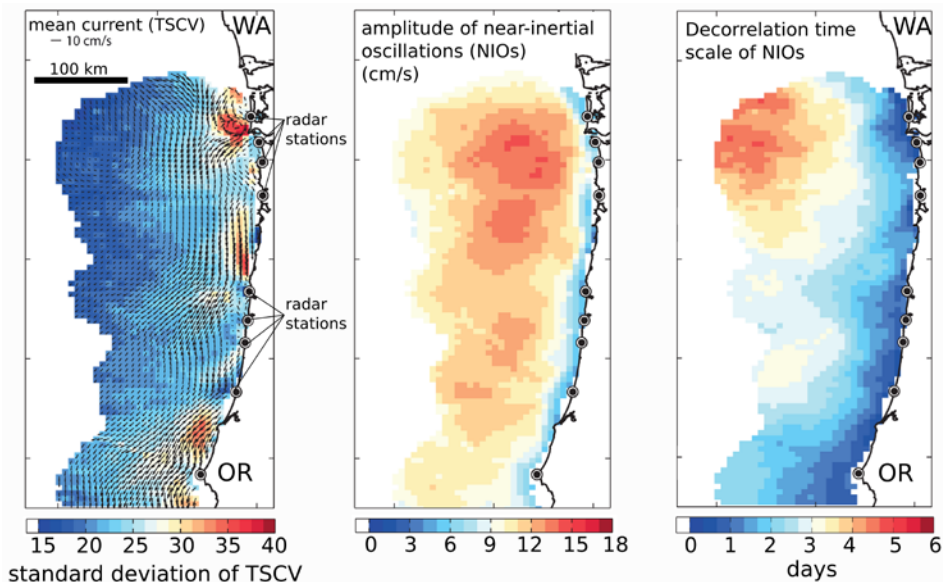


Figure 2.3. Left: mean currents (arrows) and magnitude of the standard deviation of TSCV in cm s^{-1} from the Oregon coast over 2007–08. Centre: root mean square amplitude of near-inertial oscillations, with periods around 17 hours. Right: average decorrelation time of the NIOs. Kim and Kosro, 2013, with permission from American Geophysical Society)

Extensively used since the 1990s, these Doppler radars use shore-based antennas that radiate HF radio waves (3–30 MHz) that propagate as ground waves beyond the horizon. Today, most of the coasts in the United States and some European locations have ground HF Doppler radars available, but the coverage still remains very sparse in most coastal regions (GCOS 2016). Each system typically covers a 100×100 km area of the ocean, with a maximum range of 300 km from the coast (Rubio et al., 2017). HF-radar systems are used for science and societal applications such as investigating larval dispersion and ecosystem connectivity, tracking oil spills and supporting search and rescue operations (Rubio et al., 2017). While far from ubiquitous across all coastlines of the world, where available, HF-radar measurements have led to a revolution in our understanding of coastal ocean-surface dynamics.

Fig. 2.4 (left) shows the time-space scales of dominant ocean-atmosphere phenomena that are relevant to the TSCV. Based on the user needs identified in Section 2.2, it highlights where the SKIM will operate specifically to resolve TSCV and wave related Stokes drift (described fully in Sections 2.5). These map onto user needs set out in Section 2.3.

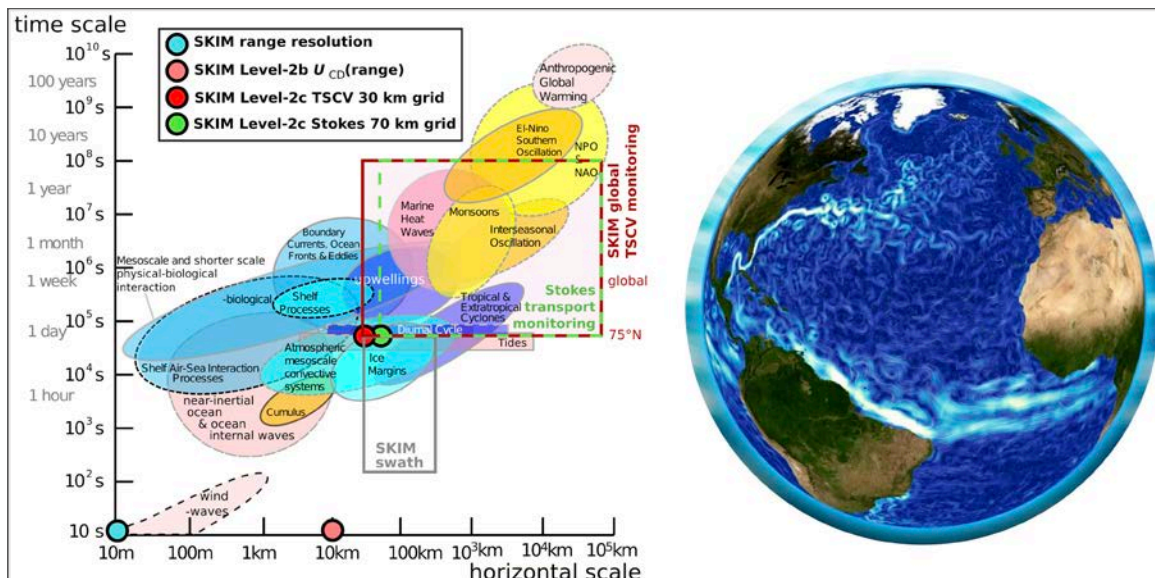


Figure 2.4. Left: time-space scales of ocean-atmosphere phenomena that are relevant to ocean–atmosphere fluxes (from Cronin et al. 2019), highlighting where the SKIM mission will globally monitor the TSCV (red box), and its component the Stokes Drift. The fundamental spatial resolution of SKIM measurements are shown as coloured dots. The red box highlights the time-space scales captured by systematically mapping TSCV at 30 km gridded resolution (SKIM Level-2c products). The green box highlights the time space scales mapped for Stokes drift (SKIM Level2c and Level-2d products). Right: example simulated TSCV over the Atlantic Ocean as expected from SKIM, revealing the complex structure of an ocean in motion (Level-2d 10-day product from the SKIMulator, Gaultier, 2019).

At the very heart of the Sea surface KInematics Multiscale monitoring (SKIM) mission is a simple idea that an instrument employing an analogous Doppler technique to coastal HF-radar can be flown in low Earth orbit to measure directly ocean TSCV. This will provide a quasi-synoptic, regular, repeat coverage and dense sampling over the global ocean. With such a mission, the TSCV will extend the highly successful coastal HF-radar network to the global ocean to address the Living Planet ocean challenges. SKIM is our ‘HF-radar in space’.

SKIM will be the first satellite mission to provide Doppler measurements that can directly retrieve the TSCV and its components every few days. SKIM is a multi-scale mission,



resolving, for the first time from space, the wave-induced Stokes drift that is essential for estimates of surface transport such as oil and chemical spills, and floating marine plastic debris.

This chapter demonstrates *why* the SKIM mission is urgently needed to deliver the scientific research necessary to address the Living Planet Challenges in a timely manner. It also identifies *what* is required to address *user community needs*. Chapter 3 traces *how* specific SKIM research objectives address user needs. Chapter 4 then *traces user needs* to product and measurement performance requirements that are used to develop the SKIM mission concept in Chapter 5.

2.1 The Importance of Ocean Currents: Scientific and Societal Issues of Concern

The ocean is a vast, largely unexplored part of our planet. Covering nearly three quarters of Earth’s surface, the global ocean holds a large part of the known biodiversity and over 60% of the planet’s biomass (Boeuf, 2011). It provides society with natural resources from an immensely diverse and well-adapted ecosystem, including food, materials and energy, and is essential for international trade, recreational and cultural activities (Lubchenco, 1998). A thriving blue economy is emerging that to support societal needs linked to the *Grand Challenge* set by the United Nations Sustainable Development Goals (Visbeck et al., 2014).

Most importantly, within the Earth system, the ocean is fundamental to regulating our climate (IPCC, 2014) largely through interactions across its incredibly dynamic surface that is in perpetual motion. Ocean-surface currents are ‘centre stage’ in the integrated Earth system, this is why the Global Climate Observing System (GCOS) identifies the ocean surface current as an Essential Climate Variable (ECV, GCOS, 2016; OOPC 2017). It is through the ocean surface interface that the atmosphere and ocean communicate with each other and the signatures of this conversation are found in the ocean surface kinematics and dynamics. Not only are Earth observation data needed to monitor and detect change in the ocean, but also to provide timely information critical to adapting to change in many natural, managed and human systems (Fig. 2.5).

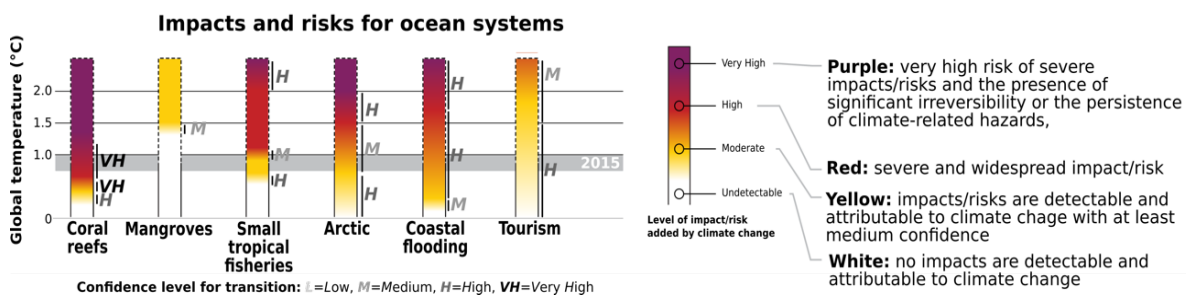


Figure 2.5. Reasons for concern and risks associated with global warming. Six of the 10 natural managed and human systems featured in the IPCC special report on global warming of 1.5°C are associated with the ocean, with high to very high confidence that they will be severely impacted by a global warming of 1.5° and more. (Adapted from Figure SPM.2 from the Summary for Policymakers in IPCC, 2018: Global Warming of 1.5°C. An IPCC Special Report on the impacts of global warming of 1.5°C above pre-industrial levels and related global greenhouse gas emission pathways, in the context of strengthening the global response to the threat of climate change, sustainable development, and efforts to eradicate poverty [Masson-Delmotte, V., P.Zhai, H.O. Pörtner, D. Roberts, P.R. Shukla, J. Skea, A. Pirani, Y. Chen, S. Connors, M. Gomis, E. Lonnoy, R. Matthews, W. Moufouma-Okia, C. Péan, R. Pidcock, N. Reay, M. Tignor, T. Waterfield (eds.)].).

Biological growth in the oceans is a key component of Earth's carbon cycle, and the source of most of our planet's biomass. Marine ecosystems develop within niche environments (temperature, light, nutrients) that are fine-tuned to the surface kinematics and dynamics of the TSCV. Surface ocean ecosystems are influenced profoundly by ocean-atmosphere coupling and lateral eddy fluxes of heat, salt and other bio-geochemical properties. Humanity depends on this biomass for feeding a rapidly growing global population. Ocean fisheries alone, not counting aquaculture, support the full protein need of 600 million people on a daily basis (FAO, 2018) and a rich source of micronutrients that are important for health (e.g. in coastal megacities, Golden et al., 2016). To ensure future food security (UN SDG 2 zero hunger), we must be able to manage fisheries and reduce the impact of pollution events, such as oil and chemical spills along with reducing the amount of marine plastic debris that threaten our marine ecosystems.

The ocean is the largest thermal reservoir on Earth, having absorbed over 90% of all anthropogenic heat (Hansen et al. 2011, Dieng et al., 2015). It is preferentially heated in the Tropics by incoming solar radiation and cools at high latitudes by outgoing longwave radiation losses with a net budget that is generally well known (e.g. Trenberth and Fasullo 2017, Dewitte and Clerbaux 2017). Due to the high heat capacity of water the ocean stores heat and, via the system of global ocean currents, the excess heat in the equatorial regions is redistributed to higher latitudes as the Earth systems perpetually strives to maintain thermal dynamic equilibrium. Away from the tropics, flow instability in the western boundary currents results in the generation of enhanced eddy kinetic energy contributing to global mesoscale eddy field that overall contains more than half of the kinetic energy of the global ocean circulation. In the extension regions of the Kuroshio and Gulf Stream, strong oceanic fronts develop that due to ocean-atmosphere interactions that contribute towards anchoring atmospheric storm tracks (Minobe et al., 2008, Nakamura et al., 2004). Besides the importance of ocean-atmosphere interaction on the scales of the mean circulation, the interaction at the eddy scale was found to be an important aspect of the climate system. It affects the energy conversion between mean circulation and mesoscale eddy field thereby setting the main pathway of the Kuroshio and Gulf Stream extensions (Ma et al., 2016).

The actual transport of heat, freshwater and material is the results from the combination of all these motions, with a large fraction characterised by high variability in space and time. *In situ* current-meter data and high-resolution simulations revealed strong eddy heat transport in western boundary currents, the Antarctic Circumpolar Current and in the equatorial region (Wunsch, 1999, Jayne and Marotzke, 2002). In particular, the equatorial region that is dominated by Tropical Instability Waves (TIWs) shows a strong convergence of eddy heat fluxes. Heat advection by the mean currents and the diapycnal mixing associated with the vertical shear of mean and eddy motions represent instead strong cooling terms (Hummels et al., 2014). They have to balance the strong heat budget residual in the equatorial oceans that results from the mean surface heat flux, with an annual mean advection flux up to -150 W m^{-2} at the equator (Schlundt et al. 2014). This is very large and is not resolved by observations today. Poor simulation of ENSO is often linked to this bias in which the cold upwelled water in the eastern equatorial Pacific extends too far west (Santoso et al., 2019).

The TSCV is required to monitor the surface component of the global ocean circulation (e.g. Le Traon et al., 2019) and the regulation of our climate (GCOS, 2016) as the climate crisis develops.

In the clear blue open ocean waters, solar radiation is absorbed in the top 50 m. This contributes to one of the most important features of the ocean: its stratification in layers of different density. The surface mixed-layer, intimately linked to the ocean-surface dynamics and kinematics, is always in contact with the atmosphere and, through turbulent exchange across the ocean–atmosphere interface, the immense ocean interior connects intimately to the atmosphere. The ocean has absorbed about 25% of all anthropogenic carbon dioxide (CO₂) emissions since 1870 (Le Quéré et al., 2018). A combination of physical and biological activity and internal ocean circulation makes the ocean the only long-term sink of CO₂ emissions (Sabine et al., 2004). Thus, the absorption, through atmosphere–ocean exchange, of both anthropogenic heat and CO₂ has helped to slow climate change, but it comes at a cost, as it is causing the ocean to fundamentally change.

Hot, sour, breathless and under pressure

The combination of warming, long-term absorption of CO₂ resulting in reduced pH (ocean acidification), and reduction in oxygen (Oschlies et al., 2018) is putting considerable stress on the ocean (Turley et al., 2013 and WMO). These stressors combined with intensified fishing (FAO 2018) and pollution (e.g. van Sebille, 2015) are rapidly degrading ocean health (e.g. Gruber, 2011), and much is already seriously degraded with losses in structure and function, impacting services to humanity (IPCC 2014, United Nations, 2016, IPBES 2019). In the future many parts of the ocean are likely to experience the combination of more than one environmental stressor, known as compound events, which will likely coincide with areas of high productivity and fisheries (Turley et al., 2013). New emerging threats, such as ocean heat waves, will require new knowledge to enable predictions on their impact on the marine system and the goods and services that it provides (Frolicher and Laufkotter, 2018). All of these anthropogenic issues are influenced, or intimately controlled, by the TSCV, transport and atmosphere–ocean exchange.

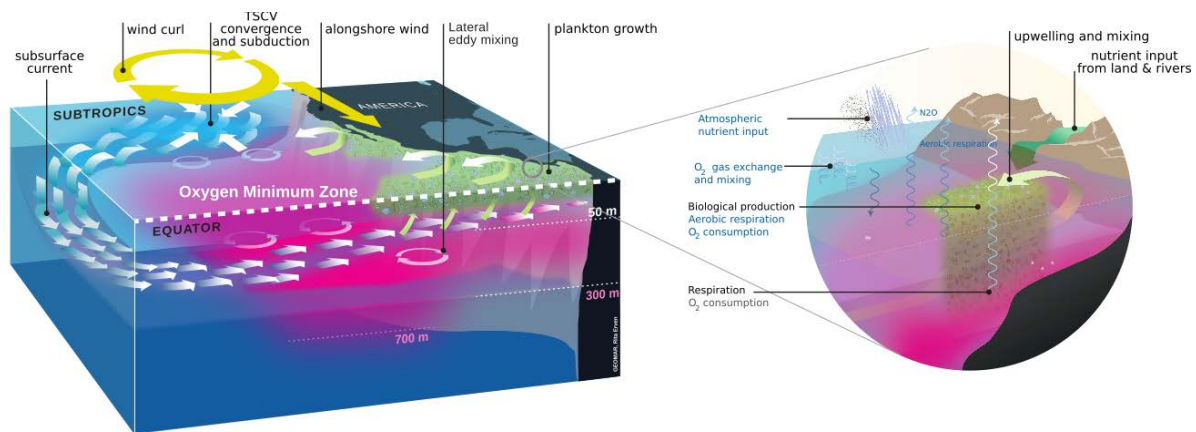


Figure 2.6. The TSCV (wide white arrows) driven by the wind is a key aspect in thermocline ocean ventilation. Schematic view of thermocline ventilation patterns with, as an example, a focus on the eastern subtropical North Pacific Oxygen Minimum Zone (OMZ). The wind-stress curl in the subtropics drives a convergence of surface currents and subduction of oxygenated waters that, via ocean interior circulation or western boundary currents, reaches biotically productive upwelling regions at the eastern boundary. High oxygen demand, together with weak oxygen supply due to reduced circulation and warming, (which reduces the amount of oxygen that is dissolved in water) results in dangerously low oxygen levels. The inset shows processes particularly relevant to OMZs connected to eastern boundary upwelling. (R. Erven, GEOMAR).



As the climate changes, wind-driven ocean-surface currents are modified, leading to different patterns of sea-surface temperature (a tracer of the TSCV), including ocean heatwaves (Bond et al., 2015). These are already causing widespread mortality of marine species, shifts in ecosystem structure, the closure of commercially important fisheries and quota reductions (Frolicher et al., 2018). They appear to be increasing in strength, with 87% of events attributed to human-induced warming (Frolicher et al., 2018) with profound consequences for ecosystems (Mills et al., 2013, Smale et al., 2019, Pinsky et al 2019). This is combined with a general reduction of the concentration of oxygen associated with a number of factors in which surface-current patterns play a leading role (Fig. 2.6).

This is leading to profound changes in ecosystems and threatening the fragile ocean food web (Orr, 2005). The excess heat absorbed by the ocean results in thermal expansion and sea-level rise, increasing stratification, and reduced dissolved oxygen, threatening marine life. Anthropogenic activities are rapidly degrading ocean health (e.g. Gruber, 2011; van Sebille, 2015) with losses in structure and function, impacting services to humanity (IPCC 2014, United Nations, 2016, IPBES 2019).

A rapidly changing Arctic Ocean

These changes and degradation are amplified in the Arctic Ocean with large temperature anomalies (Overland and Wang, 2018) and receding sea-ice cover – with predictions anticipating summer ice-free Arctic Ocean by 2030 (IPCC, 2018). The societal impacts of a rapidly changing Arctic are complex, uncertain and ambiguous for Europe which has led to the creation of *An Integrated European Union Policy for the Arctic* (EC, 2016). How will the Arctic Ocean TSCV and subsurface circulation respond when the ocean–atmosphere interface is more exposed in a changed world? How will sea-ice distribution and dynamics change? What will be the impact on society, not just in Europe but globally? What will the ocean surface currents look like and how will they impact the growth and retreat of sea-ice? How will changes impact Arctic ecosystems and the societies that live and work in the region?

The impact of increasingly reduced sea-ice cover in the Arctic Ocean and for increasingly longer periods of time, will change the TSCV and general ocean circulation patterns. More open water leads to an enhancement of waves with consequent impacts on the dynamics, development and retreat of the sea ice edge (e.g. Overeem et al., 2011). As permafrost melts increased organically loaded river discharge into the Arctic Ocean may lead to changes in local ecosystems. River discharge is an important variable form many scientific and operational applications related to water resources and aquaculture management in the coastal zone. Methods based on conventional satellite altimetry (e.g. Tarpanelli et al., 2013) are now emerging as a mature technique to monitor discharge and facilitate the management of coastal aquaculture. (The same techniques can be used to monitor water storage in lakes and reservoirs e.g. Gao et al., 2019).

The IPCC (2018) identifies the Arctic Ocean a region at very high risk of severe impact (Fig. 2.5). In the Arctic Ocean rapid changes in wind–wave–current regimes are expected by 2030 (IPCC, 2018). To address this challenge, measurements of the TSCV are required in the Arctic Ocean.

Ocean atmosphere interaction and the TSCV

By 2030 we may expect changes in wind–wave–current regimes at the ocean surface (IPCC, 2018) . Such a regime shift is already taking place with larger exchange between the ocean



and atmosphere (Barton et al., 2018) that has far-reaching impacts, from fisheries (Fossheim et al., 2015) to major influences on weather and climate across Europe (Screen 2017, Coumou et al., 2018). For example, changes in rainfall in South America and West Africa and Atlantic hurricanes are all sensitive to conditions in the Tropical Atlantic, but are driven by complex dynamic and kinematic exchange between the ocean, atmosphere, land and between ocean basins (Foltz et al., 2019).

The inadequate status of our knowledge in ocean TSCV for ocean atmosphere interaction parameterisations and modelling has been documented by the international community (Cronin et al., 2019). While Earth observation has taken a major role in many of the ocean-atmosphere flux estimates, it has been unable to provide a measure of the TSCV and its component Stokes drift. The OceanObs19 community requirement (Cronin et al., 2019) is for products with three-hourly, 25-km (and an aspirational goal of hourly at 10 km) heat flux and wind-stress fields over the global, ice-free ocean with breakthrough one-day random uncertainty of 15 W m^{-2} and a bias of less than 5 W m^{-2} . In order to meet this target, regular, repeat coverage of the TSCV is needed to compute wind stress relative to ocean surface (Brodeau et al., 2017). SKIM will, for the first time, deliver *exactly* the measurements required by the OceanObs community: TSCV, Stokes drift and surface waves.

The climate crisis

There are new emerging threats that will require additional scientific knowledge and capability, including the increasing occurrence of weather and ocean extremes (e.g. Frölicher and Laufkötter, 2018), climate tipping points in ocean biogeochemistry and ecosystems (Foltz et al., 2019) and more intense tropical storms. These are compounded by higher sea level and reduced coastal protection due to degraded coral reefs that threaten the very existence of low-lying islands and their fragile societies. Dedicated satellite altimeter missions have been used very successfully to monitor global sea level variability for several decades. Of particular importance is the need to understand how the synthetic aperture radar altimeter measurements e.g. Copernicus Sentinel-3 and the Sentinel-6 reference altimeter mission, are aliased with long-wave swells leading to regional biases in the satellite sea level record. SKIM is unique in that it can continuously map both sea-surface height and the directional wave spectra that can be used to study the global and regional impact of swell and sea state on measurements of sea level. SKIM measurements can also be used to investigate the sea-state bias corrections that are the largest uncertainty term in satellite altimetry today potentially reducing the uncertainty on Copernicus Sentinel-6 and Sentinel-3 sea level estimates from space.

Expanding our understanding of the ocean TSCV and its influence on ocean–atmosphere exchange processes and the health of our ocean is key for ensuring a healthy and productive planet for future generations.

2.2 Relevance to the ESA Research Objectives for Earth Observation

All of the effects and issues discussed in this chapter are intrinsically entwined with *the motion of the ocean surface* and its interactions with the atmosphere, which links the ocean circulation, primarily driven by atmosphere–ocean interactions, to sea level, the transportation of material (e.g. oil, marine plastic debris) away from and toward the coasts; all of which impacts the ecosystems services on which humanity relies. These are

encompassed within all the Living Planet ocean challenges that define the ESA strategy for Earth observation (ESA 2015, Fig. 2.7). These are linked to the UN Societal Development Goals in Chapter 8.



Figure 2.7. SKIM and ESA Living Planet Challenges: TSCV and waves are key to address all five ocean challenges, and can contribute to other cryosphere, atmosphere and solid Earth challenges. (S. Hervé, University of Brest)

2.3 User Needs for Ocean Surface Current Measurements

SKIM will be the first satellite mission to provide Doppler measurements that can *directly* retrieve the ocean TSCV with quasi global coverage, regular, repeat measurement every few days: SKIM is our HF-radar in space. As noted by Fox-Kemper et al. (2019) in the context of challenges and prospects for global ocean circulation models, “*The proposed satellites capable of simultaneously constraining wind, wave, and currents such as SKIM, will be highly valuable in evaluating the formulation of high-resolution the coupled wave-ocean-sea ice simulations.*”

Regular, repeat-coverage measurements of surface ocean-currents are requested to monitor ocean dynamics and kinematics as an Essential Climate Variable (GCOS 2016) to support climate applications and services for oceanography and marine meteorology (WMO, 2019), for global ocean science and services (e.g. Dohan and Maximenko, 2010). There are specific needs in the equatorial regions (Foltz et al., 2019; Smith et al. 2019) and for numerical ocean prediction (NOP, e.g. Fox-Kemper et al., 2019).

Villas Bôas et al. (2019) set out the requirements and challenges for integrated observation and modelling of winds, waves and currents for the next decade. They highlight the simultaneous measurements of absolute surface currents, ocean-surface wind vector, and directional wave spectrum from Doppler satellites as a significant but important challenge for the next decade. As noted by Villas Bôas et al. (2019), “*...surface winds, currents, and waves are coupled variables hence require integrated observations and modelling. Future Doppler oceanography satellites concepts ... [such as] SKIM have the potential to help fill*



in some of the identified observational gaps and to deliver systematic and global joint observations of surface winds, currents, and waves.”

2.3.1 User Needs for TSCV

User needs for TSCV for the oceanographic and marine meteorology community are maintained in the World Meteorological Organisation OSCAR database (<https://www.wmo-sat.info/oscar/variables/view/116>).

The TSCV requirements applicable to SKIM are summarised in Table 2.2.

Application area	Precision (m s ⁻¹)	Horizontal resolution (km)	Revisit (Days)	Coverage	Timeliness (days)
Nowcasting/very short-range forecasting (e.g. oil spill response, Safety of life at sea)	<0.01	15 (g:10)	0.5	Global	0.5 (g:0.25)
Open Ocean applications	0.2 (g:0.1)	100 (g:50)	3 (g:1)	Global	72 (g:24)
Coastal Ocean Applications	0.1 (g:0.05)	5 (g:1)	1 (g:0.5)	Global	1 (g: 0.25)
Numerical ocean forecasting (open ocean)	0.2 (g:0.1)	10 (g:5)	24 (g:6)	Global	2 (g:1)
Numerical ocean forecasting (coastal ocean)	0.1 (g:0.05)	5 (g:1)	12 (g:3)	Global	2 (g:1)

Table 2.2. Total Surface Current Velocity measurement requirements for oceanography and marine meteorology from the WMO OSCAR database <https://www.wmo-sat.info/oscar/variables/view/116>. ‘g’ denotes goal value.

In general, the requirements shown in Table 2.2. overlap with the user needs expressed in Dohan and Maximenko (2010), with specific needs in the equatorial regions (Foltz et al., 2019) and for numerical ocean prediction (Fox-Kemper et al., 2019) and from Villas Bôas et al. (2019) who set out the requirements and challenges for the next decade. It is clear that the Nowcasting requirements are extremely challenging and are not likely to be met completely from a space-based solution using current technology. However, estimates of Stokes drift at large scales (70 km) will approach the precision requirement.

User needs for the ECV for surface currents are expressed by the Global Climate Observing System (GCOS, 2016) Working Group for climate in support of implementing a climate observing system (Table 2.3). For the climate record stable data sets are required that impose requirements the SKIM mission. GCOS (2016) notes that, “*The existing surface current observations include moorings and land-based HF-radars are local, frequent, but limited in coverage. ... Satellite-based synthetic aperture radiometry (SAR) interferometry and range Doppler shift have recently demonstrated the capability to detect the surface current.*”

Application area	Precision (m s ⁻¹)	Horizontal resolution (km)	Revisit (Days)	Coverage	Stability
Surface ocean current (TSCV) Essential Climate Variable (ECV)	0.05	30	weekly	Global	Not Specified

Table 2.3. Total Surface Current Velocity measurement requirements for the GCOS ECV ‘ocean surface current’ (GCOS, 2016).



GCOS is concerned with the long-term climate record and thus a mission duration of at least five years is required (preferably ≥ 7 years) in order to planetary scale phenomena such as El Niño with timescales of 2-7 years (e.g. Trenberth and Hurrell, 1994; Cane, 2005; McPhaden et al., 2006, Godoi et al., 2019).

Ignoring orbit constrains and the impact of rain and calm seas, from these user needs the following generic user need for TSCV addressing many of the user needs described here is derived: SKIM should measure the TSCV with a combined standard uncertainty $\leq 0.15 \text{ m s}^{-1}$ (goal: $\leq 0.1 \text{ m s}^{-1}$) or 15% of the TSCV at a gridded resolution of 30 km with a mean revisit of ≤ 10 days at the equator. As a goal, the global mean TSCV uncertainty of 0.05 m s^{-1} for a 10 day mean TSCV product will meet GCOS requirements. In addition to support transport estimates, SKIM should provide measurements of Stokes drift with a combined standard uncertainty $\leq 0.02 \text{ m s}^{-1}$ (goal: $\leq 0.01 \text{ m s}^{-1}$) or 15% of the Stokes drift (whichever is greater) with a mean revisit of ≤ 10 days at the equator.

2.3.2 User Needs for Ocean Waves

The SKIM mission is designed to view the TSCV through the surface ocean waves as explained in Chapter 4 and Chapter 6 and essential wave measurements are specified for that purpose. A directional wave spectrum that is not 180° ambiguous is required in order to properly attribute the wave Doppler component to the proper direction.

Besides this specific SKIM need, wave measurements will be available to the community for direct applications. User needs for ocean waves have been reviewed by the marine meteorology community under the WMO-IOC Joint Commission on Oceanography Marine Meteorology (Swail et al., 2009, Ardhuin et al., 2019). User needs for the ECV for sea state are expressed by GCOS (2016) and WMO (2017) (Table 2.6). For the climate record, stable data sets are required that impose requirements the SKIM mission as reviewed by Ardhuin and Dodet (2019).

parameter	Precision	resolution (km)	Revisit	Coverage	Stability
Significant wave height:	0.1 m or 5% to 10%	25	3 hourly	Global	5 cm/decade
Mean direction	10°	Not determined	N.D.	Global	N.D.
Mean period	0.1 to 1 s	Not determined	N.D.	Global	N.D.

Table 2.4. Surface-wave measurement requirements for the GCOS ECV ‘ocean surface current’ (GCOS, 2016).

There are no explicit requirements for power spectral densities, in particular for the directional wave spectrum because there are, today, no measurements of the directional spectrum, with in situ instruments providing at best the first 5 Fourier components of the directional distribution at each frequency. However, from the requirements on the wave height, mean direction and mean frequencies it is possible to define associated requirements for the spectral range.

Figure 2.8 shows a global average of surface elevation Power Spectral Density (PSD), $E(f)$, and the associated PSDs for surface velocities, Stokes drift, and surface slopes. Because the high frequency part of the spectrum is in equilibrium with the local wind, it is generally possible to estimate high frequency properties, say above 0.4 Hz, from lower frequencies. As



a result, a 10% accuracy on the wave height can be achieved by resolving wavelengths from 30 to 500 m. The 2% to 6% (95% of the ocean) of the energy at wavelength longer than 500 m can be neglected in most oceanic conditions, and the 5 to 10% shorter than 30 m (95% of the ocean) can be recovered with 20% uncertainty from the energy at longer wavelengths.

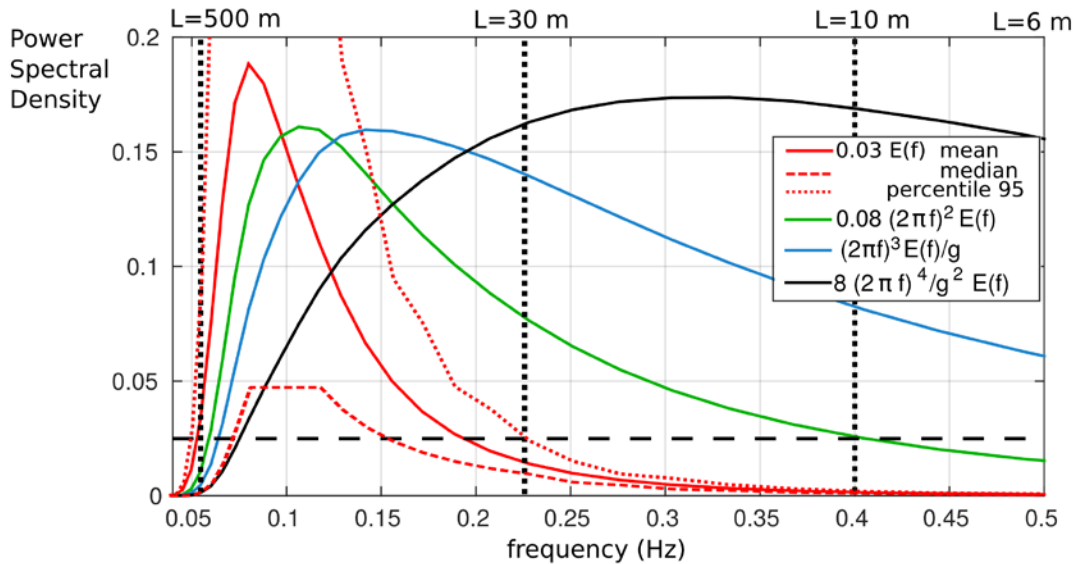


Figure 2.8. Global average over the year 2014 of normalised ocean wave spectra and associated properties. $E(f)$ is the surface elevation spectrum (red line) which is highly variable for $L > 30\text{m}$. When multiplied by $(2\pi f)$ to the power 2, 3 and 4 it gives the power spectral density of surface orbital velocities (green line), Stokes drift (blue line) and surface slopes (black line). (F. Ardhuin, LOPS)

Ignoring orbit constrains and the impact of rain and calm seas, from these user needs the following generic user need for waves is derived: SKIM should measure the directional wave spectrum with combined standard uncertainty of $\leq 30\text{ cm}$ or 10% (whichever is greater) with Significant wave height, H_s , between 1–25 m, and directional resolution $\leq 10^\circ$ in all directions for wavelengths of $\leq 30\text{--}500\text{ m}$. Measurements should be acquired simultaneously with TSCV with a mean revisit of ≤ 10 days at the equator.

2.3.3 User Needs for Nadir Altimetry

A nadir beam is included in the design of the SKIM mission that can act as a conventional synthetic aperture radar (SAR) altimeter. A performance equal to or better than the Jason class of altimeter is required if SKIM is to make a meaningful contribution to the altimeter sea level record. The key performance requirements are (Desjonquères, et al., 2010):

- Altimeter range: $\leq 1.7\text{ cm RMS}$ (goal at 1.5 cm) at 1 Hz sampling rate, for 2m H_s sea state, and a 11 dB sea surface backscatter coefficient
- Significant wave height (H_s): 10% or $\leq 40\text{ cm}$, whichever is greatest
- Wind speed: $\leq 1.5\text{ m s}^{-1}$

This allows SKIM to explore beyond geostrophy by comparing the TSCV and the conventional measure of geostrophic currents based on sea surface height measurements. In addition, it allows SKIM to monitor river and characteristics and explore the potential of Doppler measurements in that application domain.

2.4 Why SKIM?

Currents have been estimated routinely from space for 25 years using satellite altimetry – why do we need another satellite mission for the same purpose?

Because we do not have global data on the TSCV

The ocean surface current – in contact with the atmosphere – can only be measured directly through the motion of the sea surface. Ocean motion is precisely defined as the TSCV that is usually referred to as ‘surface current’. TSCV is connected to deeper ocean layers through turbulent mixing, and the convergent/divergent surface expressions of subduction and upwelling (that are also important connections from the surface to the layers below). It has an important role for all the Living Planet ocean challenges. Coastal HF-radar is able to provide TSCV measurements in some coastal regions, but there is no terrestrial technology available today to extend these measurements to provide global ocean coverage. SKIM provides that solution as a HF radar in space.

SKIM includes a nadir beam altimeter that will be used, in combination with other altimeters, to determine the geostrophic current. Figure 2.9 shows typical examples of estimates of surface currents from altimetry (in green) compared with other data sources, including altimetry-assimilating models (in black). The disagreement at all time-scales is discussed below in further detail. It should dispel any complacency on the perceived level of knowledge of the ocean-surface current in contrast to the general term ‘ocean current’.

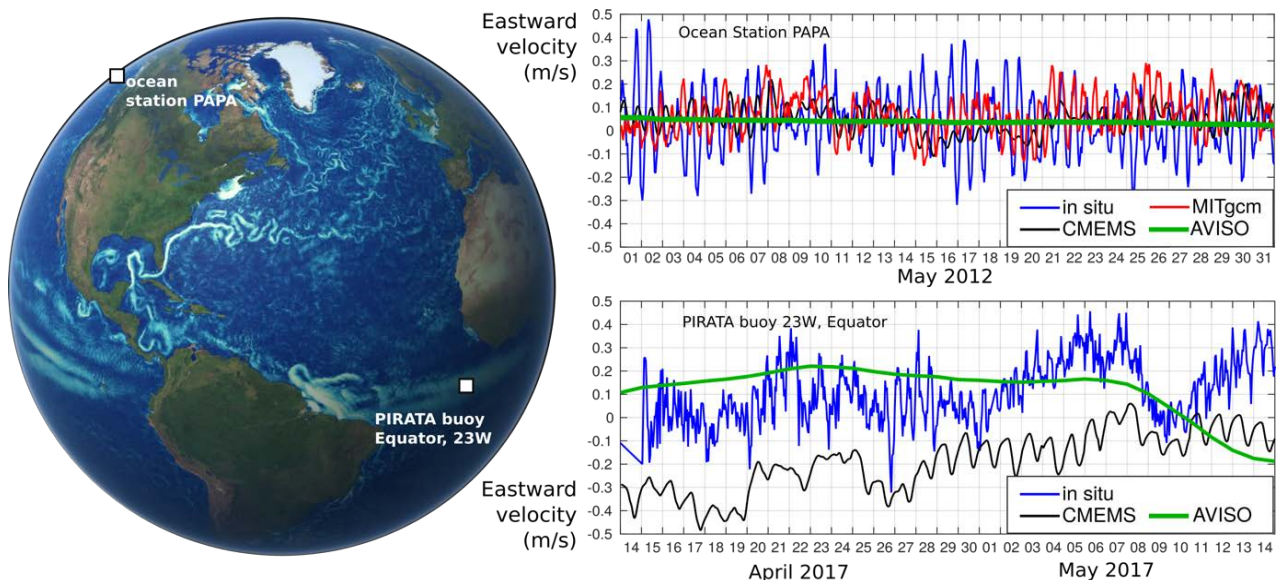


Figure 2.9. Time series of typical ocean conditions showing surface current speed (left) and time series of eastward current component (right), provided by the MITgcm 1.5 km resolution model, AVISO altimetry portal, CMEMS operational 1/12° global ocean model. The *in situ* data from the North Pacific Ocean location (Cronin et al., 2018) and equator (Bourles et al., 2008) are at 15 and 11 m depth, and show the importance of near-inertial motions and diurnal variability that is weakly captured in models and absent in altimetry. (LOPS)

Geostrophic currents and TSCV

As a matter of fact, satellite altimeters give access to a well-approximated surface current in very specific circumstances, and otherwise is a better representation of the subsurface current at depth, just like the atmospheric pressure gives an indication of the wind above the

atmospheric boundary layer. At large space and time scales, and away from the equator, sloping sea level is associated with a pressure gradient that is balanced by the Coriolis force associated to the current. This is the geostrophic balance, and the geostrophic current is the part of the velocity field that is in equilibrium with the pressure gradient. Deviations from this balance are termed ‘ageostrophic motions’ and are, among other effects, influenced by friction in boundary layers. The TSCV vector $U=(U_x, U_y)$ may thus be interpreted as the sum of a ‘geostrophic current’ $U_g=(U_{gx}, U_{gy})$, and the ‘ageostrophic component’. The approximation of the TSCV provided by a near-surface current meter is very different from altimetry-derived currents (Fig. 2.9) . The fact that the geostrophic current can only be a small part of the real current is obvious in time series from open ocean-surface current metres that are often dominated by near-inertial oscillations (Fig. 2.9). This demonstrates that measurements are urgently needed to extend the coverage of HF-radars to the open ocean.

A Grand Challenge in the Tropical Ocean

The Coriolis force goes to zero at the equator and it is not possible use satellite altimetry to derive geostrophic current in these regions. Instead the global array of drifting buoys are used together with sea surface temperature measurements from satellite radiometers (Rio and Santoleri, 2018). But this is far from an ideal solution.

Figure 2.10 shows a decade of ocean-surface current measurements from a variety of *in situ* data sources in the Tropical Atlantic Ocean. Because surface flows diverge away from the equator, even when drifters are deployed in that region, they are rapidly transported away towards the subtropics. While fixed moorings are present in the equatorial oceans, they are few in number and cannot adequately sample the geographic variability of the TSCV in those regions. Today’s *in situ* observing system only allow near-surface current measurements at 10 or 15 m depth, thanks to a few buoys in the tropical oceans, and less than four drifter measurement per year in a 30×30 km grid box within the equatorial ocean.

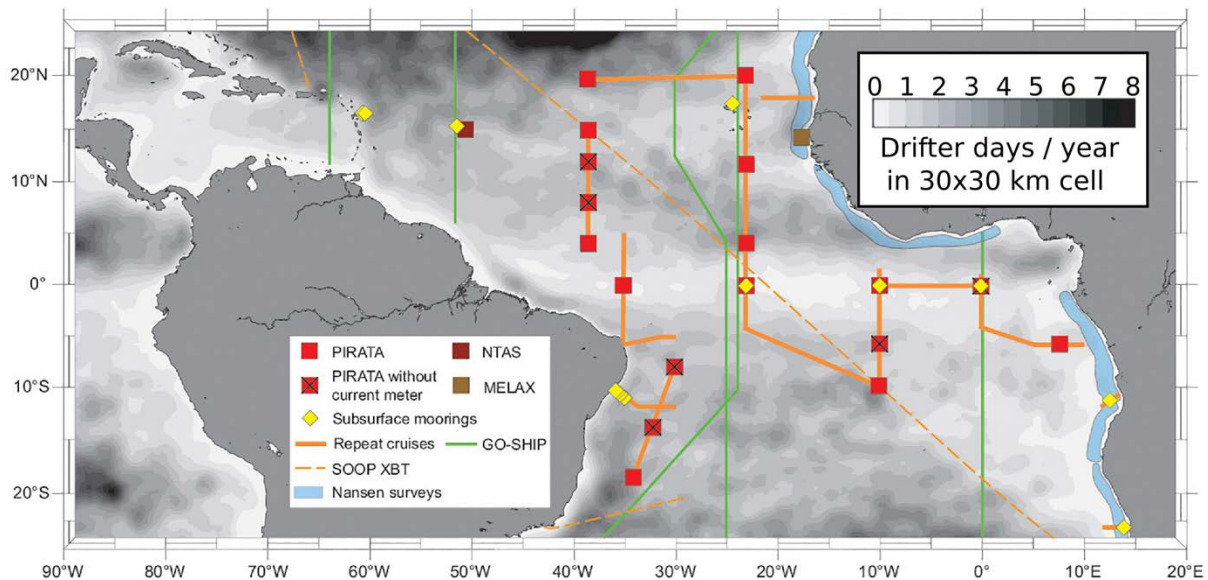


Figure 2.10. Summary of all observations in the Tropical Atlantic for a decade 1997–2017. The grey shading indicates the number of drifting buoy measurements per year in a 30×30 km square. A satellite mission such as SKIM would provide at least 60 measurements per year in each 30×30 km square. (G. Foltz, NOAA).



This sampling density is insufficient to resolve many oceanic processes such as the mean and seasonal circulation, the equatorial waves spectrum, and tropical instabilities. It is clear that there is a fundamental measurement challenge in the Tropical Atlantic Ocean (e.g. Cravatte et al., 2016) and indeed, all equatorial oceans (e.g. CLIVAR, 2018).

Having access to TSCV data is critical to progress our understanding of tropical ocean dynamics, including both atmosphere–ocean interaction and the strong connection between the ocean surface and interior. This can be uniquely and directly addressed by SKIM TSCV measurements. There are TSCV components that are uniquely accessible using SKIM Doppler velocity measurements that have important implications for scientific development and societal applications.

2.5 Unique Characteristics of TSCV

The TSCV is characterised by the co-existence of different flow patterns and phenomena that have a physical expression on the sea surface. These expressions are embedded in the surface roughness of the ocean surface that can be measured. The type and scales of the processes contributing to ocean surface currents are set out in Table 2.5.

Typical ocean process	Length Scale (L, km)	Velocity scale (U m s ⁻¹)	Adjustment Time scale (T)	Vertical scale (m)
Wind driven boundary layer	10 - 1000	0 - 0.5	Hours to weeks	O(10)
Orbital motion of surface waves	0.01 - 1 ¹	0 - 2	Hours to weeks	O(30)
Stokes Drift	10 - 1000	0 - 0.5	Hours to week	O(5)
Langmuir	0.01 – 0.1	0 - 0.5	Hours	O(10)
Internal waves	1 - 20	0.05 - 2.5	Hours to days	O(100)
Equatorial currents	100 - 5000	0 - 2	Days to seasons	O(50)
Western boundary currents	10 - 500	0.1 - 2	3 days to seasons	O(500)
Tropical instability waves	100 - 1000	0 - 1	Month	O(100)
Large eddies, fronts	10 - 100	0.1 - 2.5	Days to weeks	O(500)
Coastal upwelling	1 - 20	0 - 0.5	Several days	O(100)
Tidal currents (on shelf)	1 - 500	0 - 5	Hourly	200 m
Inertial currents	10 - 200	0 - 0.3	1 – 5 days (coherence > period)	O(100m)
Kelvin waves				
- coastal trapped	~ 30	~ 2	Days to weeks	Full Depth
- equatorial trapped	~ 250	2.8	Days to weeks	Full Depth
Rosby waves	> 200	0.05 – 0.2	Monthly to seasonal	O(1000)
Local coastal currents	1 - 30	0.1 - >>5	Hours	O(1 m – full depth)
Surf zone currents	0.05 - 2	0.1 - 3	Hours to days	Full depth (0-10 m)

Table 2.5. Type and scale factors of typical processes contributing to ocean surface currents. Process features that will be challenging to fully resolve with SKIM are highlighted grey text. All other scales will be accessible by SKIM measurements.

A fundamental interface of the Earth system is between the ocean and the atmosphere through which all exchange of heat, momentum, gas and mass must be accomplished. On either side of this interface boundary layers are present, in which friction and mixing processes dominate where motion is not primarily horizontal, but also involves vertical

¹ The orbital wave motions oscillate at the scale of the wavelength (0.01 to 1 km – that can be resolved using SKIM) but their variance is coherent at scales of 10 to 1000 km.

exchange. In the ocean, this boundary layer typically has a dimension of the order of 10 m, characterised by a vertically homogeneous slab that moves horizontally (Price et al., 1986). However, the actively mixed layer is variable due to diurnal and seasonal stratification (Fig. 2.11), freshwater from rain and land run-off, and can be shallower than 1 m.

The TSCV, denoted as vector U , has a markedly different impact on long-term drift behaviour compared to its usually defined components, the geostrophic current U_g , derived from altimetry, the mean wind-driven current U_{Ek} and the extremely important wave-induced Stokes drift, U_s (OOPC 2017). The long-term average velocity of particles at the ocean surface is well described by the sum of the three terms, $U \approx U_g + U_{Ek} + U_s$. Each of the three terms plays an important and specific role (Fig. 2.10). It is the ageostrophic motions (i.e. those not in balance with the pressure gradients), in this case $U_{Ek} + U_s$, that are important for surface convergence, and thus the aggregation of floating material such as plastic litter, but also define cross-shelf exchanges, including the export of carbon from land to the deep ocean.

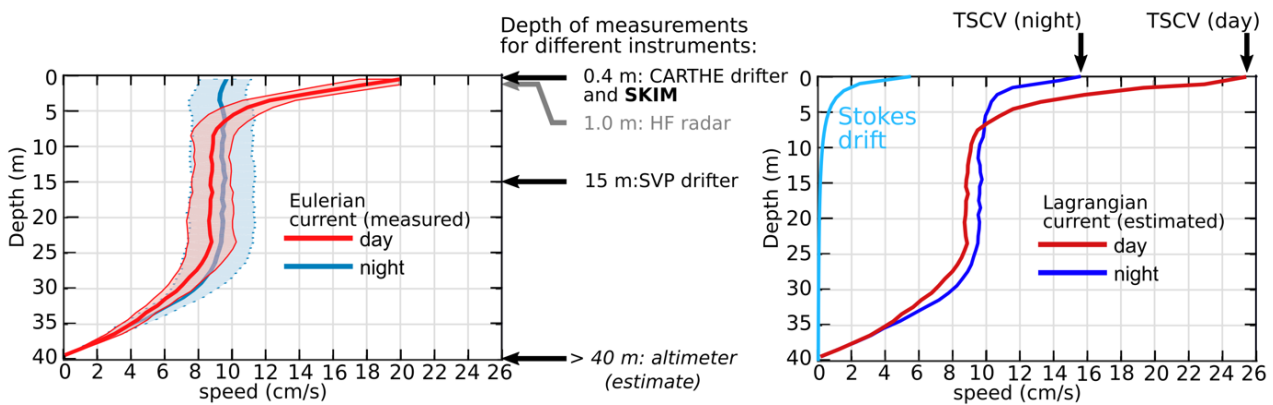


Figure 2.11. (left) Daytime and night-time average vertical profiles of the Eulerian mean velocity U_E and (right) profiles of the Lagrangian mean velocity, that is the sum of U_E and Stokes. Measurements of U_E and Stokes were obtained from a surface acoustic Doppler current profiler attached to a 50-m drogued drifter. The data collected around 26N 36W in August–September 2012 are analysed by Sutherland et al. (2016). (L. Marié, LOPS)

Owing to the properties of the mixing layer, the TSCV may be representative of a layer that varies in thickness between 0.10 m and tens of meters depending on stratification, and it has been very difficult to measure routinely. Stratification of the ocean refers to its density separation into layers owing to the dependence of the density on temperature, salinity and pressure. Stratification can lead to effective de-coupling of the upper-ocean water from that at depth (e.g. during strong diurnal heating or shallow halocline conditions leading to a ‘slippery’ shallow layer where water at the surface can flow freely over that at depth (see Kudryavtsev and Soloviev, 1990). Only the measurements in the top few metres of the ocean, such as provided by un-drogued and shallow-drogued drifters (e.g. Lumpkin et al., 2017) that follow the surface-water motion (Novelli et al., 2017) or coastal HF-radars, can be representative of the surface mixed layer in most conditions, providing an estimate of the TSCV.

Alternative measurement techniques, at a fixed position or with drifting instruments drogued below the depth where the wave-induced Stokes drift U_s becomes negligible, measure the Eulerian mean flow U_E , i.e. the total flow $U - U_s$ (Jenkins, 1989, Niiler et al., 1995). By measuring the sea-level gradients, altimeter measurements miss the difference

between the geostrophic current that often dominates below the mixed layer: the difference between the geostrophic current that often dominates below the mixed layer and the TSCV is 25 cm s^{-1} in the daytime case shown in Fig. 2.11.

2.5.1 Stokes Drift and Waves

SKIM will be the first satellite mission to provide global repeat coverage measurements of Stokes drift every few days.

Waves dominate the surface velocity field with oscillations of a few metres per second and wavelengths generally from a few metres to 500 m. These oscillations nearly cancel, leaving a residual horizontal velocity known as the Stokes drift. (e.g. Fig. 2.10). At the surface, the Stokes velocity vector U_S is one of the sub-variables of the TSCV (OOPC, 2017), transporting floating material with a typical velocity of 10 cm s^{-1} . Most of the Stokes drift comes from wavelengths between 5 m and 60 m that are not resolved by today's routine wave measurements from satellites and can only be diagnosed indirectly. As a result, there are currently no measurement of Stokes drift in the open ocean (Ardhuin et al., 2019a). The Stokes drift is only significant over a depth that is a small fraction of the wavelength, and it does not transport properties mixed on a larger vertical scale, such as heat or carbon (Hasselmann 1970, Raschle and Ardhuin 2009). Hence U_S can be neglected in the long-term transports of water-mass properties at mid-latitudes (e.g. Lozier et al., 2019). Knowledge of U_S is particularly important to explain properly the exchange between the upper ocean and the deeper layers (Li et al., 2016), which, for example, is relevant for the ventilation of the Southern Ocean and strong but variable uptake of CO_2 in that region (Le Quere et al., 2018).

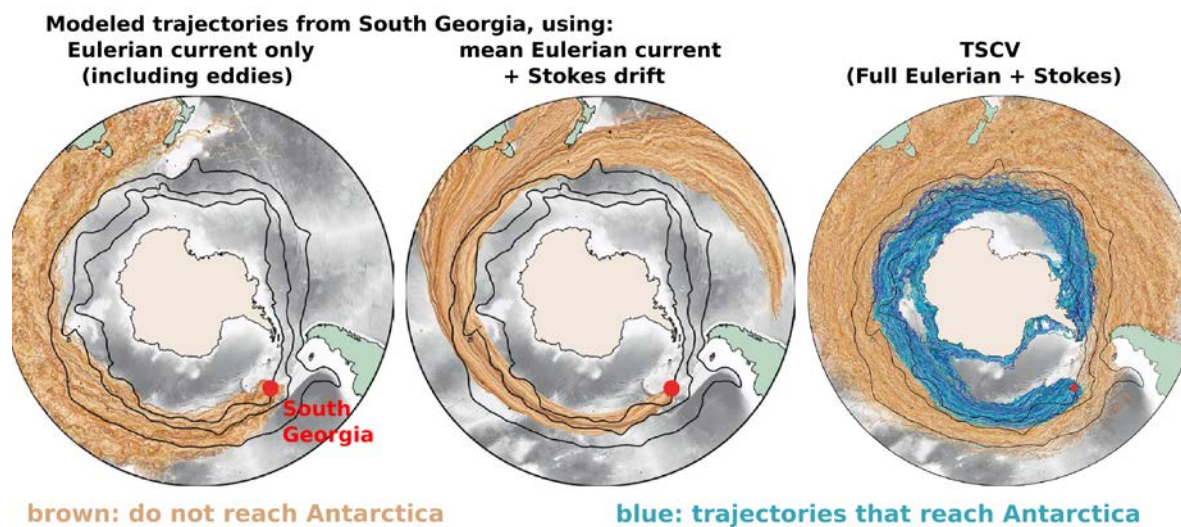


Figure 2.12. Simulated trajectories of floating material leaving South Georgia, including Eulerian currents from US Navy HYCOM $1/12^\circ$ resolution model, and/or Stokes drift from LOPS $1/2^\circ$ WAVEWATCH III wave model). As analysed by Fraser et al. (2018) connecting South Georgia to West Antarctica requires both components of the TSCV. (E. van Sebille, Utrecht University)

However, Stokes drift is extremely important to explain the connectivity of ecosystems and the transport of all material at the surface of the ocean. Stokes drift is the *exact* measurement that is required to monitor the trajectory and fate of oil/chemical spills, marine plastic debris and for maritime search and rescue operations. Application of Stokes drift by dedicated marine pollution and search and rescue models would have a significant impact on the

successful management of such disasters. Recently it has been shown that Stokes drift allows material to cross the Southern Ocean Polar Front, against the wind-driven transport. This was discovered recently by Fraser et al. (2018), using genetic analysis of kelp rafts found on Antarctic Peninsula shores: the kelp does not grow there but it originates in South Georgia (Fig. 2.12). Because kelp rafts are home to a wide range of marine species, this finding has important implications for biodiversity:

“Antarctica’s long-standing ecological differences have been the result of environmental extremes that have precluded the establishment of temperate-adapted taxa, but such taxa nonetheless frequently disperse to the region. Global warming thus has the potential to allow the establishment of diverse new species –including keystone kelps that would drastically alter ecosystem dynamics –even without anthropogenic introductions.” (Fraser et al., 2018).

It is thus impossible to understand ocean biodiversity without a full knowledge of the TSCV including Stokes drift.

In the presence of waves, it is useful to separate the TSCV in a quasi-Eulerian current (as measured by a fixed current-metre located below the wave troughs) and the Stokes drift, the average motion due to waves alone (Jenkins, 1989). The vertical profile of the quasi-Eulerian current, its magnitude and surface angle, will depart from the simplified theory of Ekman (1905). In particular, the surface angle can range between 45 and 80°, depending on wind speed and stratification. As a result, the drift of floating material at the surface has very different patterns when one considers only geostrophic currents, with very weak convergence, Ekman currents, Stokes drift or the combination of the three (Fig. 2.13).

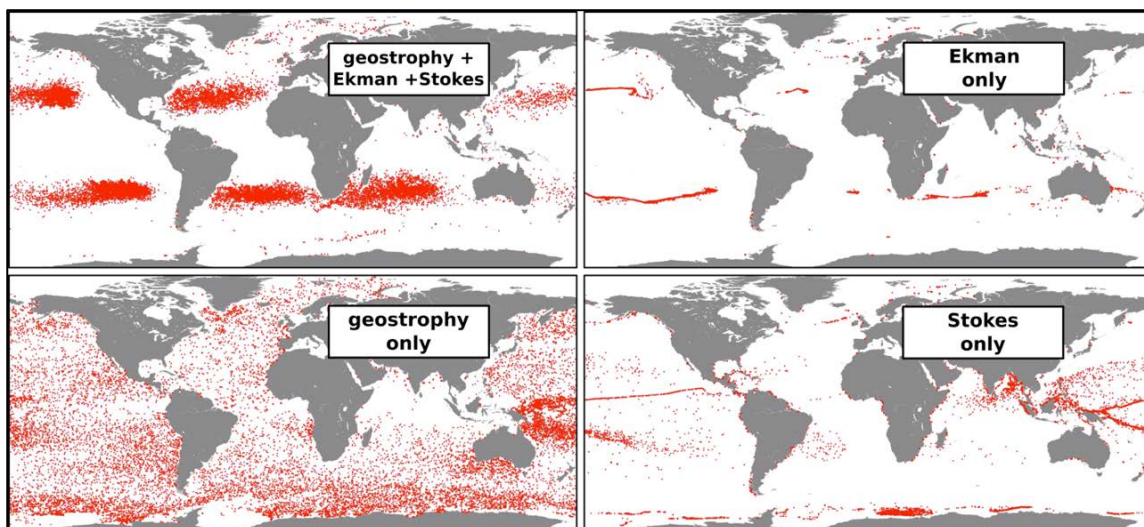


Figure 2.13. Numerical simulation of the distributions of surface particles (for example representing marine plastic debris) after 10 years, starting from a uniform distribution. The four panels show the effect of three components of the surface current combined, or their effect taken separately. (Adapted from Onink et al., 2019)

The Stokes drift has a direct contribution to the TSCV, but also a very strong influence on the other component by influencing mixing (Ardhuin and Jenkins 2006, Belcher et al., 2012).

2.6 Measuring TSCV Globally: Estimating Currents from Satellite Observations of Sea Level

2.6.1 Effective Resolution of Sea-level Measurement

Due to the dominant geostrophic balance at large scales and away from the equator, it is customary to estimate the surface geostrophic current from a combination of satellite altimetry sea level and gravimetry measurements (Rio et al., 2014). Altimetric measurements of surface-geostrophic currents are a proven technology that is part of the global ocean-observing system. Satellite altimetry provides a combination of operational data in low inclination 66° orbits (e.g. from the Jason satellites), complemented by polar-orbit satellites including Copernicus Sentinel-3, CryoSat and SARAL-AltiKa.

Satellite altimeters measure Sea Surface Height Anomalies (SSHA) relative to a mean dynamic topography, or sea level relative to the geoid (Bruinsma et al., 2013).

A first limitation of altimetry is its nadir-only measurement, hence having to rely on the slow evolution of the ocean at large scales to be able to measure its variability in space and time. Ballarotta et al. (2018) investigated the effective spatial and temporal resolution of sea-surface height maps derived from three altimeters (Fig. 2.14). At mid-to-high latitudes the temporal scales of these products are between 14- and 28-day periods, coherent with the temporal correlation scales applied in the mapping process. As a result, the faster and smaller mesoscale structures, in particular in the North Atlantic and Arctic, are escaping the watch of the altimetry constellation. Models assimilating along-track SSHA (e.g. ECCO, Forget et al., 2015; CMEMS, Lellouche et al., 2018) can improve on the resolution of the data alone but the dynamics of the along-track unobserved features ($L < 100$ km) is not controlled, and the dynamics between tracks is not well constrained. A swath-based solution such as SKIM with a mean revisit of ≤ 10 days in Equatorial regions would be a dramatic improvement on the capability provided by altimetry today.

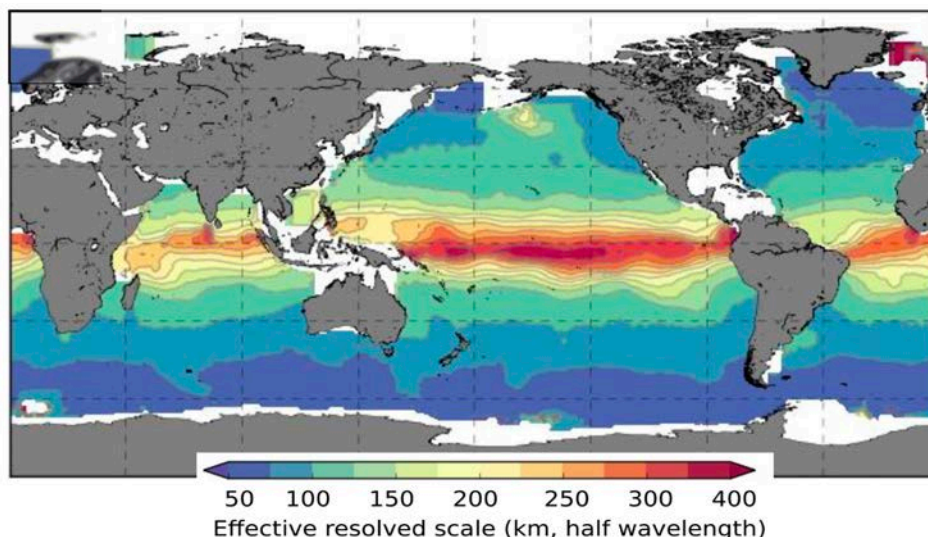


Figure 2.14. Effective spatial resolution in km of the DUACS-DT2018 3-altimeter multimission maps for the global ocean. The resolution ranges from 50 km at high latitudes to 400 km near the equator, with a mean resolution at mid-latitude near 100 km. Resolution here is defined as half the resolved wavelength. (M. Ballarotta, CLS).

2.6.2 Challenges when Estimating Ocean Currents from Sea Level Measurements

Unlike satellite altimetry, the TSCV includes ageostrophic components of the ocean surface current that often dominate at the surface. Among them are forced motions such as the strong near-inertial oscillations driven by the wind observed at Ocean Station PAPA (Fig. 2.9). Internal ocean or coupled ocean–atmosphere instabilities cannot be predicted if the relevant component of the ocean velocity field is not observed. This is particularly a problem at the equator where even state-of-the-art numerical models cannot reproduce the variability at monthly time scales (Foltz et al., 2019) as shown in Fig. 2.9.

2.6.3 Quantifying the Observation Gap

Because no observations are available, how much of the TSCV is contained in the geostrophic current can only be estimated with an analysis of state-of-the-art numerical models. A reference simulation of the Eulerian current in the full global ocean at 1.5 km resolution (MITgcm) is able to resolve all the spatial scales at which geostrophy is relevant, and a large part of the other component of the current.

Torres et al., (2018) have shown that current velocities can exceed 50 cm s^{-1} in all the large current systems and on tide-dominated continental shelves (Fig. 2.15, left). The fraction of the kinetic energy that is explained by the geostrophic balance is above 50% only in the large boundary current and frontal current systems such as the Gulf Stream and the Antarctic Circumpolar Current (Fig. 2.15, centre), even when considering daily-averaged values.

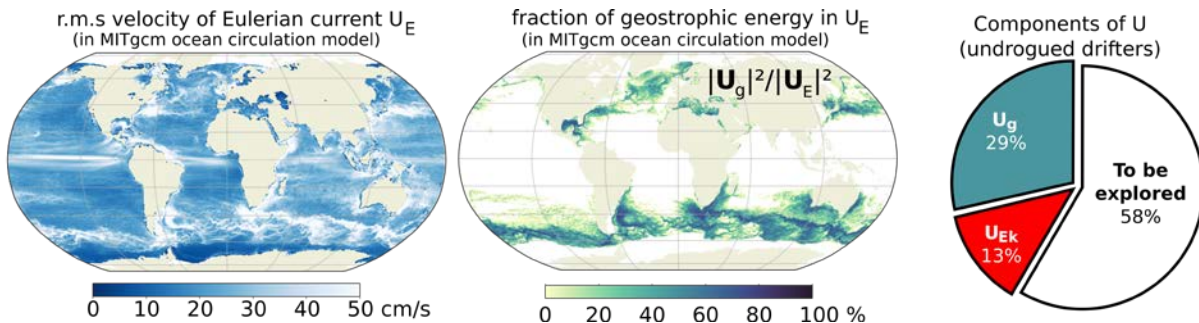


Figure 2.15. Left: Mean TSCV magnitude, Centre: mean fraction of kinetic energy associated with the geostrophic current U_g , based on a global ocean simulation at 1.5 km resolution (Rocha et al., 2016). Right: pie-chart showing the fraction of kinetic energy, measured by drifters that is explained by satellite derived U_g and U_{Ek} . (A. Ponte, LOPS and H. Etienne, CLS)

It is possible to get a proxy for the TSCV, U , by considering 20 years of *in situ* un-drogued SVP-type drifter data, and correcting for the direct effect of the wind on their velocity (LOPS, 2019). Using altimeter-derived maps of U_g , and an empirical model to estimate U_{Ek} , the residual vector velocity $U - U_g - U_{Ek}$ is relatively weak in the large currents, but accounts for 58% of the surface-ocean kinetic energy (Fig. 2.15, right). Most of this residual has a coherence time larger than three days and can be captured with a satellite measuring surface velocity with such a revisit time. This long coherence is due to processes such as tides and near-inertial oscillations (e.g. Kim and Korso, 2013), but it is also due to the part of the geostrophic current that is not resolved in space or time by today’s satellite altimetry constellation.

The relatively lower fraction of non-geostrophic current in the drifter data is clear evidence for how little we know about the TSCV and how uncertain models are. A recent statistical comparison of the Torres et al. (2018) model with drifter data shows differences of a factor of two in the magnitude of different processes, the model overestimating internal waves, but underestimating wind-forced near-inertial motions (Yu et al., 2019, see also Fig. 2.9).

In summary, 50–75% of the kinetic energy of the Eulerian current is not captured by satellite altimetry, nor by any other observation system, and begs to be explored using SKIM.

2.7 Innovation and Advancement of European Earth Observation Capability: Inventing Doppler Oceanography from Space

There is no mission flying today that can estimate the TSCV with quasi-global coverage and regular repeat sampling.

Instead of ocean topography inferring geostrophic flows from ocean topography, one can measure surface-ocean velocities directly. Based on Envisat C-band synthetic aperture radar (SAR), and more recently Sentinel-1 SAR imagers, ESA (2015b) notes that the capability to measure and interpret ocean geophysical Doppler velocities was a significant achievement of the past decade (Chapron et al., 2005). It was made possible by the massive acquisition of data from Envisat ASAR instrument, followed by the analysis of the geophysical part of the Doppler centroid. In particular it was recognised that ocean waves are the source of a large, about 2 m s^{-1} , ‘wave Doppler’ (U_{WD}) contribution to the geophysical velocity (Chapron et al., 2005; Martin et al., 2016; Nouguier et al., 2018).

The feasibility of such measurements was demonstrated at global scales with Envisat Advance SAR (ASAR): the Doppler centroid provides a measurement of a mean ocean-surface velocity, in the line-of-sight, as detected by a radar. Although noisier, this is equivalent to across-track interferometry (ATI, Romeiser et al., 2014). Collard et al., (2008) demonstrated measurements of equatorial currents using Doppler centroid estimates from Envisat ASAR wave-mode.

The possibility of using existing C-band SAR systems led to a rapid development of methods for estimating U_{WD} using a wind-based proxy called C-DOP (Mouche et al., 2008, Hansen et al., 2011) and first scientific applications (Rouault et al., 2010). This development was considerably reduced by the end of Envisat in 2012 and the lack of routine SAR data until the launch of Copernicus Sentinel-1 in 2014.

Today, acquisitions by Copernicus Sentinel-1 operating in wave mode over the open ocean provide zonal maps of the radial line-of-sight TSCV near-zonal component about every three months at a resolution of about 100 km. Three months averaging is used to reduce noise from individual measurements. From these measurements, seasonal maps of the TSCV at 100 km in nearly zonal directions are obtained with unprecedented accuracy. These data provide a view that is consistent with a 20-year drifter climatology, allowing a first investigation of interannual variability. A gyroscope-based pointing solution (OceanDataLab, 2019) and a novel analysis of wave resolved SAR images down to 40 m wavelength (Li et al., 2019) were used to estimate both the non-geophysical Doppler and U_{WD} accurately. Both developments will be used for SKIM and will contribute directly to the accuracy of the SKIM products. Sentinel-1, however, is limited to only the line-of-sight

component of TSCV, that may give some estimate of the vector when combining ascending and descending passes (Fig. 2.16), but it is unable to provide an accurate estimate of the meridional component that contains the divergence away from the equator. These data fall short of user needs for TSCV identified earlier.

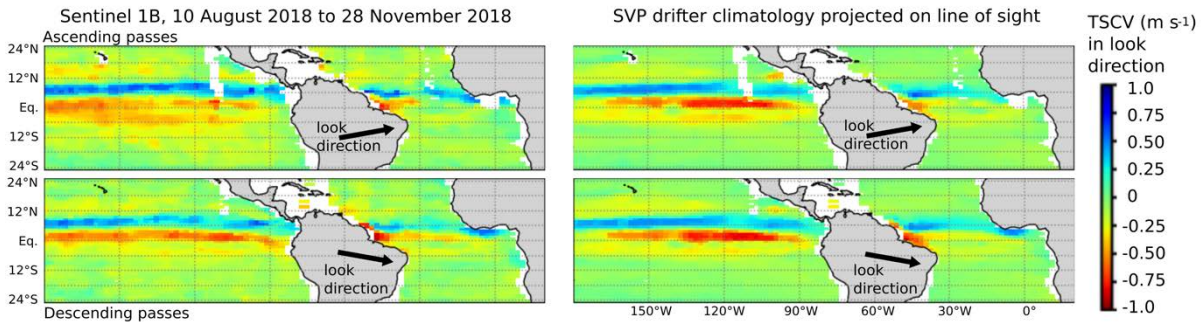


Figure 2.16. Left: mean radial line-of-sight TSCV for August–November 2018 using wave-mode data from Copernicus Sentinel-1B (SAR scenes of 20×20 km every 100 km). Right: climatology of SVP drifter velocity derived from 20years of data projected on the same look direction (OceanDataLab).

Because applications require the full velocity vector, from drift to divergence and atmosphere–ocean exchanges, efforts have been devoted to developing techniques for vector measurements. These include squinted ATI SARs (Buck, 2005) on which the Wavemill and SEASTAR Earth Explorer proposals were based (Buck et al., 2011) and for which an airborne instrument was built and demonstrated (Martin et al., 2016, 2018). The alternative possibility of the Doppler Centroid Anomaly (DCA) technique has led to specifically designed airborne instruments (Rodriguez et al., 2018) and future satellite concepts (Bourassa et al., 2016; Ardhuin et al., 2018; Rodriguez 2018; Chelton et al., 2019). ATI and DCA approaches are clearly complementary for high resolution versus global monitoring, as concluded at the 2018 Doppler Oceanography from Space community building workshop (Ardhuin et al., 2019).

Given the limited duty cycle of a single SAR system and the necessity for additional elevation and azimuth views necessary to obtain both components of TSCV, the use of a scanning real-aperture radar appears as the only feasible option today for a global mapping capability with a revisit that resolves the coherence time scale of the non-geostrophic current.

In terms of advancing European radar technology to measure surface waves, the recently launched CFOSat missions carries the SWIM radar instrument (Hauser et al., 2017). It uses an innovative rotating Ku-band radar approach to measure ocean-surface waves at many different azimuths. However, SWIM is not doppler enabled and cannot provide estimates of the TSCV.

SKIM, as a fast-track Explorer mission, will develop the SAR imager Doppler approach of Chapron et al. (2005) further by extending the rotating beam concept of CFOSat’s SWIM in the form of a Doppler wave-current scatterometer concept to uniquely, and for the first time, measure the TSCV and its component Stokes drift with a quasi-synoptic, regular, repeat coverage over the global ocean.

As a fast track mission, SKIM builds directly on and significantly advances European Earth observation development and understanding to implement a new class of Doppler wave-current scatterometer that can directly measure the TSCV.



Such a mission would initiate routine Doppler oceanography from space with enormous potential for subsequent missions in an operational context.

2.8 TSCV and Numerical Modelling

Today, circulation models are capable of simulating ocean currents in response to atmospheric wind, tides, and buoyancy forcing. A question remains: How well do such simulations represent reality?

Their full validity in dynamical regimes readily accessible through SKIM, has never been tested except at a few locations (e.g. Scott et al., 2010) or using the sparse global Surface Velocity Program drifter array (Elipot et al., 2016). A synthesis of the Copernicus Marine Environmental Monitoring System (CMEMS) model performance on surface current (see example in the Tropical Atlantic in Fig. 2.9) was made by Rémy et al. (2019). For the mean error, the modelled zonal current is typically within 5 cm s^{-1} of the SVP drifter data, but up to 40 cm s^{-1} along the equator for the western half of the Pacific. Random errors typically lead to 60 km distances of three-day drift end-points, corresponding to a constant 23 cm s^{-1} error over 3 days.

Providing high-resolution maps of the surface current, SKIM will reveal details that will help test theories and models, involving especially the wind-driven currents and wave-driven drift and mixing. On the other hand, model results will also be essential for interpreting SKIM data that are being sampled irregularly for some of the relevant time scales, with ‘entangled’ contributions of rapid physical processes in snapshots measured at each satellite pass. Artificial intelligence or machine learning can be used to identify patterns and statistical descriptions embedded in datasets with applications to Earth-system science that will certainly emerge in unforeseen areas. Essential aspects here involve: response of the upper ocean to wind forcing, the vertical structure of resulting flow fields, the dissipation of wind energy, resulting mixing and transports and their convergences.

Of particular importance is the revolution offered by fully coupled ocean–atmosphere model systems from climate to weather forecasting time scales (e.g. Williams et al., 2019). It is the TSCV and wave spectrum that are most relevant to such systems because wind–wave–current interaction governs, to first order, all exchanges of heat, gas, mass and momentum between the atmosphere and the ocean. A particular new aspect of modelling involve Stokes drifts and the impact on momentum and matter transports (Belcher et al., 2012). While global NOP traditionally were not coupled to surface-wave models, great efforts have been made recently towards a consistent ocean–wave–atmosphere coupling (Harris 2018, Lemarié et al., 2015, 2019, Beljaars et al., 2017), also including sea ice (Boutin et al., 2019). Respective parameterisations show success with respect to improving tracer fields and transport characteristics. However, only very limited tests could be done owing to the lack of relevant observations. For the first time in the history of oceanography and ocean modelling SKIM will supply these observations and thus will allow for further improvement of existing parameterisation. This is expected to lead to a new modelling framework for ocean and coupled climate models.

Models are usually being used alone or in combination with observations to study ocean or environmental processes and mechanisms as well as to predict changes. However, they can also be improved by combining them with the observations in a formal sense through data

assimilation. SKIM data will be assimilated into the models and will thus improve answers to ESA’s Living Planet challenges.

Today, significant incremental progress has been made in ocean forecasting (e.g. Schiller et al., 2015) with the inclusion of tides, improved surface forcing/surface fields and waves/current interactions and many models stand ready to assimilate wave-current data such as that from SKIM (e.g. Tonani et al., 2015, Chassignet and Sandery, 2013, Villas Bôas et al., 2019). Satellite data are being assimilated on a regular basis, including sea surface temperature, ocean colour and, particularly, altimetry – providing a dynamical pressure boundary condition. SKIM data would be entirely complementary by providing a surface layer horizontal velocity field. Impacts have to be determined, though, as this type of data were never assimilated before. To assimilate Stokes drift data requires further developments before the full potential can be inferred. We envision that along with the next generation of ocean models containing active Stokes drift modules, also the assimilation capabilities of these models will be extended. SKIM data will be an essential driver and benefit to such an evolution.

Given the acute responsibility of teams working in extremely challenging situations such as oil, chemical spill or harmful algal bloom response, marine search and rescue activities (where TSCV estimates are a critical input for success) access to regular repeat-coverage TSCV is essential. Figure 2.17 shows the progress envisaged 30 years ago in climate models for integrating a dedicated ocean-wave model (Hasselmann, 1990), which is now a reality for some of the climate models used in the IPCC AR6.

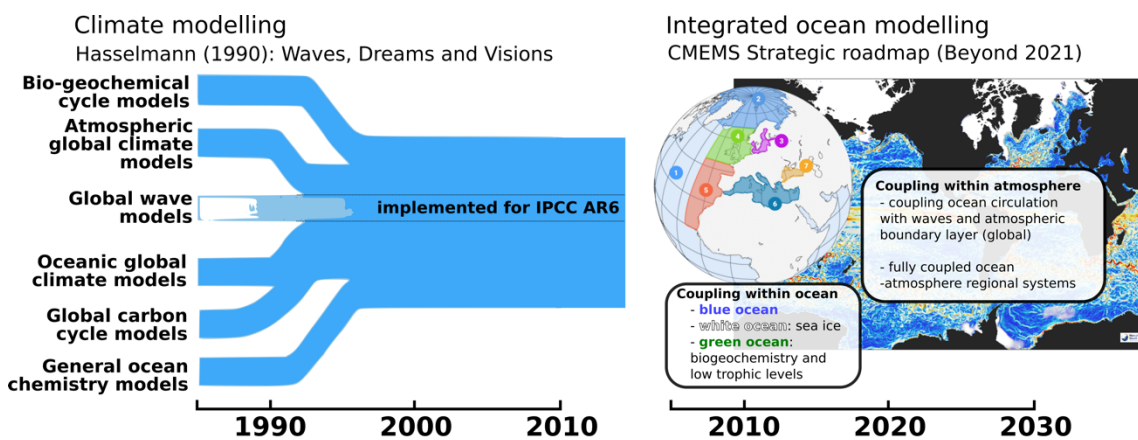


Figure 2.17. Left climate model integration over the past 30 years to (right) the development of operational integrated ocean modelling system (CMEMS). The steady increase in the resolution of models requires a strong dynamic coupling of ocean and atmosphere, via the TSCV for the momentum and mechanical energy equations. (After K. Hasselmann, University of Hamburg, and CMEMS)

The same type of effort, after combining biogeochemistry and sea ice with ocean circulation, is taking place in the Copernicus Marine Environment Monitoring Service. In that context, given the higher resolution (CMEMS will operate a 3-km global ocean model by 2025), a proper representation of surface layer processes is much more critical (e.g. Renault et al., 2017, 2019). Ocean–atmosphere coupling, including TSCV, is one of the major research and development efforts both for CMEMS and ECMWF because it is critical for both the oceanic and atmospheric dynamics. Data assimilation for coupled systems is one particular area of



intense research, and TSCV data, when available, would be a key variable to control the state of the coupled model. SKIM will certainly accelerate and contribute to these endeavours in a significant capacity.

2.8.1 The Scientific Delta of SKIM

Providing direct estimates of mesoscale TSCV at space and time scales less than 100 km and for three-ten days has great potential for validating, improving (via data assimilation) and, controlling the quality of NOP forecasts of ocean-surface currents. As noted by Schiller et al (2016) representing new scientific challenges for the international Global Ocean Data Assimilation Experiment (GODAE) OceanView user community: “*The predictive capability of the [ocean] forecast systems could, already be limited by our ability to initialize (constrain) errors with the observational coverage. Constellations of 3–4 satellite altimeters resolve a useful fraction of the variance of the sea surface height, but it may be that swath altimeters, or fine-resolution surface currents based on the matching of drifting patterns within images, could provide significantly more information on the near-surface mesoscale currents.*” SKIM TSCV measurements are designed to address this exact user need. Furthermore, since SKIM has a wide swath, it has the capacity to bring a significant impact to our integrated view of the Earth that would otherwise require multiple satellites.

SKIM will bring a unique and significant scientific and technical delta compared to the current international capability: existing Earth observation systems rely on constraining assumptions (geostrophic and Ekman balances), that do not hold for all scales of motion and in specific regions, and thus only provide one portion of the TSCV field. As shown by Fig. 2.9 and Fig. 2.12, this cannot be sufficient for many applications. Ocean-based alternatives are limited by their cost including logistics. In situ sensors are very sparse, and unable to resolve the required space and time scales. Many operational agencies and research institutions have invested in the deployment of HF radars along the coast. Their measurement coverage is limited to about 300 km from the shore.

On average data from today’s altimeter constellation explains only 29% of the variance of TSCV estimated from un-drogued drifters (Fig. 2.15). Where available, HF radars are reducing search and rescue areas by a factor 3 (Futch and Allen, 2019) in the coastal zones. We expect a similar reduction in 3-day drift prediction error globally, from 60 km with state-of-the-art models (Remy et al., 2019) to under 40 km for 70% of the world ocean. SKIM will also decompose the TSCV in Stokes drift and Eulerian currents, providing an estimate of the relevant velocity scales in the mixing layer.

SKIM will be the first satellite mission to provide wide-swath Doppler measurements that can directly retrieve the global ocean-surface current at scales of about 30 km every few days. SKIM, as our ‘HF-radar in space’, will directly address one of the most challenging and fundamental questions in modern oceanography and marine meteorology:

How do the kinematics and dynamics of the ocean TSCV influence the integrated Earth system at the ocean–atmosphere interface?

2.8.2 Complementarity

SKIM measurements of the TSCV are highly complementary (and certainly do not replace) satellite altimetry. SKIM will extend the coastal HF-radar network, with ground-based systems providing sub-hourly monitoring of rapidly evolving coastal processes in regions of particular interest, to all oceans up to a latitude of 83°N.

The measurement of TSCV, because they are representative of the ice drift or a well-defined mixing layer, are complementary to measurement of all ocean properties for which transport is important, this includes sea-ice concentration and thickness, sea-surface temperature, sea-surface salinity, ocean colour and associated constituents of sea water (suspended material, phytoplankton classes etc.), ocean vector-winds and the associated work of the wind on the TSCV, which is a major source of energy for ocean circulation. In this respect, the contemporaneous measurement by MetOp-SG(1B) and SKIM will be unique, providing the means to prepare for future Doppler scatterometer missions by exploring the sensitivity of SKIM Doppler and cross-polarised MetOp-SG(1B) scatterometer (SCA) data in high wind (Mouche et al., 2012, 2017) and extremely low-wind conditions.

Other measurements can also greatly benefit from, and contribute to, the SKIM mission, in particular, the separation of rapid processes entangled in single-pass measurements. It is expected that SKIM will fly at the same time as when wide-swath altimetry is available from SWOT (Morrow et al., 2019). The combination of TSCV and sea-surface height across a swath would be a truly unique dataset for the analysis of the complex interactions of balanced (i.e. geostrophic) and unbalanced (internal waves, near-inertial oscillations) motions.

2.9 Timeliness

The rapidly evolving biodiversity and climate crises, including the opening up of the Arctic Ocean, are calling for rapid action. SKIM will provide unique measurements of TSCV that address a long-standing and embarrassing observational gap. For every accident at sea, including recent losses of commercial airplanes or major environmental crisis (oil spills, marine plastic debris and the garbage patches, ecosystems and fisheries protection etc) it should be possible to track debris back to a source. Yet, disappointing performance regarding radioactive traces and debris from the Great East Japan tsunami reveal how little is known about surface drift beyond climatology, and how inadequate are, very often, today's numerical ocean models right at the surface (Ollitrault et al., 2010, Maximenko et al., 2018). TSCV data is thus urgently needed and SKIM can deliver this data.

The joint analysis of MetOp-SG(1B) and SKIM would be extremely beneficial to both missions. SKIM can produce useful data even in the absence of MetOp-SG(1B), although with a reduced performance.

The SWOT mission is planned for launch in 2021. It is possible that its three-year life may get extended, in which case SKIM, with a launch in 2025, could collect data at the same time as SWOT, providing a unique dataset. As discussed in Section 2.6, SKIM alone, but even more so SKIM in combination with MetOp-SG(1B) and/or SWOT, would provide a unique dataset for the validation of the new generation of coupled ocean–wave–atmosphere models that will be operational in 2022 and beyond.



It is clear that measurements of powerful, complex and highly variable ocean-surface currents and their associated surface kinematics are fundamental to our understanding of ocean circulation and atmosphere–ocean interaction, which influence the Earth system at short-time scales, from wind waves and weather, through to long-term climate.

SKIM measurements are urgently needed by the oceanographic and marine meteorological community to address the climate crisis and challenges facing our oceans today. It is timely to capitalise on the European knowledge and technical capability to take Doppler ocean measurements from space to the next level for science and societal benefit. These data will be used to address a question that is still challenging modern oceanography and marine meteorology:

How do the dynamics of the ocean TSCV influence the integrated Earth system?

2.10 Summary of SKIM User Needs

The user needs identified in Table 2.6 are derived from the information within this Chapter and supported by references. They are each traced to Living Planet Challenges.

ID	Description	Reference	ESA Living Planet Challenge (LPC)
SUN-1	SKIM should provide measurements of the TSCV over the global ocean with regular repeat coverage. <i>[This sets requirements on orbit choice, swath width, sampling, payload performance and products.]</i>	Le Traon et al. (2019), GCOS (2016), OOPC (2017), Foltz et al. (2019), Fox-Kemper et al. (2019), Villas Bôas et al. (2019), Dohan and Maximenko (2010), Schiller et al. (2015), WMO OSCAR (2019), Cronin et al. (2019)	Ocean: 1,2,3,4 Atmosphere:2, 4
SUN-2	SKIM should provide measurements of Stokes drift with a combined standard uncertainty $\leq 0.02 \text{ m s}^{-1}$ (goal: $\leq 0.01 \text{ m s}^{-1}$) or 15% of the Stokes drift (whichever is greater) with a mean revisit of ≤ 10 days at the equator. <i>[This sets requirements on orbit choice, swath width, sampling, payload performance and products.]</i>	OOPC (2017), Ardhuin et al. (2019a), Ardhuin and Jenkins (2006), Belcher et al.,(2012), Li et al.,(2016), Fraser et al. (2018), Cronin et al. (2019), Le Quere et al. (2018), Onink et al. (2019).	Ocean: 1,2,3,4 Atmosphere:2, 4
SUN-3	SKIM should provide estimates of the geostrophic velocity. <i>[This implies the need for a nadir altimeter capability and associated performance, and products]</i>	GCOS (2016), GCOS (2016)	Ocean: 1,2,3,4
SUN-4	SKIM should provide measurements measure the directional wave spectrum with combined standard uncertainty of $\leq 30 \text{ cm}$ or 10% (whichever is greater) with Significant wave height (H_s), between 1–25 m, and directional resolution $\leq 10^\circ$ in all directions for wavelengths of $\leq 30\text{--}500 \text{ m}$. Measurements should be acquired simultaneously with TSCV with a mean revisit of ≤ 10 days at the equator. <i>[This sets requirements on sampling, instrument performance and products.]</i>	WMO OSCAR (2019) GCOS (2016)	Ocean: 1,4 Atmosphere:2, 4
SUN-5	SKIM should provide measurements in the Arctic Ocean.	WMO OSCAR (2019) GCOS (2016)	Ocean: 1,2,3,4 Cryosphere: 1,4

	<i>[This sets requirements on orbit choice, swath width, sampling, and products.]</i>		Atmosphere:2, 4
SUN-6	SKIM should prioritise Equatorial oceans where no altimetry data are available. <i>[This sets requirements on orbit choice, swath width, sampling, and products.]</i>	Foltz et al., (2019), Fox-Kemper et al., (2019)	Ocean: 1,2,3,4 Atmosphere:2, 4
SUN-7	SKIM should be capable of making measurements over land surfaces to explore inland water using SKIM. <i>[This sets requirements on orbit choice, swath width, sampling, payload performance and products.]</i>	Tarpanelli et al. (2013)	Land: 2
SUN-8	SKIM should provide TSCV at a spatial resolution of 30 km.	GCOS (2016)	Ocean: 1,2,3,4
SUN-9	SKIM should provide TSCV with a mean revisit of one week (≤ 10 days at the equator). <i>[This sets requirements on orbit choice, swath width, and sampling.]</i>	GCOS (2016)	Ocean: 1,2,3,4
SUN-10	SKIM should measure the TSCV with a combined standard uncertainty $\leq 0.15 \text{ m s}^{-1}$ (goal: $\leq 0.1 \text{ m s}^{-1}$) or 15% of the TSCV at a gridded resolution of 30 km with a mean revisit of ≤ 10 days at the equator. <i>[This sets requirements on sampling, payload performance and products.]</i>	WMO OSCAR (2019) GCOS (2016)	Ocean: 1,2,3,4
SUN-11	SKIM should maximise synergy with other satellites to leverage the societal application of SKIM data. <i>[This sets requirements on orbit choice, swath width, and sampling.]</i>	Cronin et al. (2019), Schiller et al., (2015), Villas Bôas et al., (2019), Le Traon et al. (2019),	Ocean: 1,2,3,4,5 Cryosphere: 1,4 Atmosphere:2, 4
SUN-12	SKIM should have a lifetime of ≥ 5 years (goal of 10 years) in order to planetary scale phenomena such as El Nino with timescales of 2-7 years. <i>[This sets requirements on orbit choice and mission design.]</i>	GCOS (2016), Godoi et al. (2019), Trenberth and Hurrell, (1994) Cane, (2005) McPhaden et al. (2006)	Ocean: 1,2,3,4,5 Cryosphere: 1,4 Atmosphere:2, 4 Land: 2
SUN-13	SKIM should have a wide swath to maximise coverage and minimise revisit. A wide swath is needed to capture mesoscale structures, tidal flows and TSCV kinematics in a single pass to facilitate applications, to aid interpretation and derivation of uncertainty estimates. <i>[This sets requirements on mission design.]</i>	SKIM team	Ocean: 1,2,3,4,5 Cryosphere: 1,4 Atmosphere:2, 4
SUN-14	SKIM should launch as early as possible since no global repeat coverage measurements of TSCV and component parts are available today.	GCOS (2016)	Ocean: 1,2,3,4,5 Cryosphere: 1,4 Atmosphere:2, 4 Land: 2
SUN-15	SKIM should explore the different data processing approaches to retrieve Doppler-derived parameters. <i>[This sets requirements on mission design.]</i>	SKIM team	Ocean: 1,2,3,4,5 Cryosphere: 1,4 Atmosphere:2, 4 Land: 2
SUN-16	SKIM should provide individual TSCV vector component measurements for use in data assimilation systems. <i>[This sets requirements on products.]</i>	Tonani et al., (2015), Chassignet and Sandery, (2013), Villas Bôas et al., (2019), Forget et al. (2015), Lellouche et al. (2018)	Ocean: 1,2,3,4 Cryosphere: 1,4 Atmosphere:2, 4



SUN-17	SKIM should provide a gridded product including TSCV, Stokes drift, waves directional spectrum and other parameters for each orbit. <i>[This sets requirements on products.]</i>	Cronin et al. (2019)	Ocean: 1,2,3,4,5 Cryosphere: 1,4 Atmosphere:2, 4
SUN-18	SKIM should provide integrated products for different temporal resolutions including daily, 3-day and 10-day resolutions. <i>[This sets requirements on products.]</i>	GCOS (2016)	Ocean: 1,2,3,4,5 Cryosphere: 1,4 Atmosphere:2, 4
SUN-19	SKIM should provide conventional nadir altimetry products of at least the quality of Jason-3 with the following specification: Altimeter range: ≤ 1.7 (goal at 1.5 cm) at 1 Hz sampling rate, for Significant wave height (H_s)=2m, and a 11 dB sea surface backscatter coefficient, H_s : 10% or ≤ 40 cm, whichever is greatest , Wind speed: $\leq 1.5 \text{ m s}^{-1}$ <i>[This sets requirements on sampling, payload performance and products.]</i>	Desjonquères, et al., (2010), Tarpanelli et al. (2013)	Ocean: 1,2,3,4,5 Cryosphere: 1,4 Land: 2
SUN-20	SKIM should adhere to the GCOS climate monitoring principles.	GCOS (2016)	All Living Planet Challenges
SUN-21	SKIM should strive to deliver data products within 24 hours from measurement at the point of pickup for user. Altimetry products that require precise orbit determination (POD) are limited by the delay associated with POD services of 48 hours.	WMO (2019)	Ocean: 1,2,3,4 Cryosphere: 1,4

Table 2.6. SKIM user needs and traceability.

3 RESEARCH OBJECTIVES

Research objectives are developed in this chapter building on the science and research topics discussed and the user needs established in Chapter 2 summarised in Table 2.6.

The upper ocean is changing, but remains poorly observed and often ignored in the present environmental crisis. Consequently, the United Nations has called for a Decade of Ocean Science for Sustainable Development (2021–30) towards reversing the cycle of ocean decline. Using the unique measurements of SKIM, the influence and importance of TSCV in regulating our ocean, weather and climate at a wide range of spatial and temporal scales is identified in the Living Planet Challenges (LPC) of the ESA Earth Observation Living Planet Programme (ESA, 2015a). This can be linked to the *Grand Societal Challenge* of mitigating and adapting to the climate crisis for which the United Nations has defined a 2030 Agenda and Sustainable Development Goals (SDG, UN, 2015).

SKIM responds directly to all of these ‘calls for action’ that naturally focus SKIM’s research objectives into two complementary targets.

3.1 Aim and Objective

Despite their importance for science and society, and the identification of ocean Total Surface Current Velocity (TSCV) as an Essential Climate Variable (ECV, GCOS 2015; OOPC, 2017), regular, densely sampled, direct measurements of the ocean TSCV and its components from space has, so far, eluded the Earth observation community. To address this situation the *aim* of the SKIM mission is:

To measure directly and simultaneously, the ocean TSCV (an Essential Climate Variable), its component Stokes drift and Eulerian current, to quantify their role in ocean–atmosphere processes and the societal impact at the global and regional scale.

This aim serves a single **primary research objective** that is still challenging modern oceanography and marine meteorology:

How do the dynamics of the ocean TSCV influence the integrated Earth system?

This single primary research objective transcends the boundaries of physics, chemistry, biology, meteorology and climatology. It focuses a wide range of science challenges at the frontier of Earth system research that require access to the TSCV and its component parts (Stokes drift and Eulerian components) over the global ocean.

3.1.1 The Ocean–Atmosphere Interface in the Earth System

The surface layer of the ocean is continuously in intimate contact with the atmosphere over 71% of the Earth’s surface. This vast boundary layer is the breathing skin and gearbox of planet Earth. Uniquely connecting the overlying atmosphere to the deeper ocean, TSCV variability results in mesoscale resonant ‘ringing of the ocean’ (Klein et al., 2004). Wind–wave–current processes regulate all physical processes that depend on a velocity component at the ocean–atmosphere interface.

Practically no measurement of TSCV has been available so far to quantify the dynamics, and understand the character and the role of these interactions within the Earth system. While successful, coastal high-frequency (HF) radar installations cover just a small fraction of the



ocean surface. SKIM will directly resolve this situation and provide a unique ability to measure directly wind–wave–current interactions over the quasi-global ocean every few days.

For the first time, SKIM brings a ‘HF-radar in space’ to observe the world ocean.

A first target is to:

T1: To map and apply TSCV and its components to generate better estimates of atmosphere–ocean exchanges of heat, gas and momentum, accounting for the full interplay between the surface ocean and the lower atmosphere, and improve knowledge of upper ocean mixing and lower-atmosphere boundary conditions.

The intimate connection of the ocean through the atmospheric and ocean boundary layers, from the scales of viscosity to the global scale (Ferrari and Wunch, 2008) are largely controlled by the ocean–atmosphere interface and the TSCV. SKIM will provide a step change in our ability to infer convergence/divergent signals over the global ocean to explore vertical exchange from global to mesoscales.

Surface TSCV divergence is the defining signature of upwelling regions, and SKIM measurements at 30 km resolution will uniquely measure these features to address Living Planet Challenge (LPC) ocean 2:

Mesoscale and sub-mesoscale circulation and the role of the vertical ocean pump and its impact on energy transport and biogeochemical cycles .

Using SKIM TSCV and its component parts, we expect to discover new ocean currents at the mesoscale that have never been measured before – such as those recently found close to Madagascar (Ramanantsoa et al., 2018) and close to Iceland (Harden and Pickard, 2018). The TSCV signatures of mesoscale eddy systems and powerful western boundary currents that impact the full troposphere via atmosphere–ocean fluxes (Minobe et al., 2008), will be studied in detail. For example, the ‘eddy killing’ effects of the TSCV to the wind stress can work against surface motion and control important features of large mesoscale currents (Renault et al., 2016, 2019). By applying the unique measurements of SKIM, we expect to reduce the predictive uncertainty in the dynamic upper-ocean transport of heat, salinity, and biogeochemistry concentration.

Armed with this unique information of the surface ocean mesoscale dynamics, SKIM measurements can contribute a better knowledge of the exchange velocity of soluble gases such as carbon dioxide. LPC ocean-4 focuses on:

Physical and biogeochemical atmosphere–ocean interaction processes on different spatiotemporal scales and their fundamental role in weather and climate.

and LPC-atmosphere 2:

Interactions between the atmosphere and Earth’s surface involving natural and anthropogenic feedback processes for water, energy and atmospheric composition.

Using SKIM measurements, fundamental scientific research to address the ocean-atmosphere exchange community needs (Cronin et al., 2019). If the impact of the TSCV is largely ignored in parameterisations of heat and momentum turbulent fluxes, significant systematic biases are evident (Edson et al. 2013). These are due to wind–TSCV–wave interactions (Shi, 2017). Brodeau et al., (2017) estimate the mean effect of TSCV on wind



stress as $\pm 0.005 \text{ N m}^{-2}$ with the largest uncertainties amounting to $0.02\text{-}0.025 \pm 0.005 \text{ N m}^{-2}$. SKIM will provide, for the first time, deliver *exactly* the measurements required by the OceanObs community: TSCV, Stokes drift and surface waves. SKIM data will enable the exploration of: new wave–current dependent surface flux parameterisations that outperform wind speed dependent parameterisations under a wide range of wind, wave and TSCV conditions; new flux-profile relationships that account for both stratification, wind–wave–TSCV induced turbulence perturbations in the ocean–atmosphere boundary layer; new surface flux and flux-profile relationships that account for directional differences between the wind–wave–TSCV fields; new scale-dependent flux parameterisations for nested high-resolution models; new coupled large-eddy simulations with sufficient accuracy to simulate wind–wave–TSCV interaction near the ocean surface that can be validated using SKIM data.

SKIM will provide unprecedented sampling of ocean TSCV and component parts that will revolutionise our present understanding of eddy fluxes of heat, carbon and freshwater. The impact will be particularly important in the Tropical Oceans, which encompass 75% of the global ocean, and in the rapidly changing Arctic Ocean. Improved sampling is critical for heat transport estimates and preconditioning of ice melt as subsurface warm and saline Atlantic waters can be brought to the surface by mesoscale stirring, vertical mixing, and toward the coast where they impact glaciers.

Addressing LPC-atmosphere 4:

Interactions between changes in large-scale atmospheric circulation and regional weather and climate,

is an extremely urgent issue given the retreat of Arctic sea ice over the last four decades opening up the surface Arctic Ocean to new forcing. This is expected to be ice-free in summers beyond 2030 with profound impacts on European and global atmospheric circulation, weather and climate. Seasonal ice minima are routinely reported and with thinner sea ice remaining each year. Understanding how the Arctic Ocean will respond in terms of its circulation will fully exploit TSCV measurements in this region. SKIM will provide unique TSCV and directional wave measurements to help answer fundamental questions including: What will the kinematics of the ocean TSCV look like in a changed Arctic? How will they impact the seasonal and geographical characteristics of sea ice? How will this impact Arctic societies? As for most other satellite missions, full coverage of the Arctic Ocean will not be possible using SKIM due to swath limitations imposed by the payload viewing geometry and choice of orbit. Studies will therefore focus on the Arctic Ocean up to 82° North.

SKIM carries a nadir synthetic aperture radar altimeter that has a design performance suitable for use in the sea-level record. But in addition, SKIM uses off-nadir beams to determine the TSCV and wave directional spectrum. These features will be used to quantify differences between TSCV measurements at mesoscale (i.e. including near-inertial currents, Stokes drift, Ekman currents, mean ageostrophic currents, etc.) compared to mean geostrophic currents derived from conventional nadir-pointing altimetry. In this way, SKIM will make a direct and unique contribution to the multi-mission altimeter constellation and contribute to LPC-ocean 5:



Sea-level changes from global to coastal scales and from days (e.g. storm surges) to centuries.

This is a contribution to SDG-13 (climate action). Because SKIM has a wide swath and measures the *total* surface current velocity, it will also contribute to the knowledge of global tidal currents, including internal tide and the cascade of tidal energy towards ocean mixing. These data are expected, by the end of the 5-year duration SKIM mission to improve our understanding of ocean circulation and the resolution of mean ocean dynamic topography. Finally, SKIM will be used to uniquely investigate the sea state bias uncertainty term present in all altimetry missions using a combination of highly resolved waves and its nadir beam. Reducing the uncertainty in sea state bias, the largest term in altimetry uncertainty budgets, will significantly improve the sea level record. Potentially, if a solution can be found, this has implications for the historical record of altimetry measurements.

3.1.2 Transport of Material at the Ocean Surface Including Marine Plastic Debris.

A second scientific target follows from the deeper knowledge of wind—wave—TSCV—sea ice interaction and coupling derived from T1. This is to:

T2: Determine the transport by waves and currents and wave-related degradation of material at the ocean surface including plankton, nutrients, carbon, oil, and marine plastic debris.

T2 is driven by a strong demand from the research community and society at large – especially for pollution that affects 153 countries sharing transboundary waters (e.g. SDG-6, clean water and sanitation). It should put an end to the embarrassing truth revealed each time a disaster occurs at sea: we do not know well the TSCV of Earth’s ocean.

SKIM ocean TSCV and its component parts provide the most relevant velocities of floating material, such as marine plastic, and the velocity of material entrained below the Stokes depth (which is probably the case for microplastics). This need was demonstrated during the Great East Japan Tsunami disaster (e.g. Sunichi and Nubuo, 2015) and the resulting plume that traversed the Pacific Ocean, as the forecast and analysis of its trajectory were poorly constrained (e.g. Maximenko et al., 2018). This is largely due to the lack of TSCV measurements available to constrain models and, in particular, estimates of Stokes drift that is essential for surface transport calculations of floating materials.

These quantities are uniquely measured by SKIM.

Van Sebille et al. (2019) show clearly the importance of these TSCV components by demonstrating the remarkable transit of marine plastic debris across the Antarctic Circumpolar Current to make landfall on the Antarctic Peninsula. The unique measurements of SKIM are also fundamental quantities to study connectivity of ecosystems between the open ocean, land and small islands. This is particularly important to address LPC-ocean 1:

The evolution of coastal ocean systems, and address interactions with land, in response to natural and human-induced environmental perturbations.

The surface transport of heat, the weaker mixing and lower oxygen levels, river discharge of nutrients and agricultural run-off, contaminants and their dispersion in surface freshwater plumes are all agents in the environmental crisis that affects the ocean including aquaculture



and fish stocks. Adapting to and mitigating these crises requires new management and marine spatial planning that is not possible without measurements of the TSCV. Hence, SKIM will contribute to LPC-ocean 3:

The responses of the marine ecosystem and the associated ecosystem services to natural and anthropogenic changes.

This will be a decisive contribution to the United Nations Sustainable Development Goal 14 (life below water). The recent Intergovernmental Science-Policy Platform on Biodiversity and Ecosystem Services Global Assessment on Biodiversity and Ecosystem Services (2019) notes that:

“Sustaining and conserving fisheries and marine species and ecosystems can be achieved through a coordinated mix of interventions [...]. Specific actions could include, for example, ecosystem-based approaches to fisheries management, spatial planning, effective quotas, marine protected areas, protecting and managing key marine biodiversity areas.”

SKIM will provide a unique TSCV information that will directly contribute to these activities. Notably, the potential to determine river discharge using the SKIM nadir beam will be useful to determine changing river inputs due to permafrost melt and their impact in the Arctic Ocean.

3.2 Potential Additional Research Contributions of SKIM

SKIM is focussed on deriving a new generation of TSCV measurements: a HF-radar in space. Going beyond the primary mission objectives, a number of potential exploration, research and application topics that can uniquely exploit SKIM measurements have been identified by the SKIM Team (2019). Without doubt, since measurements of the TSCV and its components over the global ocean do not yet exist, SKIM may have other applications, some yet unforeseen, possibly requiring specific onboard or on-ground processing. Secondary research objectives include:

- To measure and investigate sea-ice motion and characterise the wave-TSCV-sea ice interaction (i.e. break-up, growth, kinematics, e.g. Stopa et al., 2018) in the marginal ice zone at sub-daily timescales (addressing *LPC-Cryosphere 4*).
- To explore the vertical shear of ocean-surface currents, by demonstrating for the first time in space, a tuneable Delta-K method (addressing: *LPC-ocean 1, 2, 3 and 4*).
- To determine the occurrence of extreme sea states and dangerous or freak waves by combining unique information on wind–wave–current interactions; improve ocean modelling capabilities (circulation, sea ice and waves) by providing a unique observations of global mesoscale flows that can be used to test parameterization and/or assimilate in ocean state (addressing: *LPC-ocean 1, 2, 3, 4 and 5; LPC-atmosphere 2 and 4 and LPC-cryosphere 2 and 4*).
- To improve the knowledge of extreme total water levels at the coast by measuring the incoming wave energy flux coastal sea level (addressing: *LPC-ocean 1*).
- To measure precipitation (addressing: *LPC-atmosphere 2 and 4*).
- To explore new techniques to measure flows in major rivers, estuaries and lakes (addressing: *LPC-land 2*).

3.3 SKIM Mission Objectives

To address the science research objectives and the user needs established in Chapter 2 summarised in Table 2.6, the following primary mission objectives have been established:

Over the global sea ice and precipitation-free ocean and inland seas from 82°S to 82°N:

1. Measure and investigate the TSCV with a combined standard uncertainty² in the across-track direction, U_{AC} , and along-track direction, U_{AL} , $\leq 0.15 \text{ m s}^{-1}$ (goal: U_{AC} and $U_{AL} \leq 0.1 \text{ m s}^{-1}$) or 15% of the TSCV (whichever is greater) at a gridded resolution of 30 km with a mean revisit of ≤ 10 days at the equator a for at least 70% of the ocean surface (accounting for rain and gaps in coverage).
2. Measure and investigate the directional wave spectrum with combined standard uncertainty of $\leq 30 \text{ cm}$ or 10% (whichever is greater) with significant wave height, H_s , between 1–25 m, and directional resolution $\leq 10^\circ$ in all directions for wavelengths of $\leq 30\text{--}500 \text{ m}$. Measurements should be acquired simultaneously with TSCV at a gridded spatial resolution of $\leq 70 \text{ km}$ with a mean revisit of ≤ 10 days at the equator.
3. Measure and investigate Stokes Drift with a combined standard uncertainty $\leq 0.02 \text{ m s}^{-1}$ (goal: $\leq 0.01 \text{ m s}^{-1}$) or 15% of the Stokes drift (whichever is greater) at a gridded resolution of 70 km with a mean revisit of ≤ 10 days at the equator a for at least 70% of the ocean surface (accounting for rain and gaps in coverage). The Stokes drift has larger spatial scales compared to TSCV as a result of atmospheric forcing.

It is recognised that SKIM gridded measurements of the TSCV at 30 km will be challenged in the coastal zones up to 30 km from the shoreline. This is due to the complex local current structures in this region being at sub-grid scale and the highly variable characteristics of waves in these waters (although suitable algorithms to address these issues will be attempted). Nevertheless, individual footprint measurements of TSCV vector components and directional wave spectral information will be useful in many areas – especially via data assimilation using numerical ocean prediction systems.

3.3.1 Summary

The SKIM ocean measurements will offer new opportunities to directly address the Living Planet Ocean Challenges. These measurements are required to gain scientific knowledge to explore strategies that can address the larger societal *Grand Challenges* embodied in GCOS ECV needs the United Nations Societal Development Goals, and emphasized in the World Climate Research program (WCRP) Strategic Plan for 2019-2028.

Given the present climate crisis and the profound impacts anticipated on society, the SKIM mission, *our HF-radar in space*, is both necessary and urgent.

² This is the combined standard uncertainty including systematic uncertainty and random uncertainty, following the Joint Committee for Guides in Metrology (JCGM) Guide to the expression of uncertainty in measurement (GUM), (BIPM, 2008).

4 OBSERVATIONAL REQUIREMENTS

This chapter outlines the fundamental observation approach and provides the observational requirements for the SKIM mission, relating directly to the science research objectives in Chapter 3 and the user needs established in Chapter 2 (summarised in Table 2.6). Level-2 product specifications are then translated into Level-1 radar measurement requirements that form the basis of the SKIM system that is presented in Chapter 5.

4.1 Observational Approach

For the first time, a dedicated satellite mission will routinely provide Doppler measurements, to directly measure the ocean TSCV. By extending the very successful and established principles of coastal High-Frequency (HF)-radar systems (that determine the TSCV in coastal areas) to the world ocean, SKIM will provide an analogous ‘HF-radar in space’. SKIM will then deliver regular, repeat coverage, measurements of the ocean TSCV and components with quasi-global coverage every few days.

The observational approach of SKIM is based on Doppler signals that are acquired at different radar elevation and azimuth angles. These are then combined to determine the ocean TSCV. To achieve this, the SKIM uses a unique conically scanning, multibeam Ka-band Doppler Wave-Current Scatterometer (DWCS). The conical scan provides wide-swath coverage and the azimuth viewing angle diversity required to retrieve vector velocities and directional wave measurements.

This approach is the only means to provide a cost-effective solution to address the total absence of TSCV and component measurements (i.e. Stoke drift) in many parts of the world that are necessary to address ESA Living Planet Ocean Challenges.

SKIM employs the following measurement techniques:

1. **Pulse-pair analysis** (phase-difference) to directly measure the Doppler centroid associated to the Line-of-Sight (LoS) velocity for a number of off-nadir beams at different azimuth and elevation angles.
2. **Spectral analysis of the wave-related modulation of Normalised Radar Cross-Section (NRCS)** of the sea-surface using rotating off-nadir beams to provide directional ocean wave spectra.
3. **Nadir along-track altimetry capability** (unfocussed synthetic aperture radar) to estimate sea-surface height (SSH) and significant-wave height (H_s)
4. A proof of concept of a **Delta-K time-analysis** (wave-front matching dispersion) to provide a measurement of velocity that is more selective of the contributing waves, and closer to the principle of coastal HF-radars.

The combination of Ka-band radar measurements with a near-nadir incident angles means that radar scattering at the surface can be completely described using very practical physical optics. The NRCS is governed by the specular surface slope distribution. Importantly, it minimises the need to disentangle different scatter contributions.

The instantaneous motion of the sea surface is captured by measuring the phase difference of consecutive radar echoes (pulse-pairs). The phase difference provides an unbiased estimator of the Doppler centroid. The Doppler centroid provides a LoS velocity, which after



removing the known component due to the motion of the satellite, is controlled by the motion of the sea-surface slopes. In order to maintain high coherence between the consecutive pulses, the radar must be operated at a very high pulse repetition frequency (PRF) of $\sim \geq 32$ KHz. This is traced to meet mission objective 1 (TSCV).

Further, short capillary waves with wavelength less than 8 mm on the ocean surface are rare due to surface tension restoring forces. At Ka-band and 6° or 12° incidence, the surface is sampled at a wavelength of 4 cm or 2 cm, respectively. Therefore, by using Ka band SKIM samples most of the ocean waves.

The high-resolution, range-resolved measurements, when combined with the ‘matching wavefront technique’ proposed by Jackson (1981), can be exploited to retrieve the ocean-surface wave directional spectrum. Each radar intensity measurement is an average in the azimuth direction, perpendicular to the range direction. It efficiently filters out wave modulations with azimuths away from the range direction. This has been demonstrated using airborne radars (Jackson, 1981), and such a principle is now operating in space with the Ku-band SWIM radar on CFOSat. SKIM develops this approach further by proposing measurements in Ka-band that provide a reduced footprint (10 km one-way at -3dB rather than 18 km at Ku-band) enhancing reflectivity modulation. Furthermore, SKIM has a smaller range resolution so that shorter wind-wave components, ~ 30 m and possibly less, become accessible compared to 50–70 m for SWIM. In addition, the high resolution of SKIM in both range and azimuth will also be used to remove outliers within the radar footprint, such as reflection from ships, precipitation, and to correct for Doppler bias owing to variations of backscatter power with azimuth.

These aspects are traced to mission objective 2 (waves) as and mission objective 1 (TSCV) since high fidelity ocean surface wave directional spectrum, $E(k, \theta)$, is required as input to the TSCV retrieval algorithm described in Chapter 6.

A proof-of-concept Delta-K technique (Alpers and Hasselmann, 1978) will be implemented, selecting parts of the bandwidth to select and analyse the time-evolving sea surface reflectivity at the associated narrow range of wavelength. Compared to the Doppler centroid, the resulting Doppler shift will only relate to a particular surface scale, matching the delta-K frequency which can be chosen in the megahertz range. This selection provides an independent approach to use Doppler measurements to determine the ocean TSCV. Combining several delta-K frequencies, it may yield estimates of the vertical variation of the current (Stewart and Joy 1974). This is traced to mission objective 1 (TSCV) from SUM-15 in Table 2.1.

4.1.1 From Doppler Velocity to TSCV: the SKIM Measurement Principle

The SKIM measurement equation

The fundamental measurement equation for a radar payload designed to measure velocity at the surface of the Earth from a spacecraft flying at a speed of about 7 km s^{-1} is:

$$V_{LoS}(\theta, \varphi) = V_{NG}(\theta, \varphi) + U_{GD}(\varphi) \cdot \sin \theta \quad (4.1)$$

From non-moving radar measurements, a non-zero LoS velocity, V_{LoS} , can be interpreted as a geophysical Doppler velocity in the azimuth direction, φ , after projecting on a plane surface (i.e. correcting for the incidence angle, θ). From a moving platform, an additional non-

geophysical Doppler velocity V_{NG} appears, associated to the velocity of the radar aboard the satellite relative to the solid Earth. This V_{NG} is dependent on geometric LoS pointing, as described in Chapter 5 and contains additional terms related to radiometric miss-pointing coming from azimuthal and spatial NRCS gradients within the azimuth span of the beam footprint, as described further in this Chapter.

The general principle of the SKIM TSCV measurement starts from V_{LoS} , then subtracts the non-geophysical velocity, V_{NG} , then projects on a plane surface, i.e. correcting for the incidence, θ . This gives the horizontal geophysical Doppler velocity $U_{GD}(\varphi)$ in azimuth φ :

$$U_{GD}(\varphi) = (V_{LoS}(\theta, \varphi) - V_{NG}(\theta, \varphi)) / \sin \theta \tag{4.2}$$

For stationary land or sea-ice surfaces $U_{GD} = 0$.

The radar measurement is averaged over a finite -3 dB footprint size (in the order of 9 km diameter for SKIM one-way antenna gain) to smooth out all fluctuations due to wave motions. In addition to the mean surface-water movement, the sub-pixel correlation between instantaneous velocities and backscatter intensities leads to an intensity-weighted mean ‘wave Doppler’ contribution $U_{WD}(\varphi)$ that is the average phase speed³ of the dominant short wind-waves contributing to the backscatter. $U_{WD}(\varphi)$, is a function of the sea state and of the radar properties (Mouche et al., 2008, Nougquier et al., 2018). This was demonstrated by Chapron et al., (2005) for C-band and Nougquier et al. (2018) for Ka-band (Fig. 4.1).

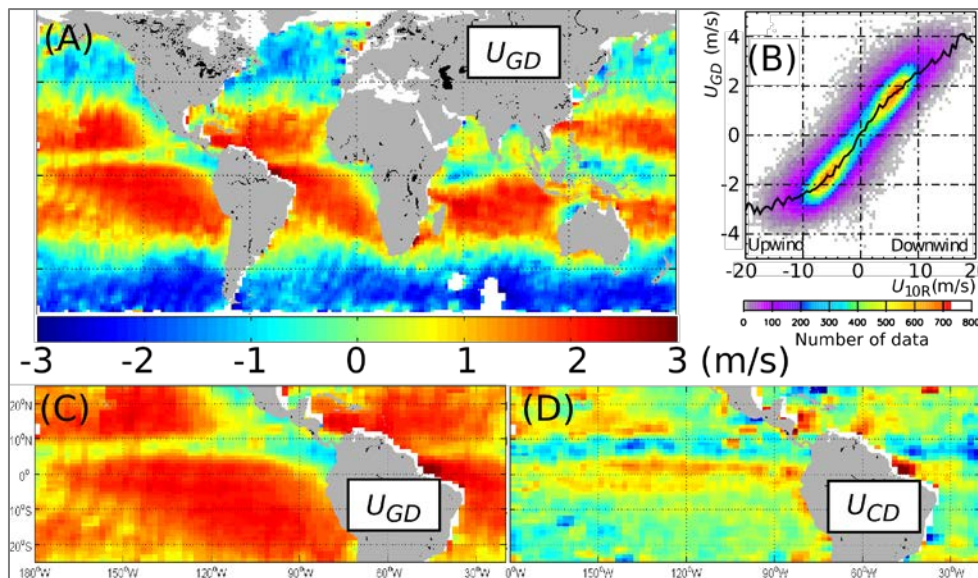


Figure 4.1. (a) Example of geophysical Doppler velocity from Envisat wave-mode data acquired in VV polarisation at an incidence angle $\theta=23^\circ$, for descending tracks. (b) Empirical relation found between the geophysical Doppler and the local wind projected on the range direction. Using a wind-based proxy for the wave-induced Doppler U_{WD} given by the black curve in (b), the surface current U_{CD} is estimated in (d) as $U_{GD} - U_{WD}$ for the region detailed in (c). (Adapted from Chapron et al., 2005 and Collard et al., 2008).

³The phase speed of surface gravity waves appears for near specular reflection because it is the wave slope times the orbital velocity (LOPS, 2019). For Bragg scattering, this speed is replaced by the phase speed C_B of the Bragg waves.

The wave Doppler component

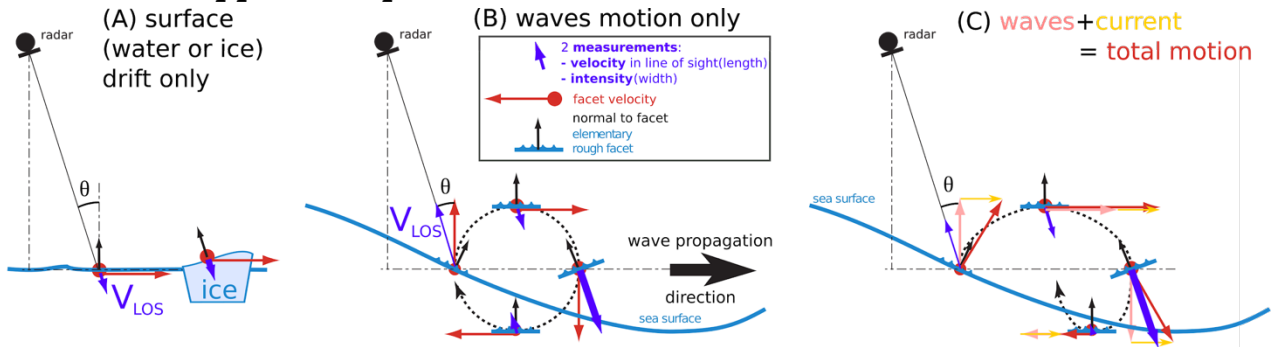


Figure 4.2. How a Doppler radar measures the line of sight velocity, V_{LOS} , the radar intensity σ^0 , and their sub-footprint combination. Left: over smooth water or ice surfaces, Centre: considering wave orbital motion only and Right: wave motion plus a current velocity. (Adapted from Rodriguez et al., 2018).

Because the contributing waves are generated mostly by the local wind, the quantity $U_{WD}(\varphi)$ is strongly correlated to $U_{10,R}$, the radial component of the wind speed projected in direction φ , as illustrated in Fig. 4.1 using Envisat data. For a fixed value of $U_{10,R}$ the root mean square (RMS) variation of $U_{GD}(\varphi)$, Δ_C , is of the order of 1 m s^{-1} . The residual is caused by variations in the sea state, TSCV, errors in the wind estimate and errors in U_{NG} . It averages out when many satellite passes are combined (Rouault et al., 2010). Therefore, measurements of the surface-wind velocity are extremely useful to estimate the wave Doppler component $U_{WD}(\varphi)$, discussed below.

Identical to coastal HF radars that operate at 3–40 MHz (Barrick et al., 1974; Stewart and Joy, 1974), the measured Doppler velocity vector component is the sum of an intrinsic wave phase velocity and a shift caused by the current in which the waves propagate as shown in Fig. 4.2 and further described in Chapter 6.

Over sea ice (Fig. 4.2, left), the vertical motion is negligible, and therefore so is $U_{WD}(\varphi)$: the measured velocity corresponds to the ice drift (Kraemer et al., 2018). Over the ocean surface (or inland waters), the instantaneous velocity is dominated by the motion of wind-generated waves that is strongly correlated with the radar intensity, σ^0 , (Fig. 4.2, centre panel).

The current Doppler component

From the sensor physics, the time-evolving sea-surface Ka-band reflectivity is conveniently controlled by the sea-surface slope time-evolution. The resulting $U_{GD}(\varphi)$ thus directly relates to the Stokes drift, including the surface current contribution. The combined effect of waves and currents (Fig. 4.2, right) gives the area-averaged geophysical Doppler $U_{GD}(\varphi)$ when looking in azimuth φ . It can then be decomposed as the sum of two terms: the current Doppler velocity, $U_{CD}(\varphi)$, and a wave Doppler, $U_{WD}(\varphi)$, i.e.:

$$U_{GD}(\varphi) = U_{CD}(\varphi) + U_{WD}(\varphi) \tag{4.4}$$

with the ‘current Doppler’ contribution, $U_{CD}(\varphi)$, being the projection of a single vector component of the TSCV along the azimuth of the radar.

To generate a complete TSCV vector U_{CD} , radial vector component measurements with sufficient azimuth diversity are combined as a horizontal current vector component in the cross-track direction (U_{AC}) and separately in the along-track direction (U_{AL}) as shown in Fig. 4.3.

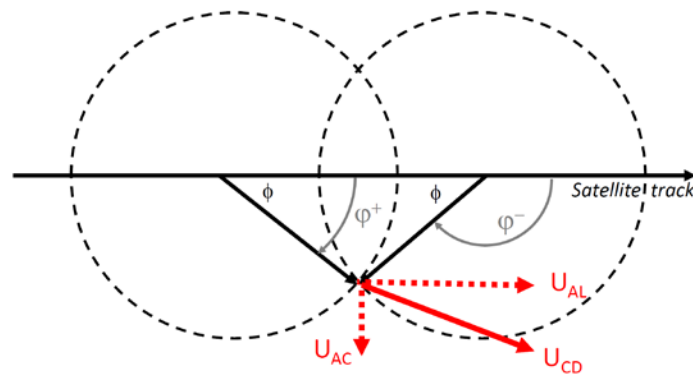


Figure 4.3. Retrieval of the horizontal current vector $U_{CD}=(U_{AC},U_{AL})$ from radial measurements $U_{CD}(\varphi+)$ and $U_{CD}(\varphi-)$ in at least two look azimuths $\varphi+$ and $\varphi-$. (Adapted from Rodriguez et al. 2018, A. Battaglia, University of Leicester).

Individual radar “snapshot” (i.e. at the 10 km footprint scale) measurements of $U_{CD}(\varphi)$ are expected to be noisy ($0.1 - 0.5 \text{ m s}^{-1}$) given the random element of the sea surface scatterers and local variability of U_{WD} (that dominates the measurement). This can be mitigated by combining a number of snapshot measurements acquired at different azimuths as a weighted least-square average at a suitable grid resolution. In the case of SKIM, this is 30 km as requested by GCOS (2016). A similar approach is used by satellite scatterometers.

SKIM will apply unique Doppler wave—current—scatterometer measurements from space both as individual “snapshots” or as gridded velocity fields, to explore the kinematics and dynamics of the ocean surface to open a new era of global Doppler Oceanography from space.

4.2 Level-2 Product Requirements to Address Mission Objectives

SKIM products are designed to provide flexibility in processing and utility for applications. Table 4.1 describes each Level-2 product highlighting their purpose, content and traceability to SKIM user needs (Table 2.6).

It is recognised that SKIM gridded measurements of the TSCV at 30 km will be challenged in the coastal zones up to 30 km from the shoreline and close to the sea-ice edge using the current version 1.0 U_{WD} algorithm discussed in Chapter 6. This is due to the complex local current structures in this region being at sub-grid scale and the highly variable characteristics of waves in these waters. Further algorithm development will lead to solutions based on measurement campaigns and theoretical treatment in future Phases of the mission. Nevertheless, individual footprint measurements of TSCV vector components and directional wave spectral information will be useful in many areas – especially via data assimilation using numerical ocean prediction systems.

Level-2a and Level-2b products include Line of Sight (LoS) measurements at the radar footprint scale that are useful for assimilation in a coupled ocean-wave modelling system or for further analysis. Separate Doppler derived current and wave contributions are available in Level-2b products. These are analogous to scatterometer backscatter measurements in different azimuths. The 1D directional wave spectrum is also included in Level-2b products. Level-2c products are the primary product of SKIM containing the TSCV, Stokes drift and wave directional spectrum (Gaultier, 2019).

Finally, multi-temporal gridded fields are provided in Level-2d products that can be obtained with a variety of ‘standard’ analysis approaches and different level of sophistication



(e.g. geo-statistical merging methods, via data assimilation capitalising on the advective properties offered by numerical ocean models). These methods will not be described further in this report.

Name	Description and Application	Format and Resolution
Level-2a_WR (Wave Radial)	Level-2a_WR is a fundamental user product for data assimilation and is an input to higher order processing traced to SUN-16 in Table 2.6. It contains spectra of σ^0 and Doppler modulation for each footprint and uncertainties. It is computed in radar scan geometry for each SKIM measurement cycle. It includes measurements from all beams along the ground track of each beam.	One NetCDF like file per orbit. Resolution is the instrument measurement footprint.
Level-2a_UGD (Geophysical Doppler)	Level-2a_UG is a user product for data assimilation and is an input to higher order processing traced to SUN-16 in Table 2.6. It contains horizontal surface geophysical Doppler velocity, U_{GD} , and uncertainties. It is computed in radar footprint level for each SKIM measurement cycle. It includes measurements from all beams along the ground track of each beam.	One NetCDF like file per orbit. Resolution is the instrument measurement footprint.
Level-2b_NAL (Nadir Altimetry)	Level-2b_NAL is a fundamental user product contributing to the international altimeter constellation. It is an input to higher order processing traced to SUN-3, SUN-7, and SUN-19 in Table 2.6. It includes Sea Surface Height (SSH), significant wave height (Hs), wind speed, σ^0 , all geophysical corrections and ancillary data (commensurate with international altimeter standards) and uncertainties.	One NetCDF like file per orbit conforming to altimeter community standards. Resolution: 0.5 x >8 km (width of product depends on sea state) at ≥ 4 Hz sampling.
Level-2b_WDS (Wave Directional Spectrum)	Level-2b_WDS is a fundamental user product that has relevance to many users interested in data assimilation. It is an input to higher order processing traced to SUN-4 and SUN-16 in Table 2.6. It includes estimates of the 1D slice directional wave spectrum $E(k, \varphi)$ and uncertainties at radar footprint level.	One NetCDF like file per orbit. Resolution is the instrument measurement footprint.
Level-2b_U (Radial TSCV)	Level-2b_U is a fundamental user product that has relevance to many users interested in data assimilation. It may represent water movement or ice movement depending on the target surface. It is an input to higher order processing traced to SUN-1, SUN-2 and SUN-10 in Table 2.6. It contains estimates of U_{CD} , the radial component of the TSCV (i.e. after the wave Doppler component, U_{WD} , has been separation from Level-2a_UGD measurements) together with uncertainties. It is computed in at footprint level in radar scan geometry, for each cycle, and all beams along the ground track of each beam. Radial Stokes drift, $Us(\varphi)$, and U_{WD} (estimation containing wave Doppler direction, φ_{WD} , and wave Doppler magnitude, M_{WD}) separated from L2A_UGD measurements are included.	One NetCDF like file per orbit. Resolution is the instrument measurement footprint.
Level-2c (single orbit product)	Level-2c is the primary user product that has relevance to many users. It is an input to higher order processing traced to SUN-1, SUN-2, SUN-3, SUN-4, SUN-5, SUN-6, SUN-8, SUN-9 and SUN-11, SUN-16, and SUN-17 in Table 2.6. This is a primary product with relevance to all users. It contains estimates of all geophysical quantities and uncertainties derived from	One NetCDF like file per orbit. Resolution TSCV 30 km posted on a 5 x 5 km



	<p>the SKIM mission on a regular latitude x longitude grid across the swath for each SKIM orbit.</p> <p>U_{CD} is posted at a resolution of 5 km x 5 km with data constructed from a search radius of ~15 km. There is no background model used in the restitution.</p> <p>$E(\varphi,k)$ computed for boxes of 70 x 70 km in satellite geometry. It is not a fixed grid oriented with meridians and parallels. This is used in higher order processing to estimate wave Doppler direction and magnitude. The Stokes drift vector U_{SR} is posted at a resolution of 5 km x 5 km with data constructed from a search radius of about 35 km</p>	<p>gridded swath map in satellite geometry.</p>
<p>Level-2d (multi-temporal product)</p>	<p>Level-2c is the primary user product that has relevance to many users. It is an input to higher order processing traced to SUN-1, SUN-2, SUN-3, SUN-4, SUN-5, SUN-6, SUN-8, SUN-9 and SUN-11, SUN-16, SUN-17, and SUN-18 in Table 2.6.</p> <p>It contains the same quantities as Level-2c products but integrated over a temporal period. It is provided on a regular latitude x longitude grid aggregated in time from 1 to n days depending on the user application. The baseline product is defined for of 3-day (general ocean user product) and 10-days (climate user) period.</p>	<p>One NetCDF like file per integration period (3 days and 10 days).</p> <p>Resolution TSCV 30 km posted on a 5 x 5 km gridded map.</p>

Table 4.1. SKIM Level-2 product definitions.

4.3 Level-1b Observation Requirements

For traceability, please refer to Chapter 5 for a detailed discussion of scientific requirements specification at Level-1b and their impact on the SKIM mission design.

4.3.1 Beam Pointing Requirements

Doppler quantities are extremely sensitive to mis-pointing and variations in mis-pointing – particularly in the yaw direction and to meet the mission requirements, the pointing knowledge in azimuth and incidence angle must be accurately known. In practice, measuring a 1 cm s⁻¹ velocity from a spacecraft flying at 7 km s⁻¹ requires a very accurate knowledge of the geometry: the azimuth angle must be known within 1.4 microradians while the elevation angle, θ , accuracy is even more strict, by a factor $\tan(\theta)$, which translates to an accuracy requirement for altitude with respect to the sea surface of the order of 5 cm (LOPS, 2019b). The incidence angle is well constrained by the off-nadir beam and nadir-beam range measurements and requires a knowledge of surface elevation gradients within ~5 cm across the swath.

Following discussions across the Phase A team, azimuth knowledge error PSD requirements for SKIM have been specified for a design that is considered feasible based on modern startracker and high-performance fibre-optic gyroscope (gyro). It was assumed that Attitude Orbit Control System (AOCS) sensors are mounted on the instrument, that is itself isostatically mounted on the platform. It was also assumed that the maximum limit for the PSD specification is ~33 Hz (timescale of 30 ms) as science data will only be collected at frequencies lower than this.

The SKIM instrument pointing performance requirement is expressed in terms of the power spectral density (PSD) for the platform contribution to pointing knowledge. In this way, an envelope can be directly used in performance simulations. This avoids having to make

spectral assumptions to interpret time-domain requirements. Typical platform contributions to an azimuth knowledge error are expected to be dominated by:

1. Startracker errors that can be approximately bounded by a flat PSD.
2. Gyro angle random walk error where the PSD follows a downward sloped line.
3. Gyro quantisation leading to a flat PSD contribution.
4. Structure flexible mode vibrations above gyro-Nyquist sampling with harmonics at several relatively predictable frequencies.
5. Reaction-wheel-induced micro-vibrations above gyro sampling with harmonics at frequencies that depend partly on reaction wheel speed.
6. Thermal mechanical misalignments between startracker and LoS.
7. Other aspects specific to a particular implementation solution.

A credible but conservative scenario was developed by the SKIM Mission Advisory Group including key AOCS pointing knowledge error PSD contributors for SKIM as shown Fig. 4.4 (left). This approach was necessary to specify requirements because an actual SKIM mission scenario requires hardware design and trade-offs supported by complex simulations. These were not available at the start of the Phase A study. The scenario was based on the pointing budget error (3σ error budget or 99% probability) available at the start of Phase A and feedback from the CFOSat and Surface Water Ocean Topography (SWOT) mission teams and translated into the SKIM context.

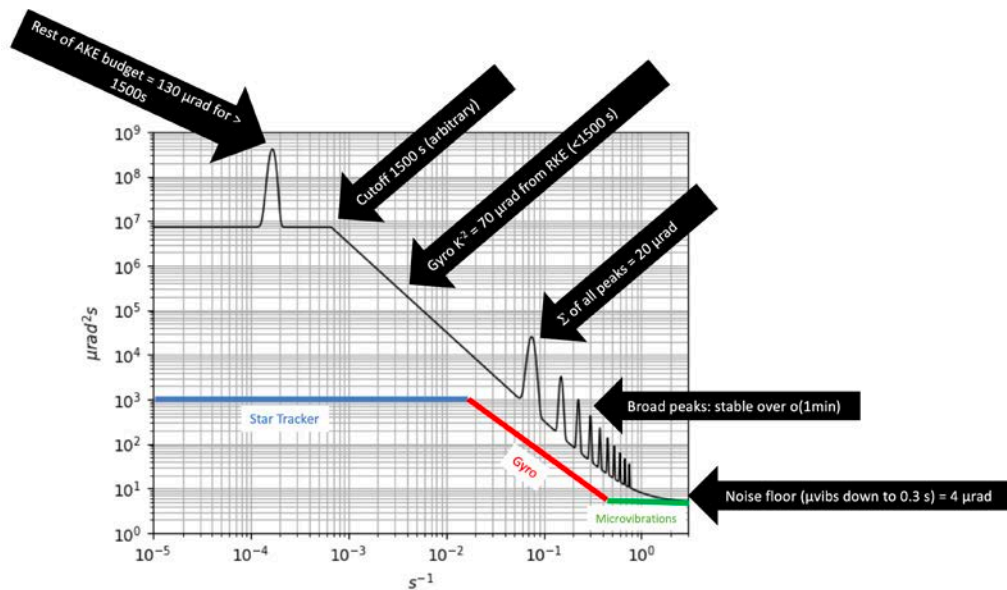


Figure 4.4. Conservative azimuth pointing error PSD scenario highlighting the role of startracker noise, gyro errors and SKIM rotating feed-plate micro-vibrations. (SKIM MAG)

The main sources of pointing error (noting that each of them may have multiple subcomponents) were included:

- Feed horn plate drive mechanism where misalignment and friction create an azimuth error at the rotation frequency.



- Feed horn plate rotation and harmonics where yaw error may be caused by sources that are not constant during a rotation.
- Micro-vibrations caused by platform momentum wheels or thermal snaps which drive the performance of higher frequencies.

At low frequencies, a startracker is the best source of knowledge, while for high frequencies, a gyro becomes more relevant. The transition frequency is approximated by the intersection of the startracker PSD envelope and the decreasing gyro random walk line. A flat noise-level envelope is assumed at very high frequencies (micro-vibrations) where a rigid link between the gyro and the instrument Line of Sight can no longer be assumed or where the frequency exceeds the gyro-Nyquist sampling. The startracker PSD level assumes an integrated total knowledge error of 1 arcsec up to the PSD corner frequency.

Micro-vibrations can be induced by a solar array drive mechanism, platform momentum wheels, thermal snaps at the terminator etc. In general, all transfer function and normal modes of the platform are poorly known. A gyro is used to report the platform and antenna pointing and can be modelled as a K^{-2} slope, the integration of the gyro-random walk error, to drive the pointing performance for scales ranging from ~1 min to ~1 h. It terminates as background noise, driving the performance of the highest frequencies, e.g. those caused by mismatch between gyro measurement and actual antenna pointing.

Considering the SKIM feed horn plate rotation and spin mechanism, any (small) misalignment and bearing friction will lead to an azimuth error at the rotation frequency of the antenna:

- Yaw error may be caused by sources that are not constant during a rotation (e.g. friction). This would create higher order harmonics (secondary peaks) with decreasing amplitude.
- Some of these harmonics have periods of a few seconds or less.
- Each harmonic may have its own stability/decorrelation time (i.e. peak width that could be controlled by design of the rotation mechanism and yaw angle monitoring hardware).

Thermo-elastic distortions (TED) are azimuth-varying but almost never time-varying for the same signature with each feed horn plate rotation for one satellite revolution, or even a few hours. Very narrow spectral peaks with known frequencies emerge as ‘narrowband’ errors because of this property. Other errors, i.e. gyro or startracker errors, are time-varying but not azimuth-dependent. They are more random and affect many frequencies in an unpredictable way, hence their name of ‘broadband’ errors.

SKIM requires a strategy that relies on a high-quality technical solution that limits broadband errors to an acceptable level to meet the TSCV requirements. Chapter 5 presents the hardware solution for SKIM and performances in which narrowband errors contain most of the pointing error variance. As this is the case, a data-driven fine-pointing calibration approach is used to mitigate the remaining residual mis-pointing. The approach is to recognise and remove spectral signatures from the Doppler shift time series spectrum that are clearly due to non-geophysical effects. The assumption of spectral separation between geophysical and non-geophysical signals places requirements on the system design. The fine-pointing algorithm developed for SKIM is explained in Chapter 6. Simulation results of the system implementation and fine-pointing approach are presented in Chapter 7.

4.3.2 Doppler Performance

Doppler performance is traced to SUN-1, SUN-2, SUN-9, and SUN-10 and to meet mission objectives for TSCV.

A fundamental requirement for the SKIM mission is to achieve a precision for U_{GD} that is commensurate with user needs set for U_{CD} . The principle of the SKIM Doppler measurement relies on the estimation of the phase of the correlation between successive pulses. Such ‘Pulse-Pair’ processing is a well-known technique (Zrnic, 1977) used in meteorological radar. Ideally, phase differences over various time lags provide the mean scatter velocity. From analytical developments, the probability distribution of the phase differences can be cast in terms of the coherence function. In practice, over the ocean surface, very short time lags must be used. The method is discussed and demonstrated for aircraft Doppler ocean-current measurements by Rodriguez et al. (2014).

For SKIM, numerical simulations were performed using the IFREMER Remote Sensing Sea Surface Simulator (R3S) which is a deep simulator designed to study the interaction of radar electromagnetic waves with the ocean surface (Nouguier, 2019). This determined that a high 32 kHz PRF is required to allow a large Doppler bandwidth (~15 kHz, maximum at 90° azimuth angle) to ensure large signal coherency and provide accurate Doppler measurements.

To meet SKIM TVSC performance and address the mission objectives for TSCV, the radial surface velocity precision will follow the requirements in Table 4.2.

Incidence angle	Azimuth 45°	Azimuth 3° and 357°	Azimuth 90°
12°	12.5 (10)	5 (3)	20 (15)
6°	17.5 (15)	5 (3)	25 (20)

Table 4.2. Required radial velocity precision (in cm s^{-1}) and goals in parentheses.

4.3.3 Loose Formation Flight with MetOp-SG(1B)

These requirements are traced to SUN-11 in Table 2.6 and to all mission objectives.

The unique data from SKIM and data from other satellite missions that are likely to be in orbit at the same time (2025+) will be mutually beneficial. A scientific trade-off to determine if SKIM should fly in loose formation with a complementary mission has therefore been conducted. The SKIM orbit has been selected based on the following criteria:

1. To independently address the SKIM primary objectives by addressing coverage and revisit requirements.
2. To maximize the sampling capabilities of SKIM that yield the best Level-2 multi-pass products.
3. Access to high latitudes to sample ocean currents over the Arctic Ocean. This implies a polar orbit. If a sun-synchronous orbit is used then tidal aliasing of the solar tidal components will occur. However, this is a major tidal component that can be derived using tidal modelling (e.g. Saynisch et al., 2018).
4. To ensure cross-overs with other relevant missions. This is relevant to identify rapidly evolving surface current components such as inertial currents whose period is equal to $2\pi/f$, with f being the Coriolis parameter. Cross-overs near half the inertial period will allow to estimate the local inertial current components being almost at 180° of



each other and subsequently use this estimate to validate the predicted corrections needed to reach Level-2d products.

5. To maximise match-up with other satellite missions that can provide independent measurements to generate better SKIM products, for SKIM product verification, and develop innovative synergy products including:
 - **Wind vector:** to further constrain the wave Doppler determination and for use in synergy scientific applications
 - **Precipitation:** Ka-band is hampered by precipitations and data must be carefully flagged
 - **Total column water vapour:** to correct the nadir beam for wet-tropospheric path delay
 - **Sea ice edge location:** using imagery at the SKIM Level-2c product level

The MetOp-SG(1B) satellites are planned and secured in an operational context and are assumed to be available as part of an existing operational system serving numerical weather prediction. The payload complement includes an ocean SCAtterometer (SCA) and a multichannel Microwave Imager (MWI) with channels of 18.8–183 GHz with varying spatial resolutions of 50 (low-frequency) to 10 km Above 35 GHz). MWI can be used to retrieve atmospheric measurements and SCA vector measurements. Synergy with MetOp-SG(1B) SCA will be extremely useful for wave Doppler estimation and exploration of advanced air–sea interaction studies, i.e. wind–wave–current interaction.

For heavy precipitation, the SKIM measurements will be obviously contaminated by precipitation and must be flagged. At lower precipitation rates flagging is more challenging. A microwave radiometer can be used to determine precipitation rate but SKIM does not carry a microwave radiometer. For this purpose, MetOp-SG(1B) MWI can readily provide information to flag precipitation within the SKIM swath, and a measurement of wet-tropospheric correction for the SKIM nadir beam. MWI channels dedicated to precipitation monitoring centred at e.g. 31, 50–53, 89, and ~118GHz and will be used to flag SKIM data. The SKIM nadir correction for range delays induced by atmospheric water vapour loading can use MWI channels entered at e.g. 23.8 and 118 GHz. MWI can also provide useful information of sea ice.

The choice of MetOp-SG(1B) imposes an orbit choice on the SKIM mission of collocations are to be attained with MWI and SCA. MetOp-SG(1B) will use a frozen sun-synchronous orbit inclined at 98.7° with a mean local solar time at the descending node of 09:30 and a repeat cycle of 29 days. For optimal global sampling, sub-cycles that optimise revisit for mesoscale ocean TSCV structures at a frequency depending on their scales must be considered. The MetOp-SG(1B) orbit has 5-day sub-cycle, which is an important sub-cycle having good coverage as a function of revisit time, increasing from 23% at one day, 62% at 3 days, 86% for 5 days and 95% for 10 days.

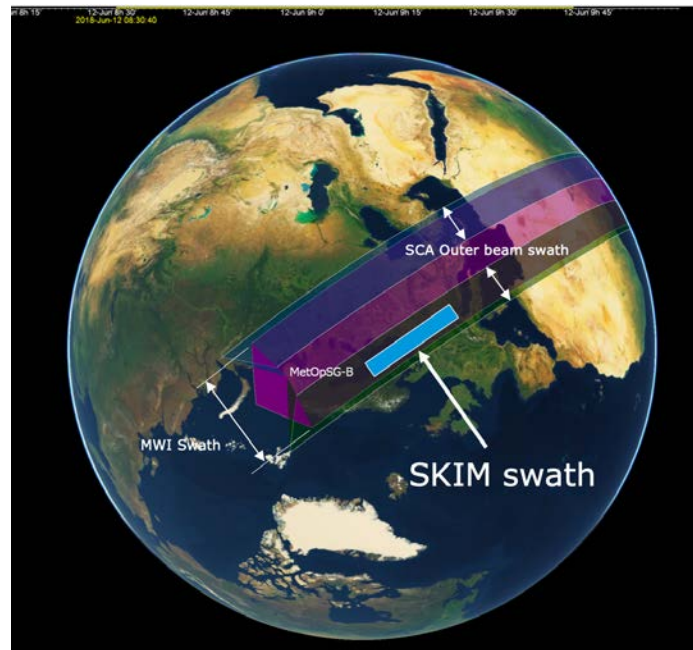


Figure 4.5. Configuration of loose formation of SKIM with MetOp-SG(1B) highlighting overlapping swath.

In terms of loose formation design, the primary objective is to achieve total overlap of SKIM and MWI observations with contemporaneous measurements for rain flagging. The secondary objective is to maximise SKIM and SCA swath overlap from the equator to mid-latitudes. As SCA has a gap of 525 km centred at the satellite nadir position, the loose formation design should maximise the collocation of SKIM and SCA measurements over the ocean surface. This concept is shown in Fig. 4.5.

The impact of a time separation of <10 minutes between many geophysical products appears very good at first glance because at a scale of 10–30 km, the statistical properties of the ocean surface will not have changed sufficiently to introduce significant uncertainty into the final products. Yet, 10 minutes is too long with respect to changes in atmospheric state due to the onset, variation in intensity and vertical position of precipitation. Movement of atmospheric rain bands at 14 m s^{-1} corresponds to $\sim 8.5 \text{ km}$ which approximately matches a SKIM footprint. This will introduce uncertainty into SKIM rain flagging and ideally, temporal collocation should be minimised to $\leq 150 \text{ s}$.

These issues imply that loose formation flight design optimises time of separation between the two satellites with reference to the MWI swath on the ground.

4.3.4 Mission Phasing

To address SUN-1, SUN-7 and SUN-15 in Table 2.1, the SKIM mission is foreseen to implement different mission phases.

The primary mission phase will focus on ocean and sea-ice surfaces through regular repeat coverage measurements during a sustained Ocean Measurement Phase (OMP) to address SUN-1 and mission objectives. This will be the primary mode of operation for the SKIM mission.



In addition, the SKIM mission must be capable of acquiring measurements systematically over land surfaces (SUN-7) to explore the use of SKIM for inland water monitoring (Living Planet Challenge Land 2) and in support of future mission development. Therefore, a limited duration Land Measurement Phase (LMP) will be implemented through the collection of systematic measurements over all land surfaces for one to n orbit cycles depending on scientific priorities and technical constraints.

Finally, noting the need to explore scientifically and technically new data processing and measurement approaches (e.g. slowing, or even stopping, the skim feed horn plate rotation to explore alternative measurement configurations) it must be possible to implement a Scientific Exploration Phase (SEP) as requested by SUN-15. This will allow alternative measurement and acquisition scenarios to be implemented. The SEP phase will be of limited duration typically for some cycles depending on scientific priorities and technical constraints.

4.3.5 Swath Width

At Level-2, a wide swath is required to meet coverage and revisit requirements requested by SUN-9 and SUN-13. In addition, a wide swath is necessary to capture mesoscale structures, tidal flows and TSCV kinematics in a single pass to facilitate applications, to aid interpretation and, for derivation of uncertainty estimates.

Based on the SKIM orbit choice constrained by MetOp-SG(1B) and the need for a 12° off-nadir beam angle (see Section 4.3.6), SKIM should implement a swath width ≥ 290 km.

4.3.6 Coverage and Revisit

These requirements are traced to user needs in Table 2.6 and Mission objectives in Chapter 3. Given the relatively limited swath width of SKIM, revisit should be considered as a mean revisit.

There are no specific revisit requirements for the LMP or the SEP (i.e. there is no requirement to modify the SKIM orbit). SKIM should be developed in such a manner that measurements over land surface are possible (SUN-7).

During OMP, SKIM will acquire scientific measurements over all ocean (including sea ice) surfaces up to 82° North and South, marginal seas and inland seas greater than 50 sq. km. A buffer zone of ≥ 10 km over the land surface should be used to account for uncertainty in the specific land masks used. This traces to SUN-1, SUN-5, and SUN-6. True global ocean coverage (i.e. no 'hole at the pole') would require a larger swath than possible if requirements on beam elevation (related to the need to measure waves) are to be preserved.

For OMP, the revisit must adequately sample kinematic variability at latitudes $>70^\circ$ in a manner that is compatible with monitoring smaller scale motions found there (due to a smaller Rossby radius of deformation). A revisit of less than one day is required for this purpose. The driving requirement is revisit over the equatorial currents which is not as critical owing to the larger scale of ocean structures that are not monitored at all today. At the equator, the revisit time should be ≤ 10 days when including ascending and descending tracks and is the more significant requirement. This approximately translates to the GCOS (2016) request for weekly revisit capability assuming a location at 45° north or south of the equator.



4.3.7 Number of Beams and Beam Characteristics

The fundamental design of the SKIM instrument requires at least one off-nadir beam rotating around the nadir pointing beam to properly sample a wide swath. In practice, several beams are used to ensure adequate sampling. The wide swath required by SKIM (SUN-13) implies at least one off-nadir pointing beam with an incidence angle $>11^\circ$.

Using Ka-band provides advantages in that the projected footprint on the sea surface is relatively small. The footprint is ideally elongated in the elevation direction to sufficiently sample and perform the analysis of the range-resolved reflectivity modulations. The SKIM radar instrument should have an aperture compatible with a ≥ 6 km footprint diameter (1-way, full width -3dB) for all beams in the elevation direction when projected onto the sea surface.

Sufficient off-nadir pointing samples are required to ensure effective measurement density within the SKIM swath, so that an accurate estimate can be derived from a collection of geophysical Doppler measurements (U_{GD}). The ensemble of samples must have sufficient azimuth diversity to ensure the number of near orthogonal crossovers are sufficient to derive an accurate TSCV.

For optimal measurement accuracy, a range of incidence angles between $\geq 6^\circ$ and $\leq 12^\circ$ are required to secure sufficient sampling across the swath. Beam scanning should then ensure a coverage with azimuthal diversity of at least 45° within a 30 by 30 km cell.

A nadir beam is required to provide a reference beam for radar tracking purposes. This beam will also ensure good signal tracking for all off-nadir beams. It will also act as a classical delay Doppler radar altimeter to estimate Sea Surface Height (SSH), significant wave height (H_s), wind speed (U_{10}) and normalised radar cross section (σ^0). These products are standard for the altimetry community and imply a measurement sampling rate of > 4 Hz. The user need for a nadir beam is traced to SUN-3, SUN-7 and SUN-19.

4.3.8 Radar Performance

As experimentally obtained (Yurovsky et al., 2017a, 2017b), at the low-incidence angles used by SKIM and over a wide range of environmental conditions, sea-surface Ka-band reflectivity does not differ between VV or HH polarisation. A choice of VV polarisation has been made for the SKIM mission.

4.3.8.1 Nadir Beam Range Performance

Accurate SSH measurements that are to make a useful contribution to sea-level estimates from space require stringent range bias stability. The range bias stability for the SKIM nadir-pointing beam will be ≤ 2 mm yr⁻¹ over the mission duration (five years). Range bias and stability can be derived from overpass of a transponder or crossover analyses with other altimeter missions.

Accurate SSH measurements at nadir place stringent range error requirements on the SKIM nadir pointing beam. Nadir echoes are mainly affected by speckle noise and thermal noise. Speckle noise is the major contributor; it is due to the coherent nature of the radar illumination and cannot be minimised. However, averaging several echoes into a waveform reduces speckle reduction significantly.



The SKIM nadir beam should have a performance at least equal to the current generation of satellite altimeters. SUN-19 requests a performance equivalent to the Jason-3 altimeter. The random range noise for the SKIM instrument nadir pointing beam should be ≤ 1.5 cm (goal: < 1 cm) at a $H_s = 2$ m and wind speed = 7 m s^{-1} ($\sigma^0 = 8$ dB) at 1 Hz (1σ , zero mean). The specified altimeter random error assumes a perfect Brown model (or Haynes model) echoes.

4.3.8.2 Nadir Beam σ^0 Performance

These requirements are traced to SUN-5 and SUN-19 in Table 2.6.

Based on data from the AltiKa altimeter, a σ^0 dynamic range of 5 dB to 20 dB over global ocean surfaces is required for the nadir beam.

In the polar regions (ice and calm water leads), data from the AltiKa altimeter show that a σ^0 dynamic range of 0 to 50 dB is required. Following conventional altimetry, the total absolute accuracy of the nadir pointing beam σ^0 measurement should be better than ± 0.5 dB (1 sigma, zero mean), after appropriate calibration.

4.3.8.3 Nadir Beam Data Processing

SKIM plans to implement an onboard Range Migration Correction (RMC) algorithm that provides an efficient approach to reduce the data volume (a solution developed and implemented for the Sentinel-6 Poseidon-4 altimeter). However, the approach uses approximations leading to Doppler stack mis-alignment: a fixed RMC matrix is applied for mean altitude, mean sea-surface slopes are not accounted for and the accuracy of radial velocity estimates are relatively poor compared to that available on ground. Onboard RMC can be reversed on ground (solution developed and implemented for the Copernicus Sentinel-6 Poseidon-4 altimeter) without loss of useful information so that Doppler stack misalignment can be corrected (requiring I and Q signals). Accurate SAR processing is then applied on ground including: optimal sea-ice processing, fully-focussed SAR, SAR multi-looking, RMC stacking, ACDC, pulse-pair amongst others. Simulations suggest that 64 range bins and 16 Doppler bands are required to achieve good performance (64 and 128 range bin noise levels are identical for range, H_s and σ^0).

If onboard RMC is not reversible, this implies Level-2 processing must account for onboard errors in the echo modelling otherwise, large H_s and SSH errors are expected. This makes the Level-2 processing more complicated, risky and less processing options are possible. Therefore, any onboard RMC processing applied to the SKIM nadir-pointing beam will be reversible on ground.

4.3.8.4 Range Resolution of the Off-nadir Beams

These requirements are traceable to the Mission objectives and SUN-2 and SUN-4 in Table 2.1.

The ‘matching wavefront technique’ (Jackson, 1981, Jackson et al., 1985a; 1985b) requires a very high range resolution. Using Ka-band, a large bandwidth can be considered to provide a high vertical range resolution compared to other instruments. Using Sentinel-1 C-band wave-mode data, a clean signal is obtained at a range resolution of 3–4 m. Considering about 2048 range gates for a footprint of 10 km at 12° , a range resolution of ~ 4 m is obtained projected on ground with reference to the WGS-84 ellipsoid. Beams at other incidence angles



may have different range resolutions. For SKIM, a 200 MHz bandwidth is proposed implying a slant range resolution of ~ 0.75 m, leading to ~ 4 m radial resolution at 12° . After on-board processing for range migration correction (RMC), the resulting resolution is reduced.

For oblique beams, the measurement of wave-induced modulations and proper acquisition on all surfaces requires an on-ground projected range resolution ≤ 6 m. This will ensure sufficient performance to analyse range-resolved radar-reflectivity modulations, below Nyquist requirements to sample scales ≤ 30 m wavelength.

4.3.8.5 Normalised Radar Cross Section Dynamic Range of the Off-nadir Beams

These requirements are traceable to the Mission objectives.

The reference σ^0 curves, as a function of wind speed and incidence angle that will be used for SKIM are provided by Vandemark et al. (2004) and Walsh et al. (2008). Other curves confirm the basic relationship including Yurovsky et al., (2017a, 2017b), Walsh et al. (2008) and Yan et al. (2019).

Using the Global Precipitation Measurement (GPM), the characteristics of σ^0 at Ka-band (35.5 GHz) are starting to be well understood (e.g. Nouguier et al., 2016, Yan et al., 2019). The GPM satellite, launched into a Sun-synchronous orbit on February 27 2014, carries the first spaceborne Ku/Ka-band dual-frequency precipitation radar providing measurements from the tropical zone to 65° N/S. The Ka precipitation radar operates at with a nadir-oriented antenna that scans a 125-km ground swath providing a 5 km \times 5 km surface footprint for incidence angles up to 9° .

In order to extend the range of incidence angles to those of SKIM ($11-12^\circ$), numerous airborne studies are available (e.g. Walsh et al., 1998, Tanelli et al., 2006) that confirm the theoretical fall-off analysis of the relative backscatter power (Walsh et al., 2008, Nouguier et al., 2016). As interpreted, the near-Gaussian fall-off provides sea-surface slope statistical parameters, in line with Ku-band measurements, but closer to expected optical signals, exhibiting similar dependence on wind speed and wind direction. In particular, the predicted effects of the most energetic long waves must be considered.

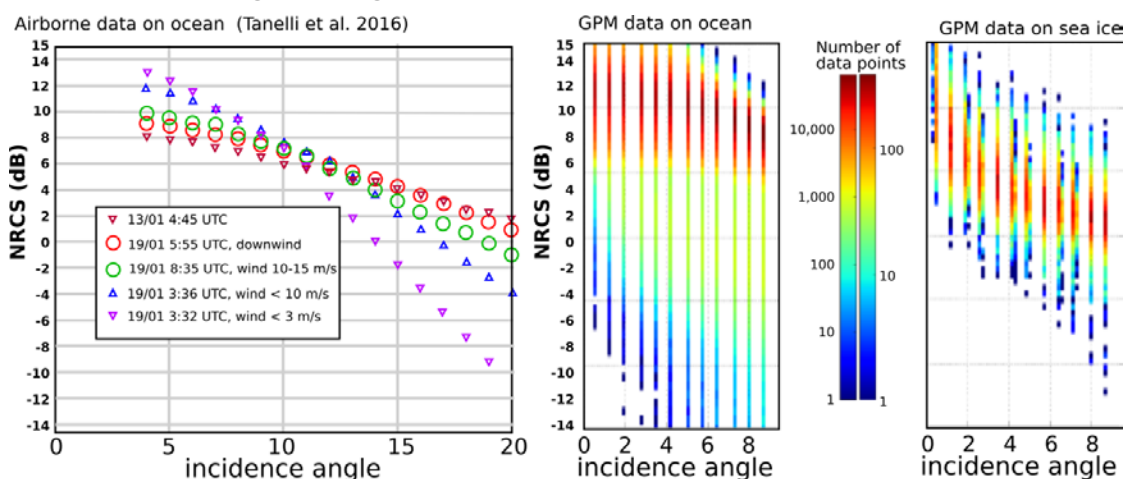


Figure 4.6. NRCS variation with incidence angle over the ocean and sea ice. Left: derived from the Airborne Precipitation Radar-2 (APR-2, Sadowy et al., 2003) for a few cases analysed by Tanelli et al. (2006), and from GPM KaPR data for (centre) ice-free ocean and (right) sea ice, with many more data but limited to 9° incidence in the available Level-2 data. (A. Mouche, LOPS/N. Longépé, CLS)

Figure 4.6 shows an example of off-nadir airborne data for Ka-band. The minimal variation of σ^0 in the incidence range of 10–12° for moderate wind speeds (which is why SKIM has chosen this incidence angle). It is complementary to the extensive GPM Ka-band measurements over ocean surfaces: a dynamic range of -15 to 15 dB is required.

The GPM mission has recently acquired Ka-band measurements at higher incidence angles including 12°. However, these data are not yet available to the community for analysis but will be studied in the context of the SKIM Phase-B1. In particular, the analysis of σ^0 over sea ice will benefit from the wider swath and longer acquisition record. A dynamic range of -15 to 15 dB is required for SKIM off-nadir beams with a ≤ 0.1 dB radiometric resolution.

4.3.8.6 Radiometric Resolution (precision)

These requirements are traceable to the Mission objectives.

The ocean-surface wave modulation spectrum performance depends on the radar capability to detect weak reflectivity modulation. The lowest sea-wave wavelength detection for SKIM has an objective set at ≤ 30 m. Reflectivity modulation can be as low as 0.2 dB, which drives a requirement on radiometric resolution. Considering observed spectra from Leckler et al. (2015), relative modulations of σ^0 are $\sim 8\%$ in the downwind direction for wavelengths 10–20 m, azimuthally averaged over 200 m. This reduces to 2.5% (which is 0.1 dB) for the SKIM. Resolving waves at ≤ 30 m wavelength thus requires a modulation sensitivity of ≤ 0.1 dB. This also matches the precision required to interpret elevation and azimuth variation cross-section according to a given geophysical model function.

4.3.8.7 Radiometric Accuracy

These requirements are traceable to the Mission objectives.

The absolute radiometric accuracy of each beam should be ≤ 1 dB (goal of 0.5 dB). AltiKa specifies σ^0 absolute bias after in-flight calibration lower than 0.7 dB, with a 0.2 dB stability (relative accuracy, which includes noise and non-calibrated drifts errors). The antenna gain may vary during the rotation and this alone will affect the radiometric accuracy. The total absolute accuracy ≤ 0.5 dB (after calibration over the lifetime of the mission) and radiometric stability for each beam ≤ 0.15 dB is required (the former for a stable climate record and the latter for consistency of measurement).

To allow detailed reprocessing and calibration/validation activities, access to antenna gain patterns is required by the scientific community. It is noted that based on the experience with SWIM on CFOSat, characterisation should be available with an azimuthal resolution much better than 45°.

4.3.8.8 Relative Radiometric Accuracy: the Impact of NRCS gradients on V_{NG}

The measured velocity is averaged over the antenna footprint with a separation of the echoes in the range direction (Fig. 4.7 left). Any non-homogeneity of the backscatter across the footprint introduces a difference, δ , between the apparent pointing azimuth φ_a and the true boresight angle φ_b (Fig. 4.7 right).

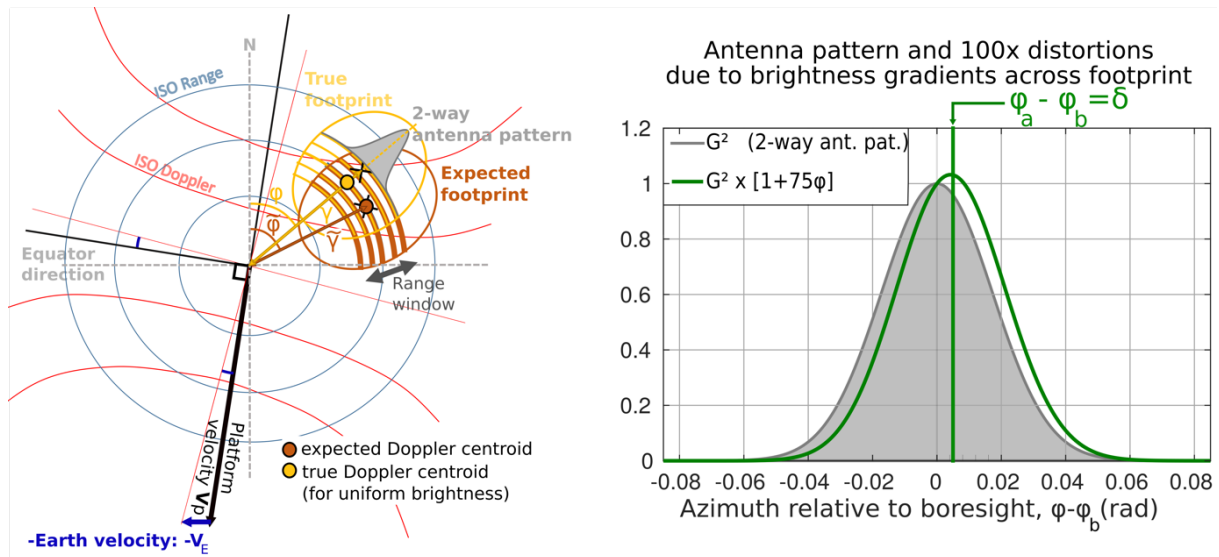


Figure 4.7. Left: the effect of pointing knowledge error. Right: apparent additional mis-pointing resulting from the effective antenna pattern distortions induced by a linear NRCS gradients $\sigma^0=1+75 \varphi$ which is typically 100 times the expected true variability of NRCS. (LOPS)

The difference, δ , induced by fluctuations with wavelengths shorter than $\sim 1/3$ of the 1-way footprint diameter are generally negligible (LOPS 2019b). The effect places requirements on the relative radiometric accuracy during one rotation of the beams. This effect of the σ^0 gradient is also included in V_{NG} . This can, to first order, be estimated from vector wind measurements (for the largest scales). For the σ^0 gradients that only impact one footprint (due to gradients in current and wind), the effect is treated as a random fluctuation parameterized based on SARAL-AltiKa measurements (LOPS 2019b). Further processing can be considered (e.g. applying an unfocussed SAR method to analyse backscatter variations in azimuth) if necessary. The estimation of δ can then be used to flag data and/or be included the effective pointing and calculation of V_{NG} .

The relative radiometric accuracy within a SKIM radar beam will be ≤ 0.1 dB (1-sigma, zero mean). It is likely that the antenna gain may vary during the rotation and this alone will affect the radiometric accuracy.

4.3.8.9 Radiometric Stability

This requirement is traced to the need for a stable data set if it is to contribute to the TSCV ECV (GCOS, 2016) and SUN-20 in Table 2.6.

The radiometric stability for each SKIM beam, after calibration, will be ≤ 0.5 dB over the five-year minimum life of the mission. It may be more advantageous to consider stability over an annual period and over the mission lifetime. In this way, performance metrics could be computed each year. The radiometric stability for each SKIM beam, after calibration, will be ≤ 0.2 dB over a single orbit.

4.3.8.10 Radiometric Accuracy Between Beams

This requirement is traced to the mission requirements.



Consistency between beam measurements is obviously important because U_{CD} vector component are estimated from different beams will be combined. In addition, there are implications for the fine-pointing algorithms described in Chapter 6 should the radiometric characteristics of beams change significantly over several rotations of the feed horn plate. The relative radiometric accuracy between all SKIM beams will be ≤ 0.15 dB (goal 0.05 dB) over one full rotation of all beams both 1-sigma, zero mean. 0.1 dB A goal of ≤ 0.05 dB is set.

4.3.9 Precise Orbit Determination

This requirement is traced to the mission requirements.

Precise Orbit Determination (POD) is a critical part of the SKIM mission. Typically, a GNSS receiver will provide the data necessary for POD processed on ground to achieve the overall mission performance. Real-time navigation and datation information from this equipment typically drives spacecraft navigation and datation functions as well as the control of any nadir beam open-loop tracking function if implemented. A GNSS solution provides position and velocity relative to the adopted reference system to support open loop operation including the satellite height above reference ellipsoid and altitude rate derived from a navigation solution.

The satellite position should be determined in the nadir direction as in near-real-time (NRT, ≤ 3 hours) to ≤ 10 cm (goal: 8 cm). For slow-time critical (STC, ≤ 48 hours) the requirement is ≤ 5 cm (goal 3 cm) and for non-time critical (NTC, ≤ 1 month), ≤ 5 cm (goal: ≤ 3 cm). This assumes the use of all onboard equipment and links to a POD service (e.g. The Copernicus POD service, Fernandez et al., 2016).

Orbital solutions computed may use different GNSS processing schemes, models and software. For the Copernicus POD service, typical accuracy in 3D RMS is in the order of 1.5 cm for all satellites. Satellite laser ranging measurements can be used as an independent means to validate the orbital accuracy. The NRT specification is required for onboard tracking and potential use of any open-loop tracking commands. The orbit radial component navigation solution precision (RMS) will be ≤ 3.0 cm. This is derived for the end-to-end range performance uncertainty estimation for the SKIM nadir-pointing beam.

Owing to the stringent pointing requirements for the Doppler SKIM mission startracker, angular position of the antenna and other relevant data will be required to precisely reconstitute SKIM pointing and as input to Level-2 retrieval algorithms applied by the user community. Access on ground to all startracker quaternions to monitor pointing is required by the scientific community.

In addition, access on ground to all high resolution gyro startracker data are requested to support on-ground pointing reconstruction. Access to GNSS position, velocity and time at high resolution is also requested to monitor pointing and radial velocity. This is required to allow re-computation and validation of instrument pointing.

Individual unprocessed (high resolution) attitude sensor data (e.g. from each startracker, gyro and GNSS) should be available on ground in addition to any onboard AOCs solution.

4.3.10 Geolocation Requirements

This requirement is traced to SUN-11 in Table 2.6.

Geolocation accuracy is driven by the need to ensure that the location of SKIM measurements is correct and can be used together with other satellite and *in situ* data. As SKIM is producing vector-based products that are to be used in ocean-model systems, the geolocation accuracy must be much less than the typical model analysis grid cells (which is ~2 km). However, for direct assimilation into other model systems that have high spatial resolution (~1 km) a geolocation accuracy of ≤ 0.1 km is required. The absolute geolocation accuracy of SKIM measurements in all beams at Level-1b, measured at the centre of the range window, should be ≤ 0.1 km (1-sigma, zero mean) with reference to the WGS84 ellipsoid.

The spatial resolution of MetOp-SG(1B) MWI measurements at the highest resolution are 10 km and geolocation accuracy for these measurements is set at < 2.5 km (1σ , zero-mean). The nominal spatial resolution of MetOp-SG(1B) SCA is 25 km gridded cells, although 12.5 km gridded products will be available. The geolocation accuracy for SCA is set at < 1 km (1σ , zero-mean see Rostan et al., 2016). The SKIM geolocation accuracy requirement of ≤ 0.1 km easily satisfies the colocation with MetOp-SG(1B) MWI and SCA geolocation accuracy.

4.3.11 Product Delivery Latency

This requirement is traced to SUN-21 in Table 2.6.

Accurate orbits from a POD service will only be available within 48 hours of data reception (i.e. short-time critical). This sets a limit on product timeliness for high-quality nadir-beam altimetry products.

Otherwise, all Level-1 products will be made available to the users with a latency of ≤ 24 hours from sensing. Obviously, for emergency applications such as safety of life at sea, oil or chemical spills, a near real-time timeliness for TSCV and Stokes drift measurements of ≤ 3 hours from data acquisition at the point of user pickup would be needed. This is traced to nowcasting user requirements set out in Chapter 2. This must be considered in later phases of mission development.

4.3.12 Mission Lifetime

This requirement is traced to SUN-12 in Table 2.6.

To assess the full potential of Doppler oceanography and anticipate technological challenges for a future generation of missions a lifetime of five years or more is required, with a goal of 10 years.

SKIM scientific objectives are targeted at multiple time scales, from local snapshots of TSCV to a long-term analysis of the rapidly evolving Arctic and Antarctic waters. To be able to identify and characterise the interactions and dynamics of ocean-surface currents, wave directional spectral properties, and discriminate the processes and characteristics in high latitudes to the equatorial current systems, a lifetime of ≥ 5 years is required. To sample one major climatic extreme event, such as an El Niño event (e.g. Trenberth and Hurrell, 1994; Cane, 2005; McPhaden et al., 2006, Godoi et al., 2019), a minimum duration of ≥ 5 years is needed (ideally 7–10 years). A lifetime of ≥ 5 years is the minimum requirement to monitor



the seasonal variability of TSCV and, in particular, the seasonal and interannual characteristics of the Arctic and equatorial surface-current systems (amongst other areas).

4.3.13 Scientific Diagnostics and Algorithm Evolution

This requirement is traced to SUN-15 in Table 2.6.

Since SKIM will implement significant on-board processing to mitigate the need to send large data volumes to ground from a 32 KHz PRF radar, access to low-level data prior to On-Board Processing (OBP) is required for a limited duration. This data will be used to verify the OBP and to evolve, if required, new approaches to use the SKIM radar. This implies that OBP software is implemented in a manner that is fully reconfigurable.

The requirement is set at a maximum of 1 minute of unprocessed data per SKIM orbit which is sufficient to study the low-level performance of the SKIM payload over time and consider alternative processing approaches to the measurement data.

For mission analysis at Phase A, the SKIM MAG has derived a mask indicating which areas RAW data should be acquired according to the geophysical challenges that may require additional algorithm development. The mask is shown in Fig. 5.28 and will be fine-tuned during Phase E1 depending on specific needs (always maintaining a limit of 1 minute per orbit).

4.4 Level-1 SKIM Products

Two SKIM Level-1b product are described in Table 4.3.

Name	Description and Application	Format and Resolution
Level-1a-RAW	This is a user product for research and development for algorithm development and testing. It has high relevance to specialist users and instrument engineers and is linked to SUN-15. L1A-RAW is a specialised raw radar data with minimum onboard data processing applied. It is repackaged from Level-0 source packets. This product is extremely large and only a very limited amount of data (one minute per orbit) will be sent to ground.	One NetCDF per orbit. Native to SKaR instrument.
Level-1b	This is the fundamental data product used for all higher order processing and addresses all user needs in Table 2.6 It contains instrument and detailed engineering data (quaternions, satellite velocity vector, pointing information, onboard temperature sensors, radar antenna position etc.) in instrument geometry, projected on ground. Notably, the product will include high-frequency samples from AOCS sensors to assist in the computation of non-geophysical Doppler. The Level-1b processor produces products containing observation data in engineering units: Power detected, range selected, and multi-looked waveforms. Coherently averaged, correlated pulse pair waveforms. Unfocussed SAR processed off-nadir beam power gates and Doppler bins. Unfocussed SAR processed nadir beam: range power gates Doppler bins. Delta-K dispersion relationship anomaly data. Calibration and geolocation is applied at this level. Data is projected in ground range coordinates, assuming the WGS84 ellipsoid model for Earth. An additional product, L1B_NGD provides an estimate for the non-geophysical Doppler velocity due to platform motion and non-ideal antenna patterns. This is the baseline instrument user product for all users.	One NetCDF like file per orbit. Radar range gates across azimuth and engineering data

Table 4.3. SKIM Level-2 product definitions.

5 MISSION ELEMENTS

This chapter provides the technical description of the SKIM mission, as derived from the preparatory activities in Phase A. Two technical baseline concepts are described that respond to the mission requirements defined in previous chapters. The concepts were developed in two parallel Phase A system studies by two industrial consortia led by Airbus Defence and Space S.A.U. and OHB System AG, respectively. Both consortia shared the same subcontractor (Thales Alenia Space France) for the main radar instrument because of the significant amount of heritage derived from the SWIM instrument on CFOSat. Whenever relevant, two implementation concepts (Concepts A and B) are described to present the different implementation options capable of meeting the mission requirements. The figures below are courtesy of the respective industrial consortia.

After an overview of the mission architecture and the orbit characteristics (Sections 5.1 and 5.2) the space segment is described in detail (Section 5.3) followed by the launcher, ground segment and operations concept (Sections 5.4, 5.5, 5.6). The overall mission performance is summarised in Chapter 7.

5.1 Mission Architecture Overview

The key architectural elements of the SKIM mission are shown in Fig. 5.1. The space segment comprises a single spacecraft carrying a Ka-band radar called SKaR (SKIM Ka-band radar). The space segment comprises a single spacecraft carrying a Ka-band radar called SKaR (SKIM Ka-band radar). The platform will be a standard low-Earth orbit platform, including a Precise Orbit Determination (POD) package consisting of a fully redundant Global Navigation Satellite System (GNSS) assembly and a Laser Retro Reflector (LRR).

The satellite will be operated in a near-polar, Sun-synchronous quasi-circular frozen orbit at an average altitude of 832 km. The orbit is designed to maximise collocated and simultaneous observations with MetOp-SG(1B)'s scatterometer (SCA) and Microwave Imaging radiometer (MWI) instruments. This is achieved by a separation in the Local Time of Descending Node (LTDN) of 23 min with respect to the MetOp-SG(1B) orbit. Concept A has been optimised for a westward LTDN shift, whereas Concept B has been optimised for an eastward shift. A time separation along the orbit of 30 s (when observed from an Earth-fixed reference frame) with SKIM flying ahead of MetOp-SG(1B) ensures a safe and stable loose formation.

The operations scenario foresees a continuous nadir-looking observation of all large water and sea ice surfaces (exceeding an area of 50 sq km) between the latitudes of 82° North and South.

The baseline launcher Vega-C will inject the satellite into its target orbit. The SKaR data will be downlinked to the ground station(s) via a radio link in the X-band. Concept A assumes ground stations in Kiruna (Sweden) and Maspalomas (Spain), whereas Concept B uses a single ground station in Svalbard (Norway). The SKIM mission will nominally last five years with sufficient propellant to last seven years.

The ground segment uses the generic Earth Explorer ground segment infrastructure and comprises the Flight Operation Segment (FOS), including the Telemetry, Tracking and Command (TT&C) ground station and the flight operations control centre, and the Payload

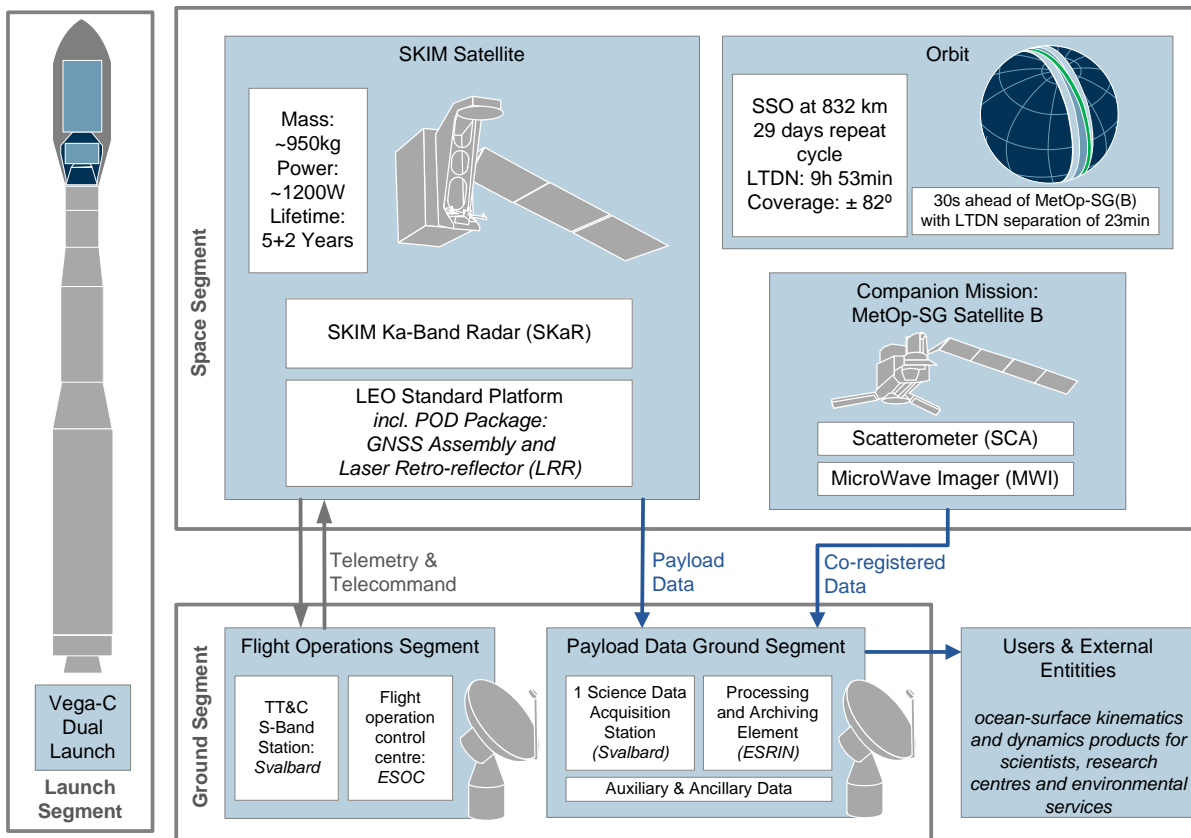


Figure 5.1. SKIM mission architecture for Concept B.

Data Ground Segment (PDGS), including the Science Data Acquisition Station, the Processing and Archiving Element and the Mission Planning and Monitoring Element. The PDGS receives auxiliary data, such as wet/dry troposphere model data, Digital Elevation Models (DEMs) and the SCA/MWI data, to be used in the end-to-end system calibration and processing of the SKaR data.

5.2 Mission Analysis and Orbit Selection

A number of orbits have been considered for the SKIM mission, looking for the optimum combination of science return, mission complexity and revisit time. By flying in loose formation with MetOp-SG(1B), SKIM can benefit from independent and quasi-simultaneous wind vector measurements taken by the Ku-band SCA. Furthermore, the data from the multi-channel MWI can be used to apply a wet-tropospheric correction across the entire swath of SKIM, without adding instruments to the SKIM spacecraft.

5.2.1 Flight Configuration with MetOp-SG(1B)

The selection of the SKIM orbit and flight configuration with MetOp-SG(1B) in Chapter 4 are driven by the maximisation of the collocated and simultaneous observations with the SCA and MWI instruments. The SCA instrument features a very large swath consisting of two lateral bands of 660 km with a 525-km nadir gap in between (Fig. 5.2, left). The MWI instrument is a conically-scanning passive radiometric imager, which rotates continuously

about an axis parallel to the local spacecraft vertical. MWI covers a 1600 km-wide swath centred on the sub-satellite track, as shown in the right panel of Fig. 5.2.

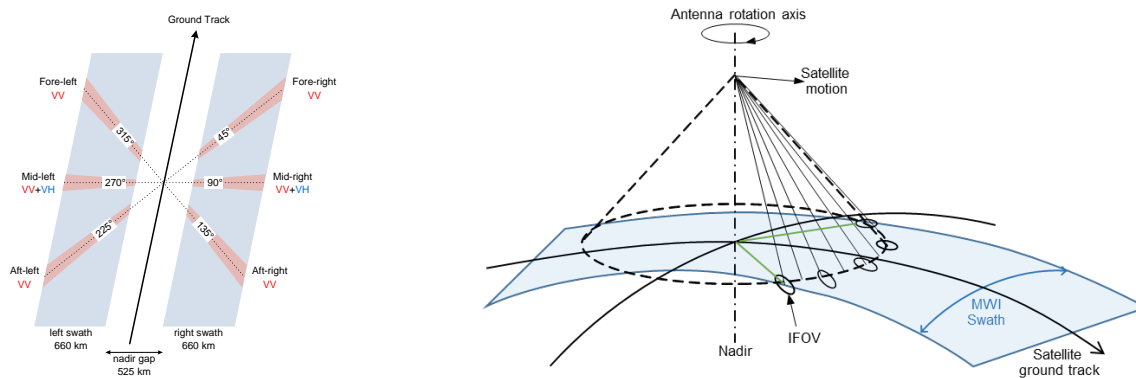


Figure 5.2. MetOp-SG(1B) SCA swath geometry (left) and MWI swath geometry (right).

Fig. 5.3 shows the overlap of the SKIM swath and the SCA and MWI swaths over one orbit, for the ascending pass. To maximise the spatial and temporal overlap of observations with MWI and SCA, SKIM flies in a loose formation with MetOp-SG(1B), in the same orbit, but shifted in Local Time of Descending Node (LTDN). This configuration means that the SKIM swath is always within the MWI swath, while total overlap with the SCA swath is achieved in the latitude band between 47.2°N and 47.2°S. Partial overlap is achieved from 47.2°N to 71.6°N (and the symmetric band with respect to the equator). Figure 5.4. shows the relative geometry of SCA (blue, shaded), MWI (green, dashed) and SKIM (red, transparent) swaths for Concept B in an ascending pass at low latitudes (left) and high latitudes (right). This performance fully complies with the scientific requirements for SKIM.

The SKIM reference orbit is Sun-synchronous and frozen, being in the same orbit as MetOp-SG(1B). The orbit properties for Concept B are summarised in Table 5.1. The orbit has a 29-day repeat cycle and an LTDN of 09:52:52. The frozen orbit keeps a constant altitude profile as a function of the argument of latitude, shown in Fig. 5.5. The orbit reference altitude, defined as the difference between the mean semi-major axis of the orbit and the Earth equatorial radius, is 817.5 km, while the average altitude over the geoid is 832.2 km.

Mean Orbital Elements		Orbit Characteristics		SKIM – MetOp-SG(1B) Characteristics	Formation
Semi-major axis	7195.59 km	Repeat cycle	14+6/29	Initial mean anomaly separation	30.0 s
Eccentricity	0.0010249	RC length	29 days	Max. mean anomaly separation	32.3 s
Inclination	98.702°	Orbits/day	14.207	Min. distance in a worst-case scenario	> 100 km
LTDN	09:52:52	Orbits/cycle	412		

Table 5.1. SKIM orbit properties for Concept B. Concept A parameters are similar, but the LTDN is at 09:06.

The satellite configuration for both concepts is explained in more detail in Section 5.3.2. The configuration for Concept A is ideally suited for use in dawn-dusk orbits, with fixed solar panels deployed towards the bottom floor of the spacecraft. The configuration for Concept B is ideally suited for use in noon-midnight orbits, with a rotating solar panel mounted on a side panel. Since the MetOp-SG(1B) orbit is roughly halfway in between, with an LTDN at

09:30, the orbit for Concept A has been optimised by shifting the LTDN westwards, closer to the dusk-dawn orbit. Conversely, the orbit for Concept B has been optimised by shifting the LTDN eastwards, closer to the noon-midnight orbit. This is illustrated in Fig. 5.6. In both cases, additional measures are required to optimise the illumination on the solar panels, as explained in Section 5.3.2.

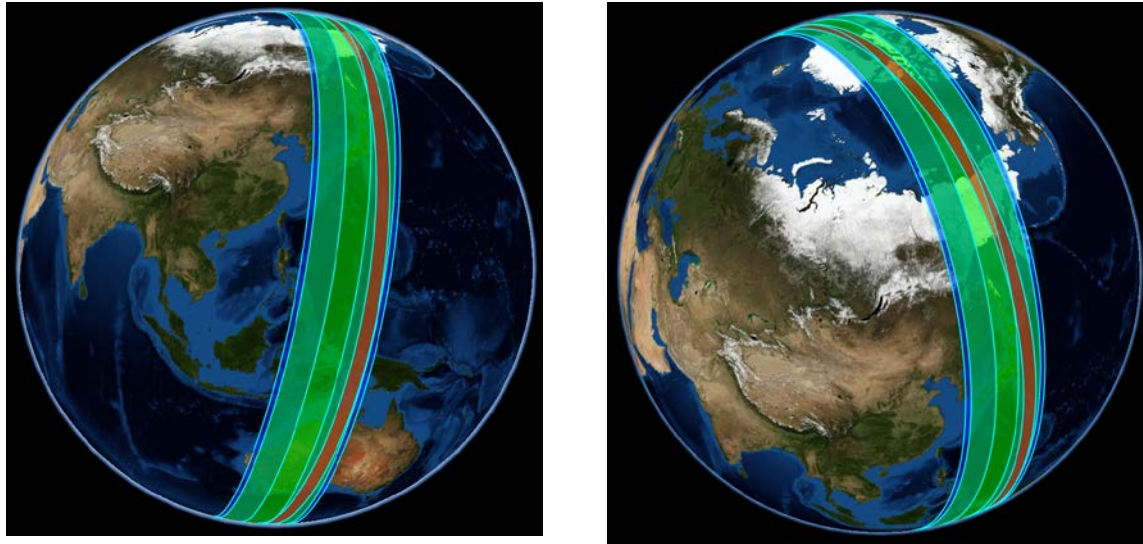


Figure 5.3. Overlap of the SKIM swath (red) and MetOp-SG(1B) SCA and MWI swaths (blue and green respectively) for an ascending pass. In this example the SKIM orbit is shifted eastwards with respect to the MetOp-SG(1B) orbit as is the case for Concept B (DEIMOS)

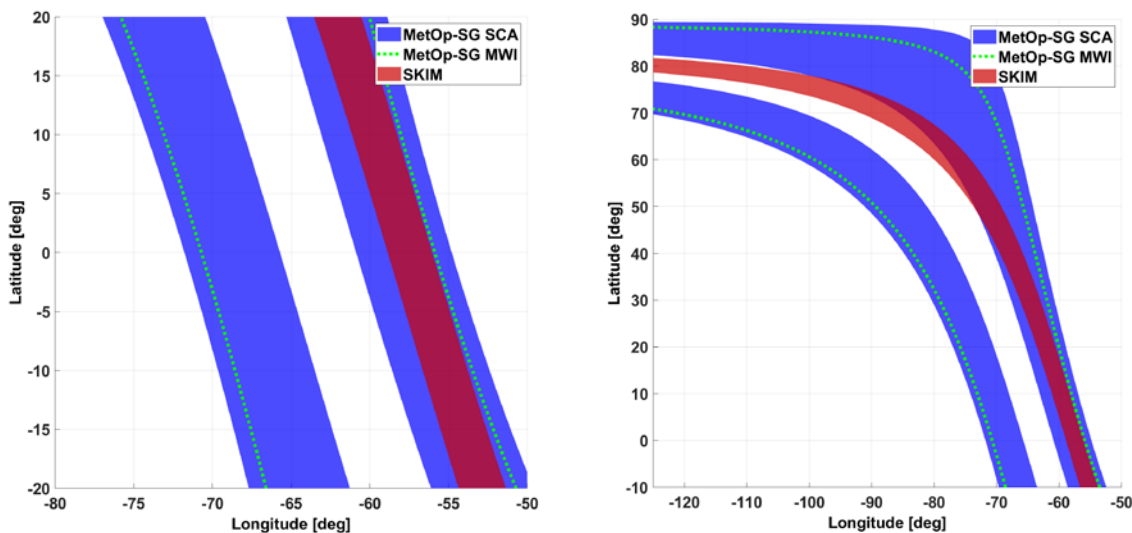


Figure 5.4. Relative geometry of SCA (blue, shaded), MWI (green, dashed) and SKIM (red, transparent) swaths for Concept B for an ascending pass at low latitudes (left) and high latitudes (right) (DEIMOS).

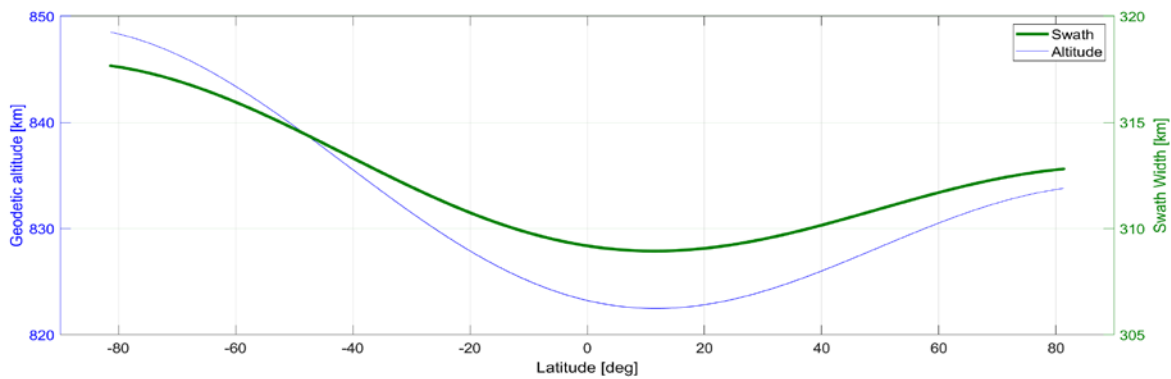


Figure 5.5. Altitude profile and swath width plotted over one repeat cycle as function of geodetic latitude for the 14+6/29 Sun-synchronous orbit. Swath width is here defined up to 12° incidence angle (DEIMOS).

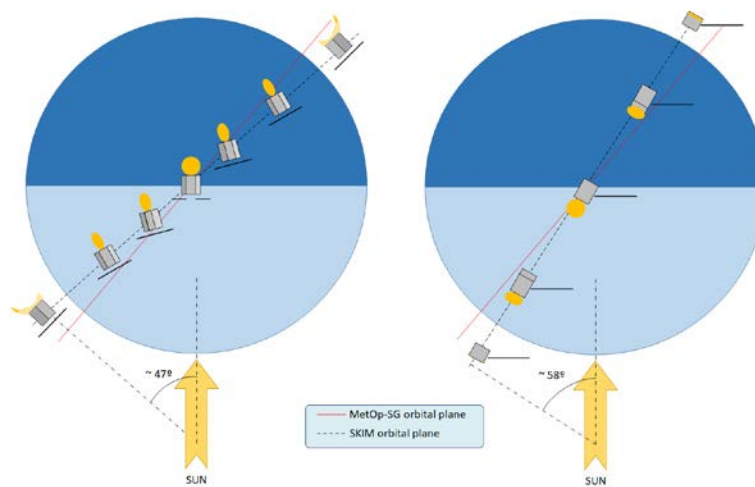


Figure 5.6. Rotation of the orbital plane (dashed) with respect to that of MetOp-SG(1B) (solid, red) as viewed down on the North Pole for Concept A (left) and Concept B (right). The yaw steering for Concept A and the canted rotation of the solar array for Concept B are also shown.

To have the same orbital period, the SKIM orbit height should be exactly the same as for MetOp-SG(1B). As the orbit planes are different, there is no risk of collision with the exception of the poles, where the orbit planes intercept. The formation is therefore designed to be passive-safe: the natural relative orbit evolution makes SKIM and MetOp-SG(1B) drift apart in nominal conditions, with the minimum satellite separation (30 seconds) large enough to avoid close approaches and radio-frequency interference. To achieve this objective, the spacecraft with the smaller ballistic coefficient (SKIM) leads the formation, while the other (MetOp-SG) follows. SKIM decays faster and drifts forward, increasing the inter-satellite separation. The swath geometry evolution is such that the SKIM swath drifts towards the east. The initial LTDN delta between the two satellites is thus selected to guarantee that the SKIM and MWI east swath bounds overlap at the maximum mean anomaly separation between the two satellites (Fig. 5.4), always achieving total overlap between the SKIM and MWI swaths.

To challenge the safety requirement and assess the formation robustness, a sensitivity analysis has been performed on the evolution of the formation, considering 2-sigma deviations of the SKIM ballistic coefficient with respect to the design value, to cover design

uncertainties and changes in the ballistic coefficient in the case of contingency situations (e.g. SKIM safe mode activation). When the 2-sigma deviation is positive, the SKIM ballistic coefficient becomes larger than that of MetOp-SG(1B). In this ‘perturbed’ scenario, the two satellites will start approaching in the nominal formation design. Also in this case, the formation is stable and features very slow relative motion, even with high solar activity (2025-26). With a selection of the initial mean anomaly separation of 30 s, the minimum distance between the two satellites will not become smaller than 100 km in the time interval between the normal ground track correction manoeuvres (implemented approximately every 18 days during 2025-26, when solar activity is high), which can also be used to reset the formation. This analysis confirms that formation safety is guaranteed in all scenarios. In case of failure of either SKIM or MetOp-SG(1B), the passive-safe, loose formation ensures that ground control has several weeks to react, far exceeding the minimum requirement of three days.

The temporal co-registration difference between the SKIM and the MetOp-SG(1B) observations is driven by the separation in LTDN and mean anomaly between orbits, the ground-track inclination and the swath shape.

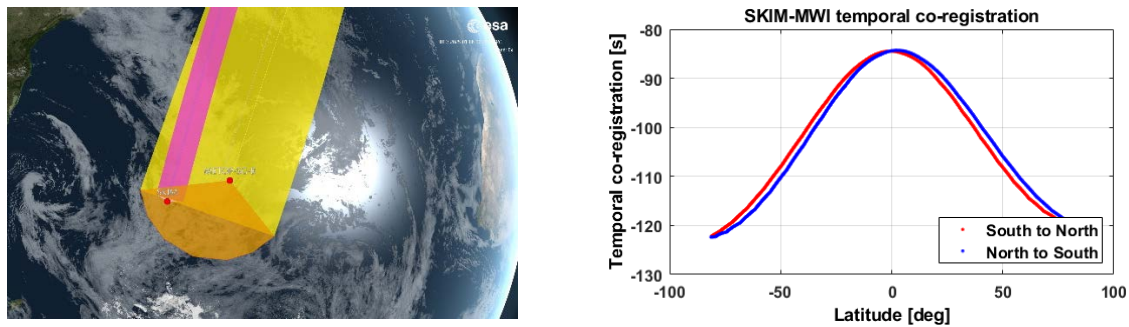


Figure 5.7. The image on the left shows the relative position of SKIM with respect to the MWI footprint (Concept A). SKIM flies ahead of MetOp-SG(1B), but its footprint trails that of MWI. The temporal co-registration between SKIM (nadir) and the MetOp-SG(1B) MWI instrument is shown as a function of latitude on the right (Concept B). The best co-registration is obtained in equatorial regions, where there is more precipitation.

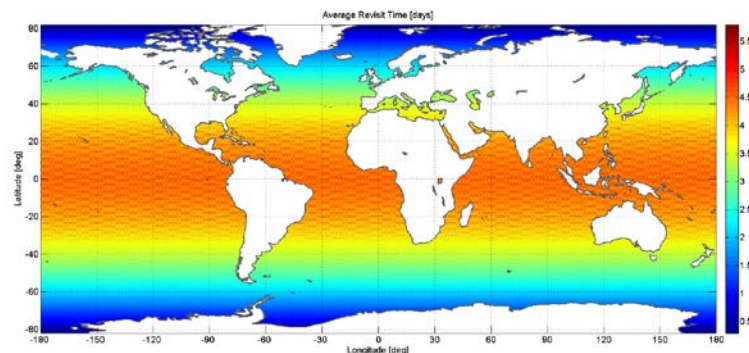


Figure 5.8. Average revisit time of SKIM over ocean and sea (DEIMOS).

Considering a mean anomaly separation between the satellites in the range of 30-32.3 s (Table 5.1), the resulting maximum temporal co-registration difference between SKIM and SCA observations is 18 s, while the maximum temporal co-registration difference is less than



125 s between SKIM and MWI observations as shown in Fig. 5.7. This temporal co-registration is fully compliant with the science requirements. If the mean anomaly separation between satellites increases, the co-registration with MWI improves while the co-registration with SCA worsens. If necessary, the initial spacecraft mean anomaly delta could be adjusted to further reduce the temporal co-registration with MWI observations (while increasing it with SCA). Figure 5.7: The image on the left shows the relative position of SKIM with respect to the MWI footprint (Concept A). SKIM flies ahead of MetOp-SG(1B), but its footprint trails that of MWI. The temporal co-registration between SKIM (nadir) and the MetOp-SG(1B) MWI instrument is shown as a function of latitude on the right (Concept B). The best co-registration is obtained in equatorial regions, where there is more precipitation.

The mean revisit time in equatorial regions is ~ 4.5 days for the SKIM orbit, assuming an Observation to Zenith Angle (OZA) of 12° at the swath edges and acquisitions over ascending and descending passes (Fig. 5.8). The coverage performance is thus compliant with the mean revisit time requirement of six days or less at the equator. The maximum revisit time is 18.5 days at low latitudes close to the equator.

5.2.2 Mission Profile

In order to achieve the target SKIM-MetOp-SG(1B) mean anomaly separation, SKIM will be launched by Vega-C into a phasing orbit with different semi-major axis (SMA), and hence different period, with respect to the reference MetOp-SG(1B) orbit. The orbital period difference triggers a relative drift between the SKIM position in the phasing orbit and MetOp-SG(1B) position in the reference mission orbit. Once the target in-plane relative position of SKIM with respect to MetOp-SG(1B) has been obtained, an in-plane manoeuvre is applied to achieve the nominal SMA of the reference mission orbit. This strategy embeds safety margins in the formation acquisition process and minimises the risk of close approaches between SKIM and MetOp-SG(1B).

The SKIM nominal mission design lifetime is five years, with seven years considered for system sizing. The orbit control strategy consists of combined in-plane and out-of-plane manoeuvres for ground-track control (GTC). Assuming a launch at the end of 2025, in-plane manoeuvres will take place every 34 days on average, with a minimum time between manoeuvres of five days around the solar activity peak. Out-of-plane manoeuvre will take place every 125 days on average, with a minimum interval between them of 66 days. The small difference in the ballistic coefficients of the SKIM and MetOp-SG(1B) spacecraft, combined with the high orbit altitude, entails slow relative dynamics even during high solar activity periods (left panel in Fig. 5.9). Throughout the SKIM lifetime, the GTC in-plane manoeuvres are triggered at time intervals that are shorter than what is needed to avoid any potential collision between the satellites. The time intervals are also shorter than what is needed to control the formation so that the temporal co-registration requirements are met. Thus the GTC in-plane manoeuvres can be tailored to reset the formation with each GTC manoeuvre and dedicated formation control manoeuvres are not needed.

The degradation of spatial co-registration due to formation evolution can be measured by monitoring the latitude band where a given percentage of overlap can be achieved, as well as the evolution of the overlap with time. Figure 5.9 (right) shows the overlap between SKIM and SCA swaths at different latitudes computed over the average time interval (i.e. several orbits) between GTC in-plane manoeuvres in the period with high solar activity. Simulations

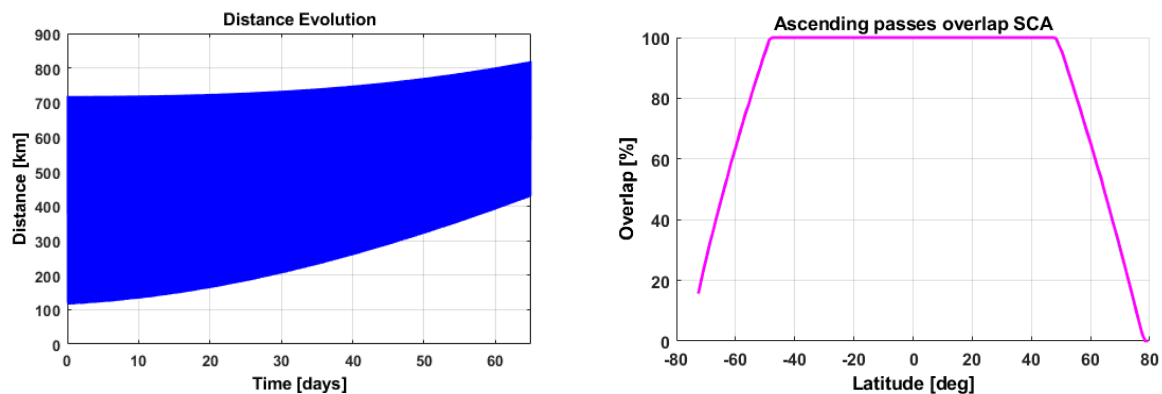


Figure 5.9. SKIM – MetOp-SG(1B) inter-satellite distance evolution (left) and evolution of the overlap between SKIM and SCA swaths versus latitude (right) with high solar activity (DEIMOS).

have been performed with different solar activity conditions. The spatial co-registration performance with SCA is always very stable and its degradation negligible even during the high solar activity period. The overlap with MWI swath is always total.

SKIM will fly in an altitude range characterised by high density of space debris. Therefore, six collision avoidance manoeuvres per year are envisaged. Each manoeuvre involves raising the attitude by 200 m, not followed by any circularisation, and subsequent in-plane manoeuvre to place the spacecraft back into its nominal orbit (more information in Section 5.6.5).

In order to comply with the Space Debris Mitigation Policy and Guidelines, SKIM will perform an end-of-life disposal manoeuvre to lower the orbit perigee to an altitude that guarantees safe uncontrolled decay within 25 years (more information in Section 5.6.6).

5.3 Space Segment

5.3.1 Overview

The top-five key drivers for the design of the SKIM satellite are:

1. The satellite, including a relatively voluminous instrument antenna, must fit in the Vega-C dual launch configuration.
2. To fit within the Earth Explorer 9 programmatic constraints, the instrument must be compatible with a small or medium size standard platform.
3. Sufficient power must be generated to support the radar instrument with a very high duty cycle (always observing when over the ocean).
4. SKIM must fly in the MetOp-SG(1B) orbit.
5. Extremely good pointing knowledge is required over the timescales of interest.

Two industrial teams have come up with two different solutions, even though the instrument design is the same for both. Both concepts can meet the requirements, and are, up to the level that can be determined in Phase A, technically feasible with adequate margins.

The top-level satellite configuration is described in Section 5.3.2 below. Sections 5.3.3 and 5.3.4 provide more details about the payload and the platform respectively. Evidence about the feasibility of the concepts is provided in the system budgets in Section 5.3.5.

5.3.2 Satellite Configuration

For both Concepts, the SKIM space segment consists of a single satellite carrying the SKaR instrument and flying in loose formation with MetOp-SG(1B). Both concepts have the SKaR antenna mounted on the top panel of the platform to provide a clear view of Earth. The antenna bench consists of a Carbon Fibre Reinforced Plastic (CFRP) support structure that maximises mechanical and thermal decoupling from the aluminium top panel of the platform via a set of titanium kinematic mounts. In order to meet the stringent pointing knowledge requirements, both concepts integrate the attitude sensors on the antenna bench. The concepts adopt different flight configurations, which are driven by their respective designs for the electrical power subsystem, as explained in Section 5.2.1. Consequentially, both concepts also adopt a different orientation of the instrument with respect to the orbital plane as illustrated in Fig. 5.6.

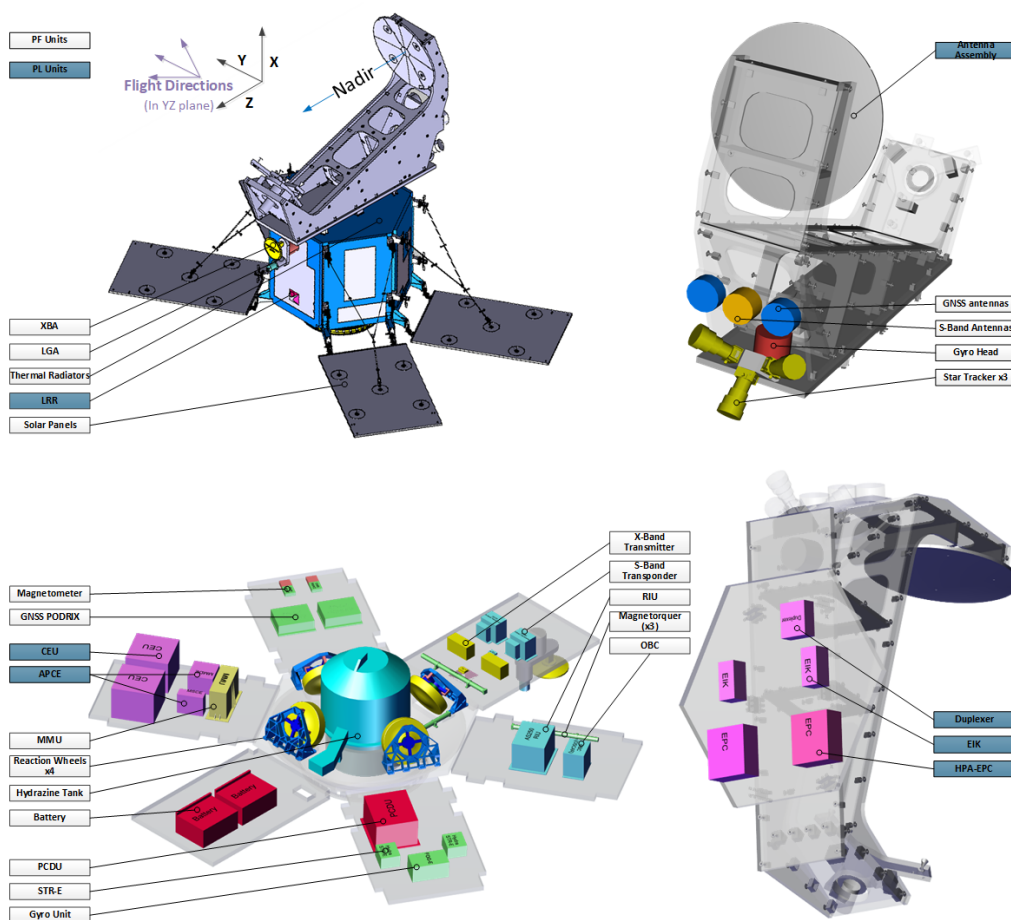


Figure 5.10. Satellite configuration for Concept A.

The hexagonal shape of the platform structure of Concept A maximises the internal volume, providing the space to accommodate both platform and payload units. The four solar panels deploy outwardly from the lateral panels of the hexagon in a petal configuration, as shown in Fig. 5.10. In a dawn-dusk orbit, this would allow the solar panels to be aligned with the orbital plane to obtain near-orthogonal illumination over most of the orbit. At the local time of the MetOp-SG(1B) orbit however, the angle of the incident illumination on the orbital

plane (the beta-angle) is close to 45°. By yaw steering around the nadir, the illumination on the solar panels can be optimised so that it is near orthogonal at the poles and ~45° at the equator. The yaw steering enables the use of much smaller solar panels and platform than would otherwise be needed to accommodate the power needs of the mission. An important advantage of the yaw steering is that direct Sun exposure on the antenna is minimised and limited to the shielded back of the antenna. This reduces the thermo-elastic deformations of the antenna, making it easier to achieve the required pointing knowledge. Concept A avoids the need for a Solar Array Drive Mechanism (SADM) as a potential source of antenna pointing errors.

The top panel of the platform hosts the instrument power electronics, High Power Amplifier (HPA) and the Duplexer. This allows for a short harness to run between the units and the antenna. This panel also offers the radiator area and deep space view required for removing the heat from these high-dissipation units. The rest of the SKaR units, i.e. Central Electronics Unit (CEU) and Antenna Power and Control Equipment (APCE) are mounted on one of the hexagon lateral panels. In this configuration the GNSS antenna and one of the S-band antennas are mounted on the SKaR antenna to achieve an unobstructed field-of-view (FoV).

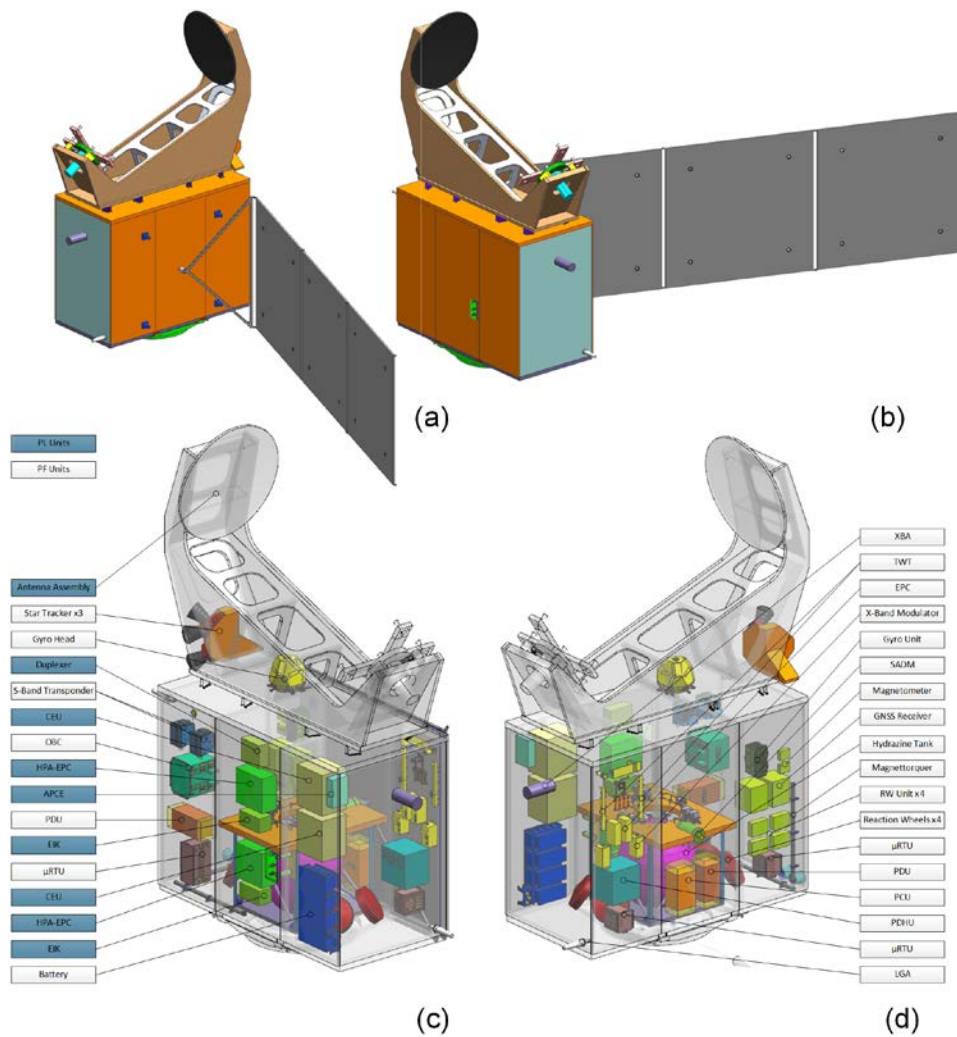


Figure 5.11. Satellite configuration for Concept B.



The satellite configuration for Concept B is shown in Fig. 5.11. The antenna is mounted in the in-flight direction. This allows orbit corrections (altitude raising) to be made without any attitude change of the spacecraft. A single Solar Array (SA) wing is mounted on the side of the spacecraft. By canting the SA backwards by 30° and tracking the Sun around the orbit, a near orthogonal illumination of the SA is obtained throughout the orbit. A SADM rotates the SA by one revolution each orbit. Yaw steering is not required for Concept B.

The Nucleus standard platform used in Concept B has a parallelepiped shape and offers a modular concept with 6 main radiator panels. Each of these panels can be exchanged based on the specific mission needs. For SKIM, one and a half panels are populated with instrument electronics. All electronic units of the payload are mounted on these panels, with ample space for radiators facing the far side of the Sun. The larger size of the platform provides a top panel with optimum support for the payload antenna during launch. It also allows all antennas to be mounted on the platform, including the S- and X-band and the GNSS antennas, whilst ensuring an unobstructed FoV.

5.3.3 Payload

5.3.3.1 Overview

SKIM carries one main instrument, the SKIM Ka-band radar, or SKaR instrument. The instrument combines an accurate state-of-the-art nadir-looking altimeter with novel Doppler enabled wave and current scatterometer capabilities. The instrument uses heritage from the SWIM instrument, developed by CNES, and currently flying on the Chinese-French CFOSat mission. The antenna concept is that of a multi-beam conical scanner, with an offset reflector illuminated by a set of feed horns on a rotating plate. With respect to its predecessor, SKIM adds a Doppler capability to measure motion of the ocean surface. To optimise its Doppler measurement sensitivity, it operates at Ka-band rather than the Ku-band chosen for SWIM. The antenna is roughly twice the size of the SWIM antenna to allow for the longer focal length required at Ka-band. The scanner technology is upgraded to facilitate Doppler measurement stability.

The following Sections address the observation principles and the description of the main instrument. In addition to SKaR, the payload includes a POD sensor complement to enable nadir altimetry to reach the required performance. The POD function is provided by the platform and described in more detail in Section 5.3.3.11.

5.3.3.2 Observation Principles and Technical Requirements

The SKaR observation principle is to gather sparsely distributed samples by scanning a set of beams across a wide swath of approximately 300 km, as shown in Fig. 5.12. One nadir beam provides high accuracy altimetry measurements, and five off-nadir beams gather surface velocity and wave spectrum measurements. There are two off-nadir beams with an incidence angle of 6° and three with 12° incidence angle. The rotating beams provide a sampling pattern over the swath, which requires interpolation in the higher-level processing chain to derive image products. Due to the conical scan, the same surface area is revisited several times with different azimuth angles, allowing 2D wave spectra and velocity vectors to be measured on the surface. The sampling pattern is a function of rotation speed and beam placement, both of which have been optimised to minimise interpolation errors. The speed of rotation around the nadir direction can be selected in the range from three to eight



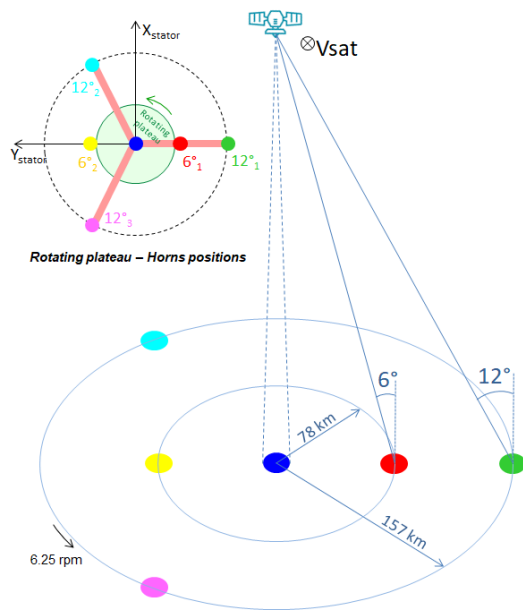
revolutions per minute and is currently set at 6.25 rpm. The beam sequencing is programmable to optimise the sampling of the different beam ground footprints over the swath. The instrument chronogram is sequential, with pulses being transmitted and received on one beam before switching to the next one, as illustrated in Fig. 5.13.

An infinite number of possibilities exist to design the sampling pattern of the scanner, by varying the number of beams, the incidence angles, their azimuth position on the rotating plate, the rotation speed of the scanner, and open and closed burst mode operation of the radar. The baseline presented in this report is the result of extensive trade-offs that involved technical considerations as well as science performance aspects.

A cycle is a burst of pulses transmitted on the same beam (nominally 1024 pulses are transmitted on each beam in the current design). The measurements collected over one cycle are averaged onboard to reduce noise, so that typically one sample per cycle is obtained. As explained in Section 5.3.3.7, the instrument can also transmit all received pulses in raw data mode to investigate and improve the onboard algorithms while the mission is flying. The sequence of cycles that takes one sample from each beam constitutes a macro-cycle. A macro-cycle will contain the nadir beam used for altimetry measurements and range tracking for all beams, as explained in Section 5.3.3.9. A set of macro-cycles can be defined in the radar data base to construct a so-called mega-cycle. A mega-cycle nominally completes one turn of the conical scan, so that the scanning pattern on the surface repeats itself with the period of the mega-cycle.

The radar operates in open burst or interleaved mode, which means that each cycle is divided into three time periods:

1. Pulses are transmitted at a specific Pulse Repetition Frequency (PRF). A number of pulses can be transmitted before the first pulse is received due to the round trip delay. By definition this number is the Ambiguity Rank (AR). The empty receive windows are used to perform real-time calibration of the radar transfer function (electronics) and of the thermal noise of the current beam.
2. Interleaved operation: NIMP-AR echoes are received in time windows that are interleaved between the transmitted pulses, where NIMP is the number of pulses per cycle.
3. The remaining AR echoes still in flight are received. For technological reasons, pulses are still generated by the radar but not used (if the next cycle is not on the same beam, nominal case).



Incidence	nadir	6°	12°
scan radius (km)	0	78	157
look angle (°)	0	5.3	10.6
nb of beams	1	2	3
Beam width (°, 1-way, elev.)	0.57	0.58	0.65
beam width (°, 1-way, azi.)	0.57	0.60	0.65
footprint (km, elev.)	8.3	8.6	9.9
footprint (km, azi.)	8.3	8.8	9.7
scan velocity (km s ⁻¹)	0	51	103
Range resolution (m)	0.75	7.2	3.6

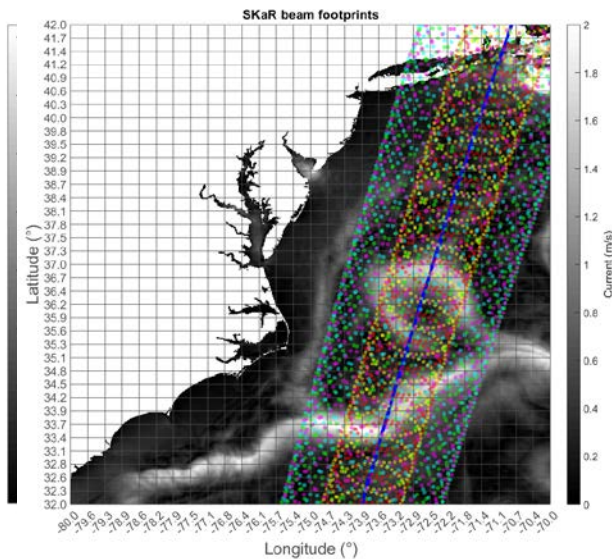
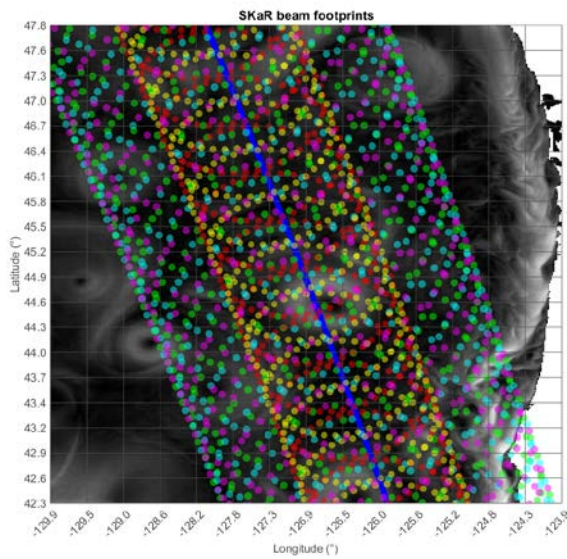


Figure 5.12. Instrument observation geometry (top left), geometry parameters (top right) and corresponding ground footprints plotted over a current field of the Oregon coast (bottom left) and over the Gulf Stream (bottom right). Grid cell size is approximately 30 km.

During the cycle and macro-cycle the PRF is kept constant. Since the altitude changes along the orbit, the radar adapts to the varying round-trip delay by stepping the PRF between macro-cycles. The adaptation of the PRF needs to consider the range variations between the satellite and Earth’s surface, the required margins to switch between transmit and receive modes and the range swath width to be measured (duration of the receive echo window).

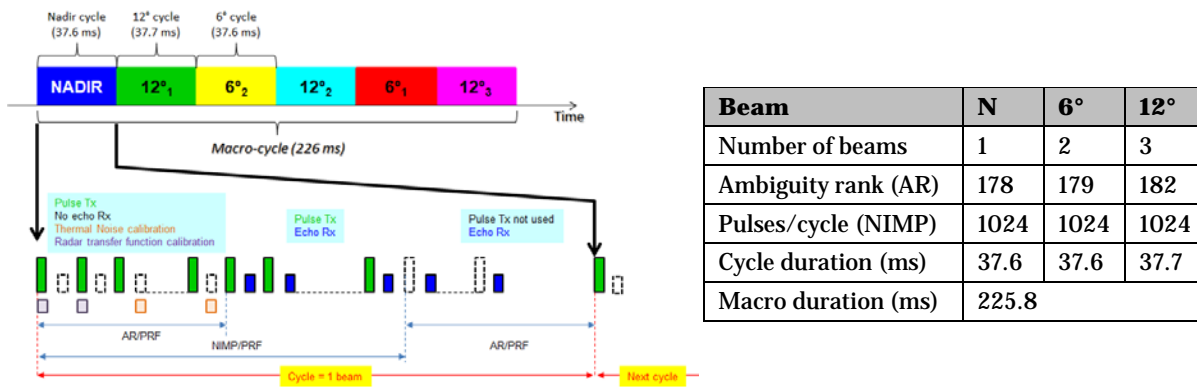


Figure 5.13. Instrument beam sequence and chronogram parameters.

Four types of measurements are provided by SKaR:

- Wave scatterometry: with the off-nadir beams, the backscatter modulation spectrum is obtained through incoherent processing of the Real Aperture Radar (RAR) waveforms.
- Line of sight (LoS) velocity measurements: thanks to the high PRF (32 kHz), consecutive pulses are coherent. By correlating pairs of consecutive pulses and coherent averaging, pulse-pair echoes are obtained. The radar can estimate the LoS Doppler velocities from the phase of the pulse-pair echoes (Eq. 5.1).
- Nadir altimetry: high-precision nadir altimetry is implemented for the nadir beam corresponding to non-ambiguous unfocussed SAR processing (PRF=32 kHz).
- Delta-k processing: experimental product, which involves beating two signals corresponding to two slightly different carrier frequencies. A resonant spike appears, which corresponds to the propagation velocity of gravity waves whose wavelength satisfies the dispersion relation of ocean waves and its anomalies (current).

From the phase of the range-resolved pulse-pair echoes, a Doppler modulation spectrum is obtained, which is used in the higher level processing, together with the backscatter modulation, to calculate the component of the measured LoS velocity that is due to orbital motion of the waves rather than underlying currents.

Doppler scatterometry uses pulse-pair processing, a well-known technique also used by meteorological radars, to measure the mean Doppler velocity in the radar LoS (Doviak, 1993). Measurements of the amplitude and phase of the mean radar signal are obtained from the cross-correlation product of two successive echoes (see Eq. 5.1). In the pulse-pair equation, $s(t)$ is the received radar echo as a function of time lag t . U_{LoS} is the velocity measured by the radar along the line of sight. P_s is the radar echo power, P_b the thermal noise power and ρ is the correlation between two successive echoes.

$$\langle s(t).s^*(t + PRI) \rangle = \rho. \bar{P}_s e^{j\phi} \tag{Eq. 5.1a}$$

$$\text{Amplitude: } |\langle s(t).s^*(t + PRI) \rangle| = \rho. \bar{P}_s \tag{Eq. 5.1b}$$

$$\text{Phase: } \hat{\phi} = \arg[\langle s(t).s^*(t + PRI) \rangle] = -\frac{4\pi.PRI}{\lambda}. U_{LoS} \tag{Eq. 5.1c}$$

$$\text{Individual echo power: } \langle s(t).s^*(t) \rangle = \bar{P}_s + \bar{P}_b \tag{Eq. 5.1d}$$

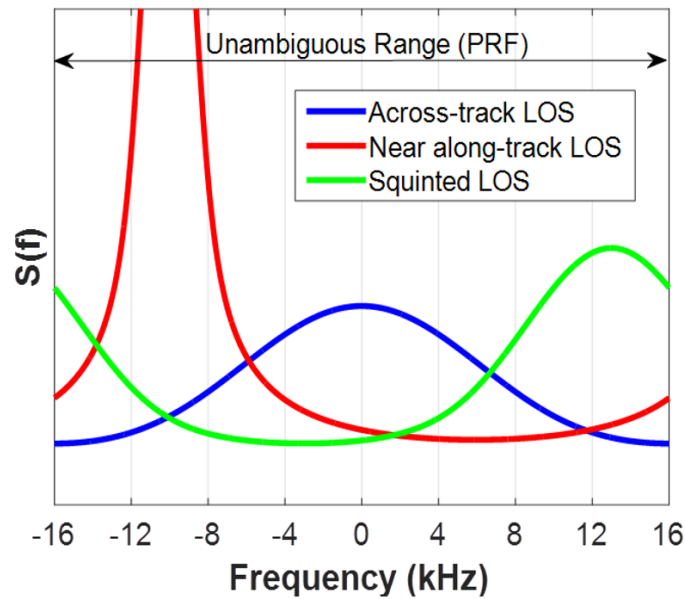


Figure 5.14. Echo Doppler spectrum for different beam azimuth positions.

The measured phase is proportional to the velocity of the scatterers illuminated by the radar and corresponds to an estimation of the mean Doppler spectrum of the echo. The width of the echo Doppler spectrum depends on the azimuth scan position (largest width in the across-track direction, orthogonal to the satellite velocity vector), which affects the angular correlation between subsequent pulses and then the accuracy of the phase measurement. The Doppler spectrum width is directly related to the antenna beam width.

The radar pulses will be transmitted with a PRF that correctly samples the width of the Doppler spectrum. The worst-case conditions are for the 12° beam at 90° azimuth angle (blue curve in Fig. 5.14). Therefore, a PRF around 32 kHz is selected to maintain enough correlation between pulse-pair signals. The accuracy of the measurements is further improved by averaging several pulse-pairs.

Parameter	Requirement	Comment
Instrument type	Ka-band Doppler wave scatterometer and nadir altimeter	Translation of Ku-band wave power scatterometer SWIM to Ka-band Doppler wave scatterometer
Observation type	Conical scan around the nadir direction	Full directional observations (360° sampling)
Observed incidence angles	One beam towards nadir multiple off-nadir beams >6°	Nadir altimetry + Low incidence Doppler scatterometry (wave+current) Two beams at 6° and three beams at 12°
Nadir beam sampling rate	>4 Hz	4.4 Hz (nominal configuration) (Equivalent to 4.5 kHz altimeter)
Swath width	>290 km	309 – 317 (see Fig. 5.5)



Parameter	Requirement	Comment
Beam polarisation	VV	Nadir beam: linear rotating with antenna scan Off-nadir beam: linear vertical in the radial direction
RF centre frequency	35.75 GHz	Centred in the allocated ITU bandwidth
RF signal Bandwidth	200 MHz	Limited by high power amplifier 200 MHz Chirp
Range resolution	≤6 m at 12° incidence	0.75 m slant range resolution (200 MHz chirp), ~3.6 m radial resolution at 12°, 6m after RMC and averaging
Antenna pointing Absolute Knowledge error (AKE)	Power spectral Density (see Section 5.3.3.8)	Drives thermo-elastic design and on-ground antenna characterisation
Radiometric resolution for each beam	≤0.1 dB	Required for wave scatterometry (NRCS modulation); requires range averaging
Absolute radiometric accuracy for each beam	≤1 dB (g: 0.5 dB)	Calibration and characterization implemented
Relative radiometric accuracy within a beam	≤0.1 dB (1σ)	Drives the accuracy of the antenna pattern characterisation
Radiometric stability for each beam	≤0.5 dB	Ensured by instrument internal calibration and antenna stability
Relative radiometric accuracy between beams over one full rotation (dB)	≤0.15 dB (g: 0.05 dB)	Consistency of the backscatter measurements between beams
Nadir altimetry performances Random range noise Range bias stability	≤1.5 cm at 1 Hz (1σ) (G 1 cm) ≤2.0 mm yr ⁻¹	SKaR is designed for high accuracy altimetry
Radial surface velocity precision at an incidence angle of 12°	At 45° and 135° azimuth: ≤12.5 cm s ⁻¹ (g: ≤10 cm s ⁻¹) At 3° and 357° azimuth: ≤5 cm s ⁻¹ (g: ≤3 cm s ⁻¹) At 90° azimuth: ≤20 cm s ⁻¹ (g: ≤15 cm s ⁻¹)	Performance obtained at each beam cycle (azimuth and range multi-looking)
Radial surface velocity precision at an incidence angle of 6°	At 45° and 135° azimuth: ≤17.5 cm s ⁻¹ (G ≤15cm s ⁻¹) At 3° and 357° azimuth: ≤5 cm s ⁻¹ (G ≤3cm s ⁻¹) At 90° azimuth: ≤25 cm s ⁻¹ (G ≤20cm s ⁻¹)	Performance obtained at each beam cycle (azimuth and range multi-looking)
Surface velocity vector instrument combined noise	≤7 cm s ⁻¹ (1σ) for along-track and across-track components	Level-1 performance metric, chosen to drive the beam sampling pattern and rotation speed

Table 5.1. SKaR key functional and performance requirements. G means a goal requirement. For more background information, please refer to Section 4.3.

5.3.3.3 SKaR Architecture

Figure 5.15 shows the instrument block diagram. It comprises the following elements:

- Antenna including the main reflector and the rotary feed mechanism assembly.
- Antenna Power & Control Electronic (APCE), which operates the rotary feed motor and the switch matrix.
- HPA including the:
 - Extended Interaction Klystron (EIK)

- High voltage power supply unit for the EIK enabling the pulsed operation
- High power isolator
- Ferrite assemblies composed of two pieces of equipment:
 - Duplexer for transmitting/receiving the signal to/from the antenna
 - Switch matrix included in the rotating antenna feed mechanism to transmit/receive signals to/from each radio-frequency (RF) beam.
- CEU including digital and processing units, low level RF sections, the onboard software and onboard processing. CEU includes an internal 10 MHz reference clock used to synchronise all digital clocks and the RF local oscillator. The signal is also used by the GNSS receiver to allow fine monitoring of the SKaR reference clock.

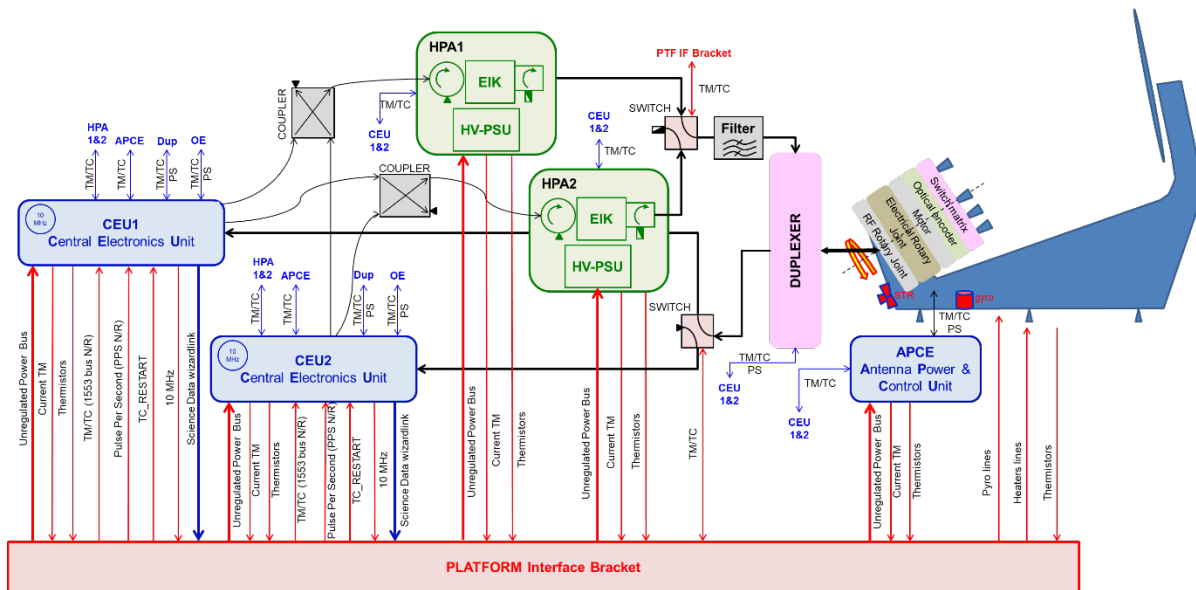


Figure 5.15. SKaR architecture overview.

The redundancy concept consists of having a nominal and redundant CEU as well as a nominal and redundant HPA with cross-strapping. Further improvements to eliminate the possibility of single point failures in the APCE and the ferrite assemblies will be studied in the next phase.

In order to avoid any effects from thermo-elastic distortions of the main spacecraft structure on the antenna LoS pointing knowledge, three startrackers and a fibre-optic gyro sensor are mounted directly on the antenna structure. The startrackers are used for attitude control and absolute pointing knowledge of the antenna reference frame and the gyro will monitor short-term attitude variation of this reference frame.

A single-sideband RF transmit pulse (linear FM) is generated by the CEU and sent at a medium power level to the HPA, which delivers a peak RF power of 1700 W (EoL) at a duty cycle of 5% and PRF of 32000 Hz on average. Then, the transmit pulses are routed by the duplexer through a circulator and a single-channel RF rotary joint to the rotating antenna feed assembly. The switch matrix located on this antenna feed assembly routes the transmit signal to the selected feed horn following the sequence defined in Fig 5.13. Only the plateau supporting the feeds rotates while the reflector is mounted in a fixed position. A synchronous motor controlled by the Antenna Power and Control Equipment (APCE) rotates the assembly

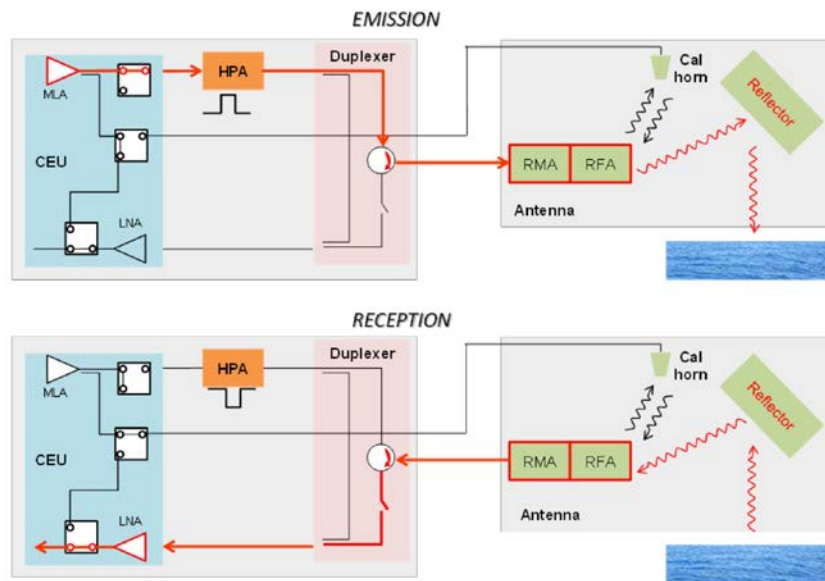


Figure 5.16. Transmitted and received radar RF signal paths. The radar signal paths (conducted and radiated) in transmission and reception are shown in red.

constant speed (fixed value between 3 and 8 rpm). It is also possible to stop the rotation at a commanded azimuth position. The azimuth position is monitored with high accuracy by a 25-bit optical encoder. Communications between APCE and the rotating assembly (switch matrix voltages, electrical commands, telemetries, etc.) is performed via an electrical rotary joint using roll rings.

In reception, the echo signal from a given beam is routed through the switch matrix, the rotary joint and the duplexer circulator to the receive chain of the CEU, where it is filtered and amplified for further processing including down conversion to base-band and analogue-to-digital conversion at 250 MHz sampling frequency (10 bit ADC). At the input of the ADCs, the signal level (echo + thermal noise) is adjusted with RF digital analogue attenuators that are controlled by the onboard gain tracking software operating in closed-loop for each beam. The receiving windows are opened to acquire just the returning echoes, thanks to an onboard range tracking capability, which can operate either in closed-loop tracking or in open-loop tracking as explained in Section 5.3.3.9.

The raw data rate of the instrument is around 1.5 Gbit s^{-1} . Therefore, the instrument has been designed with an onboard processing capability, so that the volume of the data stream can be tuned to the available downlink capacity as explained in Sections 5.3.3.6 and 5.3.3.7. The Onboard Processing (OBP) is performed inside the CEU making use of in-flight re-programmable Field Programmable Gate Arrays (FPGAs). Section 5.3.3.6 provides details of the OBP implementation and top view of the algorithms. The embedded onboard software manages all the instrument modes. Mode changes are commanded by the platform via the mil-std-1553B bus and science telemetries (instrument data products, calibration data) are transmitted to the satellite mass memory through a high-speed serial link.

5.3.3.4 SKaR Operating Modes

SKaR modes (Fig. 5.7) are divided in three categories:

- The radar modes with two possibilities of tracking modes (open-loop or closed-loop), associated with two possibilities for telemetry (OBP or OBP+RAW data, see Section 5.3.3.6)
- The calibration modes that allow to calibrate the SKaR during its lifetime
- The support modes for all other services

When SKaR is switched ON, all the units are ON and the onboard software starts in the INIT mode.

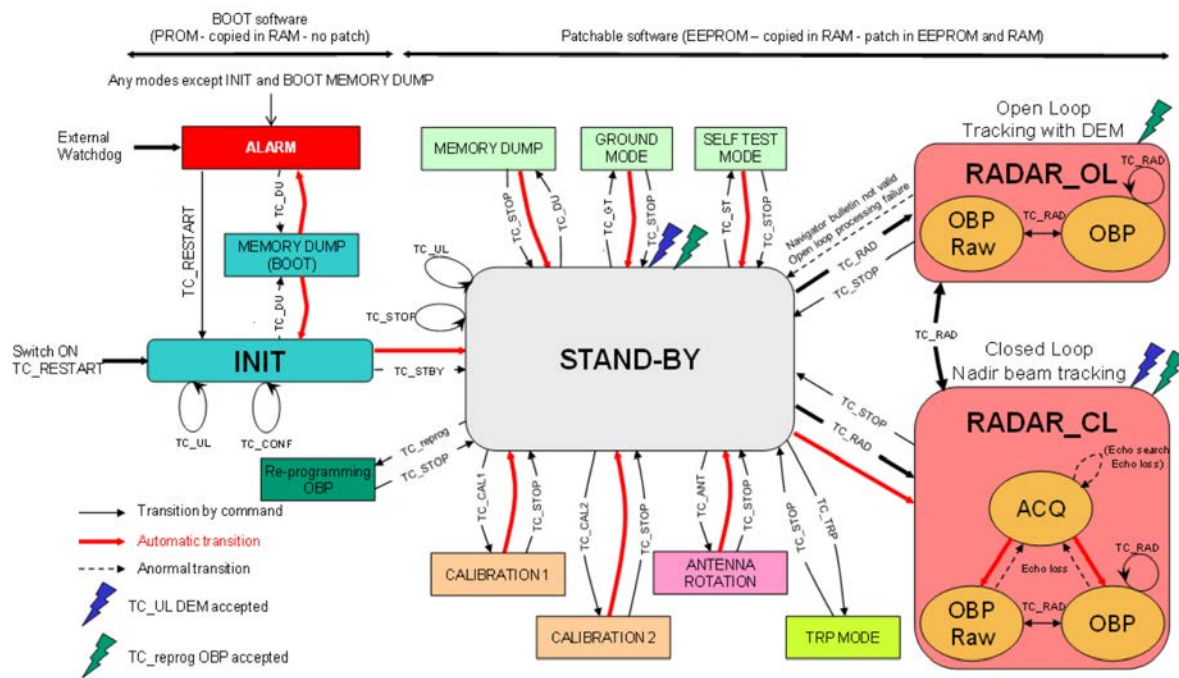


Figure 5.17. SKaR modes and transitions between different modes.

5.3.3.5 SKaR Subsystems

5.3.3.5.1 Antenna Subsystem

The antenna concept is a fixed single offset reflector illuminated by feeds on a rotating plate (Rotary Feed Assembly – RFA). The rotation of the plate in front of the reflector produces a conical scan of the beams as explained in Section 5.3.3.2. The antenna sub-system comprises of:

- a Rotary Mechanism Assembly (RMA)
- a RFA supporting the rotating horns and a switching matrix
- a parabolic reflector in offset configuration
- a mechanical structure
- a calibration horn

On SWIM, the RFA included a switch matrix so that the different beams can be time-multiplexed through one single RF rotary joint at the centre of the rotating plate. The control of the switch matrix required a slip-ring assembly in the RMA. The slip-ring technology places a limitation on the maximum speed of rotation due to its limited lifetime. Therefore, two alternative design solutions have been considered for SKIM. One is to replace the slip-ring technology with roll-ring technology, which has a much longer lifetime. Another solution is to replace the single RF rotary joint with a multi-channel rotary joint, so that the switch matrix can be integrated in the non-rotating part of the antenna. The two solutions are shown in Fig. 5.18. The baseline selected for SKIM is the roll-ring solution due to its higher technological maturity.

The overall mechanical design of the antenna is very similar in both satellite configurations, with some differences in the interfaces to the platform and platform equipment mounted on the antenna. Figure 5.19 shows the antenna for Concept A.

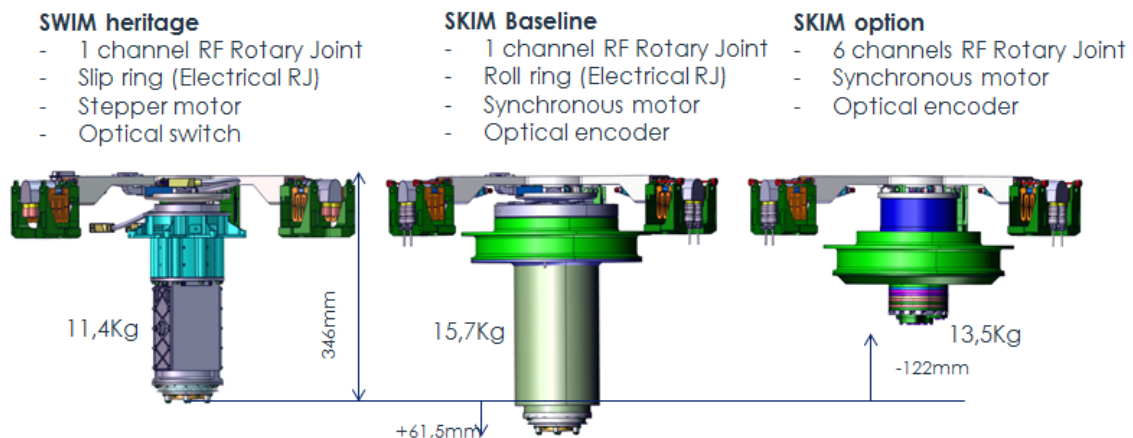


Figure 5.18. SKaR antenna RMA (middle), compared to the heritage solution from SWIM (left) and an alternative lower-TRL solution (right).

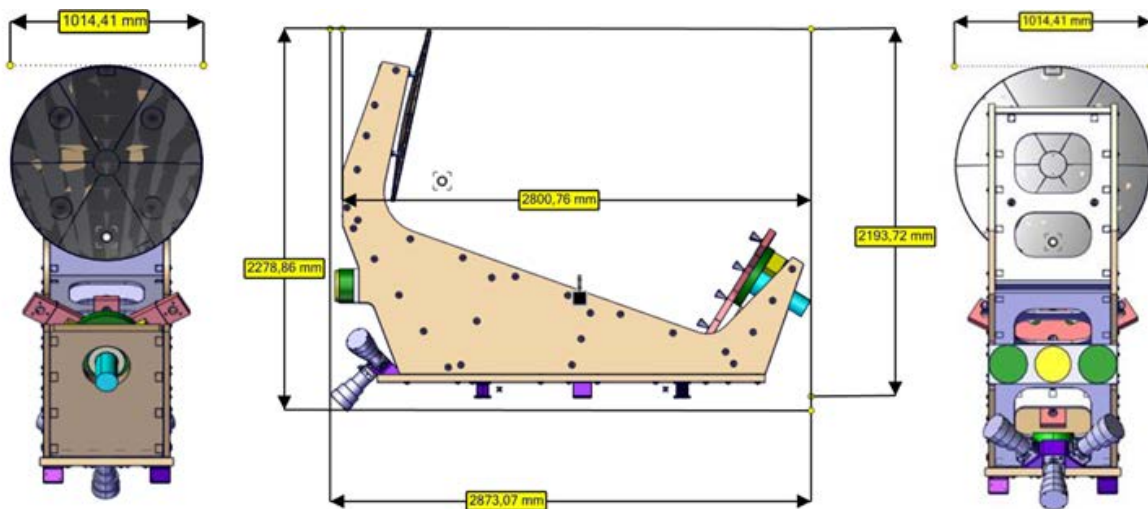


Figure 5.19. SKaR antenna for Concept A.

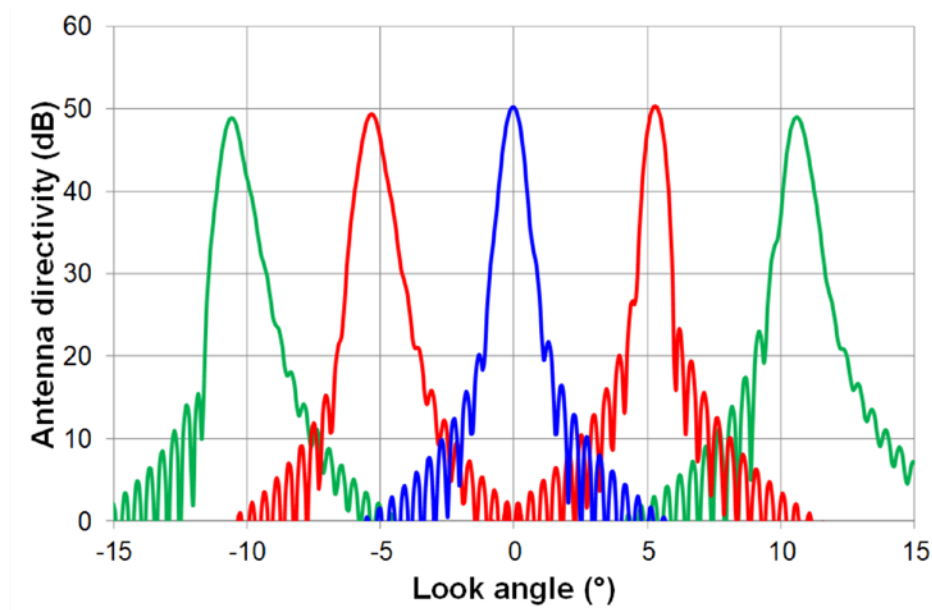


Figure 5.20. One-way antenna patterns for beam with 12° incidence angle (green), for beam with 6° incidence angle (red) and for nadir beam (blue).

5.3.3.5.2 High Power Amplifier Subsystem

The SKaR pulsed radar Ka-band HPA consists of an EIK and a High Voltage Power Supply (Fig. 5.21).

The study performed in Phase A has confirmed that the EIK used on the SWOT programme can be re-used (TRL 7) since the same RF signal centre frequency, bandwidth and output peak power are used on SKIM. On SWIM the amplifier will operate with higher PRF, but lower mean RF output power (due to shorter pulse length).

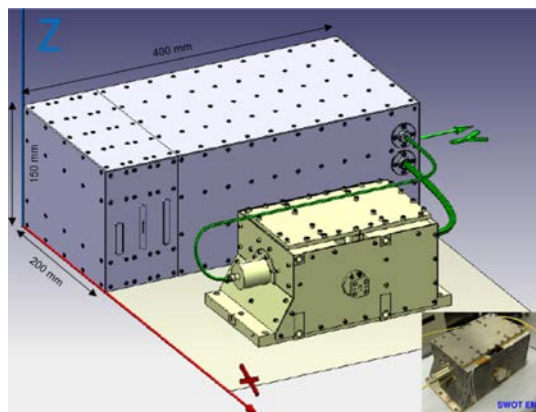


Figure 5.21. SKaR HPA mechanical model (from ASP and EIK 3D model provided by CPI).

The amplifier must be pulsed to maximise the power amplifier efficiency and to minimise power dissipation. Studies with two European suppliers with significant heritage from past and ongoing HPA power supplies have been performed during the Phase A to assess the feasibility and establish the equipment budgets. The key element for the SKIM mission is the



grid modulator module which generates the DC voltage levels required to pulse the EIK at a high operating frequency of 32 kHz. A pre-development was started in Phase A to have an early validation of the design and performances of this key element. The breadboard is shown in the middle panel of Fig. 5.22.

In the transmit RF path after the EIK a High Power Isolator (HPI) is used to protect the amplifier with respect to high RF power reflexion and to provide adequate RF load matching at the output. An HPI of similar design to the one used on the SWOT programme is required. In order to safeguard a European source, a pre-development activity with a European supplier was started in Phase A for the design, manufacturing and test of a complete Engineering Model (EM). The design is shown in the right panel of Fig 5.22.

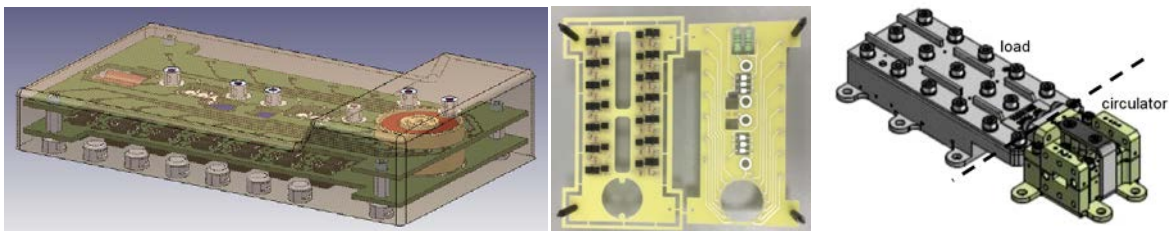


Figure 5.22. Left and middle: SKaR HV-PSU Grid modulator 3D model (from ASP) and photograph of manufactured boards before assembly and potting. Right: High Power Isolator/Circulator 3D model (from Honeywell-UK).

5.3.3.5.3 Ferrite Assemblies Unit

Ferrite assemblies include the duplexer and the switch matrix. The duplexer is used to duplex the transmit and receive signals through a single RF path to the antenna by disconnecting the receive chain while the radar is transmitting. A series of switches are required to provide sufficient isolation.

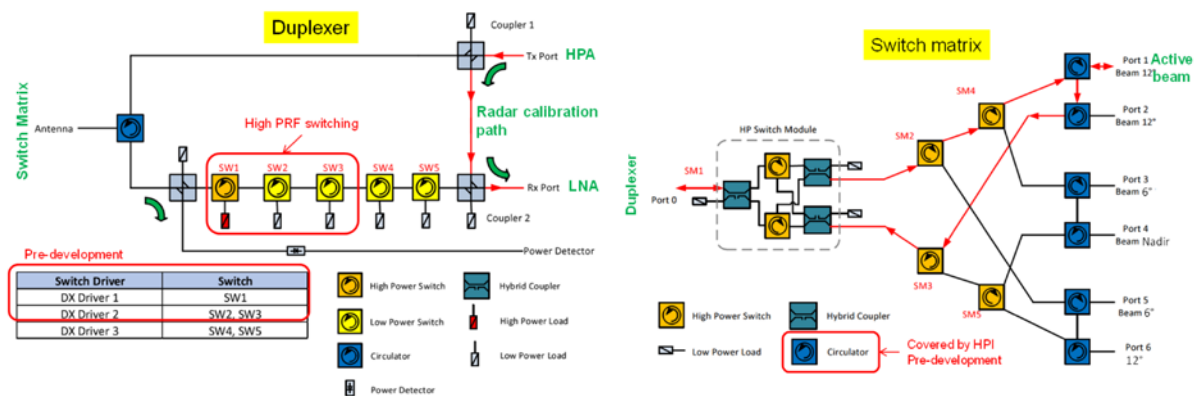


Figure 5.23. Duplexer and switch matrix synoptics. Duplexer antenna port is connected to switch matrix input port via the RF rotary joint. Ports 1 to 6 are connected to the antenna feeds.

The switch matrix is used to transmit and receive sequentially on different antenna beams. The switch matrix needs a specific mechanical design for the implementation on the rotating mechanism of the antenna (see Fig 5.24). They have significant heritage from SWIM and

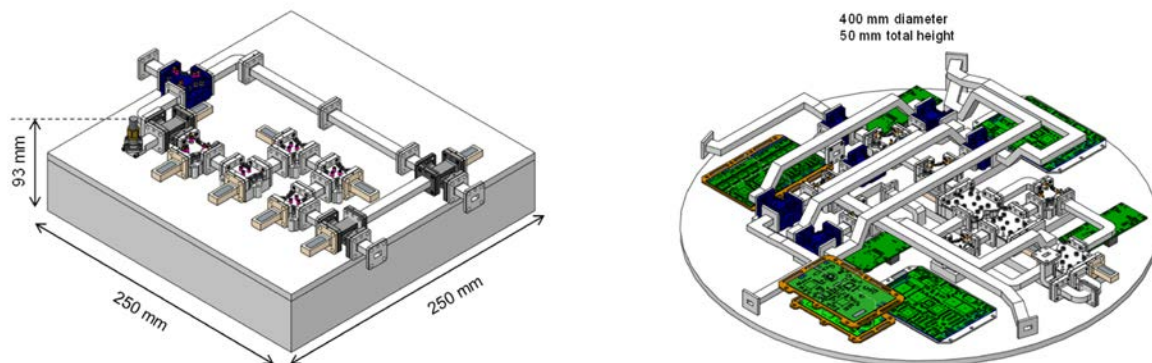


Figure 5.24. Duplexer (left) and switch matrix (right) mechanical views (Honeywell-UK).

SWOT missions, although specific improvements will be implemented for SKIM. The topology of the switch matrix for instance has been improved to enable transmit and receive on the same beam without switching, thereby reducing the power dissipation in the switch matrix.

5.3.3.5.4 Radar Central Electronics Unit

The CEU includes all digital and RF low-level functions as well as the instrument software, the onboard processing implemented in FPGAs and the hardware sequencing of the whole instrument. The architecture is based on the re-use of existing slices from the Poseidon-4 instrument on Copernicus Sentinel-6 and KaRin RFU programmes providing a well-established solution with high Technology Readiness Level (TRL).

As shown on Fig. 5.25, the CEU is composed of 9 stacked slices interconnected via a motherboard and coaxial harness:

- DSP2 slice (POS4): implements the onboard software (running on a LEON2 processor), different memories (boot PROM, SRAM, MRAM memory for application software and DEM storage), and the MIL-BUS 1553 interface. The slice includes 4 MRAM modules of 8MB each. 50% of one module is reserved for the applicative software. The available size for the DEM is 28-31 MB.
- TX_NUM slice (POS4): generates high-bandwidth digital chirp (I/Q base-band), high speed instrument sequencing signals, and digital clock signals from the 10 MHz reference provided by the RF-LO slice. It also includes 10 MHz outputs for the GNSS receiver (nominal and redundant).
- DCDC slice 1 (modified from POS4): generates towards all other CEU slices the required regulated secondary voltages from the unregulated power bus, provides the current telemetry, and performs the internal thermistor telemetries acquisition (provided in the housekeeping TM). This slice will be modified to distribute the secondary voltages to the three RF slices.
- DCDC slice 2 (standard product): generates the regulated secondary voltages to the duplexer and the switch encoder of the antenna rotating mechanism.
- RX_NUM slice: this slice is based on the POS4 slice (re-use of analogue I/Q signal acquisition chain). It will be modified to integrate the onboard processing (see Section 5.3.3.6) FPGAs and memories.

- **FORM_SEQ slice:** is based on standard digital slice heritage used to implement instrument hardware sequencer and data formatting FPGAs. The science telemetry is generated in CCSDS format, and a high data rate link to support raw data transmission to the mass memory of the PDHT is assumed, designed for the SKaR needs.
- Three RF slices from the SWOT KaRIn RFU programme are re-used:
 - The low level Tx slice which translates the baseband I,Q chirp in Ku-band and then in Ka-band at a level compatible with the HPA.
 - The RF local oscillators used for frequency translation, which are synchronised on a 10MHz reference (OCXO). This reference will be also used by the digital slices and shall be used by the GNSS receivers.
 - The Ka-band receiver in macro-hybrid technology, which performs down conversion from Ka-band to base-band.

5.3.3.6 Onboard Processing Concept

The OBP comprises three processing chains with range compressed output for all the beams:

- RAR power detection processing
- Delay-Doppler processing
- RAR pulse-pair processing

First steps of these processing chains are common:

- Acquisition
- Range compression (matched filter)
- Range migration correction

The RAR power detection processing calculates the echo power for each range gate and incoherently averages the power waveforms over a cycle. The delay-Doppler processing follows the following steps: First the 1024 pulses in a cycle are divided in 32 segments of 32 pulses. A phase ramp is applied to each segment of 32 pulses in order to offset the Doppler centroid. An FFT algorithm forms 32 Doppler beams for each segment. For the off-nadir beams, the Doppler beams are power detected and integrated over the 32 segments. No integration is implemented for the nadir beam, instead complex delay-Doppler maps are

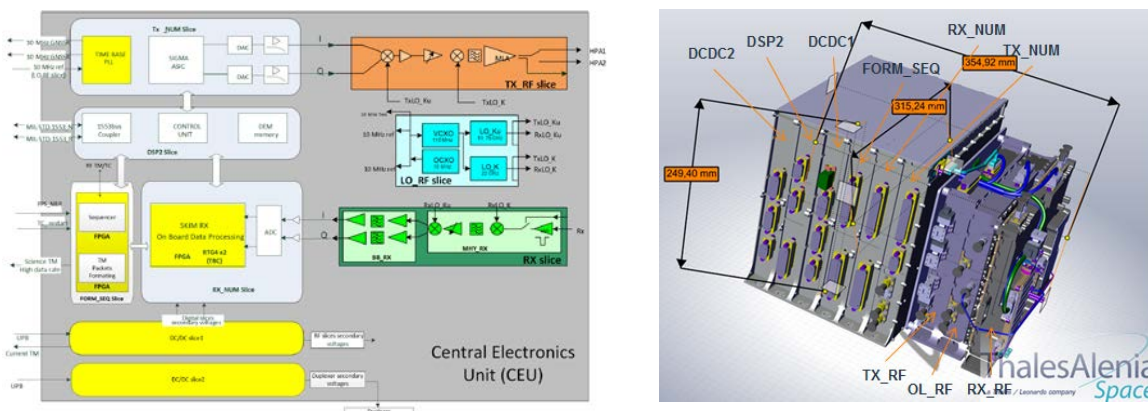


Figure 5.25. SKaR CEU internal architecture and mechanical model.

transferred to ground so that the processing is fully reversible. The delay-Doppler maps are stored after selection of the useful range gates and Doppler bins. The pulse-pair processing multiplies each echo with the complex conjugate of the previous one. Due to the antenna azimuth shift, the pulse-pair product phase varies across the cycle, and it is necessary to correct for the phase shift before coherent integration over a cycle. The OBP also includes an experimental mode called delta-K processing. It works directly on I/Q data at the output of the azimuth compression. The first step consists of computing the intensity of each azimuth compressed echo, performing a range FFT (after windowing), and selecting a part of this spectrum (in wavenumber domain). This complex spectrum is then used for computing delta-K burst pairs and a mean intensity spectrum. The processing chain is illustrated in Fig. 5.26.

A pre-development activity was started during the Phase A to design, simulate and confirm the feasibility of the implementation of the signal processing algorithms into space qualified FPGA (baseline RTG4 from Microsemi, back-up NanoXplore Ultra). The feasibility of implementing the OBP algorithms on RTG4 FPGAs is confirmed and validation on a hardware breadboard is planned for Phase-B1.

Specific to the SKIM mission is its ability to change the onboard processing during flight. The system that implements this reprogramming function is shown in Fig. 5.27. The reprogramming is performed in two steps:

- Step 1: files upload into the CEU. The bitstream is uploaded in local memory. This operation can take several orbits, but happens in parallel with normal instrument operation.
- Step2: FPGA reprogramming

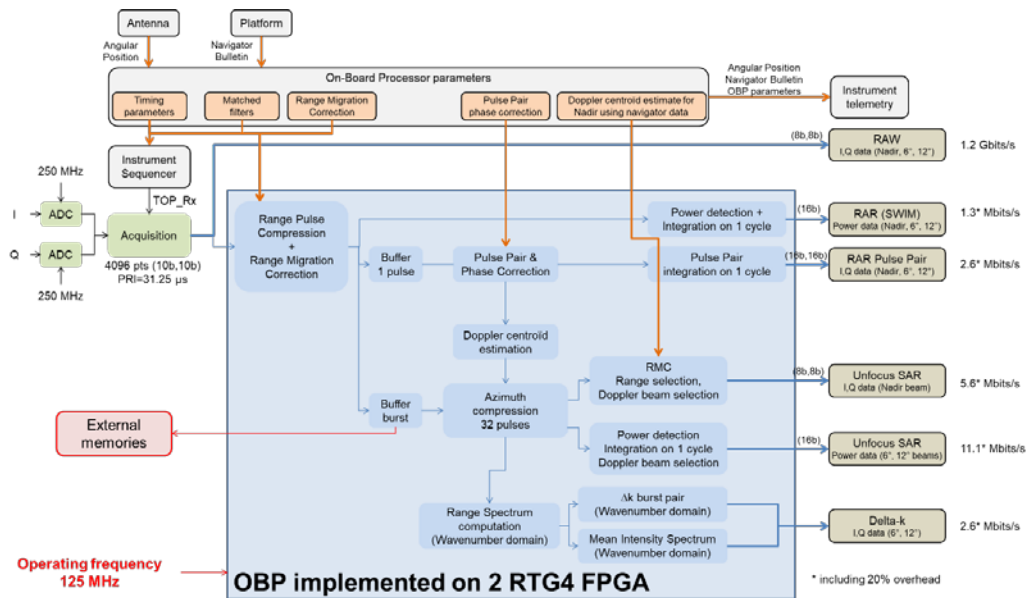


Figure 5.26. Onboard processing schematics.

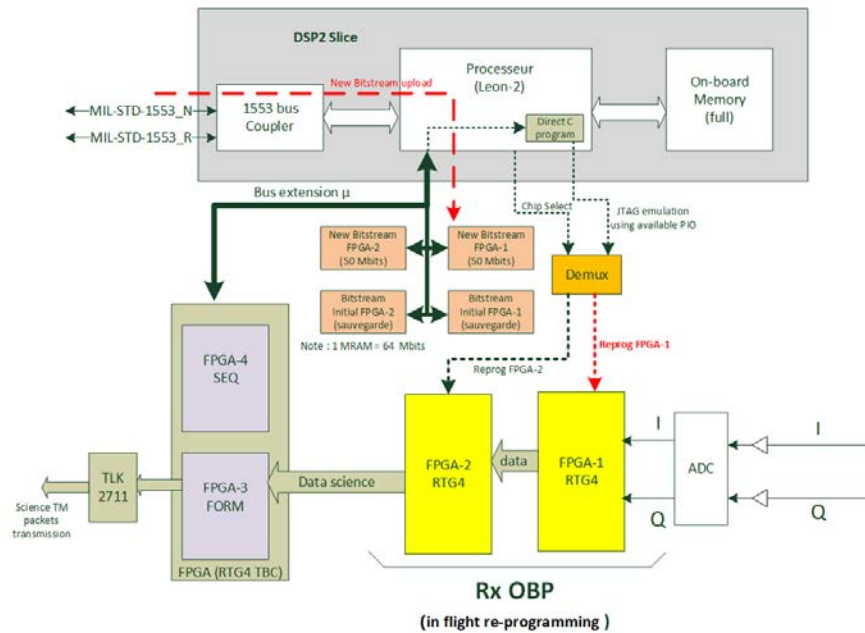


Figure 5.27. Onboard processing in-flight re-programming synoptic.

5.3.3.7 Instrument Data Rate

One of the challenges for the SKIM mission is to combine the large data rate produced by a radar instrument with the very high duty cycles required to cover all ocean surfaces. This is achieved by averaging the pulses received in a cycle onboard rather than on ground, thereby reducing the volume of data before transmission to ground. Although the onboard processing scheme is conceptually simple, it is impossible to predict future improvements to the processing scheme that may be realised while the mission is in orbit. In order to safeguard the performance of the SKIM mission, the following features will be implemented:

1. The onboard processing algorithms are encoded in FPGA chips that can be updated during flight, as explained in Section 5.3.3.6.
2. An allowance is made for a significant amount of raw unprocessed data to be downloaded, corresponding to ~1 minute per orbit. With this data the onboard processing can be monitored continuously and improvements investigated.

Figure 5.26 shows the onboard processing architecture, with the raw data stream branched off prior to the onboard processing block. The requirement for SKIM is to be able to download at least one minute of this raw data stream per orbit, in addition to the onboard processed data which is continuously acquired over all oceans and inland seas with a surface area of at least 50 km². For mission design and system sizing, an acquisition mask has been assumed for the raw data stream, corresponding to the red rectangles shown in the left plot of Fig. 5.28. Whenever the SKIM sub-satellite point crosses into these areas, it is assumed that both raw and OBP data are generated. The Mission Advisory Group (MAG) has identified this mask based on regions that are of particular scientific interest. The mask includes the following areas: Agulhas, Arctic Margins, CryoSat Box, Equatorial Atlantic, Gibraltar, Gulf Stream, Square the Cape, Iceberg Alley, ICTZ Rain Gauge and La Manche. The areas in blue correspond to all water and sea ice surfaces with an area larger than 50 km². It is assumed SKIM will only produce the OBP data stream over these areas.

The latest mask shown in 5.28 corresponds to an average of 1.56 minutes per orbit, and will be fine-tuned in later phases to correspond with one minute per orbit. The results from the data latency and memory loading analysis considered this mask, but with a slightly lower data rate from the instrument. Very large margins are available with respect to the data latency requirement and the mass memory capacity as explained in Section 5.3.4.7. In terms of total data volume to be transmitted to ground, Fig. 5.26 shows the latest data generation rates calculated for the instrument, including the delta-k data stream. These data rates result in 166 Gbit of data generated on average per orbit, assuming one minute per orbit of raw data. Both concepts are able to download all this data to ground with the baselined payload data handling subsystems, as explained in Section 5.3.4.7.

5.3.3.8 Antenna Thermo-Elastic Distortion Analysis

Accurate azimuth antenna pointing knowledge is key when measuring a 1 cm s^{-1} surface velocity from a spacecraft flying at 7 km s^{-1} . In-orbit pointing uncertainty is driven by the thermal environment and its variation at orbit scale (eclipse) and seasonal scale (solar declination). At Level-1 (prior to more elaborate processing with fine-pointing algorithms at Level-2), SKIM aims to achieve a pointing knowledge in the range of 10–30 arc seconds. Extensive Thermo-Elastic Distortions (TED) simulations have been performed to characterise the pointing behaviour for the flight configurations of both Concepts:

- Step 1: Thermal simulations
 - Selection of cold, hot and equinox orbits
 - Computations of 1200 thermal antenna maps for each orbit (5 s time step). The fine time-step is required in order to calculate the pointing Power Spectral Density (PSD).
- Step 2: Mechanical simulations to obtain the fine mechanical model of the antenna at each time step (1200 antenna displacement maps per orbit).
- Step 3: RF simulations (antenna patterns) and calculations of pointing, directivity, beam widths, etc. corresponding to each simulated orbital points (120 antenna patterns at each orbit point computed to cover the full antenna scan with 3° step).

Detailed analyses have shown that the main contribution to pointing variations come from the displacement of the reflector (translations and rotations) due to temperature variations

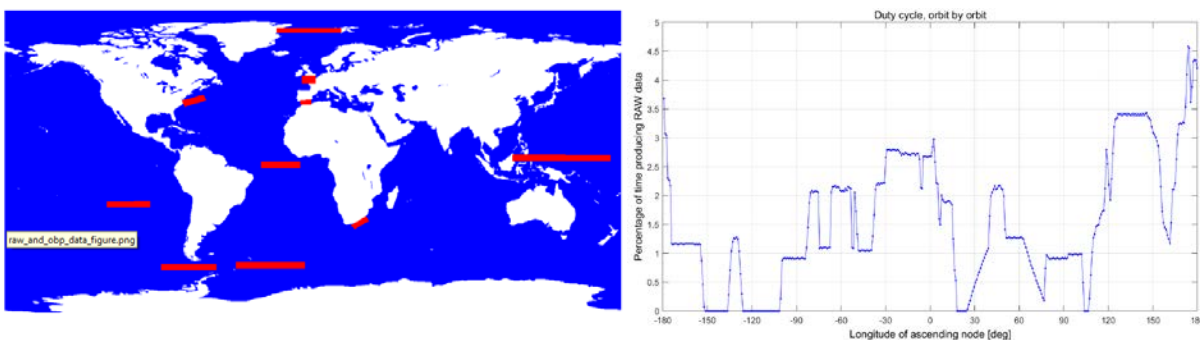


Figure 5.28. For mission design and system sizing, an acquisition mask has been assumed for the raw data (red rectangles in left plot). This corresponds to a duty cycle as a function of longitude shown in the right plot. The mean duty cycle is 1.54% or 1.56 minutes per orbit (DEIMOS).



on the lateral panels of the antenna structure. The in-orbit temperature environment is significantly colder than the ambient case on-ground, however once in-orbit very small variations occurs (few degrees depending on the satellite configuration). For Concept B the mean in-orbit temperature is around 20°C higher due to Sun illumination, but the gradients on the antenna structure are also higher.

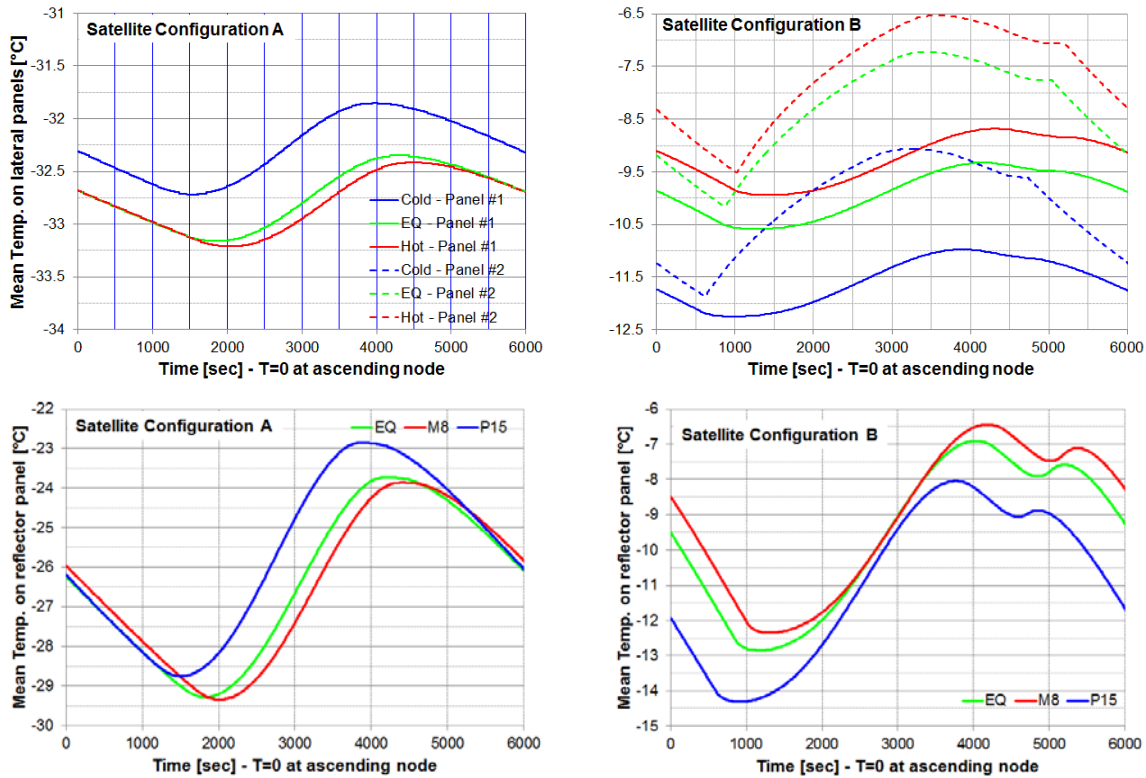


Figure 5.29. Antenna structure temperature variations in orbit, for a cold orbit (blue), equinox orbit (green) and hot orbit (red).

Looking at the mean pointing over the orbit (compared to the on-ground case), the variation as a function of scan angle is almost harmonic. This indicates that the main effect is a constant bias over the antenna scan (equivalent to an attitude modification of the antenna reference frame, the residual variable variation of azimuth over the scan is around 20 arc second peak-to-peak). The amplitude is half for satellite configuration B due to a higher antenna mean temperature in orbit (-10°C in Concept B compared to -33°C in Concept A), but this is only related to a one-off change of reference temperature.

At seasonal scale the variation as a function of scan angle of the mean pointing (compared to the equinox case) has a harmonic variation with a very weak residual (<1 arc second peak-to-peak). Concept A is more stable due to the accommodation of the antenna on the cold face of the satellite and the permanent platform yaw steering (very small temperature variations in the order of 1°C are observed).

Along the orbit, temperature variations induce variable pointing biases over the antenna scan (a few arc seconds for elevation pointing and few tens of arc seconds for the azimuth). They are quantified by calculating the PSD of the different time series as shown in Fig. 5.33.



The main component corresponds to the scan fundamental frequency. Higher harmonics have negligible energy. Also, the TED variations of the interface to the AOCs sensors (mounted on the antenna) has been investigated. These are extremely stable along the orbit and from one orbit to another, with variations well below 0.1 arcsecond.

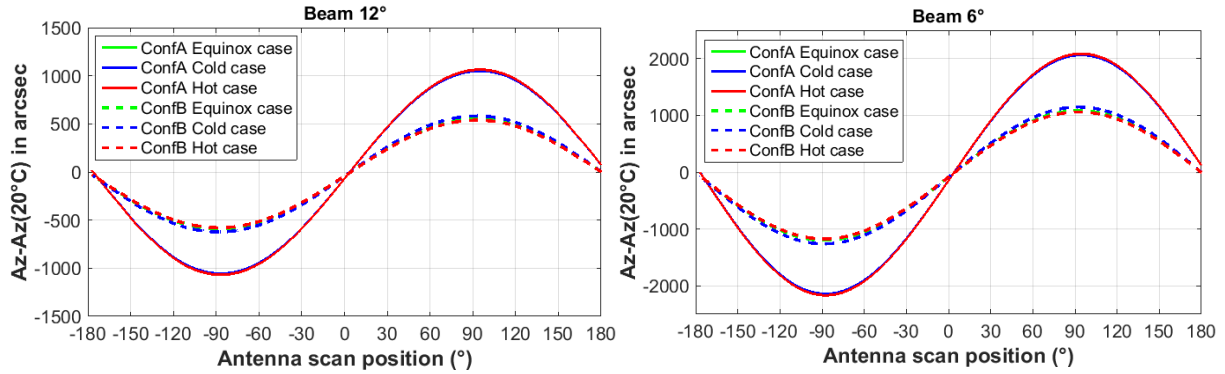


Figure 5.30. Mean azimuth pointing variations with respect to reference case (ground 20°C homogeneous case). Variations in elevation are not shown, but are 10 times weaker than the variation of the 6° beam in azimuth. These plots show the one-off variation due to in-orbit temperatures for both concepts.

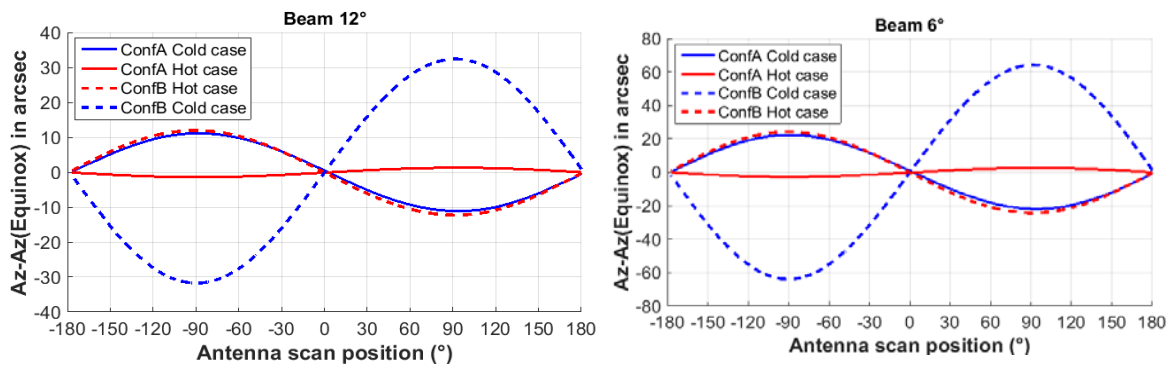


Figure 5.31. Mean azimuth pointing variations with respect to equinox case. Variations in elevation are not shown, but are 10 times weaker than the variation of the 6° beam in azimuth. These plots show the seasonal variation for both concepts due to TED.

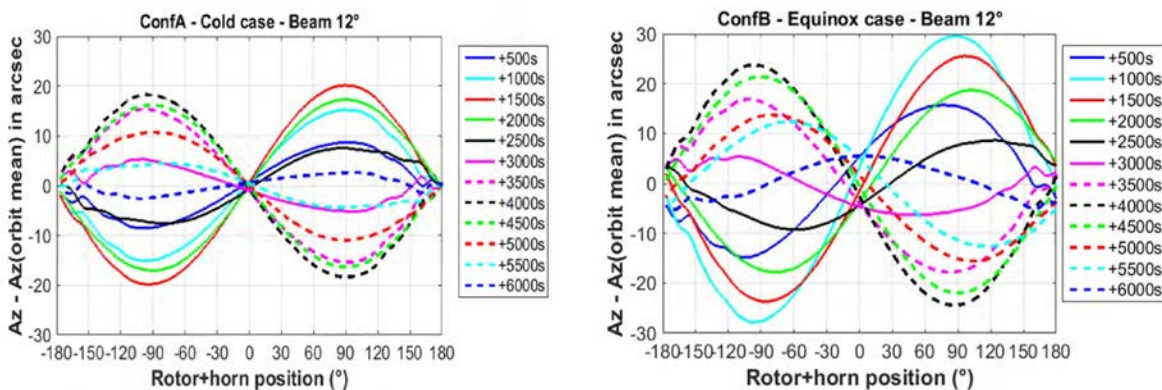


Figure 5.32. Azimuth pointing variations for 12° beam over one orbit (equinox case) with respect to orbital mean for each azimuth position. Concept A (left) and Concept B (right). These plots show the orbital variation for both concepts due to TED.

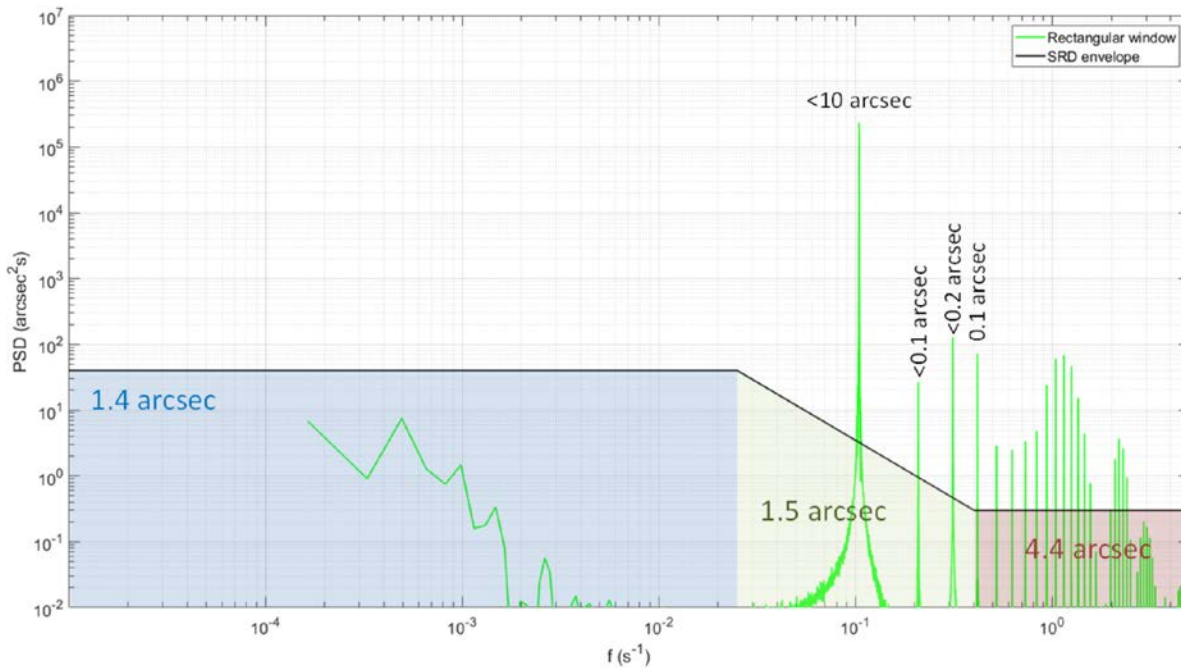


Figure 5.33. PSD azimuth pointing variation spectrum at orbit scale and seasonal scales for Concept A (for 12° beam – peaks for 6° beam are factor of two higher).

In conclusion, a mean antenna pointing over a full antenna rotation will be defined considering a mean in-orbit temperature (a large one-off deviation from ground environment by a few thousands of arc seconds). Note that launch slippage induces similar variability and will also be considered. Then, once in orbit, pointing variations are much lower. At seasonal scale, the mean pointing evolution can be modelled very well by a constant attitude bias over the antenna scan (harmonic). At orbit scale, variations are lower than 10 arcsecond (rms).

5.3.3.9 Altimeter Tracking System

The onboard software manages several tracking systems:

Range tracking enables the echo position to be controlled within the reception window. It can operate in open loop or closed loop (locked on nadir beam signals tracking). Open loop is the nominal mode to guarantee the presence of ocean echoes on off-nadir beams everywhere, even when the nadir beam is over land. Closed loop mode is a back-up mode enabling for instance DEM up-load while maintaining science data availability when the nadir beam is over ocean and in-land waters. Direct transitions between these modes can be commanded (see Fig. 5.17).

Closed-loop tracking mode

The tracking range loop is a second order loop. Its input is a range error computed at each nadir cycle from the nadir echo thanks to a range discriminator. The range discriminator is the median where the tracking gate corresponds to a fraction of the echo total energy. The range error is processed by the range tracking loop which computes a first order range instruction (for the range) and a second order range instruction (for the vertical speed). From these instructions, the onboard software computes range instructions to be applied to

each beam cycle, that is selection of the range samples of the echo for the different beams (see Fig. 5.34). The nadir instruction is used to compute from the geometry the off-nadir beams instruction considering that there is no difference of ground elevation between beams. The algorithm accounts for ambiguity rank, PRI, vertical speed and beam elevation pointing. Parameters dedicated to each beam, stored onboard (re-programmable in orbit), are used to have a fine position tuning of the echo in the range window. The range correction is applied to all radar pulses within a beam cycle considering the vertical range variation instruction (computation done by the hardware sequencer and applied during echo range compression processing).

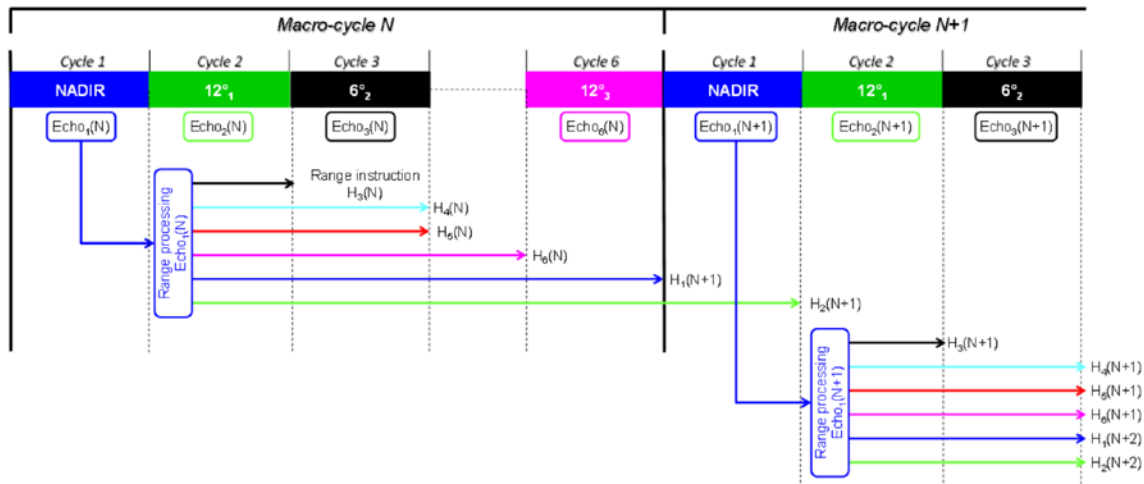


Figure 5.34. Range tracking sequencing. Same processing sequence is followed for the PRI tracking.

Open-loop tracking mode in this configuration, the instrument stops analysing the nadir return echo signals and slaves the position of the range acquisition windows using external information (navigator bulletin, DEM). Algorithm sequencing and range instruction application are the same as for the closed-loop mode. The range tracking operation will decouple the off-nadir receive window placement from the actual nadir beam, so that off-nadir beams over the ocean are correctly placed while the nadir beam tracks the land topography. Using the real-time navigator bulletin, the off-nadir range tracking algorithm will compute the range off-nadir geometry assuming a geoid reference surface. The nadir beam receive window will be correctly placed everywhere over land and ocean using a combination of the real-time navigator bulletin and one-dimensional along-track terrain elevation data (calculated on ground and stored onboard, as for Copernicus Sentinel-3/6).

Gain tracking computes echo level in real time to optimise the signal levels at the input to the Analogue to Digital Convertor (ADC), whatever the ground surface Normalised Radar Cross Section (NRCS) value by programming variable attenuators in the receive chain. Six gain loops, one for each beam, are used. The gain loop is a first order loop. A loop coefficient is applied to filter the non-significant variations of the signal level. Parameters dedicated to each beam, stored onboard (re-programmable in orbit), are used to tune the algorithms. Gain instructions are applied to RF analogue attenuators commanded by a digital command. The instruction to be applied at macro-cycle N are computed during the previous macro-cycle.

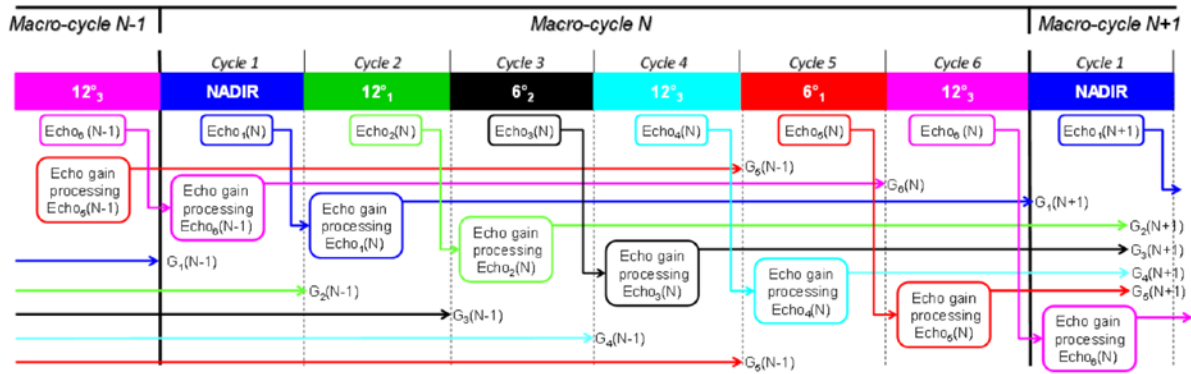


Figure 5.35. Gain tracking sequencing.

PRF tracking or Pulse Repetition Interval, PRI, adjustment along the orbit due to the altitude variations. Indeed, interval between two pulses is around 31 μ s whereas altitude variation can exceed 25 km or 167 μ s. Therefore PRI computation is done to centre the received echo between two transmitted pulses. This done for each beam at macro-cycle rhythm (4 Hz). The PRI is coded with a Least Significant Bit (LSB) equal to 16 ns.

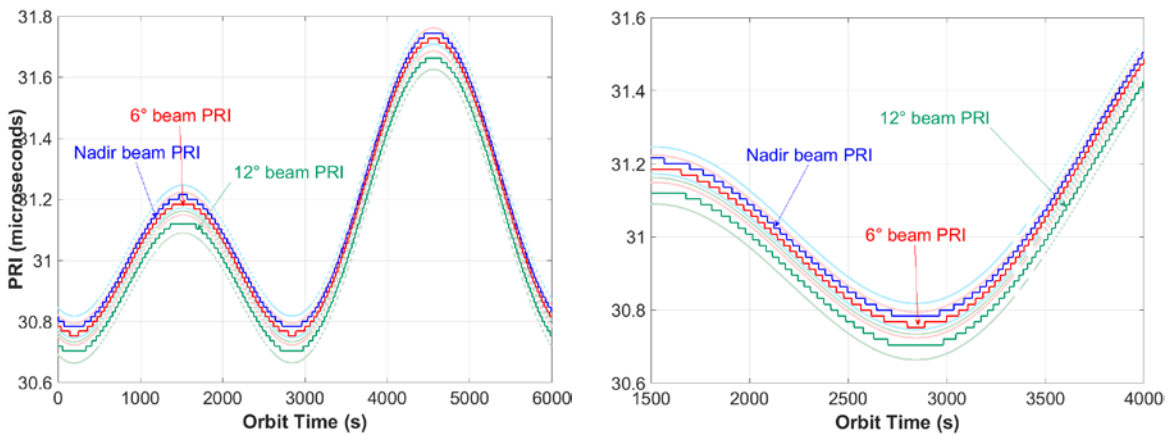


Figure 5.36. PRF/PRI tracking algorithm computation (16 ns PRI step - light coloured lines corresponds to min and max allowed PRI, a zoom is on the right).

5.3.3.10 Radar Characterisation and Calibration

5.3.3.10.1 Overview

The SKIM mission addresses different measurements types (nadir altimetry, wave and Doppler scatterometry) calling for specific calibration, characterisation and monitoring methods. Achievement of instrument performances is ensured in-orbit by:

- Continuous internal calibration of each beam (during the waiting period at the beginning of the beam cycle) of the instrument conducted transfer function and the thermal noise at the input of the receiver for the selected beam. A set of internal calibration loops are implemented in the instrument to have a complete check of all instrument conducted paths.



- Instrument ground characterisation for all the elements not included in the calibration loops or not measured with enough accuracy by the calibration loops.
- External calibration providing the possibility to check the complete instrument transfer function in orbit.
- Specific and new approach to provide accurate pointing knowledge at Level-1b processing level to the science processing higher levels thanks to correlated instrument pointing models elaborated on-ground and fed in-orbit by antenna temperature monitoring and scan angle knowledge position (optical encoder). Models will be checked and updated in-orbit using data driven methods (over ocean and non-moving stable targets) and external calibrations (ground receiver).

5.3.3.10.2 Instrument Calibration

The set of parameters to be calibrated with respect to mission performances are identified in Table 5.3. The calibration approach is based on combination of:

- Monitoring with internal calibration loops implemented in the instrument,
- Instrument ground characterisations for all the elements not included in the calibration loops or not measured with enough accuracy by the calibration loops,
- External calibration (transponder, ground receiver, known distributed stable targets) providing the possibility to check the complete instrument transfer function in orbit.

The instrument pointing calibration required for the Doppler scatterometry measurements (non-geophysical Doppler removal is addressed in Section 5.3.3.10.3).

Mission performances	Characteristic	Calibration/Characterisation
Nadir altimetry		
Range noise	Impulse response characteristics Thermal noise	Regular internal calibration sequences Estimation during each beam cycle
Range bias	Mean group delay	Regular internal calibration sequences + ground characterisation
Range bias stability	Mean group delay drift	Continuous check during each beam cycle (cal pulses in radar mode)
NRCS absolute accuracy	Radar PTx.GRx.Gant ² product	Internal calibration + Antenna ground characterisation External calibration
Absolute Pointing Knowledge	Nadir pointing bias	Data driven (Level 2 processing) External calibration over ocean during commissioning phase Estimation with re-tracking algorithm
Radiometry		
Absolute radiometric accuracy	Radar PTx.GRx.Gant ² product	Internal calibration (in-orbit) + Antenna ground characterisation External calibration
Relative radiometric accuracy within a beam	Antenna gain shape	Antenna ground characterisation External calibration
Radiometric stability for each beam	RF chains stability Antenna gain stability	Regular internal calibration sequences + ground characterisation
Relative radiometric accuracy between beams	Mean gain between beams (conducted & radiated)	Regular internal calibration sequences + ground characterisation
Doppler scatterometry		
Instrument pulse-pair phase noise	Radar Tx/Rx pulse-pair transfer function	Internal calibration loops + analyses with on- ground characterisations



Instrument drift/stability	pulse-pair phase	Radar Tx/Rx pulse-pair transfer function stability	Ensured by Pulse-pair processing (high pass filter) Continuous check during each beam cycle (cal pulses in radar mode)
----------------------------	------------------	--	---

Table 5.3. Calibration needs and methods with respect to mission performances.

5.3.3.10.2.1 Internal Calibration

Internal calibration refers to calibration measurements performed by the instrument, without requiring dedicated external calibration targets or equipment. It aims to monitor the key performances of the instrument in any orbit position:

- Instrument Range and Azimuth Impulse Response (RIR, AIR).
- Transmit power × receive gain up to the antenna feeds from the peak of the instrument impulse response (RIR).
- Instrument time delay induced by the transmit–receive loop deduced from the peak of the instrument impulse response (RIR).
- Pulse-pair phase from the peak of the instrument impulse response (RIR).
- Onboard processing transfer function.

Assuming adequate thermal control of the electronics, the instrument design is sufficiently stable to do an internal calibration once a day. However, the chosen approach is as follows:

- Use of continuous calibration pulses and free receive slots during waiting period at the beginning of each beam cycle to permanently:
 - Check the stability (range delay, pulse-pair phase, impulse response shape) of the radar transfer function.
 - Estimate the thermal noise for each beam (ensure accurate estimation since noise received by the antenna is specific to each beam location).
- Use specific calibration periods (daily/weekly/monthly, interval to be defined) to perform global check of the instrument transfer function with different calibration paths.

Four internal calibration loops are implemented (see Fig 5.37). They can be used independently or combined:

- Direct calibration loop (DCL) similar to that implemented in other altimeters. Enables the Tx/Rx transfer function of the instrument to be monitored up to the duplexer. This represents the core calibration loop, as the major components where stability could drift during the mission are included. It will be used continuously during the waiting period at the beginning of a beam cycle (a negligible part of the transmitted signal power is fed back in the receiver via the duplexer calibration path).
- Antenna calibration loop for the transmit path (TxCL). The HPA is included in this loop as well as the conducted paths of the antenna (rotary joint and transmit path of the switch matrix).
- Antenna calibration loop for the receive path (RxCL). The HPA is not included in this loop. The conducted paths of the antenna (rotary joint and receive path of the switch matrix) are included.
- CEU calibration loop (CCL): enables the electronics Tx/Rx transfer function without the HPA to be monitored.

$$ITF_{conducted} = \frac{T_xCL \times R_xCL}{CCL} \quad (\text{Eq. 5.2})$$

Eq. 5.2. shows how the complete Tx/Rx transfer function of the instrument (ITF) can be obtained by the combination of antenna calibration loops and CEU calibration loop.

For the antenna calibration loops, the transfer function between the antenna feeds on the rotating plateau and the calibration horn will be characterised on ground (as a function of scan angle). Antenna calibration loops can be performed while the antenna is rotating.

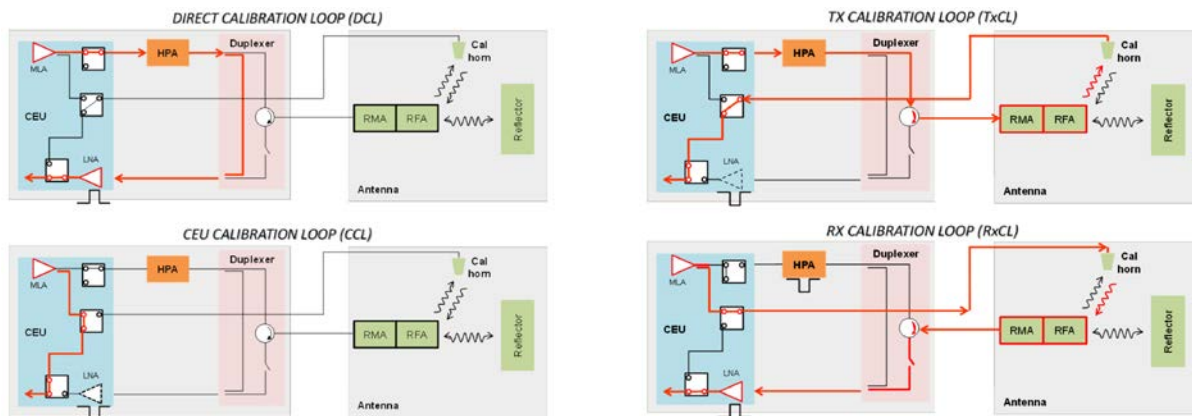


Figure 5.37. SKaR internal calibration loops.

5.3.3.10.2 External Calibration

External calibration involves the use of dedicated targets external to the instrument to obtain in orbit:

- Absolute range measurements
- Instrument total impulse response including the antenna
- Geolocation and datation accuracy system check
- Antenna gain pattern check (main lobe)
- Antenna pointing estimation (see Section 5.3.3.20.13)

Compared to internal calibration, there are more constraints associated with this calibration technique since, as it involves external means such as a transponder (point target), ground receivers and/or non-moving ground surfaces, it can only be carried out on given dates and in a given orbit position. Therefore, it will be used as an absolute calibration and for long-term monitoring of instrument drift. Use of active transponders is necessary to segregate the transponder echo from the ground clutter by applying a time delay to the incoming instrument pulse and transmit it back after amplification to the instrument. Current operational processing for Copernicus Sentinel-3 using the Gavdos transponder site in Greece allows to derive absolute range bias and product datation bias and is routinely monitored by the Copernicus mission performance centre.

The absolute power can also be derived from transponder acquisitions and future accuracy enhancement are foreseen for altimetry missions. This strategy applies to the nadir beam and can be translated to the off-nadir beams using transponders with scanning capability to



follow the satellite (as used for MetOp-SG). In addition to the active transponder sites, external calibration can be applied using either natural distributed targets (salt flats, sand deserts, rain forests) or specular stable targets (inland water). For Sentinel-3, during calibration and validation, salt-lake data with synthetic aperture radar processing has shown that the instrument point target response can be derived with good level of accuracy.

5.3.3.10.2.3 On-ground characterisation

The complete transmit and receive chains of the instrument are characterised prior to launch over the in-orbit predicted temperature range. These measurements also include characterisation of the complete internal calibration subsystem, which will monitor any transfer function variations in the radar electronics in orbit. All components that are not included in the direct calibration loop (Fig. 5.37) are specifically characterised (in-band amplitude and phase, insertion losses and group delay):

- Duplexer Tx, Rx and calibration paths
- Connecting waveguides between duplexer and antenna
- Antenna conducted Tx/Rx paths at elementary level (rotary joint, switch matrix, feed) and assembly levels.

The antenna radiated behaviour will be characterised by RF measurements (antenna gain pattern and amplitude/phase distortion as a function of scan angle) and a specific testing approach to cover SKIM pointing knowledge will be adopted (Section 5.3.3.10.3).

5.3.3.10.3 Level-1 Pointing Calibration

5.3.3.10.3.1 General approach and objective

Equation 5.3a shows that the velocity measured by the radar along the LoS (V_{LoS}). V_{NG} is the non-geophysical Doppler velocity projected on the LoS to be removed from the signal leaving the geophysical Doppler velocity V_{GD} that contains the wave and current Doppler velocity signal of interest. V_{NG} is purely due to relative motion between the spacecraft and the target, and needs to be removed from the measurements.

$$V_{LoS}(r, \varphi_{OE}) = V_{NG}(r, \alpha(\varphi_{OE})) + V_{GD}(\alpha(\varphi_{OE})) \quad (\text{Eq. 5.3a})$$

$$\begin{aligned}
 V_{NG}(r, \varphi_{OE}) = & V_{sat} \cdot \sin[\gamma(r)] \cdot \cos\alpha & \pm 1400 \text{ m s}^{-1} \\
 & - V_{Earth} \cdot \sin[\gamma(r)] \cdot (\varepsilon \cdot \cos\beta \cdot \sin\psi \cdot \sin\alpha + \cos\psi \cdot \cos\alpha) & \pm 90 \text{ m s}^{-1} \\
 & + e \cdot V_{sat} \cdot \cos[\gamma(r)] \frac{\sin(\beta - \alpha)}{\sqrt{1 + e^2 + 2e \cdot \cos(\beta - p)}} & \pm 7 \text{ m s}^{-1}
 \end{aligned}$$

$$\text{with } \alpha = \alpha(r, \varphi_{OE}) \quad (\text{Eq. 5.3b})$$

Equation 5.3b expands the V_{NG} term where r = range (radar echo time sampling), φ_{OE} is the azimuth scan position given by the optical encoder, α is the true azimuth position (differs significantly from the scan azimuthal position), γ is the look angle, other parameters are orbital elements. V_{NG} can be separated into three contributions: 1) the orbital velocity of the

spacecraft, which is the dominant component (red), 2) the rotation of Earth (yellow) and 3) the radial velocity between spacecraft and surface as it moves along the orbit (green). The dominant term in red is simply the magnitude of the spacecraft velocity, projected on the LoS, with α the azimuth angle between the velocity vector and the LoS, and γ the look angle or elevation angle to the LoS.

The uncertainty on V_{NG} due to uncertainty on α is worst in the across-track direction. For the 12° beam, an uncertainty of 1 arc second on α would result in an uncertainty of $\sim 0.7 \text{ cm s}^{-1}$ on V_{NG} (noting this corresponds to a horizontal velocity of $\sim 3.4 \text{ cm s}^{-1}$). The uncertainty on V_{NG} due to uncertainty on γ is worst in the along-track direction. For the 12° beam, an uncertainty of 1 arcsecond on γ would result in an uncertainty of $\sim 3.8 \text{ cm s}^{-1}$ on V_{NG} (noting this corresponds to a horizontal velocity of $\sim 18 \text{ cm s}^{-1}$). The question then becomes, to which LoS are these angles defined? SKIM is a real aperture radar. The look angle to the LoS is defined by the satellite position and the position of the range gates on the surface, as illustrated in Fig. 5.38. SKaR being an altimeter instrument, the range knowledge is very accurate and stable (stability better than 1 mm). The accuracy on the estimation of the look angle γ is therefore driven by the knowledge of the surface height at the location of the measurement. The azimuth position α of the LoS is defined by the Doppler centroid within a given range cell. The Doppler centroid is the position of a point target that would have the same Doppler shift as the weighted Doppler over the resolution cell of the radar. The weighing function is a combination of the antenna pattern and the NRCS distribution. In other words, V_{NG} measured by the radar depends on instrument characteristics such as the antenna patterns, but also on geophysical characteristics, including the NRCS gradients within the resolution cell and the sea surface height.

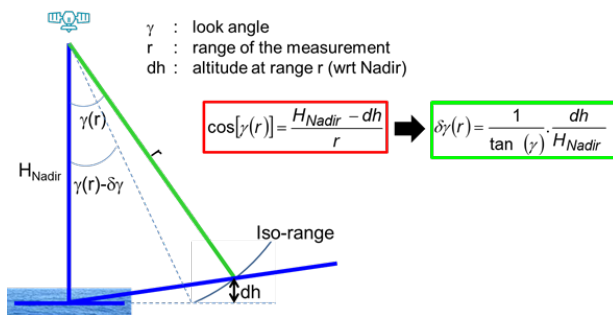


Figure 5.38.. Look angle knowledge is driven by uncertainty of sea-surface height.

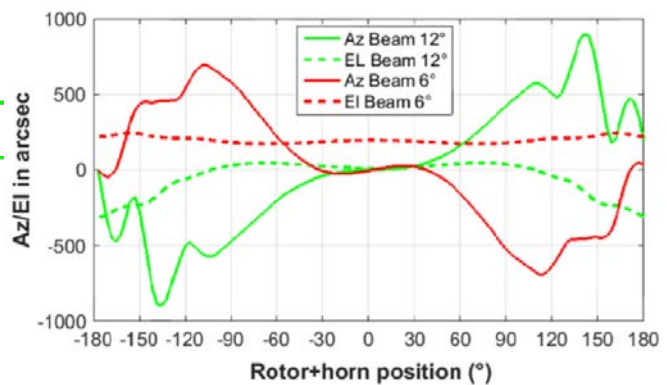


Figure 5.39. The deviation in azimuth and elevation between an ideal conical scan and that of the SKaR antenna boresight is plotted around the azimuth for Concept B, but very similar for Concept A.

The approach for SKIM is to implement at Level-1a series of calibration steps that will achieve an azimuth pointing knowledge in the order of 10-20 arcsecond, using parameters available at Level-1, such as antenna patterns, orbital position, and the antenna scan position (from the optical encoder). With regards to the look angle, the effect from geostrophic currents would typically result in sea surface heights that cause an error on the V_{NG} estimation of 37% of the current velocity and can be ignored at Level-1. For example, a 50

cm s⁻¹ current would correspond with a *dh* of 78 cm for the 12° beam (see Fig. 5.38) and cause an error of ~1 arcsecond on γ , and an error of ~3.9 cm s⁻¹ on the V_{NG} estimation.

Due to non-ideal behaviour of the antenna (asymmetry in the offset reflector design and shadowing effects from feed plate) the pointing of the RF boresight varies in elevation and azimuth ($\alpha(\varphi_{OE})$ in Eq. 5.3) with respect to a perfect conical scan by hundreds of arcseconds, as shown in Fig 5.39. In addition, the in-orbit pointing is significantly modified (several 1000 arcseconds) relative to ground due to temperature differences with ambient conditions and launch slippage (1–0g transition and hygrometry). The first objective of the pointing calibration is to acquire knowledge of this reference pointing law with scan angle. Then, at orbit and seasonal scales, the antenna pointing stability is driven by thermo-elastic variations, micro-vibrations and platform attitude stability. Micro-vibrations transmitted by the platform and created by the antenna scan mechanism are kept sufficiently low by design. The first approach at system level to obtain the antenna pointing knowledge will be based on the use of onboard sensors:

- Monitoring and knowledge of the antenna reference frame with the startrackers (absolute attitude) and gyro (relative attitude) mounted on the antenna structure.
- Measurement of the azimuth scan position (optical encoder).

By placing the AOCS sensors on the antenna, the main residual uncertainty comes from thermo-elastic deformations of the antenna. The second objective of the pointing calibration is therefore to gain knowledge on these deformations.

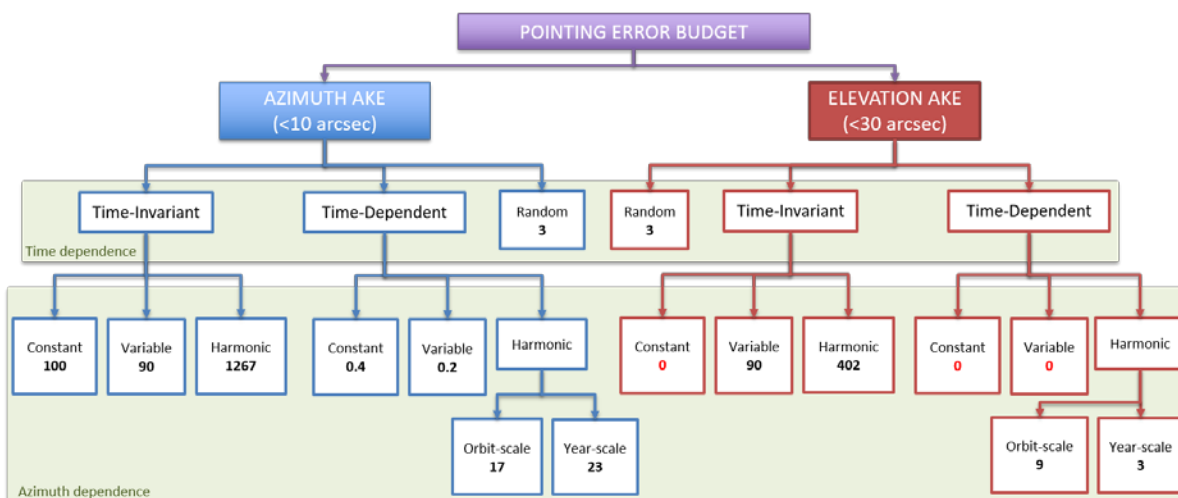


Figure 5.40. The error tree for the pointing Absolute Knowledge Error shows that time-dependent contributors to the uncertainty are relatively small, thanks to the stability of the system. This enables the use of external calibration using well controlled ground targets (receivers and/or transponders) to remove constant or slowly varying uncertainties for Concept A (isardSAT).

Various calibration methods were analysed in detail during Phase A, which can roughly be categorised in three groups:

- Use predictive models that have been correlated with on-ground characterization
- Use instrument data for data-driven calibration
- Use external calibration targets to gain information during flight

These methods are described in more detail in the following sections. Fig. 5.40 shows an error tree for the AKE. Errors are grouped in different categories depending on how they vary in time and over the conical scan. This leads to different calibration methods being proposed to address different categories of errors, as explained in more detail in Chapter 7.

5.3.3.10.3.2 Method A: Model-Based Calibration and On Ground Characterisation

Once in orbit, the variations of the pointing will mainly come from the smooth variation of the antenna temperature. For each orbital position an estimated antenna pointing will be computed from look-up tables, using temperature information extracted from antenna thermal sensors (glued at different points of the antenna) and antenna scan position (from the antenna optical encoder). Ground characterisation is required to obtain:

- A correlated thermo-elastic model. The antenna deformations (reflector, feed assembly) are measured over a wide range of temperatures by a laser tracker technique to tune the antenna thermo-elastic model. This model allows the RF model to be fed with antenna deformations for different temperatures to obtain pointing laws as a function of temperature.
- A correlated RF model. Accurate on-ground RF measurements of the pointing in a near-field test facility will enable the antenna RF model to be refined.

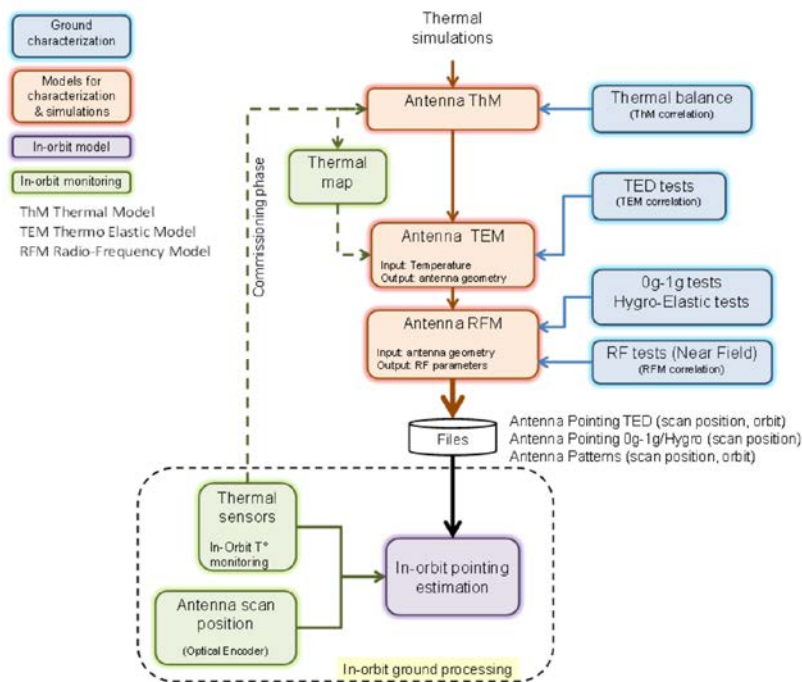


Figure 5.41. Antenna pointing behaviour in-orbit knowledge approach.

Based on these models, the thermal environment can be simulated on-ground for any position in orbit and injected in the correlated models to estimate the antenna pointing with small residual modelling errors. During the commissioning phase, thermal sensors mounted at different locations on the antenna will be used as input of the ground correlated model to



validate the on-ground pointing estimates and to tune the model as required. During routine operation, a pointing model, for instance in the form of Look Up Tables (LUT) will be used to describe:

- For thermal effects: pointing variation as a function of scan angle for different orbits (orbit sampling and number of orbits to be defined). The on-ground pointing estimation will interpolate these data for each scan angle and instrument measurement time position.
- For 1–0 g transition and hygrometry: pointing variation as a function of scan angle (constant bias along the in-orbit operation)

5.3.3.10.3.3 Method B: Data-Driven Calibration

As for any altimetry mission, satellite pointing manoeuvres will be performed during the commissioning phase to estimate the nadir beam pointing with ocean echo re-tracking and Level-2 processing techniques. Orbital cross-overs can also be used. The pointing of the off-nadir beams will require additional calibration steps, as the pointing varies with the scan angle. Since the Doppler measurement of the instrument is extremely sensitive to off-pointing, it can be used over non-moving targets to calibrate the pointing of the beams. This requires targets that are sufficiently stable and offer a sufficiently high backscatter coefficient at Ka-band (for example salt flats and sand deserts). Ocean targets can also be considered by recognising that fixed off-pointing angles of the antenna will result in a Doppler error signal with a clear harmonic signature over the scan angle. The harmonic error signals can be fitted to the data (calibration method B1). This approach is similar to the removal of the non-geophysical Doppler at Level-2 (explained in chapters 6 and 7) but applied with a coarser target accuracy.

A different variant of data-driven calibration (method B2), which can be applied on the residual calibration with method B1, is to average the geophysical signals. The error decays roughly as $1/\sqrt{N}$ with N the number of averaged values (1 measurement every 10 s). This method can be used to retrieve errors that vary with azimuth scan angle, but are fixed in time. The accuracy will depend on the geophysical contributions in the measurements. Azimuth gradient of NRCS, wave Doppler contributions and currents can each produce 1 m s^{-1} variable bias over the scan, equivalent to pointing errors of more than 30 arcseconds. Averaging over long transects is foreseen to reduce for each azimuth scan position the measurement noise and the geophysical random noise. To remove any geophysical bias however, it is necessary to disentangle different geophysical contributors, which is why for SKIM this is done in the Level-2 science processing.

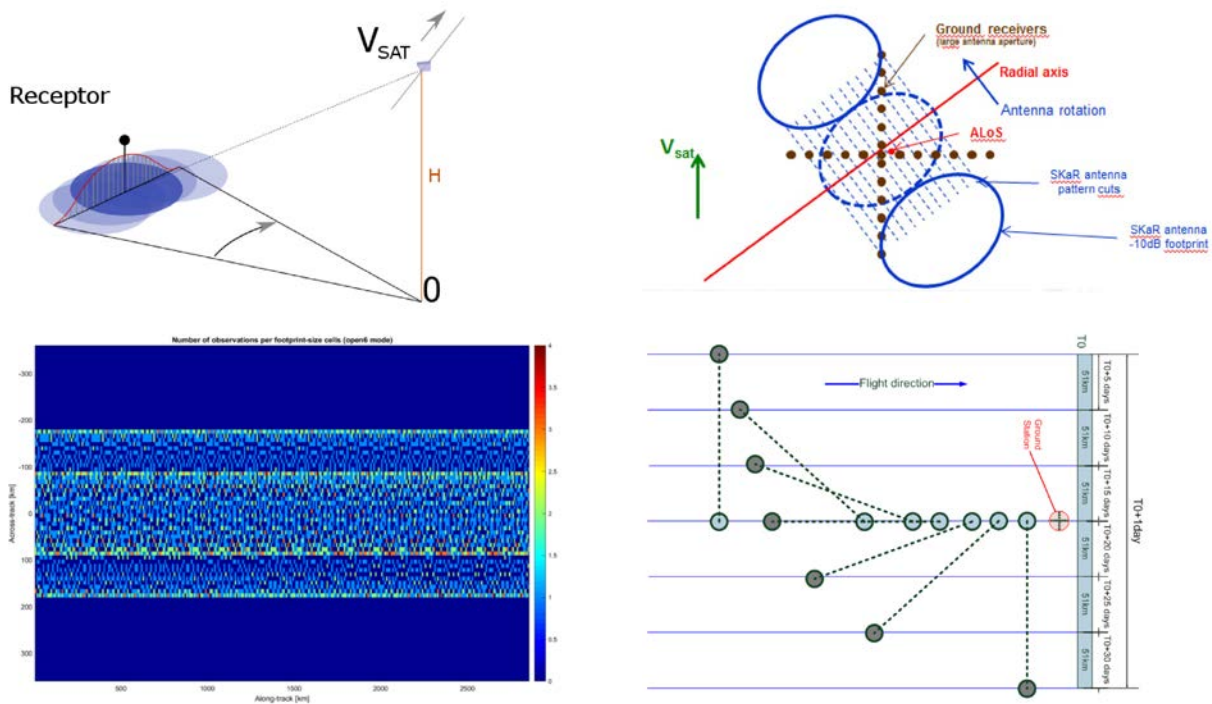


Figure 5.42. External calibration using ground receivers (top left). Calibration sites contain an array of receivers to record several cuts through the antenna pattern (top right). Concept A proposes calibration with rotating antenna, relying on statistical approach to gather sufficient antenna cuts (bottom left). Concept B proposes to stop antenna in series of deterministic azimuth positions, relying on careful selection of the calibration site latitude so that different azimuth positions can be read during subsequent passes (bottom right).

5.3.3.10.3.4 Method C: External Calibration

Model-based and data-driven calibration methods offer clear advantages in terms of complexity. However, calibration of yaw errors with data-driven approaches is more difficult due to their degeneracy with geophysical signals. Also, the amount of azimuth samples taken along the conical scan is too low for the non-geophysical signals to be orthogonal to the geophysical signals. The model-driven approach, on the other hand, cannot guarantee correct and validated calibration results once in orbit. Therefore, both concepts have complemented their calibration strategy with external calibration methods. The principle of external calibration is to measure the SKaR antenna 2D patterns when instrument beams cross the FoV of a ground receiver. Even without stopping the conical scan, the radar PRF is sufficiently high to acquire azimuth cuts with an angular spacing of samples of 4 arcseconds. Knowledge of the observation geometry between receiver and the radar as well as receiver sampling time and radar pulses emission time allows the radar antenna pattern in azimuth and elevation to be recorded. Two different variants of the external calibration approach have been proposed. For Concept A, the calibration is performed during the conical scan of the antenna and the cuts are gathered as the antenna beam sweeps over the calibration site (calibration method C1). For Concept B, a deterministic approach with the antenna fixed in a particular azimuth position is preferred (calibration method C2), and cuts through the pattern are gathered more slowly (with satellite velocity) and parallel to the flight path. This is illustrated in Fig. 5.42 A calibration site would contain 12 receivers, spread over an area of 15 km². Each receiver is approximately 1 m³ in size. For any given azimuth position a



theoretical accuracy of approximately 5 arcsecond in elevation and 0.5 arcsecond in azimuth can be obtained with a single pass (a complete error budget for external calibration will be developed in the next phase).

5.3.3.10.3.5 Summary of Level-1 Pointing Calibration Strategy

The pointing calibration strategies proposed for the two concepts both rely on a mixture of on-ground characterisation, data-driven calibration, and external calibration methods. The overall calibration strategies proposed for both concepts differ in the sequence of the main calibration steps deployed, which are also reflected in the pointing error budgets.

For Concept A, the proposed pointing calibration strategy can be summarised as follows:

1. Get pulse-pair data as a function of time, or, equivalently, as a function of optical encoder position. This could be over ocean or over non-moving, flat large areas such as salt flats.
2. Correct for Antenna azimuthal model as measured on-ground
3. Subtract non-geophysical Doppler contribution (1ω harmonic) based on a model.
4. Remove associated equivalent pitch and roll errors external to rotating plate by fitting and subtracting the 2ω harmonic. This is a continuous correction, applied over different timescales, to remove orbital and seasonal TED effects. Support from temperature monitoring, antenna temperature model and external calibration would help to reduce residual overall TED effects.
5. Estimate azimuth-variable biases by averaging the PP residuals at each azimuthal angle to compute equivalent azimuth error.
6. Iterate steps 3, 4, 5 as required.
7. Calibrate the constant bias contribution (equivalent yaw error). Different options are available, external calibration is preferred.

For Concept B, the pointing calibration strategy can be summarised as follows:

1. Use on-ground correlated models to predict in-orbit thermal behaviour, assisted by on-orbit validation using thermal sensors, as described above for method A.
2. With the antenna stopped in a particular azimuth position, perform external calibration using a calibration site with 12 receivers, spread over an area of 15 km². For any given azimuth position an theoretical accuracy of approximately 5 arcsecond in elevation and 0.5 arcsecond in azimuth can be obtained with a single pass (a complete error budget for the calibration is subject for further study). At least two different azimuth position are required BoL to identify harmonic and constant bias contributions.
3. Gather an increasing amount of azimuth positions, and interpolate in between with the help of the models from ground characterisation, to find the azimuth variable errors. Assuming calibration with 30° steps, an interpolation error of 10 arcsecond is expected.

Table 5.4 summarises the calibration strategy proposed for each concept. Chapter 7 reports on the resulting post-calibration pointing knowledge performance. Further studies are required in the next phase to determine the best overall pointing calibration approach for SKIM.

Calibration method	Id	Concept A	Concept B
Model-driven calibration using on-ground characterisation	A		√
Data-driven calibration, exploiting harmonic signatures in PP signal	B1	√	
Data-driven calibration, averaging out geophysical signals	B2	√	
External calibration, with array of ground receivers, antenna in fixed position	C1		√
External calibration, with array of ground receivers, rotating antenna	C2	√	

Table 5.4. Summary of calibration methods proposed for Concept A and B

5.3.3.11 Precise Orbit Determination Payload Complement

SKIM has very specific and demanding requirements in terms of POD to ensure the performance of the nadir altimetry product. A positioning accuracy in the nadir direction of better than 10 cm is required in near real time, and 3 cm needs to be achieved two days after observation. Both concepts achieve this performance by including two more instruments in the payload: a GNSS receiver and a LRR.

GNSS receiver: Both concepts propose the PODRIX double-frequency GNSS receiver to provide onboard position determination with an accuracy of 1 meter. The PODRIX receiver has 24 channels to maximise its precision. Furthermore, this receiver is compatible with reception of Galileo signals, which will further improve results with respect to GPS-only receivers. This equipment is also part of other radar altimeter spacecraft, e.g. Copernicus Sentinel-6, ensuring the given performances. The data from this receiver are also used by the AOCS subsystem for navigation. Centimetric resolution will be obtained after ground post-processing of the measurements obtained by the GNSS receiver. This requires the following precautions on the platform:

- The relative position knowledge of the satellite centre of mass (CoM) with respect to the antenna phase centre needs to be known accurately, which is achieved through:
 - Accurate on-ground measurement of the CoM in the spacecraft frame with an accuracy of at least 1 cm in the Xs-Ys plane and 2 cm in the Zs axis.
 - Incorporation on ground of a precise procedure for determination of CoM evolution due to the propellant consumption during the mission lifetime.
 - Accurate on-ground measurement of the position of the GNSS antenna phase centre in the spacecraft frame.
- The mechanical design and accommodation of GNSS antenna shall mitigate multipath effects by providing a surface as clear as possible in the anti-nadir panel.

The PODRIX receiver will use the 10 MHz reference provided by the SKaR in order to allow precise monitoring of the SKaR reference clock with respect to GNSS time.

Laser Retro-reflector: Satellite Laser Ranging (SLR) is used to calibrate the POD tool. A few mm accuracy on the range measurement can be obtained with SLR, providing the best possible reference. This requires the placement of a LRR on the satellite with a clear field of view towards Earth. The LRR must be accommodated as close as possible to the satellite CoM to avoid any measurement inaccuracies caused by satellite attitude motion.

5.3.4 Platform

5.3.4.1 Overview

The platforms proposed for Concepts A and B both rely on a standardised platform concept maximising recurrent elements with minor tailoring to the specific mission needs. Concept A is based on a recurrent flight proven medium-class platform already used for several missions, such as Copernicus Sentinel-5P and SEOSAT. Concept B is based on a modular standard platform that is currently being developed as a generic product line to support some of the Copernicus High Priority Candidate Missions. This platform is oversized with respect to the SKIM requirements and offers comfortable margins in terms of mass, power and consumables. Both platforms have demonstrated they can accommodate the particular needs of the instrument in terms of accommodating the antenna, achieving best-in-class pointing knowledge, power generation and heat dissipation. The platform subsystems are described in the following subsections.

5.3.4.2 Structure

The platform primary structure accommodates the payload and platform equipment providing the required mechanical strength and stiffness for the entire satellite. During launch it serves as the main load path between the antenna and a 937 mm diameter launch vehicle standard interface. The launch configurations for both concepts are shown in Fig. 5.43.

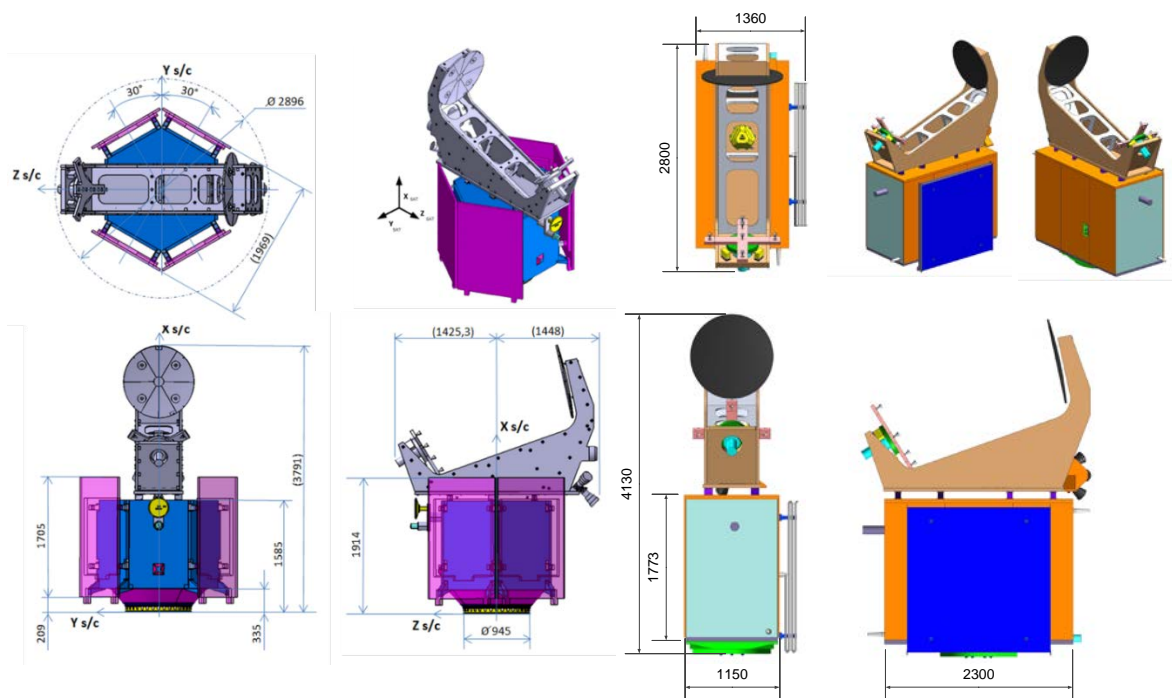


Figure 5.43. Launch configuration for Concept A (left) and Concept B (right), with dimensions in mm.

The primary structure for Concept A is hexagon with a maximum diameter of 1.7 m and a height of 1.6 m (excluding payload and solar array), and is shown in Fig. 5.44. The primary

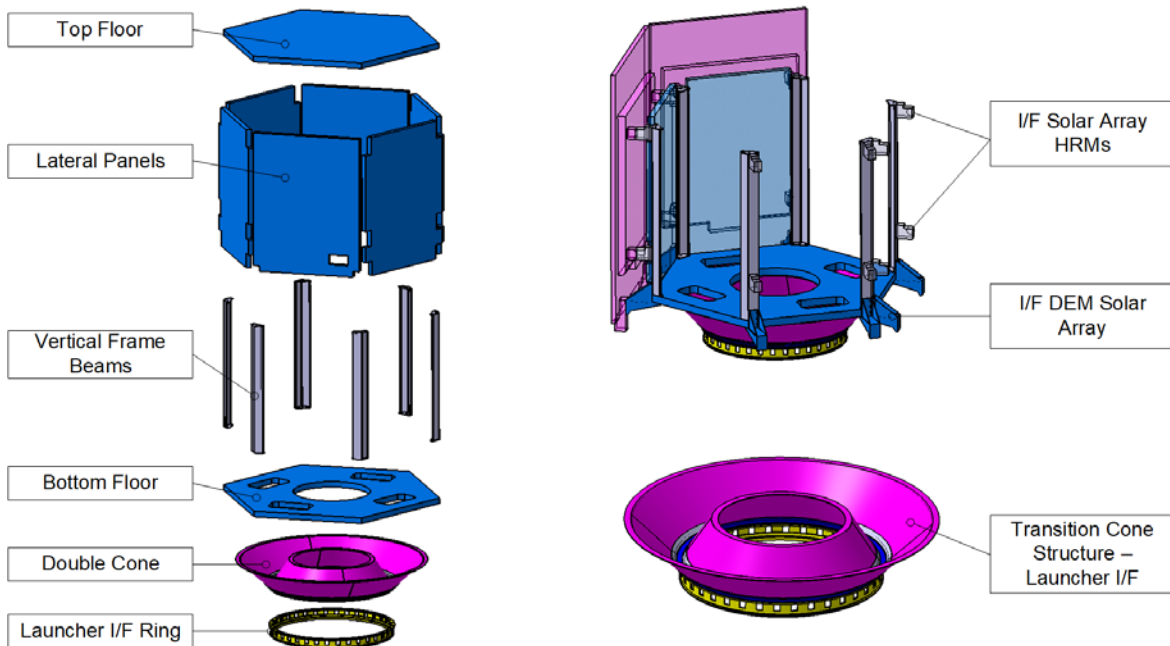


Figure 5.44. Exploded view of the platform for Concept A (left), attachment of solar panels (top right) and launcher interface adaptor (bottom right).

structural element comprises of six external panels, frame beam assemblies and a ‘double cone’ launcher interface. The six side panels are aluminium honeycomb sandwich panels, on which the platform and payload electrical units are mounted. The panels are fastened to the triangular, aluminium alloy vertical frame beams. The panels are designed to be opened during Assembly, Integration and Testing (AIT) using a set of removable hinges and mechanical bolted joints. This provides easy access to the internally-mounted equipment and the other subsystems, avoiding the need to break any electrical connections. The lateral panels contribute to the overall stiffness as a primary structure component. The six vertical frame beams run upwards from the bottom floor and connect the double bottom cone to the top floor, providing the primary load path for the payload. The lower floor is an aluminium honeycomb sandwich panel, which accommodates the four reaction wheels and harness routing between the electrical units. Four cut-outs are incorporated to allow lower accommodation of the reaction wheels. The launcher interface uses a double cone structure, interfacing the bottom floor and a dismountable Launch Interface Ring (LIR) structure. The internal cone is attached to the bottom floor close to the propulsion module to provide a direct load path. The top floor is an aluminium honeycomb sandwich panel with embedded heat pipes. Its main function is to contribute, with its high bending stiffness, to the overall rigidity of the structure and to accommodate the payload antenna, HPA and duplexer. Furthermore, the heat pipes improve heat diffusion and rejection capability of the panel, contributing to top floor thermal stability and dissipation of thermal power produced by payload electronics.

The primary structure for Concept B is cuboid. The baseline structure subsystem concept is based on eight longerons for the main load path connected to an aluminium alloy ring interfacing with the Launch Vehicle Adapter (LVA). The radiator and close-out panels are arranged in a way such that three different compartments or modules are available. To reduce the weight of the structure all of the panels are sandwich panels with aluminium

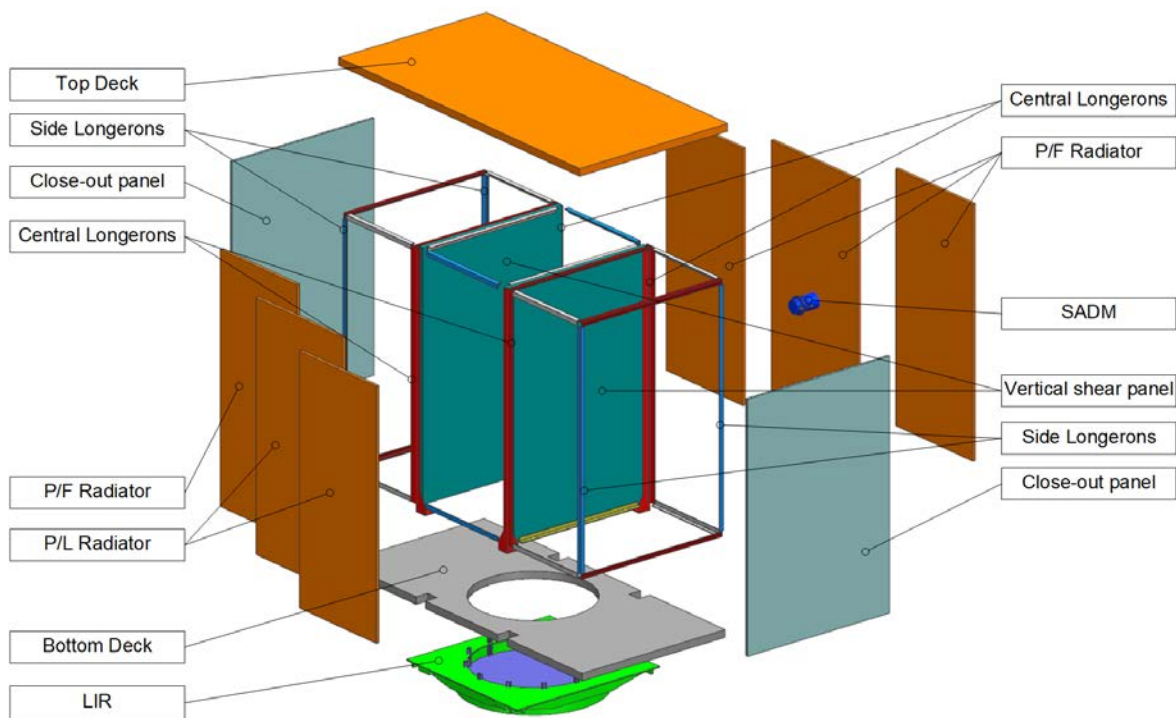


Figure 5.45. Exploded view of structure for Concept B

honeycomb core and aluminium skins. The whole structure of load-bearing longerons and panels works as a single structure. The main load path from the payload to the launcher is via the four central longerons, directly fastened to the LIR, and four vertical side panels fastened on the longerons. The top deck and bottom deck plus six side vertical panels complete the structure of the platform.

Figure 5.45 shows the exploded view of the concept structure. Unobstructed access to the instrument on the top deck allows easy integration on the platform and corresponding alignment. The concept allows the single side panels to be attached and removed separately, thus enabling a simple AIT flow. Payload units are accommodated on two platform panels, which can be delivered to the payload provider for integration of the payload units. The mounting points for the propulsion subsystem module are in the centre of the structure. Although allocations for micro-vibrations have been included in the performance budgets, dampeners on the reaction wheels and Solar Array Drive Mechanism (SADM) can be accommodated in the platform design should the need arise during the detailed design phase.

The compatibility of the structure with the launcher environment has been assessed for both concepts through dedicated mechanical analysis with Finite Element Models (FEM). Figure 5.46 shows the FEM used for both concepts, including the platform and a condensed model for the instrument. The quasi-static and dynamic analysis has been performed considering the Vega-C mechanical environment, with the spacecraft located in the upper position of the VESPA-C short adaptor. The main lateral and axial modes of both concepts are summarised in Table 5.5.

The results of the dynamic analysis show that the fundamental axial and longitudinal frequencies of both concepts are compliant with the Vega-C requirements with large

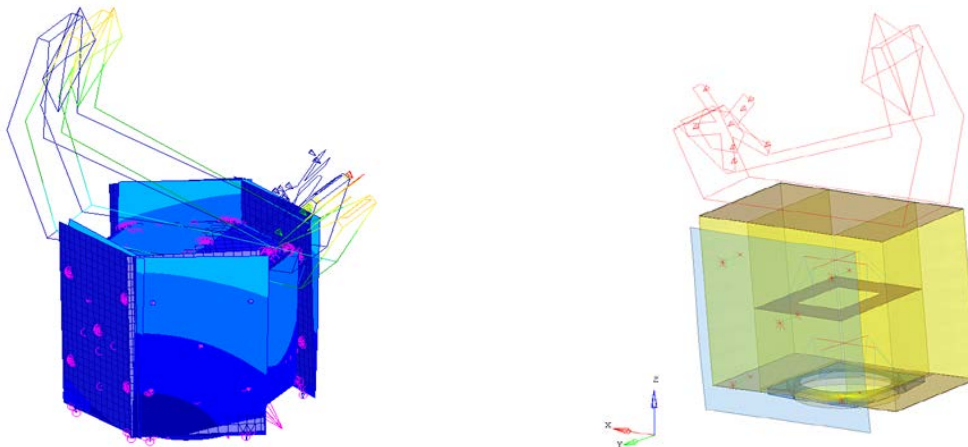


Figure 5.46. FEMs have been built to confirm the mechanical design of the platform and the antenna interface are compatible with the launcher environment. First lateral modes are shown. Left: Concept A. Right: Concept B.

Mode	Launcher (Vega-C) Requirement	Requirement with 15% Margin	Analysis Result Concept A	Analysis Result Concept B
Lateral	> 12.0 Hz	> 13.8 Hz	22 Hz	22 Hz
Longitudinal	> 20.0 Hz	> 23.0 Hz	54 Hz	79 Hz

Table 5.5. SKIM satellite analysis results versus Vega-C stiffness requirements.

margins. As usual, the sinus analysis has identified the need to perform primary notching on the main mode to not exceed the specified launcher Quasi Static Load (QSL). The coupled analysis has also confirmed that for both concepts the mechanical loads at the antenna interface are compatible with the antenna design. In conclusion, for both concepts the design is compatible with the mechanical environment specified for the Vega-C launcher and no major modification is required for the structure with respect to the standard platform.

For Concept A, thermal and thermo-elastic deformation analysis has demonstrated that the design of the top panel with embedded heat pipes keeps the delta between the hottest and coldest point on the panel below 4°C while the thermal excursion along the orbit is limited to 1°C, resulting in negligible deformation of the antenna interface.

Finally, for both concepts, compatibility with the backup launcher, Ariane 62, has been preliminary assessed, and no critical issues were identified.

5.3.4.3 Mechanisms

The mission only requires mechanisms that are readily available as off-the-shelf products with extensive flight heritage. Both concepts include Hold Down & Release Mechanisms (HDRM) to keep the solar arrays in the stowed position during launch and release them after orbit injection, locking mechanisms (e.g. reaction wheels), and propellant system valves. In addition, Concept B includes a solar array with a SADM attached to the main structure side panel. The SADM positions the solar array to optimise the power generation. Its functions are:

- Drive the solar array for optimal power generation



- Provide the solar array reference angular positions
- Transfer power from the solar array to the spacecraft
- Transfer signals between the solar array and the spacecraft with double insulated lines
- Provide the solar array electrical grounding to the platform

The actuator comprises a two-phase stepper motor with 360 steps per revolution and a Harmonic Drive gear box.

Mechanisms on the platform are a potential source of micro-vibrations that can affect the pointing performance of the instrument. This will have to be carefully assessed in the detailed design phase. If necessary, dampers can be fitted to reduce the effects of micro-vibrations.

5.3.4.4 Thermal Control

The main function of the thermal control subsystem is to guarantee operating and non-operating temperature ranges for all satellite components according to each specific requirement for all of the mission phases. The thermal control is based on a passive design supported by heater lines for specific equipment requiring heating power to remain above the minimum temperature limits during all operating modes. Inside the platform enclosure, a classical thermal control concept is suitable for the majority of the equipment.

The thermal control subsystem includes:

- Multilayer insulation (MLI) blankets and thermal washers to provide insulation and improve thermal stabilisation of critical units.
- High emissivity coatings for structural parts and equipment housings to enhance radiative heat exchanges.
- Thermal doublers to spread heat from the high-power density equipment and/or to improve the conductive coupling between some of the units.
- Radiators placed under the most dissipative equipment.
- Heater lines controlled by thermistors for the colder phases.
- Heat pipes for Concept A

The platform and antenna are thermally decoupled by means of MLIs wrapping and thermal washers at the mechanical interface. Antenna feeders are thermally controlled by the platform using a set of thermistors and heaters.

In Concept A, the antenna is mounted on the top panel, flies perpendicular to the velocity vector and faces deep space, enhancing its heat dissipation performances. Payload units with high dissipation are accommodated on the internal side of the top panel. Therefore, the thermal design implements embedded heat pipes on the top-floor, allowing excellent heat transfer to the radiators, keeping temperature gradients in the top panel well below 4°C and thermal excursion along the orbit below 1°C. This minimises thermal distortion from the platform towards the antenna.

In Concept B, the SKaR antenna flies along the velocity vector with one lateral side exposed to direct Sun illumination. The orbit is shifted in local time towards noon compared to MetOp-SG(1B) reducing the heat loads on the radiators facing the Sun. Most dissipative platform equipment and payload electronics are accommodated on the anti-Sun panels



increasing the ability of radiating the dissipated heat. This is supported by constant nadir pointing attitude in nominal operations.

For both concepts, internal sidewalls, bottom and top panel are painted black to homogenise the internal temperatures, while the non-radiative external surfaces of the platform are covered with MLI blankets. The accommodation of platform units on lateral panels is optimised to ensure heat dissipation via radiator foils and doublers when needed. The battery and propulsion module require a specific thermal control based on low emissivity coatings or blankets to provide radiative isolation from the enclosure. The propulsion module is conductively decoupled from the structure. Heater lines controlled by thermistors are provided for cold conditions. All externally mounted equipment (e.g. startrackers, etc.) has dedicated thermal control. Thermal decoupling of these elements from the platform is achieved with the use of isolating washers or low conductive mounts and MLI blankets.

5.3.4.5 Electrical Architecture

The overall system electrical architecture is similar to most Low Earth Orbit (LEO) spacecraft and is shown in Fig. 5.47 for Concept A and Fig. 5.48 for Concept B. The electrical architecture integrates the following functions:

- Command and Data Handling Subsystem (CDHS), covered in Section 5.3.4.6
- Payload Data Handling and Transmission (PDHT) subsystem, covered in Section 5.3.4.7
- Electrical Power Subsystem (EPS), covered in Section 5.3.4.8
- Telemetry, Tracking & Command (TT&C) subsystem, covered in Section 5.3.4.9

The onboard computer (OBC) acts as the command and control centre of the entire satellite and is therefore the master controller of all communications on board. The main communication is performed via two separate and redundant MIL-1553B busses, one for the platform and one for the payload. Cross strapping is implemented at the interfaces to ensure that the electrical architecture can still operate and have accessibility to redundant units in the event of a single failure. The OBC acts as the bus controller for both; all other units are remote terminals. In Concept A, non-intelligent units that are not directly linked via the main bus (e.g. some AOCS sensors and actuators, propulsion equipment, etc.) are connected via a single Remote Interface Unit (RIU). Concept B follows a more decentralised architecture, with most units connected via three Remote Terminal Units (RTU).

The science data communication link from the payload to the mass memory unit is accomplished by a Wizard Link (WZL) for high data-rate transmission. The OBC communicates with the payload via the MIL-1553B bus for payload data handling and control.

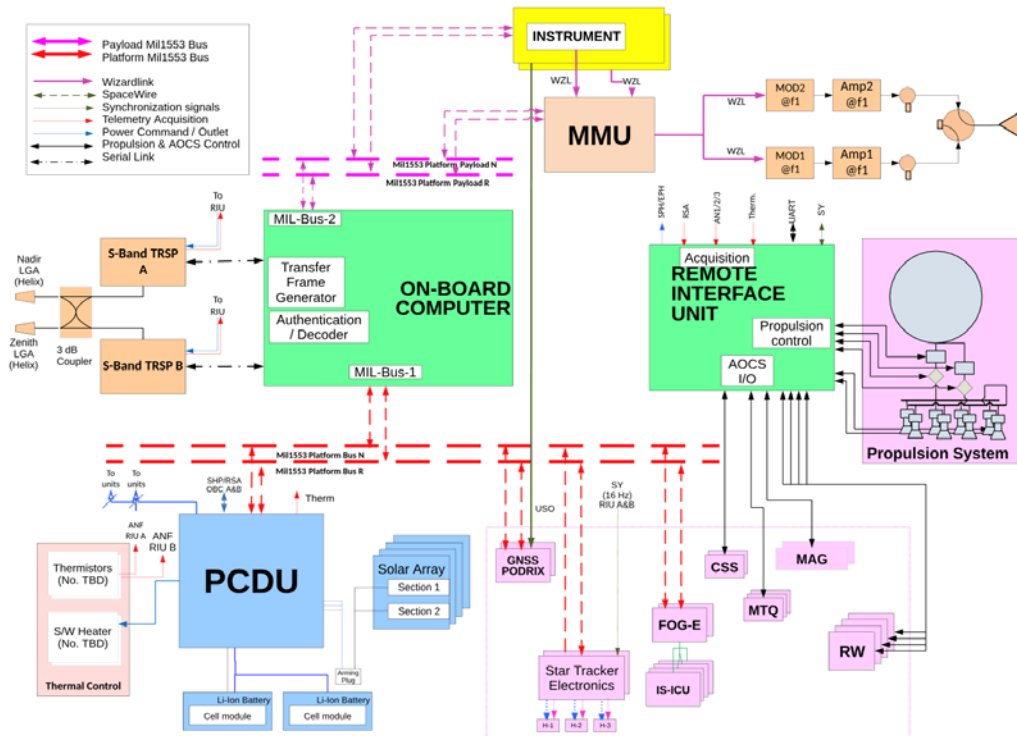


Figure 5.47. Concept A electrical architecture.

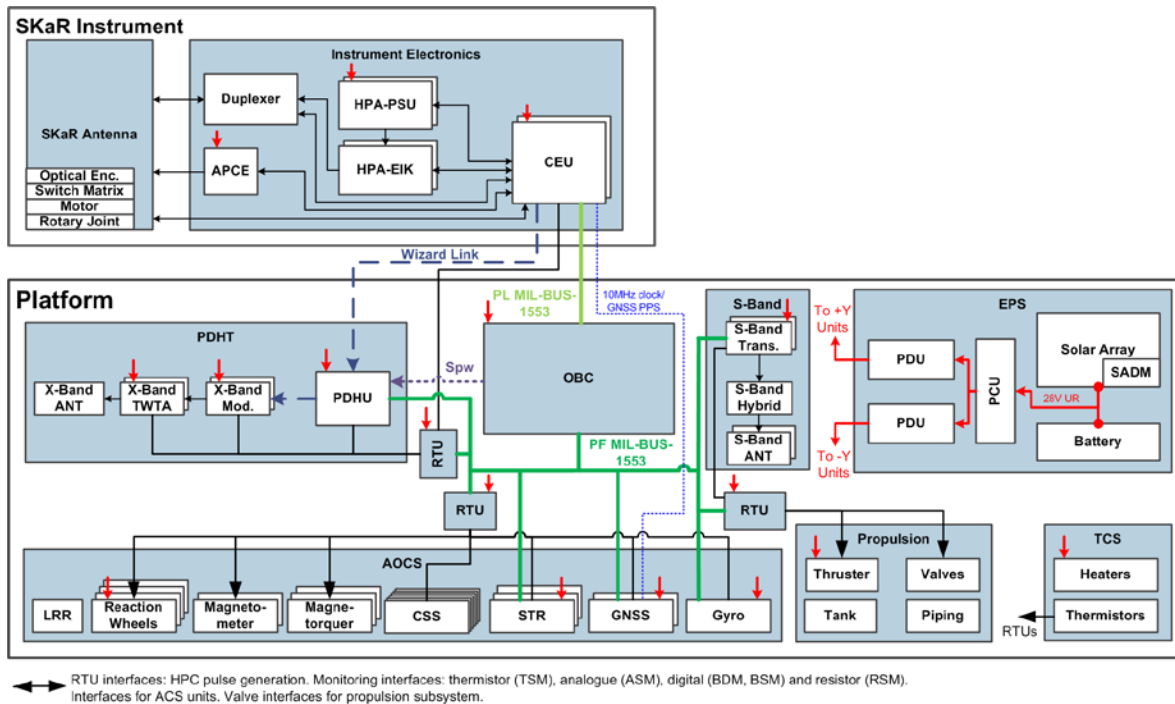


Figure 5.48. Concept B electrical architecture

5.3.4.6 Command and Data Handling Subsystem

The Command and Data Handling Subsystem (CDHS) is the core of the electrical architecture. It provides the following functions:



- Overall satellite command and control
- Supporting onboard autonomy and failure detection, isolation and recovery
- Provision and distribution of ground commands and software updates to the satellite
- Collection and storage of satellite housekeeping telemetry
- Onboard time generation, synchronisation, and distribution of time signals

The OBC provides the processing resources for the mission software, the monitoring and control of all the platform and payload units and the interfaces with the S-band communication chain. Two redundant Mil-STD-1553 data busses connect the OBC with most of the subsystem and payload units allowing the exchange of telemetry (TM) and telecommand (TC). The OBC, the payload and the PDHT are connected via a dedicated redundant MIL-STD-1553 bus. This provides the OBC with the capability of receiving, processing and storing the housekeeping telemetry (HKTM) of payload and PDHT. Furthermore, through this link, the OBC can control the payload and the PDHT and transmit HKTM ancillary data to the payload mass memory which will be integrated in the scientific data stream. The platform and payload HKTM received by the OBC is recorded in its mass memory and transmitted to the ground via the S-band communication chain.

The CDHS for Concept B has a decentralised architecture using three RTUs. They provide the interface between the MIL-STD-1553 bus connected with the OBC and some subsystem components not directly linked with the main bus (i.e. AOCS sensors and actuators, propulsion subsystem units and PDHT). For Concept A this role is fulfilled by a central RIU.

Concept B includes a Spacewire link from the OBC to the payload data handling storage unit (PDHU). This ensures that the recorded platform and payload HKTM can also be downlinked with the scientific data stream via the X-band link.

5.3.4.7 Payload Data Handling and Transmission

The PDHT ensures the scientific data gathered by the instrument are processed, stored and transmitted to ground. As explained in Section 5.3.3.7, the instrument produces 166 Gbits of data on average per orbit. For payload data storage, a dedicated mass memory (2 TB for Concept A and 1 TB for Concept B) is implemented on the spacecraft. The data is transferred from the instrument to the mass memory and on to the data downlink via the high-speed Wizard Link.

The payload data downlink is implemented using a medium capacity X-band downlink building on technology with extensive heritage within Europe, providing a maximum speed of 352 Mbit s⁻¹ for Concept A and 320 Mbit s⁻¹ for Concept B. The X-band isoflux antenna is mounted on the nadir-facing panel of the platform to provide an unobstructed FoV to the ground station.

The scientific data recorded along the orbit are downloaded to the ground station(s) once per orbit in about 11 min, through the X-band link service: Concept A considers two ground stations, in Kiruna (Sweden) and Maspalomas (Spain), while Concept B considers only a single ground station in Svalbard (Norway).

These solutions provide the capacity to download on average 230 Gbit per orbit for Concept A and 201 Gbit per orbit for Concept B. Both concepts guarantee that the maximum data latency requirement of one day can be met. For example, Concept B's onboard memory evolution and data latency map is illustrated in Fig. 5.49. A maximum of 120 GB of required

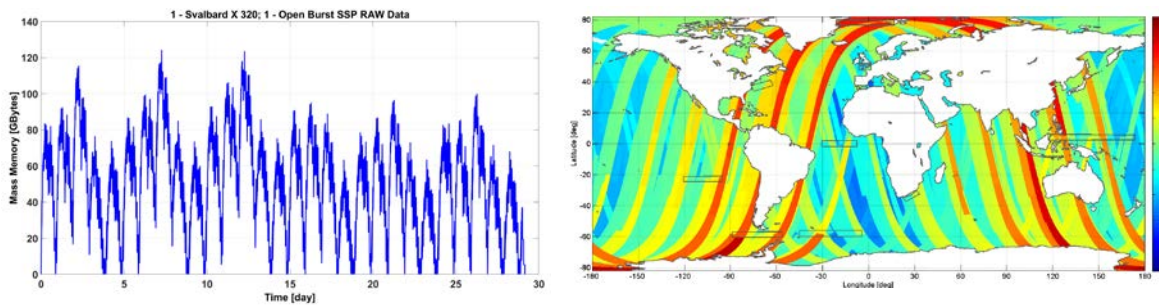


Figure 5.49. SKIM Concept B onboard memory evolution (left) and data latency map (right) in hours with X-band single channel 320 Mbit s⁻¹ downlink system and Svalbard ground station (DEIMOS).

memory load is estimated, much less than the size of the onboard memory, while the maximum latency expected for data is around 10 hours. This analysis was run with slightly different parameters than the current baseline, but the results are still valid.

Telemetry from both platform subsystems and payload are collected by the OBC. During contact with the TT&C ground station (Redu (Belgium) for Concept A and Kiruna for Concept B) the OBC transmits real-time telemetry and in case of safe mode the recorded telemetry through an S-band link. Nominally, for Concept B, recorded telemetry is transferred via the payload data X-band downlink as part of the global data stream. For Concept A, both real-time and recorded HKTMs are dumped through S-band link twice per day.

5.3.4.8 Electrical Power Subsystem

The Electrical Power Subsystem (EPS) architecture guarantees the availability of power and energy in all mission phases to all satellite subsystems and to the payload. The average power consumption is around 1000 W in nominal operation. This can be delivered by a classical EPS design which provides the following functionality:

- Generation of electrical power using a triple-junction GaAs solar array.
- Energy storage using lithium-ion batteries.
- Power regulation and distribution to all equipment through a maximum power point tracking power conditioning scheme handling the varying available solar energy over one orbit.

In Concept A, an internally redundant Power Conditioning and Distribution Unit (PCDU) distributes power from the solar array or the battery towards the platform and instrument units, and provides power and battery charge control. It distributes power lines protected by latching current limiters. Critical equipment (OBC and S-band transponder) is connected to automatically re-arming current limiters, ensuring power supply following one anomaly. The power bus is controlled by the battery voltage providing a non-regulated bus to the platform units. Power is generated by a four-wing solar array, one panel per wing, with total area of 8 m² populated with cells with 28% efficiency at Beginning of Life (BoL). The maximum power generated at EOL is 1700W. The battery will be used during eclipse, LEOP and contingency situations. It is based on two modules of Li-Ion stackable decks with a total capacity of 162 Ah, providing plenty of storage margin (heritage from Metop-SG batteries adapted to a 28 V power bus). The expected degradation during a 5 years mission is below 10%. In order to comply with the ESA guidelines on space debris mitigation a complete

passivation of the power subsystem will be exercised by a pair of electromechanical power relays in series (allowing a one failure tolerant design). Moreover, the activation of the passivation is executed in two steps: Arming and Firing.

The electrical power for Concept B is based on the use of a single articulated solar array for power generation and a single battery. The solar generator is based on a solar array wing driven by a SADM such that the Sun-incidence angle on the arrays is always kept optimal. The solar array is inclined with a cant angle of 30 degree to counteract effects of the beta angle. This is realised by connecting the solar array to the SADM by means of a yoke. In total the solar array has an array of 9.8 m², allowing to reuse the standard solar array design of the generic platform, with a fill rate of 78%. The power received from the solar generator is controlled by a maximum power point tracker on the power control unit (PCU). The PCU is responsible for charging the batteries. The loads are supplied via two distributed power distribution units (PDU) which provide the payload and platform subsystems with an unregulated 28V bus.

5.3.4.9 Telemetry, Tracking and Command

The TT&C subsystem provides S-band communication capabilities between the satellite and the ground segment. Two omnidirectional antennas ensure a communication link for all possible attitudes in nominal and non-nominal conditions. The subsystem provides the following functions:

- Command function for reception and demodulation of commands send from ground
- Telemetry function for modulation and transmission of real-time housekeeping
- Transmission of recorded housekeeping telemetry during LEOP and in safe mode
- Ranging and rate functionality for satellite orbit determination in LEOP, Safe mode and in case of GNSS failure.

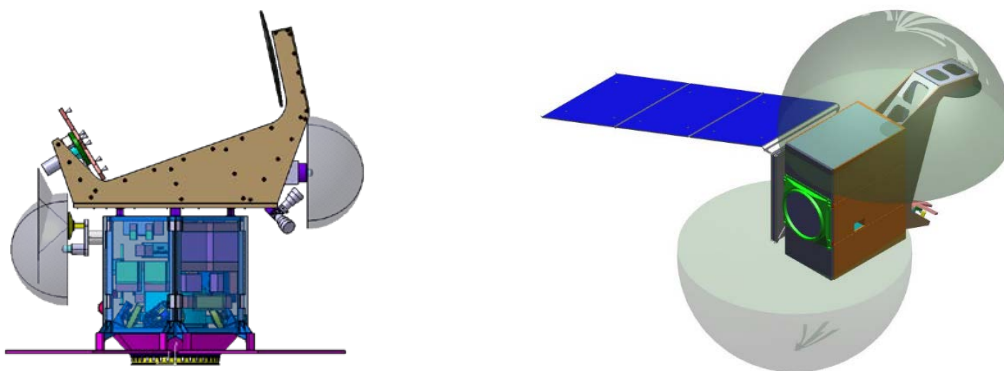


Figure 5.50. S-band antenna FoV for Concept A (left) and Concept B (right). In Concept A the GNSS and S-band antennas are mounted on the back of the SKaR antenna.

SKIM uses a flight-proven heritage S-band TT&C system, consisting of redundant transceivers and two S-band antennas each providing hemispherical coverage, thus allowing to establish communications with the SKIM spacecraft in each mission phase, from LEOP to End of Life (EoL). The receiver acquires and tracks the uplink carrier demodulating the signal to extract the 64 kbps telecommand data. The transmitter accepts the coded telemetry



signal from the OBC and the internal ranging signal from its own receiver. The telemetry signal is modulated on the carrier either with a nominal data rate of 2 Mbps or 128 Kbps in low data rate mode. For transmission of the real-time HKTM the transmission chain will be activated when in view of the TT&C ground stations (Redu for Concept A and Kiruna for Concept B).

5.3.4.10 Attitude and Orbit Control Subsystem

SKIM is a three-axis stabilised spacecraft with an AOCS based on flight-proven units and existing AOCS software inherited from previous projects. Because SKIM is a Doppler mission that measures minute surface velocities compared to its own velocity, the AOCS system needs to deliver accurate pointing knowledge, at least over the timescales of interest. For this reason, the AOCS includes a high-performance fibre-optic gyro in both concepts. The AOCS system includes the following sensors:

- Startrackers (three heads)
- Coarse Sun sensors
- Magnetometers (three)
- High-precision gyro (one)
- GNSS

SKIM is also an altimeter and requires a state-of-art POD system to deliver on-ground knowledge of its radial position. Precise double-frequency GNSS receivers form the core of the navigation function and are combined with onboard orbit propagation.

Actuation is performed using:

- Four reaction wheels,
- Three magnetorquers
- Thrusters (four in Concept A and six in Concept B)

During nominal operations the attitude of the spacecraft is three-axis stabilised and controlled with reaction wheels, providing fine actuation and slew capability, supported by magnetorquers for momentum dumping. In Concept A, the spacecraft combines a nadir-pointing attitude with a yaw steering attitude law to maximise the solar power generation and minimise the Sun illumination of the instrument. Concept B maintains a nadir pointing without any yaw steering because solar generation is maximised through the canted and rotating solar array, as illustrated in Fig. 5.6.

SKIM AOCS provides three main modes that rely on extensive heritage from previous LEO missions:

- The Normal Mode (NM) is the observation nominal mode that implements the attitude law. During this three-axis stabilised mode, high precision attitude knowledge is provided using startrackers and gyro.
- The Acquisition and Safe Hold (ASH) mode is active after satellite separation from launcher or triggered after detection of a critical failure. It benefits from the good robustness of the B-dot magnetic control law.
- The Orbit Control Mode (OCM) uses the same sensors and actuators as NM, plus the thrusters that are used to perform the orbit correction whilst performing two-axis attitude control.



For both concepts, during safe mode the spacecraft rotates around the Sun vector with the solar arrays in a fixed position pointed towards the Sun. Attitude actuation is performed with the magnetorquers.

Equipment	Redundancy	Concept A			Concept B		
		ASH	NM	OCM	ASH	NM	OCM
Sun Sensors (CSS)	2 branches in hot redundancy				X		
GNSS receiver	2 units in cold redundancy		X	X	X	X	X
Startracker (STR)	2 electronics in cold redundancy + 3 optical heads in hot redundancy		X	X	X	X	X
Gyroscope (FOG)	One unit with 4 hot redund. channels		X	X		X	X
Magnetorquer (MTQ)	3 units internally redundant	X	X	X	X	X	X
Magnetometer (MAG)	2 units in cold redundancy	X			X	X	X
Propulsion System	4×1N thrusters (A), 6×1N thrusters (B)			X			X
Reaction wheels (RW)	4 units in hot redundancy	X	X	X		X	X

Table 5.6. AOCS equipment Vs AOCS modes

5.3.4.11 GNSS and Time Distribution

The spacecraft includes two GNSS receivers that support the reception of Galileo and GPS signals and used for orbit determination. The OBC uses the GNSS signal to generate the onboard time reference. The GNSS receiver outputs a one pulse-per-second (PPS) timing signal, synchronised with the GNSS time, together with the Position-Velocity-Time (PVT) solution is has calculated. This enables the software to synchronize the Onboard Time (OBT) with the GNSS time. The OBC also provides a synchronisation signal to the CEU to synchronise the instrument internal clock. The navigation solution together with the AOCS-fused quaternions from startrackers and gyro telemetry, the onboard attitude estimation, and the quaternions measured by each sensor will be transmitted to the instrument to be part of the science ancillary data. To get the most accurate positioning performance, the GNSS antennas must be mounted so that they are free from multipath. In the case of Concept A this requires the antennas to be mounted on the back of the SKaR antenna as shown in Fig. 5.50.

5.3.4.12 Propulsion

The propulsion subsystem provides the delta-V orbital manoeuvring capability to perform:

- Launch error correction at BoL
- Initial orbit acquisition with loose formation flight with MetOp-SG(1B)
- Orbit and formation flight maintenance
- Collision avoidance
- EoL manoeuvre

For both concepts, heritage equipment and standard architectures are used for the propulsion subsystem, including hydrazine systems that are pressurised with helium and operate in blow-down mode. The typical components of the propulsion subsystem are:

- A single pressurised hydrazine tank with circa 80 kg capacity for Concept A and 170 kg capacity for Concept B
- Four (Concept A) and six (Concept B) 1 N thrusters (BoL), using two flow control valves in series in order to limit any hydrazine leak risk
- Two latching valves in parallel, one filter and two fill and drain valves
- One pressure transducer

The propulsion subsystem is a stand-alone module which can be easily integrated on the bottom panel of the platform. For Concept A, due to the spacecraft flight configuration transversal to the orbital plane, a slew manoeuvre is necessary to re-orient the spacecraft before performing any in-plane manoeuvre. For Concept B, the thrust vector is already aligned with the velocity vector allowing semi major axis rising manoeuvre without any major attitude modifications.

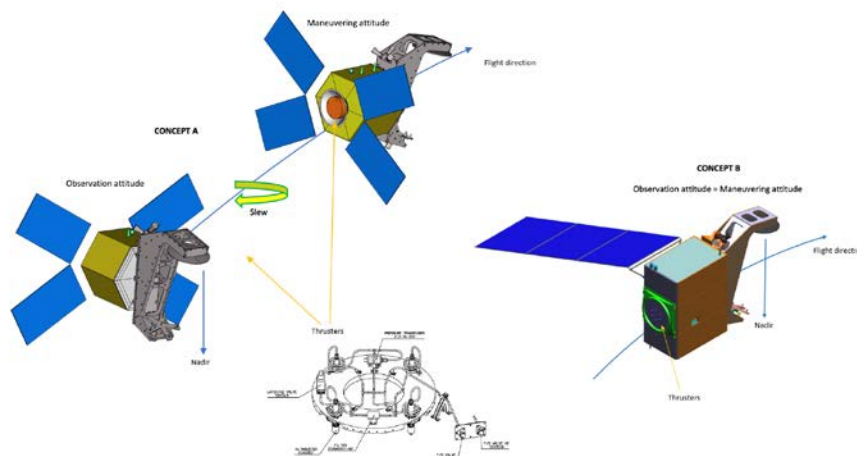


Figure 5.51. SKIM Concept A manoeuvring attitude (left) with thrusters accommodation zoom (centre) and Concept B manoeuvring attitude (right)

5.3.4.13 Software

Nominal operations of the satellite are highly autonomous thanks to the onboard software design. The broad range of functionalities within the scope of satellite onboard flight software and the typical functions addressed by the software include the following non-exhaustive list:

- Maintain TM/TC link to ground stations and other spacecrafts
- Data acquisition from sensors (Sun sensor, Earth sensor, magnetometer, startracker, gyroscope etc.)
- Data reporting
- Attitude and orbit control algorithms
- Commanding of actuators (reaction wheel, thruster, magnetorquer etc.)
- Temperature acquisition and heater control
- Health status acquisition and determination
- Evaluation of health status, failure detection and execution of corrective actions (FDIR)
- Operation of scientific payload devices



The Central Software will be based largely on heritage from previous ESA-developed missions (e.g. Copernicus Sentinel-5P, CHEOPS and SEOSAT in the case of Concept A) with the needed adaptations required by the SKIM Mission. The CDHS supports the implementation of application software and manages the packet services (PUS) which are independent from the OBC hardware. The control software for SKaR will interface with the CEU in the SKaR instrument, which has a PUS compliant command and control interface. The master timeline is managed by platform software.

5.3.5 System budgets

5.3.5.1 Mass budgets

Table 5.7 reports the mass budgets for the various cases studied and includes the following margins:

- Harness: 30%
- New units/equipment: 20 %
- Modified units/equipment: 10 %
- Recurrent units/equipment: 5 %

An additional 15% margin at system level has been applied against unpredictable mass evolutions and/or balancing needs.

Both concepts rely on standard platform solutions to reduce costs. Since the subsystems are not tailored to the mission, they are in some cases oversized with respect to the mission needs. This explains some of the differences found in the mass budgets between the two concepts.

Subsystem	Concept A	Concept B
Data Handling [kg]	18	29
Electrical Power Subsystem [kg]	64	122
Harness [kg]	96	65
X-band comm Subsystem [kg]	19	36
S-band comm Subsystem [kg]	7	7
AOCS [kg]	71	92
Structure [kg]	306	205
Thermal Subsystem [kg]	19	26
Propulsion [kg]	32	26
Platform Total [kg]	632	608
Payload Total [kg]	173	163
Dry Mass Total [kg]	804	771
System mass margin (15%) [kg]	121	116
Dry Mass with margin [kg]	925	887
Propellant [kg]	81	78 (130)*



Wet Mass [kg]	1006	965 (1016)*
Launcher performance [kg]	2020	2020
Launcher adapter [kg]	510	510
Launch margin (mass available for secondary passenger) [kg]	504	545 (494)*
Launch margin w.r.t. LV performance [%]	25%	27% (25%)*
* Values in brackets refer to Concept B satellite with full tank (177 l of N2H4 with 3:4 filling ratio)		

Table 5.7. SKIM mass budget for Concept A and Concept B

5.3.5.2 Power Budget

Table 5.8 reports the total power budgets for the two concepts, for the various operational modes. The budget includes the following margins:

- Harness electrical losses: 30%
- New units/equipment: 20 %
- Modified units/equipment: 10 %
- Recurrent units/equipment: 5 %

An additional 15% margin at system level has been applied to account for unpredictable power evolutions.

Operating Mode	Concept A	Concept B
Safe Mode	269	503
Orbit Control Mode	412	712
Observation	952	1182
Observation and Downlink	1104	1330
Observation in eclipse	952	1228
Observation and Downlink in eclipse	1104	1376
Nominal (orbit average)	975	1202

Table 5.8. SKIM Power Budget for Concept A and Concept B.

5.3.5.3 Delta-V and Propellant Budgets

The delta-V increments required for the two concepts are in Table 5.9.

Delta-v	Concept A	Concept B
Orbit injection correction and formation acquisition [m s ⁻¹]	26.4	24.4
Orbit maintenance [m s ⁻¹]	46.1	45.4
Collision avoidance [m s ⁻¹]	2.1	4.6
Deorbit manoeuvre [m s ⁻¹]	85.6	66.8
Total [m s ⁻¹]	160.2	141.2
Propellant mass incl. residuals [kg]	67.6	67.5

Total (incl. 15% margin) [kg]	78	78
Tank capacity [kg]	82.2	130
Propellant Margin [kg]	4.5	52
Propellant Margin (in excess of 15% system margin) [%]	5%	40%

Table 5.9. SKIM delta-V budget for Concept A and Concept B.

5.3.5.4 Data Rate and Volume

As explained in Section 5.3.3.7, the instrument produces the data streams listed in Table 5.10, with different data rates and duty cycles, which add up to a mean data acquisition rate of 166 Gbit/orbit. For both concepts, the payload data handling and transmission subsystem can handle the mean data acquisition rate. The data acquisition rate will be higher during some orbits, which is accommodated easily by the oversized mass memory. As shown in Section 5.3.4.7, with a realistic acquisition scenario based on a mask, all data will be transmitted to ground with a latency that always remains under 10 hours. The input parameters for the data volume analysis and the margin with respect to mass memory size are shown in Table 5.11.

Data Stream	Data rate (Mbit s ⁻¹)	Duty cycle (min/orbit)	Acquisition data rate (Gbit/orbit)
RAW	1275	1	76.5
OBP	18.1	72.1	78.3
DKP	2.6	72.1	11.2
TOTAL			166

Table 5.10. SKIM mean data acquisition rate per orbit.

Data rate and volume	Concept A	Concept B
Acquisition data rate [Gbit/orbit]	166	
Downlink rate [Mbit s ⁻¹]	352	320
Downlink capacity [Gbit/orbit]	230	201
Mass Memory size EOL [GB]	2000	1000
Margin w.r.t. Mass Memory Capability [%]	> 95 %	92%

Table 5.11. SKIM data rate and volume budget for Concept A and Concept B.

5.3.5.5 Pointing Budgets

Pointing budgets are reported in Chapter 6.

5.4 Launcher

The baseline launcher is Vega-C. As the introduction of Vega-C is foreseen in 2020, it can safely be assumed the launcher will be available for the nominal SKIM launch date in 2025. Vega-C is able to inject more than 2000 kg into a Sun-synchronous orbit at 817.5 km, which is the altitude of interest for the SKIM mission (MetOp-SG(1B) orbit). This is twice the

currently estimated spacecraft mass. Therefore, SKIM is compatible with a dual-launch scenario. For Vega-C the VESPA-C (Vega Secondary Payload Adapter) dual-launch adapter will be available in short and long versions. The baseline considered is a dual launch with the short version VESPA-C, with SKIM in the upper position Fig. 5.52). The mass of this launch adapter is 390 kg and it can cope with a mass up to 1500 kg (for a centre of gravity at 1500 mm), which exceeds the spacecraft mass with a comfortable margin. The Vega-C payload adapter (937 mm interface) weighs around 120 kg and can withstand a mass larger than 2000 kg. The mechanical design of the SKIM satellite will ensure compliance with the environment specified in the Vega-C user manual.

The backup launcher recommended by industry is Ariane 62, which will replace Arianespace Soyuz in the 2025 timeframe. It represents a European backup that comfortably envelopes the size and performance of Vega-C providing equivalent or even improved dual launch capability. Furthermore, the selection of a Kourou-based alternative adheres to the ESA launch policy and offers the benefit that launch range requirements, procedures and safety requirements are broadly similar to those of the nominal option. A first assessment has confirmed the compatibility of the mechanical design with the backup launcher.



Figure 5.52. Accommodation of SKIM in the Vega-C fairing on top of short VESPA-C, Concept A (left) and Concept B (right).

Elements	Mass Concept A (kg)	Mass Concept B (kg)
Spacecraft	1006	965
Vespa-c (short)	390	390
PLA 937	120	120
Total	1516	1475
Launcher performance	2020	2020
MARGIN (mass available for secondary passenger)	504 (25%)	545 (27%)

Table 5.12. SKIM launch solution mass budget



5.5 Ground Segment and Data Processing

5.5.1 Overview of Ground Segment

The current generation of Earth Explorer ground segments uses generic components configured or adapted to each mission. Following this approach, the SKIM ground segment consists of two main components, the Flight Operation Segment (FOS) and the Payload Data Ground Segment (PDGS).

The FOS includes the TT&C ground station and the Flight Operations Control Centre (FOCC). The TT&C ground station provides the following main functions:

- HKTM data acquisition
- Telecommand uplink
- Satellite tracking
- Data link with FOCC.

The FOCC is based at ESA–ESOC and will provide the following main functions:

- Satellite monitoring and control
- Flight dynamics and manoeuvre planning
- TT&C ground station network control
- Satellite operations planning
- Onboard software maintenance
- Spacecraft system data distribution
- Mission simulation
- FOS supervision.

During LEOP a dedicated ground station network provides the extended coverage needed to support operations. This network uses Estrack core and enhanced stations where possible.

The PDGS is mainly responsible for the reception of the science data from the satellite, the application of the processing algorithms and the delivery of data products to the users. It includes the following functions:

- Payload data acquisition (X-band ground station)
- Processing
- Archiving
- Data dissemination
- Payload operations planning
- Data quality control
- Calibration and validation
- User services
- PDGS supervision.

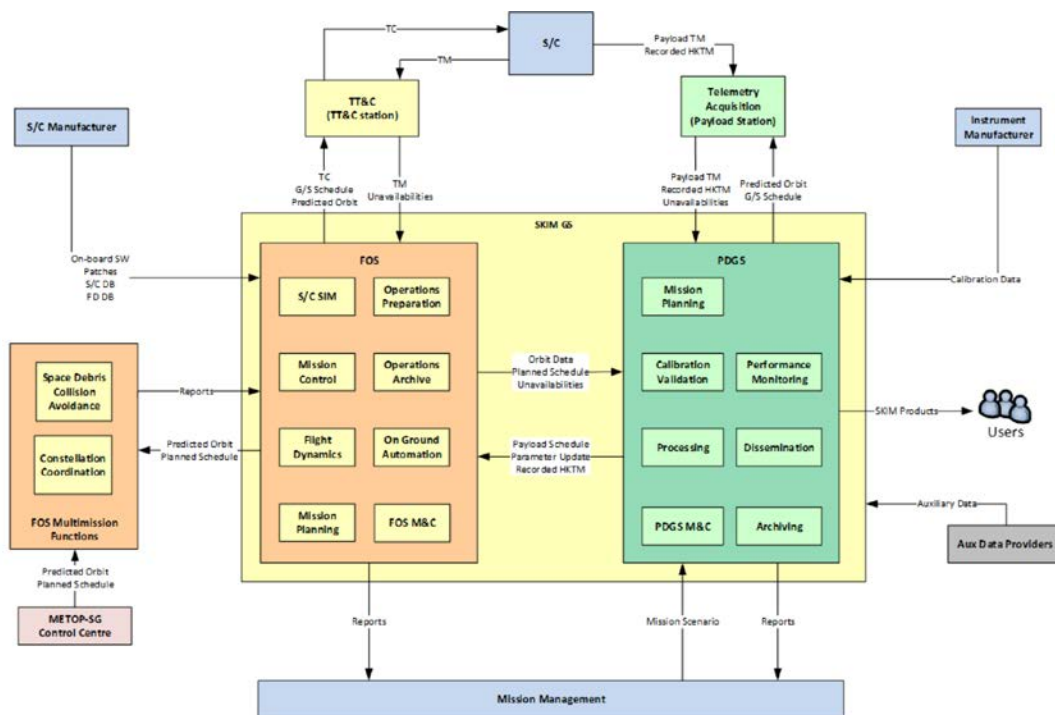


Figure 5.53. FOS and PDGS architecture (Concept B).

FOS and PDGS operations are as independent as possible. Data exchanged between these two elements are limited to mission planning requests, orbit data and for Concept B, recorded HKTMT received at the payload data ground station. Interfaces are based on existing formats and specifications supported by ESA infrastructure. In the case of SKIM PDGS, one of the user interfaces will be to the SKIM Algorithm Validation/Verification Investigation Environment (SAVVIE) described in Section 6.3. This is where onboard processing algorithms will be refined during the mission lifetime. If updates to the onboard processing are required, these will be implemented by the spacecraft manufacturer and uploaded via the FOS.

5.5.2 Flight Operation Segment

The FOS is responsible for the operations control and monitoring of the spacecraft during all operational phases of the mission from launch to end of mission. Operations control and monitoring activities include housekeeping telemetry health and performance monitoring, telecommanding of all activities using both real time commanding and loading of on board command schedules for delayed command execution, orbit control, constellation monitoring and control, reaction to space debris conjunction warnings, on board software maintenance and mission planning. The FOS is based on existing ESA hardware and software adapted to the SKIM mission where necessary.

5.5.2.1 Telemetry, Tracking and Command

For TT&C communications, one to two S-band ground station contacts per day is proposed. The Svalbard (Concept B) or Redu (Concept A) stations have been identified as suitable TT&C ground station. No modification to the ground station equipment is needed to support SKIM. The TT&C ground stations are not dedicated to SKIM, but shared with other missions.



Station allocation planning – both TT&C and PDGS – is performed by Estrack Management and Scheduling System (EMS) in cooperation with the Mission Planning System (MPS). EMS also generates the detailed operation schedule executed by Estrack ground station monitoring and control systems.

The principal task of TT&C passes in routine operations is to uplink telecommands. Real-time HKTМ will also be acquired during these passes. If stored HKTМ is downlinked via X-band (Concept B), then the HKTМ is forwarded to the FOS for processing. Ground stations which offer combined S and X-band capabilities have been proposed to optimise the ground station usage.

5.5.2.2 Mission Control System

The Mission Control System (MCS) manages all flight operations of the spacecraft, including satellite monitoring and control. This includes both real-time activities during satellite TT&C contact with the station and deferred activities on recorded telemetry data. The MCS is based on the Earth Explorer MCS, which is an extension of SCOS-2000, or its successor EGOS-CC. For SKIM a certain degree of customisation of the system is likely to be necessary (no functional modifications have been identified) according to satellite design, ground interface specifications, the final operations concept, and the existing capabilities of the MCS at the start of the ground segment implementation. There is no need to coordinate the MCS with the MetOp-SG MCS.

5.5.2.3 Flight Dynamics

Flight dynamics is a service provided to the missions that delivers orbit information and event files to the various planning entities as well as the orbital predictions used by the ground stations. It also generates command sequences that are transferred to the MCS directly or via the MPS, i.e. manoeuvres. Flight dynamics receives spacecraft monitoring data, including GNSS tracking data, and –for emergency operations or during GNSS unavailability– ranging and Doppler tracking measurements performed by the ground stations. The FDS infrastructure is standard for Earth Observations missions and is foreseen to be reused for SKIM. Some customisation may be required, in particular for external interfaces, i.e. for the format of GNSS receiver data or satellite telecommands for orbit manoeuvres. Information about the MetOp orbit is required in order to plan the orbit and formation flying manoeuvres. This is gathered by the SKIM FDS. The monitoring of the loose formation flying with MetOp-SG(1B) can be performed by the Constellation Coordination System (ESA-CCS). The ESA-CCS is a multi-mission infrastructure software, enabling information exchange between geographically distributed Mission Operations Centres. It acts as the central source of data sharing and planning visualisation. Finally, the FDS implements Space Debris Collision Avoidance manoeuvres proposed by the Space Debris Office.

5.5.2.4 Mission Planning System

The mission planning system is used and tailored for any kind of mission operated by ESA–ESOC including the Earth observation missions. It generates conflict-free schedules for the automated pass activities of the MCS as well as command sequences for loading to the satellite. The MPS will also be used to schedule the onboard payload activities based on input from the PDGS. The MPS will require configuration of mission-specific rules and



constraints. As for the MCS, some functional modification may be needed but the need for any specific modifications cannot be identified at this stage.

5.5.2.5 Flight Operation Segment Operational Approach and Implementation

The operational approach, during routine phases, is autonomous as far as possible to reduce the required manpower. The FOS is nominally operated during working hours, five days per week. In case of critical events outside working hours, the on-call engineer is alerted. Serious failures should, in principle, be excluded thanks to the spacecraft autonomy. During the launch and early orbit phase (LEOP), operations are supported by a dedicated ground station network. This uses Estrack core (i.e. Kiruna) and augmented stations (i.e. Svalbard or Troll) where possible. In general, the ground segment architecture is fixed and heavily based on the existing ESA hardware and software. Regardless of the operations model selected for nominal phase, the FOS development will still have to prepare for all reasonable eventualities. The design of the FOS is familiar in terms of the functional blocks to be used: the MCS, the automation system will execute control procedures and schedules, the flight dynamics software package will be used for orbit determination, prediction and control, and a simple mission planning system will be developed or re-used from an existing Earth Observation mission. Daily operations will be characterised by the heavy use of orbit-tagged telecommands. Thus, weekly FOS mission planning will be required, with no real time re-planning or out-of-hours support. The SKIM orbit is selected with a safe minimum distance with MetOp-SG(1B) (loose formation).

5.5.3 Payload Data Ground Segment

The current generation of Earth Explorer ground segments uses generic components configured or adapted to each mission. Data delivery to end users is required to occur within 24 hours from the time of sensing. The main driver for the PDGS design is the large data volume generated by the payload instrument. This requires download at every orbit to minimise onboard storage and downlink data rate.

5.5.3.1 Ground Stations

Science data will be downlinked (together with recorded HKTMs in the case of Concept B) using the X-band link. Concept A considers two ground stations in Kiruna and Maspalomas, while Concept B considers only a single ground station in Svalbard. These ground stations were selected to maximise overall contact time of the passes and for the ability to plan downlinks at every orbit to cope with the large data volume generated by the instrument.

5.5.3.2 Processing

The PDGS will process raw science data up to Level-1b and distribute it to the user segment using a data-driven approach. Processing starts when raw data becomes available and automatically generates data products that are archived and distributed to users. The expected data volumes require a downlink at every orbit. The processing up to Level-1b is discussed in more detail in Section 5.5.4.

5.5.3.3 Archiving and Reprocessing

The PDGS will systematically generate and archive Level-0, Level-1a and Level-1b products. The amount of data generated over the duration of the mission is estimated to be significant, as stated in table below. Reprocessing of limited datasets is expected to be managed by the



main processing chain without impacting the nominal processing. Systematic reprocessing of past data following updates in the ground processing chain require computing resources over a limited time and the current trend is to rely on reprocessing services shared with other missions.

Product type	Volume (TB for 5 years)
Level-0	7300
Level-1a	8100
Level-1b	8100

Table 5.13. Product data volumes for archiving.

5.5.3.4 Dissemination

The PDGS will systematically deliver all generated Level-1b data products to SKIM users. Access will be free and open following ESA's policy for Earth observation Level-1b data. Access to Level-0, Level-1a and calibration data products will be available for selected users, e.g. calibration and validation teams and instrument specialists. All data will be made available via the ESA generic Earth Observation data access infrastructure.

5.5.3.5 User Services

The user services support the search, access and visualisation of data products, as well as provide general mission status information and help desk. They are based on the multi-mission infrastructure for the distribution of data products to users.

5.5.3.6 Calibration/Validation Facilities

The main functions of the calibration and validation facilities are:

- Processing of in-flight calibration data and production of calibration reports, computed from the acquired data and embedded calibration information.
- Identification and characterisation of deviations extracted from the processing of in-flight calibration data for possible processing parameter updates or algorithm evolutions.
- Storage under configuration and control and verification of the calibration database.
- Support to calibration and validation teams with the provision of special calibration products and tools for data analysis and visualisation.

5.5.3.7 Instrument Performance Monitoring

This function is in charge of monitoring critical and other important parameters of the payload in order to identify failures, deviations or trends that may require corrective actions onboard or on the ground instrument processor. This function performs a systematic monitoring of data quality to ensure that products distributed to users meet a minimum level of quality. It is decomposed into several sub-functions:

- Systematic control of all generated products before distribution to users.
- Off-line tools for product analysis triggered by feedback from users.
- Report generation to present analysis results in readable format, which can be generated automatically based on time or event triggers.

5.5.3.8 Monitoring and Control

The monitoring and control function is responsible for the supervision of the PDGS operations in order to ensure that its performance and availability objectives are achieved.

5.5.4 Level-1 Data Processing

The SKIM instrument provides two kinds of L0 data products depending on the commanded mode:

1. LO_RAW Raw data, obtained from sampling and digitising the received waveforms
2. LO_OBP On Board Processed data including the following onboard data:
 - LO_NAL Range-Doppler maps of nadir beam (nadir altimetry waveform)
 - LO_RAR Incoherently averaged power waveforms (Range Aperture Radar waveforms)
 - LO_DD Range-Doppler maps of off-nadir beams (Delay Doppler waveforms)
 - LO_PP Coherently averaged correlated pulse-pairs (Pulse-pair waveforms)
 - LO_DKP An experimental product using the delta-K algorithm

In addition, the L0 data includes onboard calibration data to estimate:

- On board gain and group delay
- Relative gain of the off nadir beams
- Pulse-pair phase
- Instrument pointing error (including low-level AOCs data)

Figure 5.54 defines the sequence of on-ground processing to be applied, starting with the SKaR Instrument Source Packets (ISP). It also shows the extraction of calibration, ancillary or auxiliary data and the Calibration Long Term Monitoring (LTM) data issued from the Level 1A processing of the calibration data.

The main operations at L0 consist of filtering science & calibration data and rebuilding the time record.

The Level-1a processing operations include:

- pre-processing parameters for Level-1b:
 - instrument delay and gain
 - inversion of radar equation
 - pointing knowledge
 - coefficient for radial velocity
 - thermal noise
- Raw data operations
 - performing on-ground the equivalent of the onboard processing as explained in Section 5.3.3.6 and Fig. 5.26 in particular. The data becomes L1A_GP_xx.
 - Or prepare data without processing for the scientists in a L1A RAW product

At Level-1b, the processor produces products containing observation data in engineering units:

- Power detected, range selected, and multi-looked waveforms.
- Coherently averaged, correlated pulse-pair waveforms.
- Unfocussed SAR processed nadir beam: range power gates Doppler bins.

- Unfocused SAR processed off-nadir beam power gates and Doppler bins.
- Delta-K Dispersion relationship anomaly data.

Calibration and geo-location is applied at this level. Data is projected in ground range coordinates, assuming the WGS84 ellipsoid model for the Earth. Corresponding with the different L1a product streams (NAL/RAR/DD/PP/DKP), the processor will invoke different processing modules. An additional product, L1B_NGD provides an estimate for the non-geophysical Doppler velocity due to platform motion and non-ideal antenna patterns.

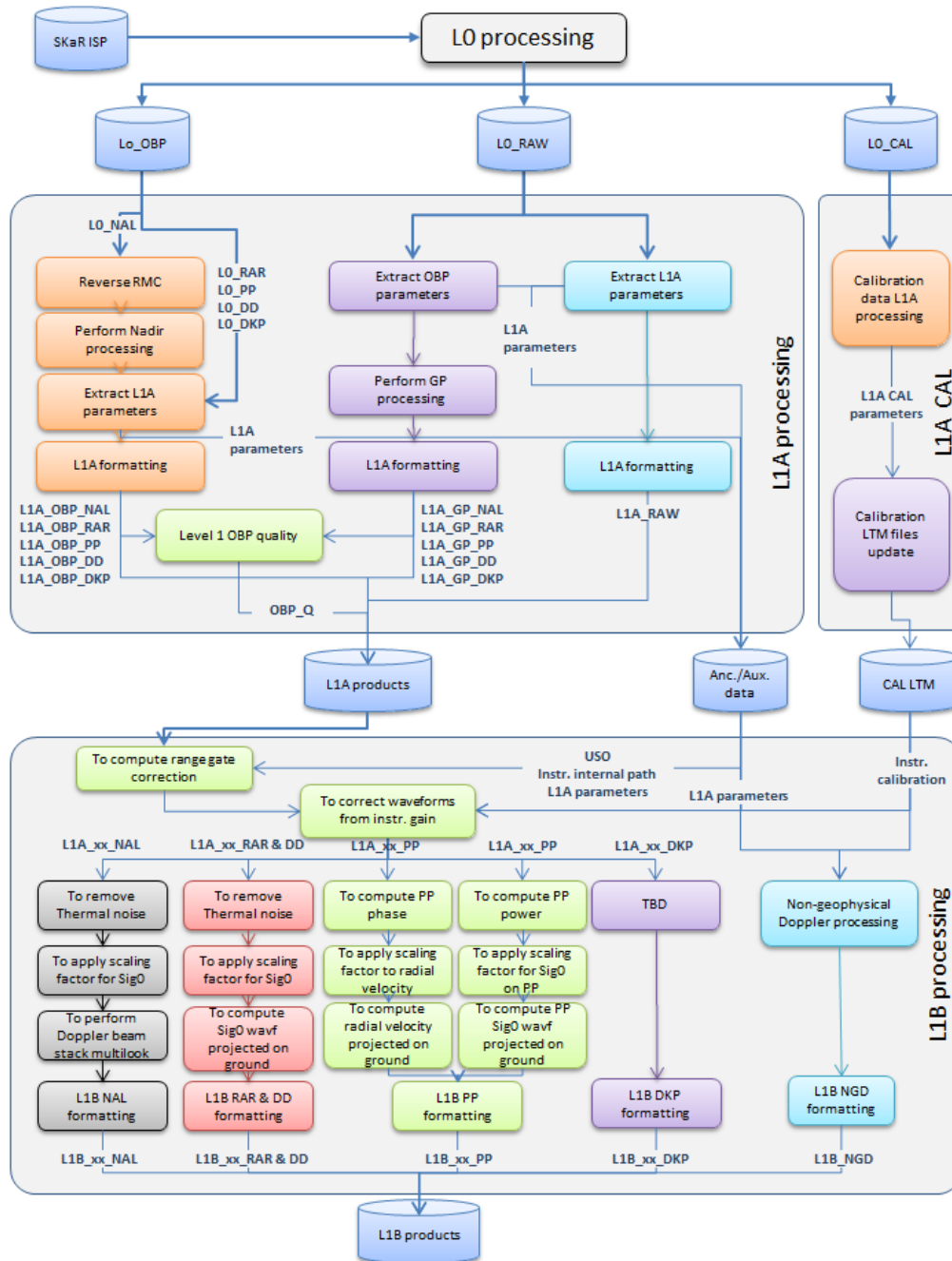


Figure 5.54. Level-1b data production in ground processing.

5.6 Operations, Utilisation and Disposal

5.6.1 Overview

The SKIM mission is divided into a number of different phases, as listed in Table 5.14. The operational aspects of each phase are described below.

Operational Phase	Duration
LEOP	~ 1 week
Commissioning Phase	≤6 months
Nominal Operational Phase	5 years (nominal) + 2 years (7 years considered to size consumables)
End-of-Life Phase (EOL)	≤2 months
Disposal	Within 25 years

Table 5.14. Mission phases and durations.

SKIM will perform observations over the oceans and inland seas larger than 50 km², defined by an imaging mask. Data is acquired on ascending and descending passes. This process allows for a high level of autonomy for both space and ground segment. The only specific external constraint of the mission is the need to fly in a coordinated orbit with MetOp-SG(1B).

5.6.2 Launch and Early Operations Phase (LEOP) and Commissioning

SKIM will be launched on a Vega-C launcher from Europe's Spaceport in Kourou, French Guiana. The LEOP covers the period from switch-over to internal power on the launch pad until the satellite is in its deployed configuration in orbit and the AOCS is operating in Normal Mode. The duration of the SKIM LEOP is estimated to be seven days.

After separation from the launcher, an autonomous initialisation sequence handles the Solar Arrays deployment, the AOCS initialisation and convergence and the S-band transponder switch-on. Ground intervention is only required if deployment fails. Upon completion of the sequence, S-band communications will be initiated and an initial satellite checkout will be completed to confirm success of the sequence. The next steps will take the satellite from the Initial Acquisition Mode to the Nominal Mode. After completion of a further checkout to confirm that the nominal attitude is being maintained, the launcher dispersion corrections will be completed. This phase also includes the SKaR antenna scan mechanism release, which will be performed during ground visibility to ensure proper monitoring of this critical activity. Once the platform key health status has been confirmed transition to next phase (commissioning) will occur. The acquisition of the SKIM – MetOp-SG(1B) loose formation is achieved with a phasing sequence, thus SKIM is launched into an initial phasing orbit 10 km below the MetOp-SG(1B) orbit. The launch time will be set in order to obtain a Local Time of Descending Node (LTDN) at 9h and 6 min for Concept A and 9h and 52min for Concept B. The resulting Right Ascension of the Ascending Node (RAAN) separation of ~6° from the MetOp-SG(1B) orbit, coupled with the 10 km difference in altitude, guarantee an extremely safe formation acquisition. Kiruna, Svalbard and Troll form the ground station



network supporting the LEOP operations, whose coverage allows the spacecraft to communicate with ground at any orbit.

The commissioning phase concerns both the platform and the payload and will last up to six months. This phase consists on the complete characterisation of the performance of the platform, payload and ground segment to verify that the system is ready for the transition into the routine operational phase and ensure the SKaR instrument is calibrated. The first part of the commissioning phase will be used to perform in-orbit functional and performance tests of all platform subsystems, including the payload data handling subsystem. For most subsystems this will take about a week although some trend analysis will be performed over the first few months in flight. Upon completion of the platform commissioning activities, the spacecraft will be in the operational orbit and attitude with the AOCS in Nominal Mode. At this point, commissioning of the SKaR instrument can begin. During the payload commissioning phase, the instrument functionality will be exercised over its full operational range with respect to all modes. For each state, HKTM and product annotations will be monitored to verify that the instrument responds correctly to the command. Level-0 products obtained in all the operational states of the instrument will be verified by monitoring a range of parameters and comparing them with expected values. External calibration of the instrument using calibration sites will be performed and the system will be verified end-to-end. Finally the validation of whole data chain, including ground processors and dissemination of science data will occur.

5.6.3 Nominal Operations

After a successful commissioning phase, SKIM will start nominal operational activities to provide data to the science community for a period of nominally 5 years. In this phase SKIM will be operated mainly via scheduled commands planned and uplinked onboard by the FOS to perform instrument observations, onboard data management, data downlink and orbit maintenance. This schedule will be uploaded typically once every five to seven days. Since the ground track repeats every 29 days, the Mission Planning Facility (MPF) generates an observation plan which is repeatable over this duration. In addition, regular payload calibration operations will be planned as part of the mission planning. Calibration and orbit control manoeuvres will take place over land, at orbital points outside the area of interest for observations. In-Plane manoeuvres are executed over the North Pole to correct orbital altitude and eccentricity and Out-of-Plane manoeuvres at the equator to correct orbital inclination. No formation flying control manoeuvres are necessary for SKIM, because the normal ground track manoeuvres are sufficient to maintain a suitable relative phasing with MetOp-SG(1B). Finally, SKIM is designed to carry consumable for a nominal lifetime of 7 years, to allow for possible mission extensions.

5.6.4 International Telecommunications Union (ITU) Constraints

The development of SKIM system will be compliant with the ITU Radio-Regulations (RR), and no significant issues have been identified.

Concerning the SKIM SAR altimeter, it operates in the band 35.5-36 GHz, which is allocated on a primary basis to the active Earth Exploration Satellite Service (EESS (active)), and is shared with the meteorological aids and radiolocation (i.e. radar systems) services. In addition, this is also a primary allocation for the terrestrial fixed and mobile services in some



African and Asian countries. The RR provide limits to the maximum mean power-flux-density produced by the sensor at the Earth surface. It is noted that radar systems operate in the range 33.4-36 GHz, and some of these may use peak transmit power in the order of kW (Technical characteristics of these systems are provided in Rec. ITU-R M.1640-1). Therefore, the SKIM radar instrument will be able to withstand such very strong emissions.

Concerning TT&C and data download, the design is compliant with the list of ESA approved standards. The proposed approach to use S-band for TTC and X-band for data download is similar to most ESA Earth observation missions, in terms of data rates and modulation schemes.

Concerning the loose formation with MetOp-SG(1B), care must be taken to avoid mutual interference. For TT&C operations in S-band, either frequency diversity and/or operational coordination are required to avoid interference. As baseline, SKIM will use different up and downlink TT&C carrier frequencies to MetOp-SG(1B). The assignment of the specific S-band frequencies for ESA missions is done by the ESA Frequency Management Office, as part of the ITU frequency filing process. For data download in X-band, both missions are using different frequencies avoiding spectrum overlap so that there is no mutual interference and it is not necessary to coordinate between the receiving ground stations.

Finally, it has to be noted that SKIM radar instrument and MetOp-SG(1B) data downlink system are using different frequency bands: EESS(active) at 35.5-36 GHz, and EESS(space-to-Earth) at 25.5-27.0 GHz. Therefore there is no interference problem between both systems.

5.6.5 Contingency Operations

The FDIR strategy will be based on a similar categorisation of the onboard failures into four of five levels, depending on the Industrial contractor. Each of the failure levels has a specific detection mechanism and resolution. Levels are defined along the following criteria (example from Concept B):

- Level 0: failure at unit level, managed by the unit, and mission not impacted by the recovery actions.
- Level 1: failure at unit level, but the unit cannot autonomously recover. Managed by OBSW.
- Level 2: similar to level 1 but not confined to single subsystem.
- Level 3: failures internal to OBC that cannot be neutralised autonomously by the OBSW. Recovery by hardware via the reconfiguration module inside the OBC.
- Level 4: failures not detected and recovered at lower levels. Managed completely by hardware through hardwired system alarms. Satellite transition to safe/survival mode.

A fundamental aspect of an FDIR approach is that survival of the satellite has priority over availability during all phases of the mission lifetime of the satellite. All FDIR functions implemented in the Onboard Software are triggered by parameter values stored in the satellite. These functions can be enabled or disabled via TC from ground and may be adapted and set according to the operational needs. A history log stores any FDIR data for investigation on ground. The ground station has the final overall control over all failure recovery activities even if the satellite performs them autonomously.



5.6.6 Disposal

An orbit decay and subsequent re-entry within 25 years has to be guaranteed to comply with space debris mitigation requirements. Uncontrolled re-entry is permissible as long as a maximum casualty risk of 10^{-4} is achieved. For both Concepts, the SKIM satellite design marginally complies with this casualty risk. Therefore, both concepts assume an uncontrolled re-entry. With an assumed launch date in 2025 and duration of seven years for the nominal operational phase, this is achieved with lowering the perigee of the orbit to an altitude of 565 km (Concept B) and close to 500 km (Concept A), which guarantees safe uncontrolled decay within 25 years (See Fig. 5.55).

For both concepts, a simulation has been performed to assess the casualty risk of the SKIM satellite re-entry. In line with ESA guidelines, a filtering criterion based on the kinetic energy at impact is applied to identify surviving elements. The simulation accounts for 100% of the total mass, with more than 60 unique elements modelled as boxes, cylinders and spheres, each composed of a single material characterised by density, melting point, specific heat capacity, heat of fusion and emissivity. Assuming an uncontrolled re-entry around year 2057 (25 years after SKIM decommissioning), about a dozen of components made of titanium and stainless steel survive re-entry and fall back to Earth’s surface. The uncontrolled re-entry approach has been accepted by the relevant ESA authorities with the recommendation of refining the analysis in the next study phase and, if necessary, study and implement some ‘design for demise’ risk mitigation measures to restore comfortable margins to the casualty risk of an uncontrolled re-entry. Improvements in the spacecraft design to include demise features and improvements of the re-entry model accuracy used for the analysis are expected to contribute to the confirmation of the compliance.

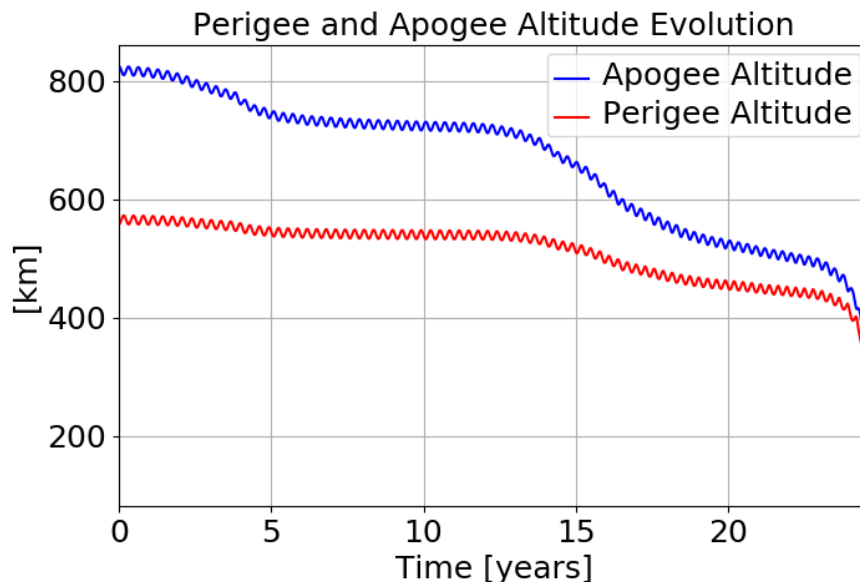


Figure 5.55. Perigee and apogee altitude evolution for SKIM EoL disposal for uncontrolled re-entry (Concept B).



6 SCIENTIFIC DATA PROCESSING AND VALIDATION CONCEPT

A Doppler measurement is the most appropriate approach to directly measure dynamic motion of the ocean surface from which a number of geophysical properties can be retrieved. These primarily include the ocean Total Surface Current Velocity (TSCV), Stokes drift, sea-ice drift, and the directional wave spectrum, $E(k, \theta)$. To this end, the SKIM Ka-band Radar (SKaR) implements the following fundamental measurement techniques:

5. **Pulse-pair measurements** (phase-difference) to directly measure the Doppler centroid associated to the Line-of-Sight (LoS) velocity for a number of off-nadir beams at different azimuth and elevation angles.
6. **Spectral analysis of the wave-related modulation of Normalised Radar Cross-Section (NRCS)** of the sea-surface using rotating off-nadir beams to provide directional ocean wave spectra.
7. **Nadir along-track altimetry capability** (unfocussed synthetic aperture radar) to estimate sea-surface height (SSH) and significant-wave height (H_s).
8. A proof of concept of a **Delta-K time-analysis** (wave-front matching dispersion) to provide a measurement of velocity that is more selective of the contributing waves, and closer to the principle of coastal HF-radars.

The SKaR instrument and related on board processing is fully described in Chapter 5. This Chapter provides an overview of the data processing algorithms used to retrieve geophysical parameters from the SKIM satellite payload, the SKIM Ka-band radar, SKaR.

6.1 SKIM Geophysical Retrieval Framework

The joint measurement of the Total Surface Current Velocity (TSCV) U_{CD} , Stokes drift, U_s , and associated wave directional spectrum, $E(k, \theta)$, defines the SKIM measurement concept. The SKIM instrument (SKaR) is a Ka-band radar, a satellite Doppler Wave and Current Scatterometer. SKIM proposes a unique approach for measuring the TSCV that extends the established grazing-angle technique used by ground-based High-Frequency (HF)-radars (e.g. Kim et al., 2018) to a moving satellite platform, operating at very high microwave frequency with a low elevation beam geometry.

The satellite platform motion relative to Earth, projected to the effective antenna pointing direction, is responsible of an additional Doppler shift called non-geophysical Doppler U_{NG} . This must be estimated and removed to obtain the radial geophysical Doppler in azimuth φ , $U_{GD}(\varphi)$, or $U_{GD,R}$ when the value of φ is well known.

Comparable to a HF-radar (using ground waves at 3–40 MHz), the SKIM Doppler velocity integrates all motion fluctuations over a finite footprint of ~9 km diameter (one-way antenna pattern at -3dB), and therefore must be decomposed as the sum of the intrinsic wave-Doppler velocity $U_{WD}(\varphi)$ and a current Doppler signal $U_{CD}(\varphi)$, associated with the TSCV (e.g. Stewart and Joy, 1974; Ardhuin et al., 2009).

The footprint-averaged geophysical Doppler $U_{GD}(\varphi)$ when looking in azimuth φ is



$$U_{GD}(\varphi) = U_{CD}(\varphi) + U_{WD}(\varphi) = U_{AL} \cdot \cos \varphi + U_{AC} \cdot \sin \varphi + U_{WD}(\varphi) \quad (6.1)$$

where $U_{CD}(\varphi)$ is the projection of the current vector in the across-track and along-track direction (U_{AC}, U_{AL}) in the azimuth of the radar.

For a satellite Doppler wave current scatterometer the wave Doppler component in the azimuth direction, $U_{WD}(\varphi)$ is a function of the sea state and of the radar properties (Mouche et al., 2008), as experimentally analysed (Yurovsky et al., 2019). At the incident angles used by SKIM, $U_{WD}(\varphi)$ is largely dominated by local short-wind waves, which results in a strong correlation with $U_{10,R}$, the wind speed at 10 m above the sea surface, projected in the radial direction.

The key to retrieving TSCV using SKIM SKaR is to combine all available measurements and retrieve the directional ocean-surface properties that are associated to very short surface-wind ruffled scales. To this end, the main algorithm processing steps are:

- Estimate the footprint-averaged radial Geophysical Doppler component in azimuth φ , $U_{GD}(\varphi)$ for all off-nadir beams at different angles. The non-geophysical Doppler, U_{NG} signal associated with the relative movement of the satellite platform the rotating Earth is removed from the Level-1b coherently averaged, correlated pulse pair waveforms. These data form the Level-2a L2A_UGD product.
- Retrieve the 1D surface wave directional elevation spectrum $E(k, \varphi)$ from the off-nadir beam backscatter modulation spectrum using the Level-1b incoherently processed real aperture radar waveforms. These data form the Level-2b L2B_WDS product.
- Estimate the wave Doppler component U_{WD} , based on analysis and processing of Level-2b L2B_WDS data and separate this from $U_{GD}(\varphi)$. A data-driven fine-pointing algorithm is applied at this point. This generates radial current Doppler $U_{CD}(\varphi)$, for all off-nadir beams. Stokes drift $U_{S,R}$ is computed from an analysis of Level-2b L2B_WDS. These data form the Level-2b L2B_U product from which the TSCV can be computed. This satisfies SUN-16 in Table 2.6.
- The TSCV is then computed on a 5 x 5 km grid by compiling all Level-2b L2B_U within a 15 km radius of each grid cell centre. A Gaussian weighted least squares combination is used to compute the TSCV U_{CD} for each grid cell. In addition, Level-2b L2B_WDS data are combined to generate the wave directional spectrum, $E(k, \varphi)$ at a grid scale of 70 x 70 km. U_{CD} , $U_{S,R}$ and $E(k, \varphi)$ form the primary SKIM Level-2c product. This satisfies SUN-1, SUN-2, SUN-4, SUN-5, SUN-6, SUN-8, SUN-9 and SUN-17 in Table 2.6.
- Further processing to combine Level-2c products as geographically mapped Level-2d products can then be performed at a temporal resolution of 10-days to address the needs the oceanography, marine meteorology and climate communities as requested by SUN-9 and SUN-18 in Table 2.6.
- The SKIM nadir beam data are processed as a conventional synthetic aperture radar altimeter to provide estimates of the sea surface height, significant wave height, H_s , normalised radar cross section and wind speed. During the Land Monitoring Phase acquisitions over rivers and lakes will be possible. This satisfies SUN-7 and SUN-19 in Table 2.6.

These main steps are illustrated in the SKIM measurement approach summarised in Fig. 6.1.



Fig. 6.1a. Step 1: Doppler velocity and roughness modulation measurements are made at Level-1b radar footprints across the SKaR instrument swath with different angular and beam elevation diversity. (ESA/Planetary Visions)



Fig. 6.1b. Step 2: the 1D-radar reflectivity modulations are determined for each footprint, to provide directional spectral information, at Level-2b_WDS, and a 2D wave spectrum is retrieved at Level-2c by combining 1D spectra over a 70×70 km grid cell. (ESA/Planetary Visions)

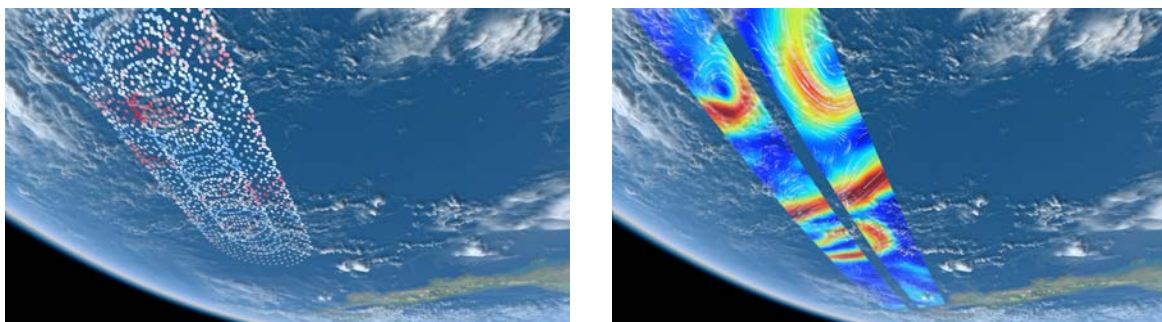


Fig. 6.1c. Step 3: the line-of-sight water velocity components are then retrieved at footprint scale (Level-2b_U) and the TSCV is retrieved at Level-2c by combining Level-2b_U data within a 15 km radius (grid-cell ≈30 km) using a Gaussian weighted least-squares approach and posted at 5 km. (ESA/Planetary Visions)

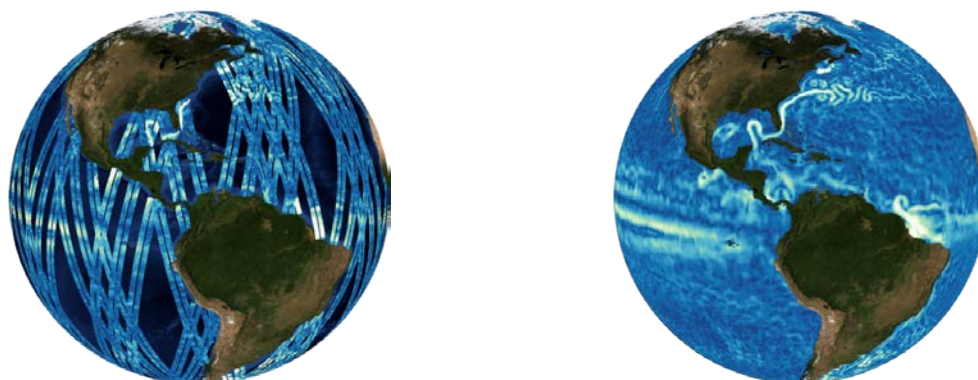


Fig. 6.1d. Step 4: Level-2c are mapped to a geographical grid on multi-temporal time scales of one to n days. Left 1-day Level-2c product, Right: 10-day Level-2d product. Simulated SKIM Level-2c and Level-2d products based on SKIM SKIMulator output (Gaultier, 2019)

The importance of azimuth sampling diversity

An important characteristic of the SKaR radar is azimuthal diversity. As for a satellite wind scatterometer, azimuthal diversity is required to retrieve both vector quantities and full directional wave-spectral properties. The link between the observation geometry of SKIM and the retrieval of TSCV is illustrated Fig. 6.2.

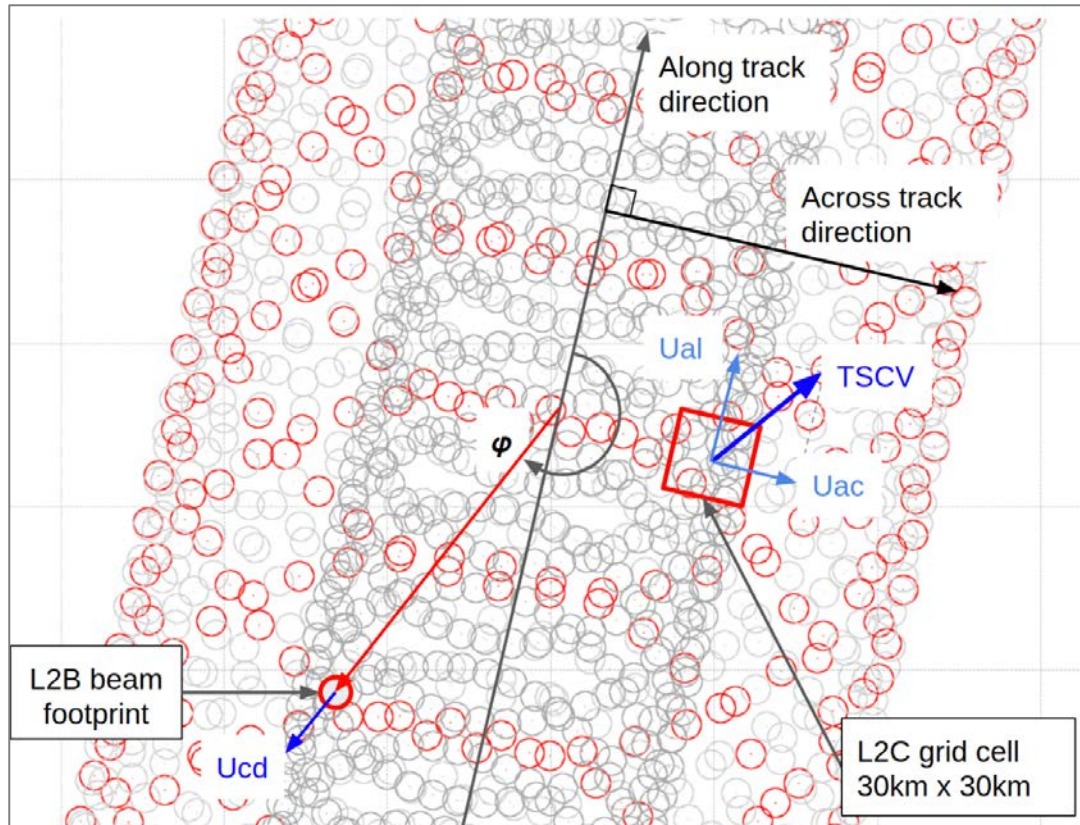


Figure 6.2. SKIM Level-2b and Level-2c product geometry and related components of surface current. Light grey circles indicate the location of 12° and dark grey circles the 6° beam footprint. Red circles indicate the beam location for one of the 12° beams. φ is the azimuth pointing line of sight direction relative to the along-track direction.

The typical coverage of SKaR footprints across the SKIM swath is shown Fig. 6.3, highlighting the associated cross-swath distribution of azimuthal sampling diversity. The number of footprints within a measurement cell, varies from 5 to 14 for 30 km cells. The impact of including both a 6° and 12° beam is clearly evident to maintain the density of measurement samples and azimuth diversity is clearly evident.

It is important to realise that at the very outer limit of the SKIM swath edge, only the cross-track vector component is measured using 12° elevation beams. At mid swath, both the 6° and 12° elevation beams are present. To construct the current vector, two non-aligned look directions are sufficient to determine the two cross-track and along-track components U_{AC} and U_{AL} , respectively. The uncertainty on each vector component is a function of the uncertainty on the radial U_{CD} measurement, amplified by a geometric dilution of precision that depends on the relative angle between each component and the azimuthal measurements (e.g. Kim et al., 2008, Rodriguez et al., 2018).

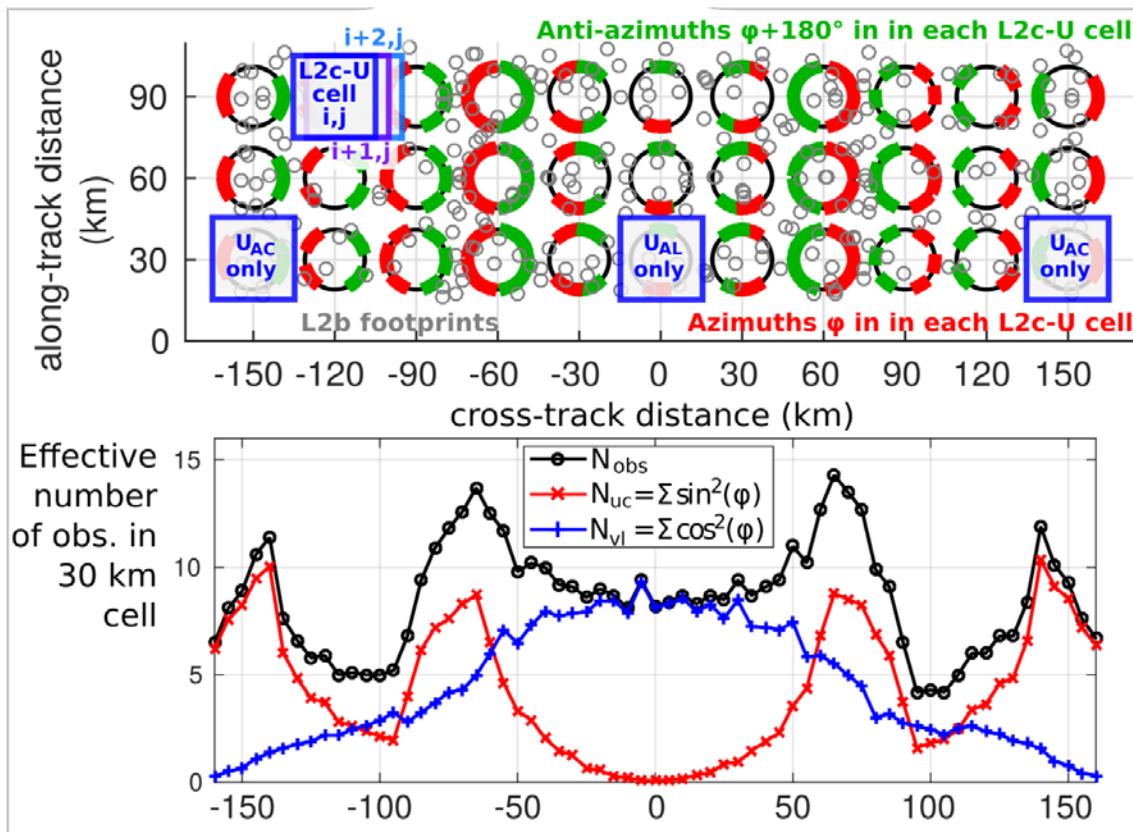


Figure 6.3. Top: directivity of measurements in 30×30 km cells across the SKaR swath that are combined to calculate a vector quantity. Between 5 and 15 measurements are available (depending on the position within the swath). Bottom: number of SKaR measurements and effective number of observations for the cross-track (red) and along-track (blue) vector components.

6.2 The SKIM Retrieval Algorithm

The SKIM algorithm is succinctly described in the flowchart of Fig. 6.4. It describes the end-to-end SKIM mission data processing approach, product levels and product relationships.

The starting point is Level-1b data (described in Chapter 4) that are generated by the Payload Data Ground Segment (PDGS) based on data from the SKIM Level-0 data processing system on board the satellite. Level-1b products include detailed engineering data related to the satellite position, velocity and time, high-resolution data from Attitude Orbit Control Sensors (AOCS) sensors, thermistor outputs from temperature sensors (notably positioned close to the SKaR antenna for thermo-elastic distortion compensation) and the position of the rotating antenna feed-plate amongst other parameters. Since the Doppler signal is extremely sensitive to mis-pointing these data are essential to generate the best pointing information possible before any fine-pointing data driven calibration is used. These data are complemented by knowledge of the antenna gain patterns around the azimuth.

Section 5.5.4 describes Level-1b processing in detail.

The specific retrieval algorithms are described in subsequent sections. Level-2 data product descriptions are provided in Chapter 4 Table 4.1 and Level-1 data product descriptions are provided in Chapter 4 Table 4.3

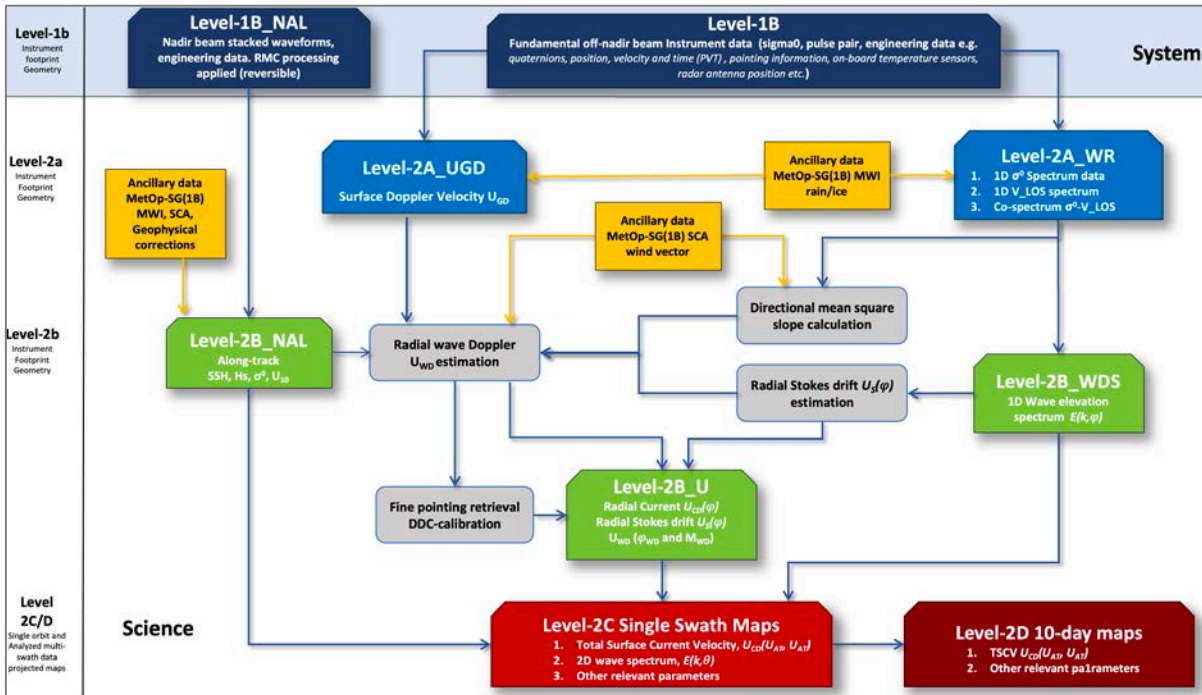


Figure 6.4. Overview of the SKIM Level-2 retrieval approach and science products.

6.2.1 Retrieving the Geophysical Doppler U_{GD} (Level-2a L2A_UGD Product)

6.2.1.1 Estimation and Correction of Non-Geophysical Doppler Velocity

The SKIM Level-2a L2A_UGD product contains the horizontal surface geophysical Doppler velocity, U_{GD} , and uncertainties for each SKIM off-axis beam computed in radar scan geometry. It is a required input to higher order processing.

The first processing step at Level-2a is to apply a non-geophysical Doppler correction to the Level-1b product and determine U_{GD} . Extracting a precise measurement of U_{GD} relies on:

- accurate measurement of V_{LoS} (function of φ , number of averaged pulse pairs, transmitted power)
- accurate estimation of the platform velocity vector V_p (rms error 0.5 cm s^{-1})
- accurate estimation of the solid Earth velocity vector V_E
- a very accurate determination of the radar pointing elevation, γ , and azimuth φ angles
- the knowledge of ocean topography, h , relative to the geoid, used for retrieving the elevation $\gamma(R)$ corresponding to each range gate, R , and projecting the V_{LoS} to the horizontal
- an estimation of the (large scale) azimuthal variation of the ocean normalized radar cross-section, σ^0 , backscatter to estimate the apparent mis-pointing, δ
- an estimation of the sub-footprint spatial variation of σ^0 (in range and azimuth) for flagging and/or refining the estimate of δ

A dedicated Level-1b L1B_NGD product contains all the system information available to make a first correction of the non-geophysical Doppler. An important reason why this

correction is not applied at Level-1b is because there are two geophysical effects (see Fig. 6.5) that interact with and alter the non-geophysical Doppler correction that need to be accounted for. These are:

- The effects of Sea Surface Height (SSH) gradients across the swath
- The effects from Normalised Radar Cross Section (NRCS) slopes in the footprint

Both effects are ignored at Level-1b, where an ellipsoid Earth and a uniform NRCS are assumed. This section explains how the processing step at Level-2a builds on the Level-1b processing by accounting for these effects. The following section explains fine pointing algorithms that are applied after separation of the wave Doppler from U_{GD} .

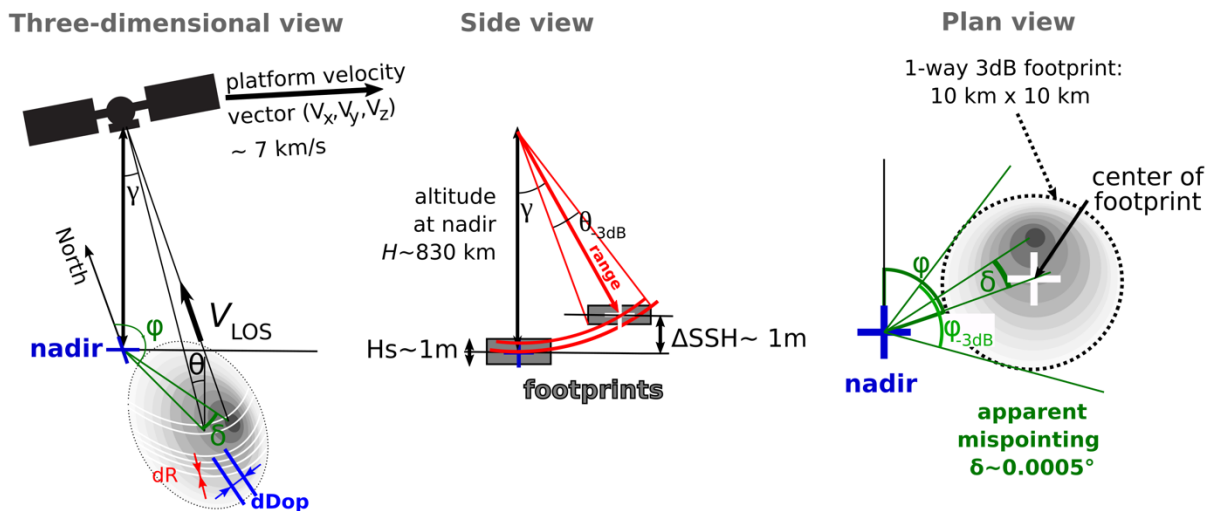


Figure 6.5. Geometry of the measurement: vertical range, horizontal range and incidence angle, and apparent azimuthal mis-pointing δ in the presence of NRCS gradients distorting the received gain pattern (grey shades). Note that for the SKIM near-nadir view, the azimuthal diversity φ_{3dB} in a footprint (exaggerated here) is much larger than the antenna beam width θ_{3dB} due to the projection on the Earth surface. (F. Ardhuin, LOPS)

Importantly, the incidence angle θ , is related to the elevation angle γ , and is obtained from the difference of range ΔR , between the ocean surface echoes at nadir and the oblique beams together with *a priori* knowledge of the difference in mean sea-surface height ΔSSH between the nadir and oblique beams. For the 12° and 6° beams a 4.8 cm and 1.2 cm error on the ΔSSH translates into an error on U_{GD} of up to 1 cm s^{-1} (LOPS, 2019).

It is planned to use the Copernicus Marine Environment Monitoring Service (CMEMS) Mean Sea Level Anomaly (MSLA) map at off-nadir locations, which is continually improved using the combined altimeter virtual-constellation measurements. Further improvements are anticipated from the SWOT mission measurements from early 2020 onwards. SKIM will take full advantage of these improvements. Tides, dynamic atmospheric corrections and geoid components will be added. Given the expected errors on SSH contributions (Table 6.2), the related Doppler error at 12° is expected to be $\leq 1 \text{ cm s}^{-1}$ for all SKIM azimuth and can be ignored. At 6° the error may be as large as 3 cm s^{-1} in along-track azimuth. At this point in the mission development this has not been studied in depth. Future development will refine the algorithm theoretical baseline document in this respect.

Source of error	12° beams	6° beams	Reference
MSLA	3.8	3.2	OSSE by Ballarotta et al. (2019)
barotropic tide	0.9	0.9	Stammer et al. (2014)
baroclinic tide	1	1	Carrere et al. (in prep)
DAC	2	2	Carrere and Lyard (2003)
geoid	1.5	1.5	Pujol et al. (2018)
RSS	4.74	4.28	

Table 6.2. Sources of errors and total root mean square error (cm) in SSH at off-nadir beam locations.

The other non-geophysical Doppler contribution is related to an apparent mis-pointing effect associated to azimuthal NRCS gradients. This effect is significant only for particular combinations of wind speed and direction, which need to be detected from the data. In practice, a local (for each Level-1b footprint) estimate of the wind vector from the MetOp-SG(1B) scatterometer (SCA) instrument will be used to compare radar measurements and expected values as a function of the SCA wind speed and direction. This information can be used to flag unfavourable conditions when the NRCS gradients would make the Doppler measurements unreliable. Flagged data will not be used for further processing. MetOp-SG(1B) SCA measurements are near contemporaneous (<150 s) and co-located with SKIM SKaR measurements. The nominal spatial resolution of MetOp-SG(1B) SCA is 25 km gridded cells although 12.5 km gridded products will be available. The geolocation accuracy is set at <1 km (1 σ , zero-mean, see Rostan et al., 2016). This allows SKaR data to be co-located precisely with SCA data to within ± 1 km worst case, which is more than adequate.

6.2.1.2 Fine Pointing Adjustment

Ocean-surface current speeds are in the range of a few cm s^{-1} to a few m s^{-1} , much smaller than a low Earth orbit satellite velocity (7 km s^{-1}) and the speed of Earth's rotation. Thus, the measured TSCV accuracy from Doppler radar backscatter data is very sensitive to the radar beam geometry because it is influenced by the projected spacecraft speed.

Maintaining accurate and precise knowledge of the SKaR radar antenna azimuth pointing is a particular challenge for the SKIM mission. Using current state-of-art technology and within realistic programmatic constraints of the mission, a coarse Level-1b non-geophysical Doppler correction can achieve a performance commensurate with the pointing calibration at Level-1b, i.e. in the order of 10 arcsecond (see Chapter 5). Elevation knowledge, which is of particular importance in the along-track direction, can be effectively managed using a combination of onboard satellite equipment and SKaR measurements. While challenging, the correction applied Chapter 5 can achieve the required performance at Level-1b.

However, effective azimuth mis-pointing (due to roll, pitch or yaw angle errors) has a large impact on the retrieval of Doppler quantities, particularly in the across-track direction. The required pointing knowledge on the equivalent line-of-sight (LoS) Doppler centroid for all beams must be of the order of 1 arcsecond to attain a TSCV uncertainty $\leq 1 \text{ cm s}^{-1}$.

A fine-pointing data driven calibration (DDC) algorithm has been developed for this purpose. It is applied after the wave Doppler has been separated from U_{GD} , using a first guess of the $U_{CD,R}$ radial current. This considerably reduces the geophysical signal variance in the frequency-bands of the non-geophysical signal. In essence, the DDC adjusts sine models for



known-frequencies (multiple harmonics of the antenna rotation frequency) that are modulated along the in-orbit position. If the error is stable in time, the sinusoidal signature of these harmonics will be unambiguously separated from the broadband and unstable signature of the ocean.

This method builds on the paradigm used by the Planck satellite for high frequency mapping (e.g. Lamarre et al., 2003; Planck Collaboration, 2016) and was found to be extremely successful. It is also similar to the DDC developed for the Surface Water Ocean Topography mission described in Dibarboure and Ubelmann (2014) and demonstrated by Rodriguez et al. (2018) using aircraft measurements.

The **Difference range Width Doppler (DWD)** method is used to account for pitch and roll error based on Doppler range distribution property. While in theory roll and pitch errors impart a very characteristic signal in the Doppler (harmonics with the conical scan), in practice the orthogonality of these signals with any geophysical signal cannot be assumed to be perfect, since only a small number of samples are gathered around the azimuth. The DWD method exploits the fact that roll/pitch errors on the Doppler signal are different depending on the chosen length of the range window. By comparing the Doppler signal obtained with different range window lengths, the error due to roll/pitch uncertainties in the spacecraft attitude can be retrieved. This method is only limited by the signal-to-noise ratio of the difference between the two range windows. Since the number of parameters to be estimated is small, a very high accuracy can be obtained, even when accounting for the higher noise of the differential signals.

The **DDC** method is used to account for the yaw error using well-defined spectral error signals. This is possible provided the error signals are sufficiently stable. The error related to the spacecraft attitude yaw shift is degenerated with a uniform current orthogonal to the spacecraft ground-projected path direction. Thus, the yaw error is almost impossible to split from the geophysical signal using only one swath. The degeneracy disappears when comparing signal from two swaths with different projected path direction. On the other hand, poor attitude knowledge is the result of stationary processes over more than one orbit. Using this stationary property of the yaw error over several swaths it is possible to split the residual Doppler signal related to the yaw error from the geophysical Doppler signal. The non-stationary part mainly occurs at short time scales and is similar to additive noise.

The performance of the SKIM DDC algorithm is reported in Section 7.4.1.

Modelling the end-to-end pointing error is complex, but the main sources of error can be separated into two types of error:

- Broadband errors affecting a wide range of frequencies in a random or unpredictable way e.g. startracker noise, gyroscope random-walk error, or micro-vibrations between the AOCS and antenna feeds. Broadband errors can be considered as time-varying due to their random nature, but not azimuth-varying because all beams are affected in the same way at all times.
- Narrowband errors affecting specific and known frequencies in a stable and coherent way. The main sources of narrow-band errors are unknown zero-gravity antenna gain pattern irregularities and thermo-elastic distortions (TED). Both errors are azimuth-varying. The former is constant in time whereas the latter is time-varying. Because SKIM uses a sun-synchronous orbit, TED related pointing knowledge errors are



almost constant (i.e. only azimuth-dependent) over a few minutes and almost perfectly repetitive with each orbit over a few days or weeks.

The approach adopted by SKIM is to rely on a high-quality hardware implementation, described in Chapter 5, to limit the broadband errors to an acceptable level (e.g. high-quality gyro). In addition, SKIM has been designed to produce well-defined and stable narrow-band peaks, which are driven by TED. As explained in Chapter 5, the gyro and startrackers are physically mounted on the antenna support frame for this reason.

In terms of implementation, the DDC signal inversion may be merged with instrument effect compensation and should be implemented using large datasets (e.g. orbit-scale). A simulated time series of pointing errors has been obtained with detailed simulations to test the effectiveness of the DDC algorithm in removing the resulting errors. The results are reported in Chapter 7.

6.2.1.3 Risk Mitigation: Cyclo-Calibration Fine Pointing Algorithm

Because in Phase A one cannot rule out the existence of additional sources of short-term errors (e.g. over a few antenna beam rotations, i.e. 30 s or so), an additional DDC algorithm has been developed as a risk mitigation contingency. This algorithm is based on the principles of cyclo-calibration (CCAL) associated with the successive views of the same region of the ocean with different azimuths (Dibarboure and Ubelmann, 2019).

In contrast to the slowly varying (i.e. narrow-band) mis-pointing error that is calibrated using the DDC algorithm, time-varying, azimuth-invariant errors (i.e. broadband errors such as gyro errors) are more challenging to calibrate because there is an ambiguity with cross-track ocean velocities. Separating both signals is not as trivial as for narrowband errors that are readily handled by the DDC approach.

Two properties can be leveraged to recover the broadband errors: 1) all beams are affected by a common error and scattered in multiple directions over a 300 km circle within the SKIM swath, and 2) almost all regions are covered by three beams sweeping a cycloid pattern (see Fig. 6.2) with different measurement times. More importantly, the ocean is almost invariant over a few tens of seconds whereas the time-varying azimuth error is not. Thus, the azimuth error signature is the same over 300 km regions, whereas the ocean velocities are not. These properties are leveraged to invert the problem and isolate the time-varying errors (or broadband errors) from the geophysical content of interest. This short-time-scale data driven approach is called cyclo-calibration (CCAL) as it uses cross-overs between the cycloids (spirals) formed by each beam on the ground.

Today, the CCAL algorithm is not required for the baseline broadband scenario, because DDC simulations (Section 7.4.2) indicate that it yields almost the same results for uncalibrated broadband errors with up to 100 times more variance than in the baseline scenario. However, it is retained and presented as a risk mitigation activity for fine-pointing.

6.2.2 Retrieving NRCS and Doppler Modulation Spectra (Level-2a L2A_WR product)

The SKIM Level-2a L2A_WR product contains spectra of NRCS and Doppler modulation for each beam footprint together with uncertainties, computed in radar scan geometry, for each



cycle and all beams along the ground track of each beam. It is a key user product for data assimilation and a required input to higher-order processing.

The physical basis of how near-nadir high-frequency microwave radar reflectivity modulation can emerge in the LoS radar direction has been explained by Jackson (1981, 1987). For the near-nadir radar beam configuration of SKIM, it essentially builds on the expected tilt modulations of radar reflectivity by the underlying surface waves (Nouguier et al., 2018). It equivalently relates to spatial interferometry between different frequencies, a dual-frequency or delta-K radar processing technique (Jackson, 1981). The technique applies identically to Ku- and high-frequency Ka-band microwave measurements. At a given radar-look direction, 1D spectra of the highly-resolved radar signals can then be evaluated. This analysis corresponds to step 2 illustrated in Fig. 6.1a.

Nouguier et al. (2018) extend the analysis of radar reflectivity signals to the range-resolved Doppler signals, and to the combination of radar reflectivity and Doppler signals. Level-2a L2A_WR products include:

- 1D spectral analysis of range-resolved NRCS (σ^0) measurements
- 1D spectral analysis of range-resolved Doppler velocity V_{LoS} measurements
- 1D spectral analysis of range-resolved $\sigma^0 \cdot V_{LoS}^*$ measurements

These spectra not only contain geophysical information related to the surface-wave directional properties, but also include the signature of the radar power transfer function of the speckle noise (Goldfinger, 1982, Madsen, 1987). This is a typical triangular-like background spectral pedestal with an amplitude proportional to the entire radar signal variance, including its associated noise contribution. The 1D power density spectrum of one intensity detected range compressed pulse, preferably an average over many successive compressed pulses, corresponding to Doppler resolved stack, will be coloured by this speckle bias signature, weighted with the windowing function used to achieve the radar pulse compression. The spectral measurement error will then decrease with:

- the number of independent looks, governed by azimuth Doppler diversity (e.g. maximal across-track, minimal along-track, for radar reflectivity modulation)
- the number of spectra, governed by the range resolution and the number of radar range gates (e.g. along-range size of the footprint to control the number of periodograms)
- the reflectivity modulation contrast, governed by the steepness of the range-resolved modulating waves and the overall short-scale roughness, the effective azimuthal beam width and ground range resolution
- narrow-band reflectivity modulation, i.e. near the wind-sea peak or swell system.

The technique is currently exploited to analyse Ku-band SWIM radar intensity signals on the CFOSat platform (Hauser et al., 2017). Fig. 6.6 shows an example of SWIM spectra with maximum energy from the southwest. SKIM, with a smaller and better-resolved footprint, is expected to outperform SWIM measurements, with enhanced radar reflectivity modulations that help to resolve directional short wind-wave spectral properties of order 20–30 m.

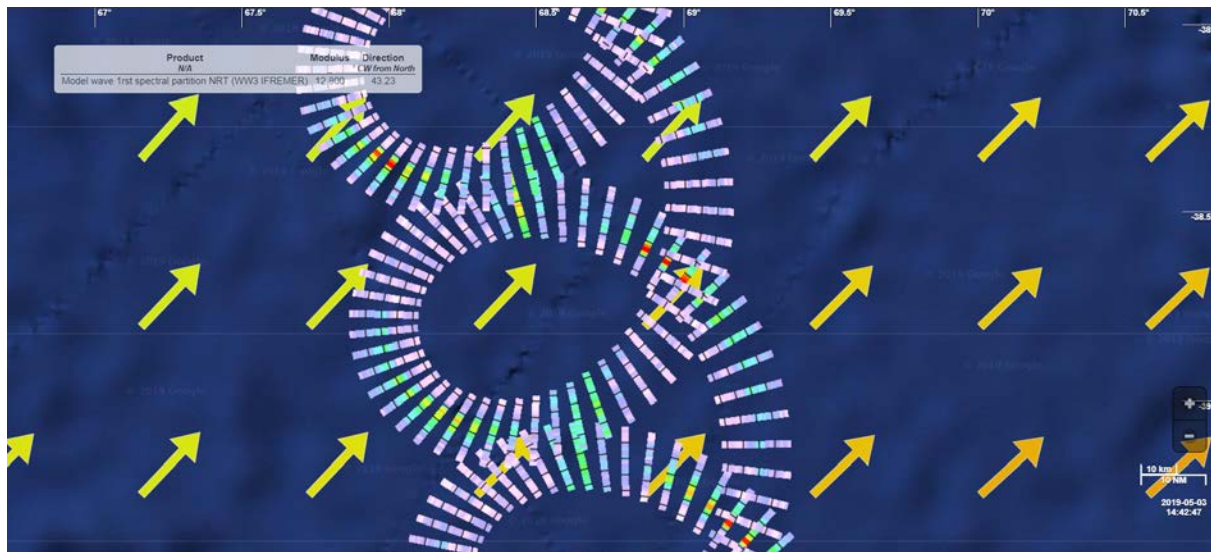


Figure 6.6. Level-2 spectra for CFOSat SWIM instrument at a beam incidence angle of 6° , similar to SKIM L2A_WR NRCS modulation spectrum. Each coloured strip represents the spectrum, with a wavelength from 800 m to 50 m. Intermediate black marks correspond to 400, 200 and 100 m measurements provided by CNES taken within a large storm system in the Southern Ocean south of India. Overlaid arrows indicate the dominant wave system in co-located WW3 model with colour representing the period (here about 13 sec). As expected, near the along-track direction, the signal is noisier due to the lack of independent samples (F. Collard, OceanDataLab/CNES).

The very-high SKIM 32 KHz Pulse Repetition Frequency (PRF) ensures high-coherency, necessary to apply the pulse-pair technique, but the effective number of independent samples is reduced. It further precludes the application of straightforward cross-spectral analysis to fully remove the noise spectral pedestal. To overcome this issue, the computation of NRCS fluctuation-spectra will closely follow a spectral estimation based on the periodogram method, and the same bias removal algorithm (Johnsen et al., 2006) that was successfully applied to the Envisat Advanced Synthetic Aperture Radar and contemporary Copernicus Sentinel-1 wave mode data. Note that, although NRCS spectra can directly be estimated from real-aperture range intensity profiles, as demonstrated for SWIM, significantly improved results are obtained using Doppler-resolved data. SKIM provides such a capability, as discussed in some depth by Johnsen and Engen (2019).

With an improved spatial resolution, comparable to SKIM 4 m ground-range resolution, Li et al. (2019) demonstrated that analysis of Copernicus Sentinel-1 wave mode measurements can be extended toward shorter-scale waves, that is, within the surface wind-wave equilibrium range. Performing 1D range-resolved spectral analysis, filtered around range-travelling intermediate wind waves (wavelengths 15–20 m), the radar cross-section variability in this range of intermediate waves quantitatively capture local wind field information, i.e. it is strongly sensitive to both wind speed and wind direction.

The SKIM-retrieval algorithm essentially builds on this potential to fully characterise the wind-driven range of surface wave scales. For highly-resolved Ka-band SKIM measurements, similar performances are expected to determine precisely both the local (wind-driven) and non-local (remote-swell system) sea-state conditions. Local wind-wave and non-local swell directional spectral properties, combined with NRCS measurements (at different incidence angles and azimuthal directions), augmented by wind vector information from MetOp-SG(1B) SCA (and numerical weather prediction ancillary information), will



serve to estimate both the local radial Stokes drift and directional mean squared slope parameter. From these latter quantities, the local $U_{WD}(\varphi)$ contribution can be specified, and compared to $U_{GD}(\varphi)$.

Access to MetOp-SG(1B) SCA data is anticipated at Level-2 through the EUMETSAT Ocean and Sea Ice Satellite Application Facility (OSI-SAF) <http://projects.knmi.nl/scatterometer/osisaf/>. Access to MetOp-SG(1B) SCA data at Level-1b will be via the EUMETSAT using operational interfaces within the ESA Payload Data Ground Segment (PDGS).

6.2.3 Retrieval of 1D Wave Spectra (Level-2b L2B_WDS Product)

SKIM's Level-2B_WDS products are azimuthal slices of the directional wave-height spectrum, $E(k, \varphi)$. The wave-spectrum is related to the NRCS σ^0 modulation spectrum by a Geophysical Model Function (GMF). At 6° and 12° incident angles, Jackson (1987) predicts the σ^0 spectrum, $S(k, \varphi)$ as:

$$S_{\sigma^0}(k, \varphi) = T\left(\theta, \frac{d}{ds}p\right) \cdot k \cdot E(k, \varphi), \quad (6.2)$$

where p is the probability density function of the slope (s) distribution, and T a function dependent on the parameters of the radar (e.g. beam-width) and azimuthal coherence of the wave field. If the wave spectrum is expressed in Cartesian coordinates as $E(k)$, with $k=(k_x, k_y)$, the σ^0 spectrum is proportional to $k^2 E(k)$, where (in both cases) this term gives the directional slope-spectrum. Using in situ data, this relation has been validated using SWIM data, and confirmed by numerical simulations, reported in Section 7.7. Since the slope distribution also controls the total σ^0 , the first term can be directly determined, after which $E(k, \varphi)$, follows directly from Eq. 6.2. The uncertainty in this estimation will then solely depend on the uncertainty of the L2A_WR product $S_{\sigma^0}(k, \varphi)$, as discussed in Section 7.5.

6.2.4 Retrieval of the Radial Surface velocity (Level-2b L2B_U Product)

The SKIM Level-2b L2B_U product is a fundamental product that has relevance to many users. It contains estimates of U_{CD} , the radial component of the TSCV (or sea-ice drift), after U_{WD} separation from L2A_UGD measurements together with uncertainties. It is computed in radar scan geometry, for each cycle, and all beams along the ground track of each beam. It may represent water movement or ice movement depending on the target surface. Radial Stokes drift $U_S(\varphi)$ in the case of a measurement over the ocean (or sea-ice drift) and wave Doppler, U_{WD} (estimation containing wave Doppler direction, φ_{WD} , and wave Doppler magnitude, M_{WD}) separated from L2A_UGD measurements are included. This is a primary product with relevance to many users and is an input to higher order processing.

6.2.4.1 Estimation of Radial Stokes Drift, U_{SR}

For range-resolved wave modulations, persistent swell waves from remote storms have directional distributions narrower than 20° . Illustrated in Fig. 6.1 step 2, the signal modulation in range disappears very quickly as the look azimuth moves away from the swell azimuth, i.e. swell systems are characterised by long-crested directional waves. In practice it requires ~ 3 to over 15 independent directional measurements (each sampling waves in

direction φ and $\varphi+180^\circ$) to specify the directional wave spectral properties $E(k,\varphi)$. Swell are thus non-local wave systems that propagate through and within each local SKIM footprint.

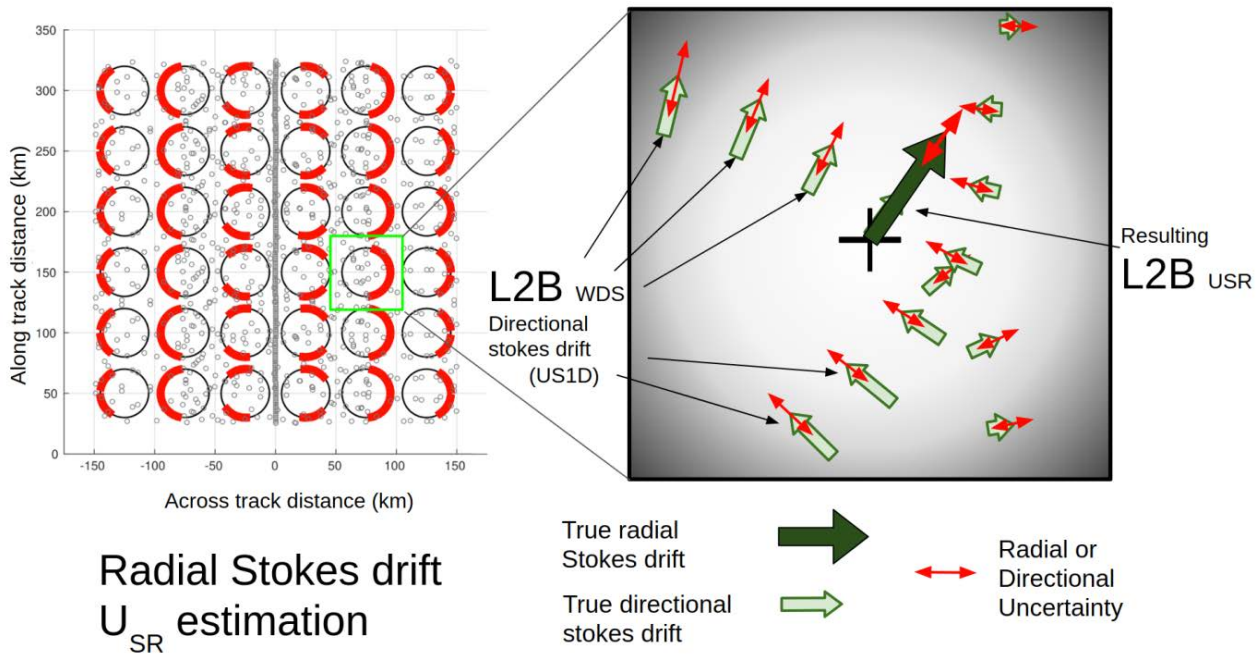


Figure 6.7. Algorithm principle to derive local radial Stokes drift estimates. Left: 70x70km cells with indication of azimuth diversity (red) used to compute the radial Stokes drift for each Level-2b beam. (F. Collard, OceanDataLab)

For the SKIM measurement geometry, a wave-measurement cell is specified with a cross-track width in the order of 70 km (Fig. 6.7) to capture the full-wave spectral properties. Because detected levels of energy will not be significant for most look directions, they can be neglected for most applications and wave-spectral properties may be estimated from a smaller measurement cell. This high directivity of the range-resolved measurement is the main strength of the wave-scatterometer principle.

The radial Stokes drift $U_{S,R}$ estimation can thus be obtained for each SKIM footprint, combining local and non-local sea-state information with NRCS measurements (at different incidence angles and azimuthal directions), all potentially augmented by ancillary wind vector from MetOp-SG(1B) SCA, and NWP outputs.

Theoretically, the Stokes drift is fully specified by the full wave directional spectrum. In practice, Modulation Transfer Functions (MTFs) and a GMF using all available inputs will be used (Ardhuin et al., 2019, LOPS 2019). Following scatterometer-analysis strategy, it is anticipated that these MTFs and GMF will be fine-tuned from the data, as also anticipated by Rodriguez et al. (2018) for higher incidence angles.

The same analysis strategy is considered to derive the directional mean squared slope parameter at each SKIM footprint.

6.2.4.2 Retrieval of Radial wave Doppler U_{WD}

Wave spectra over each footprint for azimuth φ can be integrated in spectral moments to estimate the contributions associated to resolved waves. These moments can then be integrated over directions using other neighbouring footprints at azimuth φ' .

From theory (Chapron et al., 2004, 2005, Mouche et al., 2008, Nouguier et al., 2018) and *in situ* experimental measurements (Yurovsky et al., 2018, 2019, Marié et al., 2019), the azimuth variation of $U_{WD}(\varphi)$ is dominated by a near-cosine projection of a wave Doppler vector of magnitude M_{WD} and direction φ_{WD} :

$$U_{WD}(\varphi) = M_{WD} \cos(\varphi - \varphi_{WD}) = (C_0 + \Delta C) \cos(\varphi - \varphi_{WD}) \tag{6.3}$$

Theoretically and experimentally, M_{WD} then corresponds to the ratio of the Stokes drift magnitude, U_s , and the effective mean square slope mss_{shape} (that controls the shape of radar falloff with incidence, e.g. Nouguier et al., 2018, Yurovsky et al., 2019), with the φ_{WD} , that is the direction of the Stokes drift vector. As a result, M_{WD} varies between Ku- and Ka-band measurements, due to the differing mss_{shape} , but varies very little with incidence angles $<15^\circ$ where theory predicts $C_0 = 2.5 \text{ ms}^{-1}$ for Ka band at $\theta = 6^\circ$ and 2.4 ms^{-1} for $\theta = 12^\circ$ (Nouguier et al., 2016).

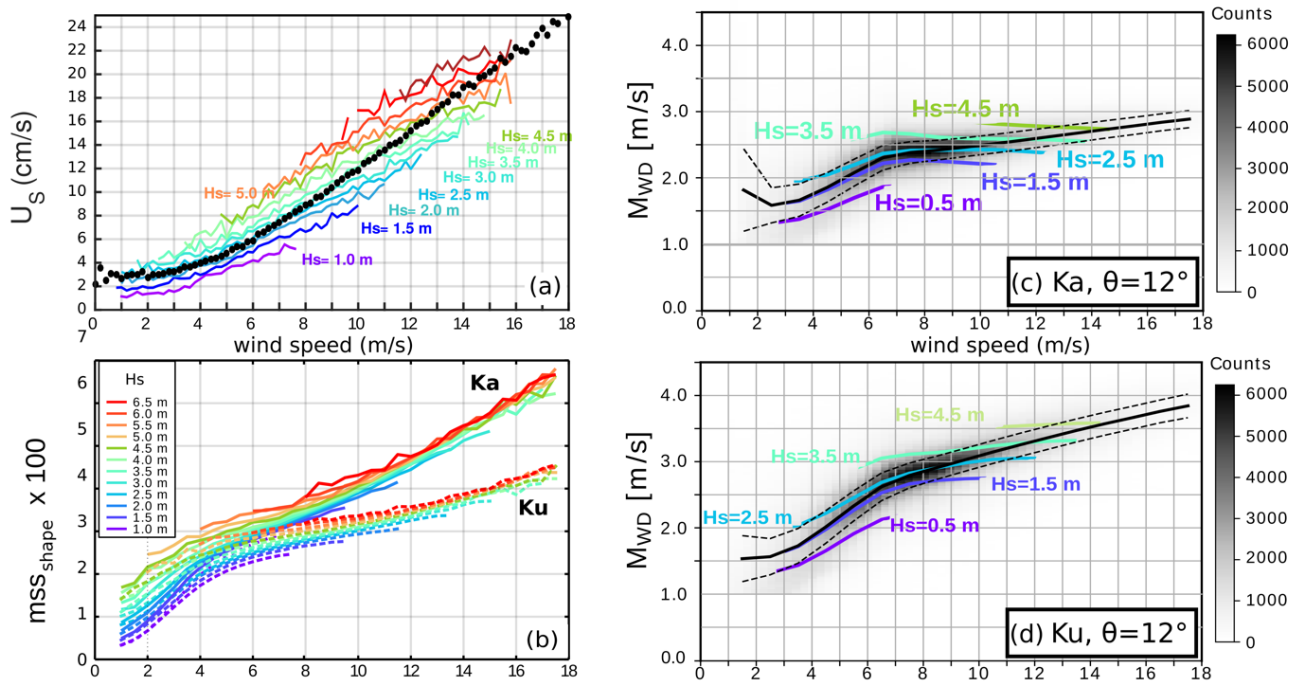


Figure 6.8. Left: measured variability of the Stokes drift from buoy (top) and mss_{shape} from GPM data (Nouguier et al., 2016) as function of wind speed and significant wave height (Hs). Right: computed Doppler magnitudes M_{WD} from six million wave spectra around the globe (LOPS, 2019). For winds $>6 \text{ ms}^{-1}$, both Stokes drift and mss_{shape} quasi-linearly increase with wind speed, leading to weak wind dependency for $M_{WD} \approx U_s/mss_{shape}$. (LOPS)

The perturbation ΔC represents the departure of the average M_{WD} relation due to variability in the sea state. ΔC is of the order of 0.2 ms^{-1} for 1 m change of Hs or for 2 ms^{-1} change in the wind speed (Fig. 6.8). ΔC can be theoretically estimated from the full directional wave spectrum. At the swath level, an accurate estimation of the Ka-band U_{WD} thus essentially requires an accurate knowledge of the directional sea-surface slope probability distribution.



This distribution is known to depend largely upon the short-wave scales of the local sea state, i.e. wind-generated surface wave scales.

Significant wave height, H_s , nadir and off-nadir NRCS measurements, including the analysis of directional radar reflectivity modulations, are used to accurately retrieve this directional sea-surface slope probability distribution. Using Ka-band, wind speed and direction can be estimated from radar backscatter at incidences above 8° in most conditions (LOPS, 2019). Numerical weather prediction models may also be used (e.g. ECMWF). However, to progress towards the highest accuracy goals, the combination of SKIM data with wind-vector data from, for example, MetOp-SG(1B) wind scatterometer (SCA) data have been studied to offer the best combination. This combination is the main driver for the choice of the SKIM orbit, as discussed in Section 4.3.3.

At footprint level, U_{WD} will be estimated using an empirically derived GMF using the following parameters:

- The radial Stokes drift $U_{S,R}$ at azimuth φ with contributions ($U_{S,1D}$) over multiple directions φ' .
- Wind vector from MetOp-SG SCA, SKIM Level-1b NRCS, possibly NWP inputs, in that order of priority, giving a magnitude U_{10} and a radial projection $U_{10,R}$
- Significant wave height H_s from nadir beam, L2a_WR and L2b_WDS products
- Mean square slope mss estimated from Level-1b NRCS, and L2a_WR products.

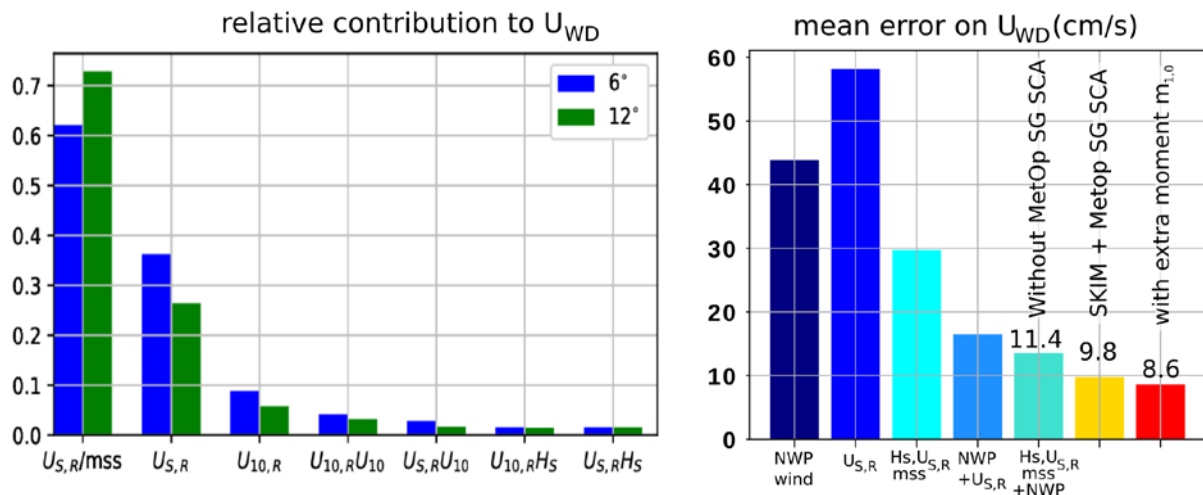


Figure 6.9. Left: relative contributions of different terms to U_{WD} . Right: mean error on U_{WD} for different GMFs applied to spectra in the Gulf Stream region (mean value of U_{WD} is 1 m s^{-1}) using only part of the parameters. The last GMF tested also includes extra wave moments $m_{1,0}$. (C. Peureux, LOPS)

The dependency of U_{WD} on the five scalar parameters, $U_{S,R}$, U_{10} , $U_{10,R}$, H_s and mss , was learned from simulated spectra and the theoretical backscatter model of Nougquier et al. (2018), providing a GMF that was implemented in the SKIMulator global simulation tool (Gaultier, 2019). It is in line with experimentally-derived platform (Yurovsky et al., 2019), and airborne measurements (Nougquier et al., 2018). The learning procedure used a simple linear-weighted combination of products and ratios, with weights shown in Fig. 6.9, and a training dataset of six million spectra from a global model simulation (LOPS, 2019b).

A family of GMFs of varying complexity was tested on independent data, from wind alone (the NWP wind speed was taken as truth plus a 1.5 m s^{-1} Gaussian noise). The reference GMF (SKIM+SCA) gives error on U_{WD} that are 20% higher than using NWP winds (Fig. 6.8). The GMF can be further refined by including a finer description of the wave field with more spectral moments.

In practice, the GMF will be learned from the data, using U_{WD} measurements where the current is known (where *in situ*, drifter or HF-radar match-ups are available), or known to be very weak. Potentially, not all parameters will be available at the local footprint (QC control), and their estimation can require some interpolation. Only U_{10} and $U_{10,R}$ are available all across the swath where MetOp-SG(1B) SCA and SKIM overlap. This can introduce errors, typically in the order of 5%, in the estimation of U_{WD} . The use of NWP fields could be used but these still have a poor temporal and spatial resolution limiting their applicability. Thus, the uncertainty in the estimation of U_{WD} will vary along the orbit. This is the reason why the SKIM orbit is designed to maximise the collocation of MetOp-SG(1B) SCA data over the ocean.

6.2.5 Retrieval of TSCV: Level-2b L2B_U to Level-2c Processing

The SKIM Level-2c product is a primary product with relevance to all users. It contains estimates of all geophysical quantities and uncertainties derived from the SKIM mission on a regular latitude by longitude grid across the swath for each SKIM orbit. U_{CD} is posted at a grid resolution of $5 \times 5 \text{ km}$ with data constructed from a search radius of $\sim 15 \text{ km}$. There is no background model used in the restitution.

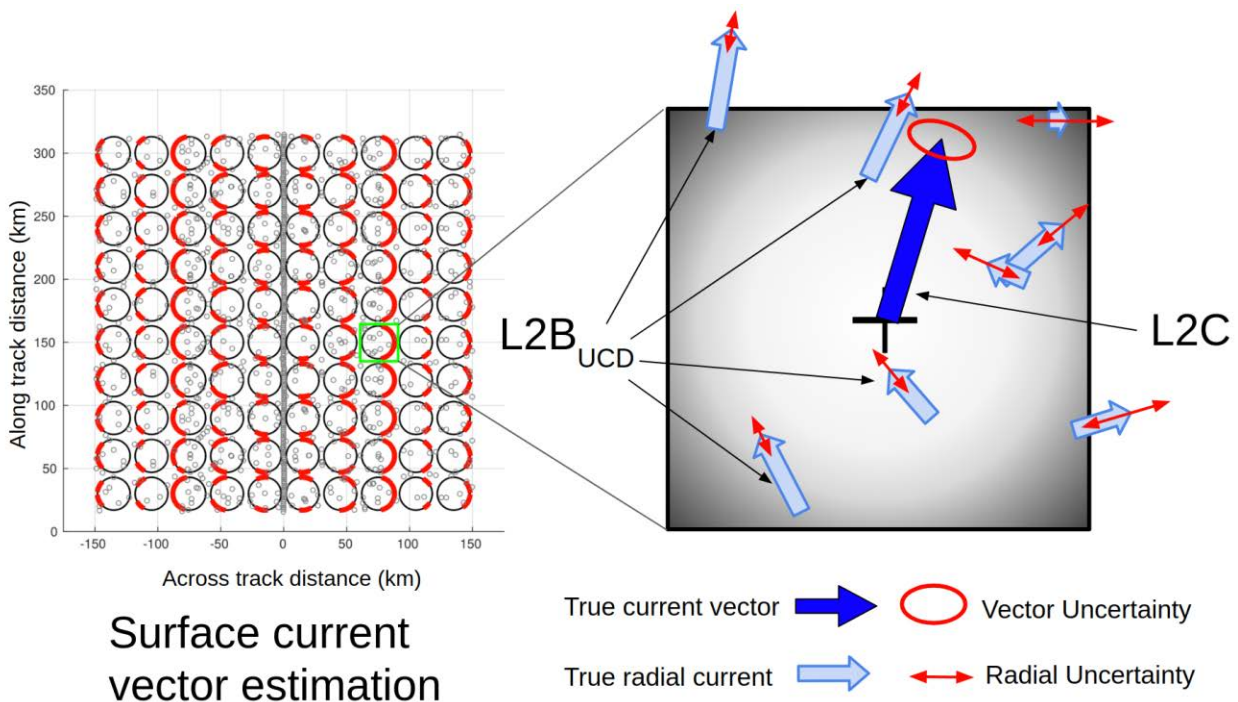


Figure 6.10. Retrieval principle to derive Level-2c vectors from Level-2b radial components. Left: $30 \times 30 \text{ km}$ cells with indication of azimuth diversity (red) used to compute the TSCV vector/uncertainty from initial Level-2b radial surface current and associated variable uncertainties. (F. Collard, OceanDatalab)

$E(k, \varphi)$ is computed for boxes of 70×70 km in satellite geometry. It is used in higher-order processing to estimate wave Doppler direction and magnitude.

Processing radial components at Level-2b to field of vectors at Level-2c follows the same methodology used for HF-radars, with radial components combined into vectors. A wide range of techniques have been used for HF-radars, as reviewed by Kim et al. (2008), from unweighted least squares, to optimal interpolation. Here we use a bi-variate Weighted Least Square (WLS) approach that is similar to that described in Kim et al. (2008) and has been implemented to stay close to the measurement data. In future phases, alternative approaches will be studied depending on the final configuration of SKIM.

The geometry and schematic algorithm principle to derive Level-2c products from Level-2b is illustrated Fig. 6.10. If at least two Level-2b observations with a different LoS are available, for example V_{los1} and V_{los3} in Fig. 6.11, one can apply the following formula to get the two components of the Level-2c velocity vector:

$$\begin{pmatrix} V_{AC} \\ V_{AL} \end{pmatrix} = (\mathbf{H}^T \mathbf{R}^{-1} \mathbf{H})^{-1} \mathbf{H}^T \mathbf{R}^{-1} \begin{pmatrix} V_{LoS1} \\ V_{LoS2} \\ \vdots \\ V_{LoSN} \end{pmatrix} \quad (6.4)$$

where \mathbf{R} is the covariance matrix of observation error, here assumed diagonal. \mathbf{R}^{-1} is a weight matrix, \mathbf{W} . The diagonal terms are set to vary as a function of prescribed uncertainty for each Level-2b observation, according to observation distance from the grid point, beam angle, wind and sea state. An inverse exponential function is considered for the distance, set to zero beyond a radius of 15 km. \mathbf{H} is the observation operator, transforming the state vector in equivalent LoS observations, therefore writing:

$$\mathbf{H} = \begin{pmatrix} \cos(\theta_1) & \sin(\theta_1) \\ \vdots & \vdots \\ \cos(\theta_N) & \sin(\theta_N) \end{pmatrix} \begin{matrix} \uparrow \\ N_{obs} \\ \downarrow \end{matrix} \quad (6.5)$$

where θ_i is the look angle as represented on Fig. 6.10 for observation i . This estimation is derived from the optimal interpolation formula assuming that the co-variances for the signal tend to infinity. No *a priori* on the statistics of the surface current signal exists, which guarantees robustness.

Along with the Level-2c solution, an uncertainty is computed following the formal error formula of weighted least-squares :

$$\mathbf{E} = (\mathbf{H}^T \mathbf{R}^{-1} \mathbf{H})^{-1}, \quad (6.6)$$

Where \mathbf{E} is a (2×2) matrix representing the error covariance of the velocity vector. In Fig. 6.11, this matrix is represented by its 1-sigma ellipses, called ellipses of uncertainty of the velocity vector.

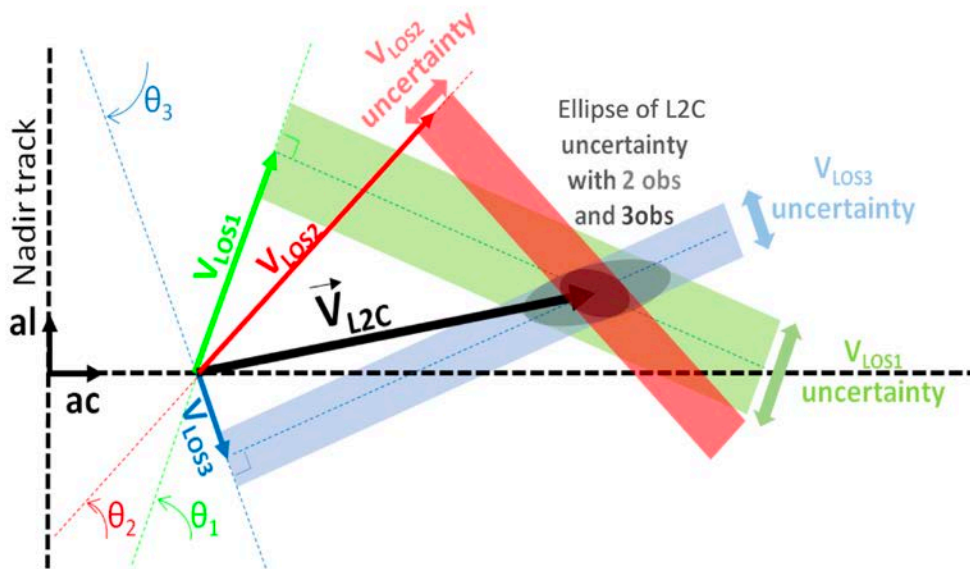


Figure 6.11. The principle of the Geometric Dilution of Precision (GDOP) from several Level-2b LoS observations (V_{LoS}) and specified uncertainties. (C. Ubelmann, CLS)

We note, in this example, that with observations 1 and 3 only, a large uncertainty remains in specific (un-sampled) directions. When additional observations at a different look angle are used (e.g. observation 2), the uncertainty is reduced. In practice: using a 15 km weighted Gaussian search radius in the processing of Level-2c the number of observations exceeds 20 with a wide diversity of look angles at medium range, favoured by the presence of multiple beam inclinations. In near range, the uncertainty is large in the across-track direction, while in far range it is large in the along-track direction.

The across-track U_{AC} and along-track U_{AL} components have missing values in the centre cells for U_{AC} , and on the outer edge of the swath for U_{AL} . These will be flagged as missing data and only one of the two components of the TSCV will be retrieved there.

There are other factors that will introduce large errors in the Level-2b $U_{CD,R}$, such as the presence of large gradients in wave properties (at the shoreline or at the ice edge), or the presence large gradients in NRCS associated with slicks or light rain. The Level-1b to Level-2b processing may also fail to produce any data for some footprints (heavy rain, very large NRCS gradient due to small islands etc.). The processing strategy will take advantage of the large number of Level-2b footprints (5 to 15) in any Level-2c cell, with all dubious data flagged using thresholding and other standard quality control techniques.

6.2.6 Multitemporal Processing to Level-2d

Level-2d data products are generated from the Level-2b data, but for multiple swaths within a 10-day time window. The same processing approach is applied, but using a map grid defined on a geographical coordinate system rather than in instrument coordinates. The weights, as described for the Level-2c processing, are a function the estimated measurement error, the spatial distance, and temporal distance within the time-window around the time of analysis. An example of a Level-2d TSCV field is presented in Fig. 6.1.



It is expected that Level-2d products will reduce uncertainties significantly assuming the correct geophysical constraints are applied. For example, additional Level-2b to Level-2d analysis approaches exploiting optimal interpolation (which also yield a useful measure of uncertainty via J_{min} cost-function statistics) exploiting dedicated background error covariance matrices, regionally specific correlation length scales, multi-scale approaches or the advective properties of ocean models will also be developed to provide the best estimate of TSCV for specific time windows of 10 days in future phases of the mission. Level-2d processing is not explained further since this is a classical operation that has many realisations in ocean science (e.g. Donlon et al., 2011).

6.2.7 SKIM Nadir Beam Processing: Conventional Altimetry

The SKIM nadir altimeter builds on the heritage SARAL-AltiKa and Copernicus Sentinel-3 altimetry missions and is processed using well-established techniques in the same manner. The algorithm theoretical baseline for nadir beam processing is described in SKIM Team (2019b). Therefore, details of the algorithm and processing for the SKaR nadir beam is not described further since the focus of the Phase A study is on the retrieval of TSCV.

However, one specific aspect is the use of MetOp-SG(1B) Microwave Imager (MWI) measurements that are co-located and near contemporaneous with the SKIM nadir beam to provide a wet tropospheric range correction (WTC). The advantage of using MWI is that a measure of water vapour and cloud liquid-water content will be available across the full swath of SKaR.

Following Picard et al. (2015), the same algorithm approach used by AltiKa will be used for SKIM. The well-established algorithm and its application is described by Obligis et al. (2006) and uses a neural-network regression approach. This relates, in the SKIM case, MWI brightness temperatures and the SKIM backscattering coefficient to water vapour, atmospheric attenuation of σ^0 , cloud liquid-water content and the WTC.

MWI channels with centre frequencies located at 18.7 GHz, 23.8 GHz, 31.4 GHz may be used for a conventional retrieval of the WTC over the ocean based on the use of 18.7 and 23.8 GHz channels. However, the footprint of MWI channels is 50 km for the 18.7 and 23.8 GHz channels and 30 km for the 31.4 GHz channel. As the WTC ideally requires a high resolution given that the footprint of SKIM is 10 km, this is not optimal.

To mitigate this issue, alternative MWI channels that are located at centre frequencies of 89 GHz and 161 GHz and have a spatial resolution of 10 km are available. These channels have sensitivity to atmospheric water vapour and cloud liquid-water content and can be used to either provide an alternative WTC solution or sharpen the WTC derived from the conventional low spatial resolution channels. The use of these channels has already been explored during development work at ESA as part of coastal altimetry radiometer studies. During future phases of the mission, the use of 10 km spatial-resolution channels, carried by MetOp-SG(1B) MWI to provide a WTC, will be explored.

6.3 Algorithm Development and Evolution after Launch

For SKIM the need is foreseen to downlink raw instrument data (L1A-RAW) corresponding to one-minute acquisition per orbit. These data will be used to investigate the characteristics of the SKaR measurements and to explore new onboard processing algorithms or optimise

those existing. SKIM's onboard processing hardware (implemented using field programmable gate array (FPGA) technology to allow algorithms to be adjusted onboard). Section 5.3.3.6 explains in detail SKIM on-board processing implementation and related hardware.

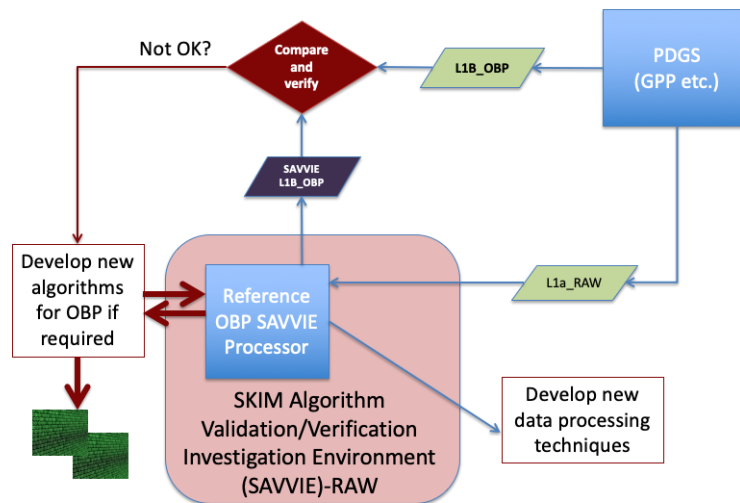


Figure 6.12. SKIM Algorithm Validation/Verification Investigation Environment (SAVVIE)-RAW environment. (ESA)

In order to use SKIM Level-1a L1A-RAW data product and facilitate rapid scientific prototyping, testing, verification and validation of algorithms and products, a parallel open source scientific suite environment is required. This is called the SKIM Algorithm Validation/Verification Investigation Environment (SAVVIE) as shown in Fig. 6.12 and will be developed and operated by the scientific community.

6.4 Validation Concept

This section presents a validation concept focused on the SKIM Level-2b and Level-2c velocity products. The aim is to monitor the in-flight performance of SKIM products and to set up a long-term approach (for the mission duration) building on operational infrastructure where possible augmented by dedicated campaigns for specific aspects during Phase-E1. At the core of the SKIM validation concept is the use of independent Fiducial Reference Measurements (FRM), (Donlon et al., 2015) that are ideally traceable to SI standards and have well-defined uncertainty budgets in place.

The validation plan is designed to detect and identify regional biases possibly associated with residual errors in the wave Doppler, rain flagging or real effects of shallow slippery layers associated with freshwater lenses and shallow mixed layers. A second aspect is the validation of gradients in the TSCV or sea-ice drift that are important for the upper-ocean dynamics, in particular for identifying eddies and upwelling regions.

For surface currents, the validation approach will rely on the global array of surface drifters, oceanographic research cruises and, for regions beyond 50 km from the shore, coastal HF-radars.

For wave spectra, the validation will use moored and drifting wave buoys, using the first five spectral moments (Ardhuin et al., 2019). Validation of swell parameters will follow standard



practice as for the Envisat and Sentinel-1 synthetic aperture wave mode. Emphasis on validation, which will be during Phase-1 of the mission, will be required to ensure that the performance of SKIM products are met.

A separate subset of *in situ* data will be used for machine learning of ocean-wave spectra variability and its impact on the wave Doppler U_{WD} , in particular in coastal regions and close to the sea-ice edge. This is particularly important given that U_{WD} is often the largest component of U_{CD} and wave Doppler separation is linked directly to the performance of SKIM products.

To validate Stokes drift specific drifters will be used that are very small and sit within the top few centimetres of the water surface. Several experimental designs have been used successfully in research experiments (e.g. Nasello and Armenio, 2016) and commercial devices are available for oil-spill clean-up operations that require estimates of TSCV and Stokes drift.

The two other products, nadir altimetry and wave spectra, will be validated using existing methods. For the nadir beam, dedicated crossovers with reference altimeters (e.g. Copernicus Sentinel-6) and *in situ* transponders (for range bias determination and monitoring) will be used. A dedicated Ka-band transponder would need to be developed for this approach as the infrastructure operated by ESA at the Permanent Facility for Altimeter Calibration in Crete, Greece, operates at Ku-band. However, due to the narrow footprint of SKIM (~9 km) stringent positioning of the transponder will be required. Furthermore, Ka-band transponders for satellite altimetry do not yet exist and would need to be developed in future phases of the mission development.

The SKIM validation strategy is thus based on a three-step approach, with a detailed validation of the different terms in the measurement equation; a global monitoring of data quality with different networks of observations; a local validation of gradients. A multifaceted validation concept will be used based on the following reference data sources is planned:

- *In situ* observations (drifting buoys, moored buoys, wave-rider buoys, current meters), in particular un-drogued drifting buoys enabled with wave measurement technology (Centurioni et al., 2017)
- Coastal HF-radar systems in shelf seas
- Dedicated campaigns (aircraft, ships) using an Aircraft AIR-SKaR instrument would need to be developed in future phases of the mission development
- Other satellite data in synergy (altimetry, SAR, optical sun-glitter, sea-surface temperature)
- Numerical models (WW3, CMEMS, FES2014)

These are briefly discussed in the following sections.

6.4.1 Validation Using In Situ Measurements

The detailed validation Level-2b U_{CD} requires the joint measurement of TSCV and wave spectra along with an estimate of the wind vector (to account for wind effects on the drifters). In principle, this can be achieved using moored buoys and dedicated research platforms, but there are very few available as shown in Fig. 6.14 (left). The tropical arrays in the three major oceanic basins TAO/TRITON, PIRATA and RAMA are undergoing important redesigns, with

opportunities for adding wave measurements where currents and wind are already available (Cravatte et al., 2016). Further investigation of all terms in the measurement equation would benefit from a dedicated field site for full spectral wave measurement (e.g. Aqua Alta platform, Fedele et al., 2013) and a fixed Ka-band radar.

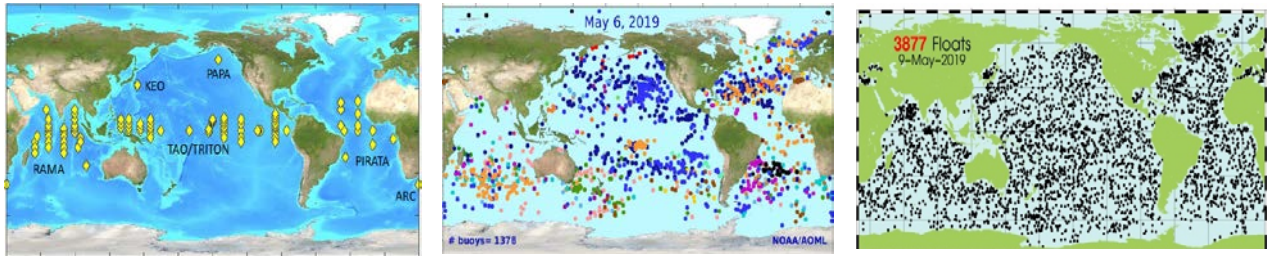


Figure 6.13. Main networks used for SKIM validation. Top: current-measuring moorings. Centre: SVP drifters. Right: Argo floats (as of May 2019). Courtesy R. Lumpkin (NOAA) and JCOMM (<http://www.jcommops.org>).

The Operational Drifting Buoy Array is managed by the Data Buoy Cooperation Panel (DBCP, <http://www.jcommops.org/dbcp/>) that coordinates the deployment and management of drifting buoys for the international community. Surface Velocity Program (SVP) drifters (Lumpkin and Pazos, 2007) are of a relatively standard design and are used to report sea surface temperature, air pressure and ocean currents. SVP drifters are drogued at a depth of 15 m as standard. However, many SVP buoys lose the drogue and become undrogued drifters (Lumpkin and Pazos, 2007) and provide a better estimate of the TSCV after windage effects have been removed.

These are augmented by new drifter designs dedicated to measuring flow in the top 1 m of the ocean surface such as the Carthe drifters (Novelli et al., 2017) used during the SKIM campaign in 2018. Other drifters (e.g. Spoo-drift spotter <https://www.sofarocan.com/products/spotter>) incorporate wave measurement sensors – although wave information may be derived from the SVP drifters themselves based on GPS techniques (e.g. Centurioni et al., 2017).

Because of the surface convergence zones very few SVP drifters are present in the Tropics (Fig. 6.13 centre). Given the importance of the Tropics for the SKIM objectives, another source of surface velocity will be used, derived from profiling Argo floats that are present at the surface for only a few hours every 7–10 days. Argo floats sample the top metre of the ocean, and they are more strongly affected by the slip relative to surrounding water under joint force of wind and waves compared to SVP drifters (Lebedev et al., 2007).

Measurements of surface currents using dedicated current meters, turbulence probes, ship drift and other devices will be exploited when available. These are maintained typically by laboratories and universities as part of dedicated research activities or campaigns. Some coordination networks exist to gain access to current measurements made by the oil and gas industry (e.g. SIMORC in the Gulf of Mexico and in the North Sea).

6.4.2 Validation Using Coastal HF-Radar

For the validation of local gradients in SKIM velocities, collocation with coastal HF-radars will be used. These are based on the same physical principle of surface motion and operate in the HF-radio band (3–30 MHz). The maximum range of 100 to 300 km from the coast,



depending on the frequency used, will allow a detailed validation of SKIM-derived gradients in different part of the SKIM swath. HF-radar data are available for a small part of the European coasts, most of the coastline around the continental United States, and a few other locations (see <http://global-hfradar.org/>, Rubio et al., 2018, Roarty et al., 2019). At their shorter ranges, under 30 km, HF-radars will be particularly useful for the validation of coastal-specific errors in SKIM data where the wave Doppler estimates are expected to be challenged due to the more complex wave fields expected in these regions.

6.4.3 Validation Using Dedicated Campaigns

Specific campaigns will be used to develop the wave Doppler estimation close to the sea ice edge and in coastal waters using ships and aircraft (such as the DRIFT4 SKIM campaign. In addition, research cruise data from the international research fleet of ships can be exploited to provide measurements of TSCV. During such activities dedicated instrumentation may be used to measure the TSCV.

A dedicated 'AIRSKaR' version for the SKIM instrument would be a considerable advantage and should be developed in future phases of the mission. Using such an instrument, data can be collected to further support the development of the SKIM Level-2 algorithms.

6.4.4 Validation Using Other Satellite Data in Synergy

The use of other satellite data including altimetry, SAR Imagers, optical sun-glitter, sea-surface temperature and ocean colour will be used in synergy to validate SKIM measurements. Each system has unique aspects (for validation/verification). Sentinel-1 wave mode can provide Doppler estimates of the single LoS ocean currents. Sentinel-2 sun-glitter gives access to high performance roughness information, the wave spectral characteristics, operates under a similar sensor physics to SKIM. Sea-surface temperature maps provide independent tracer information to interpret SKIM TSCV. Satellite altimetry can provide estimates of the significant wave height and geostrophic current. Obviously, comparisons with altimetry will be useful for geostrophic currents.

6.4.5 Use of Numerical Models

Numerical ocean models provide daily forecasts of ocean currents and waves will be used to inform the SKIM validation team of long-term performance. Tidal models (e.g. Saynisch et al., 2018) can be used to estimate the tidal component within SKIM TSCV that is uniquely measured by SKIM.

7 PERFORMANCE ESTIMATION

This chapter presents an assessment of the proposed mission and system Concept Against the mission requirements presented in Chapter 4. It includes system-level parameters introduced in Chapter 5, in particular those relating to coverage and availability.

The approach to SKIM performance assessment, the tools that have been developed and used for analysis, and the performance assessment metrics used to validate requirements is presented in Section 7.1. Level-1 product performance results are presented in Section 7.3. End to end Level-2 performance results, including regional to global scales are presented in Section 7.4. Finally, results obtained during the DRIFT4SKIM campaign in November 2018 (Marié et al., 2019), designed to validate the SKIM Level-2 retrievals, are presented in Section 7.5.

7.1 Performance Assessment Approach

The starting point of SKIM performance assessment is to define different sources of error that will be accounted for both in the analytical models so that appropriate uncertainties can be propagated through the parameterisations used by simulation tools.

A tree of uncertainties and error sources has been derived and used to establish related performance assessment metrics. Metrics are defined at algorithm and product level to provide a complete performance assessment of SKIM against requirements in an objective manner. A schematic representation of the error budget is shown in Fig. 7.1. It highlights the interconnections and implications of instrument, processing and environmental conditions on the velocity and wave-spectrum data product uncertainties. Further detailed in the SKIM End-to-End Performance Simulator (SEEPS) documentation package.

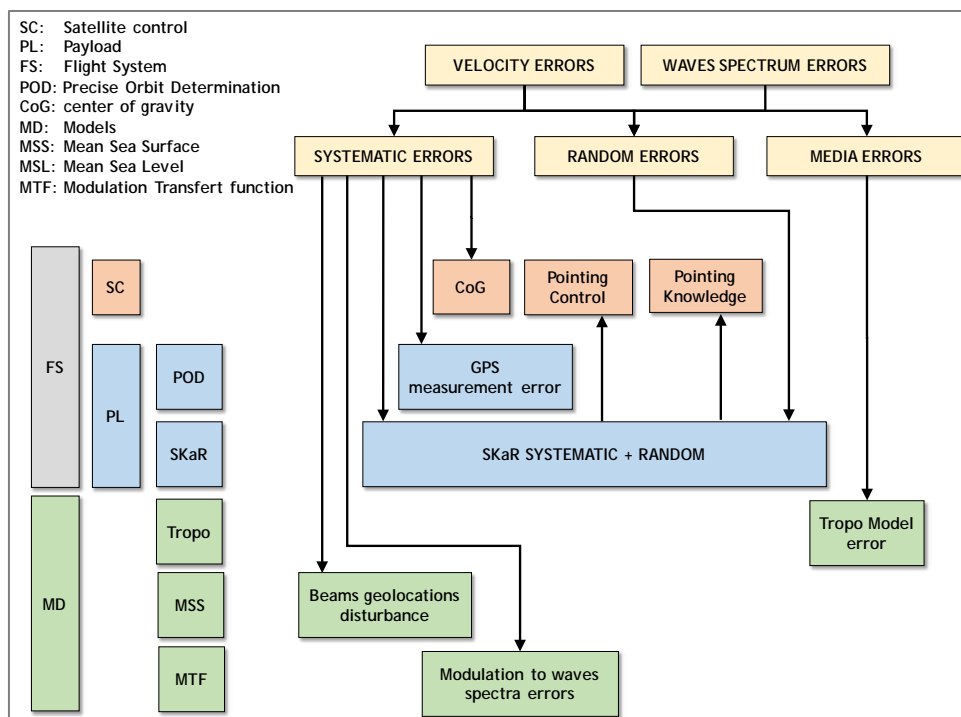


Figure 7.1. Overview of the key error budget components for the velocity and wave spectrum products. Black arrows indicate the origin of errors and uncertainties.

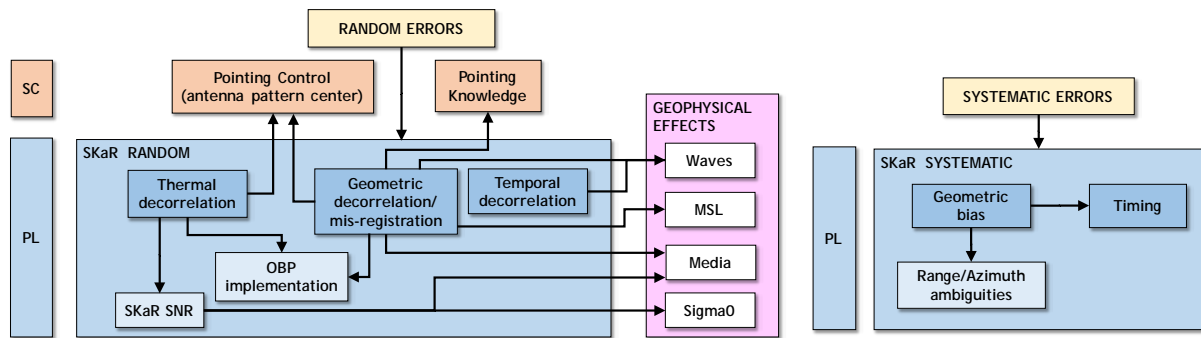


Figure 7.2. Overview of the contribution of the SKaR instrument to the random (left) and systematic (right) errors. Black arrows indicate the origin of errors and uncertainties.

Details on the systematic and random errors for the SKaR instrument can be found in Fig. 7.2. For example, ocean waves impact the geometric decorrelation that is part of the random contribution of the SKaR instrument error budget. This systematic error adds to the other sources of systematic noise and impact the radial velocity data product.

Several generic errors sources limit the accuracy of the final SKIM radial current (U_{CD}) and wave measurements including:

Random errors

These are errors related to the variance of the velocity or amplitude modulation measurements, most notably due to the intrinsic noise of the SKaR instrument. In addition, other errors that increase the variance but cannot be corrected on the ground are included. The random error contribution depends on several factors, including the system signal-to-noise ratio (SNR), the antenna angular rate, the azimuthal pointing geometry (with respect to the satellite velocity) and those inherent in the processing algorithms.

At Level-1b, these errors constrain the pointing control stability of the platform and the deployment accuracy and stability of the SKaR antennas to minimise SNR loss over the desired swath on the ground. At Level-2 random errors translate into noise on the geophysical retrievals.

Spacecraft and instrument systematic errors

These errors are typically associated with drifts or range variations that end up introducing bias in the measured products, and which could be corrected if known. Lack of knowledge in the spacecraft roll angle, system timing and phase drifts introduced by the antennas or the electronics will induce phase errors.

Sampling errors

At Level-1 these errors relate to the ability of the SKaR instrument to provide unbiased data. For example, sampling of the rotary encoder providing the position of the feed-horn plate. At Level-2 these errors relate to the representativity of measurements to reproduce the geophysical signal of interest at a given scale. The SKaR instrument is required to properly sample the geophysical field to guarantee high performance retrievals. Performance depends on the beam sampling characteristics and geometry (e.g. number of beams, beam placement, beam rotation rate, azimuth and elevation diversity) and quality of measurements (e.g. Level-1 performance, quality control of outlier identification, flagging algorithms, under-constraint of the retrieval algorithm, quality of the retrieval approach and algorithm etc.).

Model systematic errors

These errors are mostly related to the models used in the SKIM processing chains. For example, geolocation errors related to the surface topography, the SKIM wave Doppler model, background error covariance matrices and spatial-temporal correlation length scales used in Level-2d products. Any use of modulation transfer functions will suffer from simplifications used in their definition (which can be driven by the set of accessible proxies) and the estimation errors for the proxies. These will directly impact the quality of the inferred product.

Electromagnetic propagation (media) and orbit errors

The radar range measured onboard must be corrected to account for additional delays caused by propagation effects through the ionosphere and troposphere layers. They include wet and dry troposphere errors, as well as ionosphere errors, with cross-track variations within the SKIM swath. Errors in knowledge of the satellite and instrument radial positions will directly translate into phase errors. The Precise Orbit Determination (POD) suite of instruments will be used to correct radial orbit errors.

Errors related to the geophysical variability of the sea surface

At Level-1, geophysical variability of the wave fields will introduce phase biases related to radar imaging mechanisms at the sea surface, for example, spatial and azimuthal variability of σ^0 gradients. In addition, errors due to mean ocean velocities and wave motion may also introduce sea surface height gradients that cannot be corrected easily. At Level-2, this class of error impact the performance of the wave Doppler algorithm when in complex seas, close to the coast, or in strong western boundary currents. In the latter case, these will be of less importance since the SNR will be relatively high. We can also anticipate that the impact of waves may be mitigated within the SKIM on board processing (OBP) implementation.

7.1.1 Assessment Strategy

Traditionally, implementing performance simulation tools the analyses are carried out using a Monte-Carlo procedure to infer the mean value of errors and, most importantly, its variance, from many realisations that are randomly perturbed. However, it is often the case that end-to-end simulations are limited in their ability to obtain many different realisations of a given scenario because of the high computational burden. Nevertheless, end-to-end simulations provide access to any level of data products and the use of resolved data products can be used to infer uncertainty and the effective number of radar looks. These are key components that are necessary to build performance estimates.

This approach has been validated by a direct comparison of the SEEPS performance from a single simulation with the Monte-Carlo approach. At Level-1b, Monte-Carlo analysis was performed with one hundred simulations using the same orbit parameters and location and independent surface realisation under identical sea state conditions. At Level-2, random perturbations are included in the simulations as a function of both the radar Doppler sensitivity and those related to geophysical variability imposed on different input test scenes through scenario definitions.

The performance analysis is based on a SKIM canonical scenario, where moderate sea-state conditions are used with a surface wind speed of 7 m s^{-1} and a H_s of 2 m (approximate mean global wind speed and H_s). This scenario is designed to verify compatibility with the assumptions used by the performance models developed for SKIM, independently from the



instrument supplier and the end-to-end simulation teams. Additional scenarios impose geophysical perturbations for low and high sea state/wind speed conditions are used to explore SKIM performance. The instrument and platform configurations do not account for any sources of noise (e.g., pointing error) and the corresponding system parameters are used in the processing chain with a perfect knowledge.

The core of the SKIM assessment campaigns relies on the generation of scenarios showing variations from the canonical conditions in order 1) to quantify the sensitivity of the SKIM measurements from a complete system viewpoint and 2) to cover a representative range of expected geophysical conditions (as required to attain Scientific Readiness Level (SRL) = 5). This step-by-step approach is commonly used in Earth observation radar system analysis and includes any deviation related to platform, instrument and geophysical ocean-surface conditions. In particular, any deviation from the canonical scenario not well addressed by the models, such as non-Gaussian effects impacting the SKIM signals, can be properly assessed through end-to-end simulations to ensure a full assessment analysis.

7.2 End-to-End Mission Performance Tools

Given the large range of scales to be covered, from the 8 mm Ka-band wavelength to the full global view (i.e. from the radar pulse repetition interval (PRI) of ~30 microseconds to the five-year life of the mission), the SKIM end-to-end simulations have been organised around the development and application of complementary tools. This approach is similar to that developed for the radar Surface Water Ocean Topography Mission and includes both forward and retrieval models.

The SKIM End-to-End Performance Simulator resolves the ocean-surface motion at the timescale of the Pulse Repetition Interval and at spatial scales around 1 meter. Hence it can resolve most of the wind-generated waves, including a proper parameterisation of sub-metre roughness and motion (see the Geometry, Scene Generator and Instrument Models, SEEPS TN-1 report). SEEPS is capable of producing both surface velocity and wave spectral data up to Level-2c products for a segment of the SKIM orbit with a duration of up to a couple of minutes (owing to the computational burden).

The large-scale Level-2 parametric SKIMulator (Gaultier, 2019) is designed to produce surface velocities – the primary output of the SKIM mission. It uses SEEPS output to develop an uncertainty model parameterisation. It resolves spatial scales around 1 km, including Total Surface Current Velocity (TSCV), sea level and sea state (not individual wind-generated waves), and considers a satellite pass as a ‘snapshot’ (Gaultier, 2019). The SKIMulator was configured for several regional areas and with a global configuration for durations of up to one year. The output is used to verify the general behaviour of TSCV retrievals in a wide range of realistic geophysical conditions. SKIMulator is open source code and sufficiently portable as to be run by scientists on desktops or a small cluster, facilitating the analysis of output data, generation and propagation of uncertainty estimates and production of simulated TSCV maps. This approach is important because SKIM provides, for the first time, a new type of Doppler ocean data product. An open source tool will accelerate the uptake of SKIM data by the user community.

The IFREMER Remote Sensing Sea Surface Simulator (R3S, Nougier, 2019) is deep simulator designed to study the interaction of radar electromagnetic waves with the ocean surface. At high spatial and temporal resolution. The R3S tool simulates wave facets

and radar interactions at a resolution of ~80 cm. Components in the scene and instrument module are inherited from the Scalian SeaMotion radar simulation tool developed in 2007 by Scalian Alyotech, IFREMER and CLS. SeaMotion has been extensively validated by many different users. R3S and SEEPS were verified to perform identically using a number of reference test scenarios (TN-13 - SEEPS Validation Report).

The TUDelft OceanSAR simulator is an adaptation of the simulator developed in the context of the ESA MAC-SAR study (Lopez-Dekker et al., 2015) based on the simulation framework of Marull-Paretas (2013) originally designed to assess the retrieval of TSCV using the next generation of C-band SAR systems. It applies the same physical principles and approximations used by Nougquier (2019) but is optimized for Monte Carlo style simulations, trading off some fidelity in the simulation of system aspects for execution speed. This is complementary to the computationally intensive R3S implementation.

SKIM wave products have been assessed using R3S and the TUDelft OceanSAR simulators.

The SKIM nadir beam is considered separately and has been evaluated using pre-existing tools (Boy et al., 2017) developed over many years in support of nadir altimetry including the Sentinel-3 and Sentinel-6 altimetry missions (see Section 7.1.3). A numerical Doppler echo model has been adapted specifically to SKIM based on the approach used for Sentinel-3 (CLS, 2011) that has been validated using in-orbit Sentinel-3A an B data. This processing performed is fully described in SKIM Team (2019b).

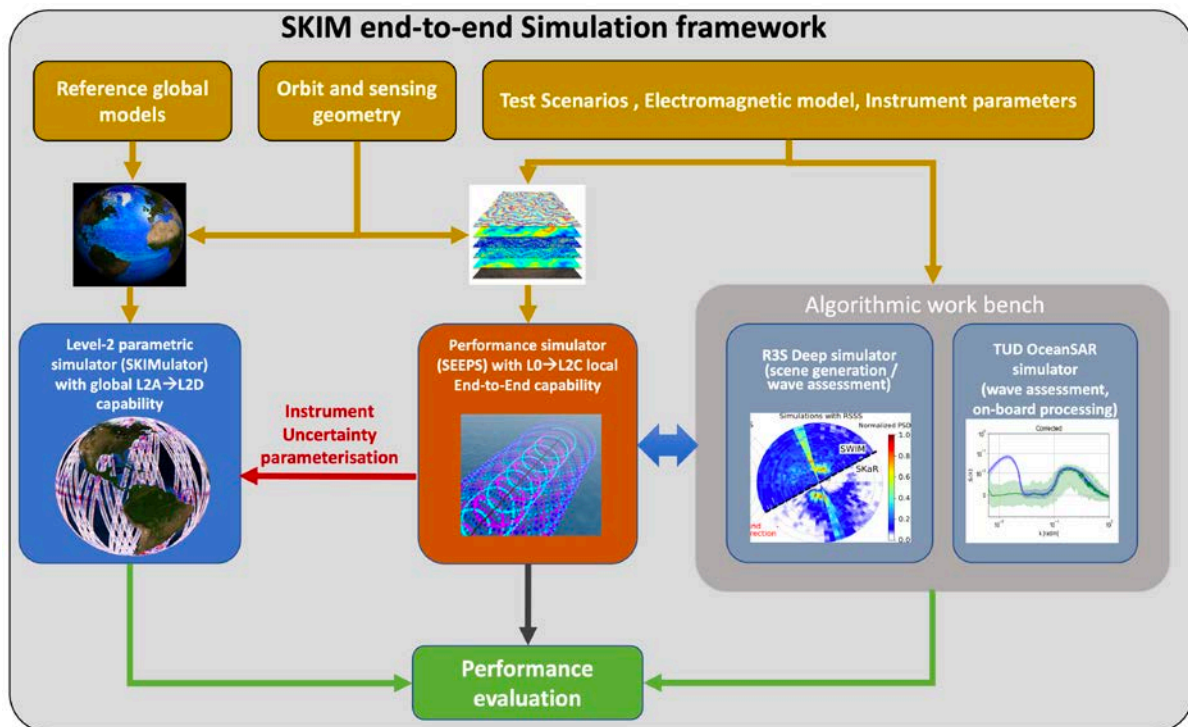


Figure 7.3. SKIM mission simulation framework for ocean surface velocity depicting the interconnection between the two tools. Each tool is designed to perform a different functionality in the performance assessment: SEEPS focussing on the detailed Level-1 instrument performance while SKIMulator is used to perform Level-2 geophysical product assessments at the global and regional scale for up to one year.

Fig. 7.3 shows how the SEEPS and SKIMulator tools are integrated into a consistent end-to-end simulation framework. SKIMulator is capable of using the Level-1 performance estimated from SEEPS as input to drive the Level-2 product performances at global level. The coherency between SEEPS and SKIMulator was verified using the reference scenarios, as defined by the science team (see Table 7.1). This verification phase is applied on Level-2c simulated data over a segment of the SKIM orbit that is common to both simulators. This analysis ensures full coherency between the components of the SKIM simulation framework in terms of 1) reliability of the underlying assumptions and 2) consolidation of the performance figures along the full set of simulated products. This is a strong asset for the SKIM end-to-end simulation framework as the assumptions used by SKIMulator are verified.

All SEEPS, R3S and the TUDelft OceanSAR simulators share the same physical assumptions (i.e., essentially comparable forward electromagnetic models), although implemented in different ways. R3S was used to confirm the validity of key parts of the SEEPS forward model, and explore the limitations of specific assumptions, instrument configuration and processing chain.

The SEEPS models were used to confirm the validity of key parts of the SEEPS forward model, and explore the limitations of specific assumptions, instrument configuration and processing chain.

7.2.1 SKIM End to End Performance Simulator (SEEPS)

SEEPS includes a complete set of end-to-end simulation modules, from the observation scenario of ocean currents, the instrument transfer function to the retrieved geophysical parameters. It is configured to easily implement any SKIM option in terms of system and instrument configurations: orbit, chronogram, incidence angles, number of horns, etc. The performance analysis is carried out on the basis of a consolidated breakdown of the error sources and uncertainties (systematic, random, geophysical, etc.) to provide a comprehensive view of SKIM mission performance figures to the user community.

Figure 7.4 depicts the SEEPS high-level architecture and an example of output simulation data. Compared to a classical ‘static scene’ simulator, for a Doppler radar mission the rapid motion of the sea surface needs to be resolved which requires a combined scene generation and instrument simulation approach. This avoids storing large amounts of data due to the range oversampling prior to the radar chirp convolution step. Components in the scene and instrument module are inherited from the SCALIAN SeaMotion radar simulation tool developed in 2007 by Scalian Alyotech, IFREMER and CLS. SeaMotion has been extensively validated by many different users.

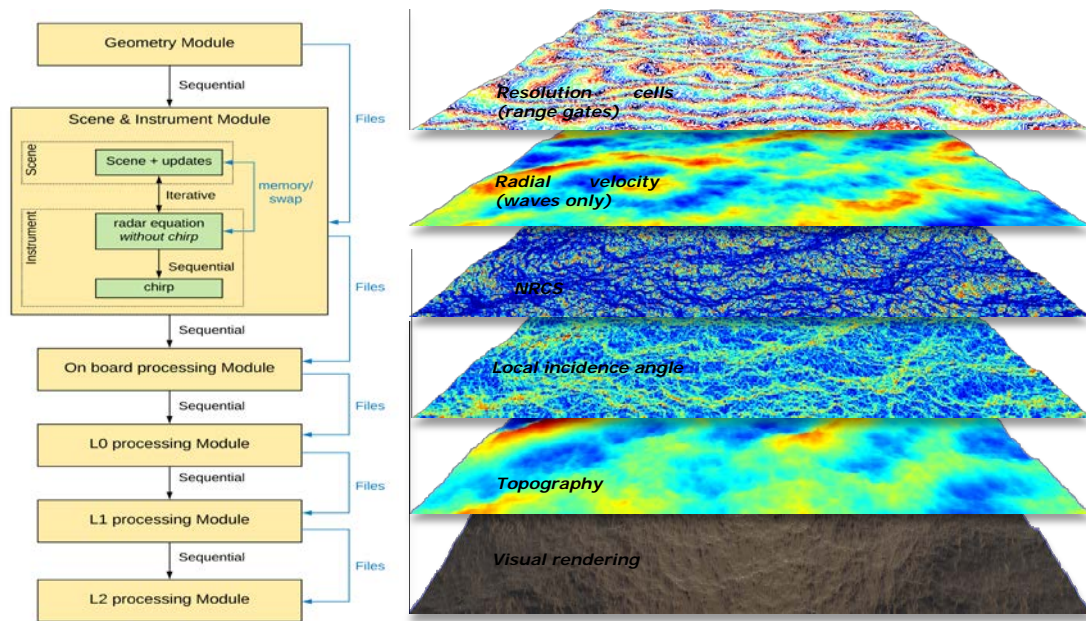


Figure 7.4. Left: Flow diagram of SEEPS processing architecture. Right: example layers of simulated data that are combined to assess performance.

7.2.1.1 Scene Generation and Electromagnetic Field Backscatter

SEEPS was designed to accurately reproduce the temporal behaviour of backscattered ocean signals for any accessible viewing geometry and without limiting hypothesis on the instrument parameters. Generating realistic phase-resolved (complex number I and Q) signals requires controlling the topography and kinematics of the illuminated surface over a wide range of time and space scales. Without resorting to strong simplifications, this can only be achieved by generating random realisations of the sea surface respecting prescribed statistics. Practically, this means setting and animating a mesh at given space and time resolutions, representing the surface topography and kinematics.

The general frame for scene generation involves a two-scale model. Waves contributing to signal modulations (in amplitude and Doppler) must be resolved in time at the pulse repetition frequency (PRF) of 32 kHz. In space, they must be resolved at the resolution of the instrument range resolution (around 4 m), covering a 32 ms cycle and the area swept by the footprint.

For the range of low incidence angles considered for SKIM, the dominant backscattering mechanism is quasi-specular. For the sea surface and at centimetric (or shorter) wavelength, it is conveniently modelled in the frame of the high-frequency limit Kirchhoff Approximation (Nouguier et al., 2019). The facet size of the scene is much larger than the wavelength and the waves contained in a facet are statistically accounted for through their power spectrum. This leads to an average normalised radar cross section (NRCS), expressed as σ^0 . The NRCS of the illuminated area is then computed as the sum of the contribution of the facets in the footprint, taken at the appropriate local angles. This approach is equivalent to the Two Scale Model (Alpers and Hasselmann, 1978), as it relies on partitioning the wave spectrum into resolved and unresolved ranges.

In SEEPS, the time-resolved complex signal is computed – rather than the NRCS only – by updating both its amplitude and phase for each pulse and in all range gates. The complex contribution from a facet is initialised in the assumption of Rayleigh-distributed amplitudes following the prescribed average NRCS. Its subsequent time evolution from pulse to pulse is then generated by updating the satellite position and the surface topography (thus modifying the pulse round-trip duration) and adding a phase shift resulting from sub-grid motions due to waves and surface current. The backscattered field, for a given pulse and range gate, is then obtained by adding the updated complex contributions from all the facets lying in the considered resolution cell. The Concept And underlying models of the SEEPS scene module is fully described in TN-1 of the SEEPS documentation package.

7.2.2 Level-2 Global Coverage Parametric SKIM Simulator

The Level-2 science simulator (SKIMulator) has been developed in a complementary manner to the SEEPS end-to-end simulator. Both SKIM industrial design configurations were used to simulate a full year of SKIM acquisitions, representative of SKIM Level-2 products. SKIMulator simulates SKIM geometry and parameterisation of geophysical and related uncertainty signals based on input from the MITgcm global ocean-circulation and sea-ice model, with a simulation at a horizontal resolution of 1.5 km (Torres et al., 2018). This model was chosen because it is the only one available globally at such a high resolution incorporating very shallow (<0.5 m) surface layer ocean currents. Its biases and properties are well known, with a particular overestimation of internal wave energy and an underestimation of near-inertial oscillations (Fig. 2.9, see also Yu et al., 2019).

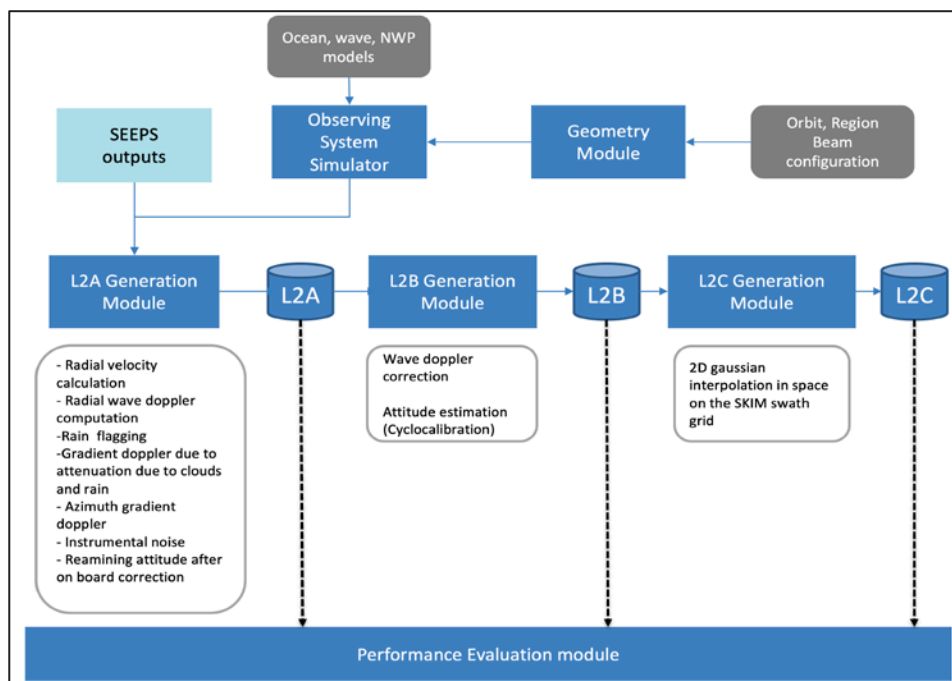


Figure 7.5. Architecture of the Level-2 global coverage parametric SKIM simulator (SKIMulator). (OceanDataLab)

Given the prohibitively high cost of running a wave model at the same resolution, moments of the wave spectrum (eq. 6.2) were obtained from a spectral discretization in 24 azimuth



and 31 frequencies (0.037–0.71 Hz) and provided at 3 km (for regional grids) to 25 km (globally) resolution in order to test specific regional effects associated with gradients of the wave field. In both cases, the version 6.05 of the WAVEWATCH III® (2018, hereinafter WW3) numerical wave model was used. This includes interaction of waves and sea ice (Ardhuin et al., 2018), forcing by winds from the operational analyses of the European Center for Medium range Weather Forecasting (ECMWF), and the MITgcm ocean-circulation model for the surface current, sea level and sea ice parameters.

The SKIMulator is implemented as a series of interconnected modules (Fig. 7.5). The geometry module generates SKIM pseudo-measurements based on MITgcm model data for a chosen region (including the entire globe, the Equatorial Atlantic, Gulf Stream or Fram Strait), a specific orbit choice (here we show results for Concept A and Concept B), and different SKaR beam configurations. The retrieval step starts from simulated Level-2b U_{GD} and nadir beam parameters. More details and illustration of the different processing steps are given by Gaultier (2019).

7.2.2.1 Test Scene Generation

The SKIMulator observing system simulator module samples the input modelled fields according to the rotating SKIM footprint geometry as input U_{CD} measurements. The wave Doppler component is then computed from modelled directional Stokes drift and added to the U_{CD} field to generate a Level-2a U_{GD} simulated product for each footprint. Uncertainties are then computed and added to the Level-2a U_{GD} as follows:

- **Instrumental error:** pulse-pair instrument noise is based on a parameterisation of validated SEEPS outputs for the reference average scenario, as a function of the NRCS simulated using WW3 outputs (mean square slope, mss , current, wind, Stokes drift) for each azimuth and beam angle. The SNR of the reference scenario and the SNR for each footprint is constructed as the reference scenario SNR multiplied by the ratio of the NRCS and the NRCS of the reference.
- **Radial wave Doppler:** parameterisation from ECMWF wind (direction and norm), H_s , radial Stokes drift, mss . The coefficients are machine-learned using the WW3 model outputs and parameterised outputs from SEEPS.
- **Pointing error simulation:** the remaining component of the attitude (after correction from the AOCS on board) is simulated. Two components are considered. The first one corresponds to the error in the estimation of the attitude by the AOCS which corresponds to a power spectrum provided by industry. The second one is implemented as fine-pointing (Chapter 6) derived from thermos-elastic deformation (TED) analysis from industry, which depends on the azimuth, the time within the orbit and the season.
- **Rain flagging:** two different methods are used – one for regional and one for global runs. For the regional method, an ensemble of rain scenes are provided on a Global Precipitation Mission (GPM) swath for each region and each time of the day. Scenes are picked randomly for each orbit and interpolated on SKIM swath as the rain is assumed to be decorrelated on the scale of SKIM revisit time. At global scale, rain rate from the Integrated Multi-satellitE Retrievals for GPM (IMERG) data set is used.



- **Rain and cloud attenuation:** similarly to the rain flag, an ensemble of scenes of gradient of radar path integrated attenuation are provided on a GPM swath for each region and each hour of the day. Scenes are selected randomly for each orbit and interpolated on the SKIM swath. The gradient (in dB) is converted into a mis-pointing and into a Doppler velocity (in m s^{-1}). At global scale, a proxy is used since the GPM scenes are only available for regional simulations at this time. Instead, a mean relationship between rain rate from the Integrated Multi-satellitE Retrievals for GPM (IMERG) data set and associated path integrated attenuation (PIA) is used.
- **NRCS gradient:** A probability density function (PDF) of along-track gradient of nadir NRCS has been derived from the AltiKa altimeter. The PDF is stretched to compute the corresponding gradient for beam at 6 and 12 ° (LOPS, 2019a). A random error is generated from the PDF and converted into an azimuthal gradient. The corresponding mis-pointing is computed and converted into a Doppler velocity (in m s^{-1}). This is fully described in LOPS (2019a,b).

This approach provides a well-controlled and computationally efficient solution that is capable of generating more than a year of global coverage Level-2a pseudo-products with the same characteristics as SEEPS output.

To verify that the SKIMulator Level-2a U_{GD} pseudo products are identical to those generated by SEEPS (within the expected uncertainty of computational numerics), specific test scene scenarios (Table 7.1) have been developed and run through both simulators.

7.2.2.2 SKIMulator Performance Evaluation Metrics

Performance metrics (M) for the SKIMulator are fully documented in SKIM-PE TN-30. In summary these are:

- M1: The RMS uncertainty of Level-2a and Level-2b radial current velocity when compared to truth.** The RMS will contain the difference between the true radial velocity (MITgcm plus Stokes drift projected on the azimuth, U_{true}) and the simulated radial velocity ($U_{skimulator}$), which includes all of the uncertainties discussed in Section 7.2.2.1. This metric will give an estimate of the level of noise expected on the measurement before and after the inversion.
- M2: RMS difference between the simulated Level-2c compared to truth.** The requirement is for Level-2c along-track and across-track components $\leq 0.15 \text{ m s}^{-1}$ or 15% (whichever is greater) and a goal of $\leq 0.1 \text{ m s}^{-1}$. As the geometry is of importance for the Level-2c reconstruction, the metric will be evaluated both the across-track and along-track velocity. The standard deviation averaged along track and as a function of the across track direction can be computed for the along track and the across track velocity. This metric can be computed on the reconstructed error-free velocity as well as for the velocity with all uncertainties considered. From these two computations, we can deduce the uncertainty resulting from the optimal interpolation alone. Then, the RMS will be computed on the eastward and the northward component of the velocity, in order to get results comparable with the velocity from the Level-2c product. Another interesting way to look at the reconstructed velocity is to compute the RMS of the direction and the norm of the velocity.



- M3: Percentage of the ocean surface covered when TSCV uncertainty is $\leq 0.15 \text{ cm s}^{-1}$ (goal: $\leq 0.1 \text{ cm s}^{-1}$) or 15% (whichever is greater).** The requirement is for at least 70% coverage. This metric is computed over a representative 30-day period and eventually a 1-year period mapped on a $1^\circ \times 1^\circ$ latitude longitude grid (for computational efficiency).
- M4: Percentage of the ocean surface covered when the SNR $> 3\text{dB}$.** The SNR is computed as the RMS of the truth (input test scene) divided by the RMS difference between the simulated Level-2c compared to truth. This metric is computed over a representative 30-day period and eventually a 1-year period mapped at a resolution of $1^\circ \times 1^\circ$ latitude longitude.
- M5: RMS difference between the wave spectral moment $P=[0, 1, 1.5 \text{ and } 2]$ compared to truth.** $P_0=H_s^2$, P_1 =wave orbital velocity variance, $P_{1.5}$ =Stokes drift and P_2 =mss. The requirement is $<10\%$ for the P^{th} moment (which efficiently integrates across the full spectrum from $\leq 30 - 500 \text{ m}$) relative to the P moment in the dominant direction (which focuses the requirement in directions for which there is a significant signal). This is consistent with the use of wave measurements in the U_{WD} retrieval algorithm.
- M6: Total RSS uncertainty of sea surface height computed for the nadir beam.** The requirement is $\leq 3.2 \text{ cm}$ after all geophysical corrections are made.
- M7: Total RSS uncertainty of significant wave height H_s , computed for the nadir beam.** The requirement is $\leq 9 \text{ cm}$ after all geophysical corrections are made.

This suite of metrics provides a simple baseline evaluation of SKIM performance at Phase A. In future, additional metrics must be defined and computed to further evaluate the performance of the SKIM instrument and output products.

7.2.3 Simulator Test Scenario Descriptions

Test scenarios are defined for both TSCV and wave simulations in the following sections.

7.2.3.1 TSCV Test Scenario Description

Table 7.1 includes the reference scenarios for simulations up to Level-2c cover ‘best’, ‘average’ and ‘worst’ case sea-state conditions, assuming a constant current, with either zero, constant or linearly variable atmospheric perturbation respectively.

The reference scenarios have been selected to stress the simulations at different levels and to ensure the consistency between the SEEPS uncertainty estimators and SKIMulator parametric error budget for a realistic and representative range of geophysical conditions using a minimum amount of computationally intensive simulations.

The best-case scenario sea-state conditions has been selected to be representative of the mean global ocean and atmosphere conditions. It uses a moderate wind of 7 m s^{-1} that is the most frequent wind speed over the global ocean and no swell. These are conditions for which the wave-Doppler retrieval model performs best. A significant surface current of 1 m s^{-1} is included (noting that the maximum surface current outside tidal regions is about 2.5 m s^{-1}) that is directed in the azimuth direction where instrument error is minimal (along track).

The wind responsible for the wave Doppler is orthogonal to the current direction, meaning no wave-Doppler correction is to be expected.

	Average	Best	Worst	Low wind	Average wind	High wind	Along track	High along-track
Wind speed (m s ⁻¹)	7	7	15	3	7	15	7	15
Wind direction (°)	90	90	90	90	90	90	0	0
Current speed (m s ⁻¹)	0.5	1	1	0	0	0	0	0
Current direction (°)	45	0	90	0	0	0	0	0
Swell height (m)	1.5	0	4	2	0	0	0	0
Swell direction (°)	45	0	90	45	0	0	0	0

Table 7.1. Reference scenarios. Here the azimuths are relative to along-track. Unless otherwise specified, all results are shown for the average-case scenario that best represents the mean global ocean atmosphere condition.

The worst-case scenario includes a relatively strong wind of 15 m s⁻¹ blowing in the same direction as a pre-existing significant swell and the underlying surface current. This results in a large wave Doppler signal with larger uncertainty that directly translates in an error on the retrieved surface current. The direction of the surface current is cross track where the instrument error is maximum. A very large swell height of 4 m together with a 15 m s⁻¹ wind leads to a significant wave height above this level in a fully developed sea. The worst-case imposes inhomogeneous backscatter across the SKIM footprint azimuth and range introducing extra non-geophysical Doppler shift uncertainty.

The average- case scenario includes the mean ocean-atmosphere situation for wind, current and swell over the global ocean. The relative direction between the waves and the current is half way (45°) between the best case (90°) and the worst case (0°).

In addition, several regional reference scenarios have been used to verify the error budget sensitivity at Level-1b L1B_U products to specific critical parameters such as low winds, high winds and both waves and current aligned with the along track direction. These are reported in later Sections.

7.2.3.2 Wave Test Scenario Description

We consider two wave test scenarios. In the first scenario, directional wave spectra retrieved by CFOSat's SWIM instrument are compared with the outputs of the R3S scientific workbench, assuming the instrument parameters of SWIM and SKIM, respectively. The R3S simulation was driven by simulated WW3 spectra for the time and location of the SWIM acquisition. This comparison serves two purposes: first, it validates that the forward modelling part of the simulation tools using existing observations; second it showcases the improvement achieved by SKIM with respect to SWIM.

In the second scenario we evaluate in detail the wave-spectrum retrieval performance for the average-case scenario specified in Table 7.1, including wind sea and swell. In this case we simulated SKIM cycles for the 12° beam with azimuth angles at 45° (the swell direction) and 90° (dominant wind–wave spectrum direction).

Each simulation was repeated in a Monte Carlo approach 100 times to allow the computation of uncertainty statistics. One specific purpose of these simulations to illustrate the performance gain that results from the use of SKIM Doppler-resolved data.



7.3 Level-1b Performance

This section presents the system and instrument Level-1b performance achieved by each mission concept developed in Phase A as presented in Chapter 5. It compares performance against requirements and provides additional information to explain and justify key performance parameters.

7.3.1 Nadir Altimetry Performance

The performance of the nadir beam is equal for both concepts. Fig. 7.5 relates the range measurement precision of the SKIM nadir beam to the Sentinel 6 SAR mode and AltiKa LRM mode performance for 16 and 32 pulses per burst as a function of H_s . The SNR of the nadir beam is 40 dB for a sigma naught of 11.5 dB, computed for a wind speed of 7 m s⁻¹. Fig. 7.6 (left) shows the range estimator random error (range noise) for a 1 second period as a function of H_s for the SKIM Nadir beam. Sentinel-6 and AltiKa altimeter performances are shown for comparison. Fig. 7.6 (right) shows range estimator random error (range noise) for a 1 second period as a function of SNR for $H_s=2$ m and for SKIM Nadir beam. Both these plots confirm that the SKIM nadir beam range noise requirement is met with significant margin.

Range bias stability of the nadir beam is related to ageing and thermal environment of the non-calibrated path, i.e. the variations over mission lifetime of the initial characterisation performed on-ground. This variation may be partially mitigated by an external calibration process (e.g. transponder). As a worst case, the long-term stability of the un-calibrated components (by the instrument internal calibration) is fully allocated to the bias stability budget.

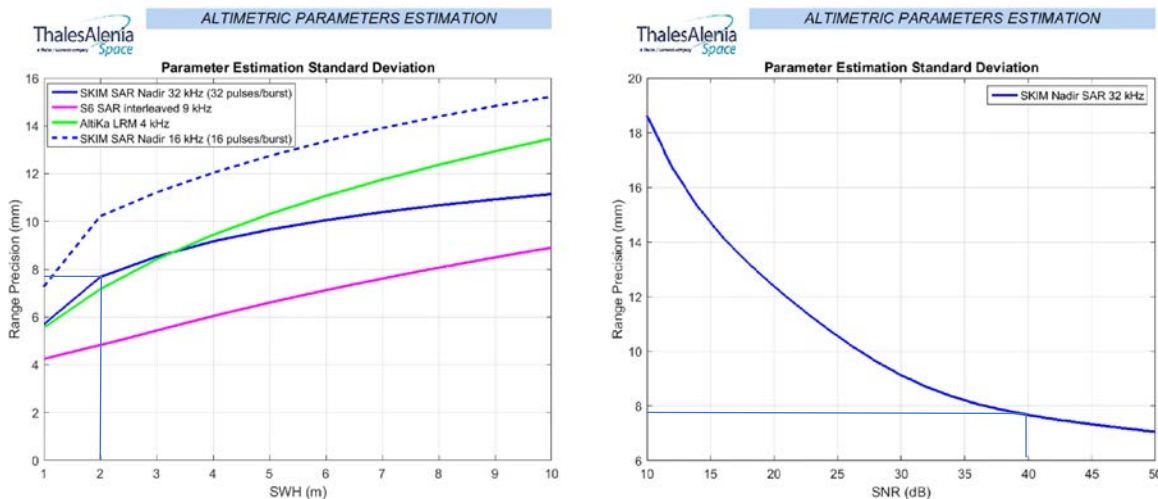


Figure 7.6. Nadir beam performance of the SKaR instrument compared to other altimetry missions in relation to significant wave height (H_s) (left) and signal to noise ratio (SNR) (right).

Contributors to the long-term range bias drift of the altimeter function are:

- Antenna conducted and radiated propagation delay stability: 6 ps = 0.9 mm
- Local oscillators frequency stability that is negligible
- Duplexer long term drift of differential group delay (1 ps = 0.15 mm)



- Harness propagation delay stability between the duplexer and the antenna port (1 ps = 0.15 mm)
- Reference clock stability. As for reference altimetry missions (Jason series, Sentinel-6), the drift of the reference clock of the altimeter is monitored during the mission duration (stability better than 10^{-9} yr^{-1} required) via the Global Navigation Satellite System (GNSS) receiver (reference clock transmitted to the GNSS).

In conclusion, the range bias stability is expected to be better than 1 mm yr⁻¹.

Requirement	Specification	Concept A/B
Nadir beam range noise at a significant wave height of 2 m, wind speed of 7 m s ⁻¹ , at 1 Hz	≤1.5 cm	≤1.2 cm
Nadir beam range bias stability over the mission duration	≤2 mm/year	≤1 mm/year
σ ₀ dynamic range covering ocean, ice infested and ice leads	0 dB to +50 dB	0 dB to +50 dB
Signal-to-noise ratio of nadir beam Doppler processed echoes over ocean and sea-ice surfaces, for the most powerful range gate of the most powerful Doppler bin	≥40 dB	43 dB (σ ₀ = 12dB)
Total absolute accuracy of nadir pointing beam NRCS	≤ 1 dB	≤ 0.9 dB TBC (0.7/0.2 dB bias/random) Better than off-nadir beams

Table 7.2. Nadir beam Level-1 performances and requirements

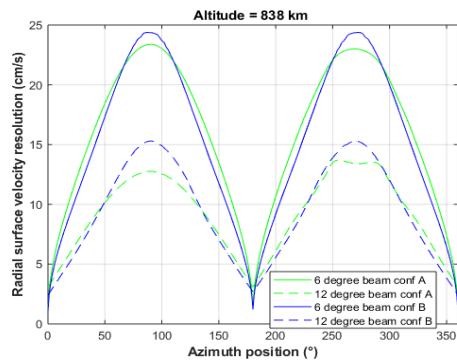
A preliminary budget has been produced for the Absolute Radiometric Accuracy (ARA) of the nadir beam, based on heritage from CFOSat SWIM. The main contributors to the ARA budget are the knowledge of the instrument gain estimated with the internal calibration and the knowledge of the antenna pattern characterised on-ground. Errors include bias, random and thermo-elastic effects in-orbit. Random errors are considered at 3-sigma. The overall budget sums to 0.9 dB, primarily driven by biases rather than random errors.

Given that SKIM will require in general a tighter control of biases, including better knowledge of the antenna patterns, it can be expected that this budget can be improved with further work in the next study phases. The performances of the nadir beam are summarised in Table 7.2.

7.3.2 Pulse-Pair Phase Performance

7.3.2.1 Performance estimation

For the off-nadir beams, the core of the Level-1b performance evaluation is the measurement precision to radial surface velocities. This precision varies with the azimuth angle of the conical scan. To second order, the variation of the performance also depends on variations in the antenna pattern, which explains the small differences in performance between the two concepts, each having adopted a different flight configuration for the antenna.



Azimuth	Concept A 6°/12° (cm s ⁻¹)	Concept B 6°/12° (cm s ⁻¹)
3°	4.26/ 3.53	3.72/ 2.85
45°	17.29/ 9.54	15.98/ 9.34
90°	23.38/ 12.77	24.36/ 15.30
135°	17.26/ 9.50	15.69/ 9.53
357°	4.27/3.53	3.72/ 2.85

Figure 7.7. Radial surface velocity resolution for Concept A and B. Table 7.3. Radial surface velocity resolution.

The performance of the radial surface velocity measurement was first established using a simplified analytical model provided by the instrument supplier. The performances obtained are shown for both the 6° and 12° beams and for both configurations in Fig. 7.7 and Table 7.3. Both concepts A and B meet the requirements. The beam-level precision requirement does not sufficiently constrain the system design. Indeed, system design parameters such as the rotation speed of the scanner and the beam placement will affect the sampling pattern of the beams in the swath, and therefore the SKIM Level-2c product performance. To capture some of the complexity of the beam placement optimisation without having all the Level-2c performance evaluation as part of the design loop, a theoretical design metric has been introduced as a Level-1 requirement for SKIM. The requirement is to achieve a combined uncertainty of better than 7 cm s⁻¹ on both the along- and across-track components of the surface velocity vector, after having combined all the line-of-sight measurements collected in any 30 by 30 km square within the swath covered by SKIM.

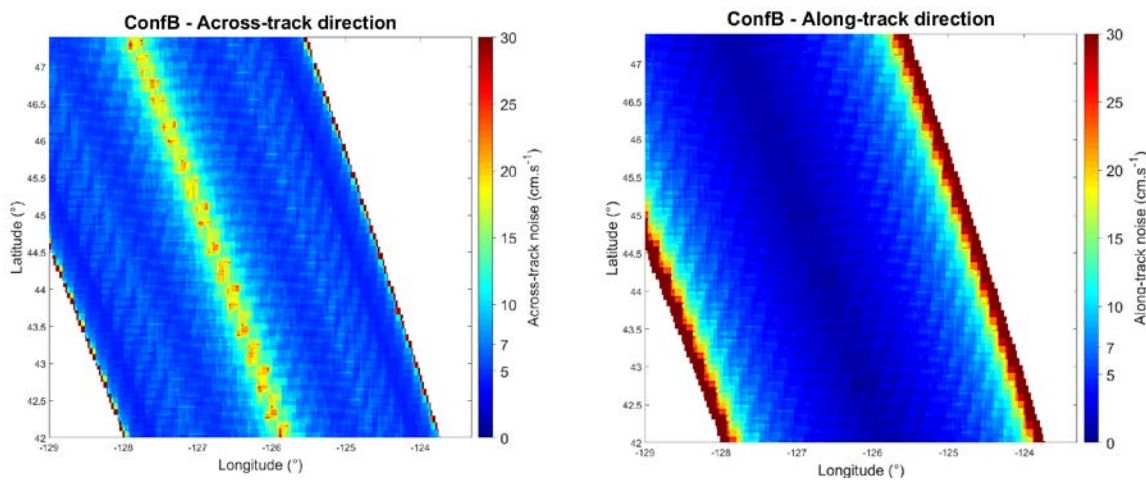


Figure 7.8. A 2-dimensional Level-1b performance metric has been devised for SKIM that considers the SKIM sampling pattern. The metric computes the sensitivity obtained for the along- and across-track components of a surface current, after vectorially combining all line of sight measurements in a sliding window of 30 by 30 km. Near the edge of the swath it is challenging to measure the along-track component, whereas close to the ground track it is challenging to measure the across-track component. Left: Concept A. right: Concept B.

Results are shown in Fig. 7.8. While this two-dimensional performance requirement allows to make qualitative comparisons between different design solutions, it is impossible at this stage to establish a quantitative traceability to higher level science performance requirements. Since the analysis against this 2D performance metric has been instrumental in the dialogue between engineering and science teams to establish the requirements reported in chapter 6, some results are shown here.

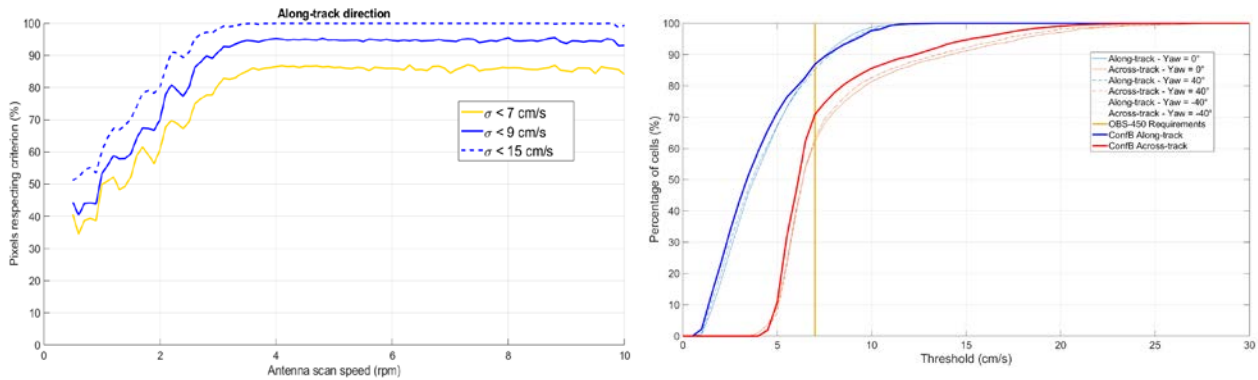


Figure 7.9. Left: The 2D performance criterion shows that for a given beam layout, performance improves with antenna rotation speed, but this improvement saturates at a certain level. Right: While for individual beams performances at a particular antenna position can differ between the two configurations, both concepts achieve a similar performance against the 2D requirement.

Fig. 7.9 (right) shows the percentage of 30 km cells in the swath with a performance above a specified threshold, for both consortia, and including multiple yaw steering attitudes for consortium A. Only minor differences in performance can be observed between Concept A and Concept B. Even though differences in performance can be observed between Concept A and Concept B for particular azimuth angles (both concepts being compliant), at swath level these differences are insignificant.

7.3.2.2 Performance Validation at Level-1b with SEEPS

Since the SEEPS simulator fully implements the pulse-pair technique used in the instrument, the performance of the Doppler velocity measurements can be simulated with more realistically simulated ocean targets and compared with the analytical performance models used by the instrument designers to verify their assumptions.

Fig. 7.10 and Fig. 7.11 plot the simulated outputs from the SEEPS for a scenario of moderate wind speed (7 m s^{-1}) with across- and along-track wind directions, together with the estimates from the theoretical models. The theoretical models and the simulations are in very good agreement. Both show differences in performance between the two concepts, depending on the azimuth angle. Over most parts of the swath these differences will cancel out however, as explained in the previous section.

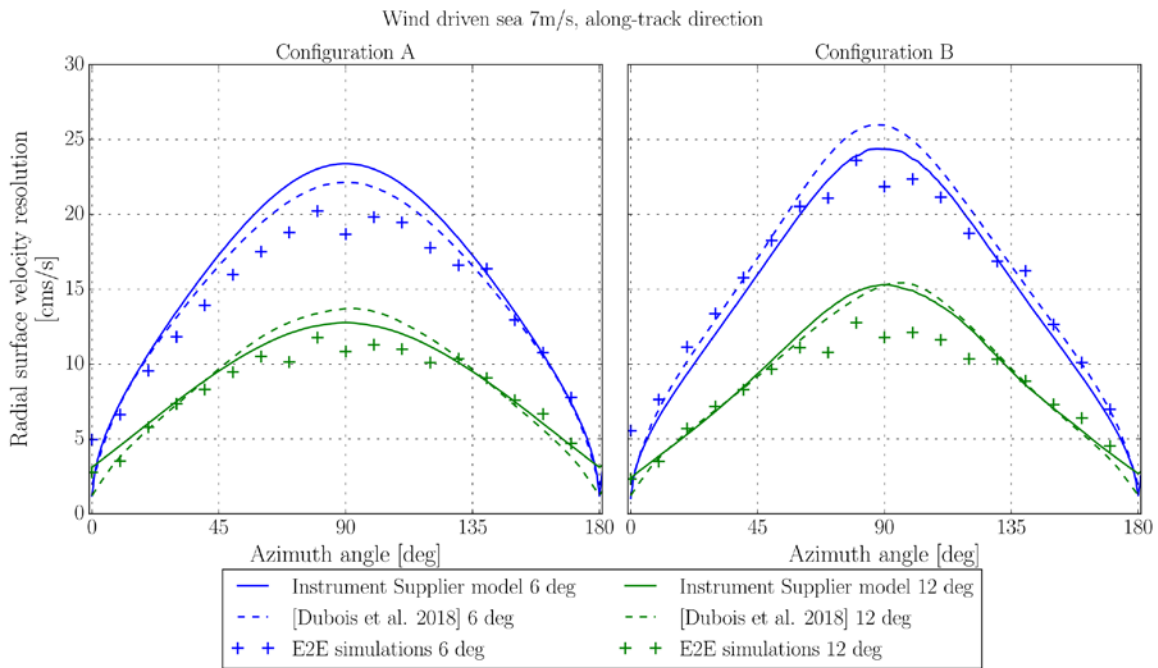


Figure 7.10. Radial surface velocity performance (rms error) as a function of azimuth angle for the along-track wind scenario (wind speed is 7 m s^{-1}). Left: Concept A. Right: Concept B.

The mean Level-1b radial surface velocity has a range dependency (whose main contribution lies in Non-Geophysical Doppler effects). In order to compare the precision obtained with the theoretical models with the SEEPS simulations, the Level-1b performance figures shown in Fig. 7.10 are computed on range-detrended data, which is equivalent to a perfect correction of the range Doppler effects. The Level-2 performance figures reported in following sections include errors in the correction of the range Doppler effects.

While the instrument supplier model and the end-to-end simulations results are generally in good agreement, near along-track and near across-track values show some differences. These are well understood and due to the following effects:

- The theoretical models calculate the precision based on the Doppler bandwidth, which increases with azimuth angle away from the along-track direction. This is partially offset by a reduction in the effective number of looks in the along-track direction, since the spacecraft motion is aligned with the range window. The second effect is mitigated by a co-registration processing step. The theoretical models assume this mitigation to be perfect, whereas the end-to-end simulation includes limitations due to the implementation of the processing algorithm (sampled signal vs. continuous signal, use of estimates vs. use of true values, ...).
- The magnitude of the range resolved pulse-pair product experiences modulations related to the backscatter coefficient (see Eq. 31 of Nouguier et al. 2018). Also, the phase of the range resolved pulse-pair-product experiences modulations related to the Doppler gradient and to the surface vertical velocity (see Eq. 33 of Nouguier et al. 2018). In a close combination with instrumental effects and the platform motion, both of these modulations are affected by moving waves, which can produce either a lack

or an excess of RMS., depending on the relative orientation of the waves, as illustrated in Fig. 7.11

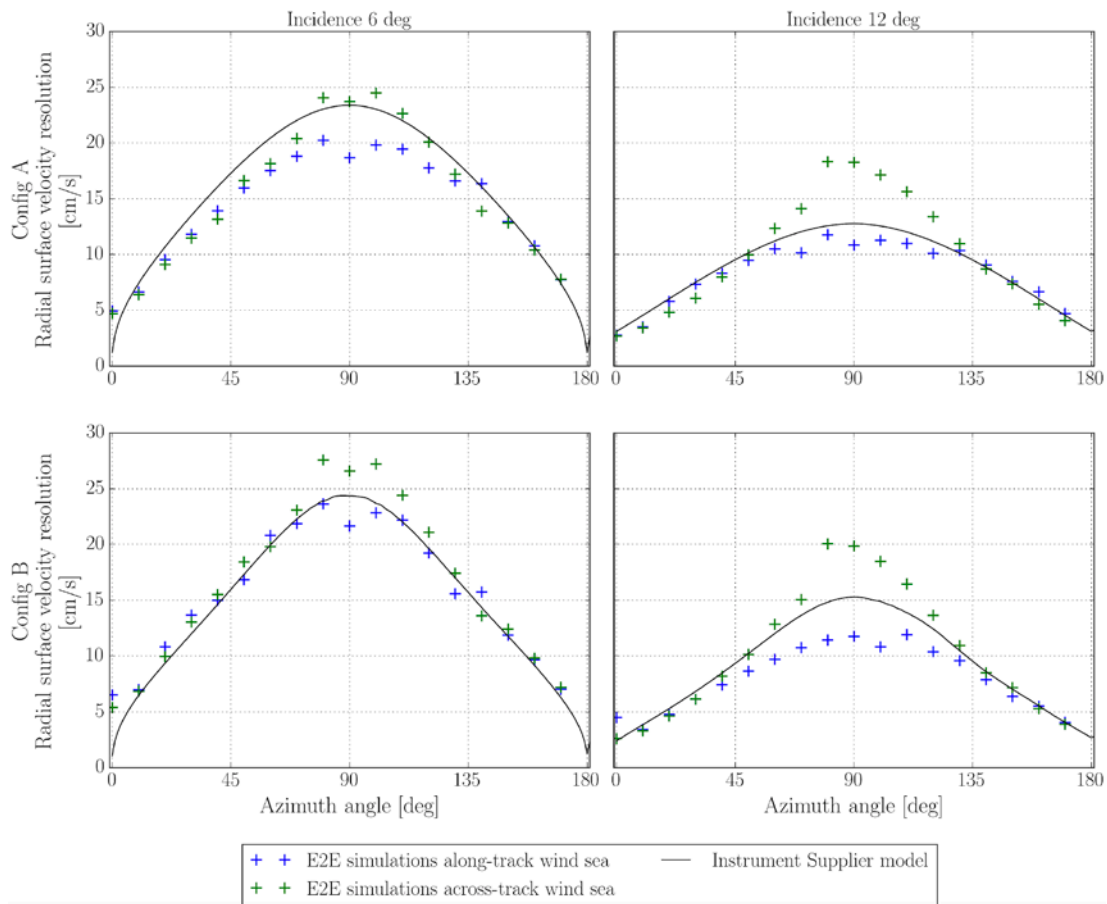


Figure 7.11. Along-track and across-track scenarios (wind speed 7 m s⁻¹): radial surface velocity performance (rms. error) as a function of azimuth angle for Concept A (top) and Concept B (bottom). Left: incidence 6 degrees. Right: incidence 12 degrees. Note that the scales for Concept A and for Concept B are different.

Table 7.4 shows the Level-1b performance of the radial surface velocities, as simulated by SEEPS, versus the Level-1b requirements. Taking due account of the wave modulation impacting the radial surface velocity precision when the observation azimuth direction and the wind vector are both cross-track oriented, both Concept A and B are compliant for all specified azimuth angles. The slight degradation for the 6° beam close to the along-track direction can be explained by the first effect mentioned above – whereby it is to be noted that the 6° beam is more sensitive to co-registration errors (driven by the range resolution) when compared to the 12° beam.

Fig. 7.12 and Fig. 7.13 show the Level-1b performance using a scenario with 15 m s⁻¹ wind. The effect of the wave modulations is more pronounced in this high wind case. The larger RMS uncertainty can be attributed to the geophysical Doppler contributions (i.e. U_{WD}) and shows that the modulations due to wave motion dynamics are fully represented within SEEPS.



Requirement	Specification (cm s ⁻¹)	Concept A (cm s ⁻¹)	Concept B (cm s ⁻¹)
At an incidence angle of 12°, radial surface velocity precision at 45° and 135° of azimuth from the along track direction (cm s ⁻¹).	≤12.5 (goal ≤10)	9 8.5	9 9.5
At an incidence angle of 12°, radial surface velocity precision at 3° and 357° of azimuth from the along track direction (cm s ⁻¹).	≤5 (goal ≤3)	3.1 3.0	2.5 2.7
At an incidence angle of 12°, radial surface velocity precision at 90° of azimuth from the along track direction.	≤ 20 (goal ≤ 15)	12.1 18.2	12.8 20.0
At an incidence angle of 6°, radial surface velocity precision at 45° and 135° of azimuth from the along track direction.	17.5 (goal ≤ 15)	15 15	17 14.3
At an incidence angle of 6°, radial surface velocity precision at 3° and 357° of azimuth from the along track direction.	≤ 5 (goal ≤ 3)	5.1 5.3	5.8 5.7
At an incidence angle of 6°, radial surface velocity precision at 90° of azimuth from the along track direction.	≤ 25 (goal ≤ 20)	18 24.1	23 27.5

Table 7.4. Main observing mission parameters at Level-1b: required and achieved nominal performance (average scenario: wind speed 7 m s⁻¹, Hs = 1.3 m). First row for along-track generated wind-sea, second row for cross-track.

It should be recalled that both the across-track and along-track vector components are required to derive the TSCV vector. At 0° and 90° azimuth only one vector component is available. Because of this, it is not possible to derive a TSCV from the Level-2c 30 km gridded products within 15 km of the swath edge and within 20 km of the centre swath. Thus, the poor performance at 90° azimuth has marginal impact on the final Level-2c product. However, at 0° azimuth the vector component has the best performance. Finally, all measurements are included in the Level-2c product for the full swath so that users may choose how to apply the measurements for a given application.

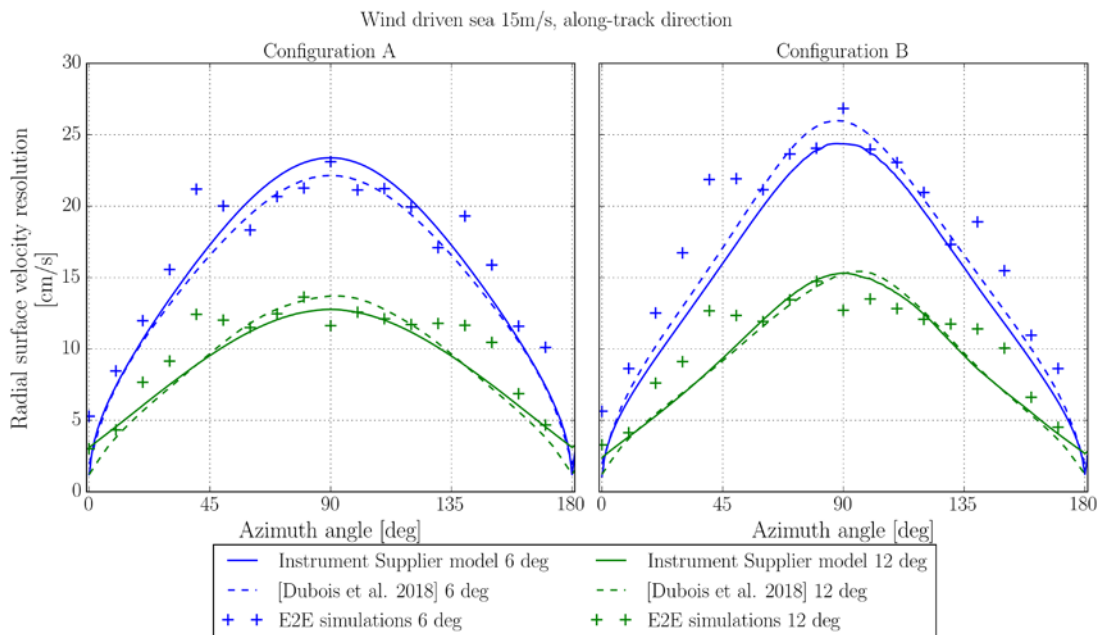


Figure 7.12. Radial surface velocity performance (RMS error) as a function of azimuth angle for canonical case of 15 m s⁻¹ surface wind speed (along-track wind generated sea surface) for Concept A (left) and Concept B (right).

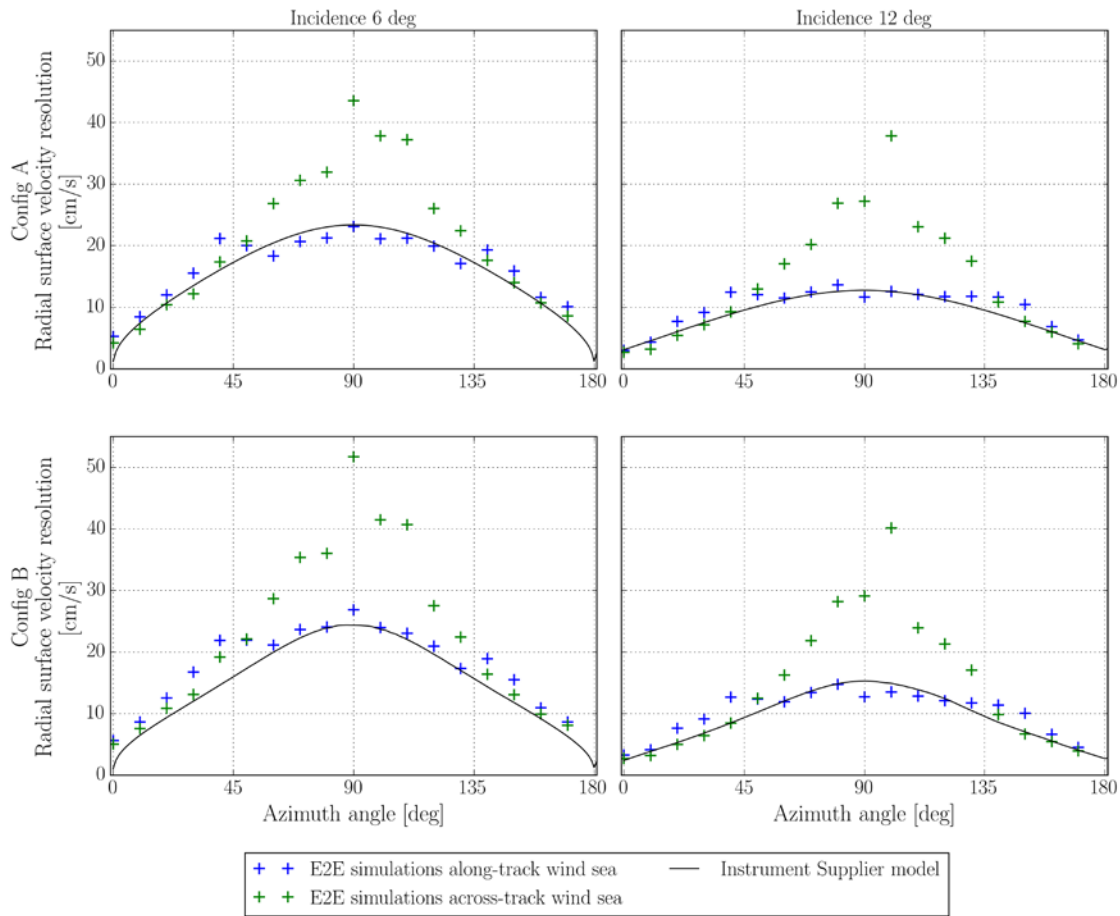


Figure 7.13. Along-track and across-track wind generated sea surface (15 m s⁻¹): radial surface velocity.

7.3.3 Level-1b Pointing Performance

SKIM relies on Level-2 (L2) pointing knowledge calibration algorithms, explained in section 7.4.1, in order to remove the non-geophysical Doppler components from the measured Doppler velocity. The approach followed for the pointing performance at Level-1 is two-fold:

1. Set Level-1 pointing requirements at a level that is challenging, but achievable with technology readily deployed for Earth Observation missions.
2. Requirements are set on the power spectral density of the azimuth knowledge error. These requirements enable the Level-2 calibration algorithms.

In practise, the requirements stemming from these two approaches drive the mission to achieve best-in-class pointing knowledge with state-of-the-art AOCS sensors, to implement thorough on-ground antenna characterisation and on-orbit calibration schemes, and to minimise antenna distortions during flight. The knowledge of the azimuth position of the Doppler centroid depends on pointing knowledge of the antenna line of sight. The knowledge of the elevation or look angle depends on radar timing and geolocation accuracy. As explained in Section 5.3.3.10.3, the azimuth knowledge is more challenging at Level-1, therefore this Section focusses on azimuth Absolute Knowledge Error (AKE) performance.



7.3.3.1 Pointing Knowledge Requirements at Level-1b

As part of the Level-1b products, SKIM will deliver an estimate of the non-geophysical Doppler velocity. SKIM aims to achieve ~10 arc seconds of AKE. The AKE performance is driven primarily by residual uncertainty after calibration. Concepts A and B have proposed different calibrations strategies as explained in chapter 5, and briefly summarised in Table 7.5 below.

Calibration method	Id	Concept A	Concept B
Model-driven calibration using on-ground characterisation	A		√
Data-driven calibration, exploiting harmonic signatures in pulse pair signal	B1	√	
Data-driven calibration, averaging out geophysical signals	B2	√	
External calibration, with array of ground receivers, antenna in fixed position	C1		√
External calibration, with array of ground receivers, rotating antenna	C2	√	

Table 7.5 Summary of the main calibration methods proposed for Concept A and Concept B and referenced from pointing budgets below using Id as lookup reference in Table 7.7 and 7.9. Further details are in chapter 5.

The pointing error budgets are too elaborate to be included in this report. Table 7.6 and Table 7.8 list the error sources that have been included in the budgets for concepts A and B, with the list for Concept B including the errors before and after on-ground antenna characterisation. The error sources are classed in different types, considering how they affect the azimuth knowledge during the conical scan. An off-pointing roll/pitch bias of the antenna for instance, would result in an error signal that is harmonic (which in this context means periodic with the period of the conical scan) but this harmonic would not change in time. This is called harmonic bias. Variable means that a signal is varying around the azimuth of the conical scan (or higher order harmonic). Different calibration approaches are being proposed to address these different error types. The different types and their characteristics are explained in Fig 7.13. The error contributors are also categorised depending on the transformation they apply to. The complete error path between the intended pointing (SNRF frame) and the Actual Line of Sight (ALoS) is illustrated in Fig 7.14.

Error source	value in arc seconds	type	transformation
instrument			
Measurement uncertainty antenna pointing	65	harmonic bias	AntRF to ALoS
Measurement uncertainty antenna pointing	49	variable bias	AntRF to ALoS
Measurement uncertainty antenna pointing	9	constant bias	AntRF to ALoS
Interpolation error of the RF azimuth pointing law	5	variable bias	AntRF to ALoS
Launch, gravity, hygro effects uncertainty on antenna	450	harmonic bias	SRF_aocs to AntRF
Launch, gravity, hygro effects uncertainty on antenna	55	variable bias	SRF_aocs to AntRF
Azimuth reference knowledge	3	constant bias	AntRF to ALoS
knowledge of feed position in-orbit	0.4	constant variable	AntRF to ALoS



knowledge of feed position in-orbit	0.2	variable	AntRF to ALoS
knowledge of feed position in-orbit	0.5	random	AntRF to ALoS
Reflector and Feed manufacturing error	280	harmonic bias	AntRF to ALoS
Impact of antenna geometry offset	900	variable bias	AntRF to ALoS
TED delta-T with on-ground characterisation at 20°C	1065	harmonic bias	SRF_aocs to ALoS
TED delta-T with on-ground characterisation at 20°C	14	variable bias	SRF_aocs to ALoS
TED seasonal	11	harmonic periodic 1 year	SRF_aocs to ALoS
TED orbital	6	harmonic periodic 1 orbit	SRF_aocs to ALoS
Microvibrations on instrument LoS induced by the RW	0	random	AntRF to ALoS
Microvibrations on instrument LoS due to rotary plate	1	random	AntRF to ALoS
platform			
AOCS roll/pitch bias	0	harmonic bias	SNRF to SRF_aocs
AOCS yaw bias	0	constant bias	SNRF to SRF_aocs
AOCS random	3	random	SNRF to SRF_aocs
Ground alignment error bias	10	constant bias	SRF_aocs to AntRF
Ground alignment error bias	10	constant bias	SRF_aocs to AntRF
Launch effect on STR bracket bias	60	constant bias	SRF_aocs to AntRF
Launch effect on STR bracket bias	60	constant bias	SRF_aocs to AntRF
Moisture error bias	20	constant bias	SRF_aocs to AntRF
Moisture error bias	20	constant bias	SRF_aocs to AntRF
Microvibrations on STR bracket (induced by RWs)	0	random	SRF_aocs to AntRF
Microvibrations on STR bracket (induced by the rotary plate)	0.1	random	SRF_aocs to AntRF
TED delta-T bias at STR bracket with respect to on ground characterisation at 20°C	5	harmonic bias	SRF_aocs to AntRF
TED orbital at STR bracket	5	harmonic periodic 1 orbit	SRF_aocs to AntRF
TED seasonal at STR bracket	1	harmonic periodic 1 year	SRF_aocs to AntRF

Table 7.6. Inputs in azimuth pointing knowledge error budget for Concept A (12° beam).

type	calibration method	before calibration	calibration residual
harmonic bias	B1	1675	0.3
variable bias	B2	123	1.1
constant bias	C2	102	3.4
constant variable	none	0.4	0.4
variable variable	none	0.2	0.2
harmonic periodic 1 orbit	repeated B1	11	2.7
harmonic periodic 1 year	repeated B1	12	2.2
random	none	3.2	3.2
TOTAL			13.5

Table 7.7. Azimuth pointing knowledge error budget (summary) for Concept A. Calibration methods are defined in Chapter 5 and summarised in Table 7.5.



Error source	value in arc seconds	after ground characterisation	type	transformation
instrument				
Measurement of RF pointing in R_ANT	9	—	Constant—bias	AntRF to ALoS
Measurement of RF pointing in R_ANT	65	—	harmonic bias	AntRF to ALoS
Measurement of RF pointing in R_ANT	49	5	variable bias	AntRF to ALoS
Interpolation Error (RF azimuth pointing wart feed azimuth position)	5	—	variable bias	AntRF to ALoS
Launch, gravity, hygro effects on antenna	450	—	harmonic bias	AntRF to ALoS
Launch, gravity, hygro effects on antenna	55	10	variable bias	AntRF to ALoS
Azimuth reference knowledge	3	3	constant bias	AntRF to ALoS
knowledge of feed position in-orbit	0.5	0.5	random	AntRF to ALoS
microvibrations of the instrument mechanism	1	1	random	AntRF to BeamF
TED delta-T with on-ground characterisation	570	20	harmonic bias	SRF_aocs to ALoS
TED delta-T with on-ground characterisation	10	10	variable bias	SRF_aocs to ALoS
TED seasonal	32	32	on-orbit TED	SRF_aocs to ALoS
TED orbital	10	10	on-orbit TED	SRF_aocs to ALoS
platform				
ground alignment errors	30	30	harmonic bias	SRF_aocs to AntRF
Launch, gravity, hygro effects on STR bracket	25	25	harmonic bias	SRF_aocs to AntRF
0.2TED seasonal (STR Bracket)	0.2	0.4	on-orbit TED	SRF_aocs to AntRF
TED orbital (STR Bracket)	0.4	5.8	on-orbit TED	SRF_aocs to AntRF
AOCS roll/pitch bias (RSS)	5.8	6.1	harmonic bias	SRF_aocs to SNRF
AOCS yaw bias	6.1	0.9	constant bias	SRF_aocs to SNRF
AOCS roll/pitch/yaw random (RSS)	0.9	0.8	random	SRF_aocs to SNRF
microvibrations from the platform	0.8	30	random	AntRF to ALoS

Table 7.8. Inputs in azimuth pointing knowledge error budget for Concept B (12° beam).

type	calibration method	before calibration	calibration residual
harmonic/constant bias	C1	53	5
variable bias	A+C1	25	10
on-orbit TED	A	42	10
Platform TED	none	0.6	0.6
random	none	1.7	1.7
TOTAL			27.3

Table 7.9. Azimuth pointing knowledge error budget (summary) for Concept B. Calibration methods are defined in Chapter 5 and summarised in Table 7.5.

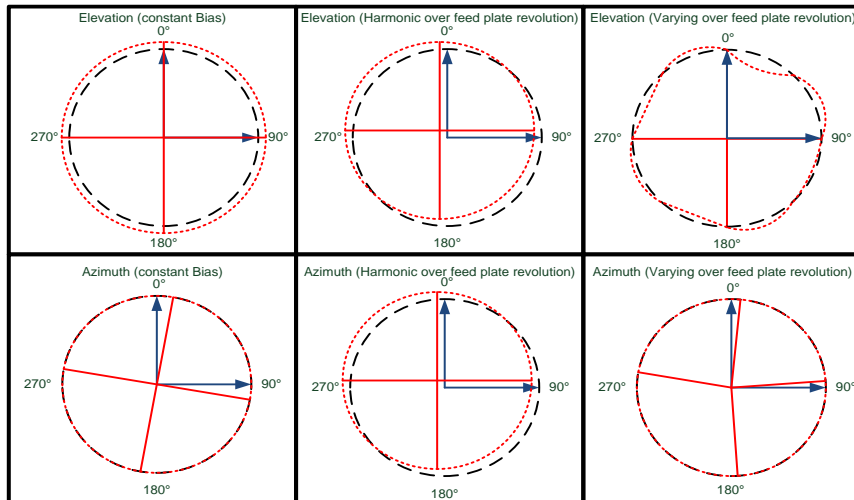


Figure 7.14. The contributors to the pointing budgets are grouped in different types, depending on how they interact with the conical scan of the instrument. This leads to different calibration methods being identified. A roll/pitch antenna offset for instance would result in azimuth and elevation changes that are harmonic (centre column) over the conical scan. Courtesy: OHB.

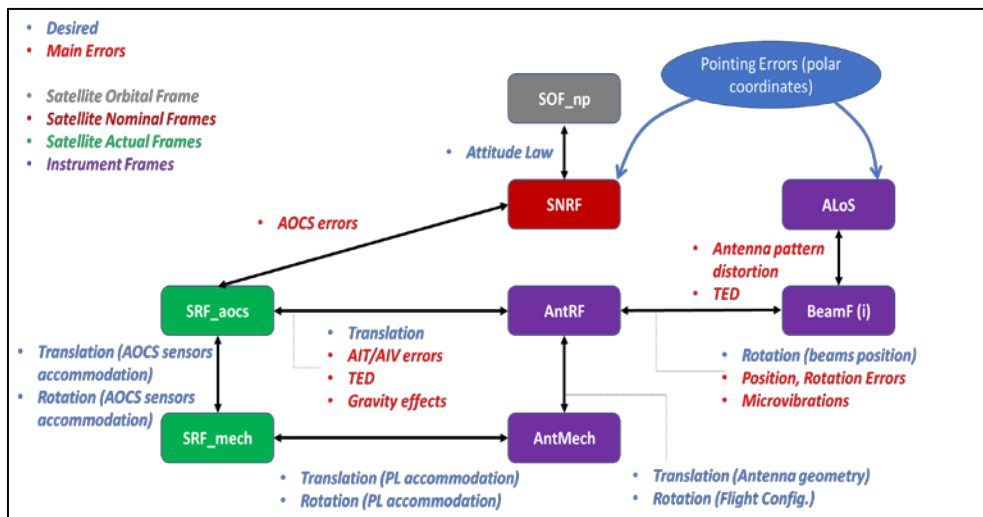


Figure 7.15. The chain of transformations between the Spacecraft Nominal Reference Frame (SNRF) and the Actual Line of Sight (ALoS) determine all the sources of uncertainty that need to be considered in the pointing budgets. In the case of SKIM, the chain of transformations has been shortened significantly by placing the AOCs sensors on the antenna. Therefore, any unknowns in the transformation to the spacecraft mechanical reference frame becomes irrelevant (to first order).

In conclusion, the achievable pointing knowledge on the azimuth angle at Level-1, with a combination of careful ground characterization and elaborate in-orbit calibration schemes, is expected to be in the order of 10-20 arc seconds. The more elaborate Level-2 algorithms can achieve an order of magnitude better performance, since they can distinguish geophysical from non-geophysical signatures in space and time and exploit that difference in a fine-pointing algorithm.

7.3.3.2 Power Spectral Density Requirements on AKE

As explained in chapter 4, AKE requirements have been set in the form of a spectral mask. The LEVEL-2 fine-pointing calibration algorithms described in chapter 6 and evaluated in the LEVEL-2 section below, have been stress-tested to cope with errors that significantly exceed the specified spectral mask. The requirement is split in two parts: First, a threshold is set for broadband noise coming from the AOCS subsystem and from micro-vibrations in the spacecraft. This mask has been set so that it is achievable with a state-of-the-art AOCS system and the best sensors currently available. Fig. 7.16 shows that the specified levels are achievable.

Second, allowance is made for narrow-band peaks protruding above the specified mask. Limits have been specified on the width, stability and integrated magnitude of these peaks. Since the AOCS sensors are mounted directly on the back-end of the antenna, the peaks are entirely governed by thermo-elastic distortions in the antenna. A very extensive thermo-elastic analysis described in chapter 5 has been performed to calculate the distortions in the antenna, over 4 different orbits. The effect of these distortions on the antenna patterns has been analysed, so that ultimately a PSD of the azimuth variations of the Doppler centroid has been established.

The results are shown for Concept A in Fig. 7.17. Not only do the results demonstrate compliance against the requirements, but the time series of the azimuth off-pointing has been fed directly into an analysis of the LEVEL-2 fine-pointing calibration algorithms. This has demonstrated that the peaks can effectively be removed, as explained in section 7.4.1 below. For Concept B the results are shown in Fig. 7.18. The PSD for Concept B is worse at the lower frequencies, because Concept B does not deploy yaw steering that keeps the antenna in the shadow. Since the levels are still low compared to the worst-case mask assumed for the stress-testing of the LEVEL-2 fine-pointing calibration algorithms, this may not be an issue, to be confirmed in next study phase. If necessary, the design can be improved in the next phase to mitigate the TED.

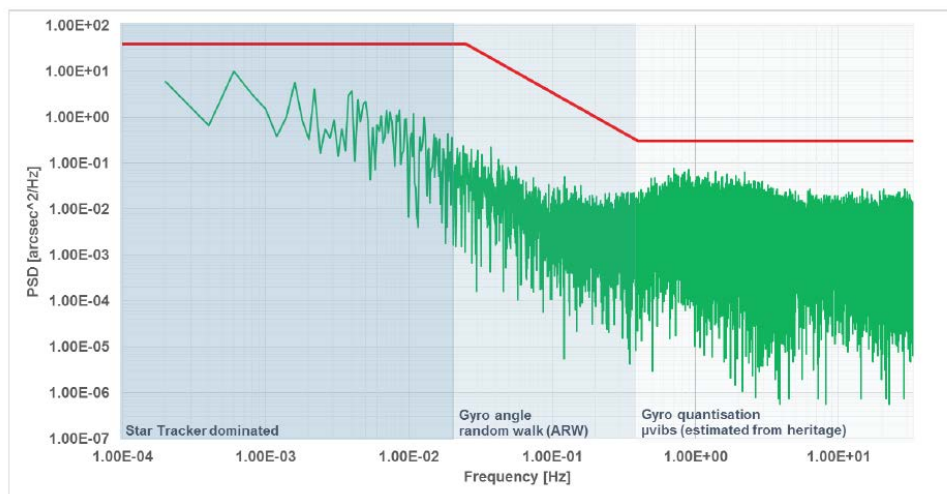


Figure 7.16. Power Spectral Density (PSD) for azimuth angle AKE, including AOCS and microvibrations, for Concept B.

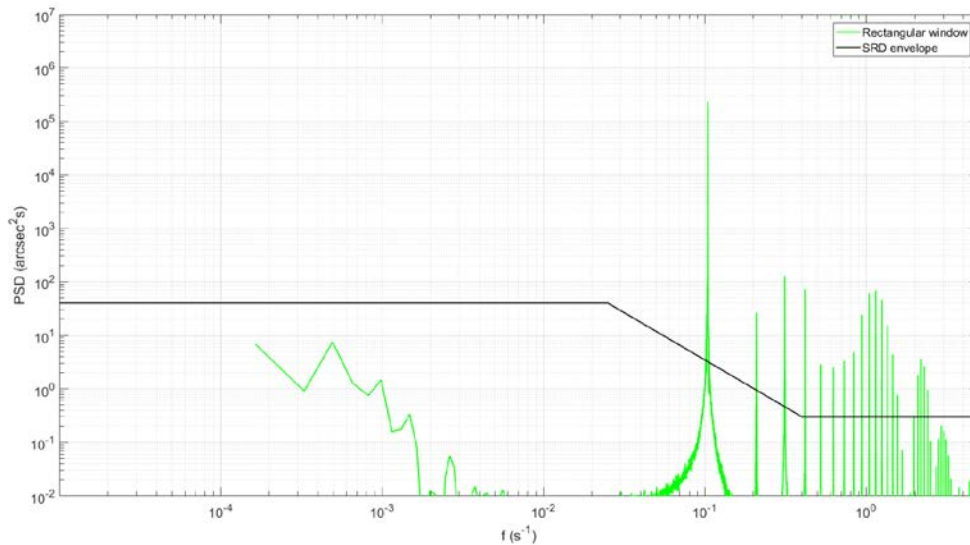


Figure 7.17. PSD of azimuth errors due to TED for Concept A (Equinox case, Beam 12°, mean pointing removed)

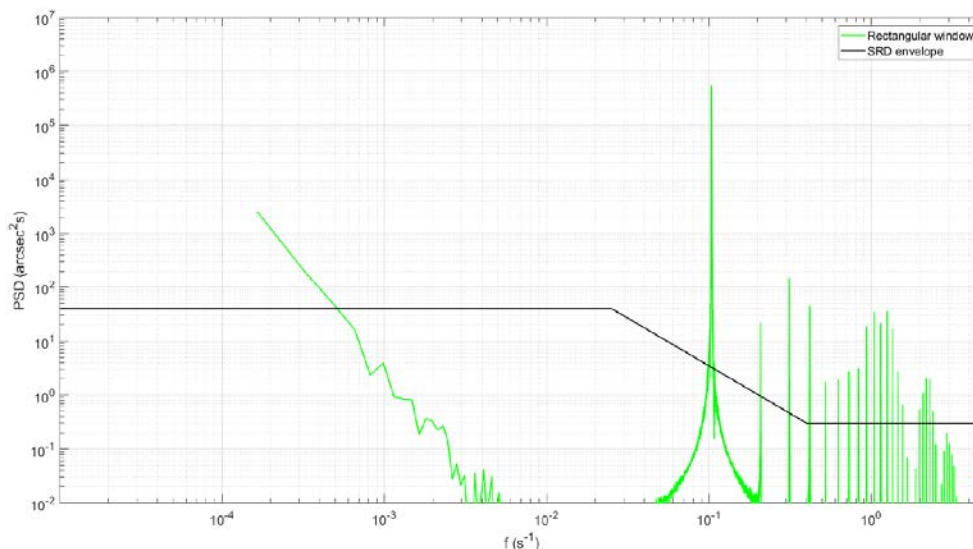


Figure 7.18. PSD of azimuth errors due to TED for Concept B (Equinox case, Beam 12°, mean pointing removed)

7.3.4 Radiometric Performance

SKIM requires a very good radiometric performance of the SKaR instrument as discussed in Chapter 4. Since it is a multi-beam instrument, relative radiometric requirements apply between the different beams, at least over short timescales. This will require regular internal calibration sequences and on-ground characterisation, as described in detail in chapter 5. The specified performance of 0.15 dB will be challenging to meet, with current performance budget showing marginal compliance. The absolute radiometric requirements are not particularly challenging and can be met with the aid of external calibration.

Requirement	Spec. value	Concept A	Concept B
Radiometric resolution of each beam (dB)	0.1	0.1	0.1
Absolute radiometric accuracy of each beam (dB)	1	0.28	0.86
Relative radiometric accuracy within a beam (dB)	0.1	0.06	0.06
Radiometric stability for each beam, after calibration, over the lifetime of the mission (dB)	0.5	0.36	0.27
Relative radiometric accuracy between beams over one full rotation (dB)	0.15	0.15	0.15

Table 7.10. Radiometric performance versus requirements for Concept A and B. Instrument level performance are common to both concepts. Performances that rely on assumptions on the external calibration may differ between the two concepts. Both are compliant, albeit the relative radiometric accuracy between beams is identified as challenging to meet.

7.3.5 Geo-location Performance

Geo-location accuracy is driven by the need to ensure that the location of SKIM measurements is correct with reference to the WGS-84 ellipsoid and for co-registration with MetOp-SG(1B) MWI and SCA data. Over the open ocean where no reference ground targets are available, geo-location relies on knowledge gained from instrument and platform pointing. Chapter 4 explains the rationale for geolocation accuracy that is set at a ≤ 0.1 km.

In the along-track direction, the required pointing knowledge on the elevation or look angle will place a driving constraint on the geolocation accuracy. This is not addressed in this section. The geolocation requirements can be met with comfortable margins. Detailed performance budgets show a performance in the order of 50 meters for both Concept A and Concept B.

7.3.6 Summary of Level-1b Requirements and Performance of the SKIM Mission

This section presents the system and instrument Level-1b performance achieved by each mission concept presented in Section 5. It compares performance against requirements and provides additional information to explain and justify key performance parameters.

The achievable pointing knowledge PSD performance is better for Concept A, due to a better thermo-elastic behaviour. Concept A also avoids the Solar Array Drive Mechanism, which may result in lower micro-vibration levels (detailed analysis of micro-vibration levels is not possible in Phase A).

While elaborate error budgets have been developed for the AKE performance, the reported figures rely primarily on the residual performance that can be achieved with the proposed calibration methods elaborated in Section 5.3.3.10.3. These will need to be investigated more deeply in the next study phase.

As explained in the next Section, the Level-2 fine pointing algorithms can cope with a pointing performance that is much worse than what is expressed in the Level-1 requirements. Even though the pointing uncertainty with Concept B is slightly worse at Level-1, after Level-2 processing the residual pointing uncertainty is expected to be similar for both concepts.

Observational Requirement	Specification	Concept A	Concept B
Mission Lifetime	≥ 5 years (goal 7 years)	Design for 5 years with 7 years consumables	
Coverage	All ocean surfaces between 82° North and South including a buffer zone of 10 km land buffer at the coastal boundary	√	√
Swath Width	≥ 290 km	√	√
Revisit	≤10 days at the Equator (average)	√	√
Radar carrier frequency	Ka-band (35.75 GHz)	√	√
Footprint size	≥ 6 km at nadir, at reference altitude (817.5 km), 3dB contour 1-way pattern	8.13 km	
Nadir beam	One nadir beam	√	√
Nadir beam range noise	≤1.5 cm at a significant wave height of 2 m and wind speed of 7 m/s (NRCS of 8dB) at 1 Hz (1σ, zero mean).	≤1.2 cm	≤1.2 cm
Nadir beam range bias stability	≤2 mm/year over the mission duration	≤1 mm/year	≤1 mm/year
σ0 dynamic range covering ocean, ice infested and ice leads	0 dB to +50 dB	√	√
Range resolution of 12° beam projected on ground with reference to the WGS-84 ellipsoid	≤6 m	3.6 m ground projected range resolution. 6 m after averaging over cycle due to RMC errors.	
The dynamic range of the instrument, expressed as NESZ range	-15 dB to 15 dB	√	√
Radiometric resolution of each beam	0.1 dB	0.1 dB	0.1 dB
Absolute radiometric accuracy of each beam (dB)	1 dB	0.28 dB	0.86 dB
Relative radiometric accuracy within a beam	0.1 dB	0.06 dB	0.06 dB
Radiometric stability for each beam, after calibration, over the lifetime of the mission (dB)	0.5 dB	0.36 dB	0.27 dB
Relative radiometric accuracy between beams over one full rotation (dB)	0.15 dB	0.15 dB	0.15 dB
Radial surface velocity precision at an incidence angle of 12°	At 45° and 135°: ≤12.5 cm s ⁻¹ (goal ≤10 cm s ⁻¹) At 3° and 357°: ≤5 cm/s (goal ≤3 cm s ⁻¹) At 90°: ≤20 cm s ⁻¹ (goal ≤15 cm s ⁻¹)	9.5 3.5 12.8	9.5 2.8 14.3
Radial surface velocity precision at an incidence angle of 6°	At 45° and 135°: 17.5 cm s ⁻¹ (goal ≤15 cm s ⁻¹) At 3° and 357°: ≤5 cm/s (goal ≤3 cm s ⁻¹) At 90°: ≤25 cm s ⁻¹ (goal ≤20 cm s ⁻¹)	17.3 4.3 23.4	16 3.7 24.4
Satellite position shall be determined in the nadir direction	Near Real Time (≤ 3 hours): ≤10 cm (goal 8 cm), Slow Time Critical (≤ 48 hours): ≤5 cm (goal 3 cm), Non Time Critical (≤ 1 month) ≤3 cm (goal 1.5 cm),	√(*)	√(*)
Absolute geo-location accuracy in all beams at Level-1b, measured at the centre of the range window.	≤0.1 km (1-sigma, zero mean) with reference to the WGS84 ellipsoid	50.1 m	49.9 m
Data Latency	24 hours from sensing	√	√
AKE spectrum	Specified spectral mask	√	TBC (**)
AKE azimuth	10 arc seconds	13.5	27.3

Table 7.11. Summary of the key Level-1b requirements and performances established in Phase A.

(*) Based on experience with Copernicus Precise Orbit Determination service (Fernández et al., 2016).

(**) The AOCs system for Concept B is compliant to the PSD mask, as shown in Fig. 7.13. At lower frequencies, the TED is causing a small non-compliance to the mask, as shown in Fig. 7.15. Simulations have shown that this non-compliance can be tolerated by the Level-2 fine pointing algorithms. Nevertheless, further mitigation will be investigated in the next phase.

7.4 Level-2 Retrieval Performance

This section reports the end-to-end Level-2 performance of the SKIM mission. The impact and performance of the SKIM fine pointing DDC and CCAL algorithms is reported in Section 7.4.1. SKIM nadir beam performance is reported in Section 7.4.2. SKIM Level-2b Level-2c TSCV performance is reported in this Section based on the use of the SKIMulator using the test case scenarios developed in Section 7.2.3.1. Performance is reported following the Metrics defined in Section 7.2.2.2. SKIM Level-2b and Level-2c wave performance is reported in this Section based on the use of the R3S and OceanSAR simulations using the test case scenarios developed in Section 7.2. Performance is reported following the Metrics defined in Section 7.2.2.2.

7.4.1 Fine Pointing Algorithm Performance

Simulations are used to demonstrate that residual mis-pointing errors can be managed without compromising the required Level-2c TSCV performance. As explained in Chapter 6 these exploit the very different space-time patterns in geophysical and non-geophysical signals within SKIM data. This near-orthogonal property is the basis of the fine-pointing Data-Driven Calibration (DDC).

The simulation of attitude error and SKIM observation was computed to validate the method proposed by Delouis (2019). The simulated attitude error model uses the oceanographic signal from the SKIMulator output and includes the best knowledge of all instrumental noise and systematic errors related to the expected performance of the SKIM AOCS, as provided by the SKIM Phase A industrial and the end of PRR. Both Concept A and Concept B have been analysed.

7.4.1.1 Evaluation of the Fine Pointing DDC Algorithm

The DWD (Difference range Width Doppler) method is used to account for pitch and roll error based on Doppler range distribution properties. The method uncertainties are only related to the noise level, without degeneracy with the geophysical signal. It can be performed early in the processing chain if required (e.g. at Level-1). If the pitch and roll variations change smoothly, then the number of parameters to fit to the model are small. Thus, the measure of each of these parameters, only affected by noise, is very accurate as the number of measurements are large compared to the number of parameters to compute.

It is possible to filter or to fit the various errors introduced by the attitude using data from several orbits, under different stability hypothesis on the expected attitude model. One, two, four, eight, 16 and 32 orbits were tested.

Figure 7.19 shows the expected residual level for the two attitude error types. The first error is associated to the focal plane rotation rate and the second error is associated to the orbit period (e.g. TED). In both cases, the pitch and roll retrieval is better than 1 cm s^{-1} at 1σ . To achieve 3σ at 1 cm s^{-1} , the attitude error must not vary during one to four orbits. This is known to be the case from the industrial SKIM TED simulation data provided by industry as input to this analysis.

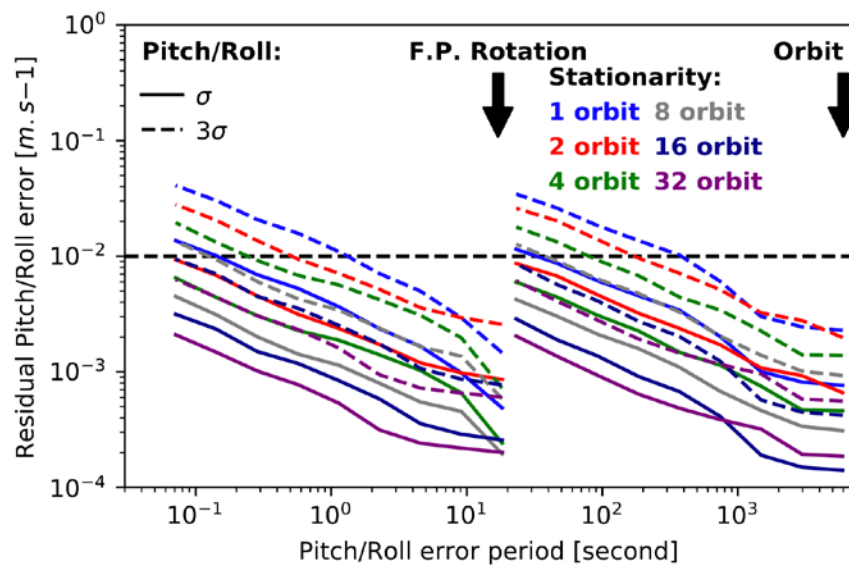


Figure 7.19. One σ (solid lines) and three σ (dash lines) pitch and roll error residual level for the attitude error related to focal plane spinning rate (smaller than the focal plane rotation) and to the orbit period for different frequency of the pitch and roll error. The residual level is shown for various hypothesis of the attitude error stability. The example shown here is for Concept A. (J-M. Delious)

For the yaw angle, the DDC method uses the differences between data taken in the same region (here a 50 km ‘pixel’) from different beams, azimuth or orbit, for which the geophysical signal should be a radial projection of the same vector. This does not account for time variation at the small scales, but the approach is a baseline to be tested on realistic simulations.

A simple filtering of the yaw error, e.g. by Fourier analysis, would unfortunately remove large-scale currents that have the same scales as the attitude signal. For this reason, the attitude pattern is fitted to a model using the difference between measurements. This leaves a residual yaw error at large scales and the small-scale structures can be considered as noise. This hypothesis was validated using simulations.

To test the impact of TED on the azimuth simulations used a time series of yaw provided by industry for a set of orbits (Concept A and Concept B). The SKIMulator, as defined in Section 7.2.2, was used with geophysical data to produce simulated time series with all errors included. The simulation used a limited TED time series of roll, pitch and yaw provided by industry for a set of orbits. Concept B has less variation in TED on average but more small-time scale structures. The SKIMulator, as defined in Section 7.2.2, was used with the geophysical data to produce simulated time series with all errors, as illustrated in Fig. 7.20 (left).

Using 10 orbits to fit the TED components in pitch and roll the DDC fine-pointing algorithm effectively removes all mis-pointing for both Concept A and Concept B (not shown).

Using 412 orbits (~29 days that is easily accommodated in the Phase-E1 commissioning phase), the variance of the residual error in TSCV using the 12° and 6° beam mis-pointing is reduced from 20 m s^{-1} to $\leq 0.04 \text{ m s}^{-1}$ after the DDC fine-pointing algorithm has been applied over 400 orbits. Better performance is attained for the 12° beam which samples a wider swath and thus a larger sample of geophysical variability. In this simulation, the dominant

effect is degeneracy with the geophysical signal that is the same for both Concept A and Concept B.

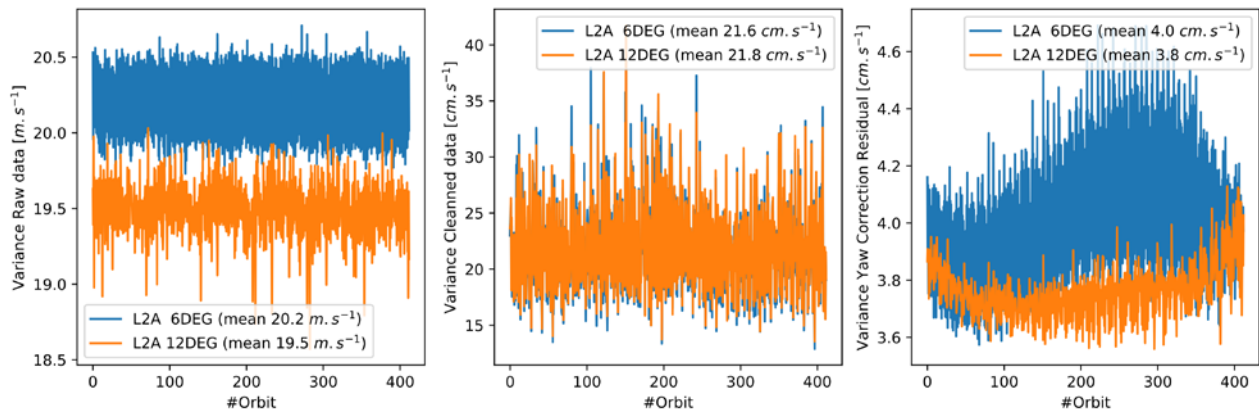


Figure 7.20. Left: Concept A time series of the TSCV input data variance in $m s^{-1}$ before DDC is applied. Centre: variance of TSCV after DDC has been applied in $cm s^{-1}$. Right: variance of fine-pointing algorithm yaw correction residual in $cm s^{-1}$ (Delouis, 2019).

The spatial distribution of these errors is very different from a geophysical signal. Figure 7.21 clearly demonstrates the dramatic impact of the DDC fine pointing algorithm, which is possible due to the proper decomposition of the signal in dimensions for which geophysical and non-geophysical signals are nearly orthogonal.

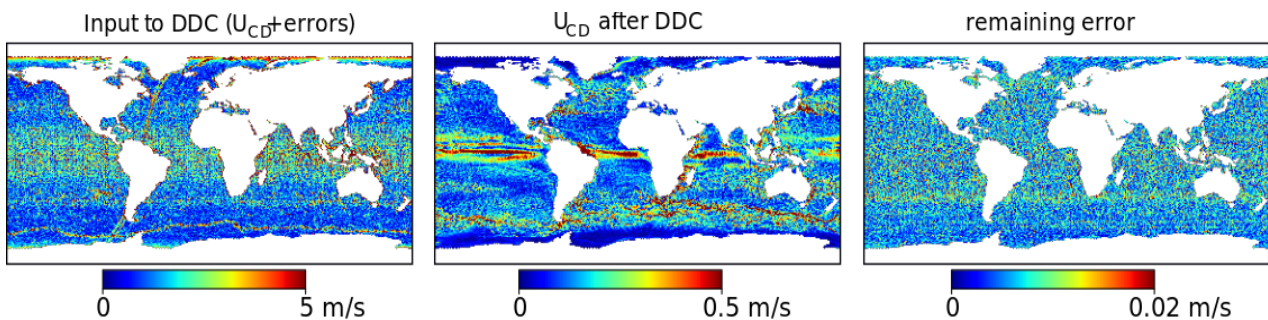


Figure 7.21. Top left: Spatial distribution of error for Concept A TSCV in $m s^{-1}$ before DDC is applied. Centre: Spatial distribution of error after DDC has been applied in $m s^{-1}$. Right: Spatial distribution of residual error in $cm s^{-1}$. Bottom: same as top line except for Concept B. (Delouis, 2019).

The residual errors shown in the right-hand panels of Fig. 7.21 can be further analysed to reveals spatial patterns in the small aliasing of the true current into the attitude error. The error can then be assigned to different processes affecting the performance of SKIM TSCV retrievals. This is shown for Concept A with an analysis of TED, random noise, residual U_{WD} uncertainty and TSCV U_{CD} in Fig. 2.22. In particular there is a remaining TED error that has a particular spatial pattern and part of the geophysical signal (U_{CD} and residual of U_{WD}) have been erroneously attributed to the pointing error.

Further progress is possible in future Phases of the mission using more detailed information from the final SKIM design. For example, no attempt has been made at this point to exploit the non-geophysical nature of the DDC residuals in Fig 7.22 that would certainly lead to further performance improvements in DDC.

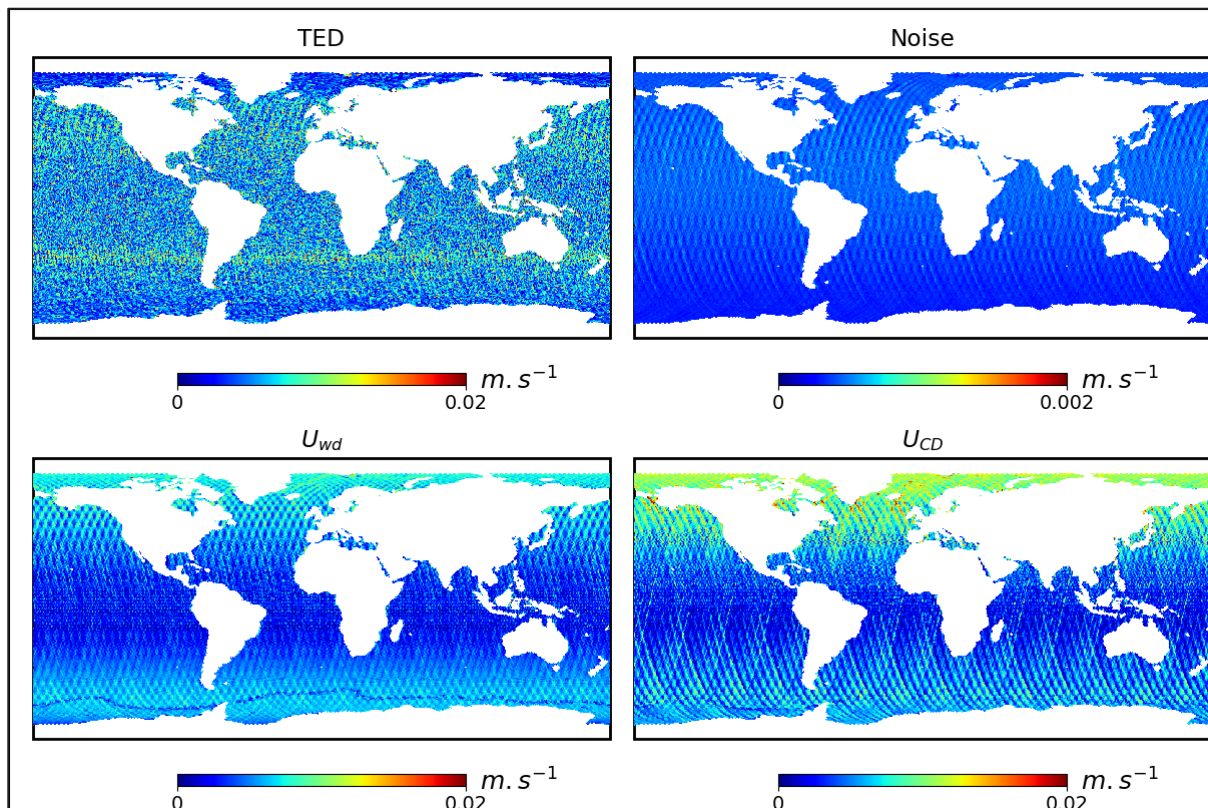


Figure 7.22. Residual yaw attitude error level associated to four processes. The residual error from TED on the top left panel, the instrumental noise on the top right, the wave Doppler on bottom left and the ocean current on the bottom right. All these plots are computed for 12° elevation beams (Delouis 2019).

In summary, simulations using data provided by industry show that it is possible to filter and to fit the various errors introduced by the attitude mis-pointing using data from several orbits, under stability hypothesis on the expected attitude model. The final error budget for the yaw is less than 4 cm s⁻¹ for SKIM Level-2c products outside coastal regions (>30km away from any coast). As the pattern of this error does not resemble the ocean current it can be efficiently separated from the geophysical Doppler. In other words, there is a significant margin for improvement with respect to the current implementation.

Given the importance of accurate pointing for a Doppler mission such as SKIM, DDC fine-pointing algorithms must be further developed and tested during subsequent phases of the mission based on the final configuration of the SKaR instrument and more up-to-date knowledge of the spacecraft and payload TED, micro-vibrations and other relevant parameter affecting mis-pointing errors.

7.4.1.2 Risk Mitigation Cyclo-Calibration (CCAL) Fine Pointing

To demonstrate that SKIM cyclo-calibration (CCAL) can meet Level-2c requirements using even using extremely conservative assumptions on the time-varying errors, an extreme ‘stress case’ scenario was designed. In this scenario, the broadband error spectrum is the baseline error multiplied by an unrealistic factor of 100 (Fig. 7.20). This assumes a lower quality AOCS as the primary source of pointing uncertainty – for example due to a degraded AOCS payload status.

Figure 7.23 shows that the Level-2b error is mitigated by a factor of 100 to 1000 using the CCAL algorithm (from the red spectrum to blue spectrum). In contrast a simpler DDC algorithm (purple spectrum) yields good results for some wavelengths, but is generally less efficient for broadband errors.

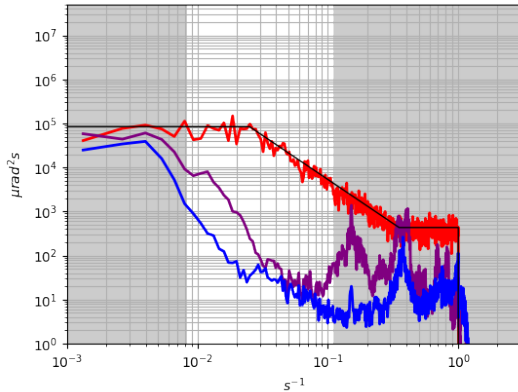


Figure 7.23. A worst-case Level-2b azimuth error PSD scenario assuming a low quality AOCS that considers the primary sources of time-varying pointing uncertainty. Red is before CCAL, blue after CCAL, and purple is after a direct DDC is used.

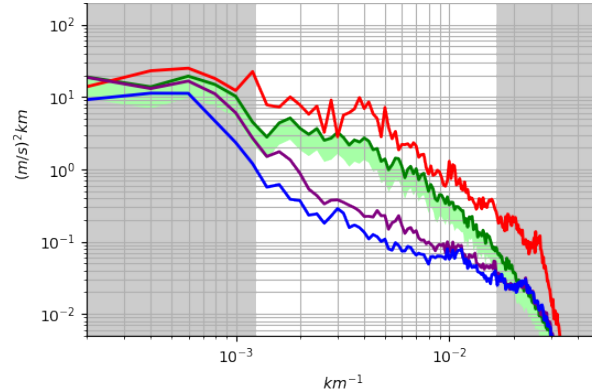


Figure 7.24. Analysis of SKIM azimuth pointing errors on Level-2c performance after CCAL. Green lines show the true geophysical signal, red is the total Level-2c error before CCAL, blue is after CCAL, and purple is after DDC.

Figure 7.24 and Table 7.12 show that, for this unrealistic and extreme stress case scenario, CCAL is required to meet Level-2c requirements. Without CCAL, the red PSD is always above the PSD of the ocean velocities (green PSD) from the SKIMulator output. In other words, the signal-to-noise ratio (SNR) is always less than zero. In contrast, after the CCAL (blue PSD) or after direct DDC (purple PSD) are used, the error is substantially reduced from 60 to 800 km. The residual error PSD after calibration is three to 10 times below the green PSD (i.e. SNR ranging from 5 dB to 10 dB). However, in this extreme test case, CCAL barely mitigates the pointing error for wavelengths smaller than 60 km in Level-2c or for a few seconds in Level-2b. Similarly, it has limited calibration capabilities for wavelengths longer than 800 km where DDC is required.

In conclusion, in this extreme stress case, the very large broadband error has been reduced to a residual that is less than the nominal pointing scenario with high-quality AOCS payload from 60 to 800 km. The algorithm has been demonstrated to mitigate extreme mis-pointing errors in L2B by a factor of 100 to 1000. L2C residual errors for the same scenario after CCAL are ~5 cm s⁻¹.

60-800 km (wavelength)	Before calibration (m s ⁻¹)	After (m s ⁻¹)	CCAL	After (m s ⁻¹)	light-CCAL
Geophysical signal	0.119				
Total Level-2c error	0.124	0.044		0.055	
Total Level-2b error	0.523	0.022		0.075	

Table 7.12. Simulated impact of applying cyclo-calibration on SKIM Level-2c U_{CD} performance (ignoring U_{WD} separation) and at Level-2b $U_{CD,R}$.

While not required at the end of Phase A, the CCAL algorithm has been developed and tested as a risk mitigation strategy for fine-pointing data driven calibration. The results presented here serve to demonstrate the robustness of the algorithm.

7.4.2 Nadir Altimetry Performance

This section describes the performance of nadir altimetry instrument. The SKIM nadir altimeter has a strong heritage from the SARAL-AltiKa and Copernicus Sentinel-3 altimetry missions. We have therefore used the end-to-end Sentinel-3 SRAL simulator, configured with the SKaR instrument characteristics (orbit, Ka band, bandwidth, range sampling, number of pulses in cycle etc.) and run thousands of simulations with different sea states.

This software, used to prepare Copernicus Sentinel-6, consists in three subsequent simulation modules, scene generation and raw data simulation (complex number I & Q radar signals). First, from a realistic ocean scene, the radar backscattering signals are simulated. The scene is digitised, composed by facets whose elevation and slope are computed using a spectrum given by Elfouhaily et al. (1997). Second, the onboard compression algorithm and down-linked data are simulated. Third, Level-1b data are processed up to the Doppler echoes (Fig. 7.25).

Range, H_s and NRCS are retrieved from simulated Doppler echoes using a re-tracking algorithm (Boy et al., 2017) and compared to the input parameters to assess the SKaR performance. The re-tracking algorithm is based on a common least-squares method which minimises the squared residuals between observed data (Doppler echo) and the expected value (model) by varying the fitting parameters. These parameters are determined if an acceptable error value is achieved. To this effect, a numerical Doppler echo model, adapted to SKIM, has been developed based on the approach described in Ray et al. (2014) which has been widely used and validated in the frame of Copernicus Sentinel-3 mission.

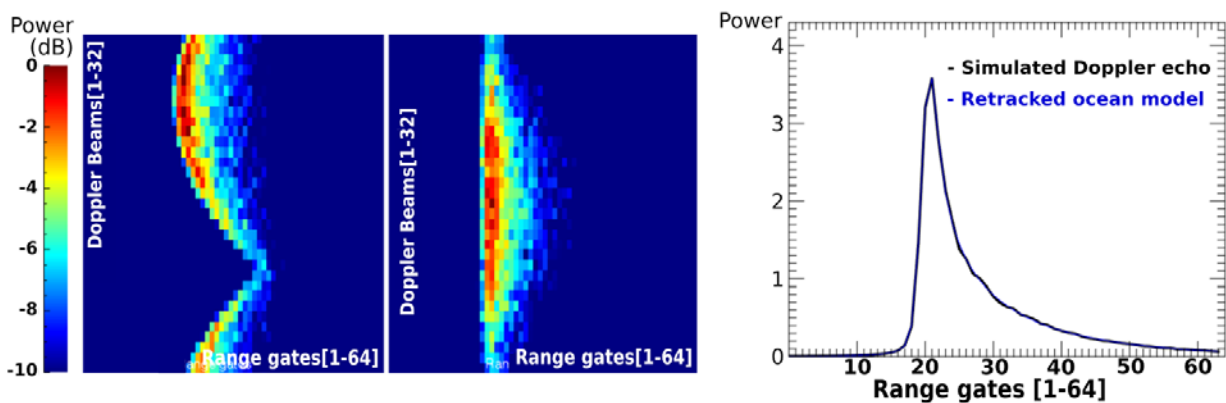


Figure 7.25. Example of simulated SKIM-NAL Level-1b nadir product. Left: Delay-Doppler Map after Doppler Beam Sharpening. Centre: Delay-Doppler Map after Range Migration Correction and Doppler centroid compensation, Right: Simulated Doppler Echo.

Figure 7.22 (right) shows the excellent agreement between simulated data (black line) and the echo model (blue line), once the re-tracking process has converged.



Using this method, Range, H_s and NRCS precisions as provided by the SKIM nadir beam with acquisitions at around 4 Hz only, are found to be better than those of the Jason-3 mission, estimated at 1.4 cm, 9 cm and 0.1 dB RMS (for the 1Hz product).

To build a complete SSH performance uncertainty (Table 7.13), additional results from the SARAL/AltiKa and Copernicus Sentinel-3 have been used.

Parameter	SKIM nadir beam uncertainty (cm)	JASON-3 GDR uncertainty (cm)
Altimeter noise	<1.4	1.7
Ionosphere	0.3 ⁽¹⁾	0.5
Sea State Bias	2.0 ⁽¹⁾	2.0
Dry Troposphere	0.7 ⁽¹⁾	0.7
Wet Troposphere	1.5 ⁽²⁾	1.2
RSS Altimeter range	3.0	3.0
RMS Orbit (radial component)	1.0 ⁽³⁾	1.0
Total RSS Sea Surface Height	3.2	3.2
Total RSS Significant wave height (H_s)	9.5 ⁽⁴⁾	11.2

Table 7.13. Preliminary End to end range performance uncertainty estimation for the SKIM nadir pointing beam (6 beam baseline configuration post PM5). ⁽¹⁾ AltiKa REX, ⁽²⁾ ECMWF model - note that SKIM will rely on the MetOp-SG(1B) MWI for wet tropospheric delay correction, ⁽³⁾ GPS solution. ⁽⁴⁾ H_s is likely to be improved via two-pass retracting to below ~3cm. Posting is at ≥ 4 Hz.

To correct the path-delay induced by the wet troposphere, altimetry missions usually host a microwave radiometer. It is not the case for SKIM but, flying in the MetOp-SG(1B) swath, SKIM will benefit from a wet tropospheric correction derived with MWI instrument with an estimated precision of ~9 mm RMS all around the orbit. Combining all errors impacting sea-surface height calculation, the total uncertainty is 2.9 cm RMS (best case with MWI) or 3.2 cm RMS (worst case with ECMWF model), which are equivalent to Jason-3 performances.

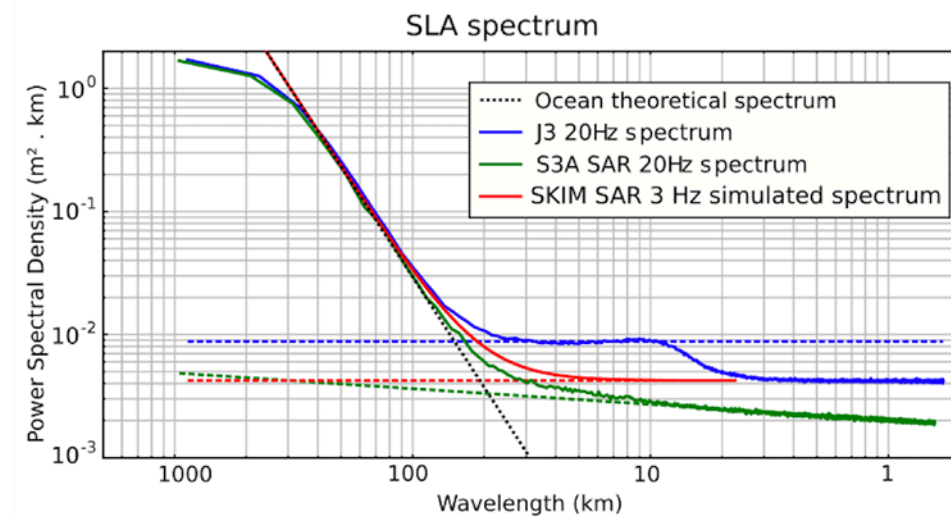


Figure 7.26. Sea-level anomaly spectrum (cycles per km) from Jason-3, Sentinel-3A and simulated SKIM. The sloping tail of Sentinel-3 is thought to be related to the impact of aliased swell waves within the SAR measurements.



Figure 7.26 shows the PSD of sea-level anomaly for Jason-3 (Ku-band Low Resolution Mode) and Copernicus Sentinel-3A (Ku-band delay-Doppler mode). On Jason-3, the SLA PSD first decreases with wavenumber following the oceanic slope. Then, the PSD is affected by a spectral hump from 5 km to 100 km (Dibarboure et al., 2014). The hump originates in a response to inhomogeneities in backscatter strength (e.g., owing to rapid changes of backscatter power induced by atmospheric and/or surface events, e.g. Dibarboure et al., 2014) not correctly captured by a low-resolution mode altimeter due to large on-ground footprint overlaps of consecutive measurements. It can corrupt wavelengths as large as 100 km and is the main contributor to the small-scale error of Jason-class missions, as discussed by Faugere et al. (2006). The PSD reaches a plateau, indicating the instrumental noise level.

The SLA PSD from Copernicus Sentinel-3 follows the same oceanic slope but then does not exhibit such a hump thanks to the delay-Doppler capability that offers a better along-track resolution (320 m) and avoids footprint overlapping. In addition, a higher noise reduction is achieved using multilooking approach. As a consequence, small-scale oceanic signals are better observed with delay-Doppler altimeter.

For these reasons, SKIM beam nadir will act as a classic delay-Doppler radar altimeter to provide clean observations from 5 km to 100 km, and with an instrumental noise level comparable to Jason-3 altimeter at 1 Hz.

Note that at Ka-band ~10% of measurements may be corrupted owing to the effects of rain on the altimeter tracking for rain rate above 1.5 mm/h. This can be flagged in SKIM measurements based on MWI data.

In conclusion, the SKIM nadir beam with existing processing algorithms will provide better performances than Jason-3 with a higher small-scale observability. Since SKIM has an ability to determine the directional wave spectrum at high fidelity, these measurements can be used with the SKIM nadir beam altimeter to study the sea-state bias error inherent to all satellite altimeters. This is significant because the sea-state bias remains the largest uncertainty term (~2cm) in the altimeter uncertainty budget today with little progress to mitigate this value.

7.4.3 Performance of Level-2 Wave Products

In this section we evaluate the performance related to the retrieval of directional wave spectra, and its translation to uncertainties in the wave-Doppler (U_{WD}) estimates. The scenarios used in this part of the analysis are described in Section 2.3.2.

7.4.3.1 Comparison Between CFOSat SWIM and SKIM

The CFOSat data used here is a typical case combining swell and wind sea, with a wind speed of 7 m s⁻¹, it was acquired on 29 April 2019, around 62°N 20°E, in the North Atlantic (<https://odl.bzh/P7K-Kfr>). The full modelled wave spectrum is used as input to the forward model of R3S (Nouguier 2019) using both a SWIM and a SKIM radar configuration. This scenario contains a wide range of wave scales, with two swells of peak wavelengths 220 and 90 m from the south and south-east, and a weak wind sea from the south-east (Fig. 7.27).

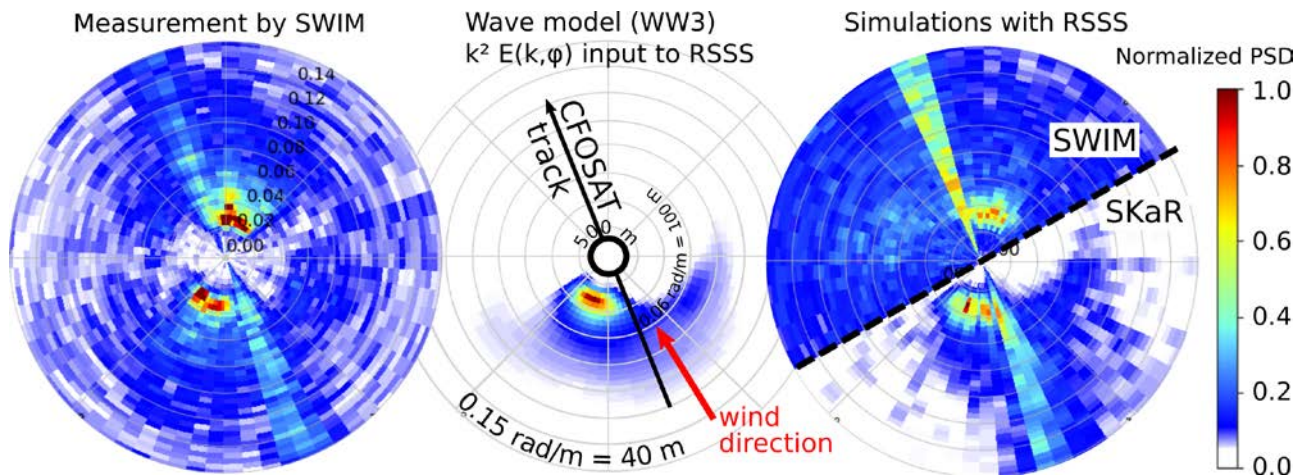


Figure 7.27. CFOSat 29 April scenario: measured and modelled Level-1b modulation spectra using a SWIM or SKaR instrument configuration. (F. Nouguier, LOPS).

The SWIM spectrum is retrieved from a unique antenna turn with the 10° incidence beam (SWIM Level-2s product). The R3S forward model is used to simulate the spectrum at 10° incidence for a CFOSat-SWIM setting and at 12° incidence for the SKIM-SKaR configuration. The NRCS spectra are nearly symmetric and we thus show only half of the antenna turn for each. Prominent features in the SWIM data are the two swell systems and a narrow wedge (10° in azimuth) of high signal around the CFOSat track direction related to over-correlation of measurements in this region.

All of these features are well reproduced by the R3S simulator (Fig. 7.28), showing that the principle of the measurement is well understood and properly simulated numerically for a realistic scenario (as required at SRL=5). Also, it appears that at 40 m wavelength there is no clear signature of the wind sea in the SWIM data, as expected from the noise-dominated simulation for these shorter wavelengths.

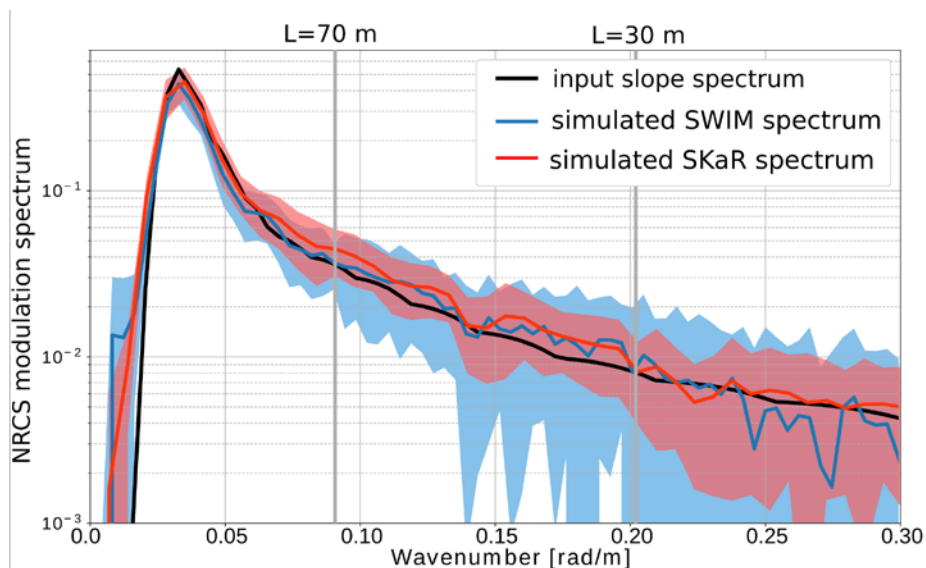


Figure 7.28. SWIM and SKIM Level-2a modulation spectra (and variability from 25 realizations) simulated using R3S (Nouguier 2019) without Doppler beam sharpening, compared to input slope spectrum in swell direction (azimuth 199°), after removing the noise pedestal (F. Nouguier, LOPS).

7.4.3.2 Reference Scenario and Error Analysis

Figure 7.29 shows 1-D intensity spectra obtained from simulated data for the average case specified in Table 7.1. In the upper panels, the instrument is looking at 90° azimuth, in the direction of the wind. In the lower panels the instrument looks at 45° degree, in the direction of the swell. The right panels show the spectra after bias removal, with the bias estimated from the data. Each plot shows two cases: in blue, the results obtained using Doppler-resolved intensity data; in green, the results obtained using the mean-intensity profiles. In each case, the plots show the average of the 100 simulations (solid lines), with the shaded areas indicating the $1-\sigma$ confidence intervals. The peak at around 0.02 rad m^{-1} corresponds to the swell, which can be clearly separated from the wind-driven wave-spectrum

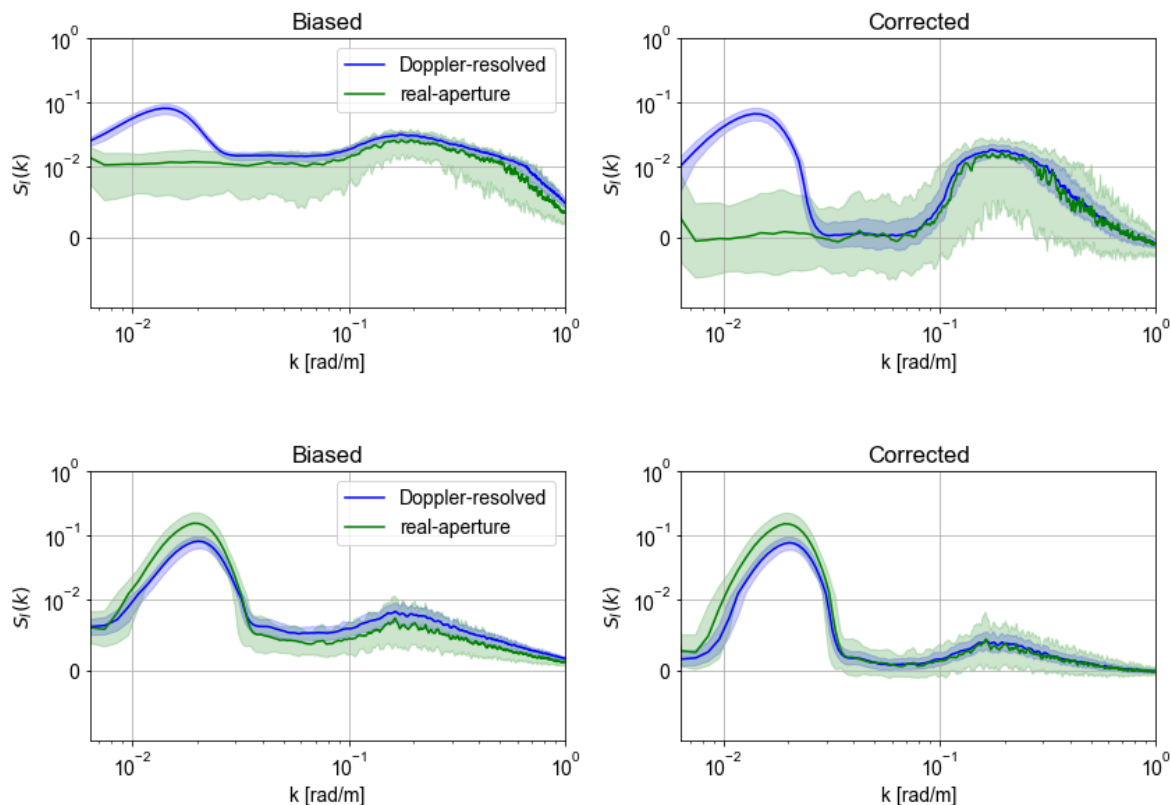


Figure 7.29. Simulated intensity spectra before and after bias removal for the average case specified in Table 7.1. Top: 12° degree beam at 90° azimuth (wind-direction). Bottom: 12° degree beam at 45° azimuth (swell-direction). The figure shows the mean of 100 simulations, with the shaded area indicated the $1-\sigma$ interval. The blue lines correspond to the Doppler-resolved case. (P. Lopez-Dekker, TU Delft)

The results illustrate several important things:

- SKIM can retrieve useful wave-spectral information up to wavenumbers of around 0.8 rad m^{-1} , or wavelengths under 10 m, greatly exceeding the requirement (30 m).
- Using Doppler-resolved data dramatically decreases the uncertainty in the retrieved spectra. This improvement results from the reduced cross-range size of the Doppler-sharpened footprint, as discussed in Chapter 6 and (implicitly) in the literature



(Jackson 1987). As expected, in the Doppler-resolved case, the sensitivity to swell modulation in directions quite far apart from radar look is largely enhanced.

Even with the simplified bias-removal algorithm used for the current analysis it is possible to remove most of the bias. As the performance improvement resulting from using Doppler resolved data is clear, it is pertinent to examine the impact of the number of pulses used for the delay-Doppler processing. A 32-pulse Doppler processing (current system baseline) performs well. Tests with a 64-pulse Doppler processing could improve performance of the delay-Doppler processing, something to be considered in the Phase-B studies.

Aside from the intrinsic value of the wave spectra, they are needed to estimate the wave-Doppler (U_{WD}). U_{WD} is derived from the p -th moments of the NRCS-spectrum,

$$M_p = \int_{k_l}^{k_h} k^p \cdot S_\sigma(k) dk, \quad (7.1)$$

with $p \in [0, 1, 1.5, 2]$. In our analyses the integration interval has been set between 0.01 and 0.6 rad/m. The normalised standard deviation

$$\sqrt{\langle M_p^2 \rangle - \langle M_p \rangle^2} / \langle M_{p,max} \rangle \quad (7.2)$$

of these moments provides an estimate of the variance of the U_{WD} estimation error. This normalisation is with respect the mean moment in the dominant direction, which for wind-driven waves corresponds to the wind direction.

For our reference scenario, the normalised standard deviation in the dominant (wind) direction is 5.5% for all values of p , using Doppler-resolved data (see Table 7.14). This doubles to approximately 11% if the real-aperture spectra are used.

In this case, at 45° azimuth, the normalised errors are lower due to the overall reduced spectral density. These results are better than the 10% set in the Mission Requirements Document in order to meet the U_{WD} estimation requirements.

Quantity	$p = 0$	$p = 1$	$p = 1.5$	$p = 2$
Dominant direction, Doppler-resolved	5.5%	5.5%	5.5%	5.5%
Dominant direction, real-aperture	10.9%	10.7%	10.9%	11.2%
45° azimuth, Doppler-resolved	3%	2.5%	2.5%	2.6%
45° azimuth, real-aperture	8%	3.7%	3.6%	3.7%

Table 7.14. Normalised spectral moments uncertainties for the reference case considered., assuming 64-pulse delay-Doppler processing. For the 32-pulse case the uncertainties for the Doppler resolved case increase with approximately a $\sqrt{2}$ factor.

7.4.4 Performance of Level-2b U_{CD}

SKIM Level-2b performance has been assessed using a specific metric (M1) based on simulations performed over regional SKIM regional scenario areas defined in Figure 7.30.

The regional test areas were chosen as follows:

- **Fram:** This area is used to study the impact of ice and the performance of SKIM in the marginal ice zone, where the computation of U_{WD} is expected to be a challenge near to the ice edge. Note that this area also serves to understand coastal areas in general.

- **Gulf Stream:** This is a very dynamic area in which TSCV is expected to have with large magnitude with rapidly evolving mesoscale and sub-mesoscale dynamics. The geostrophic is valid in this area, though as structures are moving fast, eddies and fronts are not always well captured by currents derived from altimetry.
- **Equatorial (Atlantic only):** is designed to simulate purely non-geostrophic currents and determine how well the Level-2c signal is captured in the presence of patchy rain.

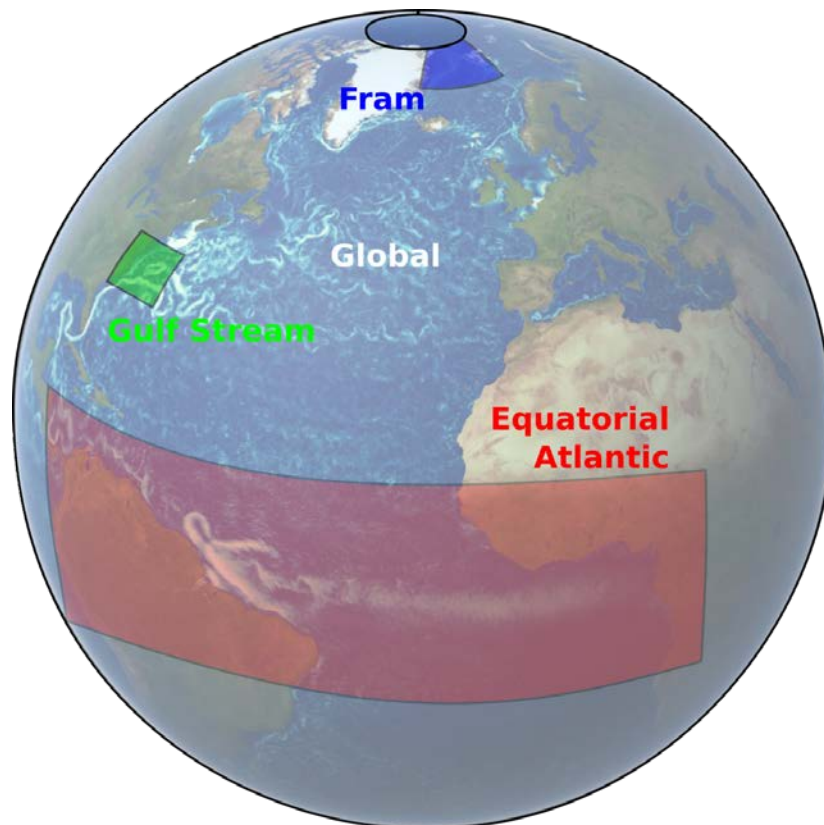


Figure 7.30. SKIMulator test scenarios areas used to evaluate Level2-b performance showing the location of the Fram, Gulf Stream and Tropics (Atlantic only) areas.

The SKIMulator includes all of the uncertainties described in Section 7.2.2.1 describing the input scene generation. These are associated to instrument V_{LOS} estimation errors, residual errors in the U_{WD} estimate, NRCS gradient, and attitude mis-knowledge. The latter two are associated to the motion of the platform via the non-geophysical Doppler V_{NG} . Statistical errors as a function of the azimuth and the beam angle have been provided by SEEPS for a given σ^0 . These curves are then interpolated proportionally to the σ^0 on each point. Random errors are generated using a normal distribution with standard deviation proportional to the interpolated curve. The remaining attitude error is computed offline using fine-pointing DDC method described in Section 7.4.1 and the computed uncertainties are added to the SKIMulator outputs.

Incidence	Region	Total U_{CD} (Us)	Instru-ment	U_{WD} residual	U_{AGD}	Attitude	RMS of “Truth” U_{CD} (Us)
6°	Gulf Stream	0.38 (0.006)	0.18	0.08	0.31	0.07	0.42 (0.058)
6°	Equator	0.38 (0.002)	0.20	0.05	0.31	0.07	0.24 (0.043)
6°	Fram	0.42 (0.010)	0.06	0.24	0.29	0.07	0.16 (0.043)
6°	Global	0.40 (0.004)	0.16	0.14	0.31	0.07	0.22 (0.045)
12°	Gulf Stream	0.19 (0.008)	0.09	0.13	0.08	0.05	0.42 (0.058)
12°	Equator	0.15 (0.003)	0.09	0.08	0.08	0.05	0.24 (0.043)
12°	Fram	0.34 (0.006)	0.11	0.31	0.08	0.05	0.16 (0.045)
12°	Global	0.24 (0.005)	0.09	0.19	0.08	0.05	0.22 (0.058)

Table 7.15. Concept A: Level-2b RMS uncertainty for the radial TSCV U_{CD} and its component the Stokes drift U_s , all in $m s^{-1}$ at 6° incidence angle and wind speed $> 5 m s^{-1}$ for the test case areas identified in Fig. 7.27. U_{WD} is the Wave Doppler and U_{AGD} is the effect of NRCS gradients.

Tables 7.15 and 7.16 report the results of the simulations for each test area as well as for the global ocean domain. Results clearly show that the uncertainty on U_{WD} is generally the largest source of uncertainty for the radial TSCV at 12° incidence and the effect of NRCS gradient, before instrumental uncertainty on VLoS is the largest source for incidence 6°. Performance is therefore driven by both the implementation of the wave Doppler correction algorithm and the instrument uncertainty.

Incidence	Region	Total U_{CD} (Us)	Instru-ment	U_{WD} residual	U_{AGD}	Attitude	RMS of “Truth” U_{CD} (Us)
6°	Gulf Stream	0.41 (0.006)	0.22	0.08	0.31	0.07	0.42 (0.058)
6°	Equator	0.40 (0.002)	0.23	0.05	0.31	0.07	0.24 (0.043)
6°	Fram	0.44 (0.010)	0.14	0.24	0.29	0.07	0.16 (0.043)
6°	Global	0.41 (0.004)	0.21	0.14	0.31	0.07	0.22 (0.045)
12°	Gulf Stream	0.41 (0.008)	0.22	0.08	0.31	0.07	0.42 (0.058)
12°	Equator	0.40 (0.003)	0.23	0.05	0.31	0.07	0.24 (0.043)
12°	Fram	0.44 (0.006)	0.14	0.24	0.29	0.07	0.16 (0.045)
12°	Global	0.41 (0.005)	0.21	0.14	0.31	0.07	0.22 (0.058)

Table 7.16. Same as Table 7.15 for Concept B.

The uncertainties on the Stokes drift are typically under 10% of the RMS value, and largest where spatial gradients in the sea state are largest (near coast, ice edge, strong currents).

These results show that Concept A marginally out performs Concept B for both the 6° and 12° off-nadir beams.

Over ice infested regions (tested here in the “Fram” case), the lower near nadir NRCS leads to higher instrument error as a consequence of SNR. Over sea ice and ~20 km away from the ice edge, the U_{WD} error is very small because only long swell waves penetrate into the sea ice. The maximum wave Doppler error occurs in a band of ~20-40 km around the ice edge due to very large gradients in the wave field that are not properly accounted for in the current implementation of the wave Doppler separation algorithm.

Future work in later phases is expected to improve the wave Doppler correction algorithm in this region by developing a dedicated algorithm for the water side of the ice edge. This would ideally be based on a combination of dedicated campaign measurements, multi-variate satellite data sets and NWP/NOP model output.

The NRCS gradient effect is based on both theory and nadir measurements from SARAL-Altika, assuming that all the measured NRCS variability is due to the ocean surface (and not to tracker noise or atmospheric effects). More campaigns will be needed in future phases to quantify this effect over both water and sea ice.

7.4.5 Performance of Level-2c U_{CD}

The SKIM Level-2c product is the main 'flagship' product from the mission serving all users. Examples are shown in Fig. 7.31. Performance at Level-2c has been assessed by running global Level-2 SKIMulator simulations using metrics M2, M3 and M4 all computed over a representative 30-day period and eventually a 1-year period mapped at a resolution of $1^\circ \times 1^\circ$ latitude longitude.

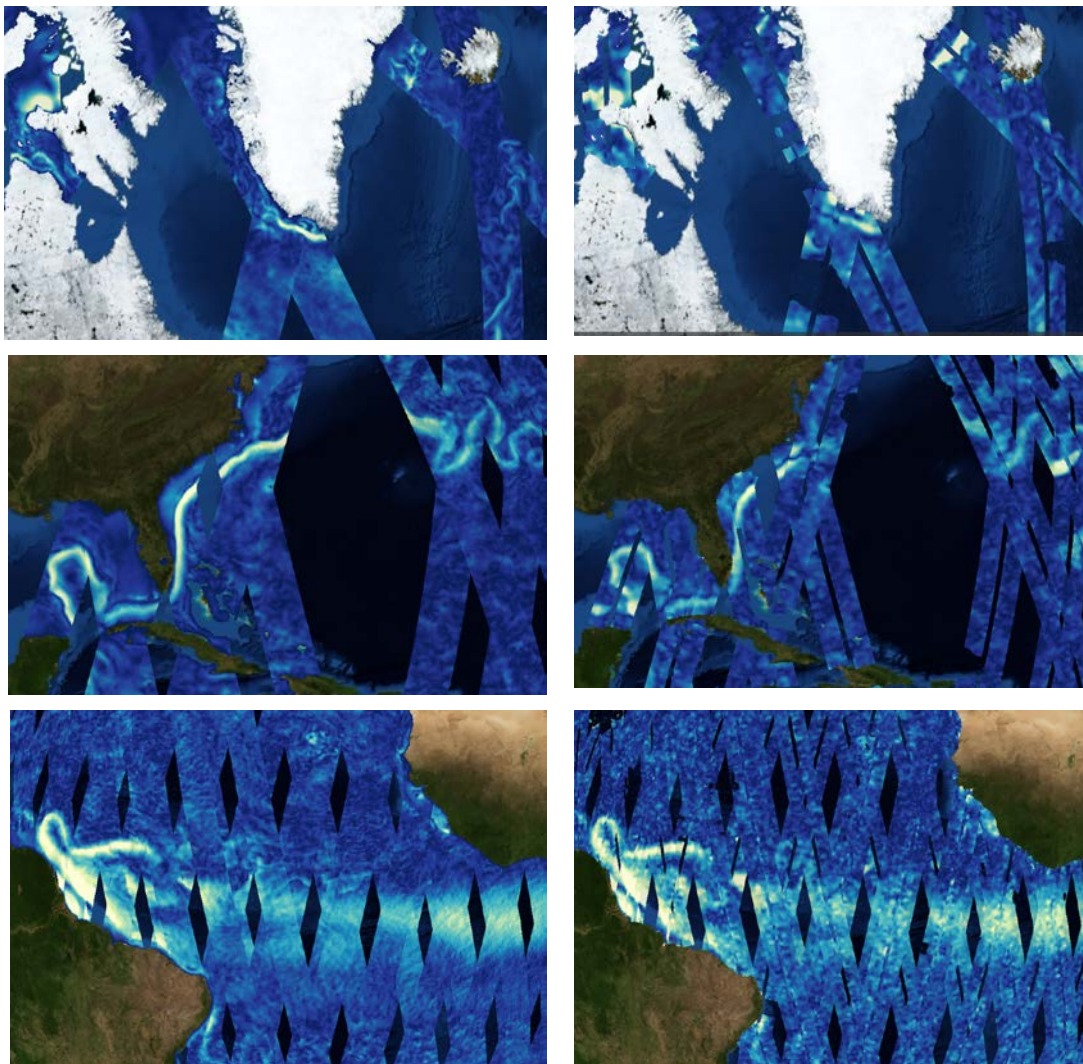


Figure 7.31. Example input (left) and Level-2c output(right) from the showing (top) Greenland current, (centre) Gulf Stream area (bottom) Tropical Atlantic area.



Additional flags have been used to quality control the simulation output data and remove these points from the performance analysis in the following way:

- When rain rates are $\leq 0.15 \text{ mm hr}^{-1}$
- When the wave Doppler estimation is $\geq 2 \text{ m s}^{-1}$ compared to the CO coefficient (i.e. deviation from the expected GMF) for a given wind speed indicating out-of-bounds algorithm failure. This is a conservative filter.
- 40 km around the satellite ground-track have been removed since there is insufficient azimuth diversity in the along-track at this across track location to construct a TSCV.
- 10 km at the edge of each swath have been removed since there is insufficient azimuth diversity in the across-track direction at this location to construct a TSCV.

It should be noted that, although the data removed around nadir and at the edge of the swath, these measurements still contain extremely accurate and useful Level-2b for one of the velocity vector components that can still be exploited.

Tables 7.17 and 7.18 present the results for performance metric M2 in both across-track and along-track directions for Concept A and Concept B. As for Level-2b_U measurements, three regional test cases have been analysed (Fig. 7.27) in addition to a global coverage simulation.

Using performance metric M2, both configurations are compliant with the specification of $\leq 0.15 \text{ ms}^{-1}$ or 15% (whichever is greater) for the TSCV in all test regions. The requirements on the Stokes drift (2.5 cm s^{-1}) are most easily met.

Region	Total UCD (Us)	Mapping	Instrument	Uwd residual	USGD	Attitude	RMS of “Truth” UCD (Us)
Gulf Stream	0.12 (0.006)	0.05	0.04	0.05	0.07	0.01	0.40 (0.055)
Equator	0.10 (0.002)	0.02	0.04	0.04	0.05	0.01	0.16 (0.042)
Fram	0.10 (0.009)	0.03	0.01	0.04	0.03	0.01	0.11 (0.030)
Global	0.11 (0.003)	0.03	0.03	0.08	0.06	0.01	0.21 (0.044)

Table 7.17. Concept A and B (same performance) Level-2c RMS uncertainty on TSCV (UCD) and Stokes drift (US) across-track component at 30 km grid uncertainty performance in m s^{-1} with wind speed $>5 \text{ ms}^{-1}$ for the test case areas identified in Figure 7.27. UWD is the Wave Doppler and USGD is the Sigma0 gradient.

Region	Total UCD (Us)	Mapping	Instrument	Uwd residual	USGD	Attitude	RMS of “Truth” UCD (Us)
Gulf Stream	0.13 (0.007)	0.04	0.03	0.07	0.04	0.01	0.32 (0.042)
Equator	0.10 (0.003)	0.01	0.05	0.05	0.04	0.01	0.13 (0.036)
Fram	0.09 (0.016)	0.04	0.02	0.06	0.04	0.01	0.12 (0.024)
Global	0.12 (0.004)	0.02	0.03	0.10	0.05	0.01	0.18 (0.039)

Table 7.18. Same as Table 7.17 for along-track current component

In order to assess the current SKIM potential to reach goal values of 0.1 m s^{-1} Additional simulations were performed using an alternative grid sizes. In this configuration the inherent noise in the Level-2b_U data will be mitigated through averaging. At a resolution of 75 km the goal requirement can be met.

Again, from these performance figures it is clear that, as for Level-2b performance, instrumental noise is not the dominant source of uncertainty in Level-2c. Performance is driven by the current implementation of the wave Doppler correction algorithm.



Doppler estimation leading to the counterintuitive conclusion that SKIM will perform best, not in the strongest TSCV regimes, but in areas characterised by relatively uniform TSCV. But in these cases, we should note that the absolute uncertainty in such strong TVSC gradients is not so important.

In addition to the work identified for ice areas, future work in later phases is expected to improve the wave Doppler algorithm as follows:

- Test the application of a multivariate machine learning approach to optimise the wave Doppler algorithm. We expect this approach to result in a parameterised geophysical model function of the wave Doppler estimation as a 3D-surface analogous to that used by operational scatterometer (the SKIM ‘Beluga’ GMF approach). In particular, during the Phase-E1 commissioning, sufficient in-flight data will be available to constrain this surface with very good accuracy and precision based on a large range of wind-wave conditions.
- Improvements based on separating the local and non-local Stokes drift estimation using external wind velocity measurements from MetOp-SG(1B) SCA and *a priori* swell spectrum information propagated from previous orbit measurements (e.g. using swell fireworks approach introduced by Collard et al., 2009).
- Further theoretical work to develop the wave Doppler estimation.

7.4.5.1 Mean Geographical Variability of Level-2c Product Performance

One important aspect of SKIM Level-2c products is understanding in which areas SKIM measurements can provide a useful information. This is a function of the SNR and as previously discussed, the uniformity of strong TSCV regimes.

Using metric M3, the percentage coverage where TSCV uncertainty is $\leq 0.15 \text{ cm s}^{-1}$ at least 70% is marginally compliant with a value of 69%. In terms of metric M4 54% coverage is attained. This latter performance is expected as the central ocean gyres are characterized by weak TSCV structures in the Truth used here. Better performance would be obtained with a more realistic Truth containing a proper level of near-inertial energy that dominates in many parts of the global ocean that is not present in the MITgcm outputs.

A further analysis using metric M2 has been performed at the global scale and is presented in Fig. 7.32. The simulation results show that SKIM Level-2c products and level-2B across-track and along-track component uncertainties are strongly reduced in Level-2c products. This is the classical reduction linked to the weighted least-squares averaging of independent measurements that leads to an error reduction by a factor $1/\sqrt{Nobs}$ where *Nobs* is the effective number of independent observations (Fig. 6.3).

The results are very good at meeting the requirements using metric M2 in all cases.

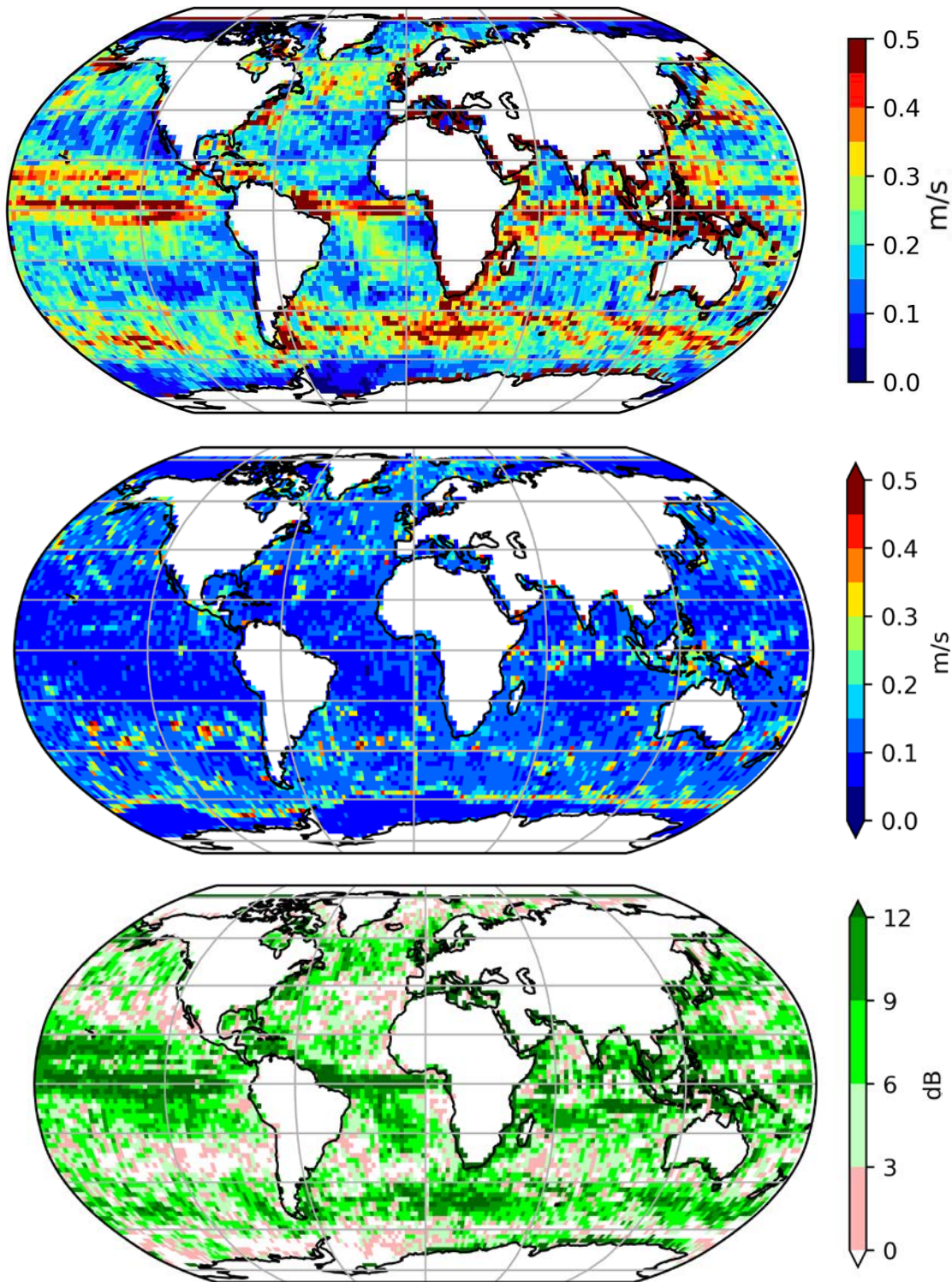


Figure 7.32. Top: reference TSCV Truth, middle: RMS uncertainty of SKIM Level-2c at 30 km resolution for a 30-day period computed by SKIMulator and mapped gridded at 1° latitude x longitude, bottom: SNR computed as the ratio of Truth (top plot) divided by simulated uncertainty (middle plot).



Figure 7.33 gives further insight into the dominant sources of errors and possible future improvements using alternative choices of processing or retrieval algorithm. The wave Doppler uncertainty dominates in the outer part of the swath. For the centre part of the SKIM swath (where beam elevation and azimuth sampling is optimal for the Phase A SKIM beam configuration) the goal requirement is approached, and the limiting factor there is expected to be the NRCS gradients. A full closed-burst acquisition mode could help because this offers a potentially better sampling capability in azimuth. This should be considered early on in Phase-B1. In general, further work in Phase-B1 should be dedicated to consider alternative beam placement that considers not just a geometric approach in terms of velocity vector construction but also accounts for beam elevation and azimuth diversity that is fundamental to reducing uncertainty in wave parameters that drive the wave Doppler correction.

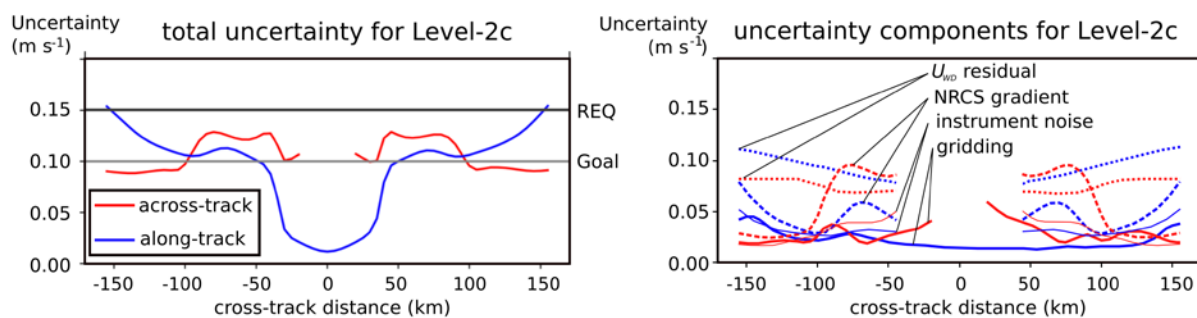


Figure 7.33: Left: global average RMS uncertainty for along-track and across-track TSCV at Level-2c using metric M2. Right: decomposition of TSCV uncertainty for cross-track (red) and along-track (blue).

7.4.5.2 Overall Performance of Level-2c

Observational Requirement	Specification	Concept A	Concept B
Level-2c TSCV	TSCV over the global ice- and precipitation-free ocean and inland seas from 82°S to 82°N at a resolution of 30 km with a revisit of ≤ 10 days at the equator and a combined standard uncertainty in UAC and UAL ≤ 0.15 m s ⁻¹ (goal: ≤ 0.1 m s ⁻¹) or 15% of the TSCV (whichever is greater) for at least 70% of the ocean surface.	Compliant with requirement and marginally compliant with goal. Goal can be reached at Level-2d or by averaging up to 75 km grid. See Table 7.17 and 7.18	
Level-2c Stokes drift	Stokes drift over the global ice- and precipitation-free ocean and inland seas from 82°S to 82°N at a resolution of 30 km with a revisit of ≤ 10 days at the equator and a combined standard uncertainty in UAC and UAL ≤ 0.025 m s ⁻¹	Compliant with requirement. See Table 7.17 and 7.18	with requirement.
Level-2c Waves	For a gridded spatial resolution of ≤ 70 km over the global ice- and precipitation free ocean and inland seas from 82°S to 82°N with a revisit of ≤ 10 days with Hs between 1-25 m with combined standard uncertainty of ≤ 30 cm or 10% (whichever is greater). The directional resolution shall be $\leq 10^\circ$ in all directions for wavelengths of $\leq 30 - 500$ m.	Compliant except for 10° sector in the along track direction. See Figure 7.26 –7.27	

Table 7.19. Summary of Level-2c compliance with requirements.

As expected, the effective SKIM Level-2c performance varies regionally owing to the combination of the various sources of uncertainty and SNR associated with patterns of the TSCV. In dynamic regions of the ocean surface (western boundary currents) where significant wave–wind–current interaction occurs, the current version of the SKIM wave Doppler algorithm is challenged. We have identified several areas for improving the current



algorithm and in addition, we suggest that alternative radar configurations (full closed-burst) are investigated in more detail during Phase-B1.

In central ocean gyres where weak TSCV prevails, as expected, the SNR of SKIM Level-2c performance is naturally poor. However, techniques based on constrained OI offer considerable promise and should be studied further as part of the SKIM Level-2d product family (Pers. Comm. C. Ubelmann, DOFS meeting 29017).

7.5 Level-2 Performance Assessment Based on Experimental Data

The physics of the Doppler velocity measurement from a microwave radar at near-nadir incidence is now well understood (Chapron et al., 2005, Yurovsky et al., 2019) and described in Chapter 4. To date, these principles have only been demonstrated in coastal regions with moderate sea states of significant wave height under 1 m (Yurovsky et al., 2018, Nougquier et al., 2018) and processing techniques slightly different for SKIM.

A version 1.0 of the SKIM U_{WD} algorithm has been developed but has not been validated using any *in situ* based data. For these reasons, a campaign was implemented (Fig. 7.34) with the Ku- and Ka-band airborne demonstrators KuROS and KaRADOC. The campaign was designed to,

- Verify the sensitivity of pulse-pair Doppler radar measurements to both currents and waves for near-nadir measurements and oceanic conditions
- Validate the version 1.0 U_{WD} algorithm.
- Verify the R3S Simulator (Nougquier., 2019) and its capability to adapt to airborne configurations.

It is not possible to mimic exactly the characteristics of SKIM using an aircraft platform. A satellite in low earth orbit has a much higher velocity (typically 7 km s^{-1}) compared to 0.12 km s^{-1} for an aircraft. As a result, the pointing accuracy is much stricter for SKIM than for an airborne instrument.

A direct translation of retrieval noise and error to the SKIM measurement is not possible due to very different platform velocity, stability and measurement geometry. In particular, the incidence and azimuth angles vary significantly on the scale of the dominant ocean wavelength, around 200 m, making it impossible to average many wavelengths with constant viewing angles.

7.5.1 Campaign Implementation

By design, the campaign location should ideally have a representative sea state, long fetch wind/wave regime, be logistically appropriate (i.e. close to port/airport, close to lab, already have suitable in water and meteorological measurement infrastructure) and importantly, have a strong tidal regime. Using the tide, a range of ocean currents can be measured from effectively no current at slack water to strong currents when in full flow depending when measurements are taken.

The DRIFT4SKIM campaign took place on 21–27 November 2018 close to Brest off the French Atlantic coast. Further details can be found in Marié et al. (2019). This is an oceanic environment, open to offshore swells, which is important to verify the limited effect of wave

development on U_{GD} . The region generally has sea states typical of the North Atlantic. The experiment was unique in the fact that it sampled a wide range of wave heights from 0.8 to 2.8 m (note that the global average is 2.5 m) while avoiding the severe storms that occurred 2 days before and after, making in situ deployments impossible. The area has a well-known tide-dominated current regime that is monitored by a 12 MHz High-Frequency radar (Ardhuin et al., 2009) operated by Service Hydrographique et Oceanographique de la Marine (SHOM). The week around spring tides of November 2018 was targeted, in order to allow for a wide range of current speeds, as well as to accommodate aircraft availability constraints. The characteristics of this location mean the DRIFT4SKIM experimental design is different from previous Doppler airborne campaigns (e.g. Martin et al., 2016; Rodríguez et al., 2018).

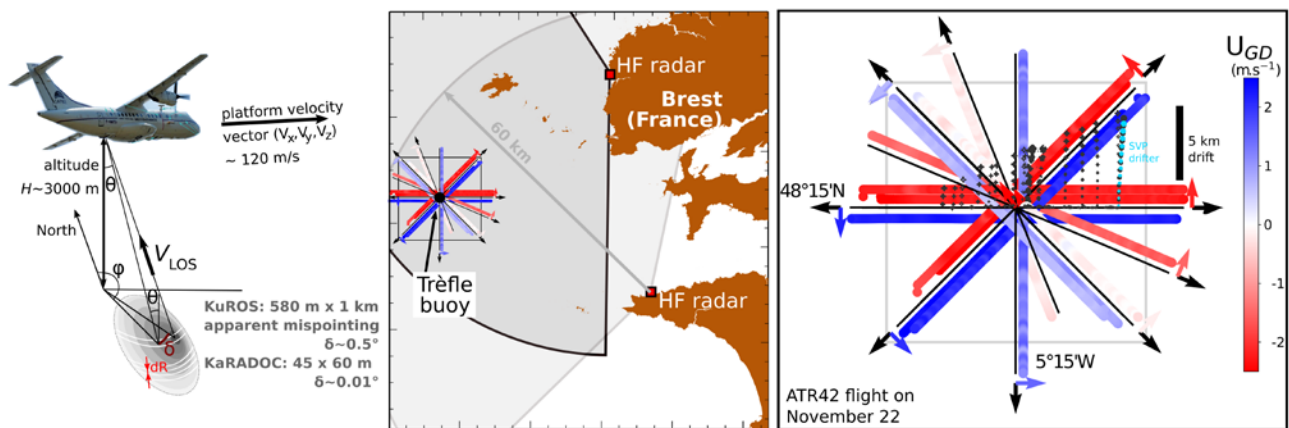


Figure 7.34. Left: measurement geometry for DRIFT4SKIM airborne measurements. Keeping the same incidence angles as SKIM gives a much smaller footprint in airborne data, which is of the order of the dominant ocean wave wavelength. Centre: location of the DRIFT4SKIM campaign showing the coverage of a HF-radar used throughout the campaign to determine TSCV and example of Doppler velocities measured by KaRADOC on 22 November. Right: magnified view of the flight paths (black lines) and KaRADOC Doppler (offset to the side) always looking to the left (see coloured arrows for look direction) and position of drifters within a one hour window, deployed from R/V Thalia steaming from east to west. The following link <https://odl.bzh/eVRHv1TE> provides an interactive summary of the campaign.

Two radars were mounted on an ATR-42 aircraft with different objectives. KuROS is the airborne demonstrator for SWIM and was developed for calibration and validation activities. It is a Ku-band radar with a wide beam that is designed to mimic the azimuthal averaging of a satellite system, hence it has a wide azimuthal aperture $\theta_{3dB}=10.6^\circ$ (one-way antenna gain) of 580 m that can effectively average short wind-waves not aligned with the look azimuth.

KuROS has a Doppler capability that was used in relative terms to remove the wave propagation azimuth ambiguity (Caudal et al. 2014). The KuROS processing chain was adapted, following the SEEPS, in order to obtain an absolute Doppler velocity. The very wide antenna beam means that the contribution of the azimuthal gradient Doppler U_{AGD} is actually larger for KuROS on ATR42 than for SKaR on SKIM, in spite of a 60 times slower platform velocity.

In contrast, the KaRADOC system has a much narrower beam with a 45 by 60 m (2-way) footprint, and the U_{AGD} contribution is negligible. The non-geophysical aspect of the measurement is particularly discussed by Marié et al. (2019).



A range of in-situ instruments (surface current drifters, drifting and moored wave-measuring buoys), as well as two airborne Doppler radars operating in Ku- (KuROS) and Ka- (KaRADOC) bands were operated. Two types of drifters were used during the campaign including CARTHE drifters (Novelli et al., 2017), drogued around 40 cm, and SVP drifters (Niiler and Paduan, 1995), drogued at 15 m. These were deployed in the measurement areas at locations and times that resulted in the drifters being under the aircraft flight path. The following link <https://odl.bzh/eVRHv1TE> provides an interactive animation of all drifter deployments and trajectories (time animation by scrolling over the timeline).

The R/V *Thalia* worked in the offshore area providing continuous underway measurements of meteorological parameters using a Météo-France “BATOS” operational system comprising a Vaisala WXT-series sonic anemometer located approximately 10 m above sea surface. The ship also conducted a small hydrographic survey of the region. In the summer, the so-called Ushant tidal front (Le Boyer et al., 2009) has a strong influence on the current and conditions in the offshore box. CTD casts were performed from R/V *Thalia* during the campaign, that showed the water column to have a very well mixed surface-layer. The spatial homogeneity of the experimental area was also checked using the ship thermosalinograph. In addition, an infrared camera was mounted on a second aircraft which surveyed the area flying under the clouds from an altitude of 500 m to 1000 m. Interesting small-scale surface signatures could be observed on calm days, but no density-associated mesoscale structure was present.

A wide range of geophysical conditions were encountered during the one-week long campaign. The wave height during the campaign was dominated by the presence of two swell systems from North Atlantic remote storms. The swell height decreased from 2.5 to 0.9 m from the 21 to 24 November, with a peak frequency increasing from 0.07 Hz to 0.1 Hz, and a mean direction gradually veering from west to north-west. This swell contributes little to the Stokes drift (about 10% on 22/11).

7.5.2 Results

A preliminary effort to translate KuROS results to SKIM is made by Marié et al. (2019) using the SEEPS-like simulator R3S (Nouguier et al., 2019) to simulate both KuROS and SKIM data, thereby validating the main assumptions of the SEEPS algorithms.

7.5.2.1 Verification of the R3S Simulator

Yurovsky et al., (2019) confirmed with in situ experiments, a near nadir Ka-band Doppler pulse-pair radar system measures a radial geophysical Doppler $U_{GD,R}$ that contains a wave contribution $U_{WD,R}$ of the order of 2 m s^{-1} projected on the direction of the Stokes drift. The same analysis was performed on the KuROS Ku-band data showing a good understanding of the scattering mechanism.

The R3S was further used to investigate the impact of NRCS azimuthal gradients associated with the wide beam of KuROS. Fig. 7.35 clearly show that the observed large modulation in azimuth is largely due to this effect and not to the orbital velocity. Hence, KuROS measures a combination of azimuthal slopes and orbital velocities. The SKIM simulation shows some signal for 40 m and even shorter waves that was analysed in more detail with the reference scenario.

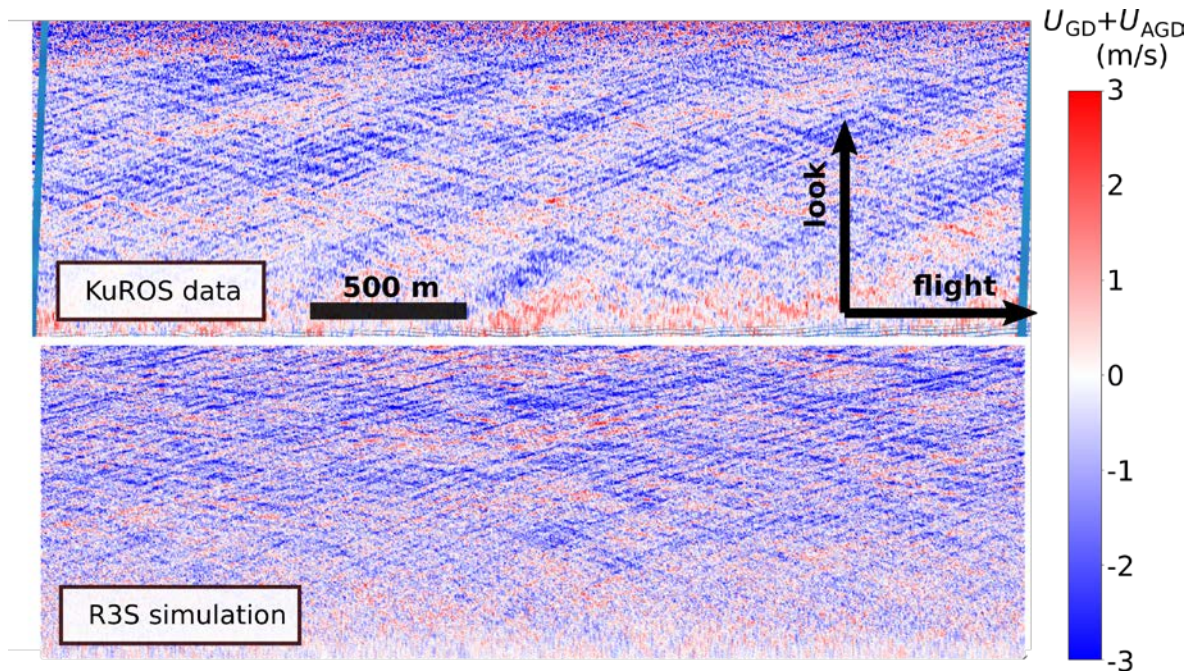


Figure 7.35. Qualitative validation of radar imaging mechanism in R3S simulations. Both the real data and simulation contain the geophysical modulation of velocities associated to surface velocities and slopes in the look direction (part of U_{GD}) and aircraft velocities and slopes in the flight direction (part of U_{AGD}), as fully discussed by Marié et al. (2019). Note that the wave phases in the R3S simulation are random and cannot be expected to match those in the data.

7.5.2.2 Validation of the SKIM Version 1.0 U_{WD} Algorithm.

As shown in Fig. 7.36 the measured Doppler varies with azimuth as predicted by the SEEPS forward model, with an expected weak dependency of the wave Doppler magnitude on sea state conditions. Between 22 and 24 November, the strong drop in wind speed from 11 to 6 m s^{-1} and waves height from 2.6 to 1.7 m only results in a 5% SEEPS-predicted change in the wave Doppler magnitude from 2.24 to 2.14 m s^{-1} .

Following the standard processing method for HF-radar TSCV (e.g. Kim et al. 2008), the current vector U_{CD} is retrieved by considering a vector decomposition, fitting the azimuthal variation (here a simple cosine function) to estimate the vector U_{GD} from which the SEEPS-simulated wave Doppler, also approximated as a vector U_{WD} , is subtracted. These results show excellent qualitative agreement between theory and measurements. To within 10%, the wave-motion contribution U_{WD} matches theoretical predictions and the v1.0 U_{WD} algorithm performance is confirmed. Simply reducing the magnitude of U_{WD} by 10%, both components of the surface current vector are recovered within 15% or 0.1 m s^{-1} , whichever is greater.

Experience with other space borne measurements (scatterometer and altimeter electromagnetic bias) shows that the retrieval strategy can be efficiently based on a calibrated Geophysical Model Function (GMF). Improving theoretical and numerical simulation can be done by gathering additional data in Phase B/C/D and during the first phase of the mission, to conduct further controlled calibration and validation, as laid out in the validation plan (section 6.2), similar to what is done for other ocean instruments.

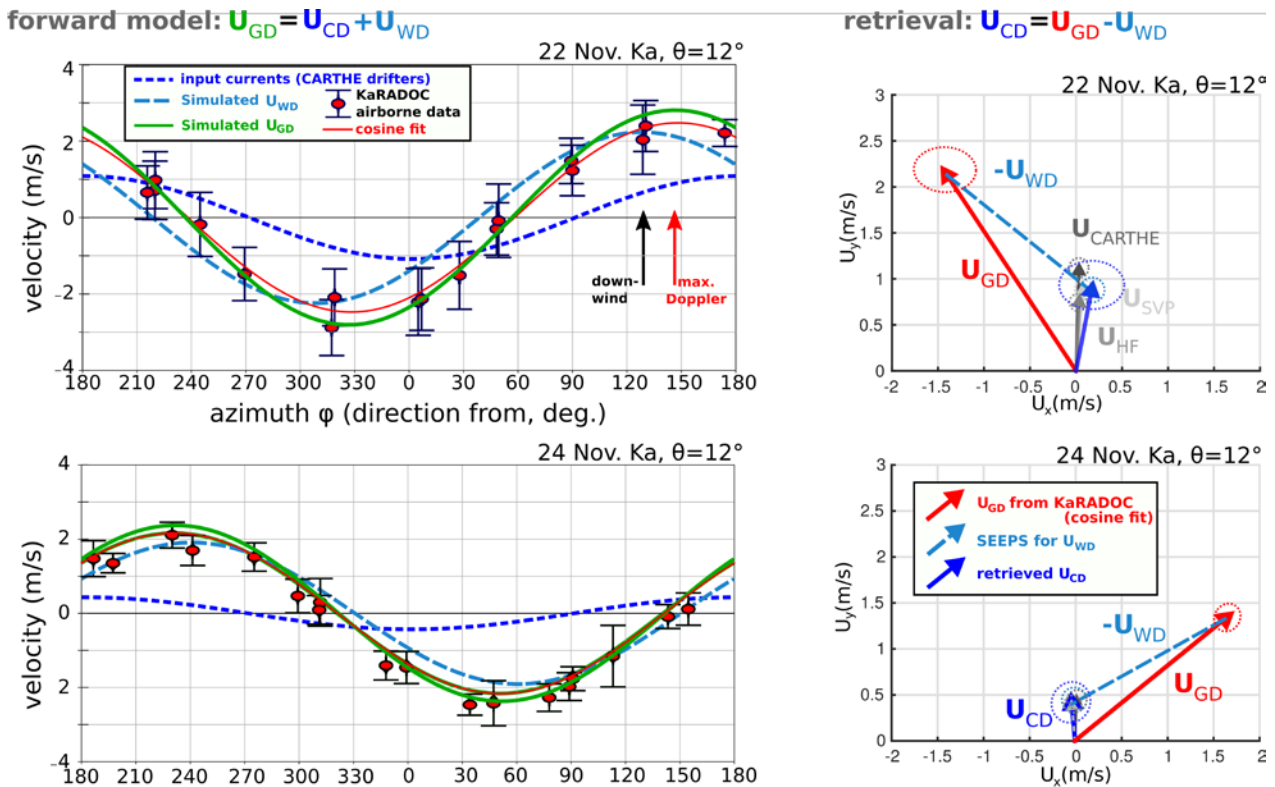


Figure 7.36. Left: validation of the wave Doppler forward model, from measured currents (CARTHE drifters) and waves (Trèfle buoy and Spotter drifters) to a geophysical Doppler U_{GD} , including a 10% reduction of U_{WD} . On November 22, Direction of Max Doppler (147°) is shifted from Max wind direction on 22/11 due to the combination of U_{CD} , from the south (181°), and U_{WD} from the south-east (128°). Right: retrieval of surface current vector U_{CD} in blue, compared to in situ measurements by HF-radar, CARTHE and SVP drifters. The uncertainties on U_{GD} are the uncertainty of the cosine fits on the left panels (Marié et al. 2019).

7.5.2.3 Summary of Campaign Results

The DRIFT4SIM campaign has successfully demonstrated the SKIM v1.0 algorithm using a combination of aircraft radar and in situ measurements. The 0.12 m s^{-1} variation of the wave Doppler between 22 and 24 November is important to capture for the Level-2c performance. It confirms the importance of having accurate wave measurements to estimate the wave Doppler. Yet, an estimation of U_{WD} based on the wind vector only would work relatively well, mitigating any mission risks due to potential limitations in determining wave spectra in regions of strong gradients. A joint wave and wind data set (which will be available during the mission) will allow for the construction of robust algorithms to remove wave biases by building synergy between the two measurements: spectra determine longer waves, whereas winds are sensitive to shorter waves. This is most important for wave conditions further away from equilibrium with the wind (see Fig. 4.2).

The measurement uncertainties on the determination of U_{WD} , demonstrated using campaign data, is consistent with the uncertainties expected from the experimental measurements. Different in situ measurements have been used all using slightly different technologies. HF-radar provides a measure over a spatial area representing the upper 2 m of the ocean surface, SVP drifters are drogued at a depth of 15 m compared to CARTHE drifters that sit in the top 1 m of the ocean surface.



The R3S simulator has been verified by adapting its capability to adapt to airborne configurations. The results obtained demonstrate both the real data and simulation output contain the geophysical modulation of velocities associated to surface velocities and slopes in the look direction (part of U_{GD}) and aircraft velocities and slopes in the flight direction (part of U_{AGD}).

The DRIFT4SKIM campaign data have confirmed the SKIM v1.0 algorithm. As SKIM will be the first satellite mission to provide wide-swath Doppler measurements, our ‘HF-radar in space’, the campaign results are an important milestone towards SKIM extending the capability of HF-radar to the world ocean.

8 MISSION CONTEXT

Building on the scientific and technical foundation of ESA’s Living Planet Program, the implementation of the SKIM mission and its unique ability to measure the Total Surface Current Velocity (TSCV), can directly contribute to long-standing Earth Observation challenges and Earth system science. These observations also have applications, and these applications generally contribute to the United Nations Sustainable Development Goals (SDGs, United Nations 2015). These goals and their specific timeline of targets are the United Nations blue print to achieve a better and more sustainable future for all by 2030. Five of the SDGs are directly relevant to SKIM (Fig. 8.1). They cover climate mitigation and adaptation measures (SDG13), marine life and biodiversity (SDG14), with clear links to sustainable marine food production (SDG12), the need to efficiently feed the world and eradicate hunger (SDG2) and the design and management of ocean energy systems for affordable and clean energy provision along with ensuring efficient and affordable energy use (SDG7).



Figure 8.1. SKIM and the UN Sustainable Development Goals: measurements of Total Surface Current Velocity (TSCV) can contribute to 5 of the 17 Goals (image credit: S. Hervé, University of Brest).

8.1 Science and societal benefit

8.1.1 Contribution to International Programmes

As specified by the Ocean Observation Panel for Climate (OOPC, 2017), many ‘derived variables’ are associated to the TSCV, including the horizontal heat and fresh-water fluxes, surface stress, kinetic energy and kinetic energy flux, upper-ocean turbulent mixing, surface turbulent heat and fresh-water/salt fluxes, ocean–atmosphere fluxes, advection of oceanic properties (biogeochemical tracers, pollutants, debris, etc.), particle dispersion and larval drift. Because the TSCV and Stokes drift give access to the representative velocity of the ocean surface mixing layer, where all constituents including salinity, temperature, gases and



nutrients are uniformly distributed, they enable the evaluation of these derived variables that are relevant for climate, food security and water quality to be quantified and studied. Similarly, as the measurement of the TSCV provides knowledge of the ocean surface kinematics and dynamics, it also enables the study and quantification of atmosphere-ocean exchange processes, that are relevant for energy, climate and water quality (SDG7, SDG13, SDG14 respectively). The following sections provide an overview of how SKIM will contribute directly to these SDGs and their associated targets.

8.1.2 Global Climate: Atmosphere-Ocean Fluxes and Transport of Heat and Carbon

8.1.2.1 Heat Transport

The poleward transport pathways of the tropical heat are only measured at a few locations, which are insufficient for understanding global intra-annual (sub-monthly) atmosphere-ocean heat fluxes and onward transport, all of which is important for understanding climate and weather forcing (Forget and Ferreira 2019). For example, the IPCC Fifth assessment report identified that different global estimates of sub-surface ocean temperatures have variations at different times and for different periods (Key Uncertainties in Observation of Changes in the Climate System, Stocker et al., 2013). Near the equator, heat is trapped and transported in the surface water layers with a very large associated uncertainty of 50-400 W/m² in the local heat imbalance (Foltz et al., 2019). TSCV measurements could reduce that uncertainty by at least a factor of two (SKIM Team, 2019), improving forecasting of rainfall patterns in the tropics at seasonal to decadal time scales (Foltz et al., 2019).

In the strongly stratified polar surface waters of the fragile and rapidly changing Arctic, the TSCV is associated to heat transport that affects both sea ice and land ice (Wood et al., 2018). TSCV observations are needed at all scales to understand this heat transport, from the Beaufort gyre (Armitage et al., 2018), to boundary currents like the Greenland current, new emerging upwelling systems (e.g. Pickart et al., 2013), hot spots of vertical mixing at continental shelf slope regions (Rippeth et al., 2015) and small mesoscale eddies which are not well observed in altimetry. The combination of SKIM data with altimetry will double the effective resolution of today's measurement of the geostrophic current (SKIM Team, 2019), contributing to better estimates of the ocean mesoscale eddies and their associated transport of heat (SKIM Team, 2019).

High latitudes are also characterized by faster near-inertial oscillations (NIOs) due to the higher Coriolis parameter. With SKIM, the analysis of these motions will benefit from faster revisit times, up to 3 times per day at 80°N. A preliminary analysis (SKIM Team, 2019) uses the long persistence of these oscillations that decorrelate on the time scale of three to 6 days (see also Fig. 2.9). This time scale is shorter than the decorrelation time scale of the geostrophic current, but still long enough to retrieve most of the NIO signal, as demonstrated in the North Atlantic with Level-2c SKIM simulated data (Fig. 8.2).

These rapid wind-driven motions are particularly important for the thinning and retreating ice. Also, the increased open water fetch and more developed waves are in turn altering the ice formation and break-up. Arctic sea ice is therefore dramatically changing, with more ice formation in the form of pancake ice (Thomson et al., 2018), making the Arctic ice appear more similar to Antarctic ice, with a wide, broken and rapidly shifting marginal ice zone (MIZ).

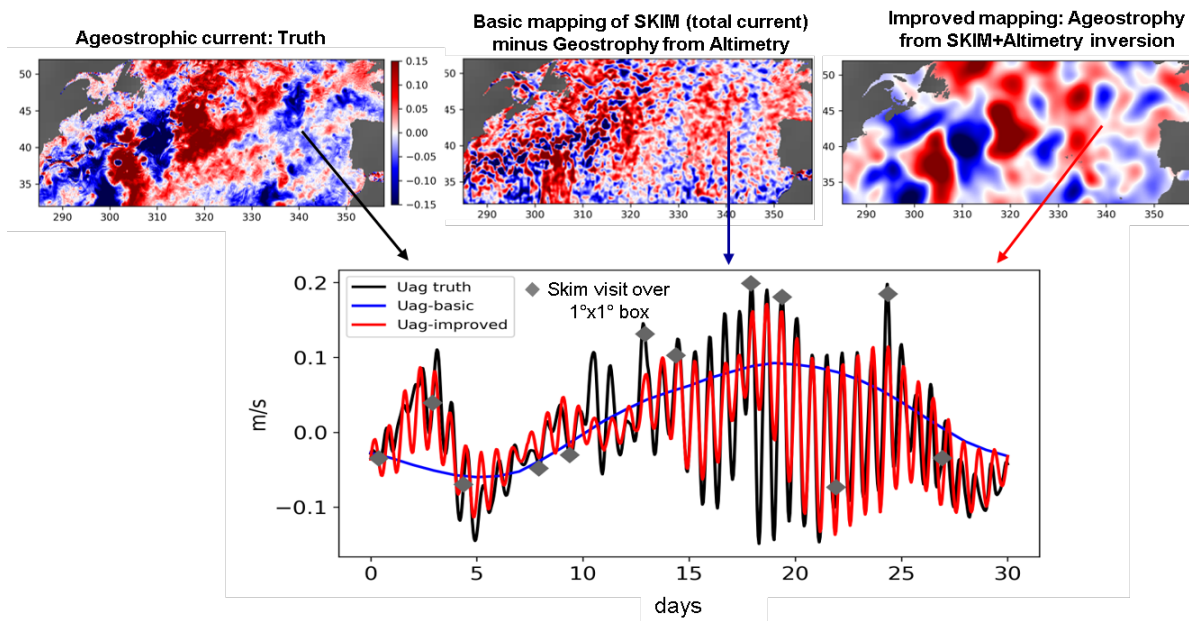


Figure 8.2. Top left: snapshot of ageostrophic surface current (m/s) in the NEMO NATL60-CJM run on November 1, 2012. Top middle: estimation of ageostrophic current at the same date, from SKIM and altimetry synthetic observations sampled in NATL60-CJM, with basic separate mapping of total current and geostrophy subtracted. Top right: improved mapping using multiple covariance functions (oscillating for NIOs) and global inversion. Bottom: time series at 42°N, 340°E of the three fields mentioned above. The grey diamonds indicate the presence of SKIM observations within a 1° box centred on 42°N, 340°E. (Figure from SKIM Team, 2019).

The MIZ is expected to cover over 50% of the Arctic sea ice by 2030 (Aksenov et al., 2017). SKIM should provide sub-daily measurements of sea-ice drift velocity close to the ice edge (Chapter 7). Such measurements are not currently possible within the highly dynamic MIZ (Sumatra et al., 2014, SKIM Team, 2019) and SKIM has the potential to provide these measurements (SKIM Team, 2019) which are needed for measuring upwelling flows, where currents, waves and sea-ice interactions are key variables (Kim et al., 2017, Meneghello et al., 2018).

8.1.2.2 Carbon Dioxide Transport.

The ocean has absorbed about 28% of all anthropogenic CO₂ emissions (Le Quere et al., 2018), slowing climate change, but this long-term absorption is reducing ocean pH (a process known as ocean acidification). As a natural sink of CO₂ the ocean is critical part of the global carbon inventory and estimates of oceanic carbon are even required for estimating land carbon uptake (see methods within Le Quere et al., 2018). The continental shelf-seas account for 10-20% of this ocean sink (Cai et al., 2006; Chen and Borges, 2009), but the global shelf-sea sink variability is poorly constrained and its strength is increasing, implying increasing acidification (Laurelle et al., 2018). Differences between shelves suggest that the coupling between the processes driving atmosphere-ocean exchange and those driving cross-shelf transport are important for controlling carbon accumulation (acidification) in the surface waters (Shutler et al., 2019). No synoptic scale monitoring approach currently exists to monitor shelf-sea carbon export (Shutler et al., 2019) and existing modelling efforts provide differing ageostrophic flows and exchanges, dependent upon the chosen model structure, bathymetry and parameterisation (Niiler, 2009; Graham et al., 2018). SKIM

cross-shelf TSCV will enable the first model-based monitoring of the continental shelf-sea carbon export (Fig. 8.3, Shutler et al., 2019; SKIM Team, 2019).

Direct measurements of surface kinematic properties from SKIM, such as the total kinetic energy (surface to ocean) flux (SKIM Level-1c product), would provide the opportunity for moving beyond simple proxies for quantifying atmosphere-ocean gas exchange and therefore reducing uncertainties in the oceanic sink of carbon. Early analysis suggests that published values of the global shelf-sea CO₂ sink could be underestimated by ~8% as they do not fully account for region specific wind-wave-current interactions and wave breaking (Holding et al., 2019). These wind-wave-current interactions will also be important for heat and momentum fluxes.

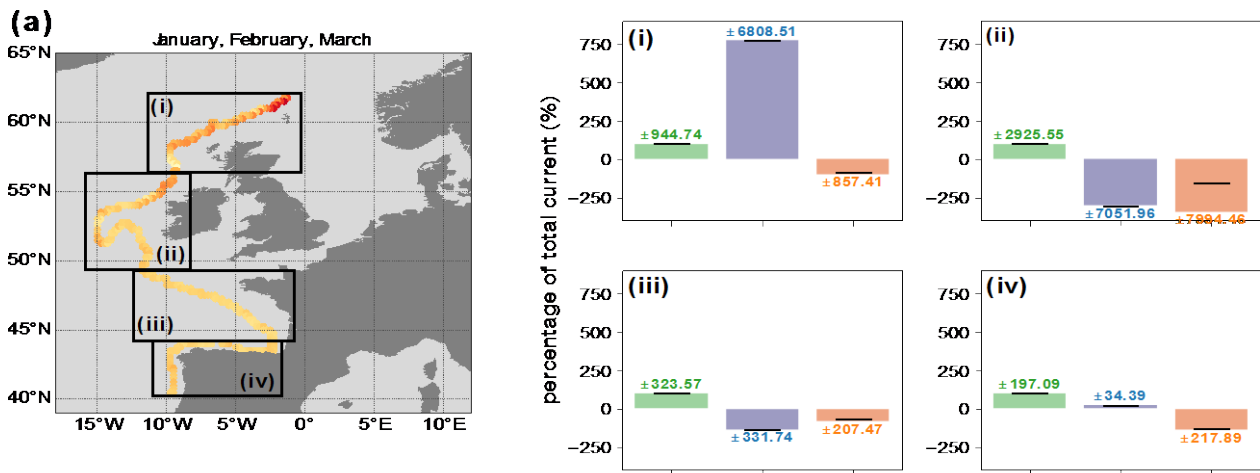


Figure 8.3. Relative contributions to surface currents across sections of the European continental shelf-edge due to geostrophic (purple), Ekman (green) and ageostrophic (orange) components during the northern hemisphere winter (January, February and March 2012) as derived from the NATL60 CJM165 simulations. The black horizontal lines show the values derived from the simulated SKIM data. Values above each bar give ± 1 standard deviation (figure from Shutler et al., 2019).

8.1.3 Marine life: Drifting Ecosystems and Debris

Pelagic organisms and ecosystems are at the mercy of ocean currents and are therefore constantly drifting. The combined warming, acidification, loss of oxygen (Oschlies et al., 2018), and intensified fishing (FAO, 2018) identify the importance for extending marine protected areas (MPAs) to the open ocean. But existing spatial planning for MPAs is unable to account for this drift. A particular problem in the tropics is the wide use of floating rafts to attract fish, called Fish Aggregating Devices, which travel across oceans and into MPAs where their existence is illegal. SKIM TSCV will allow the aggregating device trajectories to be identified for spatial planning (Scutt Phillips et al., 2019; Fig. 8.4).

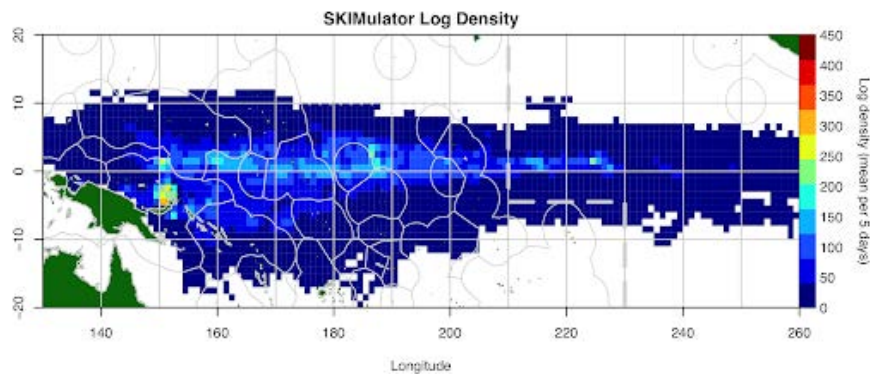


Figure 8.4. Simulated density of fish aggregating devices (mostly floating logs) in equatorial waters using simulated SKIM TSCV data as forcing. (Figure from Scutt Phillips et al., 2019).

Floating marine debris, including plastic litter has quickly become a serious and very visible threat to ocean health and thus food security. The total amount of small plastic litter (between 0.3 mm and 0.20 m in size, including microplastics) on the surface ocean is likely >200,000 metric tons (van Sebille et al., 2015). Found everywhere in our oceans, from the high Arctic (Cózar et al., 2017) to the Southern Ocean (Isobe et al., 2017), these plastics particularly accumulate in the so-called “garbage patches” in the subtropical basins (Lebreton et al., 2018). Stokes drift and the combined influence of the different ocean current components is key to studying plastic distribution (Onink et al., 2019). Clearly, the capability to monitor the trajectory of marine plastic from their sources to the ocean, and therefore any enforcement of plastic use regulation, critically depends on the availability of TSCV measurements.

8.2 Readiness of the Multiple User Communities

In the absence of global measurements of TSCV, the ocean and atmosphere scientific communities have relied upon i) proxies derived from altimeter and scatterometer data, ii) sparsely located in situ measurements from moored buoys and drifting buoys, iii) coastal HF-radar systems and iv) temporally-limited airborne campaigns (e.g. the NASA-funded sub-orbital DopplerScat program, Rodriguez et al., (2018).

The keen international interest in TSCV data is demonstrated by the large user community already using CMEMS Globcurrent and NOAA OSCAR data and the well-attended World Ocean Circulation User Consultation meeting in 2019 (>80 International participants, ESA ESRIN, February 2019).

For the majority of the ocean, proxies of the TSCV from combining altimeter and scatterometer derived estimates of the Geostrophic and Ekman currents are relied upon (e.g. Globcurrent, OSCAR). For these reasons the satellite altimetry user community represented by the Ocean Surface Topography Science Team (OSTST, 2018) has formulated this recommendation,

“The OSTST recognizes the importance of future missions such as the ESA Earth Explorer 9 SKIM candidate mission, which will provide unique opportunities to investigate direct measurement of surface currents and support the work of OSTST”.



This community contributed to the refinement of the SKIM mission requirements, research goals and plans for data uptake and validation, through the dedicated Doppler Oceanography from Space (DOFS) workshop (>100 international participants; Ardhuin et al. 2019b; see <https://dofs.sciencesconf.org/>).

The SKIM concept can benefit from existing HF-radar communities by providing global TSCV data to the Radio Oceanography Workgroup (established in 2005) and its regular workshops (now in their 15th year). For example, several methods for surface current assimilation in ocean circulation models, have been developed (e.g. Kim et al., 2008, Stanev et al., 2015), that can be transposed to the globe or other regions through exploiting SKIM TSCV measurements.

The uptake of SKIM data will benefit from the open-source SKIMulator (Gaultier 2019) that has been demonstrated in training sessions at the DOFS workshop (statistics for people external to the SKIM MAG: 19 people trained, 9 people actively using, 7 people downloaded SKIMulator data, all posts to SKIMulator forum are read >300 times demonstrating an active community interest).

Over 20 SKIM related journal articles are already either in-review, in-press or published – an example metric of the amount of community interest in SKIM.

The SKIM MAG is in active dialogue with the following communities (amongst others) that have endorsed the SKIM mission:

- Ocean Surface Topography Science Team (OSTST)
- Tropical Pacific Observing System (TPOS, see Cravatte et al. 2016, Smith et al. 2019)
- Tropical Atlantic Observing System (Foltz et al. 2019)
- SCOR WG Marine Litter
- World Ocean Circulation User Consultation Meeting participants 2019
- Surface Ocean Lower Atmosphere Study (SOLAS)
- GODAE OceanView

The SKIM mission is featured in 8 of the review papers published ahead of the decadal OceanObs'19 conference that will redefine ocean observing priorities for the next decade, making sure that in situ and satellite observations are seamlessly integrated.

8.3 Applications

Besides the applications discussed above, associated to weather and climate forecasting and projections, direct applications of SKIM are envisaged in a wide range of activities at sea and on land, including some completely new activities that are not possible without SKIM.

8.3.1 Marine Energy, from Oil and Gas to Renewables

The oil and gas industry has invested heavily in the in situ and airborne measurement of currents for a variety of applications related to production (e.g. Jeans et al., 2012, Cooper et al., 2016) for example in the Gulf of Mexico where strong 'Loop Current' meanders can lead to the arrest of oil production. More problematic still is the seismic surveys with the ship towing of kilometres of acoustic devices known as 'streamers' (Grindheim et al., 2017), with currents both making the operations difficult and corrupting the precious data on sub-seafloor reservoirs.



Offshore renewable energy, which encompasses offshore wind as well as wave and tidal energy constitutes a valuable and yet little tapped resource. Offshore wind is now in a production stage and is cost-competitive, reductions of the Levelised Cost Of Energy (LCOE) are still needed; especially considering future developments, further from the shore and in deeper water. Developments are still needed to converge towards the best designs of wave and tidal energy converters. However, the potential is clearly identified and the ocean energy industry estimates for instance that 100GW of wave and tidal energy capacity can be deployed in Europe by 2050, meeting 10% of Europe's current electricity needs (ETIP ocean, 2019).

For both fossil and renewable cases, a key element in the design process and management of operations is the availability of data allowing for an accurate characterisation of the forcing environment, namely wind, wave and current. Beyond a global or even regional mapping of the available power, the required data should provide support for the analysis and characterisation of the combined (wind, wave and current) environmental loading on the structures. For instance, the extreme loading on moorings of a floating offshore wind turbine will result from the combined action of wind on the float and turbine and of the waves and currents on the float and mooring lines (Chen and Basu, 2018). By providing the joint measurement of the three metocean forcing factors, wind, waves, and surface current, SKIM can contribute enormously to the knowledge of joint probabilities of these loading factors, leading to more efficient designs at lower LCOE.

8.3.2 Global Circulation for Disaster Management (e.g. Oil or Chemical Spill, Downed aircraft, Safety of Life at Sea)

Data assimilation of SKIM TSCV data into global (ocean) circulation models would enable the derivation of realistic trajectories for all buoyant floating materials such as surface oil (e.g. from shipping or drilling disasters) or floating debris (e.g. from aircraft accidents). This would build upon the advances made in the data assimilation of (sparse coastal coverage) HF-radar TSCV data (e.g. exploiting Kim et al., 2008, Stanev et al., 2015). This will contribute to SDG12 (responsible consumption and production), SDG13 (climate action), SDG14 (life below water) and support the international shipping industry to transition towards their responsibilities for SDG7 (affordable and clean energy).

8.3.3 Marine Meteorology and Ship Routing

The involvement of CMA CGM, the world's fourth largest shipping company. During the development of the CMEMS ESA Globcurrent and the (French government funded) OptiRoute project for shipping route optimization (using ocean current data altimetry and advanced wave modelling) use of these data resulted in a 1% reduction in their fuel costs, and can be improved on with more accurate measurement of ocean currents. Scaled to the wider shipping fleet, this can be a significant contribution of CO₂ emissions (as shipping emissions represent ~13% of the overall EU greenhouse gas emissions from the transport sector). SKIM TSCV would enable further cost and CO₂ emission reductions. Reducing and regulating ship emissions is now coming under increasing scrutiny (e.g. the International Maritime Organisation Greenhouse Gas Strategy) and is captured within SDG7 (affordable and clean energy) and SDG13 (climate action).



8.4 European Earth Observation innovation and Advancement

SKIM builds on European technologies and Earth Observation sensing physics knowledge that will deliver a unique capability that has many potential applications to assist in the development of new future satellite missions.

The next generation of satellite altimeters could leverage the demonstration of SKIM to explore beyond geostrophy using both a conventional nadir beam and off-axis rotating beams. The current configuration of SKIM provides a “best of all worlds” solution because the nadir beam delivers a well-known measurement allowing SSH measurements to be projected into the deeper ocean (below the surface) by ocean models. The rotating beams then provide the surface current that has, arguably, the most societal benefit as this is where in general, people live and work with the ocean. A future path to an operational mission providing a wide swath sampling capability would be obvious.

For many years there has been a long-running debate as to how measurements of ocean winds from space using scatterometers have been unable to definitively account for the impact of TSCV on the retrieved wind speed. By flying in loose formation with MetOp-SG(1B), SKIM will deliver measurements within the SCA swath within ~150 s. SKIM will be able to comprehensively address this issue at the relevant spatial scale providing the way for a more solid case for a future Doppler enabled scatterometer. This SKIM will improve the measurements from MetOp-SG(1B) SCA. In addition, by studying sea state bias impacts on nadir altimetry, we hope to improve the uncertainty of the long-term altimetry sea level record using new parameterisations – particularly important for the Copernicus Sentinel-6 reference altimeter and Sentinel-3.

The design of SKIM has foreseen the need to study the measurement of inland waters including rivers and lakes. This is a growing community that is now fully exploiting Sentinel-3 and in the future Sentinel-6 nadir altimeters to measure the stage-discharge relationship of rivers and the storage state of lakes. SKIM brings a new dimension of Doppler measurement's that could potentially measure flow directly from some river systems (e.g. the major tributaries of the Amazon) or from wide estuaries (e.g. the River Thames or the Elbe River).

SKIM has the potential to study terrestrial ice caps and sea ice in detail (although the steep slopes at the margins of ice caps will present a challenge). The Ka frequency nadir beam will complement existing measurements of sea ice freeboard (e.g. from CryoSat 2). Direct measurements of ice drift will be an asset for sea ice charting services especially when combined in synergy with SAR imagers and microwave radiometer measurements from space.

Finally, since SKIM offers such an innovative radar system there will undoubtedly be new and innovative measurement opportunities that have not yet been identified. The key to success is to ensure that the on-board processing scheme is flexible enough to allow future advancements. SKIM has been designed to provide this flexibility, as it will be the first satellite mission to fly Field Programmable Gate Array (FPGA) technology for the purpose of a complete remote re-programming of the on-board processors inside the instrument.

Since SKIM carries a high-power Ka band radar, its development will require the European development of some key components, such as those already started with the pre-development activities on the Low Noise Amplifier and on key components of the High-



Power Amplifier. Future Ka-band radar missions would undoubtedly benefit from these technologies being available from European suppliers.

SKIM, as the first Doppler mission capable of determining TSCV would considerably enhance European Earth Observation innovation and advancement on the international stage.

8.5 Conclusion

SKIM will directly address a long term observational gap since no regular measurements of the TSCV and its associated kinematics and dynamics have been made from space – despite the need for such measurements as expressed by the international scientific users and operational communities (e.g. ESA GlobCurrent User Requirements Document, the World Ocean Circulation user requirements, the Climate community (GCOS 2016) document and the large international community deploying sparse coastal HF-radar systems).

There is an urgent need for SKIM to help provide these measurements to address the Living Planet ocean challenges and respond to the *Grand Challenges* raised by the international community in this report.

In this way, SKIM, our HF-radar in space, will address the science and societal needs from regional-scale applications such as for example, shipping, human safety at sea and ecosystem management, to global-scale scientific research and applications targeted at mitigating the climate crisis.

9 PROGRAMMATICS

This chapter presents the maturity (including similarity/heritage), critical areas and risks associated with the mission-level scientific concepts (Section 9.2), and the programmatic and system level technical concepts (Section 9.3) as developed in the frame of the scientific and industrial Phase A studies. The development approach and the schedule are presented and discussed in section 9.4 with respect to the compatibility of a target launch for the ninth Earth Explorer mission by the end of 2025.

9.1 Scientific Maturity, Critical Areas and Risks

The starting point for the assessment of scientific maturity is reported in ESAPB-EO(2017)44 as follows: “*The SKIM mission feasibility has been convincingly demonstrated with end-to-end simulations. The mission concept as set out in the proposal is judged by the panel to have reached SRL 4 and is expected to attain SRL 5 by 2018*”.

Scientific maturity was assessed at the start and end of Phase A by conducting a Scientific Readiness Assessment (SRA) following the definitions of the Scientific Readiness Levels (SRLs) described in ESA (2015c). This is reported in MPRC-SRA1 (Ardhuin et al., 2019). At the end of Phase A, a second SRA was conducted, as reported in MPRC-SRA2 (Ardhuin et al., in press) to assess the development of the SKIM SRL.

Three scientific studies were conducted during the Phase A that led to a consolidation of science activities to attain SRL=5, as summarised in Table 9.1, and further detailed below.

SRL=5 Criteria	Phase A End	Evidence at end of Phase A
Algorithm developed, stable and in place.	5	Algorithm developed and v1.0 is stable. Further work to evolve wave Doppler correction is anticipated, LOPS (2019a,b) Data driven fine pointing algorithm: Delious, (2019), Dibaboure and Ubelmann (2019), performance confirmed in Section 7.4.1.
End to End simulator including processes and uncertainties	5	Descriptions of Simulators in Chapter 7 SEEPS simulator description: SEEPS TN1. Open Source SKIMulator (Gaultier, 2019) https://github.com/oceandatalab/skimulator , R3S (Nouguier et al., 2018), TUD-OceanSAR (Lopez-Dekker et al., 2015)
Error propagation model in place and verified	5	Established and evaluated in this report (Chapter 7) and in LOPS (2019a,b)
Test scenarios defined	5	Section 7.2.3 (TSCV) and Section 7.2.3.2 (waves)
Test scenarios implemented	5	SEEPS: Section 7.2.1.1, SKIMulator: Section 7.2.2.1, R3S Section 7.2.3.2, TUDOceanSAR: Section 7.4.3.2.
Assumptions of simulator	5	The SEEPS is based on Nouguier et al. (2018) which is common to R3S, SKIMulator and TUD -OceanSAR. All assumptions of SKIMulator are described in LOPS (2019a,b)
Demonstration of simulator robustness	5	Demonstration was run for campaign (Marié et al., 2019). Campaign data confirm algorithm approach validating the retrieval with in situ drifters, and HF radar
Instrument calibration and validation strategy	5	Section 6.2 of present report
Demonstrated interest of users	5	Section 8.2 of present report, over twenty journal papers including SKIM. DOFS workshop and open source SKIMulator uptake.

Evaluation of simulated data in applications	5	Section 8.3 of present report: 14 journal articles prepared and submitted or published for SKIM applications based on SKIM SciSoc study.
Scientific roadmap established	5	See Section 9.1.3 below

Table 9.1. Criteria for the 5th Scientific Readiness Level and evidence from for the SKIM concept.

9.1.1 Scientific Maturity: Key Questions for SRL

Given previous experience with Doppler measurements in C-band, and given the atmospheric attenuation properties of Ka-band, the *error model* first laid out at the proposal stage included pointing errors, wave Doppler residuals and representation errors (Arduin et al., 2018). This was refined during the phase A by including realistic pointing errors (from microvibrations to TEDs). Late in the Phase A it was found that the platform pointing is expected to be far superior to the pessimistic assumptions used to develop fine-pointing algorithms. Nevertheless, as a risk mitigation strategy, the CCAL algorithm is now in place that demonstrates the satisfactory performance in extreme mis-pointing situations. Should mis-pointing become a significant issue in subsequent mission phases (e.g. in case SKIM AOCS would suffer an anomaly in flight) data driven solutions are ready.

More can certainly be done to improve the “fine-pointing” data-driven algorithms. In particular, to exploit the non-geophysical patterns imprinted in the residuals after “fine-pointing” has been applied. Furthermore, as the SKIM mission is developed, more information will be available to further optimize the algorithms. New error sources were considered in the retrieval approach (Chapter 6), in particular the finite beam-width and NRCS gradients that contribute the non-geophysical velocity components U_{AGD} due to azimuthal gradient in the NRCS and U_{SGD} due to the spatial gradient in NRCS, both combined in an apparent mis-pointing δ . The full error model, also including negligible surface height effects, is described in LOPS (2019b).

Another important aspect is precipitation flagging, which can be detected in NRCS range gradients as demonstrated for CFOSat SWIM (Gressani et al., 2019), and low wind conditions. Techniques were developed to address this issue using SKIM data alone and these need to be refined in future phases as part of normal work. However, the benefit of using a microwave imager was identified as an extremely useful complement.

This error model is the basis of the end-to-end (E2E) measurement performance simulator framework that has been developed for SKIM. The design of SKIM E2E simulator incorporates several fundamental tools that are connected together via common orbit and sensing geometry, test scenarios, test data sets, electromagnetic models and defined performance evaluation metrics. These ensure that each tool is generating the same output for a given test scene. The SEEPS tool is the fundamental performance simulator with local coverage Level-0 to Level-2c end-to-end capability. This simulator has been designed, developed, implemented and tested during the Phase A to independently verify industrial team assumptions and mathematical models. SEEPS focusses on the instrument performance and local scales – fully representative of the coupled dynamics at both instrument and wave interaction mechanisms. However, this is insufficient to demonstrate the performance of SKIM over a wide spectrum of ocean conditions.

To address this issue, the SKIMulator (Gaultier 2019) brings the instrument performance in the context of geophysical signals at local to global scales and TED errors correlated at the



scale of multiple-orbits. This simulator has also been designed, developed, implemented and tested during the Phase A. The tool is specifically open source to foster SKIM community engagement in the development and application of the mission and will remain so throughout subsequent phases. SKIMulator is a Level-2 parametric simulator with global-coverage Level-2a to Level-2d capability that is fast and efficient allowing global data sets to be analysed for 12 months or more. SKIMulator parameterises the SKaR uncertainty characteristics generated by SEEPS and applies them to a wide range of regional and global conditions. This linkage is important expand the coverage of the SEEPS local simulation cases to the global ocean and propagate uncertainties from Level-0 to Level-2c.

A series of realistic and representative *test scenarios* was defined for the E2E simulation framework, targeting the expected dominant source of errors: the effects of instrument noise (high and low wind conditions), the influence of NRCS gradients (along and across-track wind conditions), the wave Doppler variability (case with dynamic current and near ice-edge conditions).

The E2E simulation framework was tested to reproduce the mean and modulation patterns measured during the airborne campaigns LASER (Nouguier et al. 2018) and the global scale SKIMulator was verified against numerical model inputs in error free conditions. The E2E tools were then applied to the predefined set of scenarios: simple homogeneous ocean scenarios for the swath scale, and global full-year analysis at global scale using state-of-the-art numerical model input that capture the variability of the ocean (including sea ice) including high resolution scenarios over the Gulf Stream, Fram Strait and Tropical Atlantic.

The *assumptions* of the E2E performance simulator were first described in the peer-reviewed literature (Ardhuin et al., 2018) with the additional effect of NRCS gradient discussed by Rodriguez et al. (2018) and Marié et al., (2019). The particular “fine pointing” algorithm solution is an adaptation (Delouis, 2019) of the very successful mapmaking code, SRoll, that was developed for mapping the cosmic microwave background with the Planck mission (Planck Collaboration, 2016; Delouis et al., 2019). Finally, the rain statistics used for flagging the data are described in Battaglia et al. (2019). The SKIMulator (Gaultier, 2019) is an open source software available on GitHub, fully open to scrutiny, with all underlying assumptions recalled in two technical notes (LOPS, 2019a,b).

The *robustness of the simulator* framework was demonstrated by testing it with very different airborne instrument configurations, a narrow-beam Ka band radar, and a broad-beam Ku-band radar (chapter 7 and Marié et al., 2019). The SKIM E2E simulator has already been extremely useful during Phase A. During subsequent phases of the mission further development of the SKIM E2E simulator will be required as the mission is developed and scientific understanding improves.

The calibration strategy for the retrieval algorithm was described in chapter 6 and involves the learning of Geophysical Model Functions for the wave Doppler contribution and detailed analysis of the error budget and final estimates of the TSCV (U_{CD}) and Stokes drift (U_S) combining SVP drifters, HF radars and models.

This calibration strategy was defined together with the *user community* as well as many other aspects, at the Doppler Oceanography from Space workshop (see Ardhuin et al., 2019b). Ahead of the decadal survey of necessary adjustments to the Ocean Observing system, at the September 2019 ‘OceanObs’19’ conference, a series of 68 [community white papers](#) has been accepted for publication. At least 8 of these mention SKIM as a unique data



source with game-changing opportunities, in particular for ocean–atmosphere interaction studies and the tropical ocean (Villas Bôas et al., 2019; Foltz et al. 2019; Smith et al., 2019; Fox-Kemper et al., 2019; Le Traon et al., 2019; Morrow et al., 2019; Arduin et al., 2019a,c). In all, over 20 papers have been published by the SKIM community to date, with 14 dedicated to applications of SKIM. Workshops run by the SKIM study team and international workshops and conferences show a user community that is ready to take up SKIM data for diverse applications.

More than twenty *dedicated scientific* publications using SKIM simulated data have already demonstrated the impact of SKIM measurements on a better estimation of Stokes drift and TSCV for surface drift of biological material, plastics, and illegal fishing devices (Fraser et al., 2018, Onink et al., 2019, Scutt Phillips et al., 2019). Two more papers are in review for applications on CO₂ fluxes (Shutler et al., 2019a,b) and other studies will be published shortly, including impact of SKIM data on reducing uncertainties on the heat budget in the equatorial Atlantic, and the accuracy of sea state forecasting using ocean currents (SKIM Team, 2019).

9.1.2 Critical Scientific Areas and Risks

Critical scientific issues and risk associated with the development of SKIM, identified during the Phase A and as input to future phases of the mission, are grouped into the following categories:

1. Addressing long-term observational gaps,
2. Timeliness of SKIM,
3. Stability of Mission Requirements,
4. Maturity of the SKIM retrieval algorithms,
5. Availability, testing and validity of the SKIM End-to-End simulation system,
6. Readiness of the scientific community to fully exploit SKIM measurements.

9.1.2.1 Addressing Long-Term Observational Gaps

A fundamental scientific risk for the ESA Living Planet strategy is that, despite their importance for science and society, regular, repeat coverage and densely sampled and direct measurement of the ocean TSCV from space are not available. As a consequence, the level of scientific scrutiny required to fully address the ESA Living Planet Ocean Challenges (ESA, 2015a) is not available. This claim is further strengthened by the user requirements set out in GCOS (2016), IPCC (2014), United Nations (2016), IPBES (2019).

The rapidly evolving biodiversity and climate crisis and the opening up of the Arctic ocean, are all calling for rapid action. SKIM will provide unique measurements on TSCV that address a long-standing and embarrassing observational gap: every accident at sea, including recent losses of commercial airplanes or major environmental crisis (e.g. tracking marine plastic debris, oil, radioactive marine debris following the Great Japan Earthquake, etc) has revealed how little is known about surface drift beyond climatology, and how inadequate very often are today's numerical ocean models right at the surface.

SKIM measurements are urgently needed by the oceanographic and marine meteorological community to address the climate crisis and challenges facing our oceans today.



9.1.2.2 Timeliness of SKIM

It is notable that the number of HF coastal radar installations around the shore of the United States and Europe has grown steadily in the last few years clearly highlighting the need for measurements of the TSCV. SKIM proposes a ‘HF-radar in space’ to complement this array with dense sampling and global, regular-repeat coverage. The unique Doppler Wave-Current Scatterometer measurement concept and capability has been pioneered in Europe starting from ENVISAT ASAR (Chapron et al., 2005), now building on the CFOSat SWIM mission rotating feed concept. It has gained strength with Sentinel-1 Doppler measurements over the ocean. For these reasons, the time is right to capitalise on the European leadership, knowledge and technical capability in this domain and take Doppler ocean measurements from space to the next level for science and societal benefit.

The joint analysis of MetOp-SG(1B) and SKIM would be extremely beneficial to both missions, but it is not critical that MetOp-SG(1B) is present when SKIM flies. SKIM, although with reduced performance (Fig. 6.9), could still deliver useful data. This is a specific choice of the MAG to optimize the value for money and performance of SKIM within the EE9 Fast Track framework. MetOp-SG(1B) is an operational satellite and will be launched in the 2022 timeframe with a design life of 7 years, to be followed by MetOp-SG(2B) in the 2029 timeframe to continue to provide the same capability. Furthermore, use of NWP fields may also be used as a surrogate although with expected reduced performance for the wave Doppler algorithm. The dependency on MetOp-SG(1B) SCA data is limited as a lower quality wind vector is feasible from the SKIM data itself, as already demonstrated with CFOSat SWIM.

The CFOSat mission, launched in 2018, has a design lifetime of 3 years and flies in a relatively low orbit with an altitude of 520 km. It is possible, but unlikely, that CFOSat would be available at the time SKIM flies. Cross-calibration of the commonly resolved part of the wave spectrum by SKIM and CFOSat will be performed using in situ measurements for both missions to remove any SKIM bias if present. Sentinel-1 will be available at the time SKIM flies to provide high-resolution SAR imagery and limited coverage independent single line-of-sight estimates of TSCV that will be useful for verification of SKIM measurements.

The satellite altimetry constellation will be maintained by Sentinel-3 and Sentinel-6. It is possible, but unlikely, that CryoSat, JASON-3 and AltiKa would be available at the time SKIM flies. However, if the HPCM CRISTAL mission is taken forward, this would be available.

The SWOT mission is planned for a launch 2021. It is possible that its 3-year lifetime may get extended, in which case SKIM could collect data at the same time as SWOT, proving a unique data set. As discussed in section 2.6, SKIM alone but even more so SKIM in combination with MetOp and/or SWOT would provide a unique dataset for the validation of the new generation of coupled ocean-wave-atmosphere models that will be operational in 2022 and beyond.

9.1.2.3 Stability of Mission Requirements

At the time the SKIM proposal was accepted, an orbit close to Sentinel-1 was proposed, allowing for complementary Doppler and wave information over a swath wider than SKIM alone. A critical analysis at the start of Phase A suggested that:



- The benefits for SKIM are limited due to the Sentinel-1 SAR duty cycle (part of the orbit in IW mode, the rest in wave mode),
- A higher orbit is feasible, allowing for a wider swath and more frequent revisit,
- There is a need for microwave radiometer measurements and scatterometer to support and improve inputs to the SKIM Level-2 retrievals and to expand the range of applications serving science and society.

A survey of possible companion missions with vector wind measurements, logically led to the selection of a convoy concept with MetOp-SG(1B), with additional benefits to associate accurate sea level measurements with accurate wind–wave–current measurements, considerably widening the range of SKIM research objectives (SKIM Team 2019). Following a detailed trade-off, the requirements were changed to fly in loose formation with MetOp-SG(1B). This solution offers considerable benefits, as discussed in Chapter 6, 7 and 8.

In terms of Level-2c requirements for ocean TSCV, the proposed requirement to meet TSCV at 0.1 m s^{-1} was not sufficiently specified. Further refinement of the requirement led the SKIM MAG to redefine the requirement as: “*For a 30 km grid cell, with a revisit of ≤ 10 days at the equator, the combined standard uncertainty in U_{AC} and $U_{AL} \leq 0.15 \text{ m s}^{-1}$ or 15% of the TSCV (whichever is greater) for at least 70% of the ocean surface*”. As a goal, the U_{AC} and $U_{AL} \leq 0.1 \text{ m s}^{-1}$ or 15% of the TSCV has been retained. From the analysis in Chapter 7, the goal requirement can be met at Level-2d-multi-temporal products and the requirement is met at Level-2c. The orbit change does not impact the User Requirements and needs. Instead, it clarifies the specification to assist both industry and the user community that are working on the SKIM mission.

9.1.2.4 Maturity of the SKIM Retrieval Algorithms

The retrieval algorithm for TSCV has considerably evolved during the Phase A based on research and development of sensor physics and theoretical modelling. This process culminated with a successful airborne campaign in late 2018 to verify the fundamental hypotheses of the wave Doppler algorithm. Over the past two years, the publication of campaign data from fixed platforms and airborne systems led to a much better knowledge of the wave Doppler and its variability (Yurovsky et al., 2018, 2019; Rodriguez et al., 2018; Marié et al., 2019). The backscatter over sea ice has not received the same attention and the performance analysis over ice-infested waters thus does not have the same level of maturity even though the wave Doppler is expected to be much smaller and therefore less critical. That particular topic however has great potential to complement the estimate of sea-ice drift that is not complete from other observing systems.

From previous demonstrations, using ERS-1 (van der Kooij et al., 2001), Envisat (Chapron et al., 2005) and now Sentinel-1, at first the requirement on the antenna pointing may first appear prohibitive. However, the demonstration of current vector mapping from a conically scanning Doppler scatterometer was performed for the airborne DopplerScat system (Rodriguez et al., 2019), with azimuthal calibration of the beam pointing learned from the data. It is now understood that the conical scan greatly helps to reduce the error in the pointing knowledge. Recent updates to the Sentinel-1 processing chain further confirm that platform attitude can be corrected by combining the data itself and information from the AOCS gyroscopes (Oceandatalab, 2019), even with a fixed antenna.



Algorithms to implement fine-pointing corrections for SKIM were of particular concern throughout the Phase A. However, using the industrial specification of SKIM pointing knowledge, TED and AOCS characteristics two data-driven fine-pointing algorithms have been developed and demonstrated using realistic simulated data. Late in the Phase A it was found that the platform pointing will be far superior to the pessimistic assumptions used to develop fine-pointing algorithms. Nevertheless, as a risk mitigation strategy, the CCAL algorithm now in place demonstrates the satisfactory performance in extreme mis-pointing situations. Should mis-pointing become a significant issue in subsequent mission phases (e.g. SKIM AOCS suffer an anomaly in flight) solutions are ready.

In terms of products, retrieval algorithms applicable for a realistic range of error sources (both geophysical and technical) have been demonstrated against a pre-defined performance metric reflecting observation and measurement requirements. This has been completed for the Level-2b L2B_U products measurements at footprint level and at global scales for Level-2c products. The simulations highlight that the goal of TSCV for a single swath product at 0.1 m s^{-1} remains a challenge. For multi-temporal analysis over 3-5 days, the goal is met. For 10-day simulations the requirement of GCOS (0.05 m s^{-1}) is approached. As requested by ACEO, the importance of geophysical Signal to Noise Ratio (SNR) has been studied and demonstrating that SKIM will provide extremely good performance in regions where the SNR is $> 3 \text{ dB}$ (with reference to the input test scene characteristics – see Fig. 7.32). This results in a coverage of 69% of the global ocean using the current wave Doppler algorithm.

In order to assess the current SKIM potential to reach goal values of 0.1 m s^{-1} additional simulations were performed using an alternative grid size. In this configuration the inherent noise in the L2B_U product will be mitigated through averaging. At a resolution of 75 km the goal requirement is met at Level-2c using the present v1.0 algorithms, with further improvements expected.

9.1.2.5 Availability, Testing and Validity of the SKIM End-to-End Simulation System

The SKIMulator and SEEPS share a common set of test scenes that are used to confirm that both simulators at Level-2b and Level-2c generate the same output within the bounds of numerical uncertainty. This verifies the relative performance of the tools.

The SKIM E2E simulator includes an advanced scene generation module that allows the SKaR instrument simulator to interact with the ocean surface. A two-scale approach to specification of the input spectral characteristics has been used. This is supported by detailed simulation work-bench tools (R3S, Nougier 2019) that have an extremely high resolution ($< 1 \text{ m}$) to capture the essential characteristics of the ocean surface. As shown in Chapter 7, comparisons to campaign data collected using the SKIM campaign in 2018 aircraft radar demonstrate that the simulations from R3S are comparable to reality. For the SKIMulator, state of the art ocean models (MITgcm and WW3) have been used to generate realistic test scenes for simulation experiments including regional domains to test specific and challenging regimes for the current SKIM wave Doppler algorithms. This is required to achieve SRL of 5.

The nadir beam performance of SKIM has been simulated and assessed using well established simulation frameworks independently of the off-nadir beam using standard tools and approaches developed already for Sentinel-3 and Sentinel-6. These tools have been



thoroughly validated (SRL of 5) and there is no need to ‘reinvent the wheel’ for the SKIM nadir beam performance assessment. The nadir beam performances are confirmed and SKIM will be capable of providing very good altimeter measurements, at the performance level of Jason-3 or better.

The wave spectrum measurements of SKIM have been specifically assessed by the R3S (Nouguier 2019) and the TUDelft OceanSAR (Marull-Paretas, 2013; Lopez-Dekker et al., 2015) dedicated tools developed during the Phase A study. With CFOSat SWIM now flying, tools were upgraded to assess SKIM simulations using in-flight CFOSat SWIM data (the most realistic and representative test data for SKIM available today). Directional wave spectra retrieved by the CFOSat SWIM instrument are compared with the outputs of the R3S scientific workbench, assuming the instrument parameters of SWIM and SKIM, respectively. The potential improvement achieved by SKIM with respect to SWIM is clearly demonstrated. All of the features within the SWIM measurements are well reproduced by the R3S simulator, showing that the principle of the measurement is well understood and properly simulated numerically.

These E2E tools have been developed, tested and validated using realistic and representative input test data and *in situ* campaign data. Simulation runs have been used to investigate the expected performance of SKIM, for using a full spectrum of experiments ranging from individual SKaR footprints to the TSCV at global scale and wave spectrum in support of Phase A work. This is required to meet SRL of 5.

Performance metrics have been defined and used to objectively assess SKIM performances against requirements for a predefined range of conditions (including realistic and stress test cases) using uncertainties of natural and observational nature. Outputs from the SKIM E2E simulator have been used to address scientific requirements in an end-to-end manner. This is required to meet SRL of 5.

9.1.2.6 Readiness of the Scientific Community to Fully Exploit SKIM

To attain SRL of 6 and above, a consolidation of products in collaboration with the scientific community will be pursued and achieved during phase B/C/D. Besides the scientific analysis performed with the data, realizing the full potential of the SKIM mission will require the adaptation of existing or new data assimilation schemes to most operational systems. At present, velocity assimilation has been only used in coastal areas where HF-radars are available. There is a great opportunity to integrate this in the new ocean-atmosphere coupled data assimilation systems that are under development. Whereas the coastal ocean modelling systems are ready today, there is some risk that the large-scale operational systems may not be ready in time, and these developments will have to be monitored closely. During future Phases of the mission, dedicated actions are required to prepare the ocean modelling community for application of SKIM products. Assimilation in ocean circulation models, as achieved using HF-radar data (Kim et al., 2008, Stanev et al., 2015), illustrates one approach for the global use of SKIM TSCV data. The supporting letters provided by ECMWF and CMEMS are evidence that the science community is ready for this important mobilization.

9.1.2.7 Risk Assessment Summary

No critical elements have been identified and community interest and future evolution to SRL=7 has no significant risk.

9.1.3 Scientific Roadmap

Future work in later phases is anticipated as follows:

- The performance of Doppler retrieval on sea-ice for near-nadir Ka band was not tested. Given the possible benefits of the mission, it is a high priority to acquire such data by campaign, which can probably be combined with other planned campaigns (e.g. JPL WaCM). The analysis of CFOSat/SWIM data can provide a first guidance as to the effect of ice-leads but cannot be completely transposable to SKIM due to the different backscatter in Ka and Ku bands (e.g. Armitage and Ridout, 2015), and due to the slightly different footprint geometry. Over ice infested regions (tested in the “Fram” case in Chapter 7), the expected lower near nadir NRCS leads to higher instrument error as a consequence of SNR. Over sea-ice and ~20 km away from the ice edge, the wave Doppler error is very small because only long swell waves penetrate into the sea-ice. Future work in later phases is expected to improve the wave Doppler correction algorithm in this region by developing a dedicated algorithm for the water side of the ice edge. This can be ideally based on a combination of dedicated campaign measurements, multi-variate satellite data sets and NWP/NOP model output.
- The NRCS gradient effect is based on both theory and nadir measurements from SARAL-AliKa, assuming that all the measured NRCS variability is due to the ocean surface (and not to tracker noise or atmospheric effects). More campaigns and analysis will be needed in future phases to quantify this effect over both water and sea ice.
- Improved mapping of Level-2b data within the Level-2c algorithm could yield better results compared to the simple, but honest, weighted least squares approach and should be explored.
- Test the application of a multivariate machine learning approach to optimize the wave Doppler algorithm. We expect this approach to result in an improved Geophysical Model. In particular, during the E1 Commissioning phase, sufficient in-flight data will be available to constrain this surface with very good accuracy and precision based on a large range of wind-wave conditions. A critical aspect for this will be to properly account for the correlation of wave parameters and currents (e.g. Ardhuin et al., 2017).
- During future Phases of the mission, dedicated actions are required to prepare the ocean modelling community for application of SKIM products. In terms of community development and preparation for SKIM, the SKIMulator provides an open source community tool. However, there is a need to explore an optimal approach to assimilate the full geophysical Doppler velocity (without current / wave) separation, in a coupled ocean circulation and wave model. Appropriate observations operators will be required for this purpose in addition to potentially fundamental changes to the upper ocean model configuration that can take full advantage of SKIM.
- Improve the wave Doppler retrieval, using a priori swell spectrum information propagated from previous orbit measurements (e.g. using the “swell fireworks” approach introduced by Collard et al., (2009).
- Develop tools and an approach to explore ‘beyond geostrophy’ using SKIM nadir and off-nadir simulation measurements.



- Develop tools and an approach to demonstrate the potential to combine nadir and off-nadir measurements, to help advance improved understanding of altimeter sea state bias correction reduce uncertainty in sea level measurements.
- Develop tools and an approach to assess the combined use of wind, wave, current and sea-level measurements for accurate descriptions of complex ocean-atmosphere processes using data-only and ocean–atmosphere models.
- The unique combination of SKIM and MetOp-SG(1B) flying in loose formation will enable wind–wave–TSCV synergy to be fully developed for scientific and societal benefits. Improvement in scatterometer wind estimates are anticipated based on the application of SKIM data that, for the first time, will systematically account for the impact of wave–TSCV interaction on the retrievals.
- The Data Driven Calibrated fine pointing algorithm was demonstrated based on extensive simulations of thermo-elastic distortion provided by industry. It can certainly be refined based on, for example, further analysis of where and when geophysical Doppler signals are found in the same spectral band as the non-geophysical signals.
- Investigate advanced processing to fully exploit the full capability of SKIM to arrive at high resolution imaging of surface processes, ideally in the form of imagerettes similar to Sentinel-1 wave mode.

9.2 Technical Maturity, Critical Areas and Risks

9.2.1 Summary

SKIM is considered a technically feasible mission but challenging within the programmatic constraints applicable to the EE9. For the satellite platform both concepts are based on extensive re-use of either existing and flight proven solutions (Concept A, with heritage from Copernicus Sentinel-5P and SEOSAT/Ingenio) or standard products to be developed (Concept B, with proposed re-use of the Nucleus standard platform being developed for the Copernicus High Priority Candidate Missions). Though some mission specific adaptations will be required, the relevant custom designs are all based on mature technologies and do not require the implementation of early pre-developments.

The SKaR instrument derives significant heritage from the SWIM instrument flying on board CFOSat for what concerns the overall instrument architecture and antenna design, and from the Poseidon-4 altimeter and the KaRIn Radar interferometer for what concerns the instrument electronics digital and RF stages.

The SKIM mission has two competitive industrial consortia for the platform and a single source supplier for the SKaR instrument. At platform level the re-use of standard (available or under development) products is considered beneficial for the development of the mission within the programmatic constraints applicable to the EE9. However, the single source supplier for the instrument with a strong "make" approach is considered a programmatic risk.

For the SKaR specific critical elements have been identified and are under mitigation by relevant technology pre-developments aiming at raising the TRL of the critical elements at least to 5 (and 6 whenever possible) by the end of Phase B1 (see Section 9.3.3). The on-going



and planned technology pre-developments provide good confidence about the technical feasibility of the instrument and the robustness of the risk mitigation strategy. With exception of the SKIM-specific on-board processing firmware, all critical elements will reach TRL 5 already by the end of the Phase A pre-development activities (see Table 9.1).

No criticalities have been identified for the ground segment. The loose formation flying with MetOp-SG will require interaction between ESA and EUMETSAT in future phases of the mission.

The SKIM Satellite is fully compatible with Vega C in dual launch configuration, but only on the upper position and using a short VESPA.

9.2.2 Satellite and Platform

For Concept A the proposed technical solution for the platform is based on re-use from flight proven (Copernicus Sentinel-5p) and mature (SEOSAT/Ingenio) technical designs, with minor modifications related to mission specific needs. The concept proposed re-uses the thermo-mechanical architecture developed for SEOSAT, with a modified top-panel based on heritage technology (embedded heat pipes). The thermal control requires specific design adaptation to cope with the high thermal dissipation of instruments units accommodated inside the platform. The modified structural and thermal designs are based on mature technologies and are assessed at TRL ≥ 6 . The payload mass memory functional unit might require a delta qualification and is currently considered at TRL 6. Specific modification of the on-board software (e.g. AOCS guidance laws) lowers the current TRL to 5. All other platform equipment/units have high TRL (>7). The current platform configuration (internal accommodation of platform and instrument units, thermal control design) offers no margins with respect to potential changes due to e.g. revised accommodation of highly dissipating units. This is considered a risk at this stage of the mission concept definition and will require close monitoring in the next development phases. Identified risk mitigation consists in a modification of the structure design to increase the internal volume and the surface available for the accommodation of the highly dissipating units and the required thermal radiators.

The platform technical solution proposed for Concept B is based on a platform currently being defined as a standard product in the context of the Copernicus High Priority Candidate Missions. This platform being under development, its design is less consolidated. However, this platform offers comfortable margins on the resources required by the mission. With respect to the structural design and its ability to support the instrument, feasibility has been established at Phase A level. All proposed subsystems and constituting equipment make use of mature and in most cases flight-proven technologies, though the relevance of the current qualification status to the mission specific environment will require further assessment and consolidation during the early implementation phases. It is expected that the subsystem/equipment with lower TRL (structure, Solar Array, payload data handling subsystem) will take benefit of the development in the context of any standard platform development activities to achieve higher TRL in parallel with the SKIM implementation phase. It is not clear yet to what extent the heritage of the central software will be affected by mission specific adaptations, additional interfaces, new development and verification/validation activities to ensure compatibility with the standard platform on-board computer, which has not yet been selected.



At system level the pointing stability and knowledge calibration strategy and the required on-ground characterisation activities, particularly at the level of the SKaR antenna, will require further consolidation during the early development phases.

The analysis of the re-entry casualty risk shows – for both concepts – marginal compliance with the requirement for an uncontrolled re-entry, which is the current baseline approach to achieve compliance with the relevant Space Debris regulation. This approach has been accepted by the relevant ESA authorities with the recommendation to refine the analysis in the next study phase and - if necessary - to study and implement some “design for demise” risk mitigation measures to restore comfortable margins to the casualty risk requirement for uncontrolled re-entry.

9.2.3 SKaR

The technological maturity of the SKaR instrument takes benefit from the heritage of the SWIM instrument flying on CFOSat for what concerns the overall instrument architecture and the Antenna concept. The Central Electronic Unit digital section has heritage from the subsystem under development for the Poseidon-4 altimeter to be flown on the Copernicus Sentinel-6 mission but will require specific development for the on-board processing implementation, whereas the RF section has heritage from the KaRIn Radar Interferometer, under development for the SWOT mission. The High-Power Amplifier will re-use the Extended Interaction Klystron developed for KaRIn, but will require also dedicate development for the High Voltage Power supply and the high-power isolator. The Antenna subsystem design has a strong heritage from the SWIM design, with specific development required for the Ka-Band rotary joint. For the ferrite TX/RX switching elements a re-use of the KaRIn duplexer RF and electronic boards is foreseen, specific developments/validation will be required for the High-Power Circulator and the switch drivers.

The following sections provide an overview of the current TRL status for each SKaR subsystem, a description of the on-going/planned pre-developments and the assessment of the TRL achieved at the end of the relevant pre-developments in relation to the Phase A and Phase B1 schedule, recalling that the objective is to reach at least TRL 5 (and 6 whenever possible) for the critical technologies at the end of Phase B1.

9.2.3.1 Central Electronic Unit

The current TRL of the CEU is assessed at 5/6, with all elements of the digital section at TRL 7 except the on-board processing implementation (OBP), which is considered at TRL 4. For the RF section the TRL of the relevant elements is >6 with the exception of the Low Noise Amplifier in the Ka-Band receiver currently at TRL 5 (for enhanced performance, a solution based on KaRIn heritage would be available at TRL 7 but with lower performance).

For the OBP, existing ASICs used for on-board processing in other programmes (SWIM, Poseidon 4) cannot be re-configured for SKaR application. Advanced FPGA technology shall be used for the OBP implementation to allow for flexibility and cost reduction.

The relevant technology pre-development is split in two steps. The first has been initiated during the Phase A and consists in the detailed architecture and specification of the on-board processing, the development of the software code and its implementation on a reference simulator, supporting the assessment of the achievable performance with the two candidate FPGA solutions. Furthermore, the specification of the demonstrator required to validate the



complete processing, to be designed around the selected FPGA, shall be completed in the frame of the Phase A pre-development activities. The second step, to be started at the beginning of Phase B1, consists in the development and testing of the OBP Elegant Breadboard (EBB) demonstrator to achieve TRL 5 at the end of Phase B1.

For the LNA two candidate dies have been characterised (S parameters, noise figure, reaction time) and tested (RF input power stress, long duration RF life test) confirming the Safe Operating Area with sufficient margins with respect to the nominal conditions.

Considering a successful completion of the relevant predevelopment and of the on-going activities for the heritage components, the CEU modules are expected to reach at least TRL 5 by the end of Phase B1.

9.2.3.2 High Power Amplifier

The SKaR HPA will have high heritage from the Extended Interaction Klystron developed for the KaRIn instrument for the SWOT mission, which is currently assessed at TRL 7 and which feasibility for SKIM has been confirmed in the course of the Phase A.

For the High Voltage Pulsed Power Supply two candidate solutions are being evaluated. The first one has already a high TRL of 7 for all constituting units except the grid modulator, whose current TRL is 3 and requires an early validation of the design and achievable performance for high frequency operations. A relevant pre-development has been initiated to raise the TRL of the grid modulator to 5 by the end of the Phase A.

A parallel activity for an alternative design based on heritage from the HV PPS being developed for the scatterometer to be embarked on MetOp-SG is also being pursued. In this case the elements subject to pre-developments are the grid modulator and the high voltage transformer and rectifier, currently assessed at TRL 3. In the course of the Phase A the specification/design of the relevant breadboard is being consolidated, with manufacturing and testing to be carried out during Phase B1, with objective of reaching TRL 5 by the end of Phase B1.

For the high-power isolator/circulator required at the output of the HPA it has been decided to pursue a pre-development based on European technology, the circulator developed for SWIM not being suitable for SKIM due to the lower power handling capabilities. The current TRL is 3 and a pre-development has been started in the course of the Phase A to design, manufacture and test the unit, reaching TRL 5 by the end of Phase A and expecting to reach TRL 6 during phase B1 after completion of the multipaction environmental tests. This development is also relevant to the high-power circulator required in the ferrite assembly.

The low pass harmonic filter is currently at TRL 4 and is considered not critical, since it will be based on a customised standard product. A relevant breadboard shall be designed, manufactured and tested during phase B1 with the objective to reach TRL 6.

Both consortia have highlighted the low reliability assessment of the Extended Interaction Klystron as used in SKaR and this will be subject of additional analysis/life tests, or design modification, in the next phases.

9.2.3.3 Antenna

The antenna architecture has strong heritage from the SWIM design, with a fixed single offset reflector illuminated by feeds on a rotating structure. Similarly to SWIM, the Rotary Feed Assembly includes a switch matrix, which allows to time-multiplex the different beams through a single RF rotary joint at the centre of the rotating structure.

The control of the switch matrix was achieved in SWIM via a slip-ring included in the Rotary Mechanism Assembly but this technology is not considered suitable for SKIM due to the lifetime limitation at the required rotating speed. To overcome this limitation the baseline solution for SWIM is to replace the slip-ring technology with roll-ring technology that requires a specific ball bearing configuration to be part of the pre-development in Phase B1 (proposal expected before end of Phase A).

All elements of the antenna are currently assessed at TRL >6, with the exception of the Ka-Band rotary joint, currently assessed at TRL 4 and for which a pre-development has been initiated with the objective of reaching TRL 5 by the end of Phase A.

9.2.3.4 Ferrite Assemblies Unit

The ferrite assembly unit includes the duplexer and the switch matrix. The duplexer is a custom design re-using the components (RF and electronics board) from the KaRIn instruments. The constituting elements have a TRL ranging from 3 to 7. The high-power circulator is currently assessed at TRL 3 and the pre-development addressed in the HPA Section is planned to reach TRL 5 by the end of Phase A and TRL 6 during phase B1.

For the switch drivers electronic boards there is heritage from the KaRIn development but some parts adaptation are required to cope with the higher PRF of SKIM. A Breadboard to validate the switching performance with the SKIM PRF is being developed and tested and is expected to confirm the achievement of TRL 5 by the end of Phase A.

Pre-development activity	Technology Readiness Level (TRL)		
	Start of Phase A	End of Phase A	End of Phase B1
On Board Processing Architecture	4	4	5
Grid Modulator	3	5	5
Grid Modulator – parallel option	3	3	5
Antenna 1-way Rotary Joint	4	5	5
High Power Isolator/Circulator	3	5	6
Low Noise Amplifier –Noise figure and Safe Operation Area	4	5	5
Switch Drivers	4	5	5

Table 9.1 SKIM SKaR pre-developments

9.3 Development Approach and Schedule

9.3.1 Overall Development Approach and Model Philosophy

SKIM will follow a phased development process (Phases B2/C/D/E1) with system reviews (System Requirements Review (SRR at end of B1), Preliminary Design Review (PDR at end of B2), Critical Design Review (CDR at end of phase C), etc.) to verify the status of the system design, development, procurement and integration of the development and flight models. In order to establish a robust development schedule, the instrument and platform developments can be decoupled. As reference planning to minimise project cost and schedule, both industrial consortia have proposed parallel development activities on the instrument, platform and satellite levels, with instrument integration performed during the Satellite Assembly, Integration and Test (AIT) phase.

The development approach and model philosophy at platform and satellite level is in general terms common to both concepts due to the similar approach for the platform (extensive re-use of heritage solution). For the platform the equipment re-used without modification will follow a direct Flight Model approach, most of those modified will go through a delta-qualification or will follow a proto-flight model approach.

For Concept A, a Structural Model (SM) will be developed to qualify the satellite structure, which is based on the SEOSAT one but will require some adaptation, particularly for the top floor supporting the SKaR instrument and in view of a potential enlargement of the bottom and top floors to increase the heat rejection capability of the platform. The SM will require representative mass dummies of the platform equipment and a representative structural model of the antenna assembly in order to allow for the satellite mechanical qualification and to confirm the interface loads of the platform/instrument mechanical interfaces.

For Concept B it is assumed that the heritage standard platform Structural and Thermal Model will qualify the platform for a range of missions carrying different payloads, including SKIM, although this is still pending the common platform contracts assignment. Therefore a dedicated STM for SKIM is not foreseen at this stage. It is planned to confirm the mechanical and thermal qualification at common platform level or at SKIM PFM level and the confirmation of the interface loads by analysis.

The electrical and functional verification at satellite level will be performed on a satellite Engineering Model consisting of the platform engineering model (that can be based on electrical and functional simulation models of the existing and re-used units and engineering models of the modified equipment) and of the SKaR CEU EM (or BBSI, see below) allowing an electric and functional verification of the payload/platform interfaces.

The satellite PFM (using the SM refurbished structure, if relevant, and the platform subsystems and instrument (P)FM) will be used for the thermal and EMC qualification and for completing the mechanical qualification and the functional and build acceptance.

The SKaR development approach includes the breadboards of some critical elements to be developed and tested during the Phase A/B1 to achieve a TRL of at least 5 (and 6 whenever possible) at the beginning of the development phase and mitigate the relevant development risks, as described in the previous Section.

At SKaR subsystem level an Engineering Qualification Model will be developed for the ferrite assemblies and for the duplexer/HPA, to perform early qualification/electrical, functional



and EMC verification of the subsystem and to be integrated in the instrument engineering model. All other subsystems will have an engineering model/proto-flight model (EM/PFM) approach with the exception of the Rotary Mechanism Assembly of the antenna for which a qualification model (QM) for lifetime testing will be developed. The CEU EM will be used to check the payload platform interfaces during the development with the platform engineering model or with a representative platform simulator, an early model (Breadboard Simulator Instrument - BBSI) could be developed for an early verification. The subsystems EMs shall be used for the electrical, functional and EMC verification and will be tested in the relevant temperature range at ambient pressure. Full qualification of the subsystems will be achieved at subsystem PFM level.

For the Antenna, a partial EM (part of the structure and no reflector) shall be used for early functional, electrical and EMC verification.

An antenna Structural Model (SM) is planned (TBC) for the satellite mechanical qualification and for confirming the interface loads at the platform/instrument interface.

The instrument engineering model will be representative of the whole instrument interfaces and functionalities. It will be used to check the interfaces between all subsystems, to demonstrate compliance to the functional and performance specification, to support the instrument qualification (EMC) and to prepare the PFM AIT sequence.

The instrument PFM will be mounted and tested at satellite level for functional and performance verification.

9.3.2 Schedule

The schedule for the SKIM development assumes the Phase B1 to start in October 2019 for a 1-year duration and that the Phase B2/C/D/E1 could start in March 2021 following the bidding and negotiation phase.

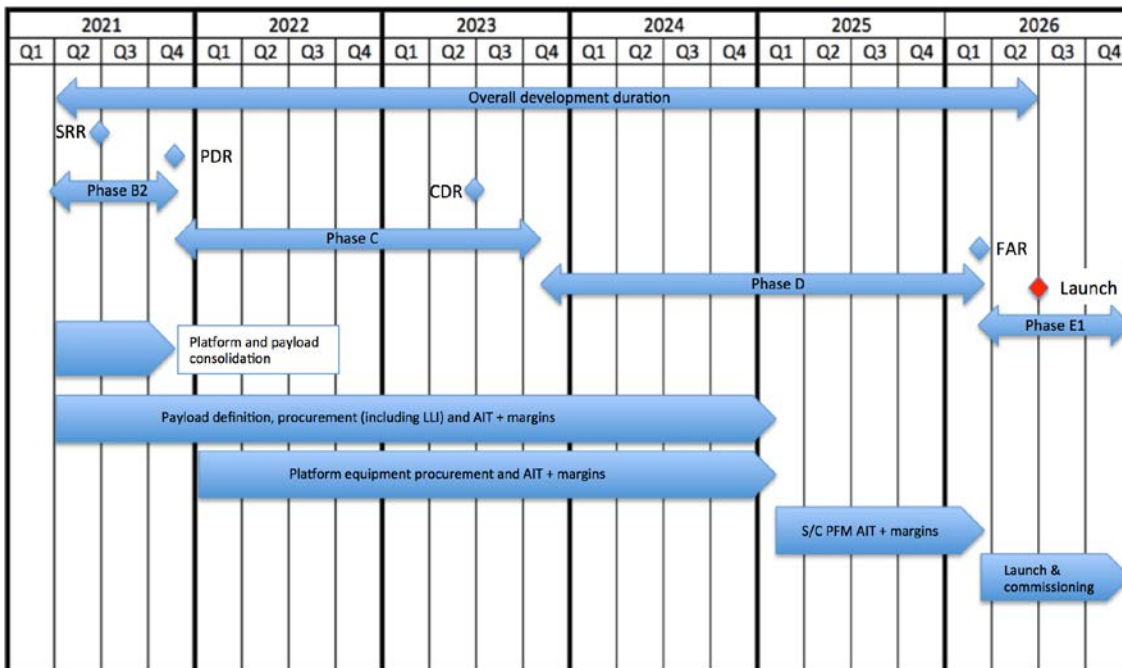


Fig. 9.1 – SKIM Development Schedule



The instrument kick-off is assumed to take place at the same time as the System Phase B2 KO. 6 months of contingency at prime level have been included. The schedule is driven by the instrument development after instrument PDR (instrument phases C/D). A launch for SKIM by the end of 2025 is not considered feasible with adequate margin. A launch by mid-2026 is considered feasible but challenging and will require an optimisation of the development approach and schedule taking into due account the associated risks.

9.4 Conclusion

The critical scientific areas of maturity and risk have been assessed and there are no major issues of concern to the scientific development of SKIM. The mission and research objectives have remained stable with respect to the original proposal. Evidence of SRL evolution has been presented based on two Scientific Readiness Assessments conducted during the Phase A that demonstrate SRL evolution from SRL=4 to SRL=5. A roadmap of science activities to further develop the SKIM mission has been established and presented in this chapter. Based on the results of the End-to-End performance simulations, the scientific campaigns and studies conducted during the Phase A, it is considered that the SKIM mission concept has reached Scientific Readiness Level 5 at the end of Phase A.

Assuming the expected successful outcome of on-going and planned technology pre-developments, the maturity of critical technologies will reach the required level prior to the start of the implementation phase. The development schedule is driven by the instrument development, calibration & characterization and test phases. The Design Development and Validation Plan and the associated schedule is not yet fully consolidated and further improvements would be necessary to recover - with margins - the launch date by the end of 2025.

SKIM will be the first satellite mission to provide wide swath Doppler measurements that can directly retrieve the global ocean surface current at spatial scales of about 30 km every few days. SKIM will be our *HF-radar in space*. SKIM will directly address one of the most challenging and fundamental questions in modern oceanography and marine meteorology:

How do the kinematics and dynamics of the ocean TSCV influence the integrated Earth system at the ocean atmosphere interface?

It is judged that the SKIM mission concept has reached the expected scientific and technical readiness level at the end of Phase A, and is sufficiently mature for implementation as Earth Explorer 9. The development schedule is compatible with a launch in the 2026 timeframe.

REFERENCES

- Aksenov, Y., E. E. Popova, A. Yool, A. G. Nurser, T. D. Williams, L. Bertino, & J. Bergh (2017). On the future navigability of Arctic sea routes: High-resolution projections of the Arctic Ocean and sea ice. *Marine Policy*, 75, 300-317, doi: 10.1016/j.marpol.2015.12.027
- Alpers, W. and K. Hasselmann (1978). The two-frequency microwave technique for measuring ocean wave spectra from an airplane or satellite, *Boundary-Layer Meteorol.*, 13, 215–230.
- Andrews, D. & McIntyre, M. E. (1978). An exact theory of nonlinear waves on a Lagrangian-mean flow. *Journal of Fluid Mechanics*, 89(04), 609. doi:10.1017/s0022112078002773
- Ardhuin, F. and A. D. Jenkins (2006). On the interaction of surface waves and upper ocean turbulence, *J. Phys. Oceanogr.*, 36, 3, 551–557. doi:10.1175/jpo2862.1
- Ardhuin, F., L. Marié, N. Rasclé, P. Forget, and A. Roland, A. (2009). Observation and estimation of Lagrangian, Stokes and Eulerian currents induced by wind and waves at the sea surface, *J. Phys. Oceanogr.*, 39, 11, 2820–2838. doi:10.1175/2009JPO4169.1.
- Ardhuin, F., F. Dumas, A.-C. Bennis, A. Roland, A. Sentchev, P. Forget, J. Wolf, F. Girard, P. Osuna, and M. Benoit (2012). Numerical wave modeling in conditions with strong currents: dissipation, refraction and relative wind, *J. Phys. Oceanogr.*, 42, 2101–2120.
- Ardhuin, F., L. Gualtieri, and E. Stutzmann (2015a). How ocean waves rock the earth: two mechanisms explain seismic noise with periods 3 to 300 s, *Geophys. Res. Lett.*, 42, 765–772, doi:10.1002/2014GL062782.
- Ardhuin, F., N. Rasclé, B. Chapron, J. Gula, J. Molemaker, S. T. Gille, D. Menemenlis, and C. Rocha (2017). Small scale currents have large effects on wind wave heights, *J. Geophys. Res.*, 122. doi:10.1002/2016JC012413.
- Ardhuin, F., Y. Aksenov, A., Benetazzo, L. Bertino, L., Brandt, P., Caubet, E., ... J. Xie, (2018) Measuring currents, ice drift, and waves from space: the Sea Surface Kinematics Multiscale monitoring (SKIM) concept. *Ocean Science*, 14, 337–354. doi: 10.5194/os-14-337-2018
- Ardhuin (2018) Preliminary Scientific Readiness Assessment SRA-1. Technical Note, SKIM-MPRC-SRA-1, ESA.
- Ardhuin (2019) Final Scientific Readiness Assessment SRA-2. Technical Note, SKIM-MPRC-SRA-2, ESA.
- Ardhuin, F., J. Stopa, B. Chapron, F. Collard, R. Husson, R. E. Jensen, J. Johannessen, A. Mouche, M. Passaro, G. Quartly, V. Swail, I. Young (2019a). Observing sea states, *Frontiers in Marine Sci.*, 6, 124, doi:10.3389/fmars.2019.00124.
- Ardhuin, F., B. Chapron, C. Maes, R. Romeiser, C. Gommenginger, S. Cravatte, R. Morrow, C. Donlon, M. Bourassa (2019b). Satellite Doppler observations for the motions of the oceans, *Bull. Amer. Meteorol. Soc.*, 100. doi:10.1175/BAMS-D-19-0039.1.
- Ardhuin F., P. Brandt, L. Gaultie, C. Donlon, A. Battaglia, F. Boy, T. Casal, B. Chapron, F. Collard, S. Cravatte, J.-M. Delouis, E. De Witte, G. Dibarboure, G. Engen, H. Johnsen, C. Lique, P. Lopez-Dekker, C. Maes, A. Martin, L. Marié, D. Menemenlis, F. Noguier, C. Peureux, P. Rampal, G. Ressler, M.-H. Rio, B. Rommen, J. D. Shutler, M. Suess, M. Tsamados, C. Ubelmann, E. van Sebille, M. van den Oever, and D. Stammer, (2019c), SKIM, a Candidate Satellite Mission Exploring Global Ocean Currents and Waves, *Frontiers in Marine Science*, 6, 209-, DOI=10.3389/fmars.2019.00209
- Armitage, T. W. K., and A. L. Ridout (2015), Arctic sea ice freeboard from AltiKa and comparison with CryoSat-2 and Operation IceBridge, *Geophys. Res. Lett.*, 42, 6724–6731, doi:10.1002/2015GL064823.
- Armitage, T.W.K., Bacon, S., Kwok R., (2018) Arctic sea level and surface circulation response to the Arctic Oscillation, *Geophysical Research Letters*, 45(13), 6576-6584.
- Ballarotta, M., C. Ubelmann, M.-I Pujol, G. Taburet, J.-F. Legeais, Y. Faugere, A. Delepouille, D. Chelton, G. Dibarboure, N. Picot and the DUACS team (2019). On the resolution of ocean altimetry maps, *Ocean Sci. Discuss.* doi:10.5194/os-2018-156
- Barrick, D. E. (1972). First order theory and analysis of MF/HF/VHF scatter from the sea, *IEEE Trans. Antennas Propagat.*, AP-20, 2–10.
- Barton, B. I., Y.-D. Lenn, C. Lique (2018), Observed atlantification of the Barents Sea causes the Polar Front to limit the expansion of winter sea ice, *J. Phys. Oceanogr.*, *J. Phys. Oceanogr.*, 48(8), 1849–1866. doi:10.1175/jpo-d-18-0003.1



- Battaglia, A., K. Mroz, D. Watters, F. Arduin, (2019): GPM-derived climatology of attenuation due to clouds and precipitation at Ka-band, *IEEE Trans. Geosci. Rem. Sens.* In Press.
- Belcher, S. E., Grant, A. L. M., Hanley, K. E., Fox-Kemper, B., Roedel, L. V., Sullivan, P. P., Large, W. G., Brown, A., Hines, A., Calvert, D., Rutgersson, A., Pettersson, H., Bidlot, J.-R., Janssen, P. A. E. M., and Polton, J. A. (2012). A global perspective on Langmuir turbulence in the ocean surface boundary layer, *Geophys. Res. Lett.*, 39, p. L18605. doi:10.1029/2012GL052932.
- Beljaars, A., E. Dutra, G. Balsamo, and F. Lemarié, (2017). On the numerical stability of surface–atmosphere coupling in weather and climate models. *Geosci. Model Dev.*, 10, 977–989, <https://doi.org/10.5194/gmd-10-977-2017>
- BIPM, (2008). Guide to the expression of uncertainty in measurement, available from <https://www.bipm.org/en/publications/guides/gum.html>
- Boeuf, G., (2011). Marine biodiversity characteristics. *Comptes Rendus Biologies*, 334(5-6), 435–440. doi:10.1016/j.crv.2011.02.009
- Bond, N. A., M. F. Cronin, M. H. Freeland, and N. Mantua, (2015), Causes and impacts of the 2014 warm anomaly in the NE Pacific. *Geophys. Res. Lett.*, 42, 3414– 3420. doi: 10.1002/2015GL063306.
- Bourassa, M. A., E. Rodriguez, and D. Chelton (2016), Winds and current mission: Ability to observe mesoscale air/sea coupling, in *IEEE International Geoscience and Remote Sensing Symposium (IGARSS)*, 7392–7395, IEEE, doi:10.1109/IGARSS.2016.7730928.
- Bourles, B., R. Lumpkin, M.J. McPhaden, F. Hernandez, P. Nobre, E. Campos, L. Yu, S. Planton, A. Busalacchi, A.D. Moura, J. Servain, and J. Trotte (2008). The PIRATA Program: History, Accomplishments, and Future Directions. *Bull. Amer. Meteor. Soc.*, 89, 1111-1125.
- Boutin, G., Lique, C., Arduin, F., Rousset, C., Talandier, C., Accensi, M., and Girard-Arduin, F., (2019). Toward a coupled model to investigate wave-sea ice interactions in the Arctic marginal ice zone. *The Cryosphere Discuss.*, <https://doi.org/10.5194/tc-2019-92>.
- Boy, F., J.-D. Desjonqueres, N. Picot, T. Moreau and N. Raynal (2017). CryoSat-2 SAR-mode over oceans: Processing methods, global assessment, and benefits. *IEEE Transactions on Geoscience and Remote Sensing*, 55, 1, 148-158, doi: 10.1038/s41586-019-1132-4
- Bruinsma, S. L., Frste, C., Abrikosov, O., Marty, J.-C., Rio, M.-H., Mulet, S., and Bonvalot, S. (2013). The new ESA satellite-only gravity field model via the direct approach,” *Geophys. Res. Lett.*, 40, 1944–8007. doi:10.1002/grl.50716.
- Buck, C. (2005). An extension to the wide swath ocean altimeter concept, in *Geoscience and Remote Sensing Symposium, IGARSS'05 Proceedings*, IEEE International, 8, 5436–5439, doi:10.1109/IGARSS.2005.1525970.
- Buck, C., Aguirre, M, Donlon, C., Petrolati, D., D’Addio, P. (2011). Steps towards the preparation of a Wavemill mission, *IEEE International Geoscience and Remote Sensing Symposium*. doi:10.1109/igarss.2011.6050098
- Cai, W.J., Dai, M.H., Wang, Y.C. (2006). Ocean–atmosphere exchange of carbon dioxide in ocean margins: A province-based synthesis. *Geophysical Research Letters* 33, L12603, doi: 12610.11029/12006gl026219.
- Cane, M.A. (2005) The evolution of El Niño, past and future. *Earth and Planetary Science Letters*, 230(3), 227– 240. <https://doi.org/10.1016/j.epsl.2004.12.003>
- Caudal, G., Hauser, D., Valentin, R., and Gac, C. L. (2014). KuROS: A new airborne ku-band doppler radar for observation of surfaces, *J. Atmos. Ocean Technol.*, 31, 2023–2245, doi: 10.1175/JTECH-D-14-00013.1.
- Cavaleri, L., B. Fox-Kemper, and M. Hemer (2012). Wind waves in the coupled climate system, *Bull. Amer. Meteorol. Soc.*, 78, 1651–1661. doi:10.1175/bams-d-11-00170.1
- Centurioni, L., L. Braasch, E. Di Lauro, P. Contestabile, F. De Leo, R. Casotti, L. Franco, and D. Vicinanza (2017). A new strategic wave measurement station off Naples port main breakwater, *Coastal Engineering Proceedings*, 1: 36.
- Chapron, B., Vandemark, D., and Jackson, F. (1994). Airborne measurements of the ocean’s Ku-band radar cross-section at low incidence angles, *Atmosphere-Ocean*, 32, 1, 179–193. doi:10.1080/07055900.1994.9649494.
- Chapron, B., F. Collard, and F. Arduin (2005). Direct measurements of ocean surface velocity from space: interpretation and validation, *J. Geophys. Res.*, 110, C07008. doi:10.1029/2004JC002809.
- Chapron, B. et al. (2017). A guideline to derive ocean surface currents from space: analysis and interpretation framework. *ESA Technical Note TN-1 from GlobCurrent Consortium*.



- Chassignet E, Sandery P. 2013. Joint GODAE OceanView –WGNE workshop on Short- to Medium-range coupled prediction for the atmosphere-wave-sea-ice-ocean: Status, needs and challenges. Modeling Whitepaper. GOV publication.
- Chelton, D.B., R.A. DeSzoeke, M.G. Schlax, K. El Naggar and N. Siwertz (1998) Geographical variability of the First Baroclinic Rossby Radius of Deformation. *Journal of Physical Oceanography*, 28, 433-460.
- Chelton, D. B., Schlax, M. G., & Samelson, R. M. (2011). Global observations of nonlinear mesoscale eddies. *Progress in Oceanography*, 91(2), 167–216. doi:10.1016/j.pocean.2011.01.002
- Chelton, D., R. Samelson, T. Farrar, J. Molemaker, and J. McWilliams (2017), Future Prospects for Estimation of Surface Ocean Velocity and Vorticity from a Winds and Currents Mission, IOVWST meeting, <http://tinyurl.com/WaCM2017>.
- Chelton, D. B., Schlax, M. G., Samelson, R. M., Thomas Farrar, J., Jeroen Molemaker, M., McWilliams, J. C., & Gula, J. (2018). Prospects for Future Satellite Estimation of Small-Scale Variability of Ocean Surface Velocity and Vorticity. *Progress in Oceanography*. doi:10.1016/j.pocean.2018.10.012
- Chen, C.T.A., Borges, A.V. (2009). Reconciling opposing views on carbon cycling in the coastal ocean: Continental shelves as sinks and near-shore ecosystems as sources of atmospheric CO₂. *Deep-Sea Res. Part II-Top. Stud. Oceanogr.* 56, 578-590.
- Chen, L., & Basu, B. (2018). Fatigue load estimation of a spar-type floating offshore wind turbine considering wave-current interactions. *International Journal of Fatigue*, 116, 421–428. doi:10.1016/j.ijfatigue.2018.06.002
- CLIVAR (2018), Report on the First Tropical Atlantic Observing System (TAOS) Review Workshop, 8 -9 February 2018, Portland US, CLIVAR Report No. 03/2018.
- CLS, (2011)Surface Topography Mission (STM) SRAL/MWR LEVEL-2Algorithms Definition, Accuracy and Specification [SD-03] [SD-07] , Reference: CLS-DOS-NT-09-119, available from https://earth.esa.int/documents/247904/351187/ALT_Level-2_ADAS.pdf
- Collard, F., A. Mouche, B. Chapron, C. Danilo, C., and J. Johannessen (2008). Routine high resolution observation of selected major surface currents from space, in Proceedings of SEASAR 2008, SP-656, (ESA -ESRIN, Frascati, Italy), ESA.
- Collard, F., F. Arduin, F., and B. Chapron (2009). Monitoring and analysis of ocean swell fields using a spaceborne SAR: a new method for routine observations,” *J. Geophys. Res.*, 114, p. C07023.
- Cooper, C., Danmeier, D., Frolov, S., Stuart, G., Zuckerman, S., Anderson, S., & Sharma, N. (2016). Real Time Observing and Forecasting of Loop Currents in 2015. Offshore Technology Conference. doi:10.4043/26920-ms
- Coumou, D., G. di Capua, S. Vavrus, L. Wang, S. Wang (2018). The influence of Arctic amplification on mid-latitude summer circulation, *Nature Comm.*, 9(2959) <https://doi.org/10.1038/s41467-018-05256-8>.
- Cravatte, S., W. S. Kessler, N. Smith, S. E. Wijffels, and Contributing Authors, 2016: First Report of TPOS 2020. GOOS-215, 200 pp. [Available online at <http://tpos2020.org/first-report/>.]
- Cronin, M., et al. (2019). Ocean–atmosphere fluxes with a focus on heat and momentum. *Frontiers in Marine Science*, in press.
- D’Asaro, E. A. (1985) The energy flux from the wind to near-inertial motions in the surface layer, *Journal of Physical Oceanography*, 15, 1043-1059.
- Delouis, J.-M. (2019): Data-driven attitude reconstruction method applied to SKIM data processing. Tech. Note SKIM-MPRC-TN4a-V1.0, ESA, May 2019.
- Delouis, J.-M., L. Pagano, S. Mottet, J.-L. Puget, L. Vibert, (2019), SRoll2: an improved mapmaking approach to reduce large-scale systematic effects in the Planck High Frequency Instrument legacy maps, arXiv:1901.11386 [astro-ph.CO]
- Desjonquères, J. D. ., G. Carayon, N. Steunou & J. Lambin (2010) Poseidon-3 Radar Altimeter: New Modes and In-Flight Performances, *Marine Geodesy*, 33:sup1, 53-79, DOI: 10.1080/01490419.2010.488970
- Dewitte, S., Clerbaux, N. (2017). Measurement of the Earth Radiation Budget at the Top of the Atmosphere—A Review. *Remote Sens.*, 9, 1143.
- Dieng, H. B., Palanisamy, H., Cazenave, A., Meyssignac, B., & von Schuckmann, K. (2015). The Sea Level Budget Since 2003: Inference on the Deep Ocean Heat Content. *Surveys in Geophysics*, 36(2), 209–229. doi:10.1007/s10712-015-9314-6



- Dibarboure, G., F. Boy, J. D. Desjonqueres, S. Labroue, Y. Lasne, N. Picot, J. C. Poisson, and P. Thibaut (2014). Investigating Short-Wavelength Correlated Errors on Low-Resolution Mode Altimetry. *Journal of Atmospheric and Oceanic Technology* 2014 31:6, 1337-1362.
- Dibarboure, G., and Ubelmann, Clement. (2014). Investigating the Performance of Four Empirical Cross-Calibration Methods for the Proposed SWOT Mission. *Remote Sensing*, 6. 4831-4869. 10.3390/rs6064831
- Dibarboure, G. and C. Ubelmann (2019). Data-driven calibration of azimuth knowledge error for the proposed SKIM mission. Tech. Note SKIM-TN4b-V1.0, ESA, May 2019
- Donlon, C. J., M. Martin, J. D. Stark, J. Roberts-Jones, E. Fiedler and W. Wimmer, (2012), The Operational Sea Surface Temperature and Sea Ice analysis (OSTIA), *Remote Sensing of the Environment*, 116, 140-158, doi: 10.1016/j.rse.2010.10.017 2011.
- Donlon, C. J., P. J. Minnett, N. Fox, and W. Wimmer (2015), Strategies for the Laboratory and Field Deployment of Ship-Borne Fiducial Reference Thermal Infrared Radiometers in Support of Satellite-Derived Sea Surface Temperature Climate Data Records in Zibordi., G., C. Donlon and A. Parr (Eds.), (2015), *Optical Radiometry for Oceans Climate Measurements*, Vol. 47 *Experimental Methods in Sciences*, Elsevier, 697 pp., ISBN: 9780124170117
- Dohan, K., and N. Maximenko, (2010). Monitoring ocean currents with satellite sensors. *Oceanography*, 23(4), 94-103. Retrieved from <http://www.jstor.org/stable/24860865>
- Doviak R. J., and D. S. Zrnic D. S. (1993). *Doppler Radar and Weather Observations*, 562 pp. Second Edition, Academic Press, ISBN: 0-486-45060-0.
- Ducet, N., P. Y. Le Traon, and G. Reverdin (2000), Global high-resolution mapping of ocean circulation from TOPEX/Poseidon and ERS-1 and 2, *J. Geophys. Res.*, 105, 9,477–19,498.
- Dufau, C., Orszynowicz, M., Dibarboure, G., Morrow, R., and Le Traon, P. Y. (2016). Mesoscale resolution capability of altimetry: Present and future. *Journal of Geophysical Research: Oceans*, 121(7), 4910-4927.
- European Commission (2016). An integrated European Union policy for the Arctic. Joint Communication to the European Parliament and the Council (JOIN/2016/021).
- Ekman, V. W. (1905) On the influence of earth's rotation on ocean currents. *Arkiv for Matematik, Astronomi och Fysik*, 2(10).
- Elfouhaily, T., Chapron, B., Katsaros, K., & Vandemark, D. (1997). A unified directional spectrum for long and short wind-driven waves. *Journal of Geophysical Research*, 102(C7), 15781–15796. doi:10.1029/97jc00467
- Elipot, S. R., Lumpkin, R., Prieto, G. A. (2010). Modification of inertial oscillations by the mesoscale eddy field, *Journal of Geophysical Research—Oceans*, 115, C09010, doi: 10.1029/2009JC005679
- Elipot, S., R. Lumpkin, R. C. Perez, J. M. Lilly, J. J. Early, and A. M. Sykulski (2016). A global surface drifter data set at hourly resolution, *J. Geophys. Res. Oceans*, 121, 2937–2966, doi:10.1002/2016JC011716.
- ESA (2015a). *Earth Observation Science Strategy for ESA: A New Era for Scientific Advances and for Societal Benefits*. ESA SP-1329/1 (2 volumes), European Space Agency, Noordwijk, The Netherlands
- ESA (2015b). *ESA's Living Planet Programme: Scientific Achievements and Future CHallenges - scientific context of the Earth Observation Science Strategy for ESA*, ESA SP-1329/2 (2 volumes), European Space Agency, Noordwijk, The Netherlands.
- ESA (2015c). *Scientific Readiness Levels Handbook*. Mission Science Division (EOP-SM), EOP-SM/2776, V1.1, European Space Agency, Noordwijk, The Netherlands.
- ETIP Ocean (2019). *Powering Homes Today, Powering Nations Tomorrow, Policy Solutions to Deliver Ocean Energy Industrial Roll-Out*. <https://www.oceanenergy-europe.eu/wp-content/uploads/2019/04/ETIP-Ocean-Integrated-Strategy-2019-LR.pdf>
- FAO (2018). *The state of world fisheries and aquaculture*. <http://www.fao.org/3/i9540en/I9540EN.pdf>
- Faugere, Y., J. Dorandeu, F. Lefevre, N. Picot, and P. Femenias, (2006), Envisat ocean altimetry performance assessment and cross-calibration. *Sensors*, 6, 100–130, doi:10.3390/s6030100.
- Fedele, F., Benetazzo, A., Gallego, G., Shih, P.-C., Yezzi, A., Barbariol, F., & Arduin, F. (2013). Space–time measurements of oceanic sea states. *Ocean Modelling*, 70, 103–115. doi:10.1016/j.ocemod.2013.01.001
- Fernandez, J., D. Escobar, F. Ayuga and P. Femenias, (2016) Copernicus POD Service Operational Experience, Space Ops conference, Paper Daejeon, Korea- May 2016, DOI: 10.2514/6.2016-2385



- Ferrari, R. and C. Wunsch (2009). Ocean circulation kinetic energy reservoirs, sources and sinks. *Ann. Revs. Fluid Mechs.*, 41, 253-282.
- Forget, G., J.-M. Campin, P. Heimbach, C. N. Hill, R. M. Ponte, and C. Wunsch (2015). ECCO version 4: an integrated framework for non-linear inverse modeling and global ocean state estimation, *Geosci. Model Dev.*, 8, 3071–3104, 2015 www.geosci-model-dev.net/8/3071/2015/ doi:10.5194/gmd-8-3071-2015
- Forget, G., D. Ferreira (2019). Global ocean heat transport dominated by heat export from the tropical Pacific, *Nature Geoscience*. doi : 10.1038/s41561-019-0333-7
- Foltz et al. (2019). The Tropical Atlantic Observing System, *Front. Mar. Sci.*, doi : 10.3389/fmars.2019.00206
- Fosheim, M., R. Primicerio, E. Johannessen, R. B. Ingvaldsen, M. M. Aschan, A. V. Dolgov, (2018). Recent warming leads to a rapid borealization of fish communities in the Arctic, *Nature Clim. Ch.*, doi:10.1038/NCLIMATE2647
- Fox-Kemper, B., Adcroft, A., Böning, C. W., Chassignet, E. P., Curchitser, E., Danabasoglu, G., ... Yeager, S. G. (2019). Challenges and Prospects in Ocean Circulation Models. *Frontiers in Marine Science*, doi:10.3389/fmars.2019.00065
- Fraser, C. I., A. K. Morrison, A. M. Hogg, E. C. Macaya, E. van Sebille, P. G. Ryan, A. Padovan, C. Jack, N. Valdivia, J. M. Waters (2018). Antarctica's ecological isolation will be broken by storm-driven dispersal and warming. *Nature Climate Change*, 8, 704-708. doi:10.1038/s41558-018-0209-7
- Frölicher, T. L., C. Laufkötter, 2018: Emerging risks from marine heat waves. *Nature Communications*, 9(1), doi:10.1038/s41467-018-03163-6
- Gao, Q.; Makhoul, E.; Escorihuela, M.J.; Zribi, M.; Quintana Seguí, P.; García, P.; Roca, M. (2019). Analysis of Retracker's Performances and Water Level Retrieval over the Ebro River Basin Using Sentinel-3. *Remote Sens.*, 11, 718.
- Gaultier, L. (2019). SKIM Simulator Documentation, Report for SKIM Performance Evaluation contract, ESA, Noordwijk, The Netherlands. See also <https://github.com/oceandatalab/skimulator>
- GCOS (2016). The Global Observing System for Climate: Implementation Needs, GCOS-200: https://library.wmo.int/opac/doc_num.php?explnum_id=3417
- Godoi, VA, Andrade, FM, Bryan, KR, Gorman, RM. (2019). Regional-scale ocean wave variability associated with El Niño–Southern Oscillation–Madden-Julian Oscillation combined activity. *Int J. Climatol.*, 39: 483– 494. <https://doi.org/10.1002/joc.5823>
- Golden, C. D., et al. (2016). Fall in fish catch threatens human health, *Nature News*, <https://www.nature.com/news/nutrition-fall-in-fish-catch-threatens-human-health-1.20074>
- Goldfinger, A. D., (1982), Estimation of Spectra from Speckled Images, in *IEEE Transactions on Aerospace and Electronic Systems*, vol. AES-18, no. 5, pp. 675-681, Sept. 1982.
- Graham, J. A., Rosser, J. P., O'Dea, E., Hewitt, H T., (2018) Resolving Shelf Break Exchange Around the European Northwest Shelf, *Geophysical Research Letters*, doi: 10.1029/2018GL079399
- Gruber (2011). Warming up, turning sour, losing breath: ocean biogeochemistry under global change. *Philosophical Transactions of the Royal Society A: Mathematical, Physical and Engineering Sciences*, 369(1943), 1980–1996. doi:10.1098/rsta.2011.0003
- Gurgel, K.-W., G. Antonischki, H.-H. Essen, T. Schlick (1999). Wellen Radar (WERA): a new ground-wave HF radar for ocean remote sensing, 37, 219–234, doi:10.1016/S0378-3839(99)00027-7.
- Hansen, J., Sato, M., Kharecha, P., & von Schuckmann, K. (2011). Earth's energy imbalance and implications. *Atmospheric Chemistry and Physics*, 11(24), 13421–13449. doi:10.5194/acp-11-13421-2011
- Hansen, M. W., F. Collard, K. Dagestad, J. A. Johannessen, P. Fabry, and B. Chapron (2011). Retrieval of Sea Surface Range Velocities From Envisat ASAR Doppler Centroid Measurements, *IEEE Trans. Geosci. Remote Sensing*, 49(10), 3582 - 3592, doi:10.1109/TGRS.2011.2153864.
- Harris, C. (2018). Coupled Atmosphere–Ocean Modelling, in *New Frontiers in Operational Oceanography*, Chassignet, E. P., A. Pascual, J. Tintoré, and J. Verron (Eds.). (2018). *GODAE OceanView*, 815pp. doi:10.17125/gov2018
- Hart-Davis, M. G., B. C. Backeberg, I. Halo, E. van Sebille, J. A. Johannessen, (2018). Assessing the accuracy of satellite derived ocean currents by comparing observed and virtual buoys in the Greater Agulhas Region, *Remote Sensing of Environment*, in press, 2018,
- Hasselmann, K. (1970). Wave-driven inertial oscillations, *Geophys. Fluid Dyn.*, 3, 463-502, doi: 10.1080/03091927009365783



- Hasselmann, K. (1990). Epilogue: waves, dreams, and visions, in *Directional Ocean wave Spectra*, 205-208, The John Hopkins University Press, Baltimore
- Hauser, D., C. Tison, T. Amiot, L. Delaye, N. Corcoral, and P. Castellan (2017). SWIM: The First Spaceborne Wave Scatterometer, *IEEE Trans. Geosci. Remote Sens.*, 57, 3000-3014, doi: 10.1109/TGRS.2017.2658672.
- Heorton, H., M. Tsamados, S. Cole, A. Ferreira, A. Berbellini, M. Fox, T. Armitage (2019). Retrieving sea ice drag coefficients and turning angles from in-situ and satellite observations using an inverse modelling framework, *J. Geophys. Res.-Oceans*, In Press.
- Holding, T., Ashton, I. G., Shutler, J. D., Land, P. E., Nightingale, P. D., Rees, A. P., Brown, I., Piolle, J.-F., Kock, A., Bange, H. W., Woolf, D. K., Goddijn-Murphy, L., Pereira, R., Paul, F., Girard-Ardhuin, F., Chapron, B., Rehder, G., Ardhuin, F., and Donlon, C. J. (2019) The FluxEngine ocean-atmosphere gas flux toolbox: simplified interface and extensions for in situ analyses and multiple sparingly soluble gases, *Ocean Sci. Discuss.*, <https://doi.org/10.5194/os-2019-45>
- Holte, J. W., L. D. Talley, T. K. Chereskin, and B. M. Sloyan (2013). Subantarctic mode water in the southeast Pacific: Effect of exchange across the Subantarctic Front, *J. Geophys. Res. Oceans*, 118, 2052–2066, doi:10.1002/jgrc.20144.
- Hummels, R., Dengler, M., Brandt, P. et al. (2014). Diapycnal heat flux and mixed layer heat budget within the Atlantic Cold Tongue, *Clim Dyn* (2014) 43: 3179.
- IPCC (2014). *Climate Change 2014: Synthesis Report. Contribution of Working Groups I, II and III to the Fifth Assessment Report of the Intergovernmental Panel on Climate Change* [Core Writing Team, R.K. Pachauri and L.A. Meyer (eds.)]. IPCC, Geneva, Switzerland, 151 pp.
- IPCC, (2018). *Global Warming of 1.5°C, Social Report*, available from <http://www.ipcc.ch/report/sr15/>
- IPBES (2019). *Global assessment report on biodiversity and ecosystem services of the Intergovernmental Science- Policy Platform on Biodiversity and Ecosystem Services*. E. S. Brondizio, J. Settele, S. Díaz, and H. T. Ngo (editors). IPBES Secretariat, Bonn, Germany.
- Jackson, F. (1981). An analysis of short pulse and dual frequency radar techniques for measuring ocean wave spectra from satellites, *Radio Science*, 16(6): 1385- 1400.
- Jackson F. C., W. T. Walton, and C. Y. Peng (1985b). A comparison of in situ and airborne radar observations of ocean wave directionality, *J. Geophys. Res.*, Vol. 90, 1005-1018.
- Jackson F. C., W. T. Walton, and P. L. Baker (1985a). Aircraft and satellite measurement of ocean wave directional spectra using scanning-beam microwave radars, *J. Geophys. Res.*, Vol. 90, 987-1004.
- Jackson F. (1987) The physical basis for estimating wave-energy spectra with the radar ocean-wave spectrometer. *Johns Hopkins APL Tech. Dig.*, 8, 70–73.
- Jayne, S. R., and Marotzke, J. (2001). The dynamics of ocean heat transport variability. *Reviews of Geophysics*, 39(3), 385–411. doi:10.1029/2000rg000084
- Jeans, G., M. Prevosto, L. Harrington-Missin, C. Maisondieu, C. Herry, J. A. M. Lima (2012). Deepwater Current Profile Data Sources for Riser Engineering Offshore Brazil, Paper No. OMAE2012-83400, 155-168, doi:10.1115/OMAE2012-83400
- Jenkins, A. D. (1989). The use of a wave prediction model for driving a near-surface current model, *Deut. Hydrogr. Z.*, 42, 133–149.
- Johnson, H. and G. Engen, (2019). Estimation of range intensity spectra. Tech. Note SKIM-MPRC-TN7-V1.0, ESA, May 2019.
- Kennedy, J. J., Rayner, N. A., Smith, R. O., Parker, D. E., and Saunby, M. (2011), Reassessing biases and other uncertainties in sea surface temperature observations measured in situ since 1850: 2. Biases and homogenization, *J. Geophys. Res.*, 116, D14104, doi:10.1029/2010JD015220.
- Kim, S. Y., E. J. Terrill, and B. D. Cornuelle (2008). Mapping surface currents from HF radar radial velocity measurements using optimal interpolation, *J. Geophys. Res.*, 113, C10023, doi:10.1029/2007JC004244.
- Kim, S. Y. & Kosro, P. M. (2013). Observations of near-inertial surface currents off Oregon: Decorrelation time and length scales. *Journal of Geophysical Research: Oceans*, 118(7), 3723–3736. doi:10.1002/jgrc.20235
- Kim, T.-W., H. K. Ha, A. K. Wählin, S.H. Lee, C.-S. Kim, J. H. Lee, and Y.-K. Cho (2017). Is Ekman pumping responsible for the seasonal variation of warm circumpolar deep water in the Amundsen Sea?. *Continental Shelf Research* 132, 38-48.



- Klein, P., G. Lapeyre, W. G. Large (2004). Wind ringing of the ocean in presence of mesoscale eddies. *Geophysical Research Letters*, 31(15). doi:10.1029/2004gl020274
- Kræmer, T., H. Johnsen, C. Brekke, and G. Engen (2018). Comparing SAR-Based Short Time-Lag Cross Correlation and Doppler-Derived Sea Ice Drift Velocities. *IEEE Transactions on Geoscience and Remote Sensing*, 56(4), 1898-1908.
- Shunichi, K and S. Nubuo, (2015), Response to the 2011 Great East Japan Earthquake and Tsunami disaster, 373, *Philosophical Transactions of the Royal Society A: Mathematical, Physical and Engineering Sciences*, doi/10.1098/rsta.2014.0373
- Kudryavtsev, V. N., A. V. Soloviev, A. V. (1990). Slippery Near-Surface Layer of the Ocean Arising Due to Daytime Solar Heating. *J. Phys. Oceanogr.*, 20(5), 617–628. doi:10.1175/1520-0485(1990)020<0617:snslot>2.0.co;2
- Lamarre, G. G., J. L. Puget, F. Bouchet, P. A. R. Ade, A. Benoit, J. P. Bernard, J. Bock, P. De Bernardis, J. Charra, F. Couchot, J. Delabrouille, G. Efstathiou, M. Giard, G. Guyot, A. Lange, B. Maffei, A. Murphy, F. Pajot, M. Piat, I. Ristorcelli, D. Santos, R. Sudiwala, J. F. Sygnet, J. P. Torre, V. Yurchenko, D. Yvon, (2003). The Planck High Frequency Instrument, a third generation CMB experiment, and a full sky submillimeter survey, *New Astronomy Reviews*, 47, Issues 11–12, 1017-1024.
- Lebedev, K. V., H. Yoshinari, N. A. Maximenko, P. W. Hacker (2007). YoMaHa'07: Velocity data assessed from trajectories of Argo floats at parking level and at the sea surface, IPRC Technical Note No. 4(2), June 12, 2007.
- Lebreton, L. C. M., B. Slat, F. Ferrari, B. Sainte-Rose, J. Aitken, R. Marthouse, S. Hajbane, S. Cunsolo, A. Schwarz, A. Levivier, K. Noble, P. Debeljak, H. Maral, R. Schoeneich-Argent, R. Brambini, and J. Reisser (2018). Evidence that the Great Pacific Garbage Patch is rapidly accumulating plastic. *Scientific Reports*, 8(1), doi:10.1038/s41598-018-22939-w.
- Leckler, F., Arduin, F., Peureux, C., Benetazzo, A., Bergamasco, F., and Dulov, V. (2015). Analysis and interpretation of frequency-wavenumber spectra of young wind waves, *J. Phys. Oceanogr.*, 45, 2484–2496, doi:10.1175/JPO-D-14-0237.1.
- Le Quéré, et al. (2018) Global Carbon Budget 2018, *Earth System Science Data*, 10, 2141-2194, <https://doi.org/10.5194/essd-10-2141-2018>.
- Lemarié, F., E. Blayo, and L. Debreu (2015). Analysis of ocean-atmosphere coupling algorithms: Consistency and stability. *Procedia Comput. Sci.*, 51, 2066–2075, <https://doi.org/10.1016/j.procs.2015.05.473>
- Lemarié, F., Burchard, H., Debreu, L., Klingbeil, K., & Sainte-Marie, J. (2019). Advancing dynamical cores of oceanic models across all scales. *Bulletin of the American Meteorological Society*. In press. doi:10.1175/bams-d-18-0303.1
- Le Traon, P-Y, et al, (2019). From Observation to Information and Users: The Copernicus Marine Service Perspective, *Frontiers in Marine Science*, 6, 234-, DOI=10.3389/fmars.2019.00234.
- Li, Q., Webb, A., Fox-Kemper, B., Craig, A., Danabasoglu, G., Large, W. G., & Vertenstein, M. (2016). Langmuir mixing effects on global climate: WAVEWATCH III in CESM. *Ocean Modelling*, 103, 145–160. doi:10.1016/j.ocemod.2015.07.020
- Li, H., Chapron, B., Mouche, A., & Stopa, J. E. (2019). A new ocean SAR cross-spectral parameter: definition and directional property using the global Sentinel-1 measurements. *Journal of Geophysical Research: Oceans*. doi:10.1029/2018jc014638
- López Dekker, M. Völker, B. Chapron, and T. Börner, (2015) MAC-SAR: Final Report. Projektbericht. D3-4000104960, 20, <https://elib.dlr.de/96873/>
- LOPS (2019a), Forward model for currents and waves: assumptions for the SKIM lightweight simulator (SKIMulator), Tech. Note SKIM-MPRC-TN0-V1.0, ESA, May 2019.
- LOPS (2019b), Estimation of non-geophysical Doppler and wave Doppler, and inversion algorithm for SKIM, Tech. Note SKIM-MPRC-TN5-V2.0, ESA, May 2019. doi: 10.13140/RG.2.2.22907.98081/3
- Lozier, M. S., et al. (2019). A sea change in our view of overturning in the subpolar North Atlantic, *Science*, doi: 10.1126/science.aau6592
- Lubchenco, J. (1998). Entering the Century of the Environment: A New Social Contract for Science. *Science*, 279(5350), 491–497. doi:10.1126/science.279.5350.491
- Lumpkin, R., T. Özgökmen, & L. Centurioni (2017). Advances in the Application of Surface Drifters. *Annual Review of Marine Science*, 9(1), 59–81. doi:10.1146/annurev-marine-010816-060641



- Lumpkin, R and M. Pazos, (2007). Measuring surface currents with surface velocity program drifters: the instrument, its data and some results, in Griffa, A, A. D. Kirwan, A. J. Mariano, T. Özgökmen, and H. T. Rossby (Eds.), *Lagrangian Analysis and Prediction of Coastal and Ocean Dynamics*, Cambridge University press.
- Ma, X. et al., 2015: Distant influence of Kuroshio eddies on North Pacific weather patterns? *Sci. Rep.* 5, 17785.
- Ma, X., Z. Jing, P. Chang, X. Liu, R. Montuoro, R. J. Small, F. O. Bryan, R. J. Greatbatch, P. Brandt, D. Wu, X. Lin, L. Wu, 2016: Western boundary currents regulated by interaction between ocean eddies and the atmosphere, *Nature*, 535, 533-537, doi:10.1038/nature18640.
- Marié, L., F. Collard, F. Nouguier, L. Pineau-Guillou, D. Hauser, F. Boy, S. Méric, C. Peureux, G. Monnier, B. Chapron, A. Martin, P. Dubois, F. Ardhuin, 2019: Measuring ocean surface velocities with the KuROS and KaRADOc airborne near-nadir Doppler radars: a multi-scale analysis in preparation of the SKIM mission, *Ocean Science Discussions*.
- Martin, A. C. H., and C. Gommenginger (2017). Towards wide-swath high-resolution mapping of total ocean surface current vectors from space: Airborne proof-of-Concept and validation, *Remote Sensing of Environment*, 197, 58-71, doi: 10.1016/j.rse.2017.05.020.
- Martin, A., C. Gommenginger, J. Marquez, S. Doody, V. Navarro, and C. Buck, 2016, Wind-Wave induced velocity in ATI SAR Ocean Surface Currents: First experimental evidence from an airborne campaign, *Journal of Geophysical Research: Oceans*, <http://dx.doi.org/10.1002/2015JC011459>.
- Martin, A., C. Gommenginger, and Y. Quilfen 2018, Simultaneous ocean surface current and wind vectors retrieval with squinted SAR interferometry: Geophysical inversion and performance assessment, *Remote Sensing of Environment*, <https://doi.org/10.1016/j.rse.2018.06.013>.
- Marull-Paretas, G. (2013), Development of a multi-channel SAR simulator for open-oceans: OASIS, Oct. 2013.
- Maximenko, N., P. Niiler, M.-H. Rio, O. Melnichenko, L. Centurioni, D. Chambers, V. Zlotnicki, and B. Galperin (2009), Mean dynamic topography of the ocean derived from satellite and drifting buoy data using three different techniques, *J. Atmos. Oceanic Technol.*, 26,1910–1919, doi:10.1175/2009JTECHO672.1.
- Maximenko, N., Hafner, J., Kamachi, M., & MacFadyen, A. (2018). Numerical simulations of debris drift from the Great Japan Tsunami of 2011 and their verification with observational reports. *Marine Pollution Bulletin*, 132, 5–25. doi:10.1016/j.marpolbul.2018.03.056
- McPhaden, M.J., Zebiak, S.E. and Glantz, M.H. (2006a). ENSO as an integrating concept in earth science. *Science*, 314(5806), 1740– 1745.
- McWilliams (2016). Submesoscale currents in the ocean, *Proc. Roy. Soc.*, DOI: 10.1098/rspa.2016.0117.
- Meneghello, G., J. Marshall, J.-M. Campin, E. Doddridge, and M.-L. Timmermans (2018). The Ice-Ocean Governor: Ice-Ocean Stress Feedback Limits Beaufort Gyre Spin-Up. *Geophysical Research Letters* 45(20), 11-293.
- Menemenlis, D., video of surface currents from MITgcm simulation LLC4420, <https://embed.ifremer.fr/videos/c4a347b7dfdb49ac856d5a138e1adc9d>
- Mills, K. E., A. J. Pershing, C. J. Brown, Y. Chen, F. Chiang, D. S. Holland, S. Lehuta, J. A. Nye, J. C. Sun, A. C. Thomas and R. A. Wahle, (2013), Fisheries Management in a Changing Climate: Lessons from the 2012 Ocean Heat Wave in the Northwest Atlantic. *Oceanography*, Vol. 26, No. 2, SPECIAL ISSUE ON Ocean Remote Sensing With Synthetic Aperture Radar 191-195
- Minobe, S., Kuwano-Yoshida, A., Komori, N., Xie, S. P. & Small, R. J., (2018). Influence of the Gulf Stream on the troposphere. *Nature* 452, 206–U251, doi: 10.1038/Nature06690.
- Moller, D., E. Rodriguez, J. Carswell, and D. Esteban-Fernandez (2011). AirSWOT-A calibration/validation platform for the SWOT mission, *Proc. International Geoscience and Remote Sensing Symposium*, Vancouver, Canada.
- Morrow, R., Fu, L.-L., Ardhuin, F., Benkiran, M., Chapron, B., Cosme, E., ... Zaron, E. D. (2019). Global Observations of Fine-Scale Ocean Surface Topography With the Surface Water and Ocean Topography (SWOT) Mission. *Frontiers in Marine Science*, 6. doi:10.3389/fmars.2019.00232
- Mouche, A. A., Chapron, B., and Reul, N. (2008). Predicted Doppler shifts induced by ocean surface wave displacements using asymptotic electromagnetic wave scattering theories," *Waves in Random and Complex Media*, 18, 1. doi:10.1080/17455030701564644.
- Mouche, A. A., Collard, F., Chapron, B., Dagestad, K.-F., Guitton, G., Johannessen, J. A., ... Hansen, M. W. (2012). On the Use of Doppler Shift for Sea Surface Wind Retrieval From SAR. *IEEE Transactions on Geoscience and Remote Sensing*, 50(7), 2901–2909. doi:10.1109/tgrs.2011.2174998



- Mouche, A. A., Chapron, B., Zhang, B., & Husson, R. (2017). Combined Co- and Cross-Polarized SAR Measurements Under Extreme Wind Conditions. *IEEE Transactions on Geoscience and Remote Sensing*, 55(12), 6746–6755. doi:10.1109/tgrs.2017.2732508
- Munk, W. (2002). The Evolution of Physical Oceanography in the Last Hundred Years, *Oceanography*, 15(1), doi: 10.5670/oceanog.2002.45
- Munk, W. (2009). An Inconvenient Sea Truth: Spread, Steepness, and Skewness of Surface Slopes, *Ann. Rev. Marine Science*, 1:377–415, doi: 10.1146/annurev.marine.010908.163940
- Nakamura, H., Sampe, T., Tanimoto, Y. and Shimpo, A. (2004). Observed associations among storm tracks, jet streams and midlatitude oceanic fronts. *Geophys Monogr Ser 147*, 329–345.
- Nasello, C., and V. Armenio, (2016). A New Small Drifter for Shallow Water Basins: Application to the Study of Surface Currents in the Muggia Bay (Italy), *Journal of Sensors*, vol. 2016. <https://doi.org/10.1155/2016/6589636>.
- Niiler, P. P., Sybrandy, A. S., Bi, K., Poulain, P. M., & Bitterman, D. (1995). Measurements of the water-following capability of holey-sock and TRISTAR drifters. *Deep Sea Research Part I: Oceanographic Research Papers*, 42(11-12), 1951–1964. doi:10.1016/0967-0637(95)00076-3
- Niiler, P., (2009) Ageostrophic circulation in the ocean, *Oceanography in 2025: Proceeding of a workshop*, Edited by Deborah Glickson, Chapter 24, 73-76, The National Academies Press, Washington, ISBN: 978-0-309-13745-4, <https://www.nap.edu/read/12627/chapter/24>
- Nouguier, F., A. Mouche, N. Rasclé, B. Chapron, and D. Vandemark (2016). Analysis of dual-frequency ocean backscatter measurements at Ku- and Ka-bands using near-nadir incidence GPM radar data, *IEEE Geoscience And Remote Sensing Letters*, 13(9), 1310–1314, doi: 10.1109/LGRS.2016.2583198.
- Nouguier, F., B. Chapron, F. Collard, Mouche, A. A., Rasclé, N., Arduin, F., & Wu, X. (2018). Sea Surface Kinematics From Near-Nadir Radar Measurements. *IEEE Transactions on Geoscience and Remote Sensing*, 1–11. doi:10.1109/tgrs.2018.2833200
- Nouguier, F. (2019). Remote Sensing Spatial Simulator (R3S). Tech. Note SKIM-MPRC-TN6-V1.0, ESA, May 2019.
- Novelli, G., C.M. Guigand, C. Cousin, E.H. Ryan, N.J. Laxague, H. Dai, B.K. Haus, and T.M. Özgökmen, (2017), A Biodegradable Surface Drifter for Ocean Sampling on a Massive Scale. *J. Atmos. Oceanic Technol.*, 34, 2509–2532, <https://doi.org/10.1175/JTECH-D-17-0055.1>
- Obligis, E., A. Rahmani, L. Eymard, S. Labroue, and E. Bronner, (2009), September. An improved retrieval algorithm for water vapor retrieval: Application to the Envisat microwave radiometer. *IEEE Transactions Geoscience Remote Sensing* 47(9):3057–3064.
- OceanDataLab, 2019: Description of the new RVL retrieval approach, Technical Note S-1 RVL DIL2, contract 4000123040/18/I-BG, ESA, Noordwijk, The Netherlands
- Ollitrault, M., B. Blanke, C. Changsheng, N. Diansky, M. Drévilion, et al.. Estimating the wreckage location of the Rio-Paris AF447. 2010. Scientific Report from the Drift Group, Bureau d'Enquêtes Accident, Le Bourget, France. <https://hal-enac.archives-ouvertes.fr/hal-01312263>
- Onink, V., Wichmann, D., Delandmeter, P., & Van Sebille, E. (2019). The role of Ekman currents, geostrophy and Stokes drift in the accumulation of floating microplastic. *J. Geophys. Res.*, doi:10.1029/2018jc014547
- OOPC (2017). Surface Currents Specification. Report v. 5.2, www.goosoocean.org/eov
- Orr, J. C., V. J. Fabry, O. Aumont, L. Bopp, S. C. Doney, R. A. Feely, A. Gnanadesikan, N. Gruber, A. Ishida, F. Joos, RKey, K. Lindsay, E. Maier-Reimer, R. Matear, P. Monfray, A. Mouchet, R. G. Najjar, G. Plattner, K. B. Rodgers, C. L. Sabine, J. L. Sarmiento, R. Schlitzer, R. D. Slater, I. J. Totterdell, M-F. Weirig, Y. Yamanaka and A. Yool, (2005) Anthropogenic ocean acidification over the twenty-first century and its impact on calcifying organisms *Nature*, 437, doi:10.1038/nature04095
- Oschlies, A., P. Brandt, L. Stramma, S. Schmidtko, (2018). Drivers and mechanisms of ocean deoxygenation, *Nature Geoscience*, 11(7), 467–473. doi:10.1038/s41561-018-0152-2.
- Overeem, I., Anderson, R. S., Wobus, C. W., Clow, G. D., Urban, F. E., & Matell, N. (2011). Sea ice loss enhances wave action at the Arctic coast. *Geophysical Research Letters*, 38(17).
- Overland, J. E., & Wang, M. (2018). Arctic-midlatitude weather linkages in North America. *Polar Science*, 16, 1–9. doi:10.1016/j.polar.2018.02.001
- Penven, P., I. Halo, S. Pous, L. and Marié (2014), Cyclogeostrophic balance in the Mozambique Channel, *J. Geophys. Res.*, 119, doi:10.1002/2013JC009528.



- Picard, B., M.-L. Frery, E. Obligis, L. Eymard, N. Steunou & N. Picot (2015) SARAL/AltiKa Wet Tropospheric Correction: In-Flight Calibration, Retrieval Strategies and Performances, *Marine Geodesy*, 38:sup1, 277-296, DOI: 10.1080/01490419.2015.1040903
- Pickart, R. S., Schulze, L. M., Moore, G. W. K., Charette, M. A., Arrigo, K. R., van Dijken, G., & Danielson, S. L. (2013). Long-term trends of upwelling and impacts on primary productivity in the Alaskan Beaufort Sea. *Deep Sea Research Part I: Oceanographic Research Papers*, 79, 106–121. doi:10.1016/j.dsr.2013.05.003
- Planck Collaboration, N. Aghanim, M. Ashdown, J. Aumont, C. Baccigalupi, M. Ballardini, A. J. Banday, R. B. Barreiro, N. Bartolo, S. Basak, R. Battye, K. Benabed, J.-P. Bernard, M. Bersanelli, P. Bielewicz, J. J. Bock, A. Bonaldi, L. Bonavera, J. R. Bond, J. Borrill, F. R. Bouchet, F. Boulanger, M. Bucher, C. Burigana, R. C. Butler, E. Calabrese, J.-F. Cardoso, J. Carron, A. Challinor, H. C. Chiang, L. P. L. Colombo, C. Combet, B. Comis, A. Coulais, B. P. Crill, A. Curto, F. Cuttaia, R. J. Davis, P. de Bernardis, A. de Rosa, G. de Zotti, J. Delabrouille, J.-M. Delouis, E. Di Valentino, C. Dickinson, J. M. Diego, O. Doré, M. Douspis, A. Ducout, X. Dupac, G. Efstathiou, F. Elsner, T. A. Enßlin, H. K. Eriksen, E. Falgarone, Y. Fantaye, F. Finelli, F. Forastieri, M. Frailis, A. A. Fraisse, E. Franceschi, A. Frolov, S. Galeotta, S. Galli, K. Ganga, R. T. Génova-Santos, M. Gerbino, T. Ghosh, J. González-Nuevo, K. M. Górski, S. Gratton, A. Gruppuso, J. E. Gudmundsson, F. K. Hansen, G. Helou, S. Henrot-Versillé, D. Herranz, E. Hivon, Z. Huang, S. Ilić, A. H. Jaffe, W. C. Jones, E. Keihänen, R. Keskitalo, T. S. Kisner, L. Knox, N. Krachmalnicoff, M. Kunz, H. Kurki-Suonio, G. Lagache, J.-M. Lamarre, M. Langer, A. Lasenby, M. Lattanzi, C. R. Lawrence, M. Le Jeune, J. P. Leahy, F. Levrier, M. Liguori, P. B. Lilje, M. López-Cañiego, Y.-Z. Ma, J. F. Macías-Pérez, G. Maggio, A. Mangilli, M. Maris, P. G. Martin, E. Martínez-González, S. Matarrese, N. Mauri, J. D. McEwen, P. R. Meinhold, A. Melchiorri, A. Mennella, M. Migliaccio, M.-A. Miville-Deschênes, D. Molinari, A. Moneti, L. Montier, G. Morgante, A. Moss, S. Mottet, P. Naselsky, P. Natoli, C. A. Oxborrow, L. Pagano, D. Paoletti, B. Partridge, G. Patanchon, L. Patrizii, O. Perdereau, L. Perotto, V. Pettorino, F. Piacentini, S. Plaszczynski, L. Polastri, G. Polenta, J.-L. Puget, J. P. Rachen, B. Racine, M. Reinecke, M. Remazeilles, A. Renzi, G. Rocha, M. Rossetti, G. Roudier, J. A. Rubiño-Martín, B. Ruiz-Granados, L. Salvati, M. Sandri, M. Savelainen, D. Scott, G. Sirri, R. Sunyaev, A.-S. Suur-Uski, J. A. Tauber, M. Tenti, L. Toffolatti, M. Tomasi, M. Tristram, T. Trombetti, J. Valiviita, F. Van Tent, L. Vibert, P. Vielva, F. Villa, N. Vittorio, B. D. Wandelt, R. Watson, I. K. Wehus, M. White, A. Zacchei, A. Zonca, (2016), Planck intermediate results - XLVI. Reduction of large-scale systematic effects in HFI polarization maps and estimation of the reionization optical depth, *A&A* 596 A107, DOI: 10.1051/0004-6361/201628890
- Poupard, James, and Benjamin Franklin (1786). A chart of the Gulf Stream. [Philadelphia, Pa.: American Philosophical Society, 1786] Map. <https://www.loc.gov/item/2004627238/>.
- Pollard, R. T., and R. C. Millard (1970), Comparison between observed and simulated wind-generated inertial oscillations, *Deep Sea Research Oceanography*, Abstr.,17, 813–821, doi:10.1016/0011-7471(70)90043-4.
- Pinsky, M. L., A M. Eikeset, D. J. McCauley, J. L. Payne, J. M. Sunday, 2019: Greater vulnerability to warming of marine versus terrestrial ectotherms, *Nature*, 569, 108–111, doi: 10.1038/s41586-019-1132-4.
- Planetary Visions (D. Jacobs, A. Wayne, P. Eales) (2019). ESA SKIM proposal - the movie. To be published by ESA, July 2019.
- Price, J. F., Weller, R. A., and Schudlich, R. R. (1987). Wind-driven ocean currents and Ekman transport, *Science*, 238, 1534–1538.
- Ramanantsoa, J. D., Penven, P., Krug, M., Gula, J., & Rouault, M. (2018). Uncovering a new current: The Southwest Madagascar Coastal Current. *Geophysical Research Letters*, 45, 1930–1938. <https://doi.org/10.1002/2017GL075900>
- Rasche, N. and F. Arduin (2009). Drift and mixing under the ocean surface revisited. stratified conditions and model-data comparisons, *J. Geophys. Res.*, 114, C02016, doi:10.1029/2007JC004466.
- Rasche, N. and F. Arduin (2013). A global wave parameter database for geophysical applications. part 2: model validation with improved source term parameterization, *Ocean Modell.*, 70, 174–188, doi:10.1016/j.ocemod.2012.12.001.
- Ray, C., C. Martin-Puig, M. P. Clarizia, G. Ruffini, S. Dinardo, C. Gommenginger, J. Benveniste, (2014). SAR altimeter backscattered waveform model. *IEEE Transactions on Geoscience and Remote Sensing*, 53(2), 911-919, doi:10.1109/tgrs.2014.2330423.
- Rémy, E., et al. (2019). Evaluation of ocean surface current in the CMEMS global 1/12° system, Mercator Ocean, internal report for CNES.
- Renault, L., J. C. McWilliams, and S. Masson, 2017, Satellite Observations of Imprint of Oceanic Current on Wind Stress by Ocean–atmosphere Coupling, *Scientific reports*, 7, 17 747.



- Renault, L., P. Marchesiello, S. Masson, J. C. McWilliams (2019). Remarkable Control of Western Boundary Currents by Eddy Killing, a Mechanical Air-Sea Coupling Process. *Geophys. Res. Lett.*, in press. Doi:10.1029/2018GL081211
- Rio, M-H and R. Santoleri, (2018). Improved global surface currents from the merging of altimetry and Sea Surface Temperature data. *Remote Sensing of Environment*, Volume 216, Pages 770-785, ISSN 0034-4257, doi:10.1016/j.rse.2018.06.003.
- Rio et al. (2018). The new CNES-CLS18 Mean Dynamic Topography solution, in preparation.
- Rippeth, Tom P., Ben J. Lincoln, Yueng-Djern Lenn, JA Mattias Green, Arild Sundfjord, and Sheldon Bacon (2015). "Tide-mediated warming of Arctic halocline by Atlantic heat fluxes overcrouch topography." *Nature Geoscience* 8, no. 3.
- Roarty H, Cook T, Hazard L, George D, Harlan J, Cosoli S, Wyatt L, Alvarez Fanjul E, Terrill E, Otero M, Largier J, Glenn S, Ebuchi N, Whitehouse B, Bartlett K, Mader J, Rubio A, Corgnati L, Mantovani C, Griffa A, Reyes E, Lorente P, Flores-Vidal X, Saavedra-Matta KJ, Rogowski P, Prukpitikul S, Lee S-H, Lai J-W, Guerin C-A, Sanchez J, Hansen B and Grilli S (2019) The Global High Frequency Radar Network. *Front. Mar. Sci.* 6:164. doi: 10.3389/fmars.2019.00164
- Rodriguez E., D. Perkovic-Martin, C. Baldi., K. Cooper, N. Majurec, M. Neumann, F. Nicaise, G. Farquharson (2014). Ka-band Doppler Scatterometer for Measurements of Ocean Surface Vector Winds and Currents, *Earth Science Technology Forum*, 2014. https://esto.nasa.gov/forum/estf2014/presentations/B5P4_Rodriguez.pdf
- Rodriguez, E., (2018). On the Optimal Design of Doppler Scatterometers. *Remote Sensing*, 10(11), 1765. doi:10.3390/rs10111765
- Rodríguez, E., A. Wineteer, D. Perkovic-Martin, T. Gál, B. Stiles, N. Niamsuwan, R. Monje, (2018). Estimating Ocean Vector Winds and Currents Using a Ka-Band Pencil-Beam Doppler Scatterometer. *Remote Sensing*, 10(4), 576. doi:10.3390/rs10040576
- Romeiser, R., H. Runge, S. Suchandt, R. Kahle, C. Rossi, and P. Bell (2014). Quality assessment of surface current fields from TerraSAR-X and TanDEM-X along-track interferometry and doppler centroid analysis," *IEEE Trans. on Geosci. and Remote Sensing*, 52, 5, 2759–2772. doi:10.1109/TGRS.2013.2265659.
- Rostan, T., D. Ulrich, S. Riegger and A. Østergaard, (2016), MetoP-SG SCA wind scatterometer design and performance, *IEEE International Geoscience and Remote Sensing Symposium (IGARSS)*, Beijing, 2016, pp. 7366-7369. doi: 10.1109/IGARSS.2016.7730921
- Rouault, M., S. A. White, C. J. C. Reason, J. R. E. Lutjeharms, I. Jobard, (2002). Ocean–Atmosphere Interaction in the Agulhas Current Region and a South African Extreme Weather Event, *Weather and Forecasting*, 9, 306–312, doi: 10.1175/1520-0434(2002)017<0655:OAIITA>2.0.CO;2
- Rouault, M. J., A. Mouche, F. Collard, J. A. Johannessen, and B. Chapron (2010). Mapping the Agulhas Current from space: An assessment of ASAR surface current velocities, *J. Geophys. Res.*, 115, C10026, doi:10.1029/2009JC006050.
- Roughan, M., E. J. Terrill, J. L. Largier, M. P. Otero, (2005). Observations of divergence and upwelling around Point Loma, California. *J. Geophys. Res.*, 110(C4). doi:10.1029/2004jc002662
- Rubio, A., Mader, J., Corgnati, L., Mantovani, C., Griffa, A., Novellino, A., ... Puillat, I. (2017). HF Radar Activity in European Coastal Seas: Next Steps toward a Pan-European HF Radar Network. *Frontiers in Marine Science*, 4. doi:10.3389/fmars.2017.00008
- Sadowy, G. AA., A. C. Berkun, W. Chun, E. Im, and S. L. Durden (2003). Development of an advanced airborne precipitation radar, *Microw. J.*, vol. 46, no. 1, pp. 84–98.
- Santoso, A., Hendon, H., Watkins, A., Power, S., Dommenget, D., England, M., ... Delage, F., (2018). Dynamics and predictability of the El Niño–Southern Oscillation: An Australian perspective on progress and challenges. *Bull. Amer. Met. Soc.*, 100, 403–420, doi:10.1175/bams-d-18-0057.1
- Saynisch, J., Irrgang, C., and Thomas, M., (2018). Estimating ocean model uncertainties for electromagnetic inversion studies, *Ann. Geophys.*, 36, 1009-1014, <https://doi.org/10.5194/angeo-36-1009-2018>, 2018.
- Schiller et al. (2015). Synthesis of new scientific challenges for GODAE OceanView, *Journal of Operational Oceanography*, 8, s259–s271, 2015.
- Schlundt, M., P. Brandt, M. Dengler, R. Hummels, T. Fischer, K. Bumke, G. Krahnmann, and J. Karstensen (2014). Mixed layer heat and salinity budgets during the onset of the 2011 Atlantic cold tongue, *J. Geophys. Res.*, 119, 7882-7910, doi:10.1002/2014JC010021.



- Scott, R. B., Arbic, B. K., Chassignet, E. P., Coward, A. C., Maltrud, M., Merryfield, W. J., ... Varghese, A. (2010). Total kinetic energy in four global eddy ocean circulation models and over 5000 current meter records. *Ocean Modelling*, 32(3-4), 157–169. doi:10.1016/j.ocemod.2010.01.005
- Schulz, E. W., S. A. Josey, R. Verein, (2012). First ocean–atmosphere flux mooring measurements in the Southern Ocean. *Geophysical Research Letters*, 39. doi:10.1029/2012gl052290
- Screen, J. A., (2017). Far-flung effects of Arctic warming. *Nature Geoscience*, 10(4), 253–254. doi:10.1038/ngeo2924
- Scutt Phillips J, L Escalle, G Pilling, A Sen Gupta, E van Sebille (2019). Regional connectivity and spatial densities of drifting fish aggregating devices, simulated from fishing events in the Western and Central Pacific Ocean. *Environmental Research Communications*, in press.
- Sheen, K. L., Smith, D. M., Dunstone, N. J., Eade, R., Rowell, P., Vellinga, M., (2017). Skilful prediction of Sahel summer rainfall on inter-annual and multi-year timescales, *Nature communications*, 8(14966), doi: 10.1038/ncomms14966
- Shutler, J. D., Holding, T., Ubelmann, C., Gaultier, L., Collard, F., Arduin, F., Chapron, B., Rio, H.-H., Donlon C., (2019). Submitted to *Environmental Research Letters*. pre-print available at <http://arxiv.org/abs/1905.08687>
- SKIM Team (2019a). Science applications of the SKIM mission, Technical Report SKIM-MPRC TN-1, ESA, Noordwijk, The Netherlands, doi: 10.13140/RG.2.2.28532.60802/1 for version 0.5. See 10.13140/RG.2.2.28532.60802/2 etc. for later versions.
- SKIM Team, (2019b), Sea surface Kinematics Multiscale monitoring Nadir beam processing Algorithm Theoretical Basis Document, Tech. Note SKIM-TN8, May 2019, ESA.
- Smale, D.A., et al., (2019). Marine heatwaves threaten global biodiversity and the provision of ecosystem services, *Nature Climate Change*, 9, 306–312, doi: 10.1038/s41558-019-0412-1. 10.13140/RG.2.2.28532.60802/1
- Smith, N, et al. (2019). Tropical Pacific Observing System, OO'19 CWP, *Front. Mar. Sci.* 6:31.doi:10.3389/fmars.2019.00031.
- Stanev, E. V., F. Ziemer, J. Schulz-Stellenfleth, J. Seemann, J. Staneva, K.-W. Gurgel (2015). Blending Surface Currents from HF Radar Observations and Numerical Modeling: Tidal Hindcasts and Forecasts. *Journal of Atmospheric and Oceanic Technology*, 32(2), 256–281. doi:10.1175/jtech-d-13-00164.1
- Stocker, T.F., et al. (2013). Technical Summary. In: *Climate Change 2013: The Physical Science Basis. Contribution of Working Group I to the Fifth Assessment Report of the Intergovernmental Panel on Climate Change* [Stocker, T.F., D. Qin, G.-K. Plattner, M. Tignor, S.K. Allen, J. Boschung, A. Nauels, Y. Xia, V. Bex and P.M. Midgley (eds.)]. Cambridge University Press, Cambridge, United Kingdom and New York, NY, USA
- Stopa, J. E., Arduin, F. & Girard-Ardhuin, F. (2016a). Wave climate in the Arctic 1992-2014: seasonality and trends. *The Cryosphere*, 10(4), 1605.
- Stopa, J. E., F. Arduin, A. Bababin, and S. Zieger (2016b). Comparison and validation of physical wave parameterizations in spectral wave models, *Ocean Modelling*, 103, 2–17, doi:10.1016/j.ocemod.2015.09.003.
- Stopa, J. E., Sutherland, P., & Arduin, F. (2018). Strong and highly variable push of ocean waves on Southern Ocean sea ice. *Proceedings of the National Academy of Sciences*, 115(23), 5861–5865. doi:10.1073/pnas.1802011115
- Sutherland, G., Marié, L., Reverdin, G., Christensen, K. H., Broström, G., & Ward, B. (2016). Enhanced Turbulence Associated with the Diurnal Jet in the Ocean Surface Boundary Layer. *Journal of Physical Oceanography*, 46(10), 3051–3067. doi:10.1175/jpo-d-15-0172.1
- Tanelli, S. and S. L. Durden (2006). Simultaneous Measurements of Ku- and Ka-Band Sea Surface Cross Sections by an Airborne Radar, *IEEE Geoscience and Remote Sensing Letters*, 3, 359-
- Tarpanelli, A.; Barbetta, S.; Brocca, L.; Moramarco, T. (2013) River Discharge Estimation by Using Altimetry Data and Simplified Flood Routing Modeling. *Remote Sens.*, 5, 4145-4162.
- Thomson, J., S. Ackley, H. H. Shen, and W. E. Rogers (2017), The balance of ice, waves, and winds in the Arctic autumn, *Eos*, 98, doi:10.1029/2017EO066029.
- Tonani, M., M. Balmaseda, L. Bertino, E. Blockley, G. Brassington, F. Davidson, Y. Drillet, P. Hogan, T. Kuragano, T. Lee, Av. Mehra, F. Paranathara, C. A.S. Tanajura and H. Wang, (2015), Status and future of global and regional ocean prediction systems, *Journal of Operational Oceanography*, 8:sup2, s201-s220, DOI: 10.1080/1755876X.2015.1049892

- Torres, H.Klein, P., Menemenlis, Qiu, B., Su, Z., Wang, J., ... Fu, L.-L. (2018). Partitioning ocean motions into balanced motions and internal gravity waves: A modeling study in anticipation of future space missions. *Journal of Geophysical Research: Oceans*. doi:10.1029/2018jc014438
- Tournadre, J., Poisson, J. C., Steunou, N., & Picard, B. (2015). Validation of AltiKa Matching Pursuit Rain Flag. *Marine Geodesy*, 38(sup1), 107–123. doi:10.1080/01490419.2014.1001048
- Tran, N., B. Chapron, and D. Vandemark, (2007), Effect of Long Waves on Ku-Band Ocean Radar Backscatter at Low Incidence Angles Using TRMM and Altimeter Data, *IEEE Geoscience and Remote Sensing Letters*, vol. 4, no. 4.
- Trenberth, K. E., and J. T. Fasullo (2017) Atlantic meridional heat transports computed from balancing Earth's energy locally, *Geophys. Res. Lett.*, 44, 1919–1927, doi:10.1002/2016GL072475.
- Trenberth, K.E. and Hurrell, J.W. (1994) Decadal atmosphere-ocean variations in the Pacific. *Climate Dynamics*, 9(6), 303–319.
- Turley, T. Keizer, P. Williamson, J.-P. Gattuso, P. Ziveri, R. Monroe, K. Boot and M. Huelsenbeck of the Plymouth Marine Laboratory, UK Ocean Acidification Research Programme, European Project on Ocean Acidification, Mediterranean Sea Acidification in a Changing Climate project, Scripps Institution of Oceanography at UC San Diego, OCEANA; 2013 6pp. ISBN: 978-0-9519618-6-5
- Ubelmann, C., Cornuelle, B., and Fu, L.-L. (2016). Dynamic mapping of along-track ocean altimetry: Method and performance from observing system simulation experiments, *J. Atmos. Ocean Technol.*, 33, 1691–1699. doi:10.1175/JTECH-D-15-0163.1.
- United Nations, (2015). Transforming our world: the 2030 Agenda for Sustainable Development, https://www.un.org/ga/search/view_doc.asp?symbol=A/RES/70/1&Lang=E
- United Nations, (2016). The First Global Integrated Marine Assessment, <https://www.un.org/regularprocess/content/first-world-ocean-assessment>
- Vallis, G. K., 2017: Atmospheric and Oceanic Fluid Dynamics, fundamentals and large-scale circulation, second edition, Cambridge University Press, doi: 10.1017/97811075588417
- van Sebille, E., Wilcox, C., Lebreton, L., Maximenko, N., Hardesty, B. D., van Franeker, J. A., Eriksen, M., Siegel, D., Galgani, F., Law, K. L., (2015) A global inventory of small floating plastic debris, *Environmental Research Letters*, 10(12), doi:10.1088/1748-9326/10/12/124006
- van Sebille E, P Delandmeter, J Schofield, BD Hardesty, J Jones, A Donnelly (2019) Basin-scale sources and pathways of microplastic that ends up in the Galapagos Archipelago, *Ocean Science Discussions*, <https://doi.org/10.5194/os-2019-37>, in review
- Vandemark D., B. Chapron, J. Sun, G. H. Crescenti, H. C. Graber (2004). Ocean wave slope observations using radar backscatter and laser altimeters. *J. Phys. Oceanogr.*, 34, 2825–2842, doi: 10.1175/JPO2663.1.
- Verron, J., Sengenès, P., Lambin, J., Noubel, J., Steunou, N., Guillot, A., ... & Murthy, D. R. (2015). The SARAL/AltiKa altimetry satellite mission. *Marine Geodesy*, 38(sup1), 2-21.
- Villas Bôas, A. B., Arduin, F., Ayet, A., Bourassa, M. A., Chapron, B., Brandt, P., Cornuelle, B. D., Farrar, J. T., Fewings, M. R., Fox-Kemper, B., Gille, S. T., Gommenginger, C., Heimbach, P., Hell, M., C., Li, Q., Mazloff, M., Merrifield, S. T., Mouche, A., Rio, M. Rodriguez, E., Shutler, J. D., Subramanian, A. C., Terrill, E. J., Tsamados, M., Ubelmann, C. and van Sebille, E.: Integrated observations and modeling of winds, currents, and waves (2019) requirements and challenges for the next decade, *Frontiers in Marine Science*, In Press.
- Visbeck, M., U. Kronfeld-Goharani, B. Neumann, W. Rickels, J. Schmidt, E. van Doorn, N. Matz-Lück, K. Ott, and M. F. Quaas, (2014), Securing blue wealth: The need for a special sustainable development goal for the ocean and coasts, *Marine Policy*, 48, 184-191, <https://doi.org/10.1016/j.marpol.2014.03.005>.
- Vousdoukas, M. I., Mentaschi, L., Voukouvalas, E., Verlaan, M., Jevrejeva, S., Jackson, L. P., & Feyen, L. (2018). Global probabilistic projections of extreme sea levels show intensification of coastal flood hazard. *Nature Communications*, 9(1). doi:10.1038/s41467-018-04692-w
- Walsh, E. J., Vandemark, D. C., Friehe, C. A., Burns, S. P., Khelif, D., Swift, R. N., & Scott, J. F. (1998). Measuring sea surface mean square slope with a 36-GHz scanning radar altimeter. *Journal of Geophysical Research: Oceans*, 103(C6), 12587–12601. doi:10.1029/97jc02443
- Walsh E. J., M. L. Banner, C. W. Wright, D. C. Vandemark, B. Chapron, J. Jensen, and S. Lee (2008). The southern ocean waves experiment. Part III: Sea surface slope statistics and near-nadir remote sensing. *Journal of Physical Oceanography*, 38(3), 670-685. doi:10.1175/2007JPO3771.1



- Williams, K. D., Copsey, D., Blockley, E. W., Bodas-Salcedo, A., Calvert, D., Comer, R., ... Xavier, P. K. (2017). The Met Office Global Coupled model 3.0 and 3.1 (GC3.0 and GC3.1) configurations. *Journal of Advances in Modeling Earth Systems*, 10, 357–380. <https://doi.org/10.1002/2017MS001115>
- Wood, M., Rignot, E., Fenty, I., Menemenlis, D., Millan, R., Morlighem, M., ... Seroussi, H. (2018). Ocean-Induced Melt Triggers Glacier Retreat in Northwest Greenland. *Geophysical Research Letters*. doi:10.1029/2018gl078024
- WMO (2017a). Guide to the Global Observing System. Technical Report WMO No. 488.
- WMO (2017b). Manual on the WMO Integrated Global Observing System. Technical Report WMO No. 1160.
- Wunsch, C. (1999). Where do ocean eddy heat fluxes matter? *Journal of Geophysical Research: Oceans*, 104(C6), 13235–13249. doi:10.1029/1999jc900062
- Wunsch, C. (2005). The Total Meridional Heat Flux and Its Oceanic and Atmospheric Partition. *Journal of Climate*, 18(21), 4374–4380. doi:10.1175/jcli3539.1
- Yan, Q., J. Zhang, C. Fan, and J. Meng. (2019), Analysis of Ku- and Ka-Band Sea Surface Backscattering Characteristics at Low-Incidence Angles Based on the GPM Dual-Frequency Precipitation Radar Measurements, *Remote Sensing*, 11, <http://www.mdpi.com/2072-4292/11/7/754>
- Yu, X., A. L. Ponte, S. Elipot, D. Menemenlis, E. D. Zaron, R. Abernathey (2019). Surface kinetic energy distributions in the global oceans from a high-resolution numerical model and surface drifter observations, *Geophys. Res. Lett.* (in press).
- Yurovsky, Y. Y., V. N. Kudryavtsev, S. A. Grodsky, and B. Chapron (2017a). Ka-Band Dual Copolarized Empirical Model for the Sea Surface Radar Cross Section, *IEEE Trans. Geosci. Remote Sens.*, 55(3), 1629 - 1647, doi: 10.1109/tgrs.2016.2628640.
- Yurovsky, Y. Y., V. N. Kudryavtsev, S. A. Grodsky, and B. Chapron (2017b). Normalized Radar Backscattering Cross-section and Doppler Shifts of the Sea Surface in Ka-band, proceedings of the Progress In Electromagnetics Research Symposium, PIERS 2017, St Petersburg, Russia, 22 - 25 May, 2017.
- Yurovsky, Y. Y., Kudryavtsev, V. N., Chapron, B., & Grodsky, S. A. (2018). Modulation of Ka-Band Doppler Radar Signals Backscattered From the Sea Surface. *IEEE Transactions on Geoscience and Remote Sensing*, 56(5), 2931–2948. doi:10.1109/tgrs.2017.2787459
- Yurovsky, Y., Kudryavtsev, V., Grodsky, S., & Chapron, B. (2019). Sea Surface Ka-Band Doppler Measurements: Analysis and Model Development. *Remote Sensing*, 11(7), 839. doi:10.3390/rs11070839
- Zrnic, D. S. (1977). Spectral Moment Estimates from Correlated Pulse Pairs, *IEEE Trans. Aero. Electronic Sys.*, 13(4), 344 - 354. doi: 10.1109/TAES.1977.308467

ACRONYMS AND ABBREVIATIONS

ADC	Analogue to Digital Converter
AIT	Assembly, Integration and Test
AIV	Assembly, Integration and Verification
AKE	Absolute Knowledge Error
AOCS	Attitude Orbit Control system
APCE	Antenna Power and Command Electronic
AR	Ambiguity Rank
ASAR	Advanced Synthetic Aperture Radar
ATI	Across-Track Interferometry
BoL	Beginning of Life
CCAL	Cyclo-Calibration
CD	Current Doppler
CDHS	Command and Data Handling Subsystem
CDHS	Core Data Handling Software
CEU	Central Electronics Unit
CFOSat	China-France Oceanography SATellite [of CNES]
CFRP	Carbon Fibre Reinforced Plastic
CMEMS	Copernicus Marine Environment Monitoring Service
CNES	Centre national d'études spatiales
CoM	Centre of Mass
CSS	Coarse Sun Sensor
DAC	Digital to Analog Converter
DAC	Dynamic Atmospheric Corrections
DC	Doppler Centroid
DDC	Data-Driven Calibration
DH	Data Handling
DHS	Data Handling Subsystem
DMS	Dimethyl sulphide
DT	Delayed Time
DUACS	Data Unification and Altimeter Combination System
ECCO	Estimating the Circulation and Climate of the Ocean
ECMWF	European Centre for Medium range Weather Forecasting
EESS	Earth Exploration Satellite Service
EGOS-CC	European Ground Operations System Common Core
EIK	Extended Interaction Klystron
EMS	ESTRACK Management and Scheduling System
EoL	End of Life
EPC	Electronic Power Control



EPS	Electrical Power Subsystem
ESA	European Space Agency
ESA-CCS	ESA Constellation Coordination System
ESOC	European Space Operations Centre
ESRIN	European Space Research Institute
ESTEC	European Space Research and Technology Centre
FAO	Food and Agriculture Organization
FDS	Flight Dynamics System
FOCC	Flight Operations Control Centre
FOG	Fibre-Optic Gyro
FOS	Flight Operations Segment
FoV	Field of View
FPGA	Field Programmable Gate Array
FS	Flight Segment
GCM	Global Circulation Model
GD	Geophysical Doppler
GDOP	Geometrical Dilution of Precision
GNSS	Global Navigation Satellite System
GPS	Global Positioning System
GS	Ground Segment
GTC	Ground Track Control
HDRM	Hold Down and Release Mechanism
HF	High Frequency
HKTM	HouseKeeping TeleMetry
HPA	High-Power Amplifier
HRM	Hold down & Release Mechanisms
IFOV	Instantaneous Field of View
IMU	Inertial Measuring Unit
IPBES	Intergovernmental Science-Policy Platform on Biodiversity and Ecosystem Services
IPCC	International Panel on Climate Change
ITU	International Telecommunication Union
IW	Interferometric Wide swath
LCOE	Levelised Cost Of Energy
LEO	Low Earth Orbit
LEOP	Launch and Early Orbit Phase
LGA	Low Gain Antenna
LIR	Launcher Interface Ring
LOPS	Laboratory for Ocean Physics and remote Sensing
LPC	Living Planet Challenges
LRR	Laser Retroreflector



LSB	Least Significant Bit
LTAN	Local Time of the Ascending Node
LTDN	Local Time of the Descending Node
LUT	Look Up Table
LVA	Launch Vehicle Adapter
MAG	Magnetometer
MAG	Mission Advisory Group
MCS	Mission Control System
MetOp-SG(1B)	MetOp Second Generation satellite 1B
MIT	Massachusetts Institute of Technology
MITgcm	MIT General Circulation Model
MIZ	Marginal Ice Zone
MLI	Multi-Layer Insulation
MMU	Mass Memory Unit
MOC	Meridional Overturning Circulation
MPF	Mission Planning Facility
MPS	Mission Planning System
MRD	Mission Requirements Document
MSLA	Mean Sea Level Anomaly
MTQ	Magnetotorquer
MWI	Microwave Imager on MetOp-SG(1B)
NOP	Numerical Ocean Prediction
NRCS	Normalised Radar Cross Section
NRSZ	Normalised Radar Sigma Zero
OBC	Onboard Computer
OBSW	Onboard Software
OBT	Onboard Time
OZA	Observation Zenith Angle
P/F	Satellite Platform
P/L	Satellite Payload
PAH	Polycyclic aromatic hydrocarbon
PCDU	Power Conditioning and Distribution Unit
PCU	Power Control Unit
PDF	Probability Density Function
PDGS	Payload Data Ground Segment
PDHT	Payload Data Handling and Transmission
PDHU	Payload Data Handling Unit
PDU	Power Distribution Units
PIA	Path-Integrated Attenuation
POD	Precise Orbit Determination



POS4	Poseidon-4
PPS	Pulse-per-second
PRF	Pulse Repetition Frequency
PRI	Pulse Repetition Interval
PSD	Power Spectral Density
PUS	Packet Utilisation Service
PVT	Position, Velocity, Time
RAR	Real Aperture Radar
RF	Radio Frequency
RFA	Rotary Feed Assembly
RIU	Remote Interface Unit
RMA	Rotary Mechanism Assembly
RMS	Root Mean Square
RR	ITU Radio-Regulations
RSS	Root Square Sum
RTU	Remote Terminal Unit
RW	Reaction Wheel
S/C	Spacecraft
SA	Solar Array
SADM	Solar Array Drive Mechanism
SAR	Synthetic Aperture Radar
SCA	Scatterometer on MetOp-SG(1B)
SCOS	Spacecraft Operating System
SDGs	Sustainable Development Goals
SKaR	SKIM KA-band Radar
SKIM	Sea surface KInematics Multiscale monitoring
SLR	Satellite Laser Ranging
SMA	Semi-Major Axis
SRA	Scientific Readiness Assessment
SRL	Scientific Readiness Level
SSH	Sea Surface Height
SSHA	Sea Surface Height Anomaly
SSO	Sun Synchronous Orbit
SST	Sea Surface Temperature
STD	Standard Deviation
STR	Star Tracker
SWIM	Surface Wave Investigation and Monitoring (radar instrument)
SWOT	Surface Water Ocean Topography [of CNES and NASA]
TC	Telecommand
TCS	Thermal Control Subsystem



TED	Thermo-Elastic Distortions
TM	Telemetry
TRL	Technology Readiness Level
TRSP	Transponder
TSCV	Total Surface Current Velocity
TT&C	Telemetry, Tracking and Command
TWT	Travelling Wave Tube
UGD	Geophysical Doppler Velocity
UN	United Nations
VOC	Volatile organic compound
WCRP	World Climate Research Program
WD	Wave Doppler
WW3	WAVE WATER level and Current Hindcasting (WAVEWATCH III®)
WZL	Wizard Link
XBA	X-Band Antenna